

TABLE OF CONTENTS, Vol. 38, No. 1

**SYMPOSIUM ON IRON-BASED CATALYSTS FOR COAL LIQUEFACTION**

**Small Particle Catalysts**

(I. Wender, M. Farcasiu and G. P. Huffman, Organizers,  
G. P. Huffman, Presiding; Monday Morning)

THE DEVELOPMENT OF A NEW IRON CATALYST FOR THE DIRECT LIQUEFACTION  
OF COAL. R. Bacaud, M. Besson and G. Djega-Mariadassou . . . . 1

SULFATED AND MOLYBDATED IRON (III) OXIDE CATALYSTS IN COAL  
LIQUEFACTION. V. R. Pradhan, J. Hu, J. W. Tierney and I.  
Wender, . . . . . 8

PREPARATION OF ULTRAFINE CATALYST POWDERS USING A FLOW-THROUGH  
HYDROTHERMAL PROCESS. D. W. Matson, J. C. Linehan and J. G.  
Darab . . . . . 14

SYNTHESIS AND CHARACTERIZATION OF Fe AND Fe<sub>2</sub>S (PYRITE) CATALYST  
PARTICLES IN INVERSE MICELLES. A. Martino, J. P. Wilcoxon, A. P.  
Sylwester and J. S. Kawola . . . . . 20

REVERSE MICELLE SYNTHESIS OF NANOSCALE METAL CONTAINING CATALYSTS.  
J. G. Darab, J. L. Fulton, and J. C. Linehan . . . . . 27

INFLUENCE OF NANOSCALE Fe<sub>(1-x)</sub>S PARTICLES ON COAL LIQUEFACTION. G.  
T. Hager, X. X. Bi, P. C. Eklund and F. J. Derbyshire . . . . 34

COAL-LIQUEFACTION CATALYSTS FROM FERRIC SULFIDE  
DISPROPORTIONATION. D. B. Dadyburjor, W. R. Stewart, A. H.  
Stiller, C. D. Stinespring, J. -P. Wann and J. W. Zondlo . . . 39

**Mechanisms**

(Continued, I. Wender, Presiding; Monday Afternoon)

THE EFFECTS OF IRON CARBONYL-BASED CATALYST PRECURSORS ON THE  
REACTION OF 4-(NAPHTHYLMETHYL)BIBENZYL. T. Walter, S. Casey, M.  
Klein and H. Foley . . . . . 46

COMPLEX IRON CATALYTIC SYSTEMS: RELATIVE CATALYTIC ACTIVITY OF  
VARIOUS COMPONENTS. M. Farcasiu, P. A. Eldredge and S. C.  
Petrosius . . . . . 53

MOLECULAR ORBITAL CALCULATIONS FOR IRON CATALYSTS. H. F. Ades, A.  
L. Companion and K. R. Subbaswamy . . . . . 60

RESULTS OF CATALYST TESTING USING IRON-BASED CATALYSTS. J.  
Linehan, J. G. Darab and D. W. Matson . . . . . 66

TABLE OF CONTENTS, Vol. 38, No. 1

EFFECT OF A SULFIDED, NON-POROUS AEROSOL  $Fe_2O_3$  CATALYST ON THE CHEMICAL STRUCTURE OF COAL LIQUIDS FROM THE HYDROLIQUEFACTION OF A HIGHLY VOLATILE BITUMINOUS COAL. V. L. Cebolla, M. Diak, M. Oberson, R. Bacaud, D. Cagniant and B. Nickel-Pépin-Donat . . . 72

DYNAMIC STUDIES OF THE INTERACTION OF IRON SULFIDES WITH HYDROGEN. N. M. Rodriguez and R. T. K. Baker . . . . . 80

ACTIVITY AND SELECTIVITY OF DISPERSED IRON CATALYST IN COAL LIQUEFACTION AND MODEL COMPOUND REACTIONS. J. A. Guin, X. Zhan and R. Singh . . . . . 86

**Technology**

(Continued, I Wender, M. Farcasiu, G. P. Huffman, Organizers, M. Farcasiu, Presiding; Tuesday Afternoon)

DESIGN OF COAL LIQUEFACTION CATALYSTS WITH FUNCTIONS FOR RECOVERY AND REPEATED USE. I. Mochida, K. Sakanishi M. Kishino, K. Honda, T. Umezawa and S. Yoon . . . . . 93

THE EFFECT OF CATALYST DISPERSION ON COAL LIQUEFACTION WITH IRON CATALYSTS. A. V. Cugini, D. Krastman, D. V. Martello and G. D. Holder . . . . . 99

A STUDY OF DISPERSED IRON-BASED ADDITIVES IN COAL LIQUEFACTION. L. K. Lee, A. G. Comolli, E. S. Johanson and R. H. Stalzer . . 107

HYDROGENOLYTIC ACTIVITY OF SOLUBLE AND SOLID Fe-BASED CATALYSTS AS RELATED TO COAL LIQUEFACTION EFFICIENCY. W. Zmierczak, X. Xiao, J. C. H. Tsai and J. Shabtai . . . . . 117

Fe CATALYZED HYDROLYSIS. A. M. Mastral, C. Mayoral, M. T. Iaquierdo and C. Pardos . . . . . 124

IRON BASED CATALYSTS FOR COAL/WASTE OIL PROCESSING. H. G. Sanjay, A. R. Tarrer and C. Marks . . . . . 131

**Catalysts Added by Chemical Impregnation**

(Continued, G. P. Huffman, Presiding; Wednesday Morning)

DEVELOPMENT OF HIGHLY DISPERSED COAL LIQUEFACTION CATALYSTS. T. Suzuki . . . . . 137

CATALYTIC HYDROLIQUEFACTION OF COAL USING MOLYBDENUM AND IRON-PROMOTED CATALYSTS. L. L. Anderson and W. H. Yuen . . . . . 142

## THE DEVELOPMENT OF A NEW IRON CATALYST FOR THE DIRECT LIQUEFACTION OF COAL

Robert BACAUD\*, Michelle BESSON\* and Gérald DJEGA-MARIADASSOU†

\* C.N.R.S., Institut de Recherches sur la Catalyse  
2, Av. Albert Einstein, 69626 Villeurbanne cedex, France

† Laboratoire de Réactivité de Surface et Structure  
Université P & M Curie, 75232 Paris cedex 05, France

**Keywords:** ultra-fine iron catalysts, iron oxide sulfidation, coal liquefaction.

### INTRODUCTION

The present paper is a synthesis of the research conducted in a program for the development of iron based catalysts, as a part of a project supported by French government and E. C. between 1980 and 1990. The objective was to provide an evaluation of the feasibility of producing substitute natural gas and liquid transportation fuels, through liquefaction of coal. The development of liquefaction catalysts was performed at laboratory scale in our Institute and the testing of dispersed iron based catalysts was conducted in a 50 kg/d facility at CERCHAR (Charbonnages de France).

The eventual influence of a catalyst upon coal dissolution is a-priori questionable. However, considerable experimental evidence has been accumulated that demonstrates the ability of hydrogenation catalysts to increase the production of soluble compounds from coal at relatively low temperature. This conversion coincides with some hydrogenation which is also enhanced by catalysts. Although low temperature liquefaction cannot generate radical species through homolytic bond cleavage, some coal macerals - especially inertinite - contain significant concentration of free fossil radicals. The initial dissolution process makes these species accessible for further reaction and condensation. The role of catalysts in these conditions is to provide a source of active hydrogen in order to cap these radical species and to avoid retrogressive reactions.

At higher temperature, the rate of radical production increases, as well as the rate of the concomitant reactions of homolytic rupture and condensation, respectively responsible for the formation of gases and insoluble products. A fast stabilization of radical species through hydrogenation contributes to an improvement of selectivity for the production of distillate by reducing the formation of gases and solid residues. A hydrogenation catalyst will prove useful for process control at increased severity but it must demonstrate its usefulness, since it operates in a highly competitive medium where several species can assume some role in hydrogen transfer mechanisms; the more serious competitor for any additional catalyst is the pyrite contained in coals, activity of which is undeniable.

The choice of a catalyst destined to be used in the form of a flowing disposable solid is dictated by the difficulty, even the impossibility, to recover a catalytic substance mixed with unconverted coal and mineral matter. This choice implies a set of requirements must be fulfilled by the catalytic material:

- As an unrecovered reactant, its cost must be low. This primary consideration has considerably limited the range of investigated candidates.

- The solid catalyst is flowing along with the reactants. It is therefore necessary to reduce the amount of displaced substance, both for avoiding the

transport of useless material and for limiting the problems associated with sedimentation and abrasion of reactor and equipments.

- A low catalyst-to-coal ratio imposed by process optimization means the active phase must exhibit a high intrinsic activity.

We decided to develop a synthetic method for the production of a catalyst, considered as the only way of ensuring a proper control of the properties, choosing iron as the cheapest raw material. Among transition metals sulfides, iron is not extremely active (1); its low intrinsic activity must be compensated by a high dispersion. The next step of our program consisted in an investigation of the methods of preparation of highly dispersed iron oxides, considered as precursors for the in-situ generation of iron sulfide during coal liquefaction.

#### PRODUCING THE CATALYST PRECURSOR

The methods of preparation of heterogeneous catalysts attempt to increase the surface area of the solids. The easiest way consists in producing a porous substance or in supporting the active phase on a porous support. Our first approach consisted in comparing the properties of catalysts obtained by means of deposition of iron compounds on various high surface area supports.

Table I. Characteristics and liquefaction behavior of supported iron oxides

Support	BET S.m <sup>2</sup> .g <sup>-1</sup>	Pore radius nm	H increment $\alpha^{(a)}$
Carbon black	115	Non porous	0
SiO <sub>2</sub>	100	15	0
Al <sub>2</sub> O <sub>3</sub>	100	20	0
SiO <sub>2</sub> -Al <sub>2</sub> O <sub>3</sub>	600	3	8

(a): relative increment of hydrogen incorporation in coal products as compared to a non catalytic experiment.

Table I clearly illustrates the fact that an active phase, well dispersed on the porous structure of a high surface support, is completely inactive for hydrogen transfer reactions. From these results, it was evident that our attempts should be oriented towards the preparation of high external surface area iron solids. We prepared pure iron oxides by precipitation from a nitrate solution with ammonia and we tried to increase the surface by introducing small amounts of various textural promoters, coprecipitated along with iron hydroxide. Only alumina provided some positive effect upon the surface area and liquefaction activity of these solids. A change in the drying process produced a major impact than the introduction of textural promoter as illustrated by table II.

It appeared that hydrogen transfer activity in coal liquefaction is not directly correlated with surface area of the active phase but with the changes in morphology of the particles induced by spray drying.

Ours investigations turned towards the methods of preparation of highly dispersed, non porous solids. A rather simple method consisting in the hydrolysis of volatile compounds in a hydrogen-oxygen flame, currently used for commercial scale production of aerosol oxides of aluminium, silicon and titanium, had been recently adapted to the elaboration of iron oxide (2). Spherical particles are obtained with narrow particle size distribution. The mean particle size can be as small as 10 nm and can be varied through control

of the respective flows of metallic compound vapors and of the gases in the torch. The properties and liquefaction behavior of these catalysts are presented in Table II.

**Table II. Characteristics and liquefaction behavior.**  
Unsupported iron oxides

Catalysts	Drying	BET S. $\text{m}^2 \cdot \text{g}^{-1}$	H increment % <sup>(a)</sup>
<b>Precipitated oxides</b>			
Fe <sub>2</sub> O <sub>3</sub>	Oven	150	10
Fe <sub>2</sub> O <sub>3</sub>	Spray	160	15
Fe <sub>2</sub> O <sub>3</sub> -Al <sub>2</sub> O <sub>3</sub> 10%	Oven	270	4
Fe <sub>2</sub> O <sub>3</sub> -Al <sub>2</sub> O <sub>3</sub> 10%	Spray	200	18
<b>Aerosol iron oxides</b>			
Lab. scale 1		40	18
Lab. scale 2		32	18
Pilot		24	12

(a): Relative increment of hydrogen incorporation in coal products as compared to a non catalytic experiment.

#### SULFIDATION OF IRON OXIDE

The oxides obtained in a convenient divided state are the precursors of the actual catalytic phase, which results from the interaction of iron oxide with the reacting medium during liquefaction. Owing to the sulfur content of the majority of coals, the partial pressure of hydrogen sulfide can be expected to range around 0.5-2 % in the gas phase during liquefaction. During the early stage of liquefaction, before hydrodesulfurization of coal takes place, the catalyst precursor will be in contact with a highly reducing medium with low initial concentration of hydrogen sulfide; the release of sulfur from coal progressively modifies the composition of the gas phase.

Preliminary experiments revealed that iron oxide is easily transformed into a pyrrhotite Fe<sub>0.91</sub>S at moderate temperature under hydrogen sulfide partial pressure ranging from 0.2 to 1% in hydrogen (3). Although sulfidation produces a severe decrease of surface area, the resulting phase is active in the reaction of tetralin dehydrogenation in the presence of hydrogen sulfide (Table III).

**Table III. Characterization and catalytic activity of iron sulfides generated by gas phase sulfidation of an unsupported iron oxide (BET S. = 24  $\text{m}^2 \cdot \text{g}^{-1}$ )**

Treatment	Phases	BET S. $\text{m}^2 \cdot \text{g}^{-1}$	Activity $\text{mol} \cdot \text{g}^{-1} \cdot \text{s}^{-1}$ (a)
1 - H <sub>2</sub> S	Fe <sub>0.91</sub> S	3	4.10 <sup>-8</sup>
2 - H <sub>2</sub>	Fe <sub>0.995</sub> S	3	0.3.10 <sup>-8</sup>
1 - H <sub>2</sub>	Fe	2	10.10 <sup>-8</sup>
2 - H <sub>2</sub> S	Fe <sub>0.995</sub> S	0.1	0.1.10 <sup>-8</sup>

(a) Catalytic activity in dehydrogenation of tetralin at 600 K, 0.1 MPa H<sub>2</sub>

A reduction of this sulfide under hydrogen generates a considerably less active phase, identified as Fe<sub>0.995</sub>S. A preliminary reduction of iron oxide under hydrogen produces a very active metallic phase. Partial sulfidation of metallic iron completely inhibits its activity. The production of Fe<sub>0.995</sub>S by

sulfidation of metallic iron by hydrogen sulfide is very progressive and gives rise to a drastic sintering (4).

This study was completed by an examination of the influence of the protocol of sulfidation and introduction of the catalyst in the reacting medium during coal liquefaction, in the presence of a hydrogen-donor solvent (tetralin). We compared the ability of catalysts to rehydrogenate the solvent, after different sulfidation protocols described below.

- In-situ sulfidation: the catalyst precursor is introduced into the reactor along with the reactants and sulfur, then heated up to the reaction temperature.

- Pre-sulfidation: either in the gas phase, by a mixture containing 1 % hydrogen sulfide in hydrogen, or in suspension in tetralin under 1 % H<sub>2</sub>S in H<sub>2</sub> at 15 MPa total pressure.

- Flash-sulfidation: the precursor is introduced under pressure (15 MPa) in the autoclave containing the reacting medium (coal, solvent, H<sub>2</sub>S and H<sub>2</sub>) at reaction temperature.

As evidenced in table IV, only catalysts pre-sulfided in gaseous H<sub>2</sub>S or in-situ sulfided are active for solvent hydrogenation. The drastic reduction of activity caused by a pre-sulfidation in tetralin suggests that coal itself must interfere with the process of generation of the active phase from iron oxide.

Table IV. Influence of sulfidation protocol upon solvent hydrogenation during coal liquefaction (tetralin 673 K, 1% H<sub>2</sub>S)

Protocol	% Solvent dehydrogenated
In-situ	2
Gas phase pre-sulfidation	3
Liquid phase pre-sulfidation	13
Flash sulfidation	13
No catalyst	13

A systematic electron microscope examination, associated with X-ray emission micro-analysis, revealed an agglomeration of sulfide particles when the precursor was sulfided in the absence of coal; the surface of the grains was covered with an opaque, thick layer of coke probably resulting from cracking of tetraline (5). On the contrary, samples originating from in-situ sulfidation, in the presence of coal, showed that the sulfided particles preserved the particle shape of the precursor. A smooth carbonaceous deposit was evidenced at the surface of the particles. This layer, as opposed to the dense coke formed in tetralin, preserved the hydrogenation activity (6). It may result from adsorption of dissolved coal products which prevent particles agglomeration.

#### EVALUATION OF CATALYSTS IN COAL LIQUEFACTION

Using a disposable catalyst prescribes low catalyst-to-coal ratio. An evaluation of catalysts for coal liquefaction must include determining the minimum loading required for a given level of conversion. In this part of our project, we chose conditions of high severity liquefaction, i.e. high temperature and a non-donor solvent. Coke buildup occurs in these conditions for non catalytic experiments. As a tool for catalysts evaluation, we determined the minimum amount of catalyst required for unperturbed reactor operation during 1 hour runs. This arbitrary criterion, designed as "critical catalyst loading", does not attempt to define an absolute value but is

indicative of the relative performances of distinct catalysts. Some of the catalysts included in table V are representative of the improvements we obtained in the synthesis of iron oxide. The effect of increasing external surface area is evidenced, as well as the doping effect produced by incorporation of minor amount of molybdenum.

Table V. Critical catalyst loading

Catalyst	Weight % vs coal
Red mud	2.2
Fe <sub>2</sub> O <sub>3</sub> , 18 m <sup>2</sup> .g <sup>-1</sup>	0.7
Fe <sub>2</sub> O <sub>3</sub> , 71 m <sup>2</sup> .g <sup>-1</sup>	0.4
Fe <sub>2</sub> O <sub>3</sub> , 2.8 % MoO <sub>3</sub>	0.2
Fe <sub>2</sub> O <sub>3</sub> , 18 % MoO <sub>3</sub>	0.2

The influence of catalyst loading on oil yield is presented in Fig. 1 for some representative catalysts. The change in oil production is not proportional to the catalyst content and a twofold increase of catalyst percentage only causes oil yield to vary from about 40% to 50%.

The relation between the amount of hydrogen incorporated into the final liquid coal products and the percentage of catalyst is described in Fig. 2. It must be specified that the values correspond to a net H<sub>2</sub> incorporation and that the contribution of hydrogen to the formation of light gases from the organic matter of coal has been subtracted; increasing the amount of red mud for example, enhances hydrogen consumption, but this additional H<sub>2</sub> is mainly utilized for the production of gases. On the contrary, the net hydrogen incorporation augments with increasing the amount of iron oxide based catalysts, and it reaches higher levels than with Ni-Mo. As indicated above, oil production varies little with the nature and with the percentage of catalyst. Consequently, the hydrogen content of the oils produced in distinct catalytic conditions - and therefore oil quality - must vary accordingly. This is reflected by the percentage of H<sub>2</sub> incorporated into oils or into (oils + asphaltenes) reported in table VI.

Table VI. Weight % H<sub>2</sub> incorporated into oils or asphaltenes

Catalyst (1.5% vs. coal)	H <sub>oil</sub>	H <sub>oil+asphalt</sub>
Fe <sub>2</sub> O <sub>3</sub> , 71 m <sup>2</sup> .g <sup>-1</sup>	4.44	3.49
Fe <sub>2</sub> O <sub>3</sub> , 2.8%MoO <sub>3</sub>	4.38	4.05
Ni-Mo/Al <sub>2</sub> O <sub>3</sub>	3.48	2.60
Red mud	3.0	2.15

From a linear regression of the rate of hydrogen consumption versus the pressure decrease, an initial rate of H<sub>2</sub> incorporation could be deduced. The results are presented in Fig. 3. This apparent initial rate reflects the activity of the fresh catalyst. Initial activity for Ni-Mo is superior to that of pure iron oxide, although the products obtained with the former are less hydrogenated; the same is observed concerning the hydrogenation of the solvent (Fig. 4): iron based catalysts exhibit a higher activity than Ni-Mo. Although supported Ni-Mo is intrinsically a better catalyst than iron sulfide (as evidenced by its higher initial activity), its exposed active surface declines rapidly, due to the plugging of the porous structure by carbonaceous deposits. On the contrary, the surface of unsupported iron sulfides is

affected to a less extent by this phenomena, and consequently their activity can maintain at a convenient level.

## CONCLUSION

As part of a program for the production of fluid fuels through coal liquefaction, we investigated the pertinent basis for the elaboration of catalytic materials. Considering the requirements imposed by the specific conditions of use of disposable catalysts in coal liquefaction, we decided to prepare synthetic iron based solids. The prominent results of this program are summarized below:

- Catalytic activity relies upon the external surface area. Porous solids that exhibit a high surface are inactive, as compared to non porous ones.
- Nanometer-sized iron oxides (aerosol) can be produced through vapor phase hydrolysis of volatile compounds in a hydrogen-oxygen flame. They exhibit uniform spherical shape particles whose diameter can be as low as 10 nm.
- Sulfidation of these precursors generates a pyrrhotite at moderate temperature. A previous reduction of iron oxide to the metallic state must be avoided, since further sulfidation is considerably more difficult.
- Coal provides a support effect during sulfidation and prevents, up to some extent, the agglomeration of catalyst particles.
- The performances of aerosol iron oxides in coal liquefaction largely exceed those of red mud and compare favourably with commercial supported Ni-Mo catalysts. They can be improved by incorporation of minor amounts of molybdenum.
- Critical catalyst loading, indicative of the minimum catalyst-to-coal ratio compatible with reactor operability, suggests that the proposed catalysts can be used at concentration levels as low as 0.2% vs coal.

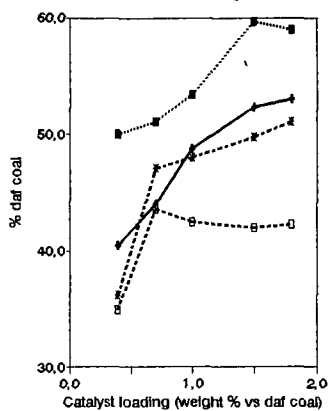
## ACKNOWLEDGMENTS

H. Charcosset, presently retired, initiated and gave the impulse to this program. His role, as a group leader of the French laboratories included in this project, has been decisive. We wish, by means of this paper, to express our gratitude for his essential contribution.

## REFERENCES

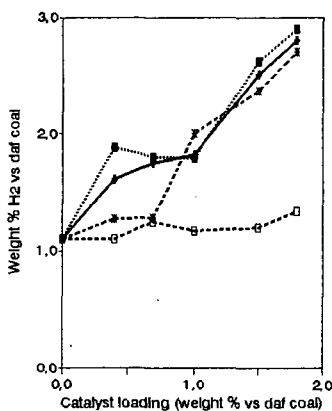
- (1) Lacroix, M.; Boutarfa, N.; Guillard, C.; Vrinat, M.; Breysse, M., J. Catal. 1989, 120, 473-477.
- (2) Vergnon, P.; Batis Landousli, H., Ind. Eng. Chem.- Prod. Res. Dev. 1980, 19, 147-151.
- (3) Andrès, M.; Charcosset, H.; Davignon, L.; Djega-Mariadassou, G.; Joly, J.P., Bull. Soc. Chim. France 1982, 11, 427-432.
- (4) Zimmer, H.; Andrès, M.; Charcosset, H.; Djega-Mariadassou, G. Applied Catal. 1983, 7, 295-306.
- (5) Djega-Mariadassou, G.; Besson, M.; Brodzki, D.; Charcosset, H.; Tran Huu Vinh, Fuel Process. Technol. 1986, 12, 143-153.
- (6) Bacaud, R.; Besson, M.; Brodzki, D.; Bussière, P.; Charcosset, H.; Djega-Mariadassou G.; Oberson, M. in: B. Delmon and G.F. Froment (Editors) "Catalysts Deactivation", Elsevier, Amsterdam, 1989, p.289.

**Fig. 1: Oil yield as a function of catalyst loading**



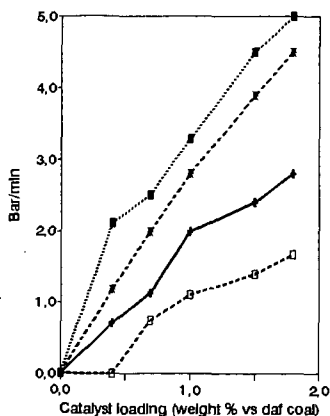
---■--- Fe-Mo    —▲— Fe    -\*- Ni-Mo    -○- Redmud

**Fig. 2: hydrogen incorporation in coal liquids**



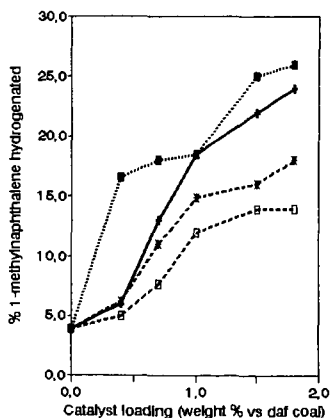
---■--- Fe-Mo    —▲— Fe    -\*- Ni-Mo    -○- Redmud

**Fig. 3: Initial rate of H<sub>2</sub> uptake Liquefaction 723K, non donor solvent**



---■--- Fe-Mo    —▲— Fe    -\*- Ni-Mo    -○- Redmud

**Fig. 4: Solvent hydrogenation Liquefaction 723K, 1 hr residence time**



---■--- Fe-Mo    —▲— Fe    -\*- Ni-Mo    -○- Redmud

## SULFATED AND MOLYBDATED IRON (III) OXIDE CATALYSTS IN COAL LIQUEFACTION

V.R. Pradhan, J. Hu, J.W. Tierney and I. Wender

Chemical and Petroleum Engineering Department  
University of Pittsburgh, Pittsburgh PA 15261

Keywords: Sulfated Iron Oxides, Low-Pyrite Coals, Pyrrhotites

### INTRODUCTION

Iron, because of its low cost, activity, and environmental acceptability, has been perceived as a potential catalyst for the first stage of coal liquefaction, namely coal dissolution. A chief objective of various methods of adding iron catalysts is to provide high catalytic surface area and fine particulate size. The initial dispersion of the precursor has a strong influence on the activity of the sulfided phases formed under liquefaction conditions. Means must also be sought to prevent agglomeration of catalyst particles so as to maintain their state of high dispersion. In the presence of enough sulfur, iron catalysts form pyrrhotites ( $Fe_{1-x}S$ ) which, along with hydrogen sulfide, function as catalysts for the hydrogenation and hydrogenolysis reactions which occur during the hydroliquefaction of coal<sup>1,2,3</sup>. Application of finely divided and chemically modified powdered solid iron oxide based catalysts used in this work shows considerable promise<sup>4</sup>. These catalysts have initial sizes in the nanophase region (1-100 nm); their ultrasmall size allows them to have dramatically different properties.

The objective of this research has been to use low-sulfur, low-pyrite coals to verify the catalytic effects of small amounts of iron added to the liquefaction reactor as sulfate and molybdate anion-promoted oxides or oxyhydroxides. We have reported on the use of sulfate-promoted iron and tin oxides for the direct liquefaction and coprocessing of Argonne Illinois No. 6 coal with tetralin and with Maya ATB heavy oil, respectively<sup>4</sup>.

The following topics will be discussed: (i) activity of small amounts of iron and molybdenum added as sulfated oxides for direct liquefaction of low pyrite coals (hvbc Blind Canyon, 0.01 wt% pyrite, and subbituminous Wyodak with 0.17 wt% pyrite), (ii) synthesis and physicochemical properties of sulfated and other anion-modified iron oxide/oxyhydroxide catalysts before use in coal liquefaction reactions, (iii) quantification of dispersion and composition of iron phases after coal liquefaction and (iv) transformation and sintering behavior of these catalysts under coal liquefaction conditions.

### EXPERIMENTAL

Starting Materials. The hvbc Blind Canyon DECS-17 coal was obtained from the Penn State Coal Sample Bank and the Wyodak subbituminous coal from the Argonne Coal Sample Bank. Elemental analyses are given in Table 1. Starting materials for catalyst preparation were iron alum [ $Fe_2(SO_4)_3 \cdot (NH_4)_2SO_4 \cdot 24H_2O$ ], ferric nitrate, urea, and 28% ammonia water. Ammonium heptamolybdate and ammonium metatungstate were purchased from the Sigma Chemical Co. and from Strem Chemicals, Inc. respectively.

Catalyst Preparation and Characterization. The sulfated oxides and oxyhydroxides of iron were prepared from either the sulfate or

nitrate salts using urea or  $\text{NH}_4\text{OH}$  as the precipitating agents, added dropwise so that the pH of the solutions changed with time. The result of the hydrolysis reaction is formation of iron oxyhydroxide ( $\text{FeOOH}$ ) with small residual amounts of sulfate anion adsorbed on the surface. The presence of sulfate anions during precipitation has been reported to bring about surface charge modifications of the precipitated particles; this affects the chemistry and kinetics of the precipitation/crystallization. The catalysts used in this study were  $\text{Fe}_2\text{O}_3$  (I),  $\text{Fe}_2\text{O}_3/\text{SO}_4$  (II),  $\text{Mo}/\text{Fe}_2\text{O}_3/\text{SO}_4$  (III),  $\text{FeOOH}/\text{SO}_4$  (IV),  $\text{Fe}_2\text{O}_3/\text{MoO}_4$  (V),  $\text{Fe}_2\text{O}_3/\text{WO}_4$  (VI) and  $\text{Mo}/\text{FeOOH}/\text{SO}_4$  (VII). These catalysts were prepared by modification of the procedure used for the preparation of  $\text{Fe}_2\text{O}_3/\text{SO}_4$  (II)<sup>4</sup>.

The following measurements were made to characterize the size and structure related properties of these catalysts: BET surface area, sulfur content, thermogravimetry (TGA), acidity measurements, thermal stability measurements, X-ray diffraction and electron microscopy. Residues of coal liquefaction experiments were also analyzed using a Phillips X-ray diffractometer and a JEOL 2000 FX STEM (100 kV beam) with an energy dispersive X-ray spectrometer (EDX) to determine composition and dispersion of catalytic phases formed under liquefaction conditions.

Reaction Studies. Tetralin was the reaction solvent (3:1 by weight to coal) and elemental sulfur (2:1 by weight to catalyst) was used for *in situ* catalyst sulfidation. Although a donor solvent such as tetralin tends to mask catalytic effects in coal conversion, its presence during coal liquefaction ensures complete conversion of the iron catalyst precursor to its sulfide via  $\text{H}_2\text{S}$  formation in 5-6 minutes at 400°C at 1000 psig cold  $\text{H}_2$ . Coal liquefaction reactions were carried out in both a 300 cc stainless steel autoclave and a 27 cc tubing bomb microreactor at 400°C and 1000 psig ambient  $\text{H}_2$  (1800 psig at reaction temperature). Coal conversions were determined using Soxhlet extraction with methylene chloride; soluble products were recovered by evaporation at 45°C under vacuum. Pentane solubles (oils) were determined by Soxhlet extraction of the methylene chloride solubles with n-pentane. Asphaltenes are the pentane-insoluble but methylene chloride soluble material.

## RESULTS AND DISCUSSION

Catalyst Synthesis and Characterization. The catalysts used are listed in Table 2 with relevant physicochemical properties. The presence of sulfate anions during precipitation was necessary to form nano-sized oxide particles which were resistant to agglomeration at high temperature.

The measure of initial dispersion of the catalysts was obtained using XRD line broadening measurements and transmission electron microscopy (TEM). The crystallite sizes of sulfated iron oxyhydroxides could not be determined by X-ray diffraction due to their low bulk crystallinity. These oxyhydroxides, after calcination, gave rise to catalyst II (high bulk crystallinity). Use of TEM revealed that catalyst IV contained very small needle-shaped, elongated, thin crystallites with average dimensions of 30 x 3 nm. Nitrogen porosimetry measurements were carried out on all catalysts. A macroporous distribution of pores was obtained for catalyst IV, indicating that individual fine particles come together to form very thin channels with average dimensions of 20-30 nm. All calcined iron oxides, completely crystalline after calcination, were 10-15 nm and

were elongated in shape as determined by electron microscopy.

The uncalcined sulfated oxyhydroxides such as IV had BET specific surface areas (120-130 m<sup>2</sup>/g) higher than the calcined oxides (80-90 m<sup>2</sup>/g). Evidence that all of the sulfated iron oxides had low porosities with pore volumes smaller than 0.2 cc/g was obtained by calculating equivalent spherical diameters from their surface area values and comparing them with diameters obtained by TEM. The values agreed within 10%.

The iron oxide surfaces were studied by FTIR and XPS. The FTIR spectrum of catalyst IV, obtained at 450°C under vacuum, showed an S=O band at 1440 cm<sup>-1</sup> similar to the S=O bonds formed in the bidentate chelating complex of sulfate anion with an oxide surface proposed by Tanabe et al.<sup>5</sup> Upon adsorption of pyridine, this band shifted to about 1500 cm<sup>-1</sup> and new bands, corresponding to coordinatively bonded pyridine (Lewis acid sites) and to pyridinium ions (Bronsted acid sites) appeared in the spectrum. XPS of the sulfated and molybdated iron oxides indicated that almost 95% of the S and Mo, both in 6+ oxidation states, were on the catalyst surface.

Reaction Studies. Coal liquefaction reactions were carried out both in a horizontally shaken tubing microreactor and a well-stirred 300 cc batch autoclave. Blank (thermal) runs were made with a previously unused microreactor to determine the catalytic activity of inherent mineral matter in the coals. Runs were also made with only elemental sulfur added to the reactor without added catalyst. Catalysts were mixed with the coal-tetralin slurry by manual stirring after being preheated in an oven at 450°C for one hour. Liquefaction experiments with sulfated iron oxides, presonicated in the reaction solvent for one hour, were also carried out; this treatment ruptured the catalyst agglomerates (about 1 nm as determined by light scattering) into smaller particles which formed a stable colloidal suspension in tetralin, thereby increasing the extent of initial catalyst dispersion.

Comparison of Catalytic Activities of Sulfated Iron Oxides and Oxyhydroxides with other Finely Divided Catalyst Precursors. Use of catalysts IV and VII (both uncalcined) resulted in total coal conversion levels similar to those obtained with their calcined forms (II and III), although higher oil yields were obtained with the calcined forms. The higher activity of calcined iron oxides for oil production is probably related to their calcination treatment at 500°C for three hours. The higher water content of the oxyhydroxides may make them more susceptible to sintering during transformation to pyrrhotites.

Activities of sulfated iron oxides were compared with those of organometallic precursor complexes such as Fe(CO)<sub>5</sub> and Mo(CO)<sub>6</sub> as well as with a fine divided (30 Å) iron oxide catalyst. Catalyst II was more active than Fe(CO)<sub>5</sub> at the same iron loading. Interestingly, 500 ppm of Mo (added as either Mo(CO)<sub>6</sub> or molybdenum naphthenate) relative to coal resulted in about the same conversion levels as 3500 ppm of Fe added as catalyst II.

Coal Conversion and Oil Yields as a Function of Catalyst Concentration. Coal conversions were carried out using the smallest catalyst loadings that gave meaningful results. Since most coals contain considerable amounts of iron as FeS<sub>2</sub>, it is difficult to obtain reliable data on the effect of small catalyst loadings on coal conversion levels. Two coals with low levels of iron, a Blind Canyon

coal with 0.02 wt% of pyrite and a Wyodak coal with 0.17 wt% of pyrite were selected to minimize the effect of inherent mineral matter. Uncalcined catalyst IV, which was as active as the calcined catalyst II, was employed for runs carried out to determine the effect of small loadings of iron (1000-5000 ppm with respect to coal) on coal conversion and on oil yields. With the Blind Canyon coal, a thermal blank conversion of 60% (maf) and oil yield of 22% were obtained. With 3500 ppm of Fe as catalyst II, conversion increased to 77% and oils to 35%. The highest conversion (87% with 48% oils) was achieved with 1% of  $\text{FeOOH}/\text{SO}_4$  (IV).

The effect of Mo loadings (20-200 ppm with respect to coal) used with 2500 ppm of iron as III was investigated. Very small amounts of Mo added to II enhanced coal conversion from 72% to 80%; the yield of oils, however, rose from 32% without Mo to 46% with 100 ppm of Mo. On increasing Mo loading to 200 ppm, total conversion was 87% and yield of oils 52%. The molybdenum in catalyst III probably forms  $\text{MoS}_2$ , which has a strong hydrogenation function so that more oil is produced at the expense of asphaltenes.

Effect of Different Anionic Modifications of Iron (III) Oxides on Coal Liquefaction Activity. Iron oxides modified with 5 wt% of molybdate ( $\text{MoO}_4$ ) or tungstate ( $\text{WO}_4$ ) anions were as active as sulfated iron oxide catalysts in terms of overall coal conversion.

All runs with the Blind Canyon coal were made with addition of elemental sulfur to the reactor. Use of S alone in a blank run (no catalyst added) resulted in 66% coal conversion with 27% oils. Iron oxides modified with either tungstate or molybdate anions resulted in slightly higher oil yields than the sulfated iron oxide. The higher activity is due to formation of highly active and well dispersed  $\text{MoS}_2$  or  $\text{WS}_2$ . These new types of anionic modifications of iron oxides bring about significant enhancement in coal liquefaction activity.

Catalyst Presulfidation and Re-use. To establish the activity of highly dispersed pyrrhotites formed from the sulfated iron oxides, we carried out presulfidation instead of *in situ* sulfidation of the catalysts by reacting them with 2:1 (by weight) of S in the presence of tetralin at 400°C and 1000 psig  $\text{H}_2$  cold for 30 minutes in the 300 cc autoclave. X-ray and electron diffraction indicated that all sulfated iron oxides were converted to  $\text{Fe}_7\text{S}_8$  with traces of  $\text{Fe}_{11}\text{S}_{12}$ . X-ray line broadening measurements and transmission electron microscopy indicated a crystal size of 20 nm for these preformed pyrrhotites, which, interestingly, contained 3 to 5 wt% of carbon derived from the solvent tetralin. The tetralin was found to have been hydrocracked, hydrogenated, and dehydrogenated during presulfidation of the sulfated catalysts.

The preformed pyrrhotites were then employed as catalysts for direct liquefaction of Blind Canyon coal at 400°C at 0.25 to 0.35 wt% iron loading relative to coal both with and without added S. The preformed  $\text{Fe}_7\text{S}_8$  was almost as active as catalyst IV at 0.35 wt% iron. Further addition of S to  $\text{Fe}_7\text{S}_8$  improved its activity, yielding 42% oils compared to 30% with larger amounts of  $\text{Fe}_7\text{S}_8$  in the absence of added S with 2500 ppm of iron. Increase in oil yields upon addition of S to  $\text{Fe}_7\text{S}_8$  indicates possible interactions between pyrrhotites and  $\text{H}_2\text{S}$  for catalyzing hydrogenolysis/hydrogenation reactions during coal liquefaction. The presence of  $\text{H}_2\text{S}$  also ensures that the iron-deficient and sulfur-rich stoichiometry of pyrrhotites is maintained.

Effect of Reaction Temperature. Catalysts I, II and III were used for liquefaction of WyodaK coal at 375, 400, and 425°C. The activities of these catalysts for production of oils from coal increased on going from 375 to 425°C except for the Fe<sub>2</sub>O<sub>3</sub> (I) catalyst, for which oils decreased somewhat. Sulfated catalysts resulted in higher yields of oils than the unsulfated ones at all temperatures.

Dispersion and Composition of Catalysts after Coal Liquefaction. To study what happened to initially added iron catalyst precursors after coal liquefaction, we carried out reactions of Blind Canyon coal with II and with Fe(CO)<sub>5</sub>. The insoluble residues containing transformed iron catalysts were characterized by X-ray diffraction and STEM coupled with an Energy Dispersive X-ray Detector. The added iron for both precursors was completely converted to pyrrhotites, highly dispersed in the insoluble organic matter in the liquefaction residue. Pyrrhotites formed from Fe(CO)<sub>5</sub> were larger (30-50 nm) than those from II (15-20 nm).

#### CONCLUSIONS

1. Sulfated iron oxides and oxyhydroxides and molybdenum promoted sulfated iron oxide were active for converting low pyrite coals to liquids at 400°C; coal conversion levels greater than 75%, compared to 66% without catalyst, were obtained with iron loadings between 2500-5000 ppm relative to coal.

2. The sulfate, molybdate and tungstate anions modified the physicochemical properties of iron(III) oxides in a similar way and were about equally effective for direct liquefaction of low-pyrite Blind Canyon coal, but slightly higher yields of oils were obtained with iron oxides promoted by molybdate or tungstate.

3. Uncalcined sulfated iron oxyhydroxides were almost as active as the calcined sulfated iron oxides, but somewhat higher amounts of oils were obtained using calcined oxides. Although initially both oxides and oxyhydroxides are highly dispersed, sulfated oxides resist sintering at high temperatures. Uncalcined sulfated oxyhydroxides have residual moisture which is probably responsible for agglomeration under coal liquefaction conditions.

4. Iron, in the form of sulfated oxides, is completely converted to highly dispersed pyrrhotites within a few minutes at 400°C. These have a composition of Fe<sub>7</sub>S<sub>8</sub> and an average particle size of 20 nm. No growth in particle size during reaction was observed. The presulfided Fe<sub>7</sub>S<sub>8</sub> is also active for direct liquefaction of coal in the presence of added sulfur.

5. A catalyst system based on anion-modified iron oxides has an initial fine size and a unique ability to resist agglomeration at higher temperatures.

#### ACKNOWLEDGMENTS

The authors acknowledge financial support from the United States Department of Energy under award DE-FC22-90PC900029 and the Exxon Education Fund. Contributions of coal samples by the Argonne Premium Coal Sample Bank and the Penn State Coal Sample Bank are also acknowledged.

REFERENCES

1. Trehwella, M.J. and A. Grint, *Fuel*, 1987, 66, pp, 1315-1219.
2. Baldwin, R.M. and S. Vinciguerra, *Fuel*, 1983, 62, pp 498-501.
3. Ogawa, T., V.I. Stenberg and P.A. Montano, *Fuel*, 1984, 63, pp. 1660-1663.
4. Pradhan, V.R., J.W. Tierney and I. Wender, *Energy & Fuels*, 1991, 5, pp 497-507.
5. Tanabe, K., H. Hattori, T. Yamaguchi, T. Iizuka, H. Matsuhashi, A. Kimura and Y. Nagase, *Fuel Proc. Tech.*, 1986, 14, pp 247-260.

Table 1. Ash-free Elemental Analyses of Coals (weight percent)

Coal	Carbon	Hydrogen	Nitrogen	Oxygen	Sulfur	Pyritic Sulfur
Wyodak	75.0	5.4	1.1	18.0	0.5	0.17
Blind Canyon	81.6	6.2	1.4	10.3	0.5	0.002

Table 2. Catalyst Characterization before Reaction

Catalyst <sup>1</sup>	Wt % SO <sub>4</sub>	Surface Area, m <sup>2</sup> /g	Average Size, nm		
			XRD	TEM	ESD <sup>2</sup>
I	0.0	26.8	46	65	41
II	3.4	81.7	12	20	14
III	3.1	81.5	12	20	14
IV	10.2	127.0	nd	16	11
V	0.0	88.0	9	15	13
VI	0.0	91.5	7	15	12
VII	9.8	120.5	nd	20	11

1. Molybdated and tungstated iron (III) oxides contained 5 wt% molybdate or tungstate.
2. ESD is the equivalent spherical diameter of the catalyst particles, calculated from the BET surface area and assuming zero porosity.

## PREPARATION OF ULTRAFINE CATALYST POWDERS USING A FLOW-THROUGH HYDROTHERMAL PROCESS

Dean W. Matson, John C. Linehan, and John G. Darab  
Pacific Northwest Laboratory,  
P.O. Box 999, Richland, WA 99352.

Keywords: Catalyst synthesis, Iron catalysts, Catalyst characterization

### ABSTRACT

The rapid thermal decomposition of solutes (RTDS) process was used to produce ultrafine iron-bearing oxide and hydroxide powders for use as coal liquefaction catalysts. The RTDS process subjects aqueous solutions containing dissolved metal salts to elevated temperatures and pressures in a flow-through apparatus. Particle formation is initiated during brief exposure of the solution to a heated region, then is quenched by abruptly cooling and depressurizing the suspension. Powders having individual crystallites on the nanometer to tens-of-nanometer size scale are readily produced by the RTDS method. Variations in RTDS processing parameters (e.g., solute concentration, flow rate, processing temperature) affect the crystallinity, morphology, and size of particles produced. Powders generated using the RTDS process were characterized using XRD, EXAFS, electron microscopy, Mossbauer spectroscopy, and BET surface area analysis.

### INTRODUCTION

The development of inexpensive and environmentally benign materials exhibiting catalytic activity toward coal liquefaction processes will enhance the economic viability of coal liquefaction as a source of liquid transportation fuels. If active materials can be developed which meet these criteria, the application of single-use "throw away" catalysts will eliminate the need for costly catalyst reclamation steps in the liquefaction process. Inexpensive iron-based materials have been shown to be catalytically active in coal liquefaction processes, although their activities are typically low compared to other, much more expensive and/or toxic molybdenum-based materials.<sup>1</sup> One approach which can be taken to counteract the inherently lower catalytic activity of iron-based materials is to increase the surface site availability per unit weight of catalyst. The production of finely divided catalyst precursor powders having particle sizes on the nanometer to tens of nanometer size scale offers specific surface areas of up to several hundred m<sup>2</sup>/g. In addition to the increase in availability of active sites, ultrafine particles have a much higher mobility within the reaction medium, increasing the potential for coal/catalyst contact.<sup>2</sup>

We have shown that ultrafine iron-bearing particles can be generated quickly in a flow-through hydrothermal process referred to as the rapid thermal decomposition of solutes (RTDS) process.<sup>3</sup> The RTDS process offers a method of generating both ultrafine iron (hydroxy) oxides and mixed metal (hydroxy) oxides using inexpensive water soluble precursors. The RTDS process is amenable to variations in a number of processing parameters. Among those readily adjusted are the precursor salt and its concentration in solution, the processing temperature and pressure, and the length of exposure to the heated region. In this report we present the results of efforts to characterize iron-bearing powders generated using the RTDS method and to relate the effects of varying processing parameters on the powder characteristics. Results of catalytic activity runs using RTDS products are presented in a companion paper.<sup>4</sup>

### EXPERIMENTAL

Details of the RTDS powder formation method have been presented elsewhere<sup>3</sup> but are summarized here for convenience. As it is used for the preparation of iron-bearing powders from aqueous solutions, the RTDS technique involves rapid transport of the precursor solution through a high temperature, high pressure region followed by an abrupt transition to low temperature and

ambient pressure. Solutions were pressurized using a high pressure reciprocating piston pump and subsequently passed through a length of stainless steel tubing which was resistively heated using the temperature regulated output from a DC power supply. Temperatures of the solutions at the downstream end of the heated tube were monitored by a thermocouple mounted in the fluid flow. Typical fluid residence times in the heated region of the apparatus were less than 2 seconds. After passing through the heated tube, the solution was depressurized by passing it through a small orifice. The resulting spray was directed into a flask immersed in an ice bath, where the resulting suspension was collected. For the purposes of investigating the RTDS process as a method of ultrafine powder production, a standard metals concentration of 0.1 M was chosen for the feed solutions.

Iron-bearing RTDS suspensions were separated by allowing the particulate fraction to settle, either gravitationally or by centrifugation. If required, additional salts were added to the suspensions to flocculate the particles and assist the settling process. Liquid above the particulate layer was decanted off, the particles were washed with deionized water, and the process was repeated. The resulting solid product was dried under flowing nitrogen or air.

A variety of techniques were used to characterize the RTDS-generated powder products. Powder X-ray diffraction (XRD) was routinely used to determine crystalline phases present in the RTDS powder product, and XRD line broadening analysis provided crystallite size data. Selected samples were also analyzed using Mossbauer spectroscopy, BET nitrogen adsorption analysis, extended X-ray absorption fine structure (EXAFS) spectroscopy, and electron microscopy.

## RESULTS and DISCUSSION

In the absence of other components, ferric nitrate solutions processed using the RTDS method yielded deep red to red-brown suspensions characteristic of polymeric ferric oxides and hydroxides.<sup>5</sup> The 0.1 M  $\text{Fe}(\text{NO}_3)_3$  solutions processed at RTDS temperatures above 250°C formed solids which settled readily, while those produced at lower temperatures (200-250°C) settled much more slowly or remained suspended until salted out.

The pH of the 0.1 M  $\text{Fe}(\text{NO}_3)_3$  solutions was roughly 2.0 as prepared, and dropped approximately 0.3 pH units during the RTDS processing. This decrease in pH resulted from hydrolysis reactions occurring under the hydrothermal conditions present in the RTDS apparatus:

$\text{Fe}^{3+} + 2\text{H}_2\text{O} \rightarrow \text{FeOOH} + 3\text{H}^+$  and  $2\text{Fe}^{3+} + 3\text{H}_2\text{O} \rightarrow \text{Fe}_2\text{O}_3 + 6\text{H}^+$ . Efforts to modify the pH of RTDS solutions by adding an acetate buffer (0.36 M sodium acetate and 0.04 M acetic acid) raised both the before- and after-processing pH values above 4.0. Processing of the buffered solution at low temperature (225°C) generated a dark reddish brown suspension that did not settle, although a solid product was salted out by addition of sodium sulfate.

The analytical results from iron (hydroxy) oxide powders produced by RTDS processing of aqueous 0.1 M  $\text{Fe}(\text{NO}_3)_3$  solutions at various temperatures are summarized in Table 1. These results suggest that at low processing temperatures (< 250°C), the phase obtained was 2-line ferrihydrite or mixtures of ferrihydrite and hematite ( $\alpha\text{-Fe}_2\text{O}_3$ ). Both XRD and transmission electron microscopy (TEM) analyses indicated that these low-temperature RTDS products consisted of powders containing crystallites smaller than 10 nm in diameter. Higher RTDS processing temperatures (300-400°C) yielded the hematite form of iron oxide exclusively, and crystallite sizes were observed to increase as a result of higher processing temperatures (Fig. 1, Table 1). The increase in crystallite size with increasing RTDS processing temperature was also reflected in the room temperature Mossbauer spectra of the powder products as a shift from the 2-line quadrupole doublet spectrum characteristic of particles less than 8.5 nm in diameter to the 6-line hyperfine spectrum which is characteristic of bulk hematite (Fig. 2).<sup>5,6</sup>

Figure 3 shows plots of the iron nearest neighbor shell radii (uncorrected for phase shift) determined from the iron K-edge EXAFS spectra of the powders produced from 0.1 M ferric nitrate solutions as a function of increasing RTDS processing temperature. At the lowest RTDS temperature (200°C), the nearest neighbor shell radii are indicative of low molecular weight oligomers. As the RTDS temperature is increased, the radii approach those which are representative of bulk hematite (2.730 Å for iron and 1.473 Å for oxygen).

The effect of adding urea (1.0 M) to ferric nitrate solutions being processed by the RTDS method was also investigated (Table 1). Decomposition of the urea to carbon dioxide and ammonia at RTDS processing temperatures resulted in a rapid rise in solution pH simultaneously with the development of hydrothermal conditions, producing a competing cation precipitation mechanism. Little effect was noted below 250°C because, at the short residence times of the solutions in the elevated temperature region of the RTDS apparatus, the decomposition of the urea was insufficient to significantly change the solution pH. At 250°C and 300°C RTDS temperatures the pH of the processed solutions was above 8.5, and the product was a reddish brown opaque gel. XRD analysis of the solid product indicated the presence of a poorly crystallized material, consisting primarily of 6-line ferrihydrite.

Catalytic activity and/or selectivity of ultrafine iron oxides may be significantly affected by the doping of other metals into the solid matrix.<sup>1</sup> Consequently, the production of iron oxide powders doped with other cations by co-precipitation during RTDS processing was investigated. Results of representative RTDS runs using additional cationic species as dopants are presented in Table 2. Empirically, the results obtained from the runs containing dopants were consistent with the results of ferric iron-only runs, although some differences were detected in secondary iron oxide phases which were produced. The principle phases identified in the resulting products were those of hematite and 6-line ferrihydrite (a hematite precursor). 2-line ferrihydrite may also have been present in some samples, but was not identified due to the weakness of its XRD pattern relative to that of the other phases. Some additional phases were identified in samples in which urea had been added to the feed solutions.

Efforts at obtaining magnetite ( $\text{Fe}_3\text{O}_4$ ) by processing a solution containing both  $\text{Fe}^{3+}$  and  $\text{Fe}^{2+}$  salts yielded only hematite and ferrihydrite phases under the conditions investigated, with the relative concentration of those phases dependent on the processing temperature. At 225°C the mixed iron system yielded both hematite and 6-line ferrihydrite, although only 2-line ferrihydrite was observed in the product of ferric nitrate only runs at similar processing conditions. At higher processing temperatures the relative concentration of hematite to 6-line ferrihydrite increased until at 400°C the product obtained was almost identical to that produced from a solution containing ferric nitrate only (Table 1). Clearly, under the RTDS processing conditions used for these experiments, the  $\text{Fe}^{2+}$  was rapidly oxidized to  $\text{Fe}^{3+}$ .

Doping of the iron feed solution with  $\text{Cr}^{3+}$  salt at a 10:1 iron to chromium ratio yielded a solid powder consisting of hematite and 6-line ferrihydrite after processing at 300°C. No distinct chromium-only phase was detected in the powder collected. Because of significant broadening of the lines in the XRD pattern due to the fine crystallite size in this material, it was not clear whether significant amounts of chromium had been incorporated into the hematite structure.

RTDS processing at 350°C of a feed solution consisting of  $\text{Fe}(\text{NO}_3)_3$  and  $\text{Ni}(\text{NO}_3)_2$  in a 2:1 mole ratio (0.067 M: 0.033 M, respectively) yielded a reddish-brown solid powder product. XRD analysis of the powder indicated the presence of only the hematite phase. No nickel-bearing phase was detected. Addition of 0.5 M urea to the  $\text{Fe}^{3+}/\text{Ni}^{2+}$  solution and processing at 350°C yielded a powder consisting primarily of the nickel ferrite, trevorite ( $\text{NiFe}_2\text{O}_4$ ), with a smaller concentration of its hydroxide precursor.

Powder generated from a  $\text{Fe}^{3+}/\text{Cu}^{2+}$  salt solution at a 350°C processing temperature consisted of a mixture of hematite and 6-line ferrihydrite. No copper-only phase was detected in the XRD analysis of the precipitated solid. Addition of 0.5 M urea to the  $\text{Fe}^{3+}/\text{Cu}^{2+}$  feed solution and processing at 350°C resulted in precipitation of the copper oxide phase, tenorite ( $\text{CuO}$ ) and a separate hematite phase. XRD results on the settled powder gave no indication of the formation of a ferrite phase similar to that observed in the  $\text{Fe}^{3+}/\text{Ni}^{2+}$  system with the use of urea as a precipitating agent.

## SUMMARY

The RTDS process is a viable method for hydrothermally generating ultrafine iron-bearing catalyst powders having crystallite sizes into the nanometer size range. Specific crystalline phases and crystallite sizes of the iron-based powders generated by this method are influenced by the

processing conditions to which the feed solutions are subjected and to the species present in those solutions.

## ACKNOWLEDGEMENTS

Pacific Northwest Laboratory (PNL) is operated for the U.S. Department of Energy (DOE) by Battelle Memorial Institute under Contract DE-AC06-76RLO 1830. The work reported here was sponsored by the DOE Office of Fossil Energy and by DOE under the Advanced Processing Technology Initiative at PNL.

## REFERENCES

- (1) Pradhan, V.R.; Herrick, D.E.; Tierney, J.W.; Wender, I. *Energy Fuels* **1991**, *5*, 712-720.
- (2) Suzuki, T.; Yamada, H.; Sears, P.; Watanabe, Y. *Energy Fuels* **1989**, *3*, 707-713.
- (3) Matson, D.W.; Linehan, J.C.; Bean, R.M. *Mater. Lett.* **1992**, *14*, 222-226.
- (4) Linehan, J.C.; Darab, J.G.; Matson, D.W. "Results of Catalyst Testing Using Iron-Based Catalysts," This proceedings.
- (5) Schwertmann, U.; Cornell, R.M. *Iron Oxides in the Laboratory*, Weinheim: New York, 1991.
- (6) Huffman, G.P.; Ganguly, B.; Taghiei, M.; Huggins, F.E.; Shah, N. *Preprints, Div. of Fuel Chem., American Chemical Society* **1991**, *36*, 561-569.

TABLE I  
RTDS Powders Produced from 0.1 M Fe(NO<sub>3</sub>)<sub>3</sub> Solutions

Added Component	RTDS Temp. (°C)	Identified Phase <sup>a</sup>	Crystallite Diameter (nm) by:			BET Surface Area (m <sup>2</sup> /g)
			XRD <sup>b</sup>	TEM <sup>c</sup>	Mossbauer <sup>d</sup>	
---	225	2-line Ferrihydrate <sup>e</sup>	<<10	2-10	---	212
---	300	Hematite	11	4-10	56% > 8.5	167
---	400	Hematite	23	20-40	100% > 8.5	---
acetate buffer	225	---	<<10	2-10	100% < 8.5	184
urea	200	---	---	---	---	---
urea	250	6-line Ferrihydrate	<<10	---	---	---
urea	300	6-line Ferrihydrate	<<10	---	---	---

<sup>a</sup>Determined by XRD

<sup>b</sup>Estimates of uncertainties in XRD size results are ± 10% for crystallites in the 10 to 120 nm range.

<sup>c</sup>TEM size estimates are qualitative and based on both bright-field and dark-field observations.

<sup>d</sup>Size distribution about 8.5 nm was based on relative areas of the quadrupole doublet vs. the 6-line hyperfine feature in room temperature spectra.<sup>6</sup>

<sup>e</sup>Two-line ferrihydrate and 6-line ferrihydrate are poorly defined hydrated iron (hydroxy) oxide phases which are distinguished from each other by the number of broad lines present in their XRD patterns.

TABLE 2  
Results of Co-Processing Aqueous Ferric  
Nitrate Solutions with Other Metal Ions<sup>a</sup> using RTDS

Other Salt	[Fe <sup>3+</sup> ]:[M]	Reaction Temperature	Identified Products <sup>b</sup>	Crystallite Diameter <sup>c</sup>
FeSO <sub>4</sub>	1:1	225°C	50% Hematite, 50% 6-Line Ferrihydrite	37 nm <<10 nm
FeSO <sub>4</sub>	1:1	300°C	90% Hematite, 10% 6-Line Ferrihydrite	36 nm <<10 nm
FeSO <sub>4</sub>	1:1	400°C	100% Hematite	32 nm
Cr(NO <sub>3</sub> ) <sub>3</sub>	10:1	300°C	40% Hematite, 60% 6-Line Ferrihydrite	12 nm << 10 nm
Cu(NO <sub>3</sub> ) <sub>2</sub>	2:1	350°C	70% Hematite, 30% 6-Line Ferrihydrite	11 nm <<10 nm
Cu(NO <sub>3</sub> ) <sub>2</sub> + Urea	2:1	350°C	30% Hematite, 70% Tenorite (CuO)	11 nm 22 nm
Ni(NO <sub>3</sub> ) <sub>2</sub>	2:1	350°C	100% Hematite	15 nm
Ni(NO <sub>3</sub> ) <sub>2</sub> + Urea	2:1	350°C	80% Trevorite (NiFe <sub>2</sub> O <sub>4</sub> ), 20% δ-(Fe <sub>0.67</sub> Ni <sub>0.33</sub> )OOH	8.5 nm <<10 nm
Ni(NO <sub>3</sub> ) <sub>2</sub> + Urea	2:1	400°C	90% Trevorite (NiFe <sub>2</sub> O <sub>4</sub> ), 10% δ-(Fe <sub>0.67</sub> Ni <sub>0.33</sub> )OOH	7.4 nm <<10 nm

<sup>a</sup>Total cation concentration 0.1 M for all starting solutions  
<sup>c</sup>By XRD line broadening

<sup>b</sup>Determined by XRD analysis

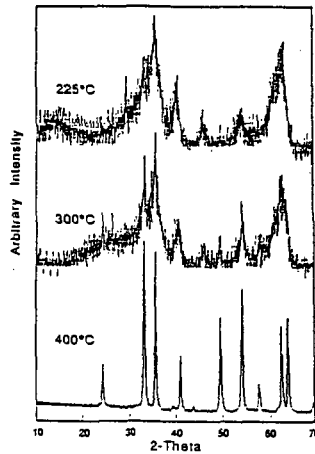


Figure 1. Variations in XRD patterns of RTDS-generated iron oxide powders as a function of increasing RTDS processing temperature.

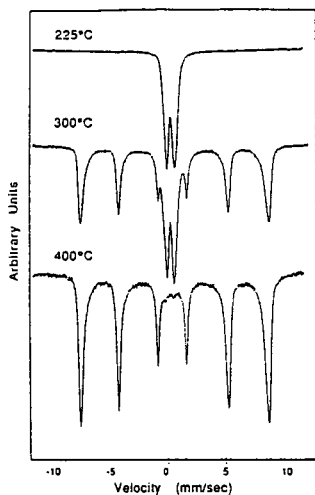


Figure 2. Variations in Mossbauer spectra of RTDS-generated iron oxide powders as a function of increasing RTDS processing temperature.

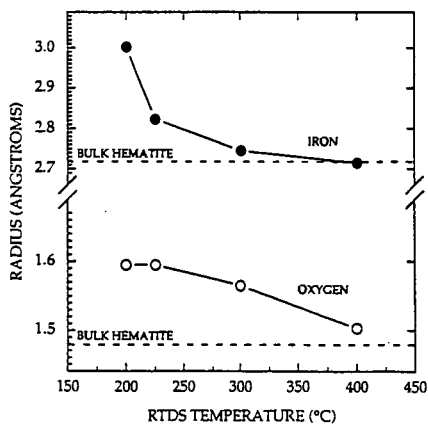


Figure 3. Plot of iron nearest neighbor radii determined from the iron K-edge EXAFS spectra of RTDS powders produced from 0.1 M ferric nitrate solutions

## Synthesis and Characterization of Fe and FeS<sub>2</sub> (Pyrite) Catalyst Particles in Inverse Micelles\*

A. Martino, J.P. Wilcoxon, A.P. Sylwester, J.S. Kawola  
Fuel Science Division, 6211  
Sandia National Laboratories  
Albuquerque, NM 87185

**Keywords:** Inverse micelles; Nanophase clusters; Coal liquefaction catalysts

### Introduction

Surfactant molecules possess two distinct moieties: a hydrophilic head group and a hydrophobic tail group. Because of the dual nature of surfactant molecules, they self-assemble in various solvents. In many two component systems of surfactant and oil, surfactants aggregate to form inverse micelles. Here, the hydrophilic head groups shield themselves by forming a polar core, and the hydrophobic tail groups are free to move about in the surrounding oleic phase. In three component microemulsion systems of water, oil, and surfactant, water is solubilized within the inverse micelle structure if the water concentration remains low. The solution takes on the structure of water droplets approximately 10-100Å in diameter dispersed in the oleic solvent with surfactant forming the boundary between the two components.

In structured solutions such as inverse micellar and oil-rich microemulsion solutions, polar chemical reactants can be compartmentalized in the interior of the surfactant aggregates. If a chemical reaction sequence is initiated, the surfactant interface provides a spatial constraint on the reaction volume. The surfactant aggregates act as micro-reactors. Metal alkoxide reactions [1], the formation of metal and semiconductor clusters [2-5], and the formation of polymer particles [6] are examples of chemical processes which have been carried out in structured surfactant solutions.

We have studied the formation of iron based clusters in inverse micelles and their use as catalysts in coal liquefaction reactions. Iron salts are solubilized within the polar interior of inverse micelles. The addition of an organic based reducing agent or water based sulfiding agent initiates respectively a chemical reduction or an exchange/replacement reaction. The inverse micelle structure acts as a reaction media and limits the final size of the particles. Particle formation is also dependent upon the particle nucleation and growth process. The initial micelle size, the nucleation and growth process, and ultimately the size of the particles is controlled by adjusting a few experimental parameters.

In order to illustrate the effects of various experimental conditions on the final particle size, we have studied a model system. CdS formation is well understood. We report the use of small angle neutron scattering, UV-visible spectrophotometry, and electron microscopy to characterize the inverse micelle solutions, the particle size, and particle elemental composition. Analogous results are observed in the formation of Fe and FeS<sub>2</sub> (pyrite). Finally, we report the use of the iron based clusters as catalysts in batch coal liquefaction reactions.

### Experimental

Alkanes of increasing hydrophobicity from hexane to hexadecane, cyclohexane, and toluene were purchased from Aldrich at 99.9+% purity. Surfactants used included didodecyltrimethylammonium bromide (DDAB) from Kodak, butyl-ethylene glycol n-dodecyl ether (C<sub>12</sub>E<sub>4</sub>) from Nikkol, and POE (6) nonylphenol from Chem Services. Metal salts used included cadmium chloride, iron(II) chloride tetrahydrate, and iron(III) chloride hexahydrate from Aldrich. Lithium borohydride in tetrahydrofuran (1M) was purchased from Aldrich. Lithium sulfide was

\* This work is supported by the U.S. Department of Energy at Sandia National Laboratories under contract DE-AC04-76DP00789.

purchased from Aldrich and prepared in a 1M solution in de-ionized, distilled water. Otherwise, all chemicals were used as delivered.

Stock solutions of 10 wt. % surfactant are prepared in various organic solvents to produce the inverse micelle solutions. The iron salts are added directly to prepare 0.001-0.01M solutions, and are mixed overnight on a stirring plate to assure complete solubilization. Concentrated aqueous cadmium chloride solutions are mixed with the stock inverse micelles solutions to prepare 0.0005-0.01M cadmium chloride microemulsions. To reduce the iron salts, the concentrated  $\text{LiBH}_4/\text{THF}$  solution is injected into the inverse micelle solutions under rapid stirring. To sulfide the iron and cadmium salts, the  $\text{Li}_2\text{S}/\text{H}_2\text{O}$  solution is injected into the inverse micelle or microemulsion solutions under rapid stirring. The reaction is carried out and the final product is stored under dry, oxygen-free conditions. The reducing agent or sulfiding agent is added in an excess molar concentration to favor the formation of the surfactant stabilized sols.

The inverse micelle and cluster solutions are studied by small angle neutron scattering (SANS), UV-visible spectrophotometry, and electron microscopy (TEM). SANS is carried out at the Low-Q Diffractometer at the Los Alamos Neutron Scattering Center. Deuterated organic solvents are used. The inverse micelle radius of gyration is determined by Guinier analysis of the scattering curve [7]:  $I = N \exp(-q^2 R_g^2/3)$ , where  $N$  is a proportionality constant,  $q$  is the scattering vector, and  $R_g$  is the radius of gyration of the inverse micelles. UV-visible spectrophotometry of the particle solutions is completed *in-situ* with a Hewlett Packard 8452A diode array spectrophotometer. Relative size and characterization of the particles is achieved through analysis of the plasmon resonances observed in metal particles and the band gap structure observed in semiconductors. Finally, TEM using a Joel 1200EX sizes the particles and selected area electron diffraction aids in the particle characterization.

Coal liquefaction of DECS-17, Blind Canyon coal is completed in a stainless steel micro-batch reactor at 400°C, a cold  $\text{H}_2$  pressure of 800 psi, and a reaction time of 30 minutes. Hexahydropyrene ( $\text{H}_6\text{Py}$ ) is used as the hydrogen donor solvent. Thermal conditions are selected to give moderate conversion of coal to relatively low molecular weight organic material. Reaction analysis consists of extracting products with THF and heptane (C7) in two separate stages, and the products are separated into categories depending on their solubility for the solvents. Insoluble organic matter (IOM) is neither soluble in THF or C7. All soluble organic matter is extracted by THF (THF solubles), and the low molecular weight fraction of this material is extracted by C7 (C7 solubles). This latter fraction of product represents potentially usable oils and gases. Product gas analysis was not completed. A description of the coal liquefaction process is detailed elsewhere [8]. The iron based catalysts were tested *in-situ* or as powders and were added to the micro-batch reactors directly.

## Results

Small angle neutron scattering results indicate that inverse micelles of  $\text{C}_{12}\text{E}_4$  in octane and dodecane increase in size with the addition of water (Figure 1). The effect of water addition is more drastic in dodecane than in octane. Also, the inverse micelle size increases as the oil hydrophobicity increases (i.e.  $\text{C}_{12}\text{E}_4/\text{dodecane}$  inverse micelles are roughly 12% bigger than  $\text{C}_{12}\text{E}_4/\text{octane}$  inverse micelles).

Transmission electron microscopy of  $\text{FeS}_2$  formed in  $\text{C}_{12}\text{E}_5/\text{octane}$  inverse micelles show ~ 10Å radius particles ( $\text{C}_{12}\text{E}_5$  is a slightly more hydrophilic analog of  $\text{C}_{12}\text{E}_4$ ). Initial concentration of the iron salt was 0.001M. The particles show no signs of aggregation and are highly dispersed, spherical, and monodisperse on the TEM grid (Figure 2). TEM results indicate  $\text{Fe}^0$  particles formed in DDAB/toluene (initial iron salt concentration = 0.001M) are ~ 12Å in radius. In addition, lattice fringe imaging indicates that the  $\text{Fe}^0$  colloids exist in the high temperature fcc  $\text{Fe}(\gamma)$  structure. Finally, CdS particles formed in  $\text{C}_{12}\text{E}_5/\text{octane}$  inverse micelles (initial cadmium salt concentration = 0.0005M) are ~14Å in radius as determined by TEM.

The electronic spectra of CdS semiconductor particles is well known [3]. An absorbance shoulder is observed in the visible wavelength range due to the formation of an electron-hole pair across the semiconductor band gap. This spectra is reproduced by UV-visible spectrophotometry in

the CdS particles produced in inverse micelles (Figure 3). Increasing water concentration in the microemulsion solution causes a red shift in the onset of visible absorbance and a red shift in the absorbance maxima. The maxima occurs just before the large solvent absorbance shoulder. The electronic spectra is not effected by the solvent. The absorbance onset and maxima are nearly identical in octane and hexadecane.

The electronic spectra of FeS<sub>2</sub> particles is also dependent on water concentration in the microemulsion solutions (Figure 4). The spectra is highlighted by several absorbance maxima which red shift as the water concentration increases in the microemulsion mixtures. The behavior of the FeS<sub>2</sub> electron spectra is analogous to the behavior of the CdS electronic spectra as a function of water content.

As further characterization of the FeS<sub>2</sub> particles, electron diffraction from a selected area on the microscope grid produces a ring pattern consistent with the FeS<sub>2</sub> pyrite structure (Figure 5).

Finally, the Fe and FeS<sub>2</sub> particles were tested as catalysts in coal liquefaction reactions. Results are shown in Table 1. Solvent dispersed Fe or FeS<sub>2</sub> catalysts show equal or lower conversion to organic products compared to the thermal (no catalyst) reactions. The liquid catalysts show high amounts of insoluble organic matter. Fe catalyst added as a powder shows equal conversion to organic products compared to the thermal runs. FeS<sub>2</sub> catalyst added as a powder shows lower overall conversion to organic products, but a higher conversion to low molecular weight products. Importantly, the catalyst selectivity for the production of low molecular weight products is greatly increased.

## Discussion

Colloid formation in the reduction and exchange/replacement processes proceed, respectively, via the following chemical reactions:  $Fe^{2+} + 2H^- \rightarrow Fe(\text{colloids}) + H_2$  and  $Fe^{2+} + S_2^{2-} \rightarrow FeS_2(\text{colloids})$ . The inverse micelles act as reaction vessels and mediate the nucleation and growth of the particles. The surfactant stabilizes the colloids and prevents flocculation and precipitation. Nevertheless, colloid stability is dependent on the high reactivity of the particles. It is necessary to use excess reactants in order to push the chemical reactions to the right and favor the formation of the colloids. In the case of the sulfiding reaction, water in the microemulsion mixtures favor the decomposition of the colloids into their respective ions. This is observed by the disappearance of the characteristic absorbance spectra of CdS and FeS<sub>2</sub>. The presence of water in the reduction reaction of iron salts may change the chemistry all together and actually lead to the formation of iron borides and oxides. Oxidation of the iron clusters is visible to the naked eye, and CdS colloids photodegrade in the presence of oxygen ( $CdS + 2O_2 \rightarrow Cd^{2+} + SO_4^{2-}$ ). The oxidation of both FeS<sub>2</sub> and CdS can be witnessed by the disappearance of their respective absorbance spectra.

Particle size control in the inverse micelle mediated synthesis of clusters is complex. It is reasonable to expect that the size of the initial inverse micelle will limit the final particle size. New particles will nucleate before existing particles grow large enough to disrupt the micelle structure. The nucleation and growth process is also governed by such variables as initial salt concentration, solution viscosity, and temperature. Any variable which increases the effective diffusion rate of the reacting ions will favor growth over nucleation and lead to larger particles.

We have attempted to elucidate the most relevant variables in the control of the final particle size. The electronic spectra of the semiconductor CdS provides us with the most facile method to determine relative particle size. The band gap of semiconductor particles increases with decreasing particle size due to quantum confinement of the charge carriers. Increasing particle size will cause a red shift in the absorbance spectra of fine particles [2]. The electronic spectra of CdS particles clearly show this behavior. Figure 1 shows that the size of inverse micelles is strongly dependent on water content and only weakly dependent on the hydrophobicity of the oil. The electronic spectra of particles synthesized in the same inverse micelles show a distinct red shift with increasing water content (Figure 3). There is little shift in the electronic spectra as the solvent changes from octane to hexadecane despite a six-fold change in solution viscosity. Clearly, the changing size of the initial inverse micelle plays a larger role in the final particle size than does ionic diffusion of reacting species as controlled by solution viscosity.

The electronic spectra of  $\text{FeS}_2$  is dependent on the water content of the reacting microemulsion system (Figure 4). If we assume that the particles grow with increasing water content, then we can infer that the electronic spectra is size dependent for the  $\text{FeS}_2$  particles. This is consistent with the formation of pyritic  $\text{FeS}_2$  which is a semiconductor. The ring pattern of the selected area electron diffraction is consistent with the structure of pyritic  $\text{FeS}_2$  and corroborates the electronic spectral data.

Iron sulfide has been studied extensively as a coal liquefaction catalyst. It is believed that pyrrhotite ( $\text{Fe}_{1-x}\text{S}$ ) is the active form of the iron catalyst under liquefaction conditions [9], and that pyrite is reduced to pyrrhotite under liquefaction conditions [10]. We have attempted to use our Fe and  $\text{FeS}_2$  (pyrite) particles as coal liquefaction catalysts. Wetting of Blind Canyon with our highly dispersed particle solutions causes coal aggregation and poor mixing. Aggregated coal which does not participate in the liquefaction process appears in the product as insoluble organic matter. Fe powder shows no improvement over thermal reactions perhaps indicating a need to sulfide the catalyst.  $\text{FeS}_2$  (pyrite) powder however shows good selectivity towards the production of low molecular weight products at the same time that the insoluble organic matter content remained high. We infer that our catalyst shows high selectivity for reducing polar functionalities within Blind Canyon. Further studies of product quality are in progress.

## Conclusions

Monodispersed, nanometer sized particles of Fe,  $\text{FeS}_2$  (pyrite), and CdS are synthesized in inverse micelle solutions. Oil rich inverse micelle solutions are characterized by a structure in which surfactant interfaces protect a polar core from the oleic phase. Iron or cadmium salts are taken up in the polar core, and the clusters are formed upon chemical reduction or chemical exchange/replacement reactions. The inverse micelles provide size and geometric constraints on the growth of the clusters and stabilize the highly dispersed sols. The effect of initial micelle size as controlled by water content influences the final particle size more than solution viscosity which regulates the nucleation and growth of the particles. We have used the size dependent electronic spectra and selected area electron diffraction to characterize the formation of pyritic  $\text{FeS}_2$ . Finally, the iron based clusters were tested as catalysts in a coal liquefaction process. While liquids wet the coal and prevent adequate mixing,  $\text{FeS}_2$  powder selectively increases conversion to low molecular weight oils.

## References

1. J.H. Jean and T.A. Ring, *Colloids and Surfaces*, **29**, 273, 1988.
2. M.L. Steigerwald and L.E. Brus, *Annu. Rev. Mater. Sci.*, **19**, 471, 1989.
3. B.H. Robinson, T.F. Towey, S. Zourab, A. Visser, and A. van Hoek, *Colloids and Surfaces* **61**, 175, 1991.
4. M. Boutonnet, J. Kizling, R. Touroude, G. Maire, and P. Stenius, *Catalysis Letters*, **9**, 347, 1991.
5. J.P. Wilcoxon and R.L. Williamson, *Mat. Res. Soc. Symp. Proc.*, **177**, 269, 1990.
6. L.M. Gan and C.H. Chew, *J. Dispersion Science and Technology*, **4**, 291, 1983.
7. G. Porod, *Small Angle X-ray Scattering*, Eds. O. Glatter and O. Kratky, pp. 24, Academic Press, 1983.
8. F.V. Stohl, Preprints of Papers Presented at the 205<sup>th</sup> ACS National Meeting, Denver, CO, 3/28-4/2/93, American Chemical Society, Division of Fuel Chemistry.
9. R.M. Davidson, *IEA Coal Research*, pp. 100, 1983.
10. T. Kotanigawa, S. Yokoyama, M. Yamamoto, and Y. Maekawa, *Fuel*, **66**, 1452, 1987.

TABLE 1. Micro-batch liquefaction results of Blind-Canyon, DECS-17 coal. Conditions: T = 400°C, P = 800 psi cold H<sub>2</sub>, t = 30 min, hexahydropyrene solvent, 2-5 wt. % catalyst. Gas analysis is not included in these results.

CATALYST	% IOM	% THF SOLS/C7 INSOLS	% C7 SOLS
thermal, average	9.9	58.0	30.1
Fe, <i>in-situ</i>	66.5	13.8	8.9
Fe, powder	6.0	60.9	30.5
Fe, surfactant	50.0	27.3	22.7
extracted liquid			
FeS <sub>2</sub> , <i>in-situ</i>	64.7	34.3	1.0
FeS <sub>2</sub> , powder	17.0	33.9	44.4
FeS <sub>2</sub> , surfactant	9.8	57.3	28.7
extracted liquid			

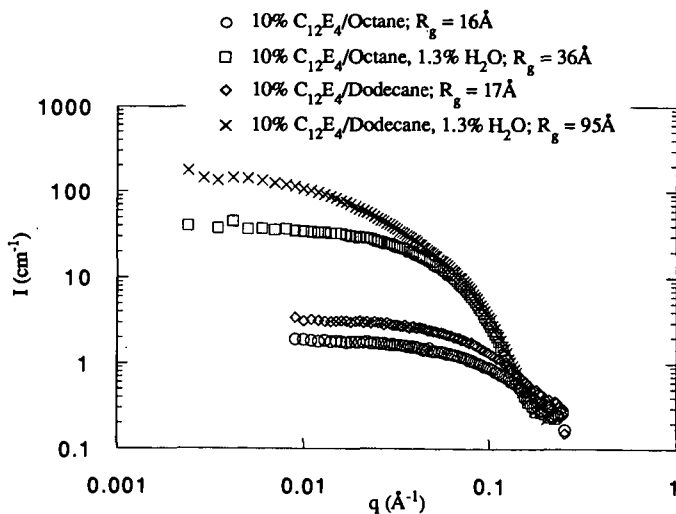


Figure 1. Small angle neutron scattering of inverse micelles. The inverse micelles grow as water concentration increases and as the oil alkane chain number increases.

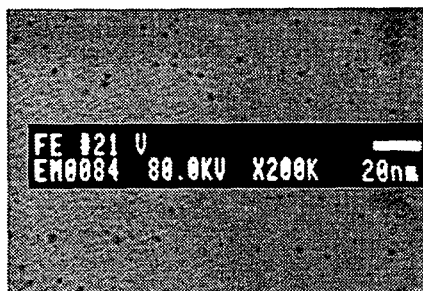


Figure 2. TEM of  $\text{FeS}_2$  (pyrite) clusters. The cluster radius is  $\sim 10\text{\AA}$ . The particles are highly dispersed and monodispersed. TEM's of Fe clusters show  $\sim 12\text{\AA}$  radius particles and CdS clusters are  $\sim 14\text{\AA}$  in radius.

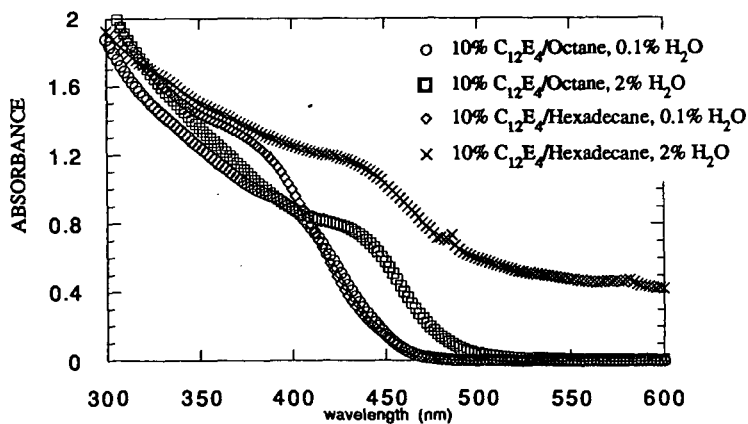


Figure 3. Electronic spectra of CdS clusters as a function of water content in two oil systems. As water content increases the absorbance maxima and onset red shift indicating an increase in the particle radius.

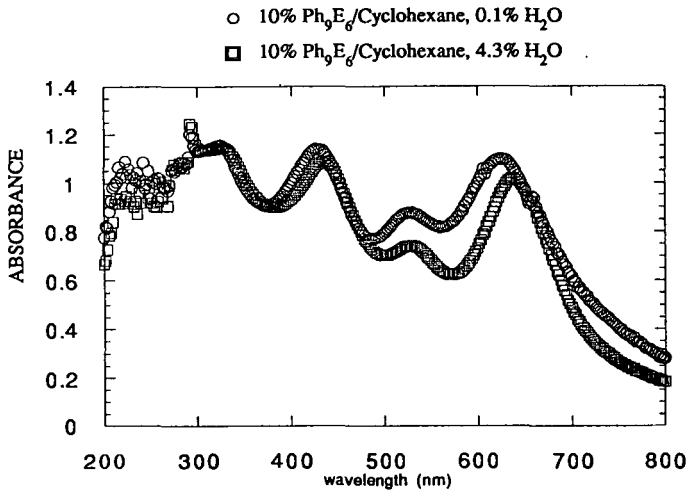


Figure 4. The electronic spectra of FeS<sub>2</sub> shows a red shift as water content increases. The size dependent band gap shift is characteristic of the semiconductor nature of pyrite.

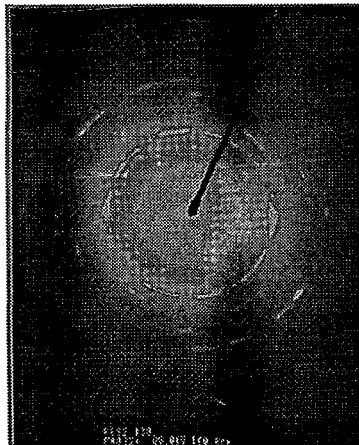


Figure 5. Selected area electron diffraction of FeS<sub>2</sub> shows a ring pattern consistent with the structure of pyrite.

## REVERSE MICELLE SYNTHESIS OF NANOSCALE METAL CONTAINING CATALYSTS

John G. Darab, John L. Fulton and John C. Linehan  
*Pacific Northwest Laboratory<sup>1</sup>, Richland, Washington 99352*

**KEYWORDS:** catalyst synthesis, EXAFS, microemulsion

### INTRODUCTION

The need for morphological control during the synthesis of catalyst precursor powders is generally accepted to be important. In the liquefaction of coal, for example, iron-bearing catalyst precursor particles containing individual crystallites with diameters in the 1-100 nanometer range are believed to achieve good dispersion through out the coal-solvent slurry during liquefaction runs and to undergo chemical transformations to catalytically active iron sulfide phases<sup>2</sup>.

The production of the nanoscale powders described here employs the confining spherical microdomains comprising the aqueous phase of a modified reverse micelle (MRM) microemulsion system as nanoscale reaction vessels in which polymerization, electrochemical reduction and precipitation of solvated salts can occur. Figure 1 shows a schematic illustration of a typical reverse micelle for the system studied here. The goal is to take advantage of the confining nature of micelles to kinetically hinder transformation processes which readily occur in bulk aqueous solution in order to control the morphology and phase of the resulting powder. A micellar approach to producing nanoscale particles has already been used on a variety of semiconductor, metal and ceramic systems<sup>3</sup>. The synthetic approach described here is unique, however, in that a much greater yield of powder can be obtained compared to the conventional reverse micelle systems (approximately 10 g/l for the MRM system vs 0.5 g/l for traditional reverse micelle systems).

We have prepared a variety of metal, alloy, and metal- and mixed metal-oxide nanoscale powders from appropriate MRM systems. Examples of nanoscale powders produced include Co, Mo-Co, Ni<sub>3</sub>Fe, Ni, and various oxides and oxyhydroxides of iron. Here, we discuss the preparation and characterization of nickel metal (with a nickel oxide surface layer) and iron oxyhydroxide MRM nanoscale powders. We have used extended x-ray absorption fine structure (EXAFS) spectroscopy to study the chemical polymerization process *in situ*, x-ray diffraction (XRD), scanning and transmission electron microscopies (SEM and TEM), elemental analysis and structural modelling to characterize the nanoscale powders produced. The catalytic activity of these powders is currently being studied.

## EXPERIMENTAL SECTION

**Powder Precursor Salts.** Ammonium ferric sulfate dodecahydrate (Fisher) and nickel sulfate hexahydrate (Fisher) were used as-received as precursor salts for iron- and nickel-bearing powders respectively.

**Preparation of the Microemulsions (MRMs).** In a 2.0-l Erlenmeyer flask 12-gm sodium dodecyl sulfate (SDS) and 80-ml of the 1.0 M aqueous metal salt solution of interest were mixed. To this slurry was added 1-l 0.12 M sodium bis(2-ethylhexyl) sulfosuccinate sodium salt (aerosol-OT or AOT) in isooctane. After rigorous stirring and gentle warming for approximately thirty minutes, an optically transparent microemulsion resulted. Two similar microemulsions were prepared using either 1.0 M aqueous sodium hydroxide or sodium borohydride in place of the metal salt containing solution. Microemulsions were used immediately after preparation.

**Preparation of Powders.** The nickel metal powder was prepared by adding sodium borohydride MRM to the nickel sulfate MRM slowly with constant stirring. Iron oxyhydroxide powder was similarly prepared by adding sodium hydroxide MRM to the ammonium ferric sulfate MRM. In both cases, after about ten minutes particle formation became apparent as the resulting microemulsion began to change color (from green to black for nickel metal formation, and from yellow/orange to red for iron oxyhydroxide formation) and scatter light. The suspension was then transferred to 500-ml nalgene centrifuge tubes and centrifuged at 6000 RPM for ten minutes. The remaining liquid was decanted off. The compacted powder at the bottom of the centrifuge tubes was then washed and centrifuged in isooctane three times. This was followed by three washings/centrifugings in each of methylene chloride and finally water. Water acidified with  $\text{HNO}_3$  was used to wash the nickel powders in order to remove salt byproducts. The wet powders were dried under vacuum at 60°C for 24 hours, then ground in a mortar and pestle.

***In Situ* Study of Particle Formation.** The sodium hydroxide MRM was added to the ammonium ferric sulfate MRM stepwise. After each addition, iron K-edge EXAFS spectra were obtained (see below) from the resulting MRM. Sodium hydroxide MRM was added until the system became translucent as a result of nucleation and precipitation of iron-bearing particles.

**EXAFS Measurements and Analysis.** Iron K-edge EXAFS spectra were obtained on beam line X19A at the National Synchrotron Light Source, Brookhaven National Laboratory. The data were recorded in a transmission mode using either powders thinly distributed onto cellophane tape, or liquids or suspensions contained in a specially prepared sample cell. For each sample, between three and fifteen scans were recorded and averaged together. Standard EXAFS data analyses were applied to the averaged data to obtain a radial distribution function (RDF)<sup>4</sup>

**Additional Characterization of Powders.** Scanning and transmission electron microscopies (SEM and TEM) and powder x-ray diffraction (XRD) were performed on the as-prepared powders. A portion of the as-prepared iron oxyhydroxide powder was sent out to a commercial analytical lab (Desert Analytical, Tuscon, Arizona) to be analyzed for Fe, C, S, Na and N.

## RESULTS AND DISCUSSION

**Nickel Powder.** Figure 2 shows an SEM micrograph of the as-prepared MRM nickel powder, indicating that the powder consists of irregularly shaped, sponge-like particles with diameters of 1-10 microns. The particles appear to be aggregates of extremely fine crystallites. XRD analysis confirms the formation of phase-pure nickel metal with an average crystallite size of 12-nm. No oxide phases were detected by XRD. However, energy dispersive spectroscopy (EDS) performed in the scanning electron microscope did detect the presence of oxygen, presumable in the form of a thin oxide layer on the surface of the nickel metal particles. Elemental and BET surface area analyses have not yet been performed on this powder.

The sponge-like morphology of the nanoscale MRM nickel metal powder, which presumably has a high surface area, makes it ideal as a highly dispersible catalyst for various industrial processes. As with most metal surfaces, a ubiquitous metal oxide layer is present on the surface of these nanoscale nickel powders; however, the total oxide content must be less than several weight percent due to the fact that no oxide phases are detected via XRD.

**Iron Oxyhydroxide Powder.** The dried powder consisted predominantly of irregularly shaped particles with diameters of 1-10 microns. TEM analysis on individual particles reveals no resolvable microstructural features, indicating that the particles are either amorphous or agglomerates of nanometer size crystallites. XRD analysis indicates that the powder has the same diffraction pattern as an iron oxyhydroxide phase typically referred to as two-line ferrihydrite<sup>5</sup>. The elemental analysis of the as-prepared powder shows that it contains 45.62 wt% Fe, 11.62 wt% C, 2.56 wt% S, 0.17 wt% Na and 0.12 wt% N. EDS analysis on the powder confirmed the presence of carbon and sulfur. BET analysis indicates that the surface area of the as-prepared powder is greater than 200-m<sup>2</sup>/gm.

**Aqueous Chemistry of Iron(III) Species.** Most 1 M aqueous iron(III) salts in bulk acidic non-complexing solutions contain octahedrally coordinated iron(III)-aquo monomeric complexes,  $[\text{Fe}(\text{H}_2\text{O})_6]^{3+}$ , in equilibrium with dimeric  $[\text{Fe}_2(\text{H}_2\text{O})_8(\text{OH})_2]^{4+}$  and trimeric  $[\text{Fe}_3(\text{H}_2\text{O})_9(\text{OH})_4]^{5+}$  species<sup>6,8</sup>. The addition of base (e.g.  $\text{NH}_3$ ,  $\text{NaOH}$ , etc.) to the non-complexing aqueous iron(III) salt solution causes polymerization of the monomeric, dimeric and cyclic trimeric species. In general, polymerization at ambient temperatures occurs via deprotonation of one or two aquo ligands and subsequent ololation which forms predominantly edge sharing linkages<sup>6,7</sup>. Livage *et al.*<sup>7</sup> discuss the formation of cyclic trimers via the ololation of hydrolyzed monomers with dimers. The addition of another monomer yields a planar tetramer. Further ololation between tetramers yields double straight-chain polymers.

Under appropriate pH conditions, sulfate ligands can chelate and remain strongly bound to the iron(III) cation even after particle precipitation, giving rise to sulfated iron oxyhydroxides with disordered polymer chains (e.g. kinked- or straight-single chain polymers)<sup>5,7</sup>. Since the synthetic technique employed here uses sulfate salts, and sulfate and sulfonate containing surfactants, these issues become critical. Chemical and structural analyses of the resulting MRM powders will be used to identify the role of sulfo ligands in the powder preparation process.

The elemental analysis of the as-prepared iron oxyhydroxide powder indicates that an appreciable amount of sulfur has been incorporated into the powder product (iron-to-sulfur molar ratio equals 10.2). Since the elemental analysis also indicates that the molar ratio of carbon-to-sulfur is 12.1 and very little sodium is incorporated into the as-prepared powder, the complexation of the iron(III) cation by dodecyl sulfate groups from the SDS seems most probable. Whether these sulfate groups actually take part in the polymerization reactions occurring in the aqueous cores of the reverse micelles or become associated with the particle surface after precipitation is still uncertain.

**Structural Modelling of the Iron-Bearing Powder.** Extracting the average number of nearest neighbors from an EXAFS spectrum, especially from those obtained from highly disordered systems (i.e., solutions, suspensions, and amorphous materials) and/or nanometer size grains like those being currently studied, often yields values which are suspect due to structural disorder and Debye-Waller damping<sup>9</sup>. Thus, only comparisons between the various nearest neighbor distances determined from the EXAFS spectra of bulk standards and of *in situ* studies of the MRM system will be considered as valid criteria in trying to elucidate the structure of the iron-bearing particles being formed.

There are primarily seven basic oxide and oxyhydroxide phases of iron which could form under the conditions used in this work: goethite ( $\alpha$ -FeOOH), akaganeite ( $\beta$ -FeOOH), lepidocrocite ( $\gamma$ -FeOOH), feroxyhyte ( $\delta'$ -FeOOH), two-line ferrihydrite (unknown structural formula), six-line ferrihydrite (see below) and hematite ( $\alpha$ -Fe<sub>2</sub>O<sub>3</sub>)<sup>5</sup>.

Goethite, akaganeite and lepidocrocite are all composed of different arrangements of double straight polymer chains connected via corner or edge sharing bonds. The primary structural order in all of these phases, i.e. the bonding in the double straight chains, are identical<sup>8</sup> and thus yield identical oxygen and iron first nearest neighbor shell radii.

In contrast, feroxyhyte, six-line ferrihydrite and hematite are built up from polymer chains and sheets containing a combination of edge, face and corner sharing linkages, and are thus distinguished from the double straight chain-based phases at the primary structural level. These three phases are all structurally similar in that two layers of the edge, face and corner sharing polymer sheets make up the feroxyhyte structure, while that of the six-line ferrihydrite contains four layers, and that of hematite contains six layers.

In terms of the oxygen and iron first nearest neighbor radii determined using EXAFS then, one can discuss whether the primary structural order of the MRM derived powder is goethite-like or hematite-like. Figure 3 shows the oxygen and iron first nearest neighbor radii determined from the EXAFS RDFs plotted versus the [OH]/[Fe] ratio. Note that as the [OH]/[Fe] ratio increases, the iron first nearest neighbor distance systematically decreases and approaches those representative of bulk phases. This indicates that the iron oxyhydroxide polymers, which may be incorporating some sulfate groups, are becoming larger and more highly condensed. The oxygen nearest neighbor distance initially increases with increasing [OH]/[Fe] ratio but then decreases and eventually approaches those representative of bulk phases. The reason for this behavior in the oxygen nearest neighbor distance is uncertain. After precipitation occurs ([OH]/[Fe] = 2.03) and the resulting powder is washed and dried, the oxygen and iron

first nearest neighbor distances become identical to those found in the goethite phase. We thus conclude that the particles formed in the MRM system are goethite-like in structure.

The XRD pattern for the proto-goethite MRM powder, however, is not representative of bulk goethite but of two-line ferrihydrite, the structure of which is still not well understood. Although two-line ferrihydrite is structurally disordered<sup>5</sup>, its primary structural has been previously investigated using EXAFS<sup>10,11</sup> and has been shown to be similar to that of goethite<sup>12</sup>. We suggest that the iron bearing powder being produced by the MRM process indeed has a goethite-like primary structure but lacks the necessary long-range order observed in bulk goethite, indicating that the particles are extremely small and/or disordered and are most likely in an early stage of development. At such early developmental stages, goethite, akaganeite and lepidocrocite are all structurally identical, i.e., double or disordered double straight polymer chains. Akaganeite and lepidocrocite generally do not form under the conditions used in this work; therefore, as a matter of convenience we have labeled this phase of the as-prepared MRM powder as "proto-goethite".

This proto-goethite structure, which may be related to two-line ferrihydrite, consists of double straight chains or disordered double straight chains with iron and/or oxygen vacancies linked together to form a secondary structure having, at best, limited order. The suggestion that the double straight chains are possibly disordered should not be surprising as it was previously noted that the presence of sulfate anions in the aqueous cores of the reverse micelles could become incorporated into the growing polymer, producing such disordered structures.

## SUMMARY

Using a modified reverse micelle process, tens-of-gram per liter quantities of micron sized particles of nanoscale nickel metal and iron oxyhydroxide were produced. The as-prepared nickel metal particles were found to consist of agglomerates of nanometer sized crystallites of nickel having a surface oxide layer. The as-prepared iron oxyhydroxide particles were determined to be either amorphous or agglomerates of nanometer sized crystallites having a structure which is proto-typical to that of goethite.

## ACKNOWLEDGEMENTS

This work was supported by the U.S. Department of Energy, Office of Fossil Energy under contract DE-AC06-76RLO 1830 and the Advanced Processing and Technology Initiative.

The assistance of Y. Ma in the collection and analysis of the EXAFS data was most appreciated.

## REFERENCES

1. Pacific Northwest Laboratory is operated for the United States Department of Energy by the Battelle Memorial Institute.
2. (a) Pradhan, V.R.; Tierney, J.W.; Wender, I.; Huffmann, G.P. *Energy & Fuels* 1991, 5, 497. (b) Pradhan, V.R.; Herrick, D.E.; Tierney, J.W.; Wender, I. *Energy & Fuels* 1991, 5, 712.
3. Steigerwald, M.L.; Brus, L.E. in *Structure and Reactivity in Reverse Micelles*; Pileni, M.P., ed.; Elsevier: New York, 1989; pp. 189-220.
4. Stern, E.A.; Heald, S. in *Handbook of Synchrotron Radiation*; Eastman, D.E., Farge, Y., Koch, E.E., eds.; North Holland: Amsterdam, 1980.
5. Schertmann, U.; Cornell, R.M. *Iron Oxides in the Laboratory*; VCH: New York, 1991.
6. Flynn, C.M. *Chem. Rev.* 1984, 84, 31.
7. Livage, J.; Henry, M.; Sanchez, C. *Prog. Solid State Chem.* 1988, 18, 259.
8. Baes, C.F.; Mesmer, R.E. *The Hydrolysis of Cations*; John Wiley and Sons: New York, 1976; pp. 226-237.
9. Lee, P.A.; Citrin, P.H.; Eisenberger, P.; Kincaid, B.M. *Reviews of Modern Physics* 1981, 53, 759.
10. Charlet, L.; Manceau, A.A. *J. Coll. Int. Sci.* 1992, 148, 443.
11. Combes, J.M.; Manceau, A.; Calas, G.; Bottero, J.Y. *Geochim. Cosmochim. Acta* 1989, 53, 583.
12. Manceau, A.; Combes, J.M. *Phys. Chem. Miner.* 1988, 283.

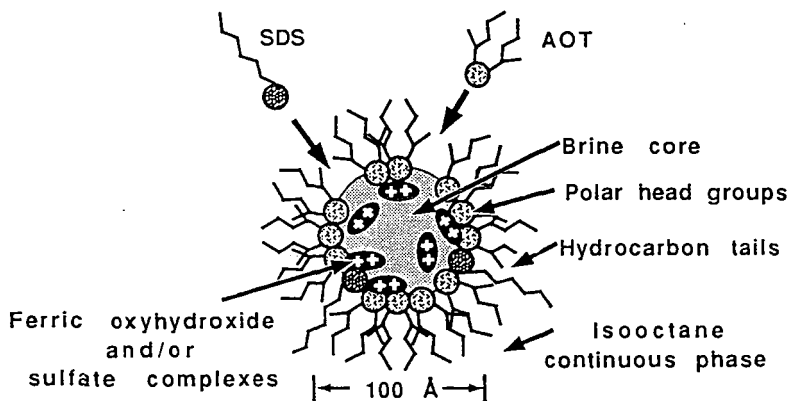


Figure 1. Schematic illustration of a typical reverse micelle for the system studied here.

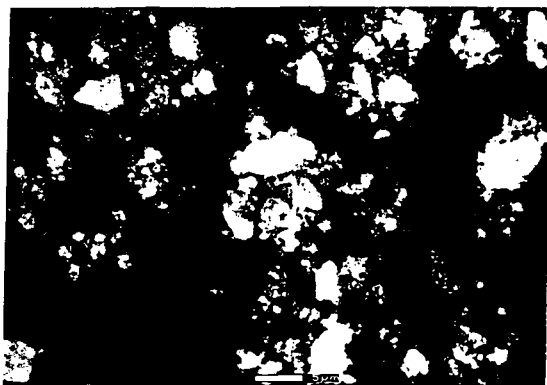


Figure 2. Scanning electron micrograph of the MRM derived nickel metal powder.

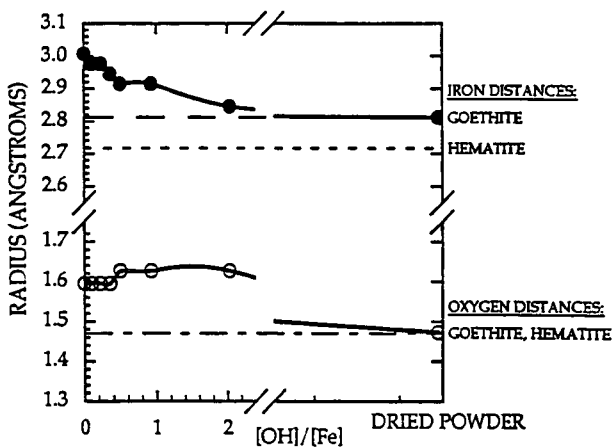


Figure 3. Oxygen and iron first nearest neighbor distances determined from the iron K-edge EXAFS of the ammonium ferric sulfate/ sodium hydroxide MRM microemulsion mixture for various [OH]/[Fe] ratios. Also indicated are the nearest neighbor distances determined for bulk goethite and hematite.

# Influence of Nanoscale $\text{Fe}_{(1-x)}\text{S}$ Particles on Coal Liquefaction

G T Hager, X X Bi, P. C. Eklund, F. J. Derbyshire  
Center for Applied Energy Research  
University of Kentucky, Lexington, KY 40511

## ABSTRACT

It has been shown that during the process of coal liquefaction, iron based catalyst precursors transform to pyrrhotite in the presence of sufficient sulfur. Due to this transformation, the activity of the catalyst initially added relative to the transformed catalyst is not known. In an attempt to address this question, the activity of nanoscale particles of pyrrhotite ( $\text{Fe}_{1-x}\text{S}$ ), generated by a laser pyrolysis technique, is being studied for the direct liquefaction of a subbituminous coal. Their activity is being compared to that of a similarly prepared iron carbide that is sulfided in situ. The particles produced by this technique have a similar size range and distribution. Comparative studies of the changes in phase and particle size of the catalysts during coal liquefaction experiments are determined by XRD and Mössbauer spectroscopy.

## INTRODUCTION

The utility of iron based coal liquefaction catalysts has been known for almost a century. The basis for their use is a combination of moderate activity and relatively low cost, compared to more active catalysts such as Mo, Ti, Ni, etc. A "red mud" iron oxide catalyst precursor was first used in commercial coal liquefaction. It was found that the addition of sulfur with the iron oxide precursor improved the processing of low sulfur coals.[1] Since then, numerous studies have examined different iron phases such as oxides, sulfides, carbides, and organometallic compounds as catalyst precursors. In most of these studies the addition of a source of sulfur has been shown to increase the catalyst activity and selectivity.

Three methods are generally used to introduce the catalyst to the coal. The first is the

physical mixing of a finely divided solid catalyst into the coal feed slurry. This is relatively straightforward and has been used extensively. The second is the addition of an oil-soluble catalyst precursor, such as iron pentacarbonyl, to the coal feed slurry. This method allows almost infinite initial dispersion of the iron. The third method is the addition of the iron to the coal itself, using either an ion exchange technique or by precipitation of a water soluble iron compound within the coal matrix. The former method can only be applied to low rank coals.

Regardless of the method of addition or the precursor composition, in the presence of sulfur the final form of the iron is generally pyrrhotite. Many studies propose that pyrrhotite ( $\text{Fe}_{1-x}\text{S}$ ) [2,3,4,10] is the active form of iron based catalysts. Indeed, pyrrhotite is the thermodynamically favored phase under liquefaction conditions in the presence of sufficient sulfur. Research has shown that a variety of iron based precursors including oxides [10], sulfides [5,6], carbides [13], and carbonyls [2,3,9] are transformed to pyrrhotite during coal liquefaction.

Some studies have been made of the kinetics of transformation of the precursor to the sulfide. Montano et al. [5,6] used *in situ* Mössbauer spectroscopy to study the decomposition of pyrite, to pyrrhotite and  $\text{H}_2\text{S}$ , in hydrogen and under liquefaction conditions. It was found that the onset of the transformation to pyrrhotite occurs at  $\sim 300^\circ\text{C}$  and is nearly complete at  $\sim 400^\circ\text{C}$ . The activation energy of the transformation decreased with decreasing particle size. Larger pyrite particles were reported to break during the transformation yielding smaller pyrrhotite particles. It was concluded that both  $\text{H}_2\text{S}$  and pyrrhotite are active as catalysts for the liquefaction process. Others have attributed the catalytic activity of pyrite to  $\text{H}_2\text{S}$  alone [11], arguing that the low surface area of pyrite should make it a very poor catalyst. This view agrees with the finding that pyrite and pyrrhotite do not exhibit any catalytic effect for the gasification of graphite [14]. The view of a synergistic effect between pyrrhotite and  $\text{H}_2\text{S}$  has been reached by other workers using both pyrite and iron oxide [10].

In a study of the liquefaction of a Victorian brown coal [8], using hematite, iron carbonyl, and impregnated iron acetate as catalyst precursors, it was concluded that, in the absence of added sulfur, the active form of the iron catalyst was reduced  $\alpha\text{-Fe}$ . This concurs with the results of a study which found that metallic iron promoted the catalytic hydrogenation of graphite at temperatures below  $1000^\circ\text{C}$  while pyrite and pyrrhotite showed no catalytic activity [14]. More recently, Weng et al. [15] have proposed that, while a synergistic effect between pyrrhotite and  $\text{H}_2\text{S}$  promotes coal liquefaction,  $\gamma\text{-Fe}$  is a more active catalyst than pyrrhotite. The fact that a substantial amount of  $\text{Fe}_3\text{C}$  was also formed during the reaction may indicate that insufficient sulfur was present for conversion of the precursor to pyrrhotite. This may be the reason for the  $\gamma\text{-Fe}$  formation.

As this brief summary indicates, the relationship between the phase of the iron catalyst and its activity is not fully understood. Neither is there any clear information

about the kinetics of precursor sulfiding, and the factors which influence this reaction. The relevance of these statements is that, even assuming that iron sulfide is an active liquefaction catalyst, the active phase may not be present during some of the critical initial reactions of coal dissolution.

The purposes of this work are to attempt to resolve these questions through: examining the effect of nanoscale iron carbide catalyst on coal liquefaction; determining the kinetics of *in-situ* sulfiding of the iron carbide; and comparing the performance when the catalyst is added in the form of nanoscale pyrrhotite. Both phases of the iron will be formed by a laser pyrolysis technique, described in detail elsewhere[13], which will ensure that the precursor particles have approximately the same size distribution. Previous studies have shown that the  $Fe_7C_3$  particles transform to pyrrhotite, in the presence of added sulfur under liquefaction conditions, while retaining their small size[13]. By comparing the activity of the presulfided catalyst to the catalyst sulfided *in situ*, the relative activity of the two may be defined. This will allow a better appreciation of the importance of sulfiding kinetics, and the attainment of the active phase, to be determined.

## EXPERIMENTAL

The coal used is a -200 mesh subbituminous Black Thunder coal which is stored in sealed foil bags prior to use, in order to reduce the effects of air oxidation. The native iron content of the coal is 0.17wt%. In liquefaction experiments 3 grams of coal and 5 grams of tetralin are charged into a 50 ml stainless steel tubing bomb reactor. The catalyst loading is 1 wt% Fe to coal. The reactors are constructed with a horizontal orientation to reduce any mass transfer limiting effects. Dimethyl disulfide (DMDS) is added at 120% of the calculated amount required for transformation of the precursor to pyrite. The sealed bombs are purged and pressurized with hydrogen to 1000 psig (cold) prior to reaction.

The bombs are agitated vertically at ~400 cycles/min while immersed in a heated fluidized sand bath. The reactions are carried out for up to 30 minutes, and at temperatures between 385°C and 415°C. Following reaction, the tubing bomb is removed from the heated sand bath and quenched in a cool sand bath. A gas sample is taken from the cooled reactor and analyzed by GC.

The products of the liquefaction experiments are analyzed by solubility class. The reactor contents are extracted with THF to determine the total conversion to THF soluble products. The THF solubles are then precipitated with pentane. The pentane soluble product is defined as the oil fraction while the insoluble portion is defined as the preasphaltene + asphaltene fraction. The THF insoluble fraction is defined as the IOM fraction. The gas yield is determined by GC and the oil yield is determined by difference.

The spent catalyst is contained in the IOM fraction and is characterized by XRD and Mössbauer spectroscopy to determine the phase and approximate size of the iron based catalyst after reaction.

## RESULTS

In order to determine the behavior of the iron carbide particles under liquefaction conditions, tubing bomb experiments were carried out in the absence of added coal. As reported elsewhere[13], it was determined by XRD that the iron carbide particles transform to pyrrhotite in the presence of added sulfur within 30 min at 385°C. Further, analysis of TEM micrographs show that the particles retain their small size and relatively narrow size distribution, with the exception of the formation a few larger crystallites.

In liquefaction studies using a subbituminous Wyodak coal the iron carbide showed moderate catalytic activity, similar to that of iron pentacarbonyl. The catalyst loading in both cases was 1 wt% Fe. The iron carbide increased the total conversion by ~10% over the thermal baseline in the temperature range from 350°C to 440°C. Further, the catalyst caused an apparent increase in the selectivity to oils over the temperature range ~350°-400°C.

The method of production of the nanoscale iron carbide particles by laser pyrolysis has been reported elsewhere.[13] A modification of this process was used to produce the nanoscale pyrrhotite. A reactant gas stream of ethylene and hydrogen sulfide is intersected with the beam from a tunable CO<sub>2</sub> laser. The pyrrhotite particles are formed in the small pyrolysis zone formed at this intersection. The size of the particles can be controlled by adjusting the reaction parameters. XRD has identified the phase of the particles as Fe<sub>(1-x)</sub>S with an average diameter of ~10nm. Work is currently in progress to determine the catalytic activity of the nanoscale pyrrhotite particles as well as their behavior during the liquefaction process.

## SUMMARY

The results of this study will allow the kinetics of the transition of iron carbide to the sulfide to be determined, and whether the transformation is sufficiently rapid so that an active catalyst is present during coal dissolution. By using two different catalysts produced by the same technique the influence of size effects on the activity are reduced. XRD and Mössbauer spectroscopy are used to determine the phase of the catalyst after the reaction. The relative importance of attainment of the active phase during the initial stages of liquefaction will be discussed.

## ACKNOWLEDGEMENTS

This work was supported in part by the Department of Energy through the Consortium for Fossil Fuel Liquefaction Science DE-FC22-90PC90029 (PCE, XXB).

## REFERENCES

- 1) Wu W R W, Storch H H, Hydrogenation of Coal and Tar, Bulletin 633, Washington, DC, USA, US Dept of the Interior, Bureau of Mines, 195pp, 1968
- 2) Herrick D E, Tierney J W, Wender I, Huffman G P, Huggins F E, *Energy & Fuels* **4**, 231-6, 1990
- 3) Suzuki T, Yamada O, Takahashi Y, Watanabe Y, *Fuel Proc. Tech.*, **10**, 33-43, 1985
- 4) Sweeny P G, Stenberg V I, Hei R D, Montano P A, *Fuel*, **66**, 532-41, 1987
- 5) Montano P A, Vaishnava P P, King J A, Eisentrout E N, *Fuel*, **60**, 712-6, 1981
- 6) Montano P A, Bommannavar A S, Shah V, *Fuel*, **60**, 703-11, 1981
- 7) Cook P S, Cashion J D, *Fuel*, **66**, 669-77, 1987
- 8) Cook P S, Cashion J D, *Fuel*, **66**, 661-8, 1987
- 9) Kamiya Y, Nobusawa T, Futamura S, *Fuel Proc. Tech.*, **18**, 1-10, 1988
- 10) Wang L, Cui Z, Liu S, *Fuel*, **71**, 755-9, 1992
- 11) Lambert J M Jr, *Fuel*, **61**, 777-8, 1982
- 13) Hager G T, Bi X X, Derbyshire F J, Eklund P C, Stencel J M, ACS Div. of Fuel Chem. Preprints, **36(4)** 1900-8, 1991
- 14) Cypres R, Ghodsi M, Stocq R, *Fuel*, **60**, 247-50, 1981
- 15) Weng S, Wang Z, Gao J, Cheng L, Wu Z, Lin D, Yu Y, Zhao C, *Hyperfine Interactions*, **58**, 2635-39, 1990

## COAL-LIQUEFACTION CATALYSTS FROM FERRIC SULFIDE DISPROPORTIONATION

Dady B. Dadyburjor, W.R. Stewart, A.H. Stilller,  
C.D. Stinespring, J.-P. Wann and J.W. Zondlo  
Department of Chemical Engineering, P.O. Box 6101  
West Virginia University  
Morgantown, WV 26506-6101

Keywords: Catalysis, Coal liquefaction, Ferric sulfide disproportionation

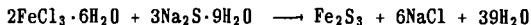
### INTRODUCTION

The use of iron-based catalysts of small particle sizes in the liquefaction of coal is widespread in laboratories and in practice due to the cost-efficiency of the catalyst and the ability of the small particles to penetrate the pore structure of the coal, at least to some extent. Of the iron-based catalysts, pyrite (PY,  $\text{FeS}_2$ ) is found indigenously in coal and has a well-documented ability [1] to enhance liquefaction rates. PY is known [2] to be converted to nonstoichiometric pyrrhotite (PH,  $\text{FeS}_x$ ,  $x \approx 1$ ) under hydrogen atmospheres at high temperatures and pressures, conditions expected in liquefaction. Whether PY or PH or a combination of the two is the catalytically active agent is a matter of current debate.

We have developed mixtures of PY and PH of small crystallite size. The mixtures contain different PH stoichiometries, and different amounts of PH and PY in intimate contact. The expectation is that the different valencies of Fe in atomic-range proximity give rise to a very efficient catalyst. These mixtures are made by disproportionating ferric sulfide ( $\text{Fe}_2\text{S}_3$ ) at various temperatures and for various times. The PH/PY ratio and the value of  $x$  defined above change with these disproportionation parameters.

### EXPERIMENTAL PROCEDURE

Ferric sulfide is prepared by mixing stoichiometric amounts of ferric chloride and sodium sulfide in a cold room below  $5^\circ\text{C}$ . The formation of ferric sulfide is instantaneous, following the reaction:



PH, PY and elemental S are the products of disproportionation, through a general reaction of the type:



The solid is washed to remove NaCl and dried. A portion of the resulting solid is separated into PH (soluble in 6M HCl) and PY (soluble in 8M  $\text{HNO}_3$ ), and the amount of Fe in each of these sulfide forms is analyzed by atomic absorption (AA). The rest of the solid is mixed with coal, solvent tetralin and  $\text{CS}_2$  presulfider for the liquefaction runs. Occasionally the solid is analyzed by X-ray diffraction (XRD) and Auger Electron Spectroscopy (AES).

Liquefaction runs were carried out in a batch tubing-bomb reactor with vertical agitation. Most experiments were performed on DECS-17 coal, a low-PY, high-exinite material. After liquefaction, the solid is analyzed for

conversion (THF-soluble material) and asphaltenes/preasphaltenes (THF-soluble, hexane-insoluble material). The amount of oil (+ gas) is obtained by difference. The THF-insoluble solid is analyzed for PH and PY.

## RESULTS

Ratios of pyrrhotite to pyrite (PH/PY) in the products of  $\text{Fe}_2\text{S}_3$  disproportionation are shown as a function of disproportionation temperature,  $T_d$ , in Table I. Note that elemental S is not shown. Table I indicates that the room-temperature disproportionation yields only PH, for all practical purposes. Increasing  $T_d$  increases the relative amount of PY in the solid. Only a few S peaks are visible in the X-ray diffraction XRD pattern for the room-temperature case; presumably the PH crystallites are too small to exhibit peaks. Disproportionation at a temperature  $T_d = 100^\circ\text{C}$  shows significant PY peaks but smaller S peaks; again the PH crystallites are X-ray-invisible. When  $T_d = 200^\circ\text{C}$ , the PH crystallites are large enough to exhibit peaks, PY peaks are larger than at  $T_d = 100^\circ\text{C}$ , and S peaks are vanishingly small.

Auger electron spectra for the PH/PY mixture after  $T_d = 200^\circ\text{C}$  are shown in Figure 1. The shape of the Fe line at around 40 eV indicates that PH of composition  $\text{Fe}_7\text{S}_8$  ( $x = 1.143$ ) is present. Further, the line shape for S indicates that the elemental form is present. The intensity ratios of the S (LVV) peak to the Fe (LMM) are plotted in Figure 2 as a function of the ratio S/Fe for standard samples of  $\text{FeS}_2$  and  $\text{Fe}_7\text{S}_8$ . Also shown in Figure 2 is the intensity ratio for the product corresponding to  $T_d = 200^\circ\text{C}$ . This allows one to estimate the amount of surface S (elemental and ionic) to surface Fe for the disproportionated product.

The PH/PY ratio of the catalyst changes after liquefaction. As can be seen in Table I, the changes depend upon both  $T_d$  and  $T_\ell$ . Table II shows the changes in the S/Fe ratio in the iron-based catalyst after liquefaction at  $T_\ell = 350^\circ\text{C}$  as a function of  $T_d$ .

In Figure 3 are plotted the overall conversion, asphaltene/preasphaltene yield and oil (+ gas) yield for DECS-17 coal as a function of the S/Fe ratio of the iron-based catalyst after liquefaction at  $T_\ell = 350^\circ\text{C}$ . Other choices of the independent variable obviously exist, yet this one appears to give linear relationships for conversion and yields. Results for the unsulfided catalysts, and for liquefaction at  $T_\ell = 400^\circ\text{C}$  with sulfided and unsulfided catalysts, have been tabulated elsewhere [3]. We did not test catalyst prepared at disproportionation temperatures higher than  $200^\circ\text{C}$  for conversion of DECS-17 coal. However, previous work [4] using Humphrey mine coal (Pittsburgh No. 8 seam) indicates that catalysts corresponding to a PH/PY ratio of unity ( $T_d = 200^\circ\text{C}$ ) have higher conversions and oil (+ gas) yields than those corresponding to larger and smaller ratios ( $T_d = 100^\circ\text{C}$ ,  $250^\circ\text{C}$ ). These results are shown in Figure 4. Because of the superior performance of the catalyst formed by disproportionation at  $200^\circ\text{C}$  for 1 h, we concentrated on this catalyst for further evaluation.

To investigate the efficacy of catalyst-coal mixing, a catalyst impregnation procedure was attempted and conversions and yields were compared to those from the "standard" catalyst preparation procedure described above. In the impregnation procedure, an aqueous solution of  $\text{FeCl}_3$  was sonicated with coal, then  $\text{Na}_2\text{S}$  was added, followed by additional sonication. After

disproportionation at 200°C for 1 h, the solid was washed with distilled water to remove NaCl, dried and then placed in the liquefaction reactor with tetralin and CS<sub>2</sub>. The conversion and oil (+ gas) yield after liquefaction at T<sub>l</sub> = 350°C for 1 h are shown in Figure 5 as catalyst preparation IDW. Also shown in Figure 5 are liquefaction results for preparation procedure IWD, wherein the washing step was carried out between impregnation and disproportionation. Comparing the results of these procedures with the "standard" procedure, labelled DWM, shows that impregnation of the catalyst yields no particular advantage.

Also shown in Figure 5 are the effects of various NaCl-washing techniques on liquefaction. In procedure DNM, the catalyst was mixed directly after disproportionation, without any washing step. Conversions and yield are noticeably lower than DWM, where the washing step is not omitted. Finally, in procedure DWAM, the catalyst was disproportionated and washed (as in DWM), but then a calculated amount of NaCl was added to the solid before mixing with coal. The liquefaction results here are very similar to those where washing was eliminated, thus indicating that the washing step eliminates only the NaCl. In Figure 5, NC represents the results for thermal liquefaction, with no catalyst addition.

Figure 6 shows the effect of catalyst loading on the overall conversion and the yield of oil (+ gas). The loading of the PH/PY mixture catalyst affects the conversion and oil (+ gas) yield of DECS-17 coal in a nonlinear manner. The conversion increases for upto 1 percent loading; at higher loadings, the conversion continues to increase but to a lesser extent. At low catalyst loadings, the yield of oil (+ gas) is less than under non-catalytic conditions. The yield is a minimum around 1 percent loading, after which the yield increases.

Finally, it is worth comparing the disproportionated catalyst with other iron-based catalysts. Figure 7 shows the overall conversion and the oil (+ gas) yield for the case of no catalyst (NC), the catalyst mixture after T<sub>d</sub> = 200°C (DFS), and an iron oxide catalyst, FeOOH, developed by Mobay Corporation and provided by Dr. Farcasiu, USDOE/PETC. Results of this catalyst are labelled IO in Figure 7. Liquefaction in each case was at T<sub>l</sub> = 350°C for 1 h.

For DFS and IO, catalyst was added corresponding to 0.5 percent Fe. The DFS catalyst was prepared according to the "standard" procedure described above. Figure 7 shows that conversions for the two sulfided catalysts are comparable and greater than the (sulfided) NC case. Unsulfided IO is comparable to the unsulfided NC. Sulfiding improves IO considerably. The yields of oil (+ gas) with both catalysts are smaller than for the NC case, with the DFS yield being somewhat less than the IO yield. This is consistent with Figure 6 which shows the oil (+ gas) yield decreasing for small additions of catalyst (less than 1 percent).

## CONCLUSIONS

Hydrothermal disproportionation of ferric sulfide yields a mixture of iron sulfides and elemental sulfur. The sulfides, FeS<sub>2</sub> and various pyrrhotites FeS<sub>x</sub>, are present as intimately mixed crystallites in small particles. The relative amount and composition of the FeS<sub>x</sub> can be controlled by varying the time and temperature of disproportionation. Thus these iron sulfides are suitable catalysts for coal liquefaction. The activity and selectivity of

these catalysts are comparable to those of other iron-based catalysts.

#### ACKNOWLEDGMENTS

The work was conducted under U.S. Department of Energy Contract No. DE-FC22-90PC90029 under the Cooperative Agreement to the Consortium for Fossil Fuel Liquefaction Science. The authors gratefully acknowledge the support.

#### REFERENCES

1. Shah, Y.T., Reaction Engineering in Direct Coal Liquefaction, Addison-Wesley, Reading, MA (1981).
2. Jagadeesh, M.S. and M.S. Seehra, J. Phys. D 14, 2153 (1981); Montano, P.A., A.S. Bommannavar and V. Shah, Fuel 60, 703 (1981).
3. Stansberry, P.G., J.-P. Wann, W.R. Stewart, J. Yang, J.W. Zondlo, A.H. Stiller and D.B. Dadyburjor, Fuel, accepted (1992).
4. Stansberry, P.G., J. Yang and J.-P. Wann, Paper presented at AIChE Annual Meeting, Los Angeles, CA (1991).

TABLE I

Pyrrhotite/Pyrite (PH/PY) Ratio Before and After Liquefaction as Functions of Disproportionation Temperature ( $T_d$ ) and Liquefaction Temperature ( $T_l$ ).

$T_d$ [°C]	PH/PY Ratios		
	Before Liquefaction	After Liquefaction	
		$T_l = 350^\circ\text{C}$	$T_l = 400^\circ\text{C}$
25	286	2.5	8.4
100	1.8	5.7	3.2
200	0.87	0.38	0.13

TABLE II

Final S/Fe Ratio in PH/PY Mixtures After Liquefaction at  $T_l = 350^\circ\text{C}$

$T_d$ [°C]	S/Fe
25	1.3
100	1.4
200	1.7

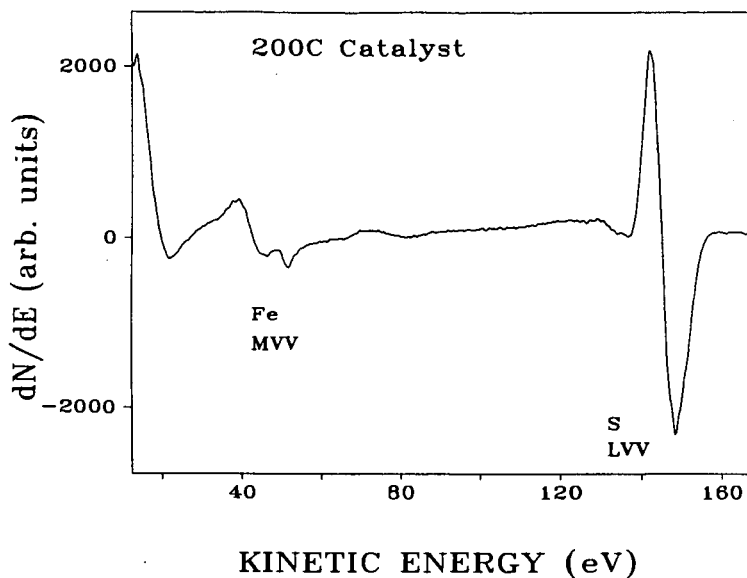


Figure 1. Auger electron spectrum for disproportionated catalyst,  $T_d = 200^\circ\text{C}$ .

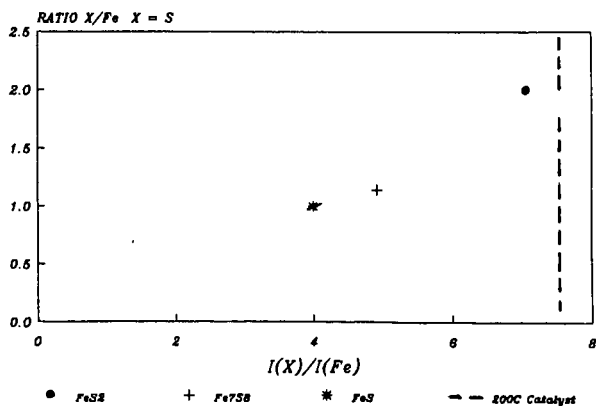


Figure 2. Sensitivity factors of Fe and S for  $\text{FeS}_2$ ,  $\text{Fe}_7\text{S}_8$ , and disproportionated catalyst,  $T_d=200^\circ\text{C}$ .

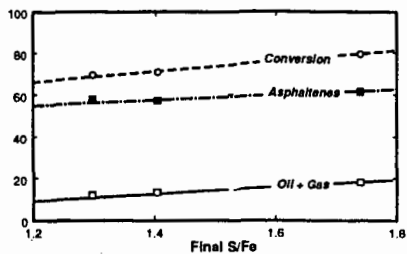


Figure 3. Conversion and yields of preasphaltenes/asphaltenes and oil(+gas) from DECS-17 coal as functions of the final S/Fe ratio of catalyst.

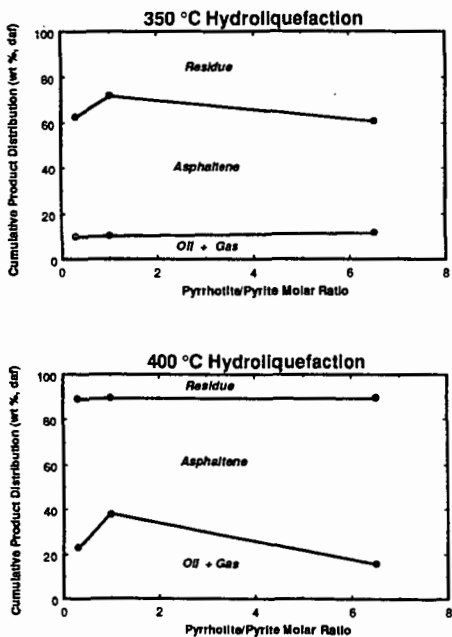


Figure 4. Conversion and yield of oil (+gas) as functions of PH/PY for liquefaction of Humphrey Mine coal [4].

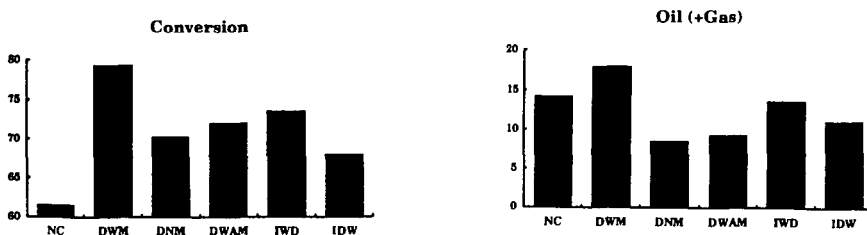


Figure 5. Conversion and yield of oil(+gas) for various procedures of catalyst manufacture. See text for nomenclature.

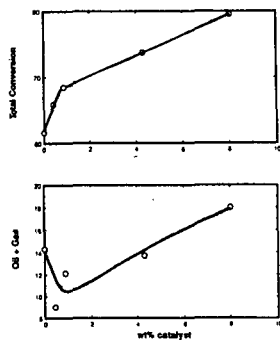
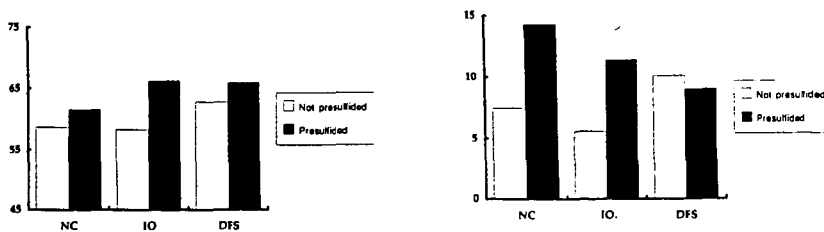


Figure 6. Conversion and yield of oil(+gas) as functions of catalyst loading.

Figure 7. Comparison of conversion (left) and yield of oil(+gas) (right) over disproportionated catalyst (DFS) and over iron oxide catalyst (IO).



## THE EFFECTS OF IRON CARBONYL-BASED CATALYST PRECURSORS ON THE REACTION OF 4-(NAPHTHYLMETHYL)BIBENZYL

Timothy D. Walter, Stephen M. Casey, Michael T. Klein, Henry C. Foley  
Center for Catalytic Science and Technology  
Department of Chemical Engineering  
University of Delaware  
Newark, DE 19716

### ABSTRACT

The reaction pathways and kinetics of 4-(naphthylmethyl)bibenzyl (NBBM) were studied in an effort to resolve certain fundamentals underlying catalysis of coal liquefaction by Fe-based catalysts. Reaction of NBBM under a hydrogen atmosphere was performed for a series of iron carbonyl-based catalyst precursors:  $\text{Fe}(\text{CO})_4\text{PPh}_3$ ,  $\text{Fe}(\text{CO})_3(\text{PPh}_3)_2$ , and  $\text{Fe}(\text{CO})_2(\text{PPh}_3)_2\text{CS}_2$ . The precursors' activities for the disappearance of NBBM were  $\text{Fe}(\text{CO})_4\text{PPh}_3 > \text{Fe}(\text{CO})_2(\text{PPh}_3)_2\text{CS}_2 > \text{Fe}(\text{CO})_3(\text{PPh}_3)_2$ . All precursors gave significantly higher rates than that for thermal reaction at 400°C. Thermolysis of NBBM was selective for cleavage at the bibenzyl bond, whereas the catalyst precursors were selective for cleavage at the naphthyl moiety. Hydrogenation activity was also observed for each of the three catalyst precursors. Possible catalytic reaction mechanisms are considered.

### INTRODUCTION

Direct coal liquefaction is the process of fragmenting the coal structure into lower molecular weight materials. Thermal liquefaction is accompanied by bond-making retrograde reactions, which can result in a more refractory solid than the original coal. This poor thermal selectivity to desirable products motivates the use of a catalyst to increase the rate and selectivity of liquefaction.

Much of the microporous coal structure<sup>1</sup> is not accessible to classical solid catalyst particles. This suggests that the use of homogeneous or fine particle catalysts, which would better access the pore structure and, in turn, the surface area of coal, could be promising for catalysis of coal reactions. The two key coal liquefaction reaction families of bond scission and hydrogenation could thus occur for coal, and not only coal-derived liquids.

Our continuing work has focused on iron-based materials. In particular, catalyst precursors that are able to form fine particle iron and iron sulfides at coal liquefaction conditions have been sought. To consider the effect of the precursor's ligands on the activity of the catalyst, the series  $\text{Fe}(\text{CO})_4\text{PPh}_3$ ,  $\text{Fe}(\text{CO})_3(\text{PPh}_3)_2$ , and  $\text{Fe}(\text{CO})_2(\text{PPh}_3)_2\text{CS}_2$  of triphenylphosphine (PPh<sub>3</sub>)-substituted iron carbonyls has been examined.

The evaluation of these catalysts involved extensive model compound reaction chemistry. This is because simple model systems, individually, mimic some of the important structural features in coal, which enables the examination of specific bond reactivities in coal. The use of well-defined hydrocarbon systems also allows focus to be placed on the catalyst and its role. The model compound 4-(naphthylmethyl)bibenzyl (NBBM) mimics some of the important attributes of coal, e.g., a fused two-ring aromatic connected to other aromatics by short alkyl chains. However, its structure, illustrated in Figure 1, is simple enough to allow for quantitative analysis.

Two studies of the reaction of NBBM have been published. Farcasiu, et al.<sup>2</sup> reacted NBBM with the hydrogen donor 9,10-dihydrophenanthrene (DHP) thermally and in the presence of a catalytic carbon material. They observed products from thermal fission of each of the bonds labeled in Figure 1, followed by radical capping with DHP derived hydrogen. Reaction with the carbon catalyst increased NBBM conversion and showed, upon subtraction of the thermal background, nearly 100% selectivity to bond A scission. The thermal and catalytic (catalyst precursor  $\text{Fe}(\text{CO})_3(\text{PPh}_3)_2$ ) reactions of NBBM under both hydrogen and nitrogen atmospheres at 420 °C have been examined by Walter et al.<sup>3</sup> They classified the main products from reaction of NBBM into three major classes: bond A scission products, bond D scission products, and

hydrogenation products. Walter et al.<sup>3</sup> proposed a reaction scheme that consists of the rupture of the thermally weak bond D, followed by bond A cleavage through ipso-substitution of a benzyl radical and subsequent liberation of a methylbenzyl radical. Bond A scission products are naphthyl phenyl methane (from benzyl ipso-substitution), naphthalene, tetralin, methyl benzyl and p-xylene (secondary product from methylbenzyl). Bond D scission products are 4-(naphthylmethyl)toluene and toluene, and hydrogenation products are hydrogenated NBBM species (e.g., 1,2,3,4-tetrahydro NBBM). The stoichiometry for bond A scission was consistent with ipso-substitution by benzyl and H<sup>•</sup> radicals, since the sum of the molar yields of naphthyl phenyl methane, naphthalene and tetralin is equal to the sum of the molar yields of methylbenzyl and p-xylene.

The objective of the present paper is to report on the reaction of NBBM in the presence of a series of substituted iron-carbonyl catalyst precursors at 400°C under a hydrogen atmosphere. We first describe the preparation of the catalytic materials, followed by a description of the reaction system and procedures. Quantitative kinetics are examined through a lumped reaction network. A consistent catalytic reaction mechanism, consisting of the insertion of catalytically bound hydrogen into the naphthalene ring leading to bond A scission and/or hydrogenation, is discussed.

## EXPERIMENTAL

**Preparation of Catalytic Materials:** The reagents for the synthesis of the catalysts, triphenylphosphine (99%, Aldrich), Fe(CO)<sub>5</sub> (99.5%, Alfa Research Chemicals) and Fe<sub>2</sub>(CO)<sub>9</sub> (99.7%, Alfa Research Chemicals), were used as received. All solvents were distilled under N<sub>2</sub> over 4 Å molecular sieve to remove oxygen and water, and reactions were performed under an atmosphere of purified nitrogen in Schlenk-type glassware to exclude air and water.

**Fe(CO)<sub>4</sub>PPh<sub>3</sub> Synthesis:** Fe(CO)<sub>4</sub>PPh<sub>3</sub> was prepared by a combined photochemical and thermal route from triphenylphosphine (PPh<sub>3</sub>) in iron pentacarbonyl (Fe(CO)<sub>5</sub>), following the synthesis procedure of Conder and Darensbourg<sup>4</sup>. This preparation procedure, which is selective to the monosubstituted product, is outlined in Figure 2a. Thus, 3 g of PPh<sub>3</sub> (0.011 mole) was added to 28 ml of Fe(CO)<sub>5</sub> (0.208 mole) under a dry N<sub>2</sub> atmosphere. The stirred solution was irradiated with a 100-Watt long-wave UV lamp for 2 hours. The lamp was then turned off and the solution was held at reflux conditions (100°C) for one hour, followed by an additional hour of reflux with the UV lamp turned on. At the end of the reaction sequence, excess Fe(CO)<sub>5</sub> was removed in vacuo. The residue was extracted with 50 ml THF and separated on a neutral alumina chromatography column in air, eluting with 75 ml THF. 50 ml of distilled water was then added and the solution volume reduced under vacuum to precipitate pale yellow crystals that were collected by filtration and purified by recrystallization from heptane. The above procedure gave a 50% yield of Fe(CO)<sub>4</sub>PPh<sub>3</sub> (based on PPh<sub>3</sub>). The product was identified through melting point comparison, 198-200°C (lit.<sup>5</sup>: 201-203°C) and spectroscopy, IR: ν(CO) (CH<sub>2</sub>Cl<sub>2</sub>): 2051, 1974, 1939 cm<sup>-1</sup> (lit.<sup>8</sup> ν(CO) (CHCl<sub>3</sub>): 2059, 1978, 1938 cm<sup>-1</sup>).

**Fe(CO)<sub>3</sub>(PPh<sub>3</sub>)<sub>2</sub> Synthesis:** Fe(CO)<sub>3</sub>(PPh<sub>3</sub>)<sub>2</sub> was prepared from Fe(CO)<sub>5</sub> and PPh<sub>3</sub> in refluxing cyclohexanol, following the procedure of Clifford and Mukherjee<sup>6</sup> outlined in Figure 2b. In this synthesis, 2 ml of Fe(CO)<sub>5</sub> (0.015 mole) and 5 g of PPh<sub>3</sub> (0.018 mole) were added to 100 ml of cyclohexanol. The solution was then refluxed (161°C) for 1 hour under N<sub>2</sub>. 100 ml of hexane was added to the reaction solution which was then cooled, giving a yellow precipitate. This relatively straightforward procedure gave a 39% yield (based on Fe(CO)<sub>5</sub>) of the disubstituted product, Fe(CO)<sub>3</sub>(PPh<sub>3</sub>)<sub>2</sub>, with a small amount of the monosubstituted derivative, Fe(CO)<sub>4</sub>PPh<sub>3</sub>, present, which was removed by silica gel chromatography. The product was identified through melting point comparison, 265-285°C (lit.<sup>8</sup>: 272°C) and spectroscopy, IR: ν(CO) (CH<sub>2</sub>Cl<sub>2</sub>): 1882 cm<sup>-1</sup> (lit.<sup>8</sup>: ν(CO) (CHCl<sub>3</sub>): 1887 cm<sup>-1</sup>).

**Fe(CO)<sub>2</sub>(PPh<sub>3</sub>)<sub>2</sub>CS<sub>2</sub> Synthesis:** Fe(CO)<sub>2</sub>(PPh<sub>3</sub>)<sub>2</sub>CS<sub>2</sub> was prepared from diiron nonacarbonyl (Fe<sub>2</sub>(CO)<sub>9</sub>) and PPh<sub>3</sub> in refluxing (46°C) carbon disulfide (CS<sub>2</sub>), as outlined by

Baird et al.<sup>7</sup> The route is outlined in Figure 2c. A mixture of 1.5 g of  $\text{Fe}_2(\text{CO})_9$  (0.004 mole) and 3 g of  $\text{PPh}_3$  (0.011 mole) in 25 ml of  $\text{CS}_2$  was refluxed under  $\text{N}_2$  for 40 minutes. The solution was cooled, and the rust-red solid,  $\text{Fe}(\text{CO})_2(\text{PPh}_3)_2\text{CS}_2$ , was precipitated by addition of diethylether (~5-10% yield based on  $\text{Fe}_2(\text{CO})_9$ ). The product was identified through melting point comparison, 133°C (lit.<sup>10</sup>: 130-134°C) and spectroscopy, IR:  $\nu(\text{CO})$  ( $\text{CH}_2\text{Cl}_2$ ): 1990, 1929  $\text{cm}^{-1}$  (lit.<sup>10</sup>:  $\nu(\text{CO})$  ( $\text{CHCl}_3$ ): 1989, 1929  $\text{cm}^{-1}$ ).

**NBBM Reactions:** NBBM (TCI Americas), dichloromethane (Fisher Scientific) and all other chemicals (Aldrich Chemical Company) were used as received. The reactions were carried out in 7  $\text{cm}^3$  stainless steel microbatch reactors. The reactant and catalyst precursor were placed in an open 10 x 75 mm glass tube within the reactor to prevent wall interactions. The loadings of NBBM and catalyst precursor were 50 mg and 1.4 wt% by iron, respectively (5 mg for  $\text{Fe}(\text{CO})_4\text{PPh}_3$ , 8 mg for  $\text{Fe}(\text{CO})_3(\text{PPh}_3)_2$ , 8.3 mg for  $\text{Fe}(\text{CO})_2(\text{PPh}_3)_2\text{CS}_2$ ), and all reactions took place under 1000 psig (cold) hydrogen pressure. The reactor was pressurized to 1000 psig with hydrogen and then discharged three times prior to heat up. This ensured reaction in the absence of air. The reactor was then plunged into a fluidized sand bath at 400°C and, after the passage of the reaction time, removed from the sandbath for cooling in an ice bath for at least 30 minutes. A known amount of biphenyl was then added to the contents of the glass tube, which was subsequently diluted with dichloromethane. The mixture was then separated in a Hewlett-Packard 5890 Gas Chromatograph with Flame Ionization Detector and a Hewlett-Packard 5890 Gas Chromatograph with a Hewlett-Packard 5970 Mass Selective Detector. Both Gas Chromatographs used Hewlett-Packard Ultra 2 columns (crosslinked 5% Ph Me Silicone) with dimensions 50 m x 0.2 mm and 0.33 mm film thickness.

## RESULTS AND DISCUSSION

The reactions of NBBM were studied at 400 °C under 1000 psig (cold) hydrogen pressure in the presence of each of the catalyst precursors ( $\text{Fe}(\text{CO})_4\text{PPh}_3$ ,  $\text{Fe}(\text{CO})_3(\text{PPh}_3)_2$ ,  $\text{Fe}(\text{CO})_2(\text{PPh}_3)_2\text{CS}_2$ ) and in the absence of a catalytic precursor.

The disappearance kinetics shown in Figure 3 reveal that the three catalyst precursors had significant activity above the thermal baseline for the disappearance of NBBM.  $\text{Fe}(\text{CO})_4\text{PPh}_3$  led to the highest conversion over most of the reaction times. Conversion in the presence of  $\text{Fe}(\text{CO})_2(\text{PPh}_3)_2\text{CS}_2$  was initially lower than in the presence of  $\text{Fe}(\text{CO})_3(\text{PPh}_3)_2$ , but by 60 minutes the trend had reversed.

Figure 4 is a plot of the yields of the three product classes, i.e., bond A scission, bond D scission and hydrogenation products, versus NBBM conversion for reaction at 400°C in the presence of the three catalyst precursors. The predominate activity for bond A scission and NBBM hydrogenation is clear. Figure 4 shows that, for the catalyst precursor  $\text{Fe}(\text{CO})_4\text{PPh}_3$ , the rate of appearance of bond A scission products decreases markedly between 120 and 150 minutes. There was very little NBBM left in the reaction mixture at this point (Figure 3); however, there was a significant amount of hydrogenated NBBM (Figure 4). The stoichiometry for bond A scission during reaction with each of the three catalyst precursors at 400 °C was consistent with the results observed by Walter et al.<sup>3</sup> and discussed earlier. Ipso-substitution by either benzyl or  $\text{H}^\cdot$  radicals can account for the observed product distributions.

Figure 5 is a simple reaction network that describes NBBM reaction in terms of the three product lumps: bond A scission products, bond D scission products and NBBM hydrogenation products. The network also includes an "other products" lump, which accounts for products not identified through gas chromatography, e.g., gases and high molecular weight products. Two additional product classes account for secondary reactions to hydrogenated versions of products attributed to bond A and bond D scission.

Quantitative kinetics analysis was accomplished by optimizing network predictions against the experimental data. Table 1 contains the best-fit values of first-order rate constants obtained by parameter estimation using a simplex optimization routine. Model predictions, with the experi-

mental data, for NBBM consumption are shown in Figure 6. The fits are good for reaction thermally and in the presence of  $\text{Fe}(\text{CO})_3(\text{PPh}_3)_2$ . However, for reaction in the presence of  $\text{Fe}(\text{CO})_4\text{PPh}_3$  and  $\text{Fe}(\text{CO})_2(\text{PPh}_3)_2\text{CS}_2$  the fits are poor, due to highly non-first order behavior.

The rate constants do provide insight into the reaction mechanisms. The values for the bond D scission constants,  $k_D$ , are independent of the presence of the three catalysts. That is,  $k_D$  for reaction with any of the catalysts is not significantly different than that during thermal reaction. This suggests that bond D scission is purely thermal and is unaffected by the presence of a catalyst. Similarly, the values for the bond A scission constants,  $k_A$ , are similar for reaction with each of the three catalysts and quite different than that for thermal reaction. This suggests that a single mechanism is responsible for the bond A scission in the presence of the three catalyst precursors. In addition, the values of the hydrogenation constants,  $k_H$ , are consistent with the higher hydrogenation activity observed for  $\text{Fe}(\text{CO})_4\text{PPh}_3$  catalyst than for the other two shown in Figure 4. Also, the slower scission of bond A in hydrogenated NBBM relative to that for bond A scission of NBBM is reflected in the relationship  $k_{HA} < k_A$  for all three catalyst precursors. Finally, all three catalyst precursors showed higher activity for hydrogenation of naphthalene ( $k_{AH}$ ) than for hydrogenation of the substituted naphthalene ( $k_H$ ).

Mechanistic insights derive from the known activity of reduced iron as an effective hydrogenation catalyst. The iron likely dissociates hydrogen into atoms that can, in turn, add to the naphthyl ring. When a hydrogen inserts at the ipso position, a thermochemically favorable  $\beta$ -scission pathway affords naphthalene and a methylbenzyl radical. This proposed mechanism is also consistent with the lack of bond A scission of hydrogenated NBBM. The destruction of the electron rich naphthalene system both decreases the molecule's ability to interact with the catalyst and removes the electronic topology required for ipso-substitution.

## CONCLUSIONS

The catalytic chemistry of NBBM at 400°C under a hydrogen atmosphere in the presence of the series of iron-carbonyl based catalyst precursors  $\text{Fe}(\text{CO})_4\text{PPh}_3$ ,  $\text{Fe}(\text{CO})_3(\text{PPh}_3)_2$  and  $\text{Fe}(\text{CO})_2(\text{PPh}_3)_2\text{CS}_2$  was examined. The three catalyst precursors showed significant activity for the disappearance of NBBM above the thermal baseline. Two of the main product classes were "bond A scission" and "NBBM hydrogenation". Quantitative network analysis examined the kinetics for each reaction family among the catalyst precursors. This analysis indicated that: bond D scission was purely thermal and unaffected by the presence of the catalyst precursors; bond A rate constants were similar for reaction in the presence of all three catalyst precursors and different from that for thermal reaction; and the hydrogenation rate constant was higher for  $\text{Fe}(\text{CO})_4\text{PPh}_3$  than for the other two catalyst precursors. A consistent reaction mechanism involves catalytic dissociation of  $\text{H}_2$  into hydrogen atoms, which are, in turn, inserted into the naphthalene system of NBBM; the naphthalene site at which the hydrogen atom is inserted determines the outcome of bond A scission or hydrogenation. The slower rate of bond A scission observed by the hydrogenated NBBM species can be qualitatively explained with decreased catalyst interaction and removal of ipso-substitution electronic topology.

## ACKNOWLEDGMENT

We would like to thank Dr. William H. Calkins, Dr. G. Alex Mills and Dr. Malvina Farcasiu for discussions in the area of coal chemistry and coal catalysis, and Dennis Kalaygian for his help in performing some of the NBBM reaction experiments. This work was supported by the United States Department of Energy Grant DE-AC22-90PC90050.

<sup>1</sup> Larsen, John W., Wernett, Patrick, "Pore Structure of Illinois No. 6 Coal", *Energy & Fuels*, **2** (5), 719-720, 1988

<sup>2</sup> Farcasiu, Malvina, Smith, Charlene, "Modeling Coal Liquefaction, 1. Decomposition of 4-(1-Naphthylmethyl)benzyl Catalyzed by Carbon Black", *Energy & Fuels*, **5**(1), 83-87, 1991

<sup>3</sup> Walter, Timothy D., Casey, Stephen M., Klein, Michael T., Foley, Henry C., "Reaction of 4-(naphthylmethyl)biphenyl Thermally and in the Presence of  $\text{Fe}(\text{CO})_2(\text{PPh}_3)_2$ ", submitted for publication, Presented at DOE Liquefaction Contractors' Meeting, Pittsburgh, PA Sept. 22-24, 1992

<sup>4</sup> Conder, H.L., and Darensbourg, M. York, "The Synthesis of Group V Substituted Derivatives of Iron Pentacarbonyl in High Yield", *J. Organomet. Chem.*, 1974, **67**, 93-97.

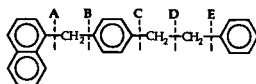
<sup>5</sup> Cotton, F.A. and Parish, R.V., "The Stereochemistry of Five-coordinate Compounds. Part I. Infrared Spectra of Some Iron(0) Compounds", *J. Chem. Soc.*, 1960, 1440-1446.

<sup>6</sup> Clifford, A.F., and Mukherjee, A.K., "Iron Carbonyl Complexes of Triphenylphosphine, Triphenylarsine, and Triphenylstibine", *Inorg. Chem.*, 1963, **2**, No. 1, 151-153.

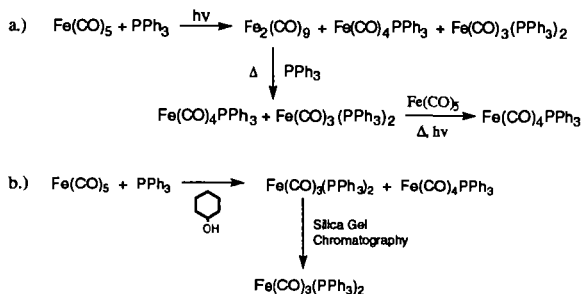
<sup>7</sup> Baird, M.C., Hartwell, jun., G., and Wilkinson, G., "Carbon Disulphide Complexes of Vanadium, Iron, Cobalt, Ruthenium, and Iridium; the Preparation of trans-Bis(triphenylphosphine)thiocarbonylhalogeno-rhodium(I) and -rhodium(III) Complexes", *J. Chem. Soc. (A)*, 1967, 2037-2040.

	$(\text{k}_1 / \text{s}^{-1}) \times 10^5$			
	Thermal	$\text{Fe}(\text{CO})_4\text{PPh}_3$	$\text{Fe}(\text{CO})_3(\text{PPh}_3)_2$	$\text{Fe}(\text{CO})_2(\text{PPh}_3)_2\text{CS}_2$
$k_A$	0.455	4.32	3.00	4.19
$k_H$	0.035	15.8	5.59	6.59
$k_D$	0.457	0.366	0.454	0.363
$k_{AH}$	4.92	42.4	18.2	17.8
$k_{DH}$	1.83	4.44	6.36	8.87
$k_{HA}$	0.112	1.72	1.33	0.549
$k_{HD}$	0.031	0.505	0	0
$k_O$	1.11	5.91	2.78	2.99

**Table1:** Regressed values for the first-order rate constants for the reaction network of Figure 5.



**Figure 1:** Model compound, 4-(naphthylmethyl)biphenyl.



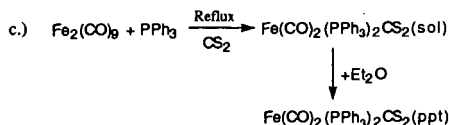


**Figure 2:** Synthesis routes for: a)  $\text{Fe}(\text{CO})_4\text{PPh}_3$ ; b)  $\text{Fe}(\text{CO})_3(\text{PPh}_3)_2$ ;  $\text{Fe}(\text{CO})_2(\text{PPh}_3)_2\text{CS}_2$ .

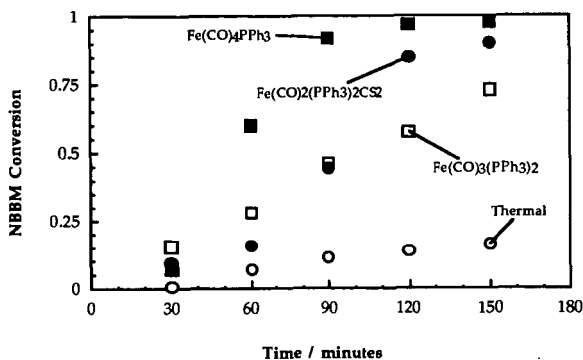


**Figure 3:** Kinetics of NBBM disappearance at 400°C under 1000 psig  $\text{H}_2$  (cold) in the presence of iron carbonyl based catalyst precursors.

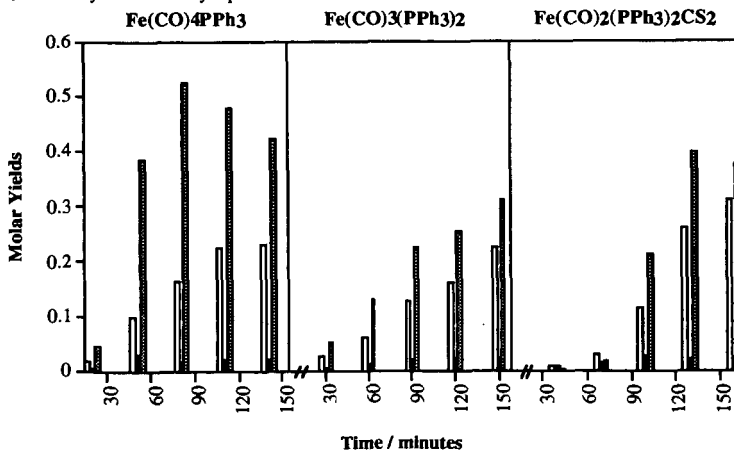


**Figure 4:** Molar yields of bond A scission, bond D scission and NBBM hydrogenation products classes upon reaction of NBBM at 400°C under 1000 psig  $\text{H}_2$  (cold) in the presence of iron carbonyl based catalyst precursors. □ Bond A Scission Products; ■ Bond D Scission Products; ▨ Hydrogenation Products.

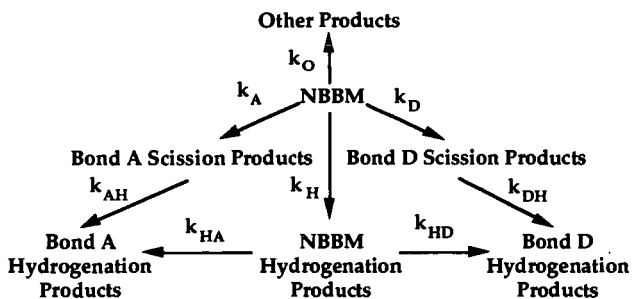


Figure 5: Lumped network for the reaction of NBBM at 400°C under 1000 psig H<sub>2</sub> (cold) in the presence of iron carbonyl based catalyst precursors.

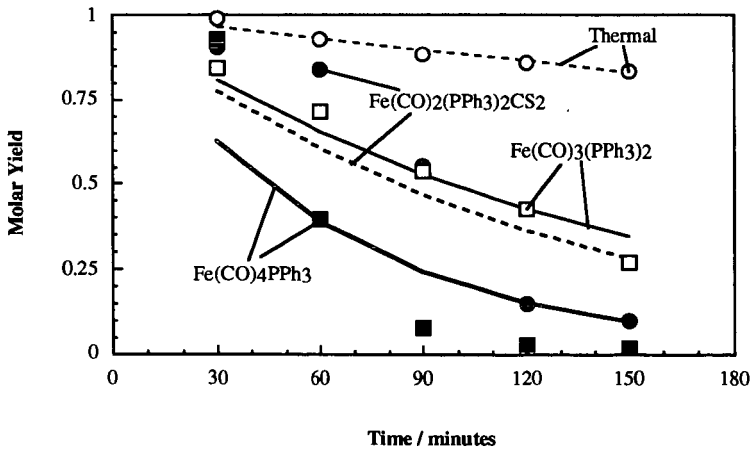


Figure 6: Model fits for the lumped network describing the reaction of NBBM at 400°C under 1000 psig H<sub>2</sub> (cold) in the presence of iron carbonyl based catalyst precursors. The lines are the predicted curves and the points are the experimentally measured values.

**Complex Iron Catalytic Systems: Relative Catalytic Activity  
of Various Components.**

Malvina Farcasiu, Patricia A. Eldredge and Steven C. Petrosius

U.S. Department of Energy  
Pittsburgh Energy Technology Center  
P.O. Box 10940, Pittsburgh PA 15236

Key words: catalytic hydrocracking, iron-sulfur catalysts, active phase.

**ABSTRACT**

Fine particle (6-8nm) iron-sulfur systems with complex chemical compositions are formed when a 3 nm iron oxide is heated with sulfur in the presence of 9,10-dihydrophenanthrene for 1 hour. These systems form small-particle pyrrhotite when heated at 320°C. The fine particle pyrrhotites are very active hydrocracking catalysts, but agglomerate rapidly during reaction at 320°C.

**INTRODUCTION**

The use of iron-based catalysts in reactions of interest for direct coal liquefaction usually involves the addition of iron compounds to the reaction mixture and the in-situ activation of the iron compounds to form iron catalysts. The composition of active iron-based catalysts has been a subject of considerable interest and several reviews have been published on the subject (1,2). It was reported that the hydrocracking of monoaromatic model compounds at temperatures of 425-435°C is catalyzed by iron-sulfur systems in the presence of hydrogen sulfide (2). The catalytic activity was tentatively explained by an interaction of pyrite with pyrrhotite and hydrogen sulfide.

We have studied the activity of some iron-sulfur catalytic systems formed in the reaction of fine-particle iron oxides with elemental sulfur and a hydrogen donor, 9,10-dihydrophenanthrene (9,10-DHP), at low temperature. In this paper we will discuss the systems formed when the above compounds are heated at low temperatures (200 - 320°C). We have found that the iron-sulfur systems formed under these conditions are very active in low temperature, selective hydrocracking of C<sub>ar</sub>-C<sub>aliph</sub> bonds, when the aromatic carbon is a part of a condensed polycyclic aromatic hydrocarbon. The composition of the iron-sulfur systems and the variation of their compositions with time under various reaction conditions have been studied by a variety of methods. We report

here our findings concerning the catalytically active components in the above described iron-sulfur system.

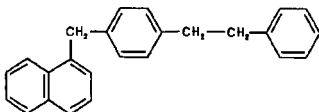
#### EXPERIMENTAL

**General.** Reagent grade chemicals and HPLC grade solvents were used as purchased unless stated otherwise. Methylene chloride was dried over 4 Å molecular sieves. Ferrihydrite ( $5\text{Fe}_2\text{O}_3 \cdot 9\text{H}_2\text{O}$ ), obtained from Mach I, Inc., King of Prussia, Pennsylvania, was vacuum dried for ca. 3 hours at 150 °C, then stored in a desiccator. The particle size reported by the vendor (3-5 nm) was confirmed by microscopic analysis and is consistent with the surface area determination by the BET method. Compound I was available from our previous work (3).

The reactions were conducted in sealed 7mm o.d. heavy walled glass tubes (Corning Glass) in a Lindberg Type 59344 muffle furnace equipped with a thermocouple.

Chromatographic analyses were conducted on a Hewlett-Packard Model 5890 Series II Gas Chromatograph equipped with a split-vent injector and connected to an HP 3396A integrator, on a J&W 30 m x 0.248 mm fused silica capillary column coated with 0.25 μm silicone SE-52, with a head pressure of 20 psi (136 KPa). The column temperature was increased from 80°C to 310°C at a rate of 8°C/min. Identification of the components was described in a previous publication (3).

**Catalyst Preparation and Activity Measurement.** In a typical experiment, ferrihydrite (2.5 mg) dried as indicated above, sulfur (2.5 mg), and 9,10-DHP (100 mg) were loaded into the glass tube which was sealed without excluding the air. The length of the sealed tube was ca. 14 cm. The tube was heated at the desired temperature for the duration indicated below, then it was cooled and stored at room temperature until use. For catalyst testing, the tube was cracked open (CAUTION: pressure buildup in the tube occurs, particularly for experiments at higher temperatures), 25 mg of the reactant, 4-(1-naphthylmethyl)bibenzyl (I), was added and the tube was resealed and heated as indicated



below. In the alternative procedure, compound I was added together with the catalyst precursors such that catalyst preparation and reaction of I were conducted in one operation. For the analysis of

products, the tube was cooled to room temperature and carefully opened, the organic materials were dissolved in the minimum amount of methylene chloride possible and filtered through a layer of anhydrous  $\text{MgSO}_4$  (ca. 0.3 g) supported by a glass wool plug in a micropipette. The tube was rinsed twice with methylene chloride (ca. 0.5 mL each time) and the washings were filtered through the same microcolumn for drying. The combined solution was concentrated to ca. 1 mL and analyzed by GLC (0.5  $\mu\text{L}$  of sample was used for each injection).

Catalyst Characterization. The particle size, chemical composition, and the crystallographic properties of the iron species formed under various experimental conditions were determined as described by Eldredge et al.(4), using XRD and Moessbauer spectroscopy. The surface area was determined by the BET method (5) from the adsorption isotherms for  $\text{N}_2$  at 77K. The samples were first outgassed for 18 hr at 95°C and less than  $10^3$  torr. A Coulter Omnisorp 100CX gas sorption analyzer operated in the fixed-dose, static-flow volumetric mode was used to measure the adsorption isotherms. Equilibration of the sample with a nitrogen dose was defined as five consecutive readings with a variance of less than 0.1 torr over a 3 second interval. A value of 0.162  $\text{nm}^2$  was used for the cross-sectional area of nitrogen.

## RESULTS AND DISCUSSION

The catalyst prepared in-situ from ferric oxide (20-80 nm) and sulfur in the presence of 9,10-DHP and reported previously (6) was found active in hydrocracking reactions of compound I at temperatures of 420-430°C. In the present study, the reactions were performed at temperature and conditions where no thermal reaction of I occurs (3). In work reported here, we have used an oxide with smaller particles (3-5 nm) as the catalyst precursor. Our goal was to prepare an iron-sulfur catalyst in an initial step, and then add the substrate I and perform the hydrocracking reaction. The temperature was varied independently in the two steps (between 200°C and 320°C for the first step and between 200°C and 400°C for the second step) and each step was normally conducted for 1 hour. Alternatively, the two steps were combined by adding the substrate from the beginning and thus synthesizing the catalyst in-situ. The conversion of I, defined as the selective cleavage of the bond adjacent to the naphthalene ring, is presented in Table 1 for both of these approaches. It can be seen that the catalyst is active even at temperatures as low as 250°C. Moreover, conversion of I reaches a maximum value of 92% in one hour at 350°C (Table 1)

The data in Table 1 also show that reaction of I at any temperature between 250 and 400°C gives the same conversion with the catalyst generated in-situ or with the material pre-synthesized at 200°C. Synthesis of the catalyst in a prior step at higher temperatures gave less active catalytic systems.

Under our experimental conditions, specifically with the reactant dissolved in 9,10-DHP, there is likely no mass transfer limitation and the rate of formation of the active phase by the

reaction of iron oxide with sulfur (or more likely with the hydrogen sulfide formed from S and the H-donor) is faster than the hydrocracking reaction. Such favorable conditions might not be available if the catalyst were generated in a very complex heterogenous medium with large excess of solids, as is the case in coal liquefaction. Therefore, preparation of active, small particle catalysts, prior to the actual coal liquefaction, is desirable.

The structural study of this Fe-S material formed after pretreatment of 3-5 nm particles of ferrihydrite for 1 hour at 200°C indicates the presence of at least four distinct components: pyrrhotite, magnetite, unreacted ferrihydrite (or hematite), and a new iron sulfide phase identified as marcasite with pyrite stacking faults (4). The composition, as determined by Moessbauer spectroscopy, is reported to be (7): 15% pyrrhotite, 19% unreacted ferrihydrite, 29% magnetite, and 37% for the new iron sulfide phase. The particle size of the pyrrhotite component in this material was in the range of 6.5-8 nm (XRD) and its calculated surface area was 150-182 m<sup>2</sup>/g. The direct surface area determination for all the components gave a surface area of 180 m<sup>2</sup>/g. The marcasite/pyrite phase is unstable at 200°C and is converted to pyrrhotite upon longer heating at that temperature. Pyrrhotite is also formed at the expense of the new phase when catalyst synthesis is conducted at higher temperature. In both cases, larger particles are obtained. When catalyst preparation was conducted at 320°C, only pyrrhotite was observed even at a short reaction time of 20 minutes. The particle size of the pyrrhotite obtained under the latter conditions was ~30 nm, with a corresponding calculated surface area of ~40 m<sup>2</sup>/g. Pretreatment at 200°C, followed by treatment for 10 minutes at 320°C, or direct pretreatment for 10 minutes at 320 °C gives pyrrhotite with particle size of 22-25 nm (corresponding surface area of 54-48m<sup>2</sup>/g). After pretreatment of 1 hour at 320°C, the particle size of the pyrrhotite was in the range of 38-50 nm (XRD) and a surface area of ~24 m<sup>2</sup>/g was calculated.

The catalytic activity of the iron-sulfur system formed at 200°C may be due to one, some, or all of the components present; i.e., to pyrrhotite, the newly identified iron sulfide phase, magnetite, or to the unreacted ferrihydrite. The ferrihydrite used alone in tests with I in the presence of 9,10-DHP was found to be catalytically inactive. For identification of the active phase in this system, we studied the conversion of compound I at 320°C as a function of time in the presence of the iron-sulfur system presynthesized at 200°C. The results are given in Table 2. Based on the conversion at 40 minutes with pyrrhotite of 24 m<sup>2</sup>/g initial surface area, a specific catalytic activity for pyrrhotite of 0.39 nmoles I/(m<sup>2</sup>hour) is calculated. X-ray diffraction data indicate that pyrrhotite is the primary material present after 20 minutes at 320°C. Assuming the only catalytically active phase present even at short reaction time is pyrrhotite, then for the 45% conversion of I in the first 20 minutes of the reaction, an average surface area of 108 m<sup>2</sup>/g can be calculated for this interval using the specific activity mentioned above. This value compares well with the observed decrease in the surface area during the first 20 minutes of reaction from ~180 m<sup>2</sup>/g

to  $\sim 41 \text{ m}^2/\text{g}$  (a calculated average would be  $110 \text{ m}^2/\text{g}$ ). Using this result along with the observation that pyrrhotite is by far the major component in the system leads to the conclusion that pyrrhotite is most likely the catalytically active phase.

The possible catalytic activity of magnetite (a major component after pretreatment of the mixture of ferrihydrite and sulfur in the presence of 9,10-DHP at  $200^\circ\text{C}$  for 1 hour) was studied using samples of genuine magnetite of known particle sizes (8). However, based on the observed conversion to pyrrhotite after 20 minutes at  $320^\circ\text{C}$ , it is unlikely that magnetite makes any important contribution to the activity under the reaction conditions reported in Table 2. The observed conversions after pretreatment at various temperatures can be explained by pyrrhotite as the catalytically active phase and by the variation of its particle size (surface area) as a function of the experimental conditions. Consequently, our present data indicate no measurable catalytic activity for the new form of pyrite-marcasite identified when the iron-sulfur system is preformed at  $200^\circ\text{C}$ , as described above. However, the stability at room temperature of the iron-sulfur system formed after pretreatment for 1 hour at  $200^\circ\text{C}$  without loss of the catalytic activity (Table 3) may be due to the fact that this complex system prevents the agglomeration of the particles.

Data by Cugini et al. (9) show that when highly dispersed  $\text{FeOOH}$  is precipitated on coal and the coal is pretreated at  $275^\circ\text{C}$  in presence of a sulfur compound, an active catalyst for coal liquefaction can be formed. It is likely that this catalyst is highly dispersed pyrrhotite and that coal prevents its agglomeration. However, in the absence of sulfur, other iron compounds are stable and can act as catalysts. When a low sulfur bituminous coal is liquefied in the presence of magnetite, a significant catalytic activity is observed and magnetite is observed as such at the end of reaction (8).

#### CONCLUSIONS

We have found that pretreatment of fine particle size (30 nm) iron oxide with sulfur in the presence of 9,10-DHP, at  $200^\circ\text{C}$  for one hour gives a high surface area mixture of magnetite, pyrrhotite, and a newly identified phase of marcasite-pyrite (4). We studied this system for hydrocracking reactions of compound I at various temperatures. The iron-sulfur mixture transforms at  $320^\circ\text{C}$  (the temperature at which we report kinetic data) into pyrrhotite. The surface area of pyrrhotite varies with the reaction time and the catalytic activity can be correlated to the surface area variation. The observed catalytic activity in the hydrocracking reaction of I is attributed under these conditions to pyrrhotite.

#### ACKNOWLEDGEMENTS

The authors gratefully acknowledge the contribution of Dr. S. Pollack, Dr. N. Johnson and Mrs. E. Frommel from PETC for their assistance with XRD analyses and helpful discussions. Technical

discussions with prof. I. Wender, Dr. B.D. Blaustein and Dr. R.P. Warzinski are gratefully acknowledged. This work was supported in part (PAE and SCP) by appointments to the Department of Energy Fossil Fuels Energy Postgraduate Research Training Program administered by Oak Ridge Institute for Science and Education.

#### DISCLAIMER

Reference in the paper to any specific commercial product, process or service is to facilitate understanding and does not necessarily imply its endorsement or favoring by the United States Department of Energy.

#### REFERENCES

1. Trawhella, M.J.; Grint, A. Fuel, 1987, 66, 1315 and references therein.
2. Narain, N.K.; Cillo, D.L.; Stiegel, G.J.; Tisher, R.E. Coal Science and Chemistry, A. Volborth editor, Elsevier Science Publishers B.V., Amsterdam, 1987, pp 111-149 and the references therein.
3. Farcasiu, M.; Smith, C.M. Energy & Fuels, 1991, 5, 83.
4. Eldredge, P.A.; Frommell, E.A.; Huggins, F.E.; Pollack, S.P., 1992, unpublished work.
5. Brunauer, S.; Emmett, P.H.; Teller, E. J. Am. Chem. Soc., 1938, 60, 309.
6. Farcasiu, M.; Smith, C.M.; Pradhan, V.R.; Wender, I. Fuel Processing Technology, 1991, 29, 199.
7. Huffman, G.P.; Huggins, F.E., personal communication.
8. Farcasiu, M.; Petrosius, S.C.; Warzinski, R.P., unpublished work.
9. Cugini, A.V.; Utz, B.R; Krastman, D.; Hickey, R.F. Prepr. Pap.- Am. Chem. Soc. Div. Fuel Chem. 1991, 36, 91.

**Table 1. Catalytic Conversion of I at Various Temperatures in the Presence of Iron-Sulfur Catalysts.**

Conditions: 25 mg I, ~100 mg 9,10 DHP, 10 wt% (based on I) ferrihydrite, 10 wt% (based on I) sulfur, 1h reaction time.

Reaction Temperature °C	Conversion of I, %			
	no catalyst pretreatment	pretreatment 1h at 200°C	pretreatment 1h at 250°C	320°C
200	0	0	0	0
250	10	9	0	0
275	31	32	10	-
300	52	54	30	10
320	79	78	48	17
350	92	92	66	38
400	94	93	87	40

**Table 2. Catalytic Conversion of I at 320°C as Function of Time.**

Time h	Catalytic Conversion % in presence of Pyrrhotite* ~24m <sup>2</sup> /g	
		Catalyst from 200°C, 1h pretreatment
0.33	~ 12	45
0.5	13	57
0.66	20	65
1	17	79

\* Pyrrhotite obtained after pretreatment for 1h at 320°C.

**Table 3. Stability of the Iron-Sulfur System Preformed at 200 °C Reaction of I at 320°C, 1 hour.**

Storage Time days	Conversion of I %
0	79
1	79
3	73

# MOLECULAR ORBITAL CALCULATIONS FOR IRON CATALYSTS

Harriet F. Ades, Audrey L. Companion, and K.R. Subbaswamy  
Departments of Physics and Chemistry  
University of Kentucky, Lexington, KY 40506-0055

**Keywords:** Iron Catalysts, Quantum Chemistry, Clusters

One of the primary questions facing scientists working in the area of direct coal liquefaction (DCL) is the state of the iron in iron-based catalysts. While much work has been done on iron-based DCL catalysts, the mechanism of catalysis is poorly understood. In order to elucidate the possible catalytic action, we have begun modeling various surfaces of FeS and  $\text{Fe}_{(1-x)}\text{S}_y$  clusters with the ASED-MO method of Anderson. We have studied the adsorption of toluene and 1-methylnaphthalene at various sites on FeS and related defect clusters and have calculated bond breaking energies of the aromatic-aliphatic linkage. One explanation of the catalytic activity of the FeS is donation of electrons to the iron surface by the adsorbate, followed by a subsequent decrease in the bond breaking energies as compared to nonchemisorbed toluene or 1-methylnaphthalene.

## A. Introduction

The development of effective and economical catalysts is the key to making direct coal liquefaction a commercially viable goal. To this end, there has been a great deal of interest in sulfided iron catalysts for coal liquefaction. Several facts are known from experiments: the presence of sulfur increases the liquefaction conversion;<sup>1</sup> molybdenum is a 'more active catalyst' for liquefaction than iron;<sup>2</sup> molybdenum produces a more highly hydrogenated product; and the addition of molybdenum to the iron sulfided catalysts greatly increases the activity of the iron catalyst.<sup>1</sup> However, the question of the state of the iron in the iron-based catalysts is still unanswered. For instance, in experiments starting with iron oxide as the catalyst it is still not known whether the iron oxide undergoes a phase transition directly to  $\text{Fe}_x\text{S}_y$  phases or it transforms to metallic iron first and then goes to form  $\text{Fe}_x\text{S}_y$ .<sup>3</sup> We address such questions through quantum chemical modeling calculations.

Two methods, both based on the EHMO method of Hoffmann,<sup>4</sup> are particularly suited for these investigations. The first, a band structure tight binding EHMO approach, developed by Whangbo,<sup>5</sup> has already been successfully employed by Zonneville, *et al.*<sup>6</sup> in explaining thiophene desulfurization on  $\text{MoS}_2$  and the formation of negatively charged ions in the scattering of oxygen from silver. This method is well suited for investigating bulk and semi-infinite surface properties of the catalyst systems.

The second, the ASED-MO method developed by A.B. Anderson,<sup>7</sup> has been used by us in the study of the possible cleavage mechanisms of model compounds of interest to investigators in the field.<sup>8-11</sup> Anderson also has used the method to study ethylene hydrogenation mechanisms on Pt surfaces and ethylene and acetylene absorption on  $\text{MoS}_2$  clusters.<sup>12</sup> In this method one models a surface by a small number of atoms (i.e., as the surface of a cluster of atoms), and is ideal for the study of the small ultrafine particle catalysts. One can thus

address whether the departure from bulk properties when the catalyst size approaches 10nm is the cause of catalytic activity.

Our goal is to investigate the active sites in both nano-size and large particles of iron-based catalysts by quantum chemical methods. Initially the adsorption of small organic molecules such as ethylene and toluene on various sites on FeS, Fe<sub>7</sub>S<sub>8</sub>, other defect structures, and pure Fe surfaces will be investigated in order to try to determine the differences in adsorptive and catalytic activity as one progresses from pure iron to the defect pyrrhotite structure. As a prelude to these complex studies, we have begun to model these interactions with cluster studies using the ASED-MO method of Anderson.<sup>7</sup>

## B. Method Used

The ASED-MO method is an attempt to improve the binding energy curve calculation in EHMO theory. There are two significant modifications. The first one is in the Hamiltonian matrix. In the ASED-MO method, as in the EHMO method, the molecular orbitals are expanded in terms of Slater type orbitals for the valence electrons. The eigenenergies,  $\epsilon_j$ , and the expansion coefficients are obtained from a solution of the secular equation,

$$|H_{ij} - \epsilon_j S_{ij}| = 0 \quad (1)$$

The Hamiltonian matrix  $H$  in ASED-MO is defined by

$$H_{ii} = -VSIE, \quad (2)$$

$$H_{ij} = \frac{K}{2}(H_{ii} + H_{jj})S_{ij} \exp(-\delta R_{ij}). \quad (3)$$

The  $S_{ij}$ 's are overlap integrals and are calculated explicitly with Slater-type orbitals (STO). The valence state ionization energies (VSIE) and the exponents in the STO's are frequently adjusted slightly from experimental or theoretical norms in order to give numbers that are in closer agreement with experiment.<sup>13</sup> Note that the off-diagonal matrix elements in (3) are different from the usual EHMO form of the Wolfsberg-Helmholz expression by the inclusion of the exponential factor. The constant,  $K$ , is taken to be 2.25 in the ASED-MO version, and the exponent  $\delta$  is 0.13au<sup>-1</sup>. The  $R_{ij}$ 's are the distances between the various atom centers in the molecule. The practical effect of the exponential factor is to produce a sharper increase in the potential curve between any two atoms than the standard standard EHMO methods.

The second modification of EHMO in the ASED-MO method is the inclusion of specific pairwise repulsion terms, derived from the consideration of the Hellman-Feynman force theorem.<sup>7</sup> Nuclear repulsion terms, attenuated by nuclear attraction integrals, are included in each pairwise repulsion term. The attraction terms are computed with classical formulae, approximating the density due to  $p$  and  $d$  electrons by spherical distributions. Inclusion of the two modifications of Anderson significantly improves the validity of EHMO calculations.

## C. Results and Discussion

The first cluster we investigated is shown in Figure 1 and consists of 19 Fe atoms in the top layer, 12 sulfur atoms in the second layer and 19 iron atoms in the third layer. This particular cluster was chosen because of its simplicity, and more realistic surfaces will

be studied subsequently. The interatomic distances were chosen to correspond to those in the idealized pyrrhotite structure.<sup>14</sup> The nearest neighbor distance between iron atoms in the same layer is 3.43 Å but 2.84 Å between layers. The Fe-S distance is 2.44 Å. This is to be compared with the nearest neighbor distance in bcc pure iron of 2.48 Å. The inner iron atoms of the cluster exhibit a charge of about +0.6 |e|. While this cluster does not have the overall stoichiometry of FeS, it is representative of the correct stoichiometry in the immediate vicinity of the adsorption sites studied.

We started by studying the adsorption of a hydrogen molecule on this cluster. The hydrogen molecule was allowed to approach the top layer of the surface perpendicularly in several different sites—i.e. head-on, bridge, and interstitial (over the exposed sulfur atom in the second layer) sites. These positions are labeled A, B, and C, respectively, in the second panel of Figure 1. The iron pyrrhotite structure was modeled by removing an iron atom from the top layer, thereby creating a vacancy in this layer. The most stable positions for the hydrogen molecule at its ASED minimum energy distance were found. In several cases, once this position was found, the hydrogen atom closest to the surface was fixed and the position of the outermost hydrogen optimized with the grid search option of the ASED program. The binding energy of the hydrogen molecule to the surface was of the order of 0.04-0.07 eV, in other words, a physisorption process is occurring. However, in the presence of the vacancy the physisorption energies slightly decrease, indicating an inhibitory effect as the iron pyrrhotite structure is formed. We next investigated the adsorption of a simple organic molecule, ethylene. The ethylene molecule, at its ASED minimum energy configuration, was brought up parallel to the surface of the cluster. In this manner, the  $p_z$  orbitals of the carbon atoms can interact with the  $d$  orbitals of iron. The ethylene molecule was allowed to approach with one carbon atom fixed directly above an iron atom and the other carbon atom along the  $x$  axis. Once the minimum energy distance above the surface of the molecule was found, the  $\text{CH}_2$  fragment not above the iron was allowed to relax until the energy of that fragment was minimized. For each of the sites studied, the binding energy of ethylene to the surface was found to be about 1 eV—i.e., a chemisorption process is occurring. There was almost no difference in binding energies whether the adsorption site was the central iron atom or one removed from the central atom. However, when a vacancy was created, the binding energy of ethylene over the vacancy site (with the sulfur layer underneath) decreased to about 0.25 eV, even after considerable relaxation of the whole ethylene molecule.

In order to compare the effect of the sulfur layer, the second layer was changed to iron (i.e., a pure iron cluster) and the same procedure followed. The adsorption in the absence of the vacancy was the same as for the iron-sulfur cluster. However, in the presence of the vacancy the chemisorption energies did not decrease as much as in the presence of a sulfur layer. Therefore, the presence of sulfur appears to have an inhibitory effect on the chemisorption ability of the cluster surface.

We next studied the adsorption of toluene and 1-methylnaphthalene on the FeS cluster. A typical geometry studied is shown in Figure 2. The ring system of toluene was kept fixed at experimental distances and kept planar. The height of the toluene molecule above the surface and bond distances, angles, dihedral angles of the ring- $\text{CH}_3$  group were optimized coarsely in this preliminary study. The binding of toluene to an iron atom of the surface is about 2.5 eV and of 1-methylnaphthalene about 5 eV. We observe a transfer of charge from the ring systems to the cluster with a resultant decrease in the ring- $\text{CH}_3$  bond breaking energy as compared to unadsorbed toluene and 1-methylnaphthalene: from 4.25 to 2.8 eV for toluene and from 4.18 to 2.6 eV for 1-methylnaphthalene (the geometry of the adsorbed molecules has

not yet been fully optimized, and so the energies are still approximate). Our initial results lead to the conclusion that the compounds are strongly chemisorbed on the catalyst surface, with a resultant transfer of charge from the molecule to the catalyst, leading to a decrease in bond breaking energies. This appears to be similar to the mechanism proposed by Farcasiu, *et al.*<sup>15</sup> in the context of the catalytic decomposition of 4-(1-naphthylmethyl)bibenzyl in the presence of carbon black. We are now in the process of doing more rigorous geometry optimizations for the cases considered above and studying other adsorption sites, the effect of iron vacancies, and modeling other surfaces which have sulfur exposed.

## D. Acknowledgement

This research was supported by USDOE contract DE-FC22-90PC90029 with the Consortium for Fossil Fuel Liquefaction Science and the University of Kentucky Center for Computational Sciences.

## References

1. Pradhan, V.R.; Herrick, D.E.; Tierney, J.W.; Wender, I. *Energy Fuels* **1991**, *5*, 712.
2. Derbyshire, F.; Hager, T.; *Prepr., Div. Fuel Chem., Am. Chem. Soc.* **1992**, *37(1)*, 312.
3. Srinivasan, R.; Keogh, R.A.; Davis, B.H. *Prepr., Div. Fuel Chem., Am. Chem. Soc.* **1992**, *37*, 1265.
4. Hoffmann, R.; *J. Chem. Phys.* **1963**, *39*, 1397.
5. Whangbo, M.-H; Hoffmann, R.; *J. Am. Chem. Soc.* **1978**, *100*, 6093.
6. Zonneville, M.C.; Hoffmann, R.; Hoek, P.J. van den; Santen, R.A. van; *Surf. Sci.* **1989**, *223*, 233 and Zonneville, M.C.; Hoffmann, R.; Harris, S.; *Surf. Sci.* **1988**, *199*, 320.
7. Anderson, A.B.; *J. Chem. Phys.* **1974**, *60*, 2477, (1974).
8. Ades, H. F.; Companion, A. L.; Subbaswamy, K. R. *J. Phys. Chem.* **1991**, *95*, 2226.
9. Ades, H. F.; Companion, A. L.; Subbaswamy, K. R. *Prepr., Div. Fuel Chem., Am. Chem. Soc.* **1991**, *36*, 420.
10. Ades, H. F.; Companion, A. L.; Subbaswamy, K. R. *J. Phys. Chem.* **1991**, *95*, 6502.
11. Ades, H. F.; Companion, A. L.; Subbaswamy, K. R. (to be published).
12. Yu, J.; Anderson, A.B.; *J. Mol. Catal.* **1990**, *62*, 223 and Anderson, A.B.; and Choe, S.J.; *J. Phys. Chem.* **1989**, *93* 6145.
13. Howell, J.; Rossi, A.; Wallace, D.; Haraki, K.; Hoffmann, R. *Quantum Chemistry Program Exchange No. 344* (Indiana University, Bloomington).
14. Fleet, M.E.; *Acta Cryst.* **1971**, *B27*, 1864.
15. Farcasiu, M.; Smith, C.; *Energy Fuels* **1991**, *5*, 83.

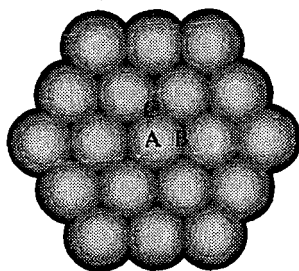
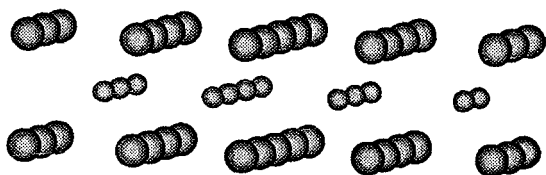


Fig. (1) Top Panel: FeS Cluster  
Bottom Panel: Adsorption site labels

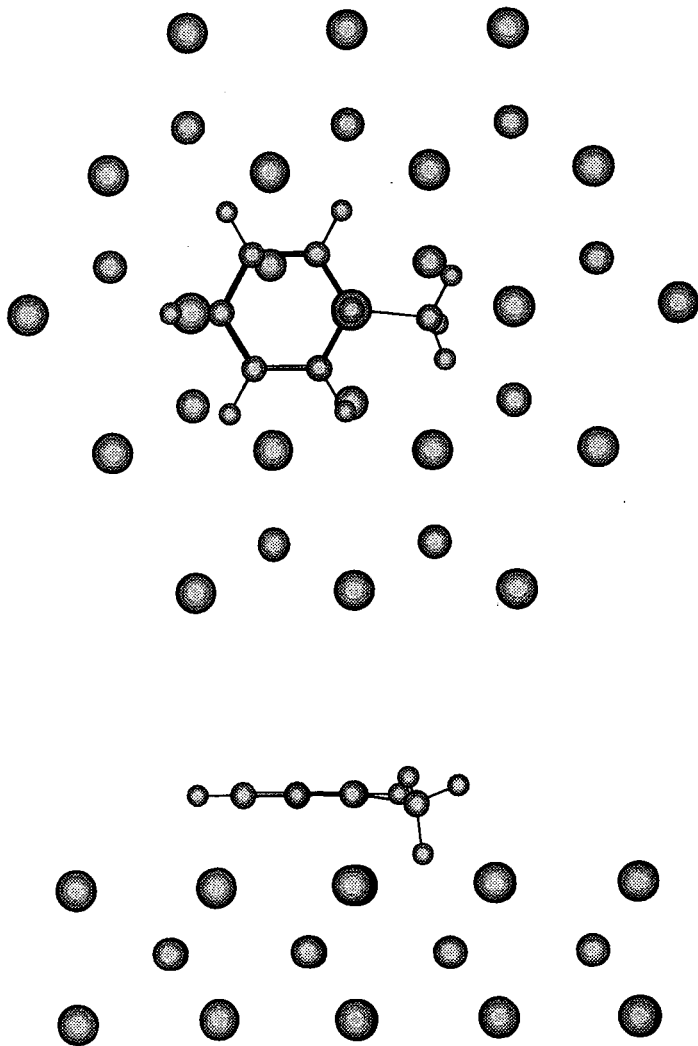


Fig. (2) Chemisorption of toluene on FeS cluster: top and side views

## RESULTS OF CATALYST TESTING USING IRON-BASED CATALYSTS

John C. Linehan, John G. Darab, and Dean W. Matson  
Pacific Northwest Laboratory<sup>1</sup>  
P.O. Box 999, Richland, WA 99352.

**Keywords:** Iron catalysts, Coal liquefaction, Model compounds

### ABSTRACT

New bulk and ultrafine iron-based coal liquefaction catalysts have been tested using coal substrates and a model compound. The results of these tests will be presented with emphasis on differences between bulk and ultrafine catalysts. The effects of catalyst size, surface area, and structure on both the model compound reactions and the coal liquefaction reactions will be compared. Special emphasis will be placed upon identifying the best catalyst precursor for optimizing THF soluble yields from coal experiments. In addition, results from different micro-reactors for coal liquefaction will be compared.

### INTRODUCTION

As coal liquefaction catalysts, iron-based products are generally inferior to the more expensive molybdenum, cobalt, or nickel-based materials. However, the lower costs of production and recovery (or in the case of some iron catalysts, non-recovery) give the iron-based materials a potential economic advantage over the more efficient precious and semi-precious metal catalysts for this application. Recent research has shown that a number of different iron-containing materials can be successfully utilized as coal liquefaction catalysts or as catalyst precursors.<sup>2-6</sup>

Pyrrhotite ( $Fe_{1-x}S$ ) or a similar iron-sulfide phase is commonly believed to be the active catalyst in coal liquefaction and model compound pyrolysis reactions,<sup>7</sup> although no specific phase has been yet been isolated as the actual catalyst species. The active iron-containing catalyst is usually generated *in situ* from an iron-oxide precursor and an elemental sulfur source under reducing conditions in the reactor vessel. Most research has concentrated on the use of common iron-oxide phases such as hematite or goethite (and their derivatives) as the iron-bearing precursor, or on non-specific iron materials produced by the reaction of various iron salts and compounds in the coal or liquefaction reactor. To our knowledge there has been no systematic effort to determine the optimum iron-containing precursor phase for producing active coal liquefaction catalysts, despite the fact that there are over ten iron-(hydroxy)oxide phases which can be easily synthesized in the laboratory.<sup>8</sup>

We have undertaken a systematic study to identify the most active iron-oxide catalyst precursor phases, the co-catalysts, and the coal pretreatments which will provide optimum yields in coal liquefaction processes. In this paper we present recent results of a study using a range of different authentic single phase iron-containing powders as catalyst precursors in coal model compound dissociation reactions. We also present the results of using ultrafine iron-containing powders synthesized by the Rapid Thermal Decomposition of Solutes (RTDS)<sup>9,10</sup> and Modified Reverse Micelle (MRM)<sup>11</sup> methods as precursors for catalysts in model compound reactions. Preliminary results of coal liquefaction runs using both fixed volume tubing bomb reactors and a flow through micro-liquefaction reactor are included.

### EXPERIMENTAL

The synthesis of iron-containing powders using MRM<sup>11</sup>, RTDS,<sup>9,10</sup> and standard laboratory procedures<sup>8</sup> has been described elsewhere. All iron-containing materials synthesized for use in this study were analyzed by X-ray diffraction (XRD) and other methods as appropriate. The model compound (naphthyl bibenzylmethane), its synthesis, and the test reactor conditions were also described previously.<sup>11,12</sup>

**Tubing Bomb Coal Liquefaction Runs** - Coal liquefaction studies were performed using the Wyodak and Blind Canyon Seam Argonne premium coals. The coal (1.2 g), iron-oxide catalyst precursor (0.01 g), and elemental sulfur (0.01 g) were loaded into 316 stainless steel tube reactors with 2 ml of tetralin and pressurized with 800 psi hydrogen. The total volume of the stainless steel vessel and the gas inlet was less than 6 ml. The vessels were placed in a fluidized sand bath at the selected temperature for a specified time. A thermocouple was placed in contact with the metal surface of the reactor, allowing indirect observation of the reaction temperature. The warmup times were typically 1 minute to 380°C, 5 minutes to 390°C and 10 minutes to 400°C. The temperature variation during an hour long run was  $\pm 3^\circ\text{C}$  once the reaction temperature was attained.

The reaction product was extracted with tetrahydrofuran (THF), and the dried insoluble residue was used to calculate the liquefaction yield. The THF extract was reduced in volume and precipitated with pentane to determine the amount of pentane insolubles. The pentane soluble fraction was calculated by difference. All yields are reported as moisture and ash free (maf).

**Micro-Liquefaction Reactor** - The micro-liquefaction reactor (Fig. 1) consisted of an in-line filter assembly attached to a HPLC pump and a capillary restrictor at the reactor exit for maintaining pressure. The stainless steel fritted cup was filled with the coal or coal/catalyst mixture, weighed, and sealed inside the micro-reactor body. Tetralin was pumped at 0.2 ml per minute through the assembly at a pressure sufficient to maintain the tetralin as a liquid at 400°C. The assembly was immersed in a fluidized sand bath at the desired temperature for the appropriate time. The dark colored tetralin fractions were collected continuously. After removal from the sand bath, tetrahydrofuran was pumped through the cooled micro-reactor until the color of the effluent was a light yellow. The coal residue was weighed after Soxhlet extraction with THF and drying. After cooling, the tetralin insolubles were filtered and weighed. Pentane was then added to the THF soluble fraction to precipitate the pre-asphaltenes, which were also filtered and weighed.

## RESULTS

Table I shows that most of the authentic laboratory-prepared oxyhydroxides, particularly lepidocrocite ( $\gamma\text{-FeOOH}$ ) and goethite ( $\alpha\text{-FeOOH}$ ), were better catalyst precursors than the oxides for carbon-carbon bond scission in naphthyl bibenzylmethane. Pure magnetite ( $\text{Fe}_3\text{O}_4$ ) and maghemite ( $\gamma\text{-Fe}_2\text{O}_3$ ) were found to be particularly poor catalyst precursors for this reaction. The proto-oxyhydroxide, 2-line ferrihydrite, was also determined to be a poor catalyst precursor for the model compound reaction. The organic products of the catalytic runs were almost exclusively methylbibenzyl and naphthalene (with some tetralin). The iron-containing products, while not rigorously characterized after the reaction runs, were typically observed as black solids with at least some ferromagnetic component.

Significant increases in the activity of the 2-line ferrihydrite, magnetite, and maghemite phases toward carbon-carbon bond scission in the model compound were noted when the materials were produced by the RTDS and the MRM methods (Table II). This increase in yields may have been due to smaller particle size or the presence of undetectable active phases in the initial catalyst precursors of the RTDS and MRM powders.

Selected coal liquefaction results utilizing tubing bombs (Table III) and using a MRM synthesized "iron-sulfide" catalyst showed that the reactivity of this catalyst appeared to change with the coal utilized. The results obtained using Wyodak coal showed an obvious improvement in both the THF soluble and the pentane soluble fractions obtained using this catalyst. There was, however, no statistical difference between the catalyzed and uncatalyzed runs when the Blind Canyon Seam coal was used with the MRM "iron-sulfide" catalyst.

The results of testing 2-line ferrihydrite catalyst precursors synthesized by the MRM method on both Wyodak and Blind Canyon Seam coals shown in Table IV. Again, a larger enhancement in the production of THF soluble products over thermal-only runs was noted when using the catalyst on the Wyodak coal. There was also an increase observed in the production of the pentane soluble fraction for both coals over the thermal-only runs when using the 2-line

ferrihydrate precursor.

Table V shows the Blind Canyon Seam coal liquefaction run results for a series of iron-oxides and oxyhydroxides produced by the RTDS method. A moderate increase in the total liquid products as well as a smaller increase in pentane solubles was observed with these catalyst precursors relative to the thermal-only run.

Figure 2 shows the liquefaction yields from Blind Canyon Seam coal when a 2-line ferrihydrate catalyst precursor produced by MRM was used in the flow-through micro-reactor. The total liquid yield in these runs was only slightly greater than in the non-catalyzed or sulfur-only thermal runs for this coal, but a definite difference was observed in the types of products formed when the flow-through reactor was used. The amounts of tetralin insolubles and pentane insolubles obtained in the catalyzed runs were significantly less than in the uncatalyzed runs.

### SUMMARY

The testing of authentic iron-(hydroxy)oxide phases with the naphthyl bibenzylmethane model compound demonstrated large differences in catalytic activity between the starting iron-containing species. Materials produced by MRM and RTDS promoted more reaction with the model compound than did the phases synthesized using literature procedures. Our testing with coals showed that ultrafine iron-oxyhydroxide powders produced by the RTDS and MRM methods were good catalyst precursors for coal liquefaction in the presence of sulfur.

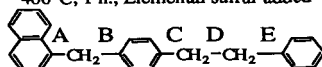
### ACKNOWLEDGEMENTS

We thank Drs. J. A. Franz, D. M. Camioni and S. T. Autrey for discussions of the model compound and coal liquefaction results. We also thank the Department of Energy, Office of Fossil Energy for supporting this work under contract DE-ACO6-76RLO 1830.

### REFERENCES

1. Pacific Northwest Laboratory is operated for the U. S. Department of Energy by Battelle Memorial Institute. This work was supported by the U. S. Department of Energy, Office of Fossil Energy under contract DE-ACO6-76RLO 1830.
2. Pradhan, V. R.; Tierney, J. W.; Wender, I.; and Huffman, G. P., *Energy & Fuels*, **1991**, *5*, 497.
3. Pradhan, V. R.; Herrick, D. E.; Tierney, J. W.; and Wender, I., *Energy & Fuels*, **1991**, *5*, 712.
4. Suzuki, T.; Yamada, H.; Yunoki, K.; and Yamaguchi, H., in *Proceedings: 1991 International Coal Symposium*, **1991**, 703.
5. Miki, K.; Yamamoto, Y.; Inabe, A.; and Sato, Y., in *Proceedings: 1991 International Coal Symposium*, **1991**, 675.
6. Bi, X-X; Derbyshire, F. J.; Eklund, P. C.; Hager, G. T.; and Stencel, J. M. *Energy & Fuels*, **1991**, *5*, 683.
7. Wei, X.-Y.; Ogata, E.; Aong, Z.-M.; and Niki, E. *Energy & Fuels*, **1992**, *6*, 868.
8. Schertmann, U. and Cornell, R. M. *Iron Oxides in the Laboratory*, Weinheim: New York, **1991**.
9. Mason, D. W.; Linehan, J. C.; and Bean, R. M. *Mater. Lett.*, **1992**, *14*, 222.
10. Matson, D. W.; Linehan, J. C.; and Darab, J. G. "Preparation of Ultrafine Catalyst Powders Using a Flow-Through Hydrothermal Process", This preprints.
11. Linehan, J. C.; Bean, R. M.; Matson, D. W.; Fulton, J. L.; and Crump, A. E. in *Preprints, Div. of Fuel Chem., American Chemical Society*, **1992**, *37*, 488.
12. Farcasiu, M. and Smith, C. *Energy & Fuels*, **1991**, *5*, 83.

TABLE I  
 MODEL COMPOUND REACTIONS  
 WITH AUTHENTIC IRON CONTAINING PHASES  
 400°C, 1 h., Elemental sulfur added



Naphthyl Bibenzylmethane

Catalyst	% Consumption	Selectivity <sup>a</sup>
<b>Controls</b>		
None	2-5%	40-60%
Sulfur Only	5-20%	50-70%
<b>Proto-Oxyhydroxide</b>		
2-Line Ferrihydrite	7%	71%
<b>Oxyhydroxides (FeOOH)</b>		
Feroxyhyte (δ')	45%	90%
Akaganeite (β)	14%	97%
Lepidocrocite (γ)	70%	93%
Goethite (α)	73%	92%
<b>Oxides</b>		
Hematite (α-Fe <sub>2</sub> O <sub>3</sub> )	37%	81%
Maghemite (γ-Fe <sub>2</sub> O <sub>3</sub> )	14%	86%
Magnetite (Fe <sub>3</sub> O <sub>4</sub> )	16%	54%

a) Selectivity is defined as [Products A + B Cleavage]/[Total Products]

Table II  
 MODEL COMPOUND RESULTS  
 WITH IRON-CONTAINING MATERIALS  
 PRODUCED BY RTDS AND MRM METHODS  
 400°C, 1 h., S added

Catalyst	% Consumption	Selectivity
<b>Controls</b>		
None	2-5%	40-60%
Sulfur Only	5-20%	50-70%
<b>RTDS</b>		
79-1 2-Line Ferrihydrite	49%	95%
79-4 Hematite	23%	83%
<b>MRM</b>		
39-39 2-Line Ferrihydrite	38%	90%
7-2 2-Line Ferrihydrite	51%	91%
7-2A Magnetite/Maghemite	77%	89%
9-2 "Iron-Sulfide"	68%	96%

Table III  
Coal Liquefaction Results Using  
MRM-Derived "Iron-Sulfide" Catalyst Precursor and Sulfur.<sup>a</sup>

Coal	Catalyst	% THF Soluble	% Pentane Soluble
Wyodak	None	71	39
Wyodak	9-2	85	46
BCS <sup>b</sup>	None	83	28
BCS <sup>b</sup>	9-2	85	28

a) Reaction conditions: 800 psi H<sub>2</sub>, 10 mg of sulfur, 400°C for 1 h.

b) BCS is Blind Canyon Seam.

Table IV  
Reverse Micelle Derived 2-Line Ferrihydrite  
Catalyst Precursors Reactions with Coals<sup>a</sup>

Coal	Catalyst	Liquefaction Temperature	% THF Soluble	% Pentane Soluble
Wyodak	None	400°C	71	39
Wyodak	7-2 + S	400°C	88	64
BCS <sup>b</sup>	None	350°C	58	23
BCS <sup>b</sup>	99-1 + S	350°C	63	32
BCS <sup>b</sup>	99-2 + S	350°C	62	30

a) Reaction conditions: 800 psi H<sub>2</sub>, 10 mg of sulfur, 1 h.

b) BCS is Blind Canyon Seam.

Table V  
RTDS Derived Iron-Oxide Catalyst Precursors  
Reactions with Blind Canyon Seam Coal<sup>a</sup>

Coal	Catalyst <sup>b</sup>	% THF Soluble	% Pentane Soluble
BCS <sup>c</sup>	None	83	29
BCS <sup>c</sup>	2-Line Ferrihydrite + S	87	30
BCS <sup>c</sup>	2-Line Ferrihydrite + S	91	30
BCS <sup>c</sup>	Hematite + S	91	35
BCS <sup>c</sup>	Hematite + S	93	36

a) Reaction conditions: 800 psi H<sub>2</sub>, 10 mg of sulfur, 400°C for 1 h.

b) Surface areas of catalyst precursors 180-215 m<sup>2</sup>/g as determined by BET.

c) BCS is Blind Canyon Seam.

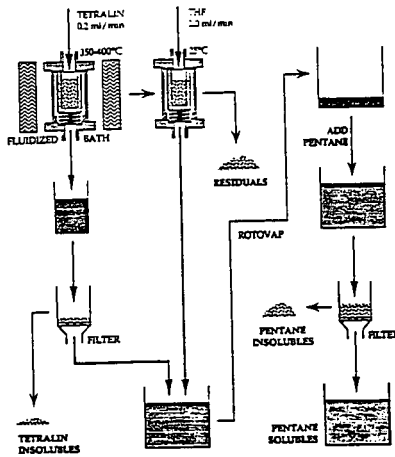


Figure 1. Schematic diagram of flow-through micro-liquefaction reactor and work-up method.

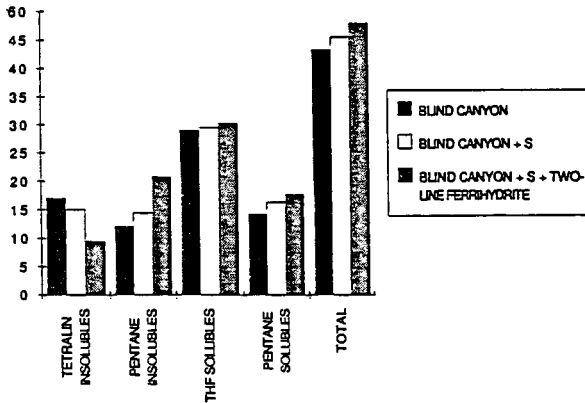


Figure 2. Liquefaction results of micro-liquefaction flow-through reactor with Blind Canyon Seam coal and a MRM synthesized 2-line ferrihydrite at 350°C for 1 hour with a 0.2 ml/min tetralin flow rate. Notice the large differences in the amount of tetralin and pentane insolubles between control and catalyzed runs.

EFFECT OF A SULFIDED, NON-POROUS AEROSOL  $Fe_2O_3$  CATALYST ON THE  
CHEMICAL STRUCTURE OF COAL LIQUIDS FROM THE  
HYDROLIQUEFACTION OF A HIGHLY VOLATILE BITUMINOUS COAL

Vicente L. Cebolla<sup>1</sup>, Moustapha Diack<sup>2\*</sup>, Michèle Oberson<sup>3</sup>, Robert Bacaud<sup>3</sup>, Dénise Cagniant<sup>2</sup> and Brigitte Nickel-Pépin-Donat<sup>3</sup>.

<sup>1</sup> Instituto de Carboquímica, CSIC. Plaza de Paraíso, 4. 50004 Zaragoza, Spain.

<sup>2</sup> Laboratoire de Chimie Organique, Université de Metz. Ile du Saulcy. 57045 Metz, France.

<sup>3</sup> Institut de Recherches sur la Catalyse, CNRS. 2, Avenue Albert Einstein. 69626 Villeurbanne, France.

\* Present address: Department of Chemistry, University of Tennessee. Knoxville, TE 37996-50.

## INTRODUCTION

Previous studies related with coal liquefaction in a batch reactor demonstrated that the pertinent parameter for the activity of a dispersed catalyst is not its total surface but the accessible external surface [1]. Thus, non-porous ultrafine aerosol oxides were synthesized by combustion of the corresponding metal chlorides in a hydrogen-oxygen flame [2-4]. Iron oxide precursors obtained in this manner, and sulfided with elemental sulfur during heating, showed a high catalytic activity for a highly volatile bituminous coal even at temperatures lower than that of most bond breaking [3]. Furthermore, the sintering of the initially dispersed iron sulfide was prevented by the presence of carbonaceous solid substances [5,6].

This work was extended to other aerosol types ( $SnO_2$ ,  $MoO_3$ ,  $SiO_2$ ,  $Al_2O_3$ ,  $NiMo/Al_2O_3$ ). Attempts were made to elucidate their active phases [7,8]. Their concentration, mode of sulfidation and introduction were also studied, as well as the effect of temperature and the solvent used [9]. Moreover, sulfided iron oxide aerosols also showed high yields in a multistage hydroliquefaction procedure [2, 10, 11].

In this paper, the effect of a sulfided aerosol  $Fe_2O_3$  on the chemical structure of oils and asphaltenes coming from the hydroliquefaction of a highly volatile bituminous coal will be compared to the effect of the other above-mentioned aerosols. For this purpose, methods of evaluation of hydroliquefaction runs in batch reactor and analytical techniques which permit differentiation between the effects of the catalysts have been developed.

## EXPERIMENTAL

### **Catalysts**

Fe<sub>2</sub>O<sub>3</sub>, MoO<sub>3</sub> and SnO<sub>2</sub> aerosol precursors were obtained by combustion of the corresponding chloride vapors. They were non-porous, with particle size lower than 50 nm and with BET surfaces from 20 to 60 m<sup>2</sup>g<sup>-1</sup>. SiO<sub>2</sub>, Al<sub>2</sub>O<sub>3</sub> and NiMo/Al<sub>2</sub>O<sub>3</sub> were commercial aerosols from Degussa and Institut Français du Pétrole (200 m<sup>2</sup>g<sup>-1</sup> S<sub>BET</sub>). More details are given in [1, 12].

### **Hydroliquefaction procedure**

This was described elsewhere [9]. Briefly, 40 g of a high volatile bituminous coal (from Freyming, France) were suspended in tetralin (95 g) with (or without in the blank run) 2% of catalyst precursor. Elemental sulfur was added in order to obtain a partial pressure of 1% H<sub>2</sub>S. The magnetically stirred reactor was pressurized (14 MPa) with H<sub>2</sub>. After the heating period (3°Cm<sup>-1</sup>), the nominal temperature (350, 400 or 430°C) was maintained for one hour before cooling.

### **Evaluation of catalytic activity in the hydroliquefaction runs**

Conversions were evaluated by parallel solvent extraction with THF, toluene and n-hexane, using microfiltration under pressure as it has been described in detail [9, 13]. The results were expressed in terms of the percentage of conversion into soluble products, calculated by the difference in weight of the insoluble fractions.

The activity of catalysts in hydrogen transfer reactions was evaluated by the extent of dehydrogenation of the solvent (expressed as the ratio of naphthalene to naphthalene + tetralin, measured by gas chromatography) and by the total consumption of hydrogen gas determined by the variation of the total pressure during a run [8, 14].

The influence of the catalyst was also confirmed by measurements of Electron Spin Resonance of the stable radicals of the THF insoluble fractions. Spectra were performed in a Varian E 112 apparatus at 9 GHz. Freyming macerals had been previously isolated by Density Gradient Centrifugation [15], and ESR parameters, also obtained at 9 GHz. Assuming that inertinite is the least reactive maceral, the percentage of "destroyed" fossil radicals in inertinite after hydroliquefaction runs can be calculated. This technique has been described in depth [16].

### **Analytical characterization of coal liquids**

Raw coal liquids were submitted to extrography [17]. A 2 g sample was dissolved in 15 ml of dichloromethane; then 16 g of activated (2 h at 120°C) silicagel were added to the solution and the mixture transferred to a column after elimination of the solvent. It was successively eluted with pentane/toluene (85/15), chloroform, chloroform/ethanol (97/3) and THF. The efficiency of extrography as a fractionation tool, advantages and structural attributions to the separated fractions have been described elsewhere [18, 19].

Derived oils and asphaltenes were separated by careful distillation of tetralin (controlled by GC/MS at 65°C under 0.27-0.4 kPa) and subsequent sequential ultrasonic extraction (Sonoclean B30 probe) in the conditions described in [20, 21].

Gas Chromatography (GC) of oils on a SE 30 glass capillary column were carried out in a Intersmat IGC 121C3 apparatus under the conditions described in [20, 21]. Identification of individual structures was out of the scope of our work. Results were summarized by retention index zones, which were calculated according to Lee et al. [22] with naphthalene,

phenanthrene and chrysene as standards. Literature reported that elution is made according to the number of total rings (aromatic or not) [23]. Index between 100-200 correspond to compounds with one ring, 200-300 to two rings, etc... This classification of ring size by retention indices can also be applied to phenolic and heterocyclic compounds, mainly nitrogen, neutral and basic compounds [23], and thiophenic structures [24].

The use of n-decane as internal standard allows a quantitative estimation (index zones) and the evaluation of non-dosed products.

Gel Permeation Chromatography (HPLC-GPC) on three  $\mu$ -styragel columns in series (1 x 500 Å + 2 x 100 Å) was applied to the oils and asphaltenes in a M-600 Waters apparatus with refractive index detection using dichloromethane as eluent [20]. Qualitative interpretation of chromatograms according to the partition in four zones as a function of the retention factor (k) was carried out on the basis of 70 model compounds, as follows:  $0.1 \leq k < 0.6$ : "asphaltenic type" of unknown structure,  $0.6 \leq k < 0.75$ : alkylated aromatics,  $0.75 \leq k < 0.85$ : non-alkylated aromatics, and  $0.85 \leq k < 1.1$ : pericondensed aromatics.

## RESULTS AND DISCUSSION

### The evaluation of catalytic effect

At the first stage of hydroliquefaction (350°C), differentiation between the effects of the catalysts is net and related to the different conversions in preasphaltenes and asphaltenes, hydrogen consumption and percentages of stabilized fossil radicals of inertinite [3]. Fe<sub>2</sub>O<sub>3</sub> and MoO<sub>3</sub> precursors were the most active catalysts (fig.1), also giving an enhancement of hydroaromatic structures (NMR <sup>13</sup>C/CP/MAS data) and breaking of ether bridges (FTIR data) in Freyming coal [8].

Taking into account that tetralin is not dehydrogenated at this temperature, and that tetralyl radicals do not stabilize fossil radicals of inertinite, a mechanism of H<sub>2</sub> dissociation on catalyst surface and subsequent migration of activated hydrogen (H<sup>\*</sup>) to stabilize the fossil radicals of inertinite, was proposed [8]. The small size of H<sup>\*</sup> would allow its diffusion into the inertinite structure.

Our results show that the catalytic effect is reduced at higher temperatures and the differentiation of catalysts by the total conversion in soluble products at 400 and 430°C is somewhat indecisive, as already observed by Makabe et al. [25]. Our total conversions are comprised in all the cases between 83 and 90% [26].

The wt% of consumed H<sub>2</sub> is more dependent on the nature of the catalyst. Tetralin donates hydrogen in the absence of added catalyst at 400°C but when used with a catalyst, the result is an increase of the contribution of gaseous hydrogen consumption [14]. Makabe et al. [25] pointed out that thermally produced coal radicals are mainly stabilized by H<sup>\*</sup> when the catalyst is active. With less active catalysts, the stabilization is due to tetralin. Therefore, catalyst efficiency can be related to its ability to dissociate H<sub>2</sub> into H<sup>\*</sup> and the ratio of hydrogen transferred from gas phase to hydrogen transferred from the solvent (H<sub>gas</sub>/H<sub>soln</sub>) is a good test to evaluate it (table 1).

The efficiency of the catalysts (at 350 and 400°C) evaluated by H<sub>gas</sub>/H<sub>soln</sub> parameters, are well related to the wt% of fossil radicals stabilized in the inertinite during hydroliquefaction at the same temperatures. Table 1 shows that trends are similar for both parameters at 350°C. The order of wt% of fossil radicals stabilized at 400°C decreases in the following order: SnO<sub>2</sub>,

~ Fe<sub>2</sub>O<sub>3</sub> ~ NiMo/Al<sub>2</sub>O<sub>3</sub> > MoO<sub>3</sub> > SiO<sub>2</sub> > no catalysts. Trends are also similar to H<sub>gas</sub>/H<sub>solv</sub>, although this last allows a clearer differentiation among catalysts. At 430°C these ratios decrease significantly as the amount of hydrogen transferred from the solvent increases because of the thermal bond cleavage.

#### The influence of Fe<sub>2</sub>O<sub>3</sub> precursor on the structural composition of coal-derived liquids

According to the results of extrography of the raw liquids (fig.2) [13, 26], the formation of PAHs (main constituents of F1 and F2 fractions) increases significantly as the temperature increases, at the expense of polar compounds (F4) and residues. However the differentiation, for a given temperature, between runs with or without Fe<sub>2</sub>O<sub>3</sub>, is not decisive using this technique, except for a small increase of the lightest compounds (F1) for Fe<sub>2</sub>O<sub>3</sub> runs (400 and 430°C).

More details about the structural analyses were found when characterization of oils and asphaltenes were performed by GC on capillary columns and HPLC-GPC.

GC data, using the classification according to ring size as previously described in Experimental, revealed the higher and significant proportion of two-nuclei aromatic compounds in the oils when the runs were performed with non-porous sulfided Fe<sub>2</sub>O<sub>3</sub> or MoO<sub>3</sub> catalyst rather than with SiO<sub>2</sub>, SnO<sub>2</sub> or NiMo/Al<sub>2</sub>O<sub>3</sub>. This effect was found at 400 and 430°C for the iron precursor (fig 3). This fact could be attributed to hydrogenolysis of ether oxide or alkyl linkages between doubled two-ringed structures rather than to hydrocracking PAHs, all structures known to exist in the products of coal liquefaction [27]. Hypothesis of hydrocracking can be eliminated because pyrrhotite Fe<sub>1-x</sub>S formed from Fe<sub>2</sub>O<sub>3</sub> aerosol does not meet the requirements of hydrogenative and acid functions, needed for a hydrocracking reaction [28, 29]. The hypothesis of hydrogenolysis is supported by literature data on model compound reactions using iron oxide catalyst [30-32] and pyrrhotite [33, 34]. The possibility of a hydrodesulfurization activity of some carbon-based iron catalysts has been also reported [35] and should also be considered.

GC and HPLC-GPC data showed the important effect of temperature for oils and asphaltenes, in general, and for a given catalyst run [26]. On one hand, the wt% of non-dosed GC compounds decrease as the temperature increases (from 400 to 430°C), the cases of SiO<sub>2</sub> and SnO<sub>2</sub> being the most significant (fig. 3). On the other hand, HPLC-GPC showed that the same increase of temperature involves degradation of the heaviest components of asphaltenes (0 < k < 0.6) (fig. 4). However, this technique did not permit the observation of differences among the catalysts for a given temperature neither for oils nor for asphaltenes.

#### ACKNOWLEDGEMENTS

The authors wish to thank CNRS-PIRSEM for financial support, H. Charcosset (Directeur du GRECO "Hydroconversion et Pyrolyse", IRC) for his encouragement and scientific assistance, and M. Besson, and M. Lambertson for fruitful discussions.

#### REFERENCES

- 1 Andrès-Besson, M., Charcosset, H., Chiche, P., Davignon, L., Djega-Mariadassou, G., Joly, J.P., and Prégermain, S., *Fuel* 1983, 62, 69.
- 2 Bacaud, R., Besson, M., Brodski, D., Bussiere, P., Cagniant, D., Cebolla, V.L., Charcosset, H., Djega-Mariadassou, G., Jamond, M., Nickel, B., Oberson, M., in "Progress in Synthetic Fuels", ed. by Bemtgen J.M., Imarisio, G., Graham & Trotman,

- London, p. 9, 1988.
- 3 Charcosset, H., Bacaud, R., Besson, M., Jeunet, A., Nickel, B., and Oberson, M., *Fuel Process. Technol.* 1986, 12, 189.
  - 4 Charcosset, H., and Genard, A., in "Synthetic Fuels from Coal; Status of the Technology", ed. by Romey, P.F.M., and Imarisio, G., Graham & Trotman, London, p. 339, 1987.
  - 5 Djega-Mariadassou, G., Besson, M., Brodzki, D., Charcosset, H., Tran Vinh Huu, and Varloud, J., *Fuel Process Technol* 1986, 12, 143.
  - 6 Bacaud, R., Besson, M., Oberson, M., Brodzki, D., Bussiere, P., Charcosset, H., and Djega-Mariadassou, G., in "Catalyst Deactivation", ed. by Delmon, B., and Froment, G.P., Elsevier, Amsterdam, p. 289, 1987.
  - 7 Besson, M., Bacaud, R., Brodzki, D., Bussiere, P., Charcosset, H., Djega-Mariadassou, G., Oberson, M., and Sharma, B.K., *Fuel* 1990, 69, 35.
  - 8 Oberson, M., Ph D Thesis, University of Lyon, France, 1987.
  - 9 Besson, M., Bacaud, R., Charcosset, H., Cebolla, V.L., and Oberson, M., *Fuel Process. Technol.*, 1986, 12, 91.
  - 10 Bacaud, R., Charcosset, H., and Jamond, M., *Fuel Process. Technol.* 1990, 24, 163.
  - 11 Bacaud, R., *Fuel Process. Technol.* 1991, 28, 203.
  - 12 Vergnon, P.G., and Batis Landoulsi, H., *Ind. Eng. Chem. Prod. Res. Dev.* 1980, 19, 147.
  - 13 Tischler, R.E., and Utz, B.R., *Ind. Eng. Chem. Prod. Res. Dev.* 1983, 22, 229.
  - 14 Bacaud, R., *Applied Catalysis* 1991, 75, 105.
  - 15 Muller, J.F., Abou Akar, A., Kohut, J.P., in "Advanced Methods for Coal Characterization", ed. by Charcosset, H., assisted by Nickel, B., Elsevier, Amsterdam, p.359, 1990.
  - 16 Nickel-Pépin-Donat, B., Jeunet, A., Rassat, A., in "Advanced Methods for Coal Characterization", ed. by Charcosset, H., assisted by Nickel, B., Elsevier, Amsterdam, p. 143, 1990.
  - 17 Alula, M., Diack, M., Gruber, R., Kirsch, G., Wilhelm, J.C., and Cagniant, D., *Fuel* 1989, 68, 1330.
  - 18 Cemy, J., Sebor, G., and Mitera, J., *Fuel* 1991, 70, 857.
  - 19 Cebolla, V.L., Weber, J.V., Swistek, M., Krzton, A., and Wolszszak, Proceedings of "Coal Structure'92, Krakow, Poland, september, 1992, and submitted to *Fuel*.
  - 20 Cebolla, V.L., Bacaud, R., Besson, M., Cagniant, D., Charcosset, H., and Oberson, M., *Bull. Soc. Chim. France*, 1987, 935.
  - 21 Cebolla, V.L., PhD Thesis, University of Zaragoza, Spain, 1987.
  - 22 Lee, M., and Vassilaros, D.L., *Anal. Chem.* 1979, 51, 768.
  - 23 Lauer, J.C., Vallés, D.H., and Cagniant, D., *Fuel* 1988, 67, 1273.
  - 24 Rostal, C.E., and Pereira, W.E., *J. High Resol. Chromatogr.* 1986, 9, 328.
  - 25 Makabe, M., Ohe, S., Itoh, H., and Ouchi, K., *Fuel* 1986, 65, 296.
  - 26 Cebolla, V.L., Diack, M., Oberson, M., Bacaud, R., Cagniant, D., and Nickel-Pépin-Donat, B., *Fuel Process. Technol.* 1991, 28, 183.
  - 27 Shinn, J.H., 1985 *Int. Conf. on Coal Science*, Pergamon, Sydney, p. 738.
  - 28 Lambertson, J.L., and Guisnet, M., *Applied Catalysis* 1984, 13, 181.
  - 29 Lambertson, J.L., and Guisnet, M., *J. Chem. Res., Synop.* 224.
  - 30 Utoch, S., Hirata, T., Oda, H., and Yokokawa, C., *Fuel Process. Technol.* 1986, 14, 221.
  - 31 Cassidy, P.J., Jackson, W.R., Larkins, F.P., Herten, P.A., Rash, D., and Marshall, M., in "Advanced Topics and Applications to Fossil Fuel Energy, ed. by Petrakis, L., and

- Fraissard, J.P., D. Reidel, Dordrecht, p. 739, 1984.
- 32 Yoshimoto, I., Itoh, H., Makabe, M., and Ouchi, K., *Fuel* 1984, 63, 978.
  - 33 Montano, P.A., Lee, Y.C., Yeye-Odu, A., and Chien, C.H., *Am. Chem. Symp. Ser.*, 301, 416.
  - 34 Ogawa, T., Stenberg, V.I., and Montano, P.A., *Fuel* 1984, 63, 1660.
  - 35 Abotsi, G.M.K., and Scaroni, A.W., *Fuel Process. Technol.* 1989, 22, 107.

**Table 1.** Evaluation of catalytic activity in coal hydroliquefaction by ESR and hydrogen balance measurements

Catalyst	% of stabilized R.		$H_{gas}/H_{soliv}$	
	350°C	400°C	350°C	400°C
Without	0	60	0.83	0.33
Al <sub>2</sub> O <sub>3</sub>	0	66	1.87	0.65
SnO <sub>2</sub>	19	77	6.29	7.74
Fe <sub>2</sub> O <sub>3</sub>	52	74	8.75	8.53
MoO <sub>3</sub>	72	68	15.62	3.17
NiMo/Al <sub>2</sub> O <sub>3</sub>	-	73	-	13.05

**Figure 1.** % of conversions (THF) of hydroliquefaction runs at 350°C.

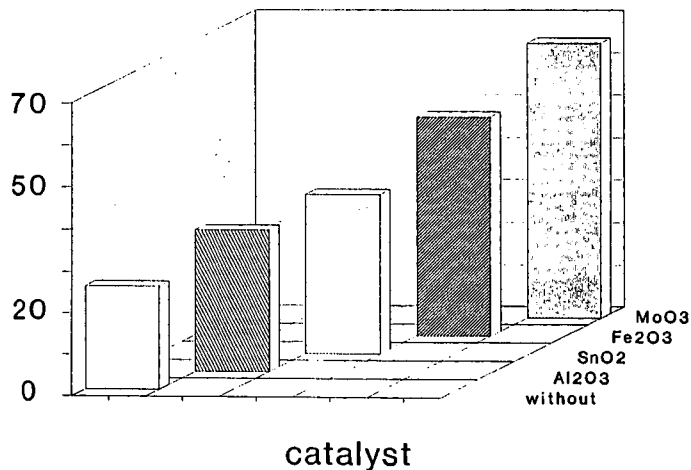


Figure 2. Iron oxide runs. Fractionation by Extrography.

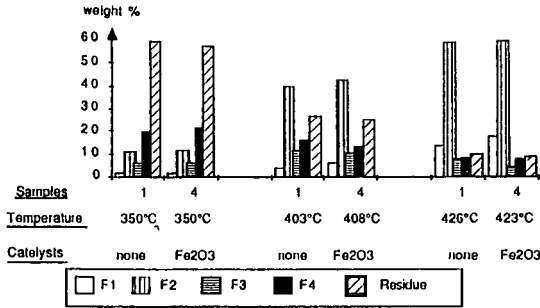


Figure 3. GC/CC analysis of oils. Classification by retention index zones.

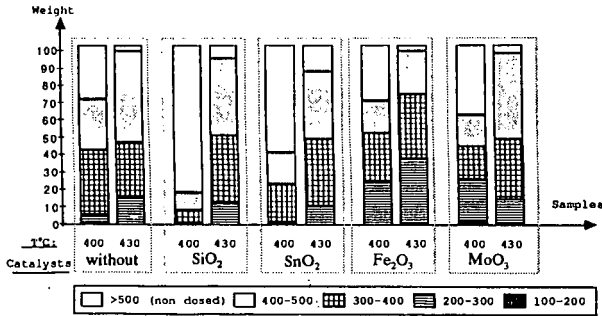
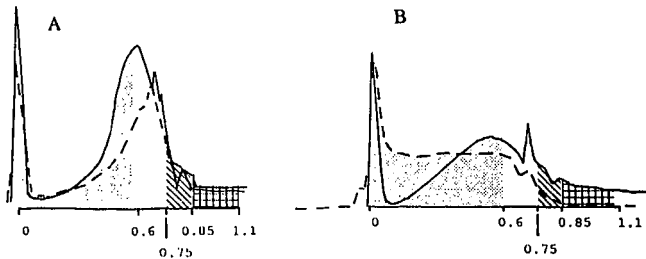


Figure 4. HPLC-GPC of oils (A) and asphaltenes (B) of iron oxide runs. (- - : 400°C; - : 430°C).



## DYNAMIC STUDIES OF THE INTERACTION OF IRON SULFIDES WITH HYDROGEN

N. M. Rodriguez, and R. T. K. Baker  
Materials Research Laboratory  
The Pennsylvania State University  
University Park, PA, 16802

Keywords: Modified iron catalysts, hydrogen spillover,  
hydrogenation of solid carbon

### ABSTRACT

*Controlled atmosphere electron microscopy and in-situ electron diffraction techniques have been used to study the manner by which various iron sulfides interact with hydrogen using graphite as a probe material. When the metal sulfide was in direct contact or physically separated from the graphite probe, pitting of the basal plane regions was observed even at room temperature. This unusual behavior is believed to result from the action of atomic hydrogen on the metal sulfide particles. These species are extremely reactive towards the  $\pi$ -electrons present on the graphite basal planes and this action leads to the creation of pits. At the low pressures used in this work, 0.2 Torr, it is clear that the atomic species can migrate not only by surface diffusion processes (spillover) but also by transport through the gas phase.*

### INTRODUCTION

The notion of using atomic hydrogen to convert carbonaceous solids to a variety of hydrocarbon products has been the subject of a number of investigations<sup>1-10</sup>. This type of study has also been extended to cover the interaction of atomic hydrogen with various coals<sup>6-10</sup>. Sanada and Berkowitz<sup>6</sup> compared the reactivity pattern arising from the interaction of atomic hydrogen with various coals to that with graphite. They found that a complex mixture of gaseous hydrocarbons was produced from the coal samples, whereas when graphite was the reactant methane was the sole product. Amano and coworkers<sup>7,8</sup> carried out a very comprehensive examination of the products generated from the interaction of a Japanese subbituminous coal with atomic hydrogen at 200°C and reported that gaseous hydrocarbons accounted for only 10 to 15% of the coal converted, the major product being a liquid which consisted of C<sub>5</sub> to C<sub>22</sub> alkanes and cycloalkanes. A somewhat different product spectrum was found by Wong and coworkers<sup>9</sup> from their investigation of the reaction of atomic hydrogen with a bituminous coal (Illinois No 6), where the major products were low molecular weight volatile hydrocarbons (methane, acetylene, ethylene and propane).

Transition metal sulfides are used extensively as hydrotreating catalysts with the most important reaction in this category been hydrodesulfurization (HDS) and there are a number of excellent reviews on this subject<sup>11-14</sup>. In such systems the precise manner by which hydrogen interacts with the sulfide catalyst is a key factor to the understanding of the mechanism. Wright and coworkers<sup>15</sup> studied the interaction of hydrogen with alumina supported molybdenum disulfide catalysts using a combination of hydrogen adsorption and inelastic neutron scattering techniques. They found that

the uptake of hydrogen was several times higher than that which was expected from nitrogen adsorption experiments. In order to account for this unusual behavior they suggested that the adsorption of extra hydrogen could arise from intercalation into the layered structure of the sulfide particles or alternatively as a result of hydrogen "spillover" onto the alumina support.

In the current investigation we have attempted to gain a clearer understanding of the manner by which hydrogen interacts with various iron sulfides as a function of temperature by using controlled atmosphere electron microscopy techniques. In these experiments graphite has been used as a probe material since its reactivity in both molecular and atomic hydrogen is well characterized

## EXPERIMENTAL

The experiments reported here were carried out in a modified JEOL 200CX TEM electron microscope, which allows one to continuously observe the behavior of a specimen as it is heated in the presence of a gas environment. In addition to being able to directly follow changes in the appearance of a specimen as it is undergoing reaction it is also possible to use the microscope in the diffraction mode and obtain information about the chemical state of the specimen at any stage of the experiment.

In this investigation two types of specimen arrangements were utilized. (a) The catalyst particles (metal sulfide) were placed in direct contact with the graphite specimen, and the observations made were limited to areas in the vicinity of the catalyst particles. (b) A microscope grid was cut in half and one section contained a pristine transmission graphite specimen and on the other, the catalyst mounted in the same manner as shown in (a). In this arrangement the catalyst and graphite probe reactant were physically separated. It was essential that when this type of specimen was placed into the environmental cell the reactant gas stream came into contact with the catalyst prior to passing over the clean graphite, the component under observation.

## RESULTS AND DISCUSSION

### *(a) Iron Sulfide/Graphite-Hydrogen*

When graphite specimens containing particulates of either  $\text{FeS}_2$  or  $\text{FeS}$  were exposed to 0.2 Torr hydrogen a very unusual pattern of behavior was observed. Immediately following the introduction of the gas attack of the basal plane regions of the graphite support took place at room temperature. This action initially took the form of the creation of very tiny pits which became visible when their width had expanded to approximately 1.2 nm and their depths reached a level sufficient to allow a contrast difference to be observed in the transmission image between the pit and the surrounding unattacked graphite.

It was evident that in the early stages of the reaction the pits tended to be generated in clusters which were aligned in definite directions with respect to the graphite substrate. Examination of numerous areas showed that the hexagonal arrangement was predominant. On continued reaction at the same temperature the pits increased in size and in a given group gradually merged with each other to form a single larger entity up to 10 nm in width. Examination of these more highly developed pits showed

that they tended to acquire a hexagonal outline and at this stage generally contained an internal region of unattacked carbon.

The intensity of the reaction increased significantly as the temperature was gradually raised to 200°C. Unfortunately, the indiscriminate mode of attack made it impossible to identify any dynamic events that could be followed for the purposes of estimating rates of graphite hydrogenation. Moreover, the gradual deterioration in quality in the transmission image due to collection of deposit on the specimen made it difficult to resolve many surface features. In studies where the temperature was held at 350°C for extended periods of time the attack became so extensive that specimens lost their integrity and experiments were normally terminated.

On continued heating to above 500°C, the sulfide particles were observed to exhibit a change in morphological characteristics from faceted structures to a more globular geometry. This transformation which occurred at about 725°C with the iron sulfides was most clearly evident with particles located at edge regions which appeared to be quite fluid and tended to wet the graphite. This behavior was a prelude to the restoration of catalytic activity, seen as the propagation of channels by these particles when the temperature was increased by a further 100°C.

A more fundamental understanding of the factors which control the ability of a supported particle to undergo morphological changes can be obtained from a treatment of the surface forces operative at the particle-support-gas interface. Consider the situation of a metal sulfide particle located at the edge site of a carbonaceous solid exposed to a hydrogen environment, as depicted in Figure 1. The contact angle,  $\theta$  at equilibrium is determined by the surface energy of the support,  $\gamma_{GS}$ , the surface energy of the metal sulfide particle,  $\gamma_{PG}$ , and the particle-support interfacial energy,  $\gamma_{PS}$ , and is expressed in terms of Young's equation:

$$\gamma_{GS} = \gamma_{PS} + \gamma_{PG} \cos \theta \quad (1)$$

or 
$$\cos \theta = \frac{\gamma_{GS} - \gamma_{PS}}{\gamma_{PG}} \quad (2)$$

If  $\gamma_{PG}$  is larger than  $\gamma_{GS}$ , the contact angle is greater than 90° and the particle is in a non-wetting state, if the reverse is true,  $\theta$  is less than 90°, then wetting occurs, and if  $\gamma_{GS} = \gamma_{PS} + \gamma_{PG}$ , then the particle will spread out over the support surface in the form of a thin film. Spreading of the catalyst particle results in the most efficient use of the additive in that the contact area between catalyst and carbon atoms is maximized.

The ability for particles to undergo the morphological transformations mentioned above indicates that a significant degree of atomic mobility exists, particularly in the surface layers. Previous studies<sup>16</sup>, have demonstrated that this phenomenon can occur below the Tammann temperature of the material constituting the particles, which is calculated from 0.52 [bulk melting point {K}]. For iron sulfides the Tammann temperature is about 480°C, and for systems such as those studied in this work, where a weak interaction exists with the support, particles will exhibit mobility at this temperature<sup>17</sup>.

In an attempt to determine whether the catalytic action could be sustained at even greater distances from the sulfide particles, another set of experiments was carried out

using a different specimen design. This involved complete physical separation of the supported metal sulfide and the graphite probe component. When this combination was treated in 0.2 Torr hydrogen then attack of the unadulterated graphite surface was once again observed at room temperature. In these systems, however, there was a modulation in the severity of the reaction compared to that where the catalyst and graphite were in intimate contact. It was significant to find that the incidence of pit formation showed a steady decline as one scanned across the graphite surface in the opposite direction to that where the sulfide catalyst particles were located.

A feature which must always be taken into consideration with experiments carried out within the electron microscope is whether the electron beam exerts any effect on either the gas or the solid under investigation. Concern that this problem was being encountered in the current work was dispelled by performing "blank experiments" in which specimens were reacted in hydrogen with the beam turned off for periods of up to two hours. When such specimens were eventually examined it was clear that there have been extensive reaction prior to exposure to the beam.

#### *(b) In-Situ Electron Diffraction Analysis*

In a final series of experiments the electron microscope was operated in the *in-situ* diffraction mode and patterns taken of the FeS<sub>2</sub>/graphite specimens at various stages of the reaction during heating from room temperature up to 850°C in 0.2 Torr hydrogen. Examination of the data summarized in Table 1 shows that reduction of FeS<sub>2</sub> to FeS and Fe<sub>7</sub>S<sub>8</sub> (Pyrrhotite) starts to occur at 240°C and at 400°C respectively, and these latter sulfides become the stable phases. At 600°C FeS appears to be the only phase present, however, on increasing the temperature to 750°C metallic iron ( $\gamma$ ) begins to appear along with Fe<sub>3</sub>C.

The major feature which emerges from this study is that the interaction of hydrogen with certain metal sulfides produces a species, which even at room temperature is highly reactive towards the  $\pi$ -electrons present on the graphite basal plane and this action leads to the creation of pits. The observation that the carbonaceous solid does not necessarily have to be in direct contact with the metal sulfide particles in order for hydro-gasification to occur, indicates that at the gas pressure used in these experiments, it is possible for the active species to be transported through the gas phase in addition to the surface migration route. The intensity of this action appears to increase with temperature up to a certain point and then come to a complete halt. Catalytic activity could, however, be regenerated by lowering of the temperature to a previously active regime.

This intriguing pattern of behavior can be rationalized according to the following arguments. At low temperature graphite can only undergo attack due to interaction with atomic species, generated from the dissociation of molecular hydrogen with metal sulfides via a reversible chemisorption process. This reaction will continue until conditions are reached which favor weakening of sulfur-metal bonds and the concomitant release of hydrogen sulfide. At higher temperatures, the sulfides are converted to the metallic state and the mode of gasification of graphite will revert to that normally associated with the metal, i.e. channeling.

## ACKNOWLEDGMENTS

Financial support for this research was provided by the United States Department of Energy, Basic Energy Sciences, Grant DE-FG05-89ER14076 and CFFLS Program Contract No DE-FC22-90-PC90029.

## REFERENCES

1. Blackwood, J. D., and McTaggart, F.K., *Aust. J. Chem.*, **12**, 533 (1959).
2. Gill, P. S., Toomey, R. E., and Moser, H. C., *Carbon* **5**, 43 (1967).
3. Vastola, F. J., Walker, Jr., P. L. and Wightman, J. P., *Carbon* **1**, 11 (1963)
4. Wood, B. J., and Wise, H., *J. Phys. Chem.*, **73**, 1348 (1969)
5. McCarroll, B., and McKee, D.W., *Carbon*, **9**, 301 (1971)
6. Sanada, Y., and Berkowitz, N., *Fuel*, **48**, 375 (1969).
7. Amano, A., Yamada, M., Shindo, T., and Akakura, T., *Fuel* **63**, 718 (1984).
8. Amano, A., Yamada, M., Shindo, T., and Akakura, T., *Fuel* **64**, 123 (1985).
9. Wong, C.-L. Chen, C.-W. and Timmons, R. B., *Fuel* **65**, 1483 (1986).
10. Gesser, H. D., and Czubryt, J. J., *Fuel* **67**, 375 (1988).
11. Massoth, F.E., *Adv. Catal.* **27**, 265 (1978).
12. Delmon, B., in *Proc. Climax Third Intern. Conf. on Chemistry and uses of Molybdenum* (H.F. Barry and P.C.H. Mitchell, eds) *Climax Molybdenum Co. Ann Arbor, Michigan 1980*, p 73.
13. Grange, P. *Catal. Rev. Sci. Eng.* **21**, 135 (1980).
14. Topsoe, H. and Clausen, B. S., *Catal. Rev. Sci. Eng.* **26**, 395 (1984).
15. Wright, C. J., Sampson, C., Fraser, D., Moyes, R. B., Wells, P. B. and Riekel, C., *J.C.S. Faraday I* **76**, 1585 (1980).
16. Derouane, E.G., Baker, R. T. K., Dumesic, J. A. and Sherwood, R. D., *J. Catal.* **69**, 101 (1981).
17. Baker, R. T. K., *J. Catal.* **78**, 473 (1982).

TABLE 1. IN-SITU ELECTRON DIFFRACTION ANALYSIS OF FeS<sub>2</sub> REACTING IN H<sub>2</sub>

TEMPERATURE (°C)	PHASES PRESENT
240	FeS <sub>2</sub> ; FeS*
300	FeS <sub>2</sub> ; FeS
400	FeS <sub>2</sub> ; FeS; Fe <sub>7</sub> S <sub>8</sub>
500	FeS <sub>2</sub> ; FeS; Fe <sub>7</sub> S <sub>8</sub>
600	FeS
700	FeS
750	FeS; Fe <sub>3</sub> C; α-Fe <sup>*</sup> ; γ-Fe

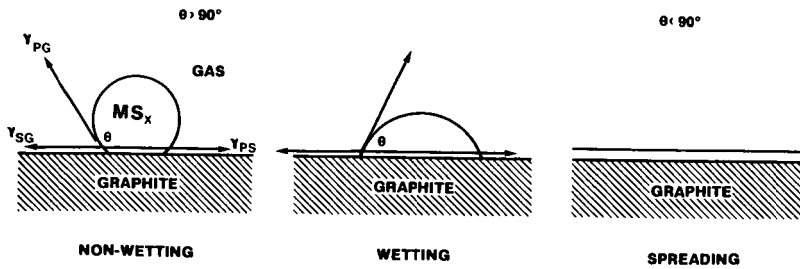


Figure 1. Metal Sulfide-Graphite-Hydrogen Interaction

\* Possibly present

## ACTIVITY AND SELECTIVITY OF DISPERSED IRON CATALYST IN COAL LIQUEFACTION AND MODEL COMPOUND REACTIONS

James A. Guin\*, Xiaodong Zhan and Ritu Singh  
Department of Chemical Engineering  
Auburn University, AL 36849

**Keywords:** Coal liquefaction, hydrogenation, iron catalyst

### INTRODUCTION

Owing to the difficulties of recovering more expensive catalysts such as Ni, Mo after use, iron has continued to be of interest as the basis of an economical and disposable catalyst for coal liquefaction. Most of the investigations on iron catalysts have focused on non-supported highly dispersed catalysts, introduced via impregnation techniques and as finely divided powder. It is believed that dispersed phase catalysts in coal liquefaction can offer several advantages over conventional ones<sup>[2,3,6]</sup>. A suitably dispersed catalyst helps to establish a highly reducing environment with the coal matrix in the presence of hydrogen, thus reducing the need for a good hydrogen donating solvent. Effective contact of coal-solvent slurries with the catalyst surface can be achieved even at low catalyst concentration. Diffusion limitations are minimized because of the small catalyst particles. In addition, certain bond cleavage reactions can be promoted during the early liquefaction step which minimize the detrimental regressive reactions. The objective of our research is to examine the catalytic activity of dispersed iron oxide catalyst in the coal liquefaction process. To lay a good foundation for this work we have also examined the selectivity and activity of several forms of iron including  $Fe_2O_3$ ,  $FeS_x$  and reduced Fe in both a continuous and a tubing bomb microreactor (TBMR) using naphthalene and biphenyl as model compounds. Coal liquefaction experiments were also performed with a small particle iron catalyst.

### EXPERIMENTAL

**Coal Liquefaction Reaction Procedures:** Coal liquefaction experiments were carried out in 45 cc tubing bomb microreactors (TBMR's) at the reaction conditions outlined in Table 1. The ratio of reaction solvent (tetralin, 1-methylnaphthalene, or mineral oil) to coal (Blind Canyon DECS-17 and Illinois #6) was 3:1. Elemental sulfur was added as a sulfur source with the DECS-17 coal. The iron catalyst employed was Fe-3 (Nanocat superfine iron oxide, Mach-1 Inc.). According to the product specification, it is  $\alpha-Fe_2O_3$  with a surface area of  $282 \text{ m}^2/\text{g}$ , and particle size of  $30 \text{ \AA}$  and approximately one-half of the atoms reside on the particle surface. For each run, two horizontal TBMR's were agitated in a fluidized sand bath that was maintained at  $400^\circ\text{C}$ . After 60 minutes reaction time, the two TBMR's were removed and quenched in water. The pentane and THF solubles formed by coal liquefaction were measured and used as an indication of catalyst activity and liquefaction reactivity for coal samples. The equation used to calculate the pentane and THF solubles is as follows:

$$\%SOLUBLES = \frac{W_o(1-M) - (I.S. - W_c \cdot \frac{2MW_{FeS}}{MW_{Fe_2O_3}})}{W_o(1-A-M)} \cdot 100$$

$W_o$ : initial weight of coal charged to bomb

A: fraction of ash in the coal

M: fraction of moisture in the coal

I.S.: weight of insolubles

$W_c$ : weight of catalyst

MW: molecular weight of specified species

**Model Compound Reaction Procedures:** The hydrogenation activities of iron catalysts with model compounds were investigated in both tubing bomb microreactor (TBMR) and continuous reactor. Table 1 shows the TBMR experimental conditions. The two model compound systems employed were 2 wt% naphthalene (NAPH) in mineral oil (M.O.) and 2 wt% biphenyl in hexadecane. The iron catalysts were Fe-2 (Strem Chemical Inc., unsupported  $Fe_2O_3$  powder) and Fe-3 as described earlier.  $CS_2$  was utilized as sulfur source at 2 wt% in the liquid solution for the Fe-2 catalyst and 0.2 wt% for the Fe-3 catalyst. The catalyst loading of Fe-2 was ten times of that of Fe-3 to keep the surface area of these two catalysts about the same. The  $H_2$  charged to the reactor was generally 1000 psig at ambient temperature. For Fe-2 catalyst, when  $CS_2$  was added to the reactants, the initial  $H_2$  pressure charged was increased to 1250 psig to compensate for  $H_2$  used in converting  $CS_2$  to  $H_2S$ . The in-situ reduction of catalysts was performed in a  $H_2$  atmosphere for 24 hrs.

The model compound system of NAPH/M.O. and Fe-2 catalyst were tested in a CDS 900 trickle bed reactor shown schematically in Figure 1, and which has been described in detail elsewhere<sup>[7]</sup>. The reactor was operated at 250°C and 1000 psi at a hydrogen flow rate of 100 ml/min (STP) and liquid feedstock flow rate of 0.2 ml/min. Nitrogen was used to purge and pressurize the reactor before starting the reaction.

The product samples collected from both the continuous reactor and the TBMR were analyzed with a Varian 3300 gas chromatograph. Temperature programming was used to improve peak resolution and decane used as an internal standard.

## RESULTS AND DISCUSSION

### Coal Liquefaction Studies

When moisture free Illinois #6 coal was used with tetralin as the reaction solvent in the tubing bomb runs, the percentage of pentane solubles (%PS) increased from 33% without catalyst to 36% with Fe-3 catalyst. For Blind Canyon coal, the %PS increased from 36% without catalyst to 44% with 2 wt.% catalyst. When sulfur was added to the coal in addition to the catalyst, the %PS increased further to 46%. This is the highest value of the pentane solubles obtained so far for any coal studied in our research.

Various other reaction solvents (e.g. mineral oil and 1-methylnaphthalene) were also used in place of tetralin; but their use did not show a significant advantage over tetralin. Figure 2 shows an overall comparison of the various reaction solvents studied. When mineral oil (a non-hydrogen donor) was used in place of tetralin, little difference was obtained between the values for pentane and THF solubles of the coals with or without catalyst. Although the use of 1-methylnaphthalene showed a similar trend as tetralin in the %PS for the coals with or without catalyst, the actual values of the %PS were somewhat lower. The percentage of THF solubles, however, increased from 74% without catalyst to 97% with catalyst. Although dispersed catalyst might be expected to reduce the influence of the reaction solvent, our study indicates that the properties of the solvent remain very significant with a dispersed catalyst.

Blind Canyon coal was used to study the effect of sintering the catalyst by preheating the catalyst alone at 400°C, 200°C, and 100°C before use. Sulfur was added to the catalyst in all liquefaction runs. The results, shown in Figure 3, show that preheating the catalyst lowers its activity presumably by lowering its surface area.

Blind Canyon coal was also used in a catalyst loading study with Fe-3 catalyst. The results, shown in Figure 4, are consistent in showing that coal conversion is increased when the number of catalytic active sites is increased; however, the effect is not great.

Model Compound Studies in TBMR In these experiments, a hydrogenation activity  $A_H$  was defined as follows to characterize the extent of hydrogenation reaction:

$$A_H = \frac{2M_T + 5M_D}{5(M_N + M_T + M_D)} \quad \text{or} \quad A_H = \frac{3M_{CHB} + 6M_{DCH}}{6(M_{BPH} + M_{CHB} + M_{DCH})}$$

Where,  $M_N$ : moles of naphthalene/gram of liquid product  
 $M_T$ : moles of tetralin/gram of liquid product  
 $M_D$ : moles of decalin/gram of liquid product  
 $M_{BPH}$ : moles of biphenyl/gram of liquid product  
 $M_{CHB}$ : moles of cyclohexylbenzene/gram of liquid product  
 $M_{DCH}$ : moles of dicyclohexyl/gram of liquid product

Fe-2 catalyst was reduced in hydrogen at 400°C, and Fe-3 catalyst was reduced at different temperatures in advance to examine the activity with naphthalene as reactant. Figure 5 showed that 200-250°C would be a suitable reduction temperature. It is likely that a higher temperature would cause the 30 Å catalyst to be sintered and thus lower the activity. Therefore, a reduction temperature of 200°C for Fe-3 was chosen for the later runs. Figure 6 indicated that, for the naphthalene hydrogenation, both the pre-reduced iron catalysts gave higher activities than their oxide forms, and sulfur almost completely poisoned both catalysts, whether in the oxide or metallic form. Similar results were obtained for the hydrogenation of biphenyl as shown in Figure 7. A notable phenomenon observed was that, in both reaction systems, secondary reactions, e.g., the conversion from tetralin to decalin, took place only when the catalysts had been reduced, even at the highest catalyst loadings. This suggests that the metallic iron is more active for

hydrogenation than iron oxide owing to active sites of greater activity rather than an increase in number of sites.

***Model Compound Studies in Continuous Reactor*** The test results of three trickle bed reaction runs with sulfur in the feed in different periods are shown in Figure 8. It can be seen that when iron oxide was used as catalyst, without sulfur in the feed, the hydrogenation activity of NAPH increased gradually to a relatively stable level. However, once the sulfur was introduced, the  $A_H$  dropped continuously to about zero after 32 hrs during this process indicating that the hydrogenation reactions have been inhibited by the presence of  $CS_2$ . The other two runs were performed by adding  $CS_2$  to the feed first and then switching to the  $CS_2$  free feed. The results (Figure 8) showed no reaction at 250°C once there was  $CS_2$  in the feed, and  $A_H$  could not be restored. This indicates that  $H_2S$  has poisoned the iron catalyst permanently for the hydrogenation reactions and/or that the sulfide form of the iron is much less active than the hydrogen reduced form. After removal of the  $CS_2$  in the feed at 48 and 92 hours, both runs showed very small, but stable  $A_H$  as the residual  $H_2S$  concentration in the reactor became smaller. This indicates that the  $FeS_x$  form of the catalyst has finite, although significantly lower hydrogenation activity than the  $H_2$  reduced form of iron. The inhibition effect of  $H_2S$  is consistent with the earlier works by Rhee<sup>[4]</sup> with NAPH hydrogenation in batch reactor using Ni-Mo/ $Al_2O_3$  catalyst and Sapre<sup>[5]</sup> with biphenyl hydrogenation in the continuous reactor using Co-Mo/ $Al_2O_3$  catalyst.

Considering the hydrogenation behavior of NAPH over iron catalysts in both continuous reactor and TBMR, we think there probably exists a corresponding reduction process before the reaction occurs when iron oxide is employed. We suggest that the active phase of iron catalyst in the hydrogenation processes investigated in the absence of sulfur may be metallic iron. We have also reported<sup>[1]</sup> that hydrogen reduced iron generally yields higher hydrogenation activity than the iron sulfide which is a much less active hydrogenation catalyst. However, the iron sulfide form may possess a higher cracking activity which may be more beneficial to coal liquefaction.

#### ACKNOWLEDGEMENTS

This work was supported by the U.S. Department of Energy Under Contract No. DE-FC22-90PC90029.

#### REFERENCES

1. Guin, J.A., Zhan, X., *Yearly Report to DOE*, 1992.
2. Hirschon, A.S., Wilson, R.B., *ACS Fuel Preprints*, p881,
3. Pradhan, V., Tierney, J.W., Wender, I., *ACS Fuel Preprints*, 5(3), p793, 1990.
4. Rhee, Y.W., Guin, J.A., *Fuel Processing Tech.*, 19, p1, 1988.
5. Sapre, A.V., Gates, B.C., *Ind. Eng. Chem. Process Des. Dev.*, 21, p86, 1982.
6. Utz, B.R., Cugini, A.V., Frommell, E.A., *ACS Fuel Preprints*, 34(4), p1423, 1989.
7. Wang, W.P., Guin, J.A. *Fuel Processing Tech.*, 28, p149, 1991.

**Table 1. TBMR Reaction Conditions**

<b>Reactant wt. (g)</b>	Coal 3	NAPH 0.24		BPH 0.24
<b>Catalyst wt. (g)</b>	Fe-3 0.66	Fe-2 0.6	Fe-3 0.06	Fe-3 0.06
<b>Solvent wt. (g)</b>	Tetralin etc. 10	Mineral Oil 12	Mineral Oil 12	Hexadecane 12
<b>Sulfur Source wt. (g)</b>	Elementary Sulfur 0.1	CS <sub>2</sub> 0.24	CS <sub>2</sub> 0.024	CS <sub>2</sub> 0.024
<b>Temp. (°C)</b>	400	350	350	300
<b>H<sub>2</sub> Pressure (psi)</b>	1250	1000 (1250)	1000	1000
<b>Time (h)</b>	1	1	1	1

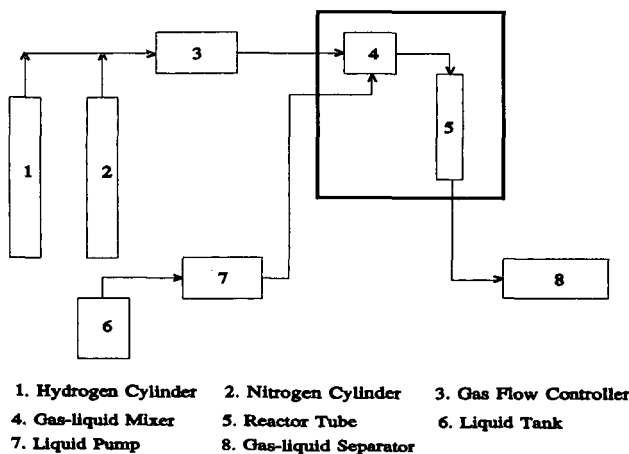


**Figure 1. CDS 900 Reactor System**

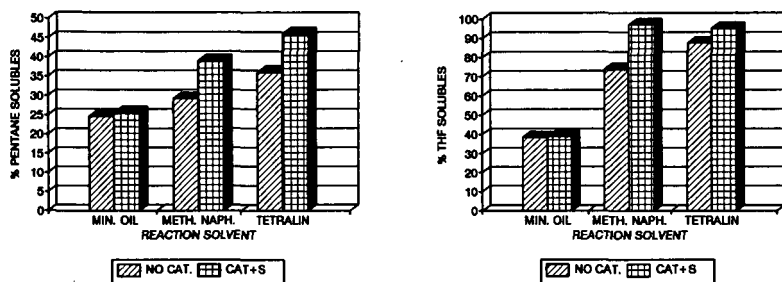


Figure 2. Comparison of Reaction Solvents using Blind Canyon Coal

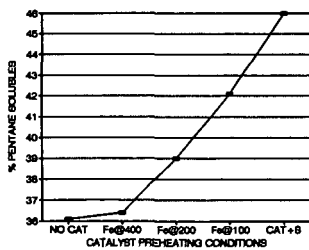


Figure 3. Effect of Preheating the Catalyst at Different Temperatures

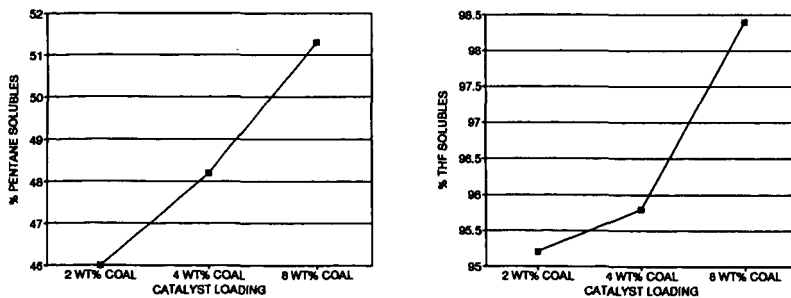


Figure 4. Comparison of Different Loadings of Catalyst

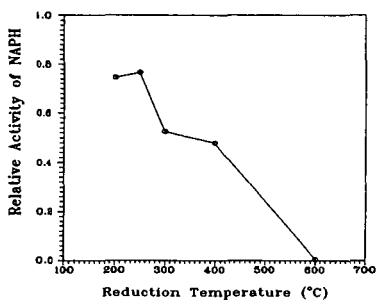


Figure 5. Effect of Reduction of Fe-3 Catalyst at Different Temperatures on NAPH Activity in TBMR

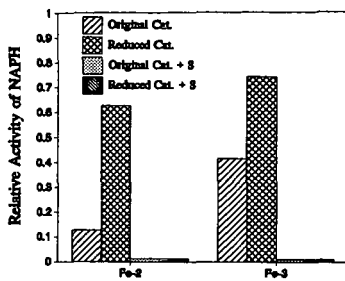


Figure 6. NAPH Hydrogenation Activity at 350 °C in TBMR

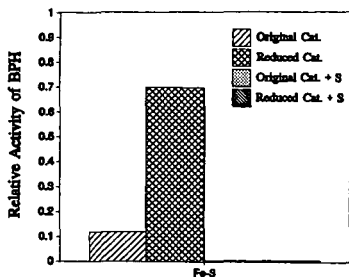


Figure 7. BPH Hydrogenation Activity at 300°C in TBMR

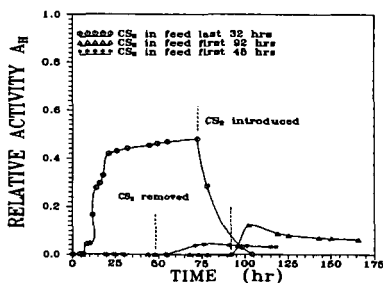


Figure 8. NAPH Hydrogenation Activity at 250°C in Continuous Reactor

## Design of Coal Liquefaction Catalysts with Functions for Recovery and Repeated Use

Isao Mochida, Kinya Sakanishi, Masahiro Kishino, Katsuyuki Honda, Tatsuya Umezawa, and Seong-ho Yoon  
Institute of Advanced Material Study,  
Kyushu University, Kasuga, Fukuoka 816, Japan

### Abstract

Active catalysts with functions for recovery and repeated use are expected to reduce the cost and waste in the coal liquefaction. The authors are going to propose basically two types of catalysts which are recoverable for the repeated use. The first type is acid-proof iron catalysts which are recoverable from the mixture with carbonate and chloride minerals. Such catalysts are applicable to particular coals such as Australian brown coal which is completely liquefied, carrying calcium and magnesium carbonates as the major minerals after the primary liquefaction.

Second type is characterized by its sulfur-proof ferromagnetism for the recovery from the minerals and carbons by gradient magnetic field. The authors are going to describe the performances of  $\text{Fe}_3\text{Al}$  powder and carbon-coated ferrite. Fine powders are essential for their high activity.

The deactivation of the catalyst by carbon and minerals in the liquefaction should be clarified, and a multi-step liquefaction scheme including coal pretreatment can be designed to minimize the deactivation.

### Introduction

Coal liquefaction has been rather extensively investigated for longer than several decades to provide clean liquid fuel from coal in order to meet the increasing demand expected in early next century. However the cost of the liquid fuel is still too high to substitute the fuel from petroleum. Several break-through ideas are strongly wanted to cut the cost currently estimated.

Cut of installation cost appears most effective. The ways are  
1) More moderate conditions

- 2) Better yields per installation, more change of coal and better conversion
- 3) Simpler scheme,
  1. hydrogen source
  2. solid-liquid separation
- 4) Stable operation for years
- 5) Cheaper catalyst and residue handling

The present authors have been studying a complete conversion of coal (no organic residue), with least amount of hydrogen donor in the reactor by multi-stage scheme which includes the coal pretreatment, coal dissolution, catalytic up-grading. The catalyst of primary liquefaction stage is a key to be developed. The authors assumed that the recovery and recycle of the catalyst from the residue is as approach to reach the objective described above.

In the present report, recovery and recycle of the catalyst for the primary liquefaction stage were studied. The basic idea is to recover the catalyst from the inorganic residues which come from the feed coal. According to the natures of inorganic residue, two approaches were examined in the present study.

1. Washing out the inorganic residues such as carbonates which are principally found in Australian brown coal

2. Recovery of the ferromagnetic catalyst from the diamagnetic residue by applying the magnetic gradient.

The catalyst deactivation and adhesion of the catalyst and minerals should be avoided by designing the scheme. The pretreatment and hydrogen transferring liquefaction as the prior to the catalytic steps are responsible. The catalyst and organic residue can be recycled to the liquefaction stage when the organic residue still carries significant amount of reactive portions.

## Experimental

### Materials

The liquefaction (hydrogen donating) solvent was a hydrogenated fluoranthene prepared by catalytic hydrogenation of commercial fluoranthene (FL) using a commercial Ni-Mo catalyst in an autoclave at 250°C, under initial hydrogen pressure of 13.5 MPa. The major component of the solvent was 1,2,3,10b-tetrahydrofluoranthene (4HFL),

which was identified by  $^1\text{H}$  and  $^{13}\text{C}$  n.m.r., quantified by g.c., and purified by recrystallization with n-hexane, removing perhydrofluoranthenes (PHFL).

#### Liquefaction procedure

Liquefaction was carried out in an autoclave (50ml volume). The ground coal (3.0g), the solvent (4.5g) and catalyst (0.9g) were transferred to the autoclave. The products remaining in the autoclave were extracted with THF, benzene and hexane. The hexane soluble (HS), hexane insoluble but benzene soluble (HI-BS), benzene insoluble but THF soluble (BI-THFS), and THF insoluble (THFI) substances were defined as oil, asphaltene, preasphaltene, and residue, respectively. A small amount (<5%) of solvent derived products, which remained in the HI-BS fraction, was corrected by g.c. analysis. The gas yield was calculated by the difference between the initial (dry ash free base) and recovered residual weights. Thus, the weight loss during the experiment was included in the gas yield.

#### Hydrogenation of 1-MN procedure

Hydrogenation of 1-MN was carried out in an autoclave (50ml volume). 1-Methylnaphthalene (1.0g), Decahydronaphthalene (9.0g) and catalyst(0.3g) were transferred to the autoclave. The reaction products were washed out with acetone. Hydrogenation conversion and products were determined with GC and GC-MS, respectively.

### Results

#### Catalytic activity of washed residue in the liquefaction of Australian brown coal.

Figure 1 summarizes the catalytic activity of the residue in the solvent washing, and ones resultfided, S-added or washed followed by resultfiding in the liquefaction of the brown coal. Basically the residues indicated similar activities, although the resultfiding enhanced activity to produce more gases. The point is that the washing removed almost completely the inorganic carbonates, concentrating the ion catalyst. Thus, the bottom recycle can be performed by avoiding the accumulation of the inorganic residues. Even if the catalyst is covered by the carbonates, such washing can remove the carbonates without diferialating the catalytic performances.

### Ferromagnetic catalysts

Two kinds of ferromagnetic catalysts are examined in the present study, Fe<sub>3</sub>Al and carbon-magnetite composite. Their catalytic activities are illustrated in Figure 2. Both of them exhibited significant activities and maintained ferromagnetic susceptibility after the liquefaction. Their susceptibility stood in H<sub>2</sub>-H<sub>2</sub>S atmosphere at 400 °C.

### Ferromagnetic support

Table 1 shows the activity of NiMo supported on Fe<sub>3</sub>Al for the hydrogenation of 1-methylnaphthalene at 380°C for 40min under H<sub>2</sub> pressure of 10MPa ; Non-trivial activities were induced by supporting NiMo on Fe<sub>3</sub>Al. The catalyst maintained the ferromagnetic susceptibility.

### Discussion

The present study indicated that the recovery and recycle of the catalyst are basically possible after the primary coal liquefaction where the inorganic residues are present to contaminate the iron catalyst. Although the catalytic activity so far revealed is not super yet, more elaborate preparation of the catalyst can improve the activity without losing functions of recovery. Smaller particle size, better dispersion and favorable catalyst-support interaction are applicable ways to enhance the activity.

The reaction scheme including coal pretreatment procedure should be also examined for further development to avoid the catalytic deactivation.

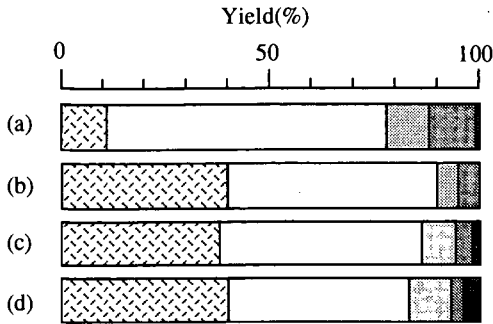


Fig.1 Effects of pretreatment for several recoverable catalyst to the liquefaction yields

catalyst: 3% addition to coal  
 solvent(75%4HFL/25% Py)/ coal= 1.5  
 single-stage used autoclave  
 380°C-40min,H<sub>2</sub>Press.10MPa

- (a) ; non-treatment Y-coal PI  
 (b) ; presulfided Y-coal PI  
 (c) ; presulfided and S-addition Y-coal PI  
 (d) ; acetic acid washing and presulfided Y-coal PI

☒ :G □ :O ▨ :A ▩ :P ■ :R

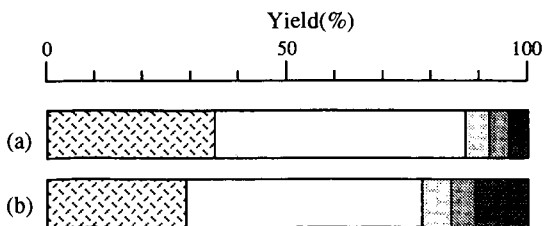


Fig.2 Effects of Fe<sub>3</sub>Al catalyst to the liquefaction yields

catalyst: 3% addition to coal  
 solvent(75%4HFL/25% Py)/ coal= 1.5  
 single-stage used autoclave  
 380°C-40min,H<sub>2</sub>Press.10MPa

- (a) ; C/Coated Magnetite, (b) ; Fe<sub>3</sub>Al

☒ :G □ :O ▨ :A ▩ :P ■ :R

Table 1 Catalysttype and 1-MN hydrogenating conversion

Catalyst (NiMo/Fe <sub>3</sub> Al)	Mo wt%	Ni wt%	Conversion %
A	10	2	9
B	10	5	13
C	5	1	5
D	10	5	20
E	10	5	23

Sulfiding conditions ( ABC:360°C 6hr D: 300 °C 3hr

E: 360 °C 3hr after 300 °C 3hr)

Reaction conditions (1-MN:1.0g DHN:9.0g

catalyst:0.3g used autoclave

380°C-40min,H<sub>2</sub>press.10Mpa.

**THE EFFECT OF CATALYST DISPERSION ON  
COAL LIQUEFACTION WITH IRON CATALYSTS**

Cugini, A.V., Krastman, D., Martello, D.V. and Holder G.D.  
U.S. Department of Energy  
Pittsburgh Energy Technology Center  
Pittsburgh, Pennsylvania 15236  
University of Pittsburgh

**INTRODUCTION**

Dispersed catalysts have been used for first stage direct coal liquefaction studies. Compared to supported catalysts, dispersed catalysts offer many advantages for first-stage coal liquefaction, such as the lack of aging and, for inexpensive catalysts, such as iron, the ability to simply dispose of the catalysts. The effectiveness of dispersed catalysts depends on the dispersion of the catalyst in the coal-vehicle system. Catalyst dispersion can potentially be improved by two methods in coal/catalyst systems: improving contact between coal and catalyst during the initial stages of coal liquefaction and optimizing the physical properties of the catalyst, i.e. increased surface area, smaller particle size, or smaller crystallite size.

Dispersion is usually treated qualitatively. Studies have shown that methods of catalyst preparation that should result in enhanced levels of catalyst dispersion also result in the highest levels of catalyst activities as measured by coal conversion to soluble or distillable products.<sup>1-7</sup> Methods of enhancing catalyst dispersion which have been investigated include developing techniques to increase the surface areas and/or reduce the particle sizes of catalysts, using aqueous catalyst impregnation of coal, and coupling aqueous impregnation with coal swelling.

Enhancing catalyst dispersion has been found to be effective with iron systems. It has been reported that the effectiveness of iron catalysts can be improved by decreasing their initial particle size.<sup>8-10</sup> However, sintering or agglomeration has been observed under liquefaction conditions.<sup>11-14</sup> Coal as well as sulfate pretreatments can act to mitigate this effect.<sup>13-15</sup>

Another means of enhancing the activity obtained with iron catalysts is to improve the contacting between the coal and catalyst. Workers have attempted to use forms of iron catalyst precursors that are soluble in oil or aqueous media. The solubilized precursor could then either be precipitated onto the coal's surface prior to charging the reactor or directly mixed with the coal/solvent mixture in the reaction. Studies have shown that

Reference in this manuscript to any specific commercial product, or service is to facilitate understanding and does not necessarily imply it endorsement or favoring by the United States Department of Energy.

catalyst pretreatments that result in enhanced levels of contacting between coal and catalyst also result in higher levels of coal conversion.<sup>3,16 and 17</sup>

Recent work at PETC has centered on the development of an iron catalyst precursor that is intimately contacted with the coal and maintains a fine particle size upon conversion to the active, sulfided phase. The procedure, reported previously,<sup>3</sup> results in the precipitation of FeOOH directly on the coal surface. Failure to intimately contact the FeOOH with the coal surface resulted in the loss of iron activity. The present study investigates the surface area and particle size changes resulting from the transformation of the precursor, FeOOH, to the active phase, presumably pyrrhotite. The effect of improved contacting between the FeOOH and coal was also investigated.

#### EXPERIMENTAL

Experiments were conducted with Blind Canyon bituminous (DECS-6, from the DOE/Penn State Coal Sample Bank) and Black Thunder subbituminous coals. Properties of the feed coals are presented in Table 1.

The catalyst precursor was added to the reactor as a dry powder, aqueous solution or by precipitation onto the coal. Hydrated iron oxide (FeOOH) was dispersed onto the feed coals by an incipient wetness impregnation/precipitation approach.<sup>3</sup> Forms of iron tested include powdered Fe<sub>2</sub>O<sub>3</sub>, aqueous ferric nitrate, aqueous ferrous sulfate, and powdered FeOOH. A sample of Fe<sub>2</sub>O<sub>3</sub>, with a nominal particle size of 1 $\mu$  (from Spang and Company) was added as a dry powder. High surface area, powdered FeOOH was prepared by precipitating FeOOH from an aqueous solution of ferric nitrate by the addition of ammonium hydroxide. The precipitate was recovered by filtration through a 0.45 $\mu$  filter, was vacuum dried at 40°C, and ground to a powder. The N<sub>2</sub> BET surface area of the FeOOH prepared in this manner was 138 m<sup>2</sup>/g. Catalyst prepared in this way was added to the reactor in a physical mixture with the coal.

The effectiveness of each catalyst precursor was determined by using each precursor in a 40-mL tubular microautoclave reactor. Experiments were conducted by adding 3.3 g coal to the reactor with 6.6 g of Panasol (a mixture of alkylated naphthalenes obtained from Crowley Chemical). Elemental sulfur (0.1 g) was added to the reactor to sulfide the catalyst precursors. The reactor was charged with 1000 psig (6.9 MPa) of hydrogen and sealed. The pressurized reactor was then heated to the liquefaction temperature in a fluidized sandbath. The heating period lasted 30-40 minutes. Following the liquefaction period (0.5 h), the reactor was cooled and depressurized. Coal conversion was calculated from the solubility of the coal-derived products in THF and in heptane as determined by a pressure filtration technique.<sup>18</sup>

Microautoclaves were also employed to investigate the transition of impregnated FeOOH to pyrrhotite. In these

experiments, FeOOH was impregnated onto carbon black rather than coal to eliminate interferences on subsequent analyses from the indigenous pyrite in the coal. The carbon black was Raven 22 Powder obtained from Columbian Chemicals Co. The iron-loaded carbon black and tetralin were heated (under  $H_2$  in the presence of  $CS_2$ ) to  $400^\circ C$  and held at temperature for 5 minutes. The products were mixed with THF and filtered through a  $0.45\mu$  filter. The filter cake, containing the iron loaded carbon, was recovered and analyzed by X-ray diffraction (XRD).

A series of iron sulfide catalysts (pyrrhotite, as analyzed by XRD) were prepared from the iron oxide precursors as well as from aqueous ferric nitrate solution and aqueous ferrous sulfate solution. The iron sulfide was prepared by adding the precursor to a 1-L autoclave containing tetralin. The mixture contained 400 g of tetralin and sufficient precursor to produce 4 g of iron sulfide. To convert the precursor to catalyst, the mixture was heated to  $400^\circ C$  and held for 0.5 h under 2500 psig (17.3 MPa) of  $H_2/3\%H_2S$  which was passed through the reactor at 4 SCFH. The recovered iron sulfide catalysts were extracted with THF.

## RESULTS AND DISCUSSION

### Catalyst Surface Area

The effect of iron oxide surface area was investigated using powdered FeOOH with a surface area of  $138\text{ m}^2/\text{g}$  and micronized  $Fe_2O_3$  with a surface area of  $5\text{ m}^2/\text{g}$ . Table 2 gives the effect of precursor surface area (iron oxide) on coal conversion. The precursor surface area does not appear to be important. This was expected to some extent since the precursor undergoes a chemical reaction to form the catalyst. The surface area of the catalyst itself is the important variable. Consequently, a series of tests were conducted to determine the relationship between the surface area of the catalyst (pyrrhotite) and the surface area of the original iron oxide. The catalyst was formed from the precursor in tetralin with an  $H_2/H_2S$  atmosphere as described in the experimental section. XRD and BET surface area were conducted on the resulting pyrrhotite. Table 3 presents the surface areas and crystallite sizes of the resulting iron sulfides (pyrrhotites). Also shown in Table 3 are the characteristics of pyrrhotites resulting from soluble iron precursors (ferric nitrate and ferrous sulfate). The analyses showed that the pyrrhotite was crystalline with estimated crystallite sizes ranging from 42 to 82 nm by XRD. The BET surface area analysis indicated that the surface area of the resulting pyrrhotite was significantly different than that of the original iron oxide. For the high surface area precursor, the surface area dropped from  $138\text{ m}^2/\text{g}$  to  $17\text{ m}^2/\text{g}$ , while the low surface area precursor increased its surface area from  $6\text{ m}^2/\text{g}$  to  $9\text{ m}^2/\text{g}$ . The similarity of the surface areas of the pyrrhotites resulting from the solid iron oxide precursors helps to explain the similar coal conversions observed with each. The surface areas of the pyrrhotites prepared by aqueous precipitation were both about  $30\text{ m}^2/\text{g}$ , which is greater than those from either of the iron oxide

precursors.

The next series of tests conducted was aimed at investigating the effect of pyrrhotite surface area on coal conversion. Table 4 presents coal conversion as a function of iron sulfide surface area and crystallite size. It appears that there is a relationship between surface area and coal conversion. Clearly the precipitated precursors produced a higher surface area pyrrhotite and subsequently higher coal conversions.

#### Impregnation

The effectiveness of catalysts formed from FeOOH depends on the method by which FeOOH is added to the system. Table 5 compares coal conversion using physically mixed FeOOH with impregnated FeOOH. The impregnated FeOOH is more active and results in higher coal conversion than the physically mixed FeOOH. As shown in Table 3, the surface area of the iron sulfide formed from powdered FeOOH (not impregnated) in tetralin dropped to 17 m<sup>2</sup>/g compared to 138 m<sup>2</sup>/g for its precursor. This large reduction in surface area produced a catalyst which resulted in lower coal conversions compared to the conversions obtained when the precursor was precipitated onto the coal.

The surface area and crystallite size for the catalyst precipitated onto the coal may not be the same as those measured for the catalysts formed in pure tetralin. The pyrrhotite formed from coal-impregnated FeOOH is not easily characterized because of the presence of pyrite and other crystalline material in the coal. Therefore, a separate preparation of impregnated carbon black was prepared in order to see what effect impregnation has on crystallite size. The impregnated carbon black was subjected to liquefaction conditions and recovered by THF extraction. XRD analysis of the iron sulfide on the carbon black revealed that the average crystallite size of the catalyst was 27 nm. This is significantly lower than the pyrrhotite crystallite size formed from powdered FeOOH (56 nm). One of the effects of impregnation of the FeOOH appeared to be the generation of smaller iron sulfide particles in the system.

#### CONCLUSIONS

In the absence of a carbonaceous support, the transformation of FeOOH to iron sulfide results in a loss of surface area, possibly due to sintering. This effect has been previously documented.<sup>11-14</sup> The loss in surface area prevents a correlation between precursor surface area and coal conversion from being established. However, an increase in the surface area of the actual (iron sulfide) catalyst does appear to improve liquefaction yields. Iron sulfide preparations with a broader range of surface area need to be investigated.

The presence of a carbonaceous support for FeOOH tends to mitigate the sintering and favors the formation of smaller particle

size iron sulfide catalysts which are likely to have higher specific surface areas. It is likely that the same effect occurs in coal impregnated with FeOOH since addition of the precursor through impregnation results in higher coal conversions. However, the better contacting between coal and catalyst achieved by impregnation may also contribute to the higher conversions.

#### ACKNOWLEDGEMENTS

The authors thank Sidney S. Pollack and Elizabeth A. Frommell for their assistance in the X-ray diffraction study.

#### REFERENCES

1. Derbyshire, F.J., "Catalysis in Coal Liquefaction: New Directions for Research," IEA CR/08, IEA Coal Research, June 1988.
2. Cugini, A.V., Ruether, J., Krastman, D., Cillo, D.L., Balsone, V., and Smith, D.N., Fuel Div. Preprints, 33(1), 6 (1988).
3. Utz, B.R. and Cugini, A.V., U. S. Patent 5,096,570, 1992.
4. Derbyshire, F.J., Davis, A., Lin, R., Stansberry, P.G., and Terrer, M.T. Fuel Proc. Tech. 12, 127 (1986).
5. Joseph, J., Fuel, 70, 459 (1991).
6. Artok, L., Davis, A., Mitchell, G.D., and Schobert, H.H., Fuel, 71, 981 (1992).
7. Weller, S.W., Proceedings: 4th International Conference on the Chemistry and Uses of Molybdenum, 1982.
8. Pregermain, S. Fuel Processing Technology, 12, 155 (1986).
9. Andres, M., Charcosset, H., Chiche, P., Dvignon, L., Djega-Maradassou, G., Joly, J.P., and Simone, P., Fuel, 62, 69 (1983).
10. Fukuyama, T., Okada, T., Takekawa, T., Matsubara, K., and Moriguchi, S., Proceedings: International Conference on Coal Science, 181 (1985).
11. Srinivasan, R., Keough, R.A., and Davis, B.H., ACS Div. of Fuel Chemistry Preprints, 37(3) 1265 (1992).
12. Bacaud, R., Fuel Processing Technology, 28, 203 (1991).
13. Djega-Maradassou, G., Besson, M., Brodzik, D., Charcosset, H., Huu, T.V., and Varloud, J., Fuel Processing Technology, 12, 143 (1986).
14. Stephens, H.P., Stohl, F., and Padrick, T.D., Proceedings: International Conference on Coal Science, 368 (1981).
15. Pradhan, V. R., Tierney, J., and Wender, I., Sixth Annual Technical Meeting of the Consortium for Fossil Fuel Liquefaction Science, 1992.
16. Garg, D. and Givens, E.N., Fuel Processing Technology, 7, 59 (1983).
17. Mitra, J.R., Chowdhury, P.B., and Mukherjee, D.K., Fuel Processing Technology, 8, 283 (1984).
18. Utz, B.R., Narain, N.K., Appell, H.R., and Blaustein, B.D., "Coal and Coal Products: Analytical Characterization Techniques" (Ed. E.L. Fuller, Jr.), Am. Chem. Soc. Symp. Ser. 205, 225 (1982).

**Table 1. Analyses of Coal Feeds**

	<b>Black Thunder</b>	<b>Blind Canyon DECS-6</b>
<b>Proximate Analysis (wt%, as received)</b>		
Moisture	19.2	4.7
Volatile Matter	34.8	42.4
Fixed Carbon	40.6	47.3
Ash	5.4	5.6
<b>Ultimate Analysis (wt%, Moisture Free)</b>		
Carbon	68.2	76.5
Hydrogen	4.8	5.9
Nitrogen	1.0	1.5
Sulfur	0.4	0.4
Oxygen (Difference)	18.8	9.9
Ash	6.8	5.8
<b>Sulfur Forms (wt%)</b>		
Sulfate	0.02	0.01
Pyritic	0.04	0.02
Organic	0.30	0.41

**Table 2. Effect of Iron Precursor Surface Area on Coal Conversion of DECS-6 Blind Canyon Coal at 425°C, 0.5 h, 1000 psig (cold) H<sub>2</sub>, 5000 ppm Fe, 0.1 g S added to 9.9 g of a 2:1 mixture of Panasol to DECS-6 Coal.**

<b>Precursor</b>	<b>Precursor Surface Area, m<sup>2</sup>/g</b>	<b>Coal Conversion(%) To:</b>	
		<b>THF Sols.</b>	<b>Heptane Sols.</b>
None	None	58	30
FeOOH	138	66	34
Fe <sub>2</sub> O <sub>3</sub>	6	73	35

**Table 3. Effect of Precursor Type and Surface Area on the Resulting Iron Sulfide Crystallite Size and Surface Area Produced in a 1-L Autoclave at 400°C, 0.5 h, 2500 psig H<sub>2</sub>/3%H<sub>2</sub>S.**

Catalyst Precursor	Surface Area m <sup>2</sup> /g	Iron Sulfide Crystallite Size, nm @ 2θ=53.2	Iron Sulfide Surface Area m <sup>2</sup> /g
Micronized Fe <sub>2</sub> O <sub>3</sub>	6	82.0	9
FeOOH	138	56.0	17
Aqueous Ferric Nitrate	n/a	43.0	30
Aqueous Ferrous Sulfate	n/a	42.1 <sup>1</sup>	32

<sup>1</sup> Calculated based on surface area.

**Table 4. Effect of Iron Sulfide Precursor Surface Area and Crystallite Size on Coal Conversion of DECS-6 Blind Canyon Coal at 425°C, 0.5 h, 1000 psig (cold) H<sub>2</sub>, 5000 ppm Fe, 0.1 g S added to 9.9 g of a 2:1 mixture of Panasol to DECS-6 Coal.**

Precursor Surface Area, m <sup>2</sup> /g	Crystallite Size, nm @ 2θ=53.2	Coal Conversion(%) To:	
		THF Sols.	Heptane Sols.
None	na	58	30
9	82.0	73	31
17	56.0	70	31
30	43.0	84	38
32	42.1 <sup>1</sup>	76	35

<sup>1</sup> Calculated based on surface area.

**Table 5. Effect of FeOOH Mode of Addition on Coal Conversion of DECS-6 Blind Canyon Coal and Black Thunder Coal at 425°C, 0.5 h, 1000 psig (cold) H<sub>2</sub>, 5000 ppm Fe, 0.1 g S added to 9.9 g of a 2:1 mixture of Panasol to Coal.**

Precursor	Coal Conversion(%) To:	
	THF Sols.	Heptane Sols.
<b>Blind Canyon</b>		
None	58	30
Physically Mixed FeOOH	66	34
Impregnated FeOOH	85	41
<b>Black Thunder</b>		
None	54	30
Physically Mixed FeOOH	64	35
Impregnated FeOOH	73	33

## A STUDY OF DISPERSED IRON-BASED ADDITIVES IN COAL LIQUEFACTION

Theo L.K. Lee, Al Comolli  
Edward Johanson, Robert Stalzer

Hydrocarbon Research, Inc.  
100 Overlook Center, Suite 400  
Princeton, New Jersey 08540

**Keywords:** Liquefaction, thermal-catalytic, iron additives

### INTRODUCTION

Iron-based additives have been extensively (1-5) evaluated for their catalytic behavior in direct coal liquefaction. The catalytic activity of these iron-based additives depends not only on their chemical composition but also on their effective contact area with the coal/solvent mixture. Various preparation techniques have been investigated (6) to produce nanoscale iron-based catalyst precursors to enhance its activities.

The activity of two different iron-based additives for liquefying a Wyoming sub-bituminous coal, Black Thunder mine coal, was evaluated in a two-stage, bench scale continuous flow unit. One of these additives, iron oxide, was introduced in form of a powder to the slurry feeding system, while the second additive was impregnated on the coal matrix using an incipient wetness technique developed at the Pittsburgh Energy Technology Center.

This paper describes the findings of the bench scale evaluations (Runs CC-7 and CC-15) which were intended to examine the relative effects of catalyst type and reactor configuration (e.g. Catalytic/Thermal or Thermal/Catalyst).

### EXPERIMENTAL

#### Coal Preparation

Black Thunder mine coal was used as feed. Analyses of the feed coals are shown in *Table 1*. The feed coals (HRI-5630 and 5828) were screened to -70 mesh and dried under nitrogen to obtain moisture content between 5-10 W% for tests when the iron additive was added in form of a powder. The impregnated coal feed (L-780) was dried to 5 to 12 W% moisture content.

The PETC incipient wetness technique involves the contact of coal with a solution of iron salt followed by precipitation (impregnation) of hydrated iron oxide on accessible coal surfaces.

The iron content of the untreated coal was 0.2 W% (dry basis), while that of the impregnated coal feed contained 0.57 to 0.65 W% of iron.

#### Start-up/Make-up Solvent

Each run was start-up with coal derived distillates. The start-up oil used in CC-7 was HRI-5648 and was derived from Wilsonville using Illinois coal as feed. This oil was also used as make-up oil in the early part of the run to supplement the process-derived oil for the recycle oil requirements. In the later part of the run, the make-up oil, if required, was made up from the accumulated process-derived oil. Run CC-15 employed filtered process derived liquids stored in Tank 4 from a recent HRI PDU run (Run 260-03) as start-up and make-up oils. Analyses of these solvents are summarized in *Table 2*.

#### Additives

In Run CC-7 the iron-based additive was in an oxide form. This additive was labelled as magnetic pigment and was purchased from Wright Industries (Brooklyn, New York). Analyses of the iron additive are shown in *Table 3*. In Run CC-15, iron was added as hydrated oxide and was impregnated on the coal matrix.

#### Liquefaction Tests

The liquefaction tests were carried out in a 20 Kg/day continuous flow unit employing two backmixed reactors, as shown *Figure 1*. An additional pretreater was added to the system in Run CC-15 for activating the iron catalyst precursor prior to the thermal stage (first stage).

Each run usually starts with coal derived distillates from Wilsonville or HRI's PDU. The unit is then brought to equilibrium by the recycling of pressure filter liquids to the coal slurry preparation section on a bi-hourly basis. Mass balance is performed every 8 or 12 hours and a daily average is then reported. Each of the conditions tested is of minimum 3 days duration to ensure the validity of the data point.

Due to the low inherent sulfur content of Black Thunder mine coal, sulfur was added in form of liquefied hydrogen sulfide to ensure proper sulfidation of the catalyst precursor as well as maintaining the supported catalyst in a sulfided state.

## RESULTS AND DISCUSSION

Coal conversion is normally calculated from the ash-to-solid (quinoline insoluble) ratio of product and comparing it with the feed coal. This assumes that non-ash portion of the product is organic unconverted coal. This is not entirely true as asking transforms mineral matter into other inorganic form. In dealing with sub-bituminous coal, HRI usually considers ash on a SO<sub>2</sub>-free basis to discount the sulfur capture by lime that might occur during asking. When additives are introduced, calculation of true coal conversion can be uncertain and imprecise. If additive contains iron as in this case, it captures sulfur from coal or coal-derived liquid or from hydrogen sulfide.

If the liquefaction product containing this sulfided iron species is ashed, the inorganic material undergoes transformation. For example, if the product contains FeS, it could be oxidized to Fe<sub>2</sub>O<sub>3</sub> or some other oxide. If it is converted to Fe<sub>2</sub>O<sub>3</sub>, it would lose weight during asking. As a result, the amount of the mineral matter in the product would be underestimated and that of the organic matter overestimated. Calculated coal conversion would then be lower than the real conversion.

A true or more accurate value of coal conversion could be arrived at if the chemical nature of the iron species in the product and in the ashed form is known. Since this information was lacking, it was assumed here that the iron species in the liquefaction product was present as pyrrhotite Fe<sub>(1-x)</sub>S with x of 0.15 and that it was converted to Fe<sub>2</sub>O<sub>3</sub> during asking.

#### Dispersed Iron Oxide

Run CC-7 was conducted to study the effect of reactor configuration in two-stage liquefaction: catalytic/thermal vs thermal/catalytic modes of operation.

The supported catalyst charged to the unit was a blend of fresh Shell 317 catalyst (12.5 W%) and the recovered catalyst (87.5 W%) from an earlier run (CC-5). The latter was obtained from the first stage of a run which also used Black Thunder mine coal. Table 4 summarizes the run plan and results. The catalytic stage temperature was maintained at 399°C. The temperature of the thermal stage was varied from 440-448°C and space velocity varied from 44-67 lb/h/ft<sup>3</sup> cat. The additive used in this run was iron oxide, the magnetic pigment supplied by Wright Industries. The rates of the additive and hydrogen sulfide were about 5.5 and 3.8 W%.

Figure 2 and 3 compares the performance of different reactor configurations. In catalytic/thermal mode of operation, increasing the thermal stage temperature from 440°C (Condition 1) to 448°C (Condition 2) increased C<sub>1</sub>-524°C distillate yield (2.0 W% maf coal) as increased coal and residuum conversions outpaced increase in gas yield. With the thermal stage at 448°C, catalytic/thermal configuration gave higher coal and residuum conversions relative to thermal/catalytic configuration (Condition 3). However, the product quality was superior in the latter case.

Compared to catalytic/catalytic mode (Run CC-4 Condition 2), thermal/catalytic and catalytic/thermal configurations gave slightly higher coal conversion, as shown in Table 4. Typically, conversion of sub-bituminous coals is quite sensitive to residence time which was less in the catalytic/catalytic mode of operation due to catalyst hold-up in the reactor. However, residuum conversion and distillate yield were higher in catalytic/catalytic configuration. The process performance in this configuration was superior with less gas yield, lighter distillate slate. Hydrogen consumption was higher, however, it was used efficiently to produce a better quality product.

#### Iron Impregnated Coal (CC-15)

The performance of iron impregnated (about 5000 ppm Fe) Black Thunder mine coal was measured in a thermal/catalytic mode of operation. The second stage contained

a fresh charge of Criterion 317 Ni/Mo catalyst. The catalyst was presulfided in situ by holding the catalyst at various temperature levels during the start-up period under a continuous stream of hydrogen sulfide and start-up oil.

The iron catalyst precursor(FeOOH) was activated with H<sub>2</sub>S at 275°C (Condition 1) and 290°C (Conditions 2 to 4). The test was conducted using constant conditions of space velocity of about 42.5 lb coal/h/ft<sup>3</sup> (supported catalyst), and temperatures of 427°C and 413°C for the thermal and the catalytic reactors, respectively. The run plan and results are given in *Table 5*.

The yield of C<sub>1</sub>-C<sub>3</sub> gas remained constant around 10.5 W% maf coal reflecting the relatively stable operation. Although the results were masked by the continuous deactivation of the supported catalyst throughout the course of the run, the process performance in term of coal conversion, 524°C conversion, and C<sub>4</sub>-524°C distillate yield were higher in tests with iron impregnated coal as compared with the untreated coal (Condition 3).

In the presence of iron additive, coal conversions varied slightly between 92.7 and 93.1 W% maf coal (Conditions 1, 2 and 4). In Condition 3, no dispersed catalyst was used. The coal conversion dropped by 2.7 W% to 90.0 W%. The decrease in residuum conversion (3.7 W%) and distillate yield (7.7 W%) were more noticeable because these performances were more sensitive to catalyst activity. Iron additive was reintroduced in Condition 4, repeat of Condition 2. The coal conversion increased back up to 92.7 W%, while the residuum conversion and distillate yield rebound to a level as projected assuming linear deactivation in catalyst activity. Interstage samples show that all coal conversion occurred in the thermal stage (at 427°C). Similar trend was observed on the effect of iron additive on coal conversion in the interstage sample, i.e. 3.7 to 4.1 W% lower when no additive was used.

The iron impregnated coal contained substantially higher nitrogen content (L-780, 2.64 W%) than the untreated coal (HRI-5828, 0.95 W%). This was probably due to the sorption of ammonium nitrate on the coal matrix during the precipitation procedure. As a result, both the interstage and the two-stage product liquids exhibited higher nitrogen content when iron impregnated coal was used, as shown in *Table 4*.

## CONCLUSION

Black Thunder mine coal was liquefied in thermal/catalytic and catalytic/thermal modes of operation to study effect of iron additive on process performance. With the limited data and variations in catalyst age, in the thermal/catalytic mode of operation, it seems that the distillate yield with 5000 ppm of finely dispersed iron (on the coal matrix) was 66.0 W% and was equivalent to, if not slight more higher, than that with 5.7 W% of magnetic pigment (Run CC-7 Condition 5). However, the selectivity toward lighter product was higher in the case of magnetic pigment reflecting the higher overall reaction severity used in the test.

## ACKNOWLEDGEMENT

The research was conducted under U.S. Department of Energy Contract No. DE-AC22-88PC-88818. Advices from staff in PETC on the preparation of FeOOH-impregnated coals for Run CC-15 are also acknowledgement.

## REFERENCE

Gary D. and Given, E.N., "Pyrite Catalysis in Coal Liquefaction", *Ind. Eng. Chem. Process Des. Dev.*, Vol 21, pp. 113-117, 1982.

Stohl, F.V. :The Effect of Iron Sulfide Surface Area Variations on Coal Liquefaction", *Fuel*, Vol. 62, pp. 69-72, 1983.

Southern Electric International, Inc., Technical Progress Report, "Run 258 with Subbituminous Coal", DOE Contract No. DE-AC22-82PC50041.

Southern Electric International, Inc., Technical Progress Report, "Run 260 with Black Thunder Mine Subbituminous Coal", DOE Contract No. DE-AC22-90PC90033, January 1992.

Hydrocarbon Research, Inc., Quarterly Reports No. 5, 6 and 11, DOE Contract No. DE-AC22-88PC-88818.

Cugini, A.V., Utz, R.G., Krastman, D. and Hickey, R.F. "Effect of Activation Conditions on Dispersed Iron Catalysts in Coal Liquefaction.", *Preprints, Fuel Chemistry Division, ACS Vol. 36, No. 1, pp. 91-102, 1991.*

**TABLE 1**  
**FEED COAL ANALYSES**

HRI No.	<u>5630</u>	<u>5828</u>	<u>L-780</u>
Moisture Content, W%	6-9	8.41	8.81
Ash Content, W% (mf)	6.69	6.95	7.15
SO <sub>3</sub> -free, W% (mf)	5.74	5.71	6.03
Ultimate Analysis, W% (maf)			
Carbon	71.90	72.51	72.38
Hydrogen	4.91	4.08	4.31
Sulfur	0.38	0.51	0.49
Nitrogen	1.04	0.95	2.64
Oxygen (by diff.)	21.77	21.95	20.18
Iron Content, W% (mf)	n/a	0.20	0.57-0.65

**TABLE 2**  
**ANALYSES OF START-UP SOLVENT**

HRI No.	5648	L-769
API Gravity	n/a	10.1
Elemental Analysis, W%		
Carbon	90.14	88.95
Hydrogen	9.85	10.08
Sulfur	0.13	0.06
Nitrogen	0.37	0.34
ASTM D-1160 Distillation,		
IBP	391	318
5 V%	413	339
10 V%	426	345
20 V%	432	358
30 V%	443	366
40 V%	450	376
50 V%	459	385
60 V%	469	398
70 V%	476	416
80 V%	483	449
90 V%	499	479
95 V%	511	517
FBP	542	524*

- Boiling point at 96 V%

**TABLE 3**  
**ANALYSES OF IRON ADDITIVES**

<u>Magnetic Pigment</u>	
Moisture, W%	0.02
Sulfur, W%	0.003
Iron, W%	61.22
Forms of Iron, W%	
Fe	0.05
FeO	25.14
Fe <sub>2</sub> O <sub>3</sub>	70.42

**TABLE 4**  
**Evaluation of Dispersed Iron Oxide (CC-7)**  
Catalyst: Shell 317 Ni/Mo    Coal: Black Thunder Mine

Run No.	7	7	7	7	7	4
Condition	1	2	3	4	5	2
<b>Mode</b>						
1st Stage	Cat.	Cat.	Therm.	Therm.	Therm.	Cat.
2nd Stage	Therm.	Therm.	Cat.	Cat.	Cat.	Cat.
<b>Temperature, °C</b>						
1st Stage	398	399	448	448	441	399
2nd Stage	441	448	399	399	399	441
<b>Catalyst Age, lb coal/lb cat.</b>						
1st Stage	658	801	—	—	—	717
2nd Stage	—	—	974	1101	1107	1088
<b>Space Velocity</b>						
lb coal/h/ft <sub>3</sub> cat.	66.9	65.6	68.3	45.7	43.8	68.9
Additive Rate, W% mf coal	5.5	5.3	5.5	5.4	5.7	5.2
H <sub>2</sub> S Rate, W% mf coal	4.5	4.7	4.3	6.3	5.4	1.8
<b>Performance, W% maf coal</b>						
C <sub>1</sub> -C <sub>3</sub>	9.96	12.01	4.81	17.41	14.10	8.81
H <sub>2</sub> Used	6.73	7.43	8.07	8.31	8.28	8.60
C <sub>4</sub> -524 °C	58.5	60.5	59.4	55.8	59.0	64.6
Coal Conversion	90.4	93.3	91.3	92.4	90.8	88.1
524 °C* Conv.	85.5	89.0	89.1	87.7	87.4	87.5
HDN	57.4	55.1	71.2	69.0	53.9	76.9

**TABLE 5**  
**Evaluation of FeOOH Impregnated Coal (CC-15)**  
**Catalyst: Shell 317 Ni/Mo    Coal: Black Thunder Mine**

Condition	1	2	3	4
<b>Mode</b>				
1st Stage	Therm.	Therm.	Therm.	Therm.
2nd Stage	Cat.	Cat.	Cat.	Cat.
<b>Temperature, °C</b>				
Pretreating	275	298	297	297
1st Stage	426	429	427	427
2nd Stage	413	412	413	412
<b>Catalyst Age, lb coal/lb cat.</b>				
2nd Stage	143	227	314	403
<b>Space Velocity</b>				
lb coal/h/ft <sup>3</sup> cat.	42.3	41.7	43.7	42.7
Additive Rate, W% mf coal	0.4	0.4	None	0.4
H <sub>2</sub> S Rate, W% mf coal	3.5	3.6	3.2	3.0
<b><u>Performance, W% maf coal</u></b>				
C <sub>1</sub> -C <sub>3</sub>	10.55	10.78	10.35	10.49
H <sub>2</sub> Used	9.26	9.0	8.14	8.34
C <sub>4</sub> -524 °C	66.1	64.1	56.4	60.2
<b>Coal Conversion</b>				
1st Stage	91.1	91.1	87.0	90.7
2nd Stage	93.1	92.7	90.0	92.7
524 °C <sup>+</sup> Conv.	89.1	87.7	84.0	85.3
HDN	90.0	87.1	66.6	82.6

**FIGURE 1 - HRI TWO STAGE EBULLATED BED BENCH SCALE UNIT**

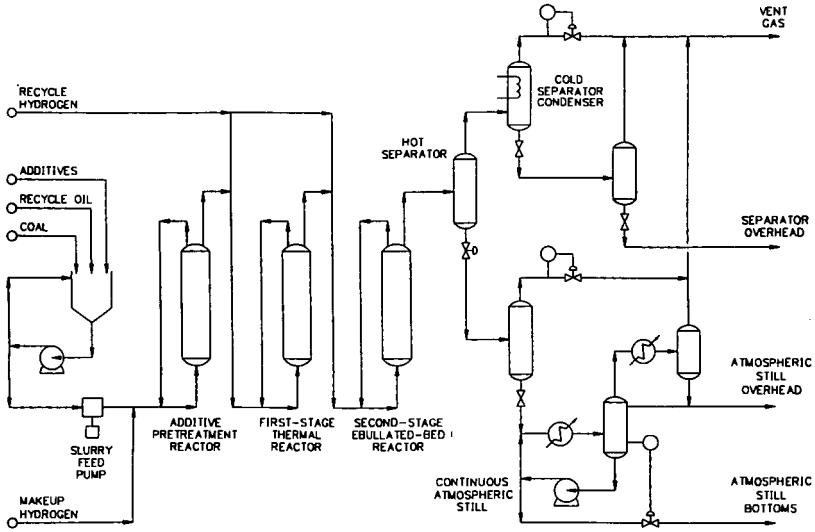


**FIGURE 2 - PROCESS PERFORMANCE OF IRON OXIDE AS ADDITIVE: CATALYTIC/THERMAL vs THERMAL/CATALYTIC**

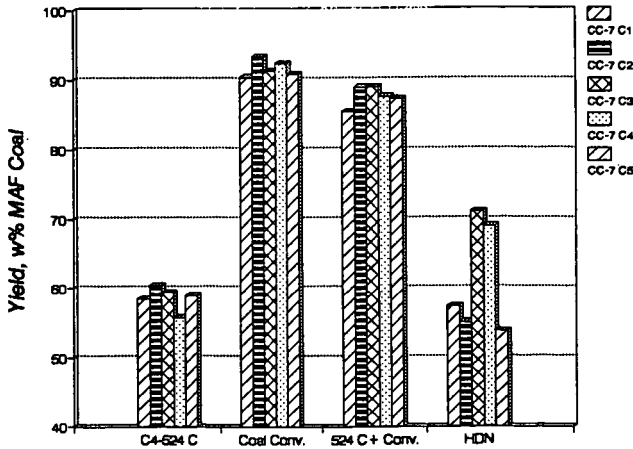


**FIGURE 3 - PROCESS PERFORMANCE OF IRON OXIDE AS ADDITIVE:  
GAS YIELD AND HYDROGEN CONSUMPTION**

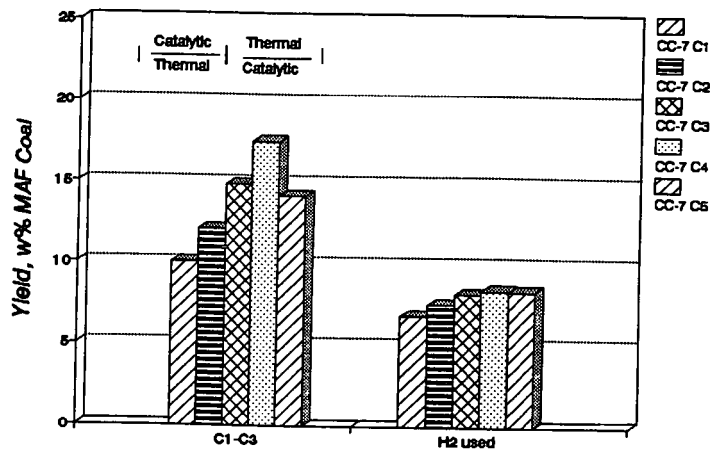
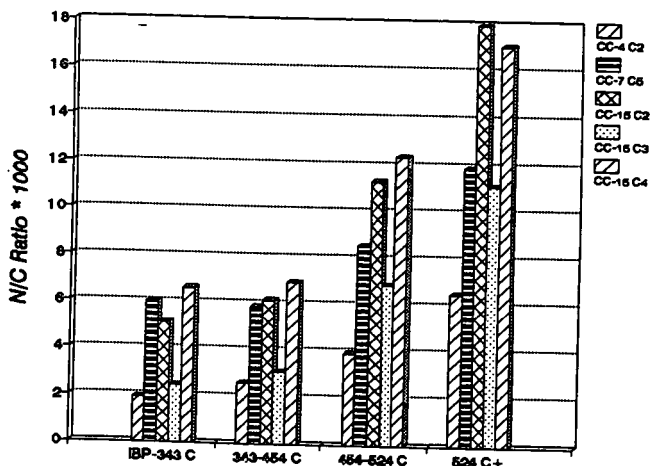


**FIGURE 4 - NITROGEN CONTENT OF SELECTED INTERSTAGE SAMPLES**



## HYDROGENOLYTIC ACTIVITY OF SOLUBLE AND SOLID Fe-BASED CATALYSTS AS RELATED TO COAL LIQUEFACTION EFFICIENCY

W. Zmierzak, X. Xiao, Jesse C.H. Tsai and Joseph Shabtai  
Department of Chemical & Fuels Engineering  
University of Utah  
Salt Lake City, Utah 84112

Keywords: Iron-based catalysts, Hydrogenolysis activity, Coal liquefaction.

### ABSTRACT

A comparative activity study of soluble and solid Fe-containing catalysts for hydrogenolysis of (1) coal-simulating compounds, i.e., 2-isopropyl-naphthalene (IPN) and diphenylmethane (DPM), and (2) a Blind Canyon coal sample (designated as DECS-17), was performed. The soluble catalysts were supported on SiO<sub>2</sub> and included aqua complexes of various Fe salts, i.e., sulfate, acetate and chloride. The solid catalysts consisted of finely dispersed superacids, i.e., Fe<sub>2</sub>O<sub>3</sub>/SO<sub>4</sub><sup>2-</sup> and ZrO<sub>2</sub>/SO<sub>4</sub><sup>2-</sup>. The soluble catalysts contain the aqua complex ion [Fe(H<sub>2</sub>O)<sub>6</sub>]<sup>3+</sup>, which is pre-formed or formed *in situ* in the presence of water, and acts as a protonic acid by ligand dissociation especially above 250°C. Kinetic rate constants for hydrodealkylation of IPN and hydrogenolytic cleavage of DPM show that at temperatures of 350-400°C the above solid superacids possess markedly higher activity as compared with that of the SiO<sub>2</sub>-supported, soluble Fe salts. In agreement with this finding, the same solid superacids were found to be effective hydrogenolysis catalysts in the depolymerization of the Blind Canyon coal sample. Therefore, small amounts (0.1-0.5 wt %) of Fe-containing solid superacids can be conveniently used in the initial step of a modified version of the previously developed HT-BCD (mild hydro-treatment-base catalyzed depolymerization) coal liquefaction procedure.

### INTRODUCTION

An important aspect of direct coal liquefaction research is the development of effective catalysts for the chemical reactions involved in the liquefaction process. A large variety of catalysts have been investigated in fundamental studies, but two groups of catalysts have attracted particular attention, i.e., (1) bifunctional metal sulfides which are believed to act mainly as ring hydrogenation but also as C-O, C-S, C-N, and C-C hydrogenolysis catalysts, and (2) soluble or solid acid catalysts which cause primarily hydrogenolytic bond cleavage<sup>(1)</sup>.

In recent years the concept of applying disposable, highly dispersed iron-based catalysts in coal liquefaction has attracted considerable interest. The advantage of these catalysts is seen in their anticipated high activity, low cost, and environmental acceptance. Iron-based catalysts which can be added to coal in the form of very fine solid dispersions include iron oxide, iron oxyhydroxide, prepared by different methods<sup>(2,3)</sup>, iron carbides<sup>(4)</sup>, and others. Alternatively, coal impregnation with soluble iron compounds has been examined using various methods<sup>(5-12)</sup>.

Numerous studies have been performed on a sulfated iron oxide catalyst<sup>(13-15)</sup>. An IR spectroscopic study, performed by Yamaguchi et al. <sup>(13)</sup> indicated the presence of surface

complexes between  $\text{SO}_4^{2-}$  ions and iron oxide. It was proposed that a chelated iron oxide-sulfate structure, containing two covalent  $\text{S}=\text{O}$  double bonds, is responsible for the strong acidity of sulfated iron oxide. Hino and Arata used this catalyst for various acid-catalyzed reactions, e.g., dehydration of ethanol<sup>[14]</sup>, and skeletal isomerization of butane to isobutane at low temperatures<sup>[15]</sup>. They pointed out that  $\text{Fe}_2\text{O}_3/\text{SO}_4^{2-}$  catalyst can be considered as a superacid.

Previous reports have shown that many iron compounds in their original form are not the active catalysts in direct coal liquefaction processes. Rather, it is assumed that such iron compounds are converted under coal liquefaction conditions, viz, in the presence of sulfur<sup>[3,16]</sup> or other sulfidation agents<sup>[17]</sup> to very active forms of non-stoichiometric pyrrhotites. The introduction of sulfate ions on the surface of iron oxide catalyst apparently enables its transformation into fine particles of pyrrhotite, which is characterized by high acidity and other properties<sup>[18]</sup>.

Shabtai et al.<sup>[5-7]</sup> have recently developed a two-stage, low-temperature coal depolymerization-liquefaction procedure. In the first step of the depolymerization stage, a coal sample is impregnated with a soluble, highly dispersed iron catalyst<sup>[19]</sup> and then subjected to mild hydrotreatment (HT) at temperatures  $\leq 290^\circ\text{C}$  and a  $\text{H}_2$  pressure of 1000-1500 psig. The mild hydrotreatment results in partial depolymerization of the coal by preferential hydrogenolytic cleavage of alkylene, benzyl etheric, cycloalkyl etheric and some activated thioetheric linkages. In the second depolymerization step, the mildly hydrotreated coal sample is subjected to base-catalyzed depolymerization (BCD) at  $\leq 290^\circ\text{C}$  with a methanolic solution of  $\text{KOH}$  or  $\text{Ca}(\text{OH})_2$ . This completes the coal depolymerization by hydrolysis (alcoholysis) of diaryletheric, aryl cycloalkyl etheric, diaryl thioetheric and other bridging groups. The sequential HT-BCD treatment results in a mixture of low M.W. (about 100-300) products, composed primarily of monocluster compounds.

In the present study the hydrogenolytic activity of soluble vs solid Fe-containing catalysts was compared, using the hydrodealkylation of 2-isopropyl-naphthalene and the hydrogenolysis of diphenylmethane as model reactions. In parallel, the activity of the two types of acid catalysts in the framework of the HT-BCD procedure (as measured by the overall yield of depolymerized coal products) was examined, using a Blind Canyon coal sample (DECS-17) as feed.

## EXPERIMENTAL

**Materials.** 2-isopropyl-naphthalene (purity, 98%) was obtained from Willey Organics. Diphenylmethane (purity, 99%) was obtained from Aldrich Chemical Company, and n-dodecane (purity, 99%) from Phillips Petroleum Company. Coal samples (DECS-17) were supplied by the Penn State Coal Sample Bank.

**Preparation of Catalysts.** Two series of catalysts were prepared.

The first series consisted of three  $\text{SiO}_2$ -supported soluble salts, i.e.,  $\text{FeCl}_3 \cdot 6\text{H}_2\text{O}$ ,  $\text{Fe}_2(\text{SO}_4)_3 \cdot 5\text{H}_2\text{O}$  and  $\text{Fe}(\text{CH}_3\text{COO})_3$ . Those were prepared by incipient wetness impregnation of  $\text{SiO}_2$  (Aldrich,

grade 62, 60-200 mesh, 150 Å) with aqueous solutions of the respective salts, followed by drying under vacuum for 24 hours at room temperature. An alternative drying procedure, which produced a more active  $\text{Fe}_2(\text{SO}_4)_3 \cdot 5\text{H}_2\text{O}/\text{SiO}_2$  catalyst involved drying of this catalyst in air at 120°C. The second series of catalysts comprised two solid superacids, i.e.,  $\text{Fe}_2\text{O}_3/\text{SO}_4^{2-}$  and  $\text{ZrO}_2/\text{SO}_4^{2-}$ , which were prepared as follows:

**$\text{Fe}_2\text{O}_3/\text{SO}_4^{2-}$ .** A solution of 25 g of  $\text{NH}_4\text{Fe}(\text{SO}_4)_2 \cdot 12\text{H}_2\text{O}$  and 50 g of urea in 1000 ml of distilled water was heated at 95°C for 2 h. The precipitate formed was filtered, washed with hot water (until no free  $\text{SO}_4^{2-}$  ions could be detected) and dried at 100°C for 24 h. The dry product was treated with 0.5 M  $\text{H}_2\text{SO}_4$  (10 ml/g of solid) with continuous stirring, and then filtered, dried at 100°C for 24 h and calcined at 500°C for 3 h.

**$\text{ZrO}_2/\text{SO}_4^{2-}$ .** 25 g of  $\text{ZrOCl}_2 \cdot 8\text{H}_2\text{O}$  was dissolved in 150 ml of water and subjected to hydrolysis at room temperature by slowly adding 28-30 %  $\text{NH}_4\text{OH}$  with vigorous mixing, until a pH=8.5 was reached. The precipitate was filtered, washed with distilled water until no free  $\text{Cl}^-$  ions could be detected, and then dried at 110°C for 24 h. The dry solid was pulverized to -100 mesh and treated with 0.5 M  $\text{H}_2\text{SO}_4$  (10 ml/g of solid) for 1 h with continuous stirring, and then filtered, dried at 100°C for 24 h and calcined at 650°C for 3 h.

**Procedure of Kinetic Hydrogenolysis Studies.** The kinetic studies of model compounds, in particular 2-isopropyl-naphthalene, were carried out in a 50 ml Microclave reactor (Autoclave Engineers) equipped with a special sampling device. Twenty grams of a solution containing 2 wt. % of 2-isopropyl-naphthalene in n-dodecane and the catalyst were introduced in the reactor and the latter was quickly closed, purged with nitrogen and then pressurized with hydrogen to an initial pressure of 800 psig. The reactor was brought to the desired temperature (350-400°C) in 12-15 min., and at this point stirring (800 r.p.m.) was started. After each sampling, at intervals of 5-10 min., some hydrogen addition was necessary to keep a constant hydrogen pressure of 1500 psig. The reaction products were analyzed by gas chromatography using a 4 m x 0.3 cm o.d. stainless steel column packed with 10% OV-17 on Chromosorb W-HP.

The treatment of the kinetic data was made on the basis of pseudo-first-order reaction in reactant concentration, viz.,

$$-\ln(1-x_i) = kWf(t/V)$$

where k is the rate constant;  $x_i$  is the conversion at time  $t_i$ ; W is the catalyst weight, and  $f(t/V)$ , (volume-corrected space time) is defined by

$$f(t/V) = \sum_{i=1}^n \frac{t_i^c - t_{i-1}^c}{V_{i-1}}$$

in which,  $n$  is the total number of intervals between the samples;  $V_{i-1}$  is the liquid volume remaining in the reactor during a given time period, and  $t'$  is the corrected time.

## RESULTS AND DISCUSSION

Table 1 summarizes the values of the pseudo-first-order kinetic rate constants ( $k_1$ ) for hydrodealkylation of 2-isopropyl-naphthalene, IPN (to yield naphthalene and propane) as a function of catalyst type. The Table also provides the values of the rate constants ( $k_2$ ) for the competing ring hydrogenation of IPN to yield 2-isopropyl-1,2,3,4-tetrahydronaphthalene. Kinetic runs were performed at two different temperatures, i.e., 350 and 400°C (for other conditions, and for the experimental procedure, see Experimental). The  $k_1$  values obtained were taken as a measure of the hydrogenolytic activity of the catalysts.

As seen, at 350°C the solid superacid catalysts 4 and 5 show markedly higher hydrogenolytic activity than the supported soluble catalysts 1 and 2. The difference in activity becomes larger with increase in reaction temperature to 400°C. The supported anhydrous  $\text{Fe}(\text{CH}_3\text{COO})_3$  catalyst shows the lowest activity among the soluble Fe salt catalysts. Addition of a small amount of water to this catalysts (see footnote d, Table 1) prior to reaction, resulted in some hydrogenolysis activity, which, however is lower than that of catalysts 1 and 2 which contain the pre-formed aqua complex  $\text{Fe}(\text{H}_2\text{O})_6^{3+}$ . The latter has been previously indicated<sup>(20)</sup> as the precursor of active, protonic acid-generating species, e.g.,  $\text{H}^+[\text{Fe}(\text{H}_2\text{O})_5\text{OH}]$ . The relatively low activity of catalyst 3, even in the presence of water, indicates that it is preferable to use pre-formed aqua complexes of Fe salts. The thermal stability of such catalysts between 250-400°C is presently being investigated in this laboratory. The very low values of the ring hydrogenation rate constants ( $k_2$ ) with the supported soluble catalysts 1-3 indicates that the latter possess essentially no ring hydrogenation activity, viz., they act as selective, monofunctional hydrogenolysis catalysts. In contrast, the  $\text{Fe}_2\text{O}_3/\text{SO}_4^{2-}$  catalyst 4 shows moderate ring hydrogenation activity, especially at 400°C ( $k_2=0.30$ ). This would indicate that under reaction conditions ( $\text{H}_2$  pressure; elevated temperature) the sulfated iron oxide may be converted to a bifunctional catalyst system containing not only a strongly acidic functional group, but also a moderately active ring hydrogenation co-catalytic component. This could explain the overall good efficiency of this catalyst under coal liquefaction conditions.

The observed extraordinarily high hydrogenolytic activity of  $\text{ZrO}_2/\text{SO}_4^{2-}$  suggests the desirability of developing active  $\text{Fe}_2\text{O}_3\text{-ZrO}_2/\text{SO}_4^{2-}$  co-catalysts. Work on such catalyst systems is presently underway in this laboratory. Parallel hydrogenolytic activity studies with diphenylmethane (DPM) as feed showed similar trends as those in Table 1. However, the rate constants for hydrogenolytic cleavage of DPM (to yield benzene and toluene) were lower, due to the slower protonation rate of the monocyclic aromatic rings in DPM, as compared with that of the bicyclic arene system in IPN.

Table 2 summarizes the total conversions of the Blind Canyon coal sample (DECS-17) into depolymerized, THF-soluble products obtained by HT-BCD treatment, using different acid

TABLE 1. Kinetic Rate Constants for Hydrogenolysis (Hydrodealkylation) and Ring Hydrogenation of 2-Isopropyl-naphthalene (IPN) as a Function of Catalyst Type<sup>a,c</sup>.

Catalyst	$k_1 \times 10^2$ (ml/g·min), hydrodealkylation		$k_2 \times 10^2$ (ml/g·min), ring hydrogenation	
	350°C	400°C	350°C	400°C
(1) FeCl <sub>3</sub> ·6H <sub>2</sub> O/SiO <sub>2</sub>	3.9	31.5	0.2	0.7
(2) Fe <sub>2</sub> (SO <sub>4</sub> ) <sub>3</sub> ·5H <sub>2</sub> O/SiO <sub>2</sub>	2.4	10.6	0.4	1.3
(3) Fe(CH <sub>3</sub> COO) <sub>3</sub> /SiO <sub>2</sub> <sup>d</sup>	0.4	6.9	0.2	0.5
(4) Fe <sub>2</sub> O <sub>3</sub> /SO <sub>4</sub> <sup>2-</sup>	6.2	99.2	4.2	30.0
(5) ZrO <sub>2</sub> /SO <sub>4</sub> <sup>2-</sup>	372.5	565.9	4.1	5.7

<sup>a</sup> In each kinetic run was used 20 g (26.7 ml) of a 2.0% by weight solution of IPN in n-dodecane.

<sup>b</sup> The amount of SiO<sub>2</sub>-supported soluble catalysts 1, 2 and 3 used in each run was 4 g. The rate constants for these catalysts were calculated on a SiO<sub>2</sub>-free basis. The amount of superacids 4 and 5 used in each run was 5000 ppm (0.5%).

<sup>c</sup> Reaction conditions: H<sub>2</sub> pressure, 1500 psig; temperature, 350 or 400°C; microclave reactor volume, 50 ml; sampling time intervals, 5-10 min.; total reaction time, 75 min.

<sup>d</sup> A calculated amount of water, needed for *in situ* formation of the Fe(H<sub>2</sub>O)<sub>6</sub><sup>3+</sup> ion was added to this supported anhydrous salt, prior to reaction.

catalysts in the HT reactor (a flow reactor system was used in this part of the study). As seen, using either the soluble aqua complexes of Fe salts (unsupported; impregnated in the coal) or solid superacids (in the form of fine dispersions; physical mixture with coal) results in a very high level of depolymerization (92.4-94.5 wt. %, calculated on the pre-extracted (THF) DECS-17 sample; MAF basis). However, the impregnated aqua complexes can be applied as acid catalysts at a mild HT temperatures (275-325°C) whereas the use of finely dispersed solid superacids in the HT treatment requires temperatures of  $\geq 340^\circ\text{C}$ .

TABLE 2. HT-BCD Treatment of Blind Canyon Coal (DECS-17) using different acid catalysts in the HT reactor<sup>a</sup>

HT Catalyst	Catalyst/Feed Ratio	HT Temp., °C	HT-BCD Conversion <sup>b</sup>
$\text{Fe}_2(\text{H}_2\text{O})_5(\text{SO}_4)_3$	1:9	325	92.7
$\text{Fe}(\text{H}_2\text{O})_6\text{Cl}_3$	1:9	300	94.1
$\text{Fe}_2\text{O}_3/\text{SO}_4^{2-}$	1:200	340	92.4
$\text{ZrO}_2/\text{SO}_4^{2-}$	1:200	340	94.5

<sup>a</sup> In each run was used 10.0 g of coal-catalyst mixture. HT reaction conditions:  $\text{H}_2$  pressure, 1500 psig;  $\text{H}_2$  flow rate, 50 sccm; total reaction time, 2 h. BCD reaction conditions: catalyst-solvent system, 10% KOH solution in MeOH; temperature,  $290^\circ\text{C}$ ; total reaction time, 1 h.

<sup>b</sup> Total yield of THF solubles (MAF basis), calculated on the pre-extracted Blind Canyon coal feed.

## CONCLUSIONS

1. Kinetic studies of acid-catalysed hydrogenolysis of 2-isopropyl-naphthalene and diphenylmethane show that (in the temperature range of  $350\text{-}400^\circ\text{C}$ ) finely dispersed solid superacids, e.g.,  $\text{Fe}_2\text{O}_3/\text{SO}_4^{2-}$  and  $\text{ZrO}_2/\text{SO}_4^{2-}$ , possess markedly higher hydrogenolytic activity as compared with that of soluble aqua complexes of Fe salts, e.g., Fe sulfate, chloride and acetate (supported on  $\text{SiO}_2$ ).

2. In agreement with the above, it is found that solid superacids, in very low concentrations (0.1-0.5 wt. %) can be conveniently applied as hydrogenolysis catalysts in the HT step of the HT-BCD coal depolymerization process<sup>5-7</sup>. The effective application of superacid catalysts in this process, however, requires HT temperatures  $\geq 340^\circ\text{C}$ , which are considerably higher than those found as optimal in the case of impregnated soluble Fe salts as hydrogenolysis catalysts ( $275\text{-}300^\circ\text{C}$ ).

## ACKNOWLEDGEMENT

The authors wish to thank the U.S. Department of Energy for financial support through the Consortium for Fossil Fuel Liquefaction Science (UKRF-4-21003-86-24; DE-FC22-89PC89851).

## REFERENCES

1. Derbyshire, F., *Energy & Fuel*, **1989**, 3, 273-277.
2. Tanabe, K., Yamaguchi, T., Hattori, H., Sanada, Y. and Yokoyama, S., *Fuel Process. Technol.*, **1984**, 8, 117-122.
3. Pradhan, V.R., Tierney, J.W., Wender, I. and Huffman, G.P., *Energy & Fuels*, **1991**, 5, 497-507.
4. Eklund, P.C., Quarterly Report on DOE Contract No. DE-FC22-90PC90029, August 1, 1991-October 31, 1991, p. 73-75.
5. Shabtai, J.S. and Saito, I., U.S. Pat. 4728418, **1988**.
6. Carlson, R.E., Critchfield, S., Vorking, W.P., Dong, J.-Z., Pugmire, R.J., Lee, M.L., Zhang, Y., Shabtai, J. and Bartle, K.D., *Fuel*, **1992**, 71, 19-29.
7. Shabtai, J. and Zhang, Y., *Proc. Int. Confer. Coal Science, Tokyo, Vol. II*, **1989**, 807-810.
8. Suzuki, T., Yamada, O., Takahashi, Y. and Watanabe, Y., *Fuel Process. Technol.*, **1985**, 10, 33-43.
9. Herrick, D.E., Tierney, J.W., Wender, I., Huffman, G.P. and Huggins, F.E., *Energy & Fuels*, **1991**, 4, 231-235.
10. Cook, P.S. and Cashion, J.D., *Fuel*, **1987**, 66, 661-668.
11. Cook, P.S. and Cashion, J.D., *Fuel*, **1987**, 66, 669-677.
12. Huffman, G.P., Ganguly, G., Taghiei, M., Huggins, F.E. and Shah, N., *Preprints ACS Div. of Fuel Chem.*, **1991**, 36(2), 561-569.
13. Yamaguchi, T., Jin, T. and Tanabe, K., *J. Phys. Chem.*, **1986**, 90, 3148-3152.
14. Hino, M. and Arata, K., *Chemistry Letters*, **1979**, 477-480.
15. Hino, M. and Arata, K. *Chemistry Letters*, **1979**, 1259-1260.
16. Suzuki, T., Yamada, H., Sears, P.L. and Watanabe, Y., *Energy & Fuels*, **1989**, 3, 707-713.
17. Marriadasou, D.G., Charcosset, H., Andres, M. and Chiche, P., *Fuel*, **1983**, 62, 69-72.
18. Farcasiu, M., Smiths, C., Pradhan, V.R. and Wender, I., *Fuel Process. Technol.*, **1991**, 29, 199-208.
19. Huffman, G.P., et al., *Energy & Fuels*, **1993** (in press).
20. Zhang, Y., Ph.D. Dissertation, **1991**, University of Utah.

## IRON CATALYSTS IN COAL HYDROGENATION

A. M. Mastral, C. Mayoral, M. T. Izquierdo, C. Pardos  
Instituto de Carboquímica, CSIC  
Apdo 589, 50080-Zaragoza, Spain

**Keywords:** coal, hydrogenation, iron

### ABSTRACT

Hydrogenation of a set of low and high rank coals was studied using iron containing species as catalyst. Three catalytic precursors were used:  $\text{FeSO}_4 \cdot 7\text{H}_2\text{O}$  (IS),  $\text{Fe}_2\text{O}_3$  (RM) and  $\text{Fe}(\text{CO})_5$  (IP). The addition of catalyst increased the conversion in important extent when low rank coals were hydrogenated and in a more moderate way with the bituminous coals under an initial hydrogen pressure of 10 MPa and in absence of solvent, dry hydrogenation. When  $\text{CS}_2$  was added to high sulphur content coals only slight increase of oils formation was observed. However, significative higher conversions to asphaltenes and oils were reached when the coal sulphur content was around 1%. It seems to be more important the amount of total sulphur than its organic or inorganic nature.

### INTRODUCTION

Coal hydrogenation processes consists in coal transformation into progressively lighter products in order to obtain oil. In general, the product distribution of processes such as hydroliquefaction and hydroypyrolysis, shows a mixture of low-molecular weight oils, asphaltenes and preasphaltenes, as well as the insoluble residue. The hydrogenation has been widely used, not only for its interest in hydrocarbon production, but also as an strategy of degradative reaction applied to coal in order to study the coal structure.

Both approaches to coal, the practical and the theoretical one, seem to be nowadays not yet resolved, regardless the great research effort that is been done, in many senses, process development, variables optimization and catalyst selection.

Iron containing compounds have been widely studied as hydrogenation catalysts, due to their relatively low cost, hydrogenation activity and iron decarboxilation potential. Several ways of iron addition to the coal can be used. Each one presents advantages and drawbacks. The iron precursors dispersion onto the coal surface is now generally considered to have a beneficial effects, that increases the amount of active catalyst surface area available at the same loads. This dispersion requires the previous dissolution of the precursors and several of the compounds of interest as liquefaction catalysts, such pyrite, iron oxide, are insoluble in common solvents. Other solid precursors have to be added by physical mixing. The organometallic species are usually added with the hydrogenation solvent; when the working procedure is dry, liquid species as  $\text{Fe}(\text{CO})_5$  can be just added to the coal previously to the introduction into the reactor. In all the cases, the active form of the iron catalyst is considered to be the iron sulphide.

The aim of this work is to study the effect of the hydrogenation temperature and catalysts on the product distribution and characteristics, when the hydrogenation is carried out in absence of solvent, keeping constants the initial hydrogen pressure and the hydrogenation time.

### EXPERIMENTAL

The work reported is part of a broader investigation (1) of dry catalytic hydrogenation of a set of 25 coals from different mining areas around the world. For this paper, the results

obtained with 9 of these coals, 6 from Spain (Ref. S9, S13, S16, S18, S20 and B23), one from USA (Illinois No 6, Ref. B19), one from Germany (Zollverein, Ref. B22) and one from UK (Bagworth, Ref. B25). The low-rank coals are from Mequinenza (S9), Andorra-Ariño (S13, S16 and S18) and Portalrubio (S20) and were selected as a function of their nature(2). The analysis of the coals are compiled in Table 1.

#### Catalyst Precursors

Three iron containing precursors with iron in different oxidation stages were used:  $\text{FeSO}_4 \cdot 7\text{H}_2\text{O}$ , Red Mud (36.5%  $\text{Fe}_2\text{O}_3$ ) and  $\text{Fe}(\text{CO})_5$ . The first one was converted "in situ" into iron sulphide by  $\text{H}_2\text{S}$  bubbling for 30 min through the alkaline aqueous solution. Then was dispersed on coal using coal as catalytic support. The two others precursors were added to coal before hydrogenation by direct physical mixing (RM) or by embedding ( $\text{Fe}(\text{CO})_5$ ). The catalyst loading was equivalent to 5% wt iron of dmmf coal.

#### Hydrogenation Procedure

The hydrogenation was carried out in small reactors type tubing bomb (160cc capacity) loaded with about 10 g of daf coal and catalyst, pressurized with  $\text{H}_2$  to 10 MPa and heated in a fluidized sand bath for 30 min at 300, 350, 400, 425, 450 and 500°C. When the coal sulphur content was low,  $\text{CS}_2$  was added.

The products work-up was according to Fig 1. The gas were analyzed by GC, the oils by elemental analysis, FTIR, TLC-FID and simulated distillation by GC. The THF-insolubles by CP-MAS 13C nmr and FTIR

## RESULTS AND DISCUSSION

As the numerical data on conversions and derived product distributions of each coal would enlarge this paper, tables 2 and 3 show the results obtained with coals Ref. S13 and B25 as representative models. However, comments on the other hydrogenated coals will be done along this paper since each coal has its own characteristics.

The selected coals, apart from low and high rank coals can be classified as high and low sulphur content coals. The percentages are calculated on "as received" basis. While the low rank coals have %S ranging from 8.6% to 5.7%, the bituminous coals show a total sulphur content around 1%, with the exception to B19 with 3.9% of total sulphur. That is the reason why to very few experiments has been added  $\text{CS}_2$ , see Table 2, when S13 coal has been hydrogenated. Coals S13, S16, and S20 have about the same organic sulphur contents (4%), while S18 has more pyritic sulphur (3.80%) and S9 has much more organic sulphur (7.78%). Not one of these coals need  $\text{CS}_2$  addition to reach high conversions in iron catalytic hydrogenation and when  $\text{CS}_2$  was added not significative variations were detected on conversion percentages nor THF-solubles; only a very slight increase in oils formation percentages were obtained.

Keeping constants the hydrogenation time and the starting hydrogen pressure, in general, the higher the temperature, the higher the conversions, the THF-solubles and the oils percentages.

The very high conversions (95% dmmf for the S9 coal) reached with these low-rank high-sulphur content coals seem to show that it does not matter the origin of the sulphur, organic or inorganic, the real point seems to be the total amount of sulphur present in order to reach the  $\text{H}_2\text{S}$  pressure to convert the iron (whatever be its original oxidation degree) from the catalytic precursor into the iron sulphide salt which is the active form (3). On the other side the SEM analysis shows that if the  $\text{H}_2\text{S}$  pressure is sufficient at the end of the processes most of the iron is in the sulphide form. The optical microscopy shows the superficial, not yet the nucleous, transformation of the pyrite nodules from the inherent mineral matter into pyrrhotite on the THF-insolubles from non-catalyzed test at 300 °C. This

transformation is complete at 350 °C.

The presence of iron catalyst increased coal conversion from 47% to 75% (IS), 60% (RM) and 59% (IP) at 350 °C and from 76% to 89% (IS), 95% (RM) and 91% (IC) at 400°C when S9 coal was hydrogenated. With the bituminous coals the difference between non-catalytic and catalytic processes was not so pronounced, but significant enlargement was reached when CS<sub>2</sub> was added.

For the B22, B23, and B25, Table 3, at the lowest temperature studied, the addition of CS<sub>2</sub> is not determinant because at this temperature there are not yet thermic nor catalytic cracking with these high rank coals, but at the medium temperatures studied, 350°C and 400°C, the CS<sub>2</sub> addition influences helping to stabilize the radicals from both thermic and catalytic cracking. The bituminous coal with an intermediate total sulphur content (B19) follows the same trends but the effect of CS<sub>2</sub> addition is significant in a minor extent.

The nature of the oils, analyzed by TLC-FID, show to be mainly aromatic and polar, with percentages in saturate compounds always minor to 3% . On polar percentages, the nature of the iron precursor is not relevant but the increase of the process temperature means a reduction of polars to the corresponding aromatic compounds.

The curves of simulated distillation, from the oils by GC analysis, show that there are not conversion into light fractions with low-molecular weight, the gas oil fraction is very scarce, always lower than 2% and the rest of the components are heavy oils.

The transformation of coal into liquids has been followed by solid state nmr spectroscopy of the THF insolubles, Tables 5 and 6. Due to the magnetic properties of this analytical technic and to the iron catalysts used, in some of the spectra was not easy the chemical shift assignation, so only the aliphatic (0-100 ppm) and aromatic (100-190 ppm) carbons have been assigned. These troubles were deeper when RM than when FeSO<sub>4</sub> was used. In order to do not lose rigor, the simplification was done in all the cases. It can be deduced a gradual diminution in the length of the alkylic chains and with increasing hydrogenation temperature, an increasing aromaticity slightly higher when red mud is the catalytic precursor. The FTIR (Fig. 2), confirms the disappearance of aliphatic chains, the decrease in oxygen groups and the aromaticity increase.

Summarizing, at the conditions studied, it can be concluded: a) The importance of the total amount of sulphur in order to reach the suitable H<sub>2</sub>S pressure, being not significant the organic or inorganic nature of the parent sulphur. b) The CS<sub>2</sub> addition does not influence the yields from high-sulphur content coals, but increases conversions and THF-solubles, mainly asphaltene formation, when about 1 % is the inherent sulphur content of coals. c) The iron of the catalytic precursor is converted into pyrrhotite in a higher extension when it comes from IS than from RM.

## REFERENCES

- 1.- Mastral A. M. et al, "Valorization of coal conversion by swelling measuring", Progress Report N°1, Contract 7220/EC/755, CSIC to ECSC, June 1990.
- 2.- Mastral A. M. et al, "Valorization of coal conversion by swelling measuring", Progress Report N°5, Contract 7220/EC/755, CSIC to ECSC, June 1992.
- 3.- Garg D. and Givens E. N., Ind. Eng. Chem. Process. Des. Dev. 1982, 21, 113
- 4.- Mastral, A.M., Izquierdo, M.T., Mayoral M.C. and Pardos C., The Journal of Coal Quality, 1992, 11, 1

## ACKNOWLEDGEMENTS

Authors are thankful to the European Community, GD XVII, ECSC, Contract 7220/EC/755 and to the Spanish CICYT ,Contract PB 413, for this work financial support.

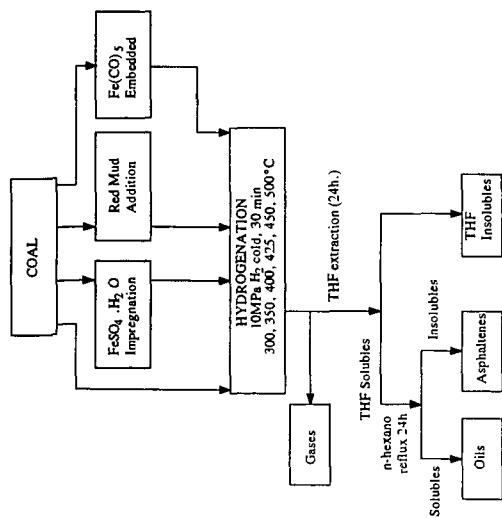


Figure 1. Diagram of the process.

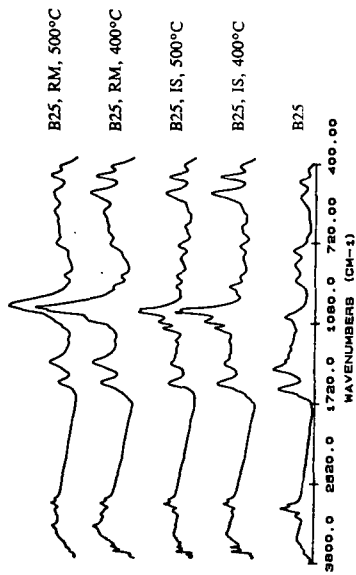


Figure 2. FT-IR spectra of THF-insolubles of B25 coal hydrogenation and raw coal.

Table 2. Conversions and product yields (daf) from S13 coal (10MPa H2 cold and 30 min).

Cat.	Tem. °C	% CS2	% Conv	%THF sol.	O/A	%Gas formation		
						COx	C1-C4	SH2
-	350	-	32.4	23.4	0.1	69	4	27
-	350	YES	37.7	26.9	0.2	71	5	25
-	450	-	80.5	56.3	0.4	46	18	37
IS	300	-	15.8	9.1	0.4	98	0	2
IS	350	-	82.0	69.6	0.1	78	6	16
IS	400	-	78.7	54.2	0.5	54	16	29
IS	425	-	80.2	48.9	0.7			
IS	450	-	84.8	51.2	1.1	45	41	14
RM	300	-	12.1	8.6	0.5	100	0	0
RM	350	-	33.1	23.2	0.3	86	8	5
RM	350	YES	35.6	23.9	0.4	79	8	14
RM	400	-	87.9	60.9	0.4	57	20	23
RM	425	-	84.4	53.5	0.4			
RM	450	-	64.7	30.9	0.8	50	39	11
IP	350	-	34.4	26.0	0.2	83	3	14
IP	350	YES	61.3	40.2	0.2	85	4	11
IP	400	-	75.8	50.9	0.2	69	20	12

Table 3. Conversion and product yields (daf) from B25 coal (10MPa H2 cold and 30 min).

Cat.	Tem. °C	% CS2	% Con.	%THF sol.	O/A	%Gas formation		
						COx	C1-C4	SH2
-	350	-	14.2	8.3	0.8	77	7	14
-	400	-	39.2	32.5	0.4	51	36	13
-	450	-	40.4	22.5	1.1	41	54	5
IS	300	-	11.3	9.2	0.3	97	0	3
IS	350	-	21.3	17.3	0.2	96	0	4
IS	400	-	70.7	55.9	0.4	56	37	7
IS	425	-	79.1	58.1	0.5	43	50	7
IS	450	-	71.7	45.8	1.3	38	59	3
IS	500	-	74.1	32.0	1.3	23	73	4
RM	300	-	5.5	9.3	0.5	100	0	0
RM	300	YES	3.6	10.5	0.3	49	1	50
RM	350	-	14.7	13.3	0.3	92	8	0
RM	350	YES	19.2	19.7	0.3	48	10	43
RM	400	-	43.9	37.9	0.4	67	31	1
RM	400	YES	69.5	60.5	0.3	45	20	34
RM	425	-	73.9	55.6	0.4	50	49	1
RM	425	YES	75.1	59.8	0.6	29	28	43
RM	450	YES	70.2	44.2	0.8	24	36	40
RM	500	YES	64.6	32.8	1.4	22	72	6
IP	350	-	12.6	12.4	0.6	98	2	0
IP	350	YES	9.2	17.1	0.4	90	3	7
IP	400	YES	71.9	61.3	0.4	60	14	25
IP	450	YES	73.7	35.8	0.8	55	33	12

Table 1. Analysis of the parent coals.

Coal Ref.	Proximate analysis (%)				C. fix.	Ultimate analysis (%)			Macerales (%vol)				
	C/H	Moist.	Ash	%MM		Volat.	C	H	N	S	tot	Vitrin.	Exin.
S 9	0.68	11.03	21.35	27.65	36.48	31.14	44.15	5.39	0.39	8.65	90.9	0.4	8.7
S 13	0.74	17.04	11.29	19.48	29.53	42.14	48.34	5.47	0.29	6.00	71.8	3.1	25.1
S 16	0.81	12.94	11.10	18.81	29.51	46.15	49.24	5.07	0.49	6.38	74.7	1.6	23.7
S 18	0.92	12.04	15.11	24.20	29.07	43.78	49.10	4.99	0.35	6.33	75.4	1.0	23.6
S 20	1.07	9.30	38.60	58.06	22.15	29.95	38.18	2.95	0.39	5.71	62.7	1.3	36.0
B 19	1.14	3.30	13.34	17.20	31.59	31.78	64.17	4.67	1.21	3.92	89.1	1.7	9.2
B 22	1.33	1.10	12.07	12.08	25.88	60.95	72.33	4.52	1.49	0.98	67.0	9.0	19.0
B 23	1.58	0.80	8.30	11.43	16.95	74.27	82.23	4.35	1.67	1.20	92.9	0.0	7.1
B 25	1.24	13.70	7.60	11.39	34.10	44.60	62.49	4.19	1.06	1.06	72.0	5.0	23.0

Table 4. Oils nature as a function of the hydrogenation variables (10 MPa H<sub>2</sub>, cold and 30 min).

Coal	Variables	Cat.	Tem.(°C)	Oil Composition (%)		
				Sat.	Arom.	Polars
S13	-	350	1.9	56.0	42.1	
S13	-	400	1.5	68.4	30.1	
S13	IS	300	2.0	39.5	58.5	
S13	IS	350	2.0	56.0	42.0	
S13	IS	400	1.4	67.6	31.3	
S13	RM	300	2.0	39.5	58.5	
S13	RM	350	2.2	49.4	48.5	
S13	RM	400	1.4	60.7	37.9	
B25	-	350	2.4	46.9	52.0	
B25	-	400	5.9	60.9	36.4	
B25	IS	300	2.1	45.4	52.5	
B25	IS	350	2.2	48.5	49.3	
B25	IS	400	2.5	57.3	40.3	
B25	IS	425	2.5	57.3	40.3	
B25	RM	300	2.8	29.0	68.3	
B25	RM	350	2.4	46.0	51.7	
B25	RM	400	2.6	58.4	38.3	
B25	RM	450	1.7	55.5	42.8	

Table 5. Aromaticity and functional groups by CP-MAS Cl<sub>3</sub> nmr of S13 THF-insolubles.

Chemical Shift(ppm)	Raw		Blank runs		S13 IS			S13 RM		
	Coal	300°C	350°C	300°C	300°C	350°C	400°C	300°C	350°C	400°C
0 - 100	33.0	25.5	21.4	53.0	26.4	22.0	68.0	35.5	24.6	
100 - 190	67.0	74.8	81.1	139.0	135.0	131.0	135.5	155.0	157.0	
Aromaticity	0.66	0.71	0.78	0.71	0.82	0.85	0.67	0.78	0.84	

Table 6. Aromaticity and functional groups by CP-MAS Cl<sub>3</sub> nmr of B25 THF-insolubles.

Chemical Shift(ppm)	Raw		B25 IS		B25 RM		
	Coal	300°C	400°C	500°C	300°C	400°C	500°C
0 - 100	33.0	35.8	15.5	7.3	34.8	26.8	11.8
100 - 190	72.0	62.9	84.3	92.7	65.2	73.2	88.2
Aromaticity	0.66	0.64	0.84	0.92	0.65	0.73	0.88

This page intentionally left blank

## IRON BASED CATALYSTS FOR COAL/WASTE OIL PROCESSING

H.G. Sanjay, Arthur R. Tarrer, Chad Marks  
Department of Chemical Engineering  
Auburn University, Auburn, ALA

**Keywords:** Coprocessing, Coal/Waste oil, Iron catalysts

### ABSTRACT

Iron based catalysts are being used in our laboratory to process coal with waste oil. Almost 1.2 billion gallons of waste oil are generated in the United States each year, posing an environmental hazard due to metal bearing compounds and high sulfur content. Waste oil is primarily paraffinic and is a poor hydrogen solvent, but contains surfactants which could help in better dispersion of the coal particles and the catalyst during liquefaction. The undissolved coal can act as a trap for the metals removed from the waste oil without significantly altering the metal content of the coal. The initial results - coal conversion over 70% and oil yield greater than 48% indicate that coprocessing coal with waste oil is beneficial. The results are preliminary and responses in coal conversion and selectivity due to different ratios of waste oil and conventional hydrogen solvents are being evaluated. The effect of various parameters such as temperature, pressure and the amount of catalyst on coal conversion and selectivity during coprocessing is being evaluated.

### INTRODUCTION

The coprocessing of coal with used oil has the potential to improve the economics of coal liquefaction. Almost 1.2 billion gallons of waste oil are generated in the United States each year, posing an environmental hazard due to metal bearing compounds and high sulfur content. The used oil must be re-refined and hydrotreated before use as a fuel or as a lube base stock. The reactions during the hydrotreatment of used oil include hydrodesulfurization (HDS), hydrodemetallation (HDM) and hydrodeoxygenation (HDO). The undissolved coal during coprocessing could act as a trap for the metals removed from the oil and the sulfur present in the oil could serve to produce the sulfided catalyst needed for liquefaction. The overall objective of this work is to evaluate the beneficial effects of coprocessing coal with waste oil using iron based catalysts.

The use of unsupported dispersed catalysts for conversion of coal to liquids via direct coal liquefaction is believed to be a very effective method to overcome the limitations of supported metal catalysts [1]. The restricted access to the reaction surface of the supported metal catalysts such as CoMo/Al<sub>2</sub>O<sub>3</sub>, used in direct coal liquefaction prevents them from influencing the reactions of coal and high molecular weight coal derived products. In addition, supported metal catalysts suffer from rapid deactivation. Unsupported dispersed catalysts provide efficient contact of coal/solvent slurries with the catalyst surface [1]. The effective dispersion of the catalysts can be achieved by different methods such as using water soluble [2] or oil soluble precursors [3] and by using finely divided powders [4]. These techniques allow formation of the active inorganic phase under reaction conditions. The addition of finely divided solid precursors with high specific surface area is considered a very effective way to achieve good dispersion and improved overall coal conversion and selectivity to oil production in direct coal liquefaction [4,5].

Iron based catalysts have the potential to be used as effective dispersed catalysts and have been employed recently for direct coal liquefaction. Iron based catalysts are cheap, readily available and disposable. Sulfated iron oxide was found to be an effective catalyst for liquefaction with 86 wt% conversion and 50 wt% selectivity for oils [6]. The addition of elemental sulfur to the catalyst was found to further increase the conversion and selectivity. It was postulated that the sulfate group inhibits agglomeration of the metal oxides and subsequently increases the surface area and catalyst dispersion [6]. Oil soluble iron carbonyls have been used in direct coal liquefaction and in coprocessing with heavy oil in a number of studies [3,7-10]. The iron carbonyls are distributed throughout the coal/solvent mixture and decompose upon heating to form very small catalyst particles active for liquefaction of coal. The addition of sulfur in either elemental form or as an organic sulfur compound favored the formation of pyrrhotite whereas the less active iron oxide ( $\text{Fe}_2\text{O}_3$ ) was formed in its absence [8]. The iron pentacarbonyl precursor was converted to pyrrhotite at the reaction conditions with time. The use of 0.5 wt% iron as iron pentacarbonyl increased the coal conversion from 39% to 82% [3]. Hematite ( $\text{Fe}_2\text{O}_3$ ) was found to be a very good sulfur scavenger during coal desulfurization [11]. The iron oxide reacts with all the hydrogen sulfide released to form pyrrhotites and prevents any reaction of hydrogen sulfide with the organic constituents of the process solvent. The formation of pyrrhotites as the major phase has also been reported when iron oxide was presulfided in a mixture of hydrogen and hydrogen sulfide under reaction conditions [12].

Waste oil is primarily paraffinic and is a poor hydrogen donor solvent. It does, however, contain surfactants which could be advantageous to liquefaction. The additives found in the waste oil such as detergent/dispersant additives, oxidation inhibitors, etc., are organic sulfur compounds [13]. These additives could help effectively disperse the coal and the catalyst precursors throughout the coal/oil slurry during coprocessing. In addition, these additives can serve as sulfur sources to convert the catalyst precursors to the more active form. The unconverted coal could act as a trap for the metals removed from the oil. This has been the case during coprocessing of coal with a heavy oil where metallic impurities in the oil were found to deposit on the coal residue or pitch [14]. The demetallation of used oil during hydrotreatment was found to be primarily due to the process of physical deposition on the catalyst bed [15].

## EXPERIMENTAL

The co-processing reactions in the tubing bomb were carried out using DECS 6 coal, waste oil (1% sulfur, 0.45% ash), tetralin as a solvent (in some cases), and superfine iron oxide ( $\text{Fe}_2\text{O}_3$ ) as a catalyst precursor. The coal was crushed and separated to obtain a particle size of less than 16 mesh. The liquid and solid reactants were then charged in the desired proportions into a tubing bomb reactor. High pressure hydrogen was added through a fine metering valve and capped with a Swagelok fitting. The bomb was leak tested by submerging it in water. The bomb was then attached to a variable-speed motor via an extension arm. The bomb was then lowered into a fluidized sand bath to maintain the reaction temperature and was shaken vertically. At the end of the desired reaction time, the motor was stopped and the tubing bomb was removed from it. The reaction was then quenched using water at room temperature. The liquid and solid reactant mixture was filtered under vacuum to separate the solid and liquid components. The liquid portion was saved for sulfur and ash analysis. The bomb and the solids collected

in the first filter were then washed with hexane to obtain the hexane-soluble fraction. The solids remaining after hexane washing were allowed to dry before weighing. The solids were then washed with tetrahydrofuran (THF) to obtain the THF solubles. This solid was also allowed to dry before being weighed. The liquid obtained from the first filter was then tested for sulfur content using a LECO sulfur determinator (SC-32) and ash content was determined using a SYBROM Thermolyte furnace.

## RESULTS AND DISCUSSION

The coal conversion during coprocessing with waste oil was defined as

Conversion =  $100 * (1-X)$  where,

$$X = \frac{W_R - W_C - W_{ash}}{W_{ash\ free\ coal}}$$

$W_R$  weight of residue remaining after THF wash,

$W_C$  weight of catalyst (it was assumed that all the iron oxide was converted to FeS)

$W_{ash}$  weight of ash in the coal

The results from coprocessing experiments are given in Table 1 (using superfine iron oxide) & Table 2 (using Fisher grade iron oxide).

The reduction in sulfur and ash are for the oil obtained after the first filter on the basis of initial analysis of waste oil. The conversion and the oil yield are very high (88% and 69% respectively) even when only coal and oil are used. The conversion increased when either tetralin or catalyst precursor (iron oxide) was added to the reaction mixture. The oil yield remained nearly same. However, both the conversion and oil yield decreased when both tetralin and iron oxide were added. The reason for this behavior is not very clear at this time and additional experiments are being conducted for confirmation. The amount of iron oxide used in these runs was the stoichiometric amount (2.5 wt% based on the oil) needed to remove all the sulfur in the waste oil. However, when the iron oxide was used in excess (1.5 times the stoichiometric amount), and the amount of tetralin was increased, the conversion and the oil yield increased as expected (89% and 48% respectively).

The reduction in the sulfur content was greater when tetralin was present in the system. This is probably due to the increased availability of hydrogen in the liquid phase when tetralin is present, leading to increased removal of sulfur by forming hydrogen sulfide. The reduction in the ash content was greater than 70% in most of the runs. The ash reduction is believed to be primarily due to the deposition of the metals on unreacted coal and residue [14,15].

## CONCLUSIONS

Coprocessing coal with waste materials such as waste oil which have expensive disposal costs offers several advantages. Unsupported dispersed catalyst precursors (iron oxide) were used in an initial study to coprocess waste oil with coal. The conversion of the coal

and the selectivity for the oil was in excess of 70% for most of the runs. The conversion and the selectivity were higher even when the catalyst precursor was not used. The sulfur and the ash content in the oil were reduced substantially during coprocessing. A detailed study is underway at present to evaluate the effect of various parameters such as different ratios of oil to hydrogen donor solvents, temperature, pressure, catalyst loading, etc., on the coal conversion and selectivity.

#### REFERENCES

- (1) Derbyshire, F., *CHEMTECH*, July 1990, 439.
- (2) Cugini, A. V., Utz, B. R., Fromell, E. A., *Prepr. Pap. - Am. Chem. Soc., Div. Fuel Chem.* 1989.
- (3) Herrick, D. E., Tierney, J. W., Wender, I., Huffman, G. P., Huggins, F. E., *Energy Fuels* 1990, 4, 231.
- (4) Marriadassou, D. G., Charcosset, H., Andres, M., Chiche, P., *Fuel* 1983, 62, 69-72.
- (5) Suzuki, T., Yamada, H., Sears, P., Watanabe, Y., *Energy Fuels* 1989, 3, 707-713.
- (6) Pradhan, V. R., Tierney, J. W., Irving, W., *Energy & Fuels* 1991, 5, 497-507.
- (7) Suzuki, T., Yamada, O., Fujita, K., Takegami, Y., Watanabe, Y., *Chem. Lett.* 1982, 1467-1468.
- (8) Suzuki, T., Yamada, O., Takehaski, Y., Watanabe, Y., *Fuel Process. Technol.* 1985, 10, 33-43.
- (9) Watanabe, Y., Yamada, O., Fujita, K., Takegami, Y., Suzuki, T., *Fuel* 1984, 63, 752-755.
- (10) Montano, P. A., Stenberg, V. I., Sweeny, P., *J. Phys. Chem.* 1986, 90, 156-159.
- (11) Garg, D., Tarrer, A.R., et al., *Ind.Eng.Chem.Proc.Des.Dev.* 1980, 19, 572-580.
- (12) Shridharani, K.G., *PhD Dissertation*, Auburn University, 1983.
- (13) Wills, J.G., *Lubrication Fundamentals*, Marcel Dekker, Inc, New York 1980.
- (14) Miller, T.J., et al., *Fuel Process. Technol.* 1989, 23, 23-38.
- (15) Skala, D.U., et al., *Ind.Eng.Chem.Res.* 1991, 30, 2059-2065.

Table 1. Coproducting Coal with Waste Oil						
CATALYST (wt%)	TETRALIN* (wt%)	TIME (min)	CONVERSION* (%)	OIL YIELD® (wt%)	SULFUR REDUCTION (%)	ASH REDUCTION (%)
6 grams of oil, 0.6 grams of DECS 6 coal						
-	-	60	87.84	69.27	35.80	84.10
2.50	-	60	96.13	65.64	28.85	89.06
-	20	60	93.03	70.39	38.30	72.22
2.50	20	60	71.48	36.27	40.40	-
3.75	60	30	88.93	47.68	54.90	90.67
9 grams of oil, 0.9 grams of DECS 6 coal						
-	-	30	88.96	80.37	27.00	80.02
-	-	60	71.50	71.77	27.20	73.27
-	-	90	88.87	87.12	-	38.22
2.5	20	60	91.88	35.31	40.80	75.82

\* catalyst precursor: superfine iron oxide ( $Fe_2O_3$ ).

+ based on amount of oil.

# tetrahydrofuran (THF) soluble MAF basis.

@ oil yield on basis of coal converted.

Reaction conditions: 400 °C, 1200 psig (at room temperature).

Table 2.  
COPROCESSING COAL WITH WASTE OIL

WASTE OIL (gms)	TETRALIN (gms)	TEMPERATURE (°C)	OIL ANALYSIS*		OIL YIELD** (MAF)
			SULFUR REDUCTION (%)	ASH REDUCTION (%)	
20	-	410	30	80	55%
20	-	430	40	65	55%
10.14	10.53	430	40	85	75%

Reaction Conditions: Blind Canyon (DECS 6) coal: 2 gms; Fe<sub>2</sub>O<sub>3</sub> (Fisher grade): 0.75gms.  
1000 psig hydrogen pressure (at room temperature)

\* Initial Analysis: Sulfur 1.01%; Ash content: 0.43%

\*\* based on initial coal charge

## DEVELOPMENT OF HIGHLY DISPERSED COAL LIQUEFACTION CATALYSTS

Toshimitsu Suzuki

Department of Chemical Engineering, Kansai University  
Suita, OSAKA JAPAN 564

### Key Words

Iron carbonyl, Coal liquefaction kinetics, Dispersed catalyst,

### Introduction

Recently much attention has been focused on the highly dispersed catalyst for coal hydro-liquefaction.<sup>1</sup> We have been developing highly dispersed catalyst for coal liquefaction since 1981.<sup>2</sup> In 1951 Weller and Peripetz first reported that the distribution of the catalyst is very important for the high activity.<sup>3</sup> However, exact roles of coal liquefaction catalyst have not been well elucidated. Until now understandings of coal liquefaction catalyst involves many contradictory arguments.

Our understanding in coal liquefaction reaction mechanisms is as follows: Thermal scission of covalent bonding in coal macromolecular structure occur to give free radicals, followed by stabilization by a hydrogen abstraction either from hydrogen donor substances or a molecular hydrogen activated on a catalyst. This process is schematically represented in Scheme I.

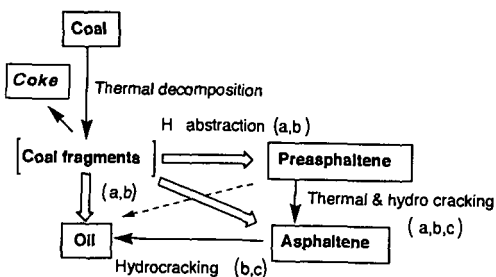
- To keep good contact between catalyst and solid coal.
- High activity toward hydrogen transfer in both coal fragment radicals and aromatic moiety.
- High activity for cracking and hydrocracking of C-C bonds.
- Cost of the catalyst should be low and recovery or recycle use of the catalyst should be easy.

From these view points, following four conditions would be required for the efficient coal liquefaction catalyst.

Among them (a) and (b) are the most significant characteristics required for the catalyst in the early stage of the coal liquefaction course shown in Scheme I.

A catalyst which fulfill all the requirement shown above cannot be found hitherto. Among many catalysts previously investigated,  $ZnCl_2$  or  $SnCl_2$  is superior in functions (b) and (c), on the other hand, iron is important in the cost of metal (d). Co-Mo and Ni-Mo catalyst employed for the hydrodesulfurization of petroleum fractions are extremely active in functions (b) and (c). However, such a supported catalyst is poor in contact between catalysts and coal (a) and in addition deactivation of catalyst is indispensable.

In several processes involved in coal liquefaction, hydrogen transfer to coal fragment radicals is the most important path in order to obtain higher coal conversion. A certain amount of coal fragment



Scheme I Coal liquefaction scheme and functions of the catalyst required in the particular steps

radicals exist in the solid coal matrix or appear as partially fused macromolecular structure of which mobility is restricted, at the early stage of the liquefaction. Under such conditions, contact between catalyst and solid coal is a very important factor to obtain higher coal conversion.

Previous attempts to use homogeneous transition metal complexes as a catalyst were not successful.<sup>4</sup> We have been noticed that iron carbonyl decomposes to give fine particles of iron metal at an elevated temperature. This prompts us to use iron carbonyl as a catalyst precursor of coal liquefaction. Iron carbonyl is freely soluble in a common organic solvent, therefore the catalyst precursor may penetrate into pore structures of coal at a lower temperature and above a decomposition temperature the precursor decomposes to a finely dispersed iron species on the solid coal. Thus good contact between the catalyst and solid coal could be attained.

#### Results of coal liquefaction with organometallic compounds<sup>5,6</sup>

Hydroliquefaction of coal with  $\text{Fe}(\text{CO})_5$  was carried out in a batch 50 mL micro autoclave under various reaction conditions. A 2.0 g of coal and 4.0 mL of vehicle oil (1-methylnaphthalene or tetralin) was charged with a certain amount of catalyst. The autoclave was heated to the desired reaction temperature and shaken. The reaction mixture was separated into preasphaltene asphaltene, and oil fractions.

The results of the liquefaction of Illinois No 6 coal (C:76.8 %) are summarized in Table I.<sup>5</sup> Since we have known that that  $\text{Fe}(\text{CO})_5$  exhibited higher catalytic effects than those of conventional iron catalyst previously reported, we wanted to carry out the liquefaction reaction at a higher reaction temperature in a short contact time. At an initial hydrogen pressure of 5.0 MPa, coal conversion was not high as expected (compare run 2 and 4). Increases in the initial hydrogen pressure to 8.0 MPa, remarkable increases in the coal conversion and oil yield were observed at a reaction time of only 20 min. At 480 °C a reaction time of 10 min is sufficient to obtain oil yield of 50 %. Conventional  $\text{Fe}_2\text{O}_3$  catalyst afforded smaller coal conversion and oil yield of 43 % (see run 10). Even in a very short reaction time (10 min), conversions to THF soluble fraction were almost constant and very high (over 93 % in the temperature range of 425 to 480 °C). However, the asphaltene and oil yields increased with an increase in the reaction temperature. This indicates that conversion of THF soluble products to oil and asphaltene fractions can not be promoted with the iron catalysts at a lower temperature.

We have extended the use of iron carbonyl based catalyst to the liquefaction of Australian low rank coals (Yallourn C: 68.2 %, Wandoan C: 76.8 %). The results are summarized in Table II.<sup>6</sup> Much lower conversions were observed in the absence of the catalyst as compared to Illinois No.6. Use of  $\text{Fe}(\text{CO})_5$  increased conversions, but the increases are not significant as in the case of Illinois No.6 coal. Addition of one to two equivalent amount of sulfur to iron greatly enhanced the catalytic activity. Several iron carbonyl derivatives also enhanced coal conversion and oil yield markedly with sulfur.

The role of sulfur in the iron catalyst was examined by X-ray diffraction study of the residues from the liquefaction reaction.

Pyrrothite has been proposed to be one of active species of iron-sulfur based catalyst by Montano.<sup>7</sup> In our case a liquefaction residue in  $\text{Fe}(\text{CO})_5$ -S system clearly showed intense peaks attributed to  $\text{Fe}_{1-x}\text{S}$  in the XRD pattern. On the other hand, that obtained in the absence of sulfur exhibited the peaks ascribed to  $\text{Fe}_3\text{O}_4$ . These findings indicate that active form of  $\text{Fe}(\text{CO})_5$  based catalyst is essentially the same as that of conventional iron oxide or iron sulfide based catalyst.

Further studies of an active form of  $\text{Fe}(\text{CO})_5$  based catalyst were done by using Mössbauer spectroscopy in the reaction with coal model compounds.<sup>8</sup> Mössbauer spectra of  $\text{FeS}_2$  or  $\text{Fe}_2\text{O}_3$ -S based catalyst after a hydrocracking reaction of diphenylmethane exhibited clear sextet signals ascribed to  $\text{Fe}_{1-x}\text{S}$ . On the other hand,  $\text{Fe}(\text{CO})_5$ -S based catalyst exhibited rather broad doublet signals in the center of the spectra, in addition to the sextet signals ascribed to  $\text{Fe}_{1-x}\text{S}$ . This absorption is probably attributed to highly dispersed paramagnetic iron species, so called superparamagnetic species.

Superiority in such a finely dispersed iron catalyst can be observed when hydrogenation of coal model compounds phenanthrene or pyrene were hydrogenated. Much higher conversion of condensed aromatic compounds to partially hydrogenated compounds were observed as compared to conventional

iron catalysts such as  $\text{Fe}_2\text{O}_3$  or  $\text{FeS}_2$ . On the hydrogenolysis of diphenylmethane or diphenylethane slightly higher activities of  $\text{Fe}(\text{CO})_5$ -S based catalyst was observed.

#### Kinetic studies of $\text{Fe}(\text{CO})_5$ based catalysts<sup>9</sup>

Further investigation of the nature of  $\text{Fe}(\text{CO})_5$  based catalyst was carried out by kinetic treatment of coal liquefaction. A kinetic model used in our study is a combined parallel and consecutive reaction paths shown in Scheme II. Where first order rate constants were estimated by computer curve fitting methods. Typical results of curve fitting in the hydroliquefaction of Yallourn coal with  $\text{Fe}(\text{CO})_5$ -S catalyst system is shown in Figure 1. The first order rate constants summarized in Table III indicate that much larger values for  $k_1, k_4$ , and  $k_5$  in all the experiments shown here. Such tendency is more pronounced in the case of low rank coal (Yallourn). This indicates that direct depolymerization of this coal into asphaltene and oil fractions predominate over the consecutive path ways via preasphaltene intermediate. This seems to strongly reflect the chemical structure of low rank coal. Yallourn coal is thought to contain small amounts of condensed aromatic ring structure and to have large amounts of ether linkages, which would easily cleave thermally. Thus even at an early stage of the liquefaction smaller molecular weight fragment radicals would be formed. Most of them abstract hydrogen from molecular hydrogen activated on the catalyst surface to give lower molecular weight products (asphaltene and oil).

Increase in the amount of catalyst markedly increased all the rate constants. As shown in Fig. 1, yields of preasphaltene and asphaltene reached maximum values at reaction times 10 and 20 min. respectively, and gradually decreased. Accordingly the yield of oil fraction increased with an increase in the reaction time. Among the rate constants  $k_2$  and  $k_5$  increased by about factor of 10 and 3 respectively with a 2.5 fold increase in the  $\text{Fe}(\text{CO})_5$ . On the other hand  $k_1, k_4$ , and  $k_5$  increased by factors of about 3.

Effects of hydrogen partial pressure, reaction temperature, and coal rank are also discussed.

From these results the role of iron catalyst is ascribed to mainly activate molecular hydrogen and transfer hydrogen to coal fragment radicals in a non hydrogen donor solvent. In this stage fragment radicals tend to recombine, if the catalyst is not effective or the concentration is not sufficient. At the late stage of the liquefaction, condensed aromatic compounds in preasphaltene and asphaltene fractions are gradually hydrogenated to yield lighter oil fraction.

All these results clearly show superiority of the highly dispersed catalyst prepared from organo-transition metal complexes. Combined with recent results, it is concluded that the catalyst used for coal hydroliquefaction played key functions for the hydrogen transfer reaction from gas phase to coal fragment radicals.

#### References

1. Fine Particle Catalyst Testing US DOE Advanced Research Liquefaction
2. Suzuki, T.; Yamada, O.; Fujita, K.; Takegami, Y.; Watanabe, Y. *Chem. Lett.*, **1981**, 1467-1468; *Fuel*, **1984**, *63*, 1706-1709.
3. Weller, S.; Peripetz, M. G. *Ind. Eng. Chem.*, **1951**, *43*, 1243.
4. Cox, J. L.; Wilcox, W. A.; Roberts, G. L. *In Organic Chemistry of Coal*; Larsen, J. W. Ed.; ACS Symposium Series 77; American Chemical society; **1978**; pp 186-203
5. Suzuki, T.; Yamada, O.; Fujita, K.; Takegami, Y.; Watanabe, Y. *Ind. Eng. Chem. Process Des. Dev.*, **1985**, *24*, 832-836.
6. Suzuki, T.; Yamada, O.; Takahashi, Y.; Watanabe, Y. *Fuel Processing Tech.* **1985**, *10*, 33
7. Montano, P. A.; Granoff, B. *Fuel* **1980**, *59*, 214-216; Bommannar, A.; Montano, P. A. *Fuel*, **1982**, *61*, 1288-1290.
8. Suzuki, T.; Yamada, H.; Watanabe, Y. *Energy Fuels*, **1989**, *3*, 707-713.
9. Suzuki, T.; Ando, T.; Watanabe, Y. *Energy Fuels*, **1987**, *1*, 295-300.

Table 1 Hydroliquefaction of Illinois No.6 Coal Using Iron Pentacarbonyl<sup>a</sup>

run	catalyst <sup>b</sup>	H <sub>2</sub> MPa	Temp °C	Time min	Conv %	Gas %	Oil %	AS %	PA %	H <sub>2</sub> %
1	none	5.0	425	60	56.7	3.7	22.8	19.2	11.0	0.5
2	Fe(CO) <sub>5</sub>	5.0	425	60	92.9	6.3	33.1	39.0	14.5	2.2
3	none	5.0	460	20	54.9	4.2	31.5	15.8	7.6	0.8
4	Fe(CO) <sub>5</sub>	5.0	460	20	84.2	5.2	40.9	25.5	17.8	2.0
5	Fe(CO) <sub>5</sub>	5.0	460	40	83.9	6.7	47.3	23.3	13.3	2.4
6	none	7.9	460	20	69.7	6.4	37.2	20.4	12.1	1.4
7	Fe(CO) <sub>5</sub>	7.9	460	20	95.0	5.6	53.1	30.5	11.4	3.0
8	Fe(CO) <sub>5</sub> <sup>c</sup>	7.9	460	20	94.8	4.6	56.2	26.2	10.2	2.7
9	none	7.9	480	10	61.2	5.3	34.9	16.2	10.1	1.2
10	Fe <sub>2</sub> O <sub>3</sub>	7.9	480	10	83.7	6.3	43.4	25.4	14.9	2.2
11	Fe(CO) <sub>5</sub>	7.9	480	10	93.9	6.4	50.4	29.5	14.0	2.8

<sup>a</sup> Coal; 2.0 g, solvent, 1-methylnaphthalene; 4.0 mL. <sup>b</sup> Fe, 0.4 mmol (1.1 wt % coal).  
<sup>c</sup> Solvent; Decalin

Table 2 Hydroliquefaction of Australian coals using iron-sulfur catalysts<sup>a</sup>

Run	Catalyst	Fe mmol	S mmol	Conv.	Gas	Oil %	AS	PA	H <sub>2</sub>
Wandoan Coal									
1	none	0	0	48.6	7.8	22.3	12.6	5.9	0.2
2	Fe(CO) <sub>5</sub>	1	0	85.2	6.9	35.5	21.0	21.8	1.8
3	Fe(CO) <sub>5</sub> -S	1	1	94.4	9.5	48.6	24.8	11.5	2.8
4	Fe(CO) <sub>5</sub> -S	2	2	94.7	7.5	47.3	27.5	12.4	2.6
5	Fe <sub>2</sub> (CO) <sub>9</sub> -S	1	1	92.7	8.1	47.7	25.8	11.1	2.6
6	Fe <sub>3</sub> (CO) <sub>12</sub> -S	1	1	94.8	7.9	46.2	27.7	12.8	2.9
7	Fe(acac) <sub>3</sub> -S	1	1	81.6	12.0	23.7	25.2	20.7	2.4
8	Red mud-S	1	1	93.2	8.7	39.3	28.5	16.7	2.4
9	Fe <sub>2</sub> S <sub>2</sub> (CO) <sub>6</sub>	1	1	93.3	8.0	42.1	29.8	13.4	3.0
Yallourn Coal									
10	none	0	0	36.7	15.0	12.9	5.4	3.4	0.8
11	Fe(CO) <sub>5</sub>	1	0	69.7	15.2	25.3	14.4	14.8	1.6
12	Fe(CO) <sub>5</sub>	2	0	92.5	18.9	30.8	22.9	19.9	2.3
13	Fe(CO) <sub>5</sub> -S	1	0.5	91.5	18.8	34.6	17.0	21.1	2.2
14	Fe(CO) <sub>5</sub> -S	1	1	97.7	16.9	41.8	21.6	17.4	3.3
15	Fe(CO) <sub>5</sub> -S	1	2	96.0	20.2	36.8	19.3	19.7	2.9

<sup>a</sup> Coal; 2.0 g, 1-methylnaphthalene; 4.0 ml, H<sub>2</sub> pressure; 5.0 MPa, 425°C, 60 min.

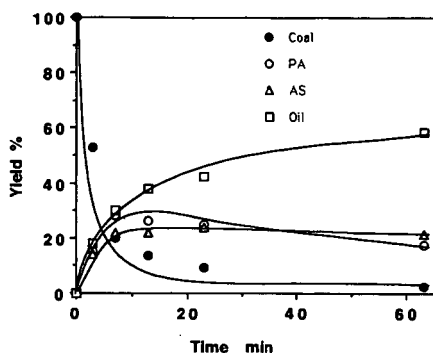
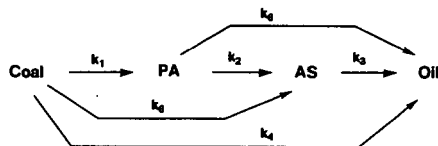


Figure 1 Observed and simulated results of kinetics in Yallourn coal hydroliquefaction  
425 °C, Fe(CO)<sub>5</sub>: 1.0 mmol, S: 1.0 mmol, PH<sub>2</sub>=5.0 MPa



Scheme II Kinetic model of liquefaction reaction

Table 3 Rate constants for hydroliquefaction of various coals with Fe(CO)<sub>5</sub> catalyst<sup>a</sup>

entry	Coal	catalyst mmol	PH <sub>2</sub> MPa	Conv. <sup>b</sup> %	rate constant, min <sup>-1</sup>					
					k1	k2	k3	k4	k5	k6
1	YL	0.40	5.0	83.5	0.0213	0.0007	0.0007	0.0366	0.0178	0.0018
2	YL	1.00	5.0	97.7	0.0740	0.0078	0.0110	0.0760	0.0550	0.0049
3	YL	0.40	7.9	89.4	0.0380	0.0070	0.0062	0.0590	0.0380	0.0037
4	YL <sup>c</sup>	0.40	5.0	87.8	0.0230	0.0024	0.0	0.0340	0.0160	0.0
5	WD <sup>c</sup>	0.40	5.0	87.4	0.0700	0.0120	0.0100	0.0300	0.0330	0.0080
6	MK <sup>c</sup>	0.40	5.0	96.8	0.1300	0.0050	0.0038	0.0100	0.0700	0.0033

a Coal 2.0 g, 1-methylnaphthalene 4.0 mL, Temperature 425 °C, b Conversion at 60 min  
c at 400 °C

Catalytic Hydroliquefaction of Coal Using  
Molybdenum and Iron-Promoted Catalysts

Larry L. Anderson, W.H. Yuen, J. Jaturapitpornsakul,  
Department of Chemical and Fuels Engineering  
D. Sommerfeld, and E. M. Eyring,  
Department of Chemistry  
University of Utah  
Salt Lake City, Utah 84112

Keywords: coal, hydroliquefaction, catalytic coal liquefaction.

**INTRODUCTION**

Coal has been liquefied to volatile liquid products by a variety of methods but the feasibility of this method of producing synthetic liquid fuels depends on conversion without extreme reaction conditions. To react coal at milder than those used in the German plants (high pressures and temperatures) requires the application of catalysts which permit reaction at reasonable rates and conversion levels. Iron has been used in many catalytic liquefaction processes because of its low cost and low environmental impact. In this study several iron catalysts and combinations tested on bituminous and subbituminous coals. The iron catalysts used were mostly ineffective at significantly increasing the fraction of coal converted to liquids. However, iron was found to migrate throughout the coal particles during the reaction holding the promise that an effective iron catalyst may still be a possibility.

Catalytic reactions were done without solvents or vehicle oils to avoid the complexity of product characterization and to simplify the procedure.

**COALS AND EXPERIMENTAL CONDITIONS**

Several coals from the Argonne Premium coal sample bank and the Penn State sample bank were used in the dry hydroliquefaction experiments. These included: Blind Canyon, Utah; Elkhorn, Illinois; Hiawatha, Utah; Pittsburgh, Pennsylvania; Wyodak, Wyoming; Illinois #6, Illinois; and Lewiston-Stockton, West Virginia coals. The proximate, ultimate, and maceral analyses have been given previously for these coals.<sup>1</sup> The experimental procedure consisted of taking the coal, either -100 mesh (Penn State - DECS-6) or -60 mesh (Argonne Samples) and impregnating the catalyst, if any, from aqueous solution onto the surface of the coal. The mixture was then dried for 4 hours at 60°C. When promoters were used with Mo catalysts the Mo was impregnated first, the mixture dried; the promoter was then added and the mixture dried again. The coal and any catalyst were placed in a tubing reactor, sealed, pressurized with hydrogen, and attached to a shaking mechanism. The reactor was then immersed into a sand bath heated to the reaction temperature. Reactions were conducted usually for one hour with shaking at 160 rpm. For some experiments the coals were first extracted with tetrahydrofuran (THF) or were demineralized with HCl and HF. Experiments were run with no catalyst or with one or more of the following: ammonium tetrathiomolybdate [(NH<sub>4</sub>)<sub>2</sub>MoS<sub>4</sub>], iron (III) chloride hexahydrate [FeCl<sub>3</sub>·6H<sub>2</sub>O], nickel (II) chloride hexahydrate [NiCl<sub>2</sub>·6H<sub>2</sub>O], nickel (II) nitrate [Ni(NO<sub>3</sub>)<sub>2</sub>], ammonium ferric sulfate [NH<sub>4</sub>Fe(SO<sub>4</sub>)<sub>2</sub>] (AFS), ferrocene [C<sub>10</sub>H<sub>10</sub>Fe], ferric citrate. After the reaction the reactor was taken out of the sand bath, quenched, and the gases vented for analysis. The liquids and solids were extracted with THF. Conversion was defined as:

$$\text{Conversion} = 100 - \frac{(\text{weight of maf THF-insolubles in product})}{\text{weight of maf coal charged}} \times 100$$

**RESULTS AND DISCUSSION**

Some preliminary experiments were done to determine the effects of different impregnation methods, reaction time, and hydrogen pressure on the liquefaction yields. Impregnation by incipient wetness (catalyst solution

just the entire coal surface) or ultrasonic treatment<sup>1</sup> (excess solution, with application of ultrasonic energy for two hours) gave essentially the same results. Liquefaction yields after 1 hour, 2 hours, and 3 hours were determined. Hydrogen pressures of 1000, 2000, and 3000 psi (at reaction temperature) were used.

Since similar results were obtained for all the coals tested most of the data reported here are for Blind Canyon, Utah coal. Some results for runs at 350, 400, and 425°C will be reported although other runs were done at higher temperatures. Above 400°C reactions gave significant gas conversion and corresponding reduced liquid yields.

Soxhlet extraction of Blind Canyon (BC) coal gave 19.9 per cent THF-soluble liquids. Hydroliquefaction without catalyst gave approximately 22 per cent liquids at 350° and 30 per cent at 400°. Several iron catalysts were tested for liquefaction effectiveness. Table 1 shows the liquid yields for Pittsburgh #8 coal at 350 and 450°. Molybdenum catalysts gave higher liquefaction yields than any other catalysts we tested in dry hydroliquefaction experiments. Figure 1 gives results for Mo (as ammonium tetrathiomolybdate) hydroliquefaction of BC coal at 400°C. The improvement of liquid yields from less than 30 per cent without catalyst to near 80 per cent with only 0.05 per cent Mo was dramatic but we also wanted to determine if further improvements could be obtained by using iron or nickel as promoters for the molybdenum catalyst.

The main results of testing iron and nickel as promoters are shown in figures 2 and 3. Both iron as iron chloride and nickel as nickel chloride were active as promoters even at low concentrations i.e. 0.01 per cent. The iron was slightly better than nickel at 350° while the reverse was true at 400°C (Figure 4).

To determine the effectiveness of our impregnation methods and to locate the catalyst materials after the reaction, we utilized electron probe microanalysis (EPMA)<sup>3</sup>. With this technique one can determine the dispersion of certain elements. To do this the insoluble product is embedded in a resin block using Petropoxy 154 and polished on a Syntron diamond paste polisher. Samples are sputter-coated with carbon to minimize charging in the electron microscope. Characteristic X-rays are collected for iron, nickel, molybdenum, sulfur and other elements with an energy dispersive spectrometer detector (CAMECA Model SX-50 detector, Courbevoix Cedex, France). Visual images of the samples are made from secondary electron and back-scattered electron images of the sample. X-ray data analysis is carried out with a Digimap program. Magnification of the samples is typically 2000 yielding a Digimap area of about 45 microns by 45 microns for each micrograph.

Figure 5 shows a coal particle in the center with sulfur accumulated around the particle (A). The Mo response in B is similar. In Figure 6A the visual image shows a coal particle while 6B shows that the dispersion of iron after reaction is uniform throughout the coal particle.

The products of the hydroliquefaction reaction were char, liquids (defined as THF-soluble), and gases. The gases were minor (2 per cent of the maf coal at 350°, 12 per cent at 400°, and 16 per cent at 425°C) products and were composed mostly of carbon dioxide and methane. As the temperature increased the fraction of the gases that were methane, ethane, and propane increased while that for carbon dioxide decreased. The liquid products were quite similar, with average molecular weights between 240 and 270. When the reaction time was increased to 3 hours the average molecular weight increased slightly to about 310. Table 2 gives compositional information on representative liquids produced from BC coal at 350°C and 400°C. <sup>13</sup>C nuclear magnetic resonance spectroscopy of the liquids produced in experiment MS-BC #28 showed that the aromaticity was 0.64, the aliphatic fraction was 0.32 and that the average molecular weight per cluster was 326. This was similar to results obtained for other liquid products.

#### SUMMARY AND CONCLUSIONS

High liquid yields can be obtained by dry hydroliquefaction when an active catalyst is applied, even at relatively mild conditions (2000 psi, hydrogen and 400°C, for one hour). Molybdenum sulfide was found to be the most effective for the conditions tested and was used in concentrations of 0.05 per cent or less (weight of Mo as per cent of maf coal). Iron and nickel were found to be active as promoters for liquefaction using Mo catalyst at 350° and 400°C. Increasing hydrogen pressure resulted in higher yields of liquid product.

#### ACKNOWLEDGEMENT

The authors would like to thank the U.S. Department of Energy through the Consortium for Fossil Liquefaction Science and the State of Utah who financially supported this research.

#### REFERENCES

1. Anderson, L.L. and J. Jaturapitpornsakul, Proc. Sixth Ann. Int. Pittsburgh Coal Conf. 1989, 1, 104-112.
2. Wann, J.P., 1987, M.S. Thesis University of Utah, Salt Lake City, Utah.
3. Sommerfeld, D.A., J. Jaturapitpornsakul, L.L. Anderson, and E.M. Eyring, 1992, Preprints Div. Fuel Chem., Am. Chem. Soc., 37, No. 2, 749-755.

TABLE 1. Hydroliquefaction of Pittsburgh #8 (HVB) coal using several iron catalysts.

Run No.	Catalyst	Temp. °C	% of maf coal	
			THF Insol.	THF Soluble (Liquefaction %)
FP-PT #5	- none -	450	65	14
FRC-PT #1	Ferrocene	450	53	28
FRC-PT #2	Ferrocene	350	67	33
FCT-PT #1	Ferric Citrate	450	42	33
FCT-PT #2	Ferric Citrate	350	62	38

Table 2. Composition of Liquid Products from the hydroliquefaction of Blind Canyon coal at 400°C and 350°C at 2000 psi hydrogen and 1 hour reaction time (except as noted otherwise).

Run #		C	H	N	S	O (diff)	H/C	O/C
<b>400°C</b>								
DECS - 6	(dmmf - mod. Parr)	81.72	6.22	1.56	0.40	10.10	0.91	0.093
MS-BC # 6	0.05% Mo	85.48	6.91	1.59	0.29	5.75	0.97	0.051
MS-BC # 7	0.03% Mo	85.36	6.91	1.49	0.32	5.92	0.97	0.052
MS-BC #28	0.03% Mo, 3 hour	86.31	7.34	1.47	0.16	4.73	1.02	0.041
MS-BC #10	0.01%Ni+0.03%Mo	85.42	7.01	1.51	-	5.76	0.98	0.051
MS-BC #12	1.00% Fe	85.57	7.18	1.72	-	5.34	1.01	0.047
MS-BC #18	0.20% Ni	84.93	6.97	1.55	-	6.36	0.98	0.056
<b>350°C</b>								
BC (Argonne)	(dmmf - mod. Parr)	81.32	5.81	1.59	0.40	10.88	0.86	0.100
MS-BCA #3	0.05% Mo	82.36	7.08	1.20	-	9.06	1.03	0.082
MS-BCA #7	1.00%Fe+0.05%Mo	79.69	6.66	1.17	-	12.19	1.00	0.115
MS-BCA #9	1.00%Ni	81.43	7.14	1.23	-	9.91	1.05	0.091

FIGURE 1.. Hydroliquefaction of Blind Canyon coal (DECS-6) at 400°C, 2000 psi hydrogen for 1 hour.

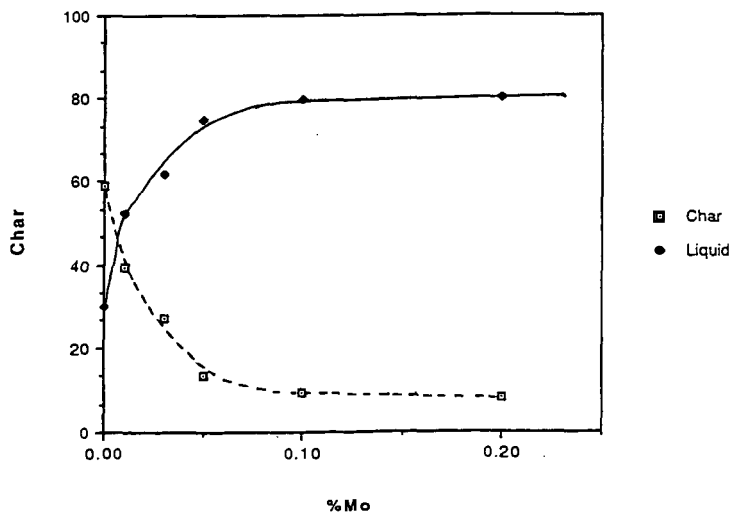


FIGURE 2. Hydroliquefaction of Blind Canyon coal (Argonne) at 2000 psi hydrogen for 1 hour at 350°.

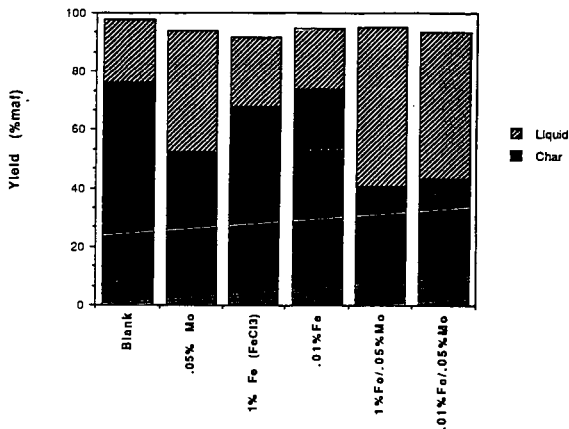
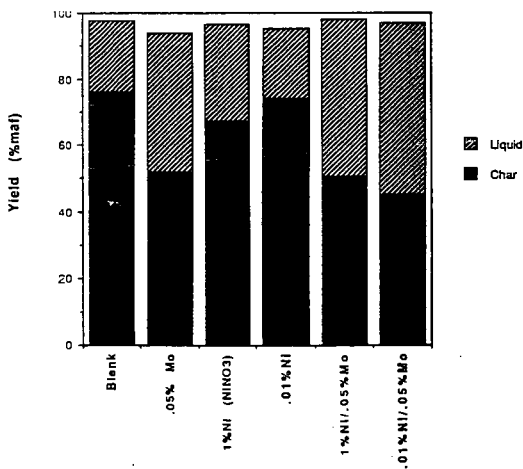


FIGURE 3. Hydroliquefaction of Blind Canyon coal (DECS-6) at 350°C for 1 hour with several different catalysts and combinations.



**FIGURE 4.** Hydroliquefaction of Blind Canyon coal at 400°C for 1 hour at 2000 psi hydrogen using iron or nickel as promoters for molybdenum catalyst (0.03% Mo).

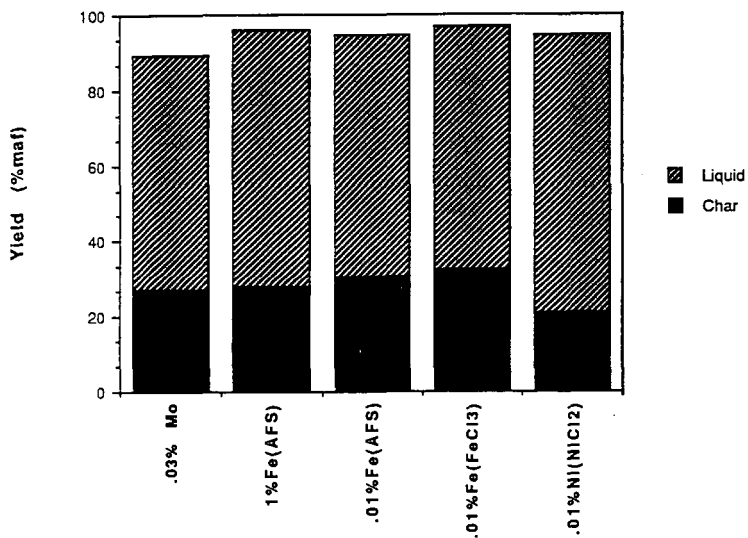


FIGURE 5. Electron Probe Microanalysis (EPMA) showing the dispersion of sulfur (A) and Molybdenum (B) for a Blind Canyon coal particle after impregnation with 1 per cent iron and 1 per cent molybdenum but before reaction.

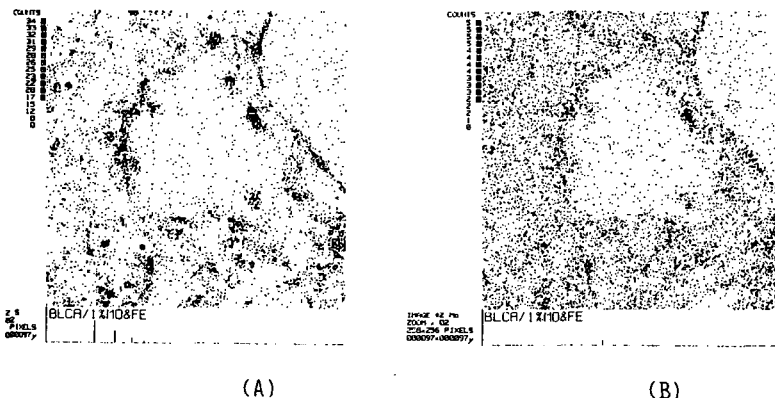
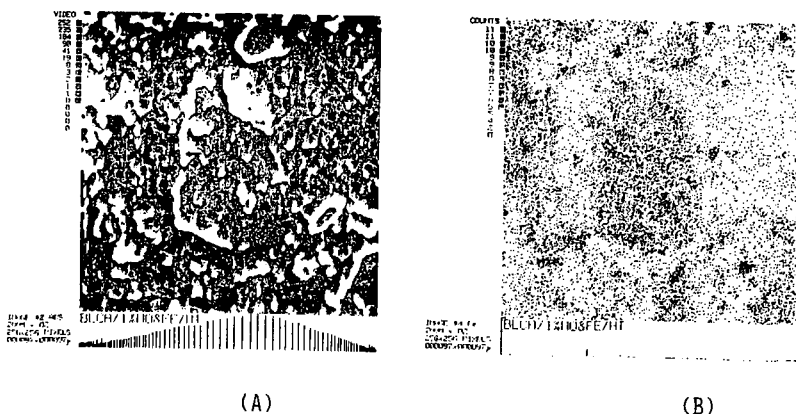


FIGURE 6. Electron Probe Microanalysis (EPMA) showing a Blind Canyon coal particle (center) after hydroliquefaction reaction. The catalyst used was 1 per cent iron and 1 per cent molybdenum. (A) shows a visual image of the coal particle and (B) shows the evenly dispersed iron through the coal particle.



## USE OF CATION-EXCHANGE TO PRODUCE HIGHLY DISPERSED IRON CATALYSTS IN LOW RANK COALS

M. Mehdi Taghiei, F. E. Huggins, B. Ganguly, and G. P. Huffman  
IMMR/CFFLS, University of Kentucky, Lexington, KY, 40506.

### Abstract

A significant enhancement of both liquefaction yields and desirable products from two lignites has been achieved by incorporating iron in the lignites by an ion-exchange process. At 5-8% iron content, total conversions approached 88% and oil yields were about 45% compared to 62% total conversion and 33% oil yield for the raw coal. The effect of catalyst loading on cation-exchanged lignites was studied to determine the concentration that results in the optimum oil yield.  $^{57}\text{Fe}$  Mössbauer and XAFS spectroscopies were used to characterize the catalyst structure and size distribution in the iron cation-exchanged lignites before and after liquefaction. The results indicate that the added iron is initially present in bimodal form, with most present as highly dispersed goethite ( $\alpha\text{-FeOOH}$ ) particles, 50-100Å in diameter, but with a significant fraction (about 30%) of the iron in particles less than 30Å in diameter, which may represent molecularly dispersed ferric ions at the ion-exchange (carboxyl) sites. With sufficient sulfur present in the system, the iron is rapidly transformed to pyrrhotite ( $\text{Fe}_{1-x}\text{S}$ ) during liquefaction.

### Introduction

A number of studies<sup>1-3</sup> have been conducted on the activity of various iron-based catalysts during liquefaction of coals of different rank. Recent research<sup>4</sup> has shown that sulfated iron catalysts can significantly enhance the conversion yield of high-rank coals. However, for lower rank coals, the improvement in conversion yield through the addition of similar sulfated catalysts has not yet been achieved. The oxygen contents of low-rank coals such as lignites are significantly higher than those of high-rank coals, and as a result, oil yields from liquefaction of low-rank coals tend to be low due to  $\text{CO}_2$  formation. A considerable portion of this oxygen derives from carboxyl groups and other oxygen functional groups. In low-rank coals, most of the exchangeable cations are associated with carboxyl groups, and a number of studies<sup>5,6</sup> have shown that the behavior of lignites in coal conversion processes is greatly affected by the amount and type of exchangeable cations present.

The results of this study indicate that iron ion-exchanged into the low-rank coals constitutes a catalyst in a state of dispersion ranging from molecular ions to particles a few nanometers in diameter. Superparamagnetic modeling of Mössbauer spectra<sup>7</sup> indicates that the iron particle size in a high-iron loaded lignite has a bimodal character, with the majority of the particle sizes ranging from 50 to 115Å in goethite form, but with a significant fraction (about 30%) less than 30Å, which may derive from ferric cations in ion-exchange sites bound to the oxygen anions of carboxyl groups. The direct coal liquefaction (DCL) total conversion and oil yields of the iron ion-exchanged Beulah and Hugel lignites used in this work were enhanced significantly compared to the raw lignites.

## Experimental

The two lignites used in this study are Beulah (obtained from Dept. of Energy Coal Sample, DECS-11) and Hagel (obtained from Pen. State Office of Coal, PSOC-1482) from the Fort Union region in North Dakota. The original iron contents of these lignites are less than 0.5 percent. The ion-exchange experiments were carried out in a 10 liter fermenter using a freshly made 0.05M aqueous solution of ferric acetate at a controlled pH of about 2.8 and a constant temperature of 60°C. The iron contents of the Beulah and Hagel lignites after the ion-exchange process were 7.8% and 5.33%, respectively. The efficiency of lower loadings (~1 wt%) of iron in the ion-exchanged lignites during liquefaction was also investigated.

### Liquefaction Experiments:

Two sets of coal liquefaction experiments were conducted. The first set of experiments was carried out with tubing bombs in a fluidized sand bath. This set of experiments was designed to investigate the effect of iron catalysts on the total yield and product distribution in the liquefaction process. The tubing reactor was first charged with a slurry mixture of lignite and tetralin in a 1:2 ratio in the presence of dimethyl disulfide (DMDS) as a sulfur donor, and pressurized to 800 psi (cold) with hydrogen. Control liquefaction experiments, using slurry mixtures of the same lignite samples with a 30Å iron oxide and with no catalyst, were run under the same conditions to compare the catalytic effects of an ultrafine particle iron oxide with those obtained for the ion-exchange catalyst. The products were separated into THF insoluble organic materials (IOM), THF soluble, toluene insoluble (preasphaltene), toluene soluble, pentane insoluble (asphaltene), and pentane soluble (oil and gas) fractions. The soluble product percentage yields were calculated on a dry, ash-free (daf) basis as follows:

$$\text{Percentage soluble products} = \frac{\text{total soluble products}}{\text{daf lignite}} \times 100$$

Pentane solubles were determined by subtracting the sum of asphaltenes, preasphaltenes and the IOM residue from the weight of the starting lignite. The results were reproducible within  $\pm 2\%$ .

The second set of experiments was designed to generate larger samples for the detailed characterization of the chemical structure and reactions of the added iron. The apparatus used to prepare the samples for these experiments was an one liter autoclave. This autoclave was connected at the top to a vessel for holding the sample prior to heating. At the bottom, four nitrogen-purged sampling lines were attached to the outlet valve of the autoclave to collect the liquefaction products directly from the autoclave without exposure to air. Liquefaction experiments in the autoclave were performed at 385°C and 400°C under 1500 psi of hydrogen pressure (cold) in the presence of excess tetralin (tetralin:coal 3:1) and dimethyl disulfide (DMDS) as a sulfur donating species.

### Mössbauer and XAFS Spectroscopies:

Mössbauer spectra for the as-received, demineralized, and ion-exchanged lignite samples were obtained using a conventional constant-acceleration-type Mössbauer spectrometer<sup>8</sup>. The samples were run at several temperatures to determine the size distribution. Calculation of the particle size distribution is described in detail elsewhere<sup>7</sup>. XAFS measurements were performed at beam line X-19A at the National Synchrotron Light Source in Brookhaven National Laboratory. Iron K-edge XAFS spectra of the samples were obtained in transmission mode using a Si(111) double crystal monochromator.

### Results and Discussion

The effect of iron concentration on liquefaction yields of Beulah and Hagel coal is shown in Figure 1. It can be seen that the asphaltene and oil conversion yields increased significantly for both ion-exchanged lignites compared to the raw coals. The preasphaltene yields, however, tend to decrease as a result of catalyst addition to the lignite. We have also compared the results obtained using a physically added 30Å iron oxyhydroxide catalyst to those obtained using cation-exchanged iron at approximately the same concentrations. The 30Å iron oxyhydroxide catalyst was provided by Mach I Inc., and its interesting structural properties are discussed in several forthcoming publications<sup>9,10</sup>. It is evident from Figure 1 that the ion-exchanged iron is a more active catalyst than the 30Å iron oxide.

Mössbauer and XAFS spectroscopies were used to characterize the structure of the cation-exchanged iron both before and after DCL. The characterization of iron-based DCL catalysts by Mössbauer and XAFS spectroscopies has been discussed in detail elsewhere<sup>11</sup>. The Mössbauer spectra of the Beulah and Hagel lignites containing cation-exchanged iron are shown in Figures 2 and 3, respectively. The spectra are fit with one or several magnetic components and quadrupole doublets (peak positions denoted by bar diagrams), and a superparamagnetic relaxation component (dashed curve). As discussed by Ganguly et al.<sup>7</sup>, at a given temperature, particles with diameter less than some critical value will give rise to a quadrupole doublet, particles with a diameter greater than some larger critical value will exhibit a six-peak magnetic hyperfine spectrum, and particles with diameters between these two values will give rise to superparamagnetic spectra. Approximate size distributions can be determined by measuring the percentages of these three components as a function of temperature and the size distribution determined in this manner for the cation-exchanged Hagel lignite with 5.33% Fe is shown in Figure 4. It is seen that the size distribution is bimodal, with approximately 70% of the particles in the 50-100Å size range, and 30% having diameters less than 30Å. Much of the iron in the latter size category may in fact be ferric iron that is molecularly dispersed and bonded to oxygen anions of the carboxyl groups in the lignite, whereas, the larger particles result from hydrolysis of either iron acetate or ion-exchanged iron to form goethite. The low-iron cation-exchanged coals exhibit similar Mössbauer spectra, but a detailed study of the temperature dependence of the superparamagnetic relaxation spectra has not yet been completed. Nevertheless, it is evident that most of the iron in these samples is contained in iron oxyhydroxide particles less than 100Å in diameter, and a significant percentage of the iron is present in the less than 30Å diameter size category.

Both the x-ray absorption near edge structure (XANES) and the radial structure function (RSF) derived from the iron K-edge XAFS spectra of the iron loaded lignites exhibit significant size related effects. Typical results are shown in Figure 5. The XANES of the Hagel lignite sample is compared to that of bulk goethite in Figure 5a, while the corresponding RSF are compared in Figure 5b. It is seen that the XANES of the iron loaded Hagel lignite sample and goethite are quite similar, with the exception of an increase in the intensity of the small pre-edge peak. This occurs because the surface iron atoms of ultrafine ferric oxide particles are no longer in centrosymmetric octahedral coordination, but in reduced coordination number sites, which cause the intensity of the pre-edge ( $1s \rightarrow 3d$ ) transition to increase. The RSF of the Hagel lignite sample and goethite exhibit similar peaks, but the peaks corresponding to the iron shell are decreased in amplitude for the iron in the lignite, consistent with a small particle size<sup>11</sup>.

Further studies are in progress (i) to determine the structure and size distribution of the cation-exchanged iron as a function of concentration, both before and after liquefaction, (ii) to investigate the use of the cation-exchange process for preparation of small particle metal oxides containing Mo, Co, Al, Ni, etc., and (iii) to evaluate the potential of these ion-exchange catalysts for lignite liquefaction.

#### Acknowledgement

This research was supported by the U.S. Department of Energy through DoE contract No. DE-FC22-90-PC90029 as part of the research program of the Consortium for Fossil Fuel Liquefaction Science.

#### References:

- 1- Herrick, D. E.; Tierney, J. W.; Wender, I.; Huffman, G. P.; Huggins, F. E. *Energy & Fuels* **1991**, *4*, 231.
- 2- Tanabe, K.; Yamaguchi, T.; Hattori, H.; Sanada, Y.; Yokoyama, S. *Fuel Proc. Technol.* **1984**, *8*, 117.
- 3- Cook, P.S.; Cashion, J. D. *Fuel* **1987**, *66*, 661.
- 4- Pradhan, V. R.; Tierney, J. W.; Wender, I.; Huffman, G. P. *Energy & Fuels* **1991**, *5*, 497.
- 5- Matsumoto, S.; Walker Jr., P. L. *Carbon* **1986**, *25*, 277.
- 6- Linares-Solano, A.; Hippo, E. J.; Walker Jr., P. L. *Fuel* **1986**, *65*, 776.
- 7- Ganguly, B.; Huggins, F. E.; Rao, K. R. P. M.; Huffman, G. P. *J. Catalysis*, **submitted**.
- 8- Huffman, G. P. *Chemtech.* **1980**, *10*, 504.
- 9- Ganguly, B.; Huggins, F. E.; Feng, Z.; Huffman, G. P. *Phys. Rev.*, **submitted**.
- 10- Zhao, J.; Huggins, F. E.; Feng, Z.; Lu, F.; Shah, N.; Huffman, G. P., *J. Catalysis*, **submitted**.
- 11- Huffman, G. P.; Ganguly, B.; Zhao, J.; Rao, K. R. P. M.; Shah, N.; Feng, Z.; Huggins, F. E.; Taghiei, M. M.; Lu, F.; Wender, I.; Pradhan, V. R.; Tierney, J. W.; Seehra, M. S.; Ibrahim, M. M.; Shabtai, J. S.; Eyring, E. M., *Energy & Fuels* **1992**, in press.

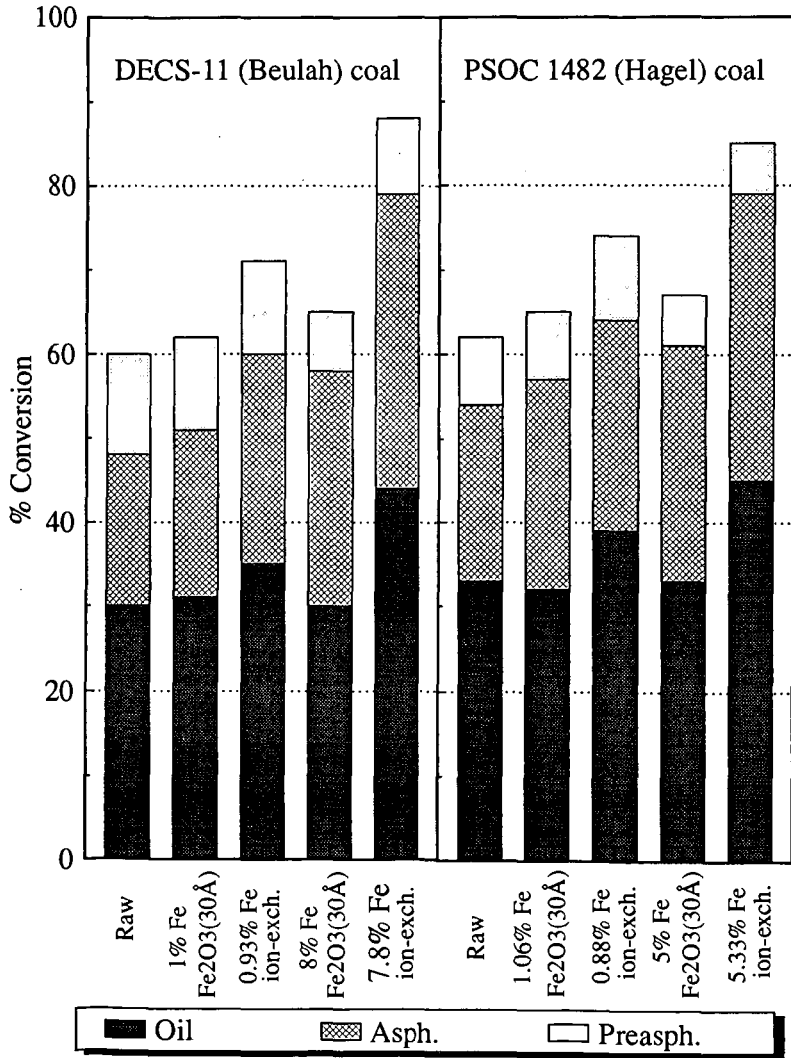


Figure 1. Comparison of liquefaction product yield for Beulah and Hagel lignites

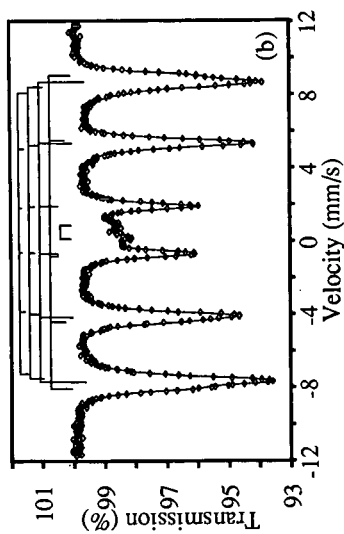
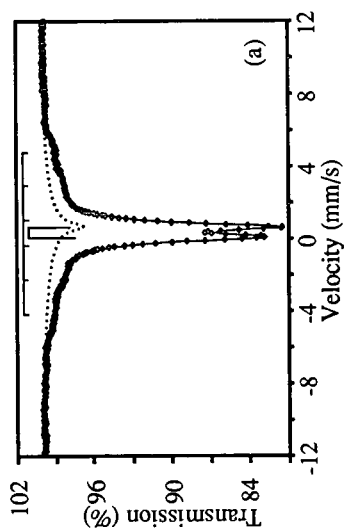


Figure 2. Mössbauer spectra of ion-exchanged Beulah lignite with 7.8% iron, (a) at room temperature, (b) at 12K.

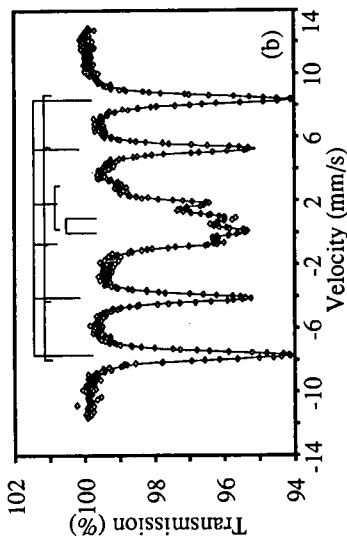
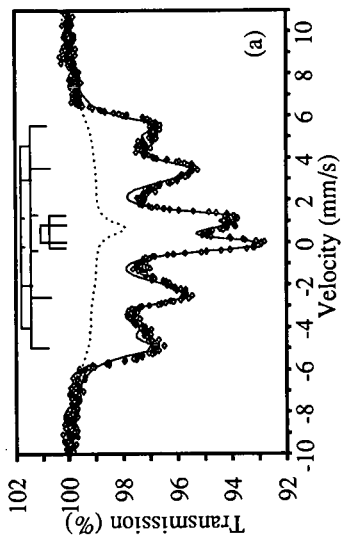


Figure 3. Mössbauer spectra of ion-exchanged Hagel lignite with 5.33% iron, (a) at room temperature, (b) at 12K.

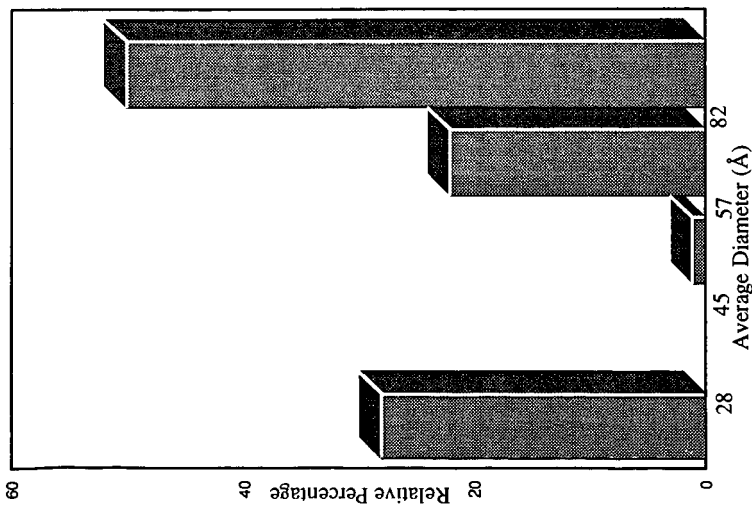


Figure 4. Size distribution of iron species in Hagel lignite containing 5.33 wt% iron.

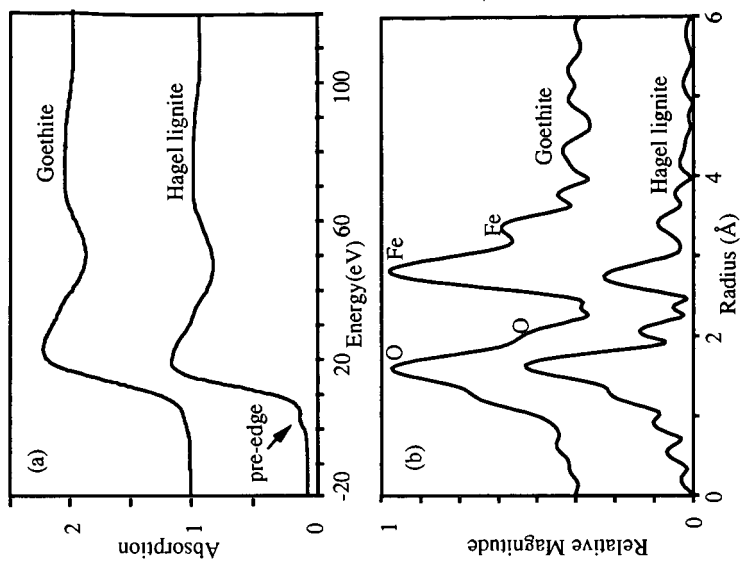


Figure 5. Comparison of iron K-edge (a) XANES, and (b) RSF of bulk goethite and iron loaded Hagel lignite.

## OPTIONS FOR IRON-CATALYZED LIQUEFACTION OF LOW-RANK COALS

Edwin S. Olson, Candace M. Buchwitz, and Mary Yagelowich  
Universal Fuel Development Associates, Inc.  
Grand Forks, ND 58201

Ramesh K. Sharma  
University of North Dakota Energy and Environmental Research Center  
Grand Forks, North Dakota 58202

Key Words: Coal liquefaction, iron catalysts, ion exchange

### ABSTRACT

Liquefaction of low-rank coals is impeded by the mineral content of the coal. Inorganic constituents such as calcium are a major factor in deposits in the process equipment, but they also disrupt the functioning of the catalyst by blocking pores, deactivating sites, or causing sintering or aggregation. A series of liquefaction tests was performed that compared ion-exchanged Wyodak coal with the as-received coal. The catalysts were impregnated iron or iron dispersed on acidic supports. Highest conversions to heptane solubles were obtained with iron impregnated (PETC method) into acid-washed Wyodak. Alternatively, solubilization of as-received Wyodak with CO/water (uncatalyzed) gave an ash-free intermediate that produced high conversions to heptane-soluble product in the subsequent catalyzed liquefaction reaction.

### INTRODUCTION

The high calcium content of low-rank coals has been recognized for some time as a potential problem in processing these coals to useful products. Operational difficulties were experienced at the Wilsonville Advanced Coal Liquefaction Research and Development Facility during the runs with Black Thunder (Wyoming) subbituminous coal due to substantial solids deposition (1). These deposits contained large amounts of calcium carbonate. In batch and continuous unit tests conducted at PETC (2), dispersed iron catalysts prepared by the PETC method exhibited poorer activities with subbituminous coals than previously obtained with bituminous coals. Swanson (3) recently reported that deposits of calcium coated the dispersed catalyst particles during tests with Black Thunder coal. Joseph and Forrai (4) examined the adverse effects of exchangeable cations (Na, K, Ca) on liquefaction of low-rank coals by ion-exchanging additional ions into the coals. The evidence cited in these reports implies that calcium deposits can rapidly deactivate the catalyst by blocking pores and active sites in the fine particles or could cause the particles to aggregate. Loss of catalytic activity for the activation of hydrogen then leads to condensation and retrograde reactions that form carbonaceous deposits and low oil yields.

Replacement of the alkaline earth cations with hydrogen ions is a possible solution. However, previous studies at EERC (5) demonstrated that noncatalytic thermal liquefaction of acid-washed lignite gave lower

conversions than the as-received coals. The lower yields were attributed to condensation reactions catalyzed by the highly acidic clays generated during the exchange process. Recently the conversions of coals washed with methanolic HCl were examined (6). This pretreatment significantly increased the conversion to THF-solubles in noncatalytic reactions. The significant increase in conversion to oils for ammonium-exchanged lignite (4) also demonstrates the potential for metal cation removal but may not be feasible for catalytic processing because of release of the ammonia. The behavior of acid-exchanged and other demineralized low-rank coal materials in liquefaction with various types of dispersed catalysts requires extensive investigation and elucidation.

This paper reports our investigations on the catalytic liquefaction of low-rank coal that was pretreated by ion exchange with aqueous acid and by thermal solubilization to a mineral-free product. A series of tests with ion-exchanged Wyodak subbituminous coal (IEW) was conducted to determine the effectiveness of various dispersed iron catalysts without the complications of the exchangeable cationic components. A second objective was to examine an alternative liquefaction scheme that produces mineral-free low-severity intermediate in a noncatalytic thermal pretreatment stage, that is subsequently liquefied with various dispersed iron catalysts in hydrogen.

## EXPERIMENTAL

### Preparation of Ion-Exchanged Coals

Acid-washed Wyodak (IEW) coal was prepared by stirring 7 g of ARW in 100 ml 1N nitric acid for one hour at ambient temperature. The acid-treated coal was separated by centrifugation and washing with water.

### Coal Liquefaction

As-received Wyodak-Clovis Point (ARW) and IEW coals were pretreated using several different techniques prior to liquefaction. The PETC-method (7) was used for both ARW and IEW. Procedures reported by Ziolo and coworkers (9) were modified to prepare  $Fe_2O_3$  dispersed on the coals. A slurry consisting of 7.0 g of ARW coal or product coal obtained from pretreatment of 7.0 g ARW, 10 wt% of catalyst (if required), 0.1 g of elemental sulfur, and 14 g of tetralin (solvent) were placed in a 70-ml Parr reactor. The reactor was evacuated and charged with 1000 psi (initial) of hydrogen gas. The reactor was heated to 425°C in a rocking autoclave (initial heatup time = 15 minutes) and left at this temperature for 60 minutes. At the end of the reaction, the reactor was cooled to room temperature, and the gases were removed. The product slurry was extracted with tetrahydrofuran (THF). The THF-insoluble product was dried under vacuum and weighed. A 4 ml aliquot of the THF-soluble was mixed with one ml solution of internal standard (a mixture of 2,2,4-trimethylpentane and n-octadecane in dichloromethane) and analyzed by GC. The remaining THF-solubles were evaporated to remove THF, and the dark oil was added to a large excess of heptane and stirred. The heptane-insoluble product was separated by centrifugation, washed with heptane, dried in vacuo at 50°C and weighed. The percent conversion was calculated on the basis of the coal (maf) that did not appear in the THF-insoluble fraction. Heptane-soluble yields were obtained by difference (100% - %THF-insolubles - %heptane-insolubles).

## RESULTS AND DISCUSSION

Wyodak subbituminous coal was treated with nitric acid to remove by ion-exchange the metal cations bound to the coal matrix. Initial thermal (noncatalytic) tests were carried out to provide a basis for comparison with the catalytic tests. These tests required heating the coal/tetralin slurry in a rocking microtube reactor for 1 hr at 425 °C with 1000 psi (cold pressure) of hydrogen. Conversion and yield data are given in table 1. The thermal reaction of as-received Wyodak coal (ARW) gave a very high conversion (89%) to THF-soluble products. These data are consistent with earlier results for low-rank coals in thermal (noncatalytic) reactions in hydrogen or carbon monoxide (5). Carbon monoxide works as well as hydrogen in the noncatalytic reactions. The conversion for the (IEW) test (86%) was lower than that for the ARW coal on a maf basis. The lower conversion is also consistent with earlier work with low-rank coals that demonstrated that acid-washing lowers the conversion. This effect was attributed to the generation of highly acidic sites on clay minerals in the coal that catalyze carbonium ion reactions that often result in condensations to higher molecular weight and less soluble products. The amounts of heptane-soluble products formed in the two thermal reactions were similar (48%). The heptane-soluble yields are obtained by difference (100% - %THF-I - %heptane-I) and include major amounts of the gaseous products (CO<sub>2</sub>, H<sub>2</sub>O, etc.) in addition to the heptane-soluble oils.

The ion-exchanged coal was then reacted in catalytic liquefaction tests with several dispersed iron catalysts, and these results were compared with similar catalytic reactions carried out with the ARW in order to determine the effect of the inorganic cations on the catalytic activity. The PETC method (7) for impregnating iron as the iron hydroxyoxide on the coal surface was utilized for preparing the dispersed iron catalyst for liquefaction of both ARW and IEW coals. Addition of iron hydroxyoxide to ARW via the PETC method resulted in a conversion to THF solubles similar to those found in the thermal reactions (88%), but the yield of heptane-solubles was substantially higher (52%). Thus the catalytic effect is demonstrated principally in the oil yield. Generation of iron hydroxyoxide on the IEW significantly improved the conversion THF-solubles as well as heptane-solubles (56%). The significant increase in yields for the IEW can be attributed to less deactivation of the catalyst by the inorganic matter.

Alternative methods for generating dispersed iron on the coal surface were also examined. Previous work at Universal Fuel Development Associates, Inc. (8) demonstrated that clay-supported iron catalysts with high concentrations of maghemite fine particles were much more catalytically active than those with hematite. Ziolo and coworkers (9) reported that maghemite fine particles can be generated on ion-exchange resins by reducing ferric ions with hydrazine and sodium hydroxide or by treating ferrous ions with hydrogen peroxide and ammonium hydroxide. Since sodium hydroxide dissolves humic acids from the low-rank coal, ammonium hydroxide was utilized instead of sodium hydroxide to prepare the maghemite fine particles on the coal surface. Treatment of the coal with ferrous chloride/ammonium hydroxide to maximize maghemite formation did not improve conversions for IEW, 92% to THF-solubles, 47% heptane-solubles. Likewise treatment with ferric nitrate/hydrazine did not improve conversions, 91% THF-solubles, 46% heptane-solubles. A reaction carried out with this same pretreated coal but

Table 1  
Catalytic Liquefaction with Dispersed Iron

Reaction Temp. = 425°C, Reaction Time = 1 hr, H <sub>2</sub> = 1000 Psi (cold) Wyodak (AR) coal = 7.0 g., Coal/Tetralin = 0.5, Sulfur = 0.15 g.				
Pretreatment	Conv. (%)	THF-I (%)	Heptane-I (%)	Heptane-S (%)
None*	89	11	41	48
Acid washed*	86	13	40	47
Fe(NO <sub>3</sub> ) <sub>3</sub> + NH <sub>4</sub> OH <sup>a</sup>	88	12	36	52
1 Acid washed 2 Fe(NO <sub>3</sub> ) <sub>3</sub> + NH <sub>4</sub> OH <sup>a</sup>	91	9	36	56
1 Acid washed* 2 Fe(NO <sub>3</sub> ) <sub>3</sub> + N <sub>2</sub> H <sub>4</sub> + NH <sub>4</sub> OH <sup>b</sup>	88	12	43	45
1 Acid washed 2 Fe(NO <sub>3</sub> ) <sub>3</sub> + N <sub>2</sub> H <sub>4</sub> + NH <sub>4</sub> OH <sup>b</sup>	91	9	45	46
1 Acid washed 2 FeCl <sub>2</sub> + NH <sub>4</sub> OH + H <sub>2</sub> O <sub>2</sub> <sup>b</sup>	92	8	45	47

\* = No sulfur was added to the reaction mixture.

a = PETC method.

b = Modified Ziolo method.

without addition of sulfur gave a similar conversion, indicating that the iron dispersed by this method is inherently inactive.

Previous work in this project was concerned with the preparation of fine iron sulfide particles supported on an acidic clay, and a preliminary report of mixed iron/alumina-pillared montmorillonite catalysis was presented (8). Catalytic liquefaction reactions of ARW and IEW were performed in tetralin using conditions similar to those above. Reactions were carried out using 10 wt% of the clay catalysts (sulfided in situ using small amount of elemental sulfur) at 425°C for one hour in 1000 psi of initial hydrogen pressure. The reaction conditions and yields data are given in table 1.

With the most active of the mixed iron/alumina-pillared clay catalysts in the presence of sulfur, the conversion of the ARW was 91% to THF-solubles with 53% heptane solubles. In the absence of sulfur required for sulfidation of the oxyiron catalyst, the conversion was substantially less, 87% to THF-solubles, with only 33% heptane-solubles. This large reduction in oil yield is attributed to the presence of the highly acidic clay and absence of any good hydrogen activation capability. The reaction of IEW coal with the active sulfided clay catalyst gave a significantly higher conversion to THF solubles, and excellent conversion to heptane-solubles (54%).

Although significant improvements in oil yields were obtained as a result of pretreating the Wyodak to remove metal cations, the economics of an ion-exchange process and subsequent disposal of the acidic waste water may not compensate for the increase in conversion and operability. An alternative liquefaction process has been utilized for many years at the Energy and Environmental Research Laboratories. This processing involves a noncatalytic thermal pretreatment under carbon monoxide atmosphere to break down the cross-links in the coal to give a high molecular weight THF-soluble intermediate in 95% yield. Mineral matter is conveniently removed from the coal solution. This cation-free low-severity intermediate is then used in catalytic liquefaction tests with hydrogen.

Several reactions of a mineral-free low-severity intermediate from Wyodak coal (LSW) were carried out with dispersed iron catalysts. A THF-soluble intermediate was obtained by thermal liquefaction in CO and was separated from heptane-soluble products and solvent(tetralin)-derived materials by solvent (heptane) precipitation to give the high molecular weight LSW intermediate for these tests. The LSW is a low-density solid at ambient temperature, but melts easily. A thermal (noncatalytic) reaction of the LSW in tetralin at 425 °C for 1 hr in 1000 psi hydrogen gave 15% conversion to heptane-solubles (Table 3). The conversions obtained for the LSW substrate cannot be directly compared with the coal conversions above, because the substrates are quite different. The 15% value for the LSW substrate represents a conversion of preasphaltenes and asphaltenes to heptane-soluble oils, whereas the 48 to 54% yields of heptane-solubles given above for coal substrates include both the more easily cleaved oil products as well as the gaseous products of liquefaction, such as significant amounts of carbon dioxide and water.

The liquefaction reaction of the LSW in tetralin with the dispersed iron/alumina-pillared clay catalyst (in situ sulfided) gave 30% conversion to heptane-solubles under the same conditions. The two-fold increase in conversion to oils for catalytic versus thermal reactions with the LSW substrate thus compares favorably with the increase of 6% (48 to 54%) found in the experiments with ion-exchanged coal described above.

The LSW intermediate was also subjected to the PETC iron dispersion treatment by stirring the low-density solid LSW with ferric nitrate solution and adding ammonium hydroxide to generate the surface-bound iron hydroxyoxide. The conversion of this material under conditions identical to those above with in situ sulfidation gave 15% heptane-solubles, the same as the thermal reaction. It is not known yet whether the iron sulfide that forms in the reaction with LSW is able to activate hydrogen, or whether some acidic component is required at this stage of liquefaction. This result may have very important implications for selecting conditions and coals for application of the PETC method to low-rank coals.

A variation of the PETC method was attempted to generate the dispersed iron catalyst on the LSW. Ethanol was used to obtain a colloidal dispersion of the LSW, which was then mixed with the ferric nitrate solution in ethanol and the ammonium hydroxide. After removal of the ethanol, the liquefaction was carried out in tetralin under conditions similar to those used above. When the dispersed iron obtained by this method was utilized, a 28% yield of heptane-soluble oils was obtained. It is now obvious that there are critical interactions between the iron and the coal surface that need to be

further elucidated and evaluated for designing a viable coal liquefaction method.

#### CONCLUSIONS

In coal liquefaction reactions that utilize dispersed iron catalysts, the catalytic activity was significantly improved by ion-exchange of cations present in the low-rank coals by aqueous acid-washing. Higher conversions to heptane-solubles were obtained with ion-exchanged Wyodak when dispersed iron catalyst was prepared by the PETC method. The ion-exchange pretreatment also improved the activity of the dispersed iron/alumina-pillared montmorillonite catalyst. A thermal pretreatment was also used to eliminate mineral matter, and the iron/alumina-pillared clay and one of the dispersed iron catalyst preparations were catalytically active.

#### 4.0 REFERENCES

1. Gollakota, S.V.; Vimalchand, P.; Davies, O.L.; Lee, J.M.; Corser, M.C.; Cantrell, Proceedings: Liquefaction Contractors' Review Meeting, U.S. Department of Energy Pittsburgh Energy Technology Center: Pittsburgh, 1991, pp 504-531.
2. Cugini, A.V.; Kratsman, D.; Hickey, R.F.; Lett, R.G., Abstracts: Liquefaction Contractors' Review Meeting, U.S. Department of Energy Pittsburgh Energy Technology Center: Pittsburgh, 1992, p 13.
3. Swanson, A.J.; Abstracts: Liquefaction Contractors' Review Meeting, U.S. Department of Energy Pittsburgh Energy Technology Center: Pittsburgh, 1992, p 8.
4. Joseph, J.T.; Forrai, T.R. Fuel 1992, 71, 75.
5. Olson, E.S.; Sharma, R.K. "Quarterly Technical Progress Report for the period July through September 1988", University of North Dakota Energy and Mineral Research Center: Grand Forks, ND, 1989.
6. Shams, K.; Miller, R.L.; Baldwin, R.M. Preprints: ACS Division of Fuel Chemistry, 1992, 37 (2), 1017-1024.
7. Cugini, A.V.; Utz, B.R.; Krastman, D.; Hickey, R.F.; Balsone, V. Preprints, ACS Div. of Fuel Chem. 1991, 36 (1), 91-102.
8. Olson, E.S.; Yaegelowich, M.L.; Sharma, R.K., Preprints: ACS Division of Fuel Chemistry, 1992, 37 (1), 262-267.
9. Ziolo, R.F.; Giannelis, E.P.; Weinstein, B.A.; O'Horo, M.P.; Ganguly, B.N.; Mehrotra, V.; Russell, M.W.; Huffman, D.R., Science 1992, 257, 219-222.

Table 2  
Catalytic Liquefaction with Iron/Alumina Pillared Clay

Reaction Temp. = 425°C, Reaction Time = 1 hr, H <sub>2</sub> = 1000 psi (cold) Coal/tetralin = 0.5, Catalysts = 10 wt%						
Coal (g)	Catalyst (wt. %)	Sulfur (g)	Conv. (g)	THF-I	Heptane-I	Heptane-S
Wyodak (AR) (7.0)	None	None	89	11	41	48
Wyodak (AR) (7.0)	APC-Fe <sub>3</sub> (10)	None	87	13	54	33
Wyodak (AR) (7.0)	APC-Fe <sub>3</sub> (10)	0.10	91	9	38	53
Wyodak (IEW) (5.34)	APC-Fe <sub>3</sub> (10)	0.10	95	5	41	54

AR = as received Wyodak  
IEW = 7.0 g AR coal was acid washed and dried

Table 3  
Catalytic Liquefaction of LSW Intermediate

Reaction Temp. = 425°C, Reaction Time = 1 hr, H <sub>2</sub> = 1000 psi (cold) Coal/tetralin = 0.5, Catalysts = 10 wt%					
Substrate (g)	Catalyst (wt. %)	Sulfur (g)	THF-I	Heptane-I	Heptane-S
LSW (1.0)	None	None	0	85	15
LSW (1.0)	APC-Fe <sub>3</sub> (10)	0.1	0	70	30
LSW (1.0)	PETC METHOD	0.10	0	73	28

## ACTIVITY OF SLURRY PHASE IRON-BASED CATALYSTS FOR HYDROGENATION AND HYDROCRACKING OF MODEL SYSTEMS

Ying Tang and Christine W. Curtis  
Chemical Engineering Department  
Auburn University, Alabama 36849-5127

### INTRODUCTION

Slurry phase catalysts have been shown to be very active for coal liquefaction. Pellegrino and Curtis (1989) compared the activity of three different types of molybdenum catalysts: an oil-soluble molybdenum naphthenate, a presulfided molybdenum on alumina, and a precipitated  $\text{MoS}_2$  catalyst. The catalyst generated *in situ* from molybdenum naphthenate was the most active in terms of hydrogenation and heteroatom removal as well as showing the highest coal conversion and product upgrading. Kim and Curtis (1990) evaluated catalyst precursors of molybdenum, nickel, and vanadium for their activity in coprocessing of coal with resid. The activity of the molybdenum and nickel precursors for coal conversion and oil production was high while that for the vanadium was low.

Comparisons of the catalytic activities of iron and molybdenum catalysts used in reactions of model coal molecules showed that  $\text{Fe}(\text{CO})_5$  or  $\text{Fe}(\text{CO})_5\text{-S}$  had high catalytic activity for hydrogenation of aromatic species (Suzuki et al., 1989). However,  $\text{Mo}(\text{CO})_6\text{-S}$  more strongly promoted hydrogenation of polyaromatic compounds as well as hydrogenation of some phenyl carbon bonds. The effect of dispersion methods had also been examined using iron catalysts in which an iron oxide ( $\text{FeOOH}$ ) precursor was dispersed onto the solid coal matrix (Cugini et al., 1991). Other iron systems, such as  $\text{Fe}_2\text{O}_3$  dispersed on carbon black, iron incorporated into coal by impregnating with  $\text{FeCl}_3$  and iron incorporated into lignite by cation exchange with a sulfated  $\text{Fe}_2\text{O}_3$ , have been used as finely dispersed catalysts for coal liquefaction and characterized by Mössbauer and XAFS spectroscopy (Huffman et al., 1991).

Finely divided iron (III) oxides and iron oxyhydroxides modified with either ( $\text{SO}_4^{2-}$ ) or molybdate ( $\text{MoO}_4^{2-}$ ) anions used in coal liquefaction have shown increased coal conversion and selectivities to n-pentane soluble products (Pradhan et al., 1991). A bimetallic catalyst,  $\text{Mo}/\text{Fe}_2\text{O}_3/\text{SO}_4^{2-}$  that consisted of 50 ppm Mo and 3500 ppm Fe, was active for coal conversion with a selectivity for oil. The effect of the pyrite to pyrrhotite ratio produced from ferric sulfide as a precursor on coal liquefaction has also been studied. A definite effect of intermediate stoichiometry of the ratio was observed on the selectivity to lighter products at higher liquefaction temperatures (Stansberry et al., 1991).

In this investigation, the effect of slurry phase iron catalysts on hydrogenation and hydrocracking reactions of model coal species was investigated. The areas investigated included (1) the effect of iron complex type on hydrogenation of pyrene and on hydrocracking of alkyl substituted naphthalenes; (2) the effect of different dispersion methods on catalytic activity of iron-based slurry catalyst precursors; and (3) the effect of combining iron with molybdenum slurry phase catalyst precursors on catalytic activity during the hydrogenation of pyrene.

## EXPERIMENTAL

The experimental reaction methods used for dispersing the catalyst precursors were (1) *in situ* where the catalyst precursor was added directly to the reaction system and reacted in the presence or absence of sulfur; (2) *ex situ* where the catalyst precursor reacted in the presence of the model compound was reclaimed and used in a second reaction and (3) two stages where the catalyst precursor was added to hexadecane, hydrogen, and sulfur and reacted for 30 min, then the model species was introduced into the reactor along with hydrogen and reacted for another 30 min.

**Pyrene Hydrogenation Reactions.** Iron slurry phase catalyst precursors were compared and utilized the *in situ* reaction method; molybdenum naphthenate was also used for comparison. The iron catalyst obtained *in situ* was generated by introducing the catalyst precursor at a level of 900 to 1100 ppm metal directly into the reaction system of 2 wt% pyrene in hexadecane. The reactants were charged into a 20 cm<sup>3</sup> stainless steel tubular microreactor and the reactions were conducted at 380 or 425°C for 30 or 60 min with a hydrogen pressure of 1250 psig at ambient temperature and an agitation rate of 550 rpm. Reactions were performed both with and without sulfur. When sulfur was present, it was introduced as elemental sulfur in a stoichiometric ratio of 3:1 sulfur to metal, presuming that either FeS<sub>2</sub> or MoS<sub>2</sub> was formed depending upon the precursor introduced.

The catalyst precursors used in the *in situ* experiments were iron (III) naphthenate, iron (III) acetylacetonate, iron (III) citrate hydrate, iron (III) 2-ethylhexanoate, iron (III) stearate, and molybdenum naphthenate for comparison. Iron (III) acetylacetonate (99% purity) was obtained from Eastman Kodak Company; iron (III) citrate hydrate (98% purity) was obtained from Aldrich Chemical Company; iron (III) 2-ethylhexanoate (8 to 11.5% Fe), iron (III) acetylacetonate (99% purity), and iron (III) stearate (9% Fe) were obtained from Strem; and the molybdenum naphthenate (6% Mo) was obtained from Shepherd Chemical. All of the catalyst precursors were used as received.

The *ex situ* catalyst was generated by collecting the catalyst solids produced during an *in situ* reaction and then drying the solids for 72 hours in a vacuum oven at 60°C. The dried solids were then introduced into the reactor containing pyrene in hexadecane solution at a level of 900-1100 ppm active metal. Hydrogen was introduced and the reaction was performed at the abovementioned conditions.

Two-stage pyrene hydrogenation reactions were performed by producing the catalyst in the first stage using a reaction system of catalyst precursor, excess sulfur, hexadecane, and a hydrogen pressure of 1250 psig at ambient temperature. After 30 min of reaction, the reactors were removed from the sandbaths, cooled, and then charged with pyrene and 1250 psig hydrogen introduced at ambient temperature. The pyrene hydrogenation reaction was then performed at 380°C for 30 min.

An analysis procedure UV-visible spectroscopy was developed for measuring the amount of organometallic complex that reacted under liquefaction conditions. The procedure developed used the metal complex dissolved in hexadecane as the reaction system. The concentration of the iron or molybdenum complex present after a given reaction time was determined by UV-visible spectroscopy. Each iron complex had to be dealt with differently in the experimental procedure because of their varying degrees of solubility in hexadecane. Iron naphthenate, iron 2-ethylhexanoate, and molybdenum naphthenate utilized hexadecane as a solvent for UV-visible spectroscopy. Iron citrate hydrate was dissolved in ethanol for analysis; iron acetylacetonate was

extracted with hot water for UV-visible analysis. For each metal complex, a calibration curve was developed using the same solvent for UV-visible analysis as was used after reaction.

The reactions using different amounts of iron and molybdenum complexes involved adding the different metal complexes *in situ* to the 2 wt% pyrene hydrogenation system. These experiments were performed at the same conditions as the previously described *in situ* reactions except that the iron and molybdenum complexes were added in weight ratios of 75:25, 50:50, and 25:75.

**Hydrocracking Reactions.** Two compounds were used as hydrocracking models: 1-methylnaphthalene and 2-hexylnaphthalene. 1-methylnaphthalene was obtained from Aldrich while 2-hexylnaphthalene was obtained from Dr. M. Farcasiu of PETC. The reaction system consisted of 2 wt% of the model compound dissolved in hexadecane. Three catalyst precursors were tested: iron naphthenate, iron stearate and molybdenum naphthenate; all of which were introduced at a level of 900 to 1100 ppm metal directly into the reaction system. Thermal baseline experiments were also performed. The reaction conditions were reaction temperatures of 380 or 425°C for 30 min with a hydrogen pressure at 1250 psig at ambient temperature and an agitation rate of 550 ppm.

**Analysis.** The reaction products obtained from the pyrene hydrogenation reactions were analyzed by gas chromatography using a Varian Model 3700 gas chromatograph equipped with FID detection and J&W DB5 30 m column. Quantitation was achieved by employing the internal standard method using p-xylene as the internal standard. The reaction products were identified comparing retention times with those of authentic compounds and by identifying unknowns by GC-mass spectrometry using VG70 EHF GC-mass spectrometer.

The product slates were determined for each reaction and the amount of hydrogenation of the aromatic determined. The percent hydrogenation is defined as the moles of hydrogen required to produce the product slate as a percentage of the moles of hydrogen required to produce the most hydrogenated liquid product. The most hydrogenated liquid product from naphthalene was considered to be decalin, from pyrene, perhydropyrene, from 1-methylnaphthalene, 1-methyldecalin and from 2-hexylnaphthalene, 2-hexyldecalin. Percent hydrocracking is defined as the mole percent of the products that have undergone hydrocracking.

## RESULTS AND DISCUSSION

**Pyrene Hydrogenation Reactions.** Of the five slurry phase catalysts tested for their activity for pyrene hydrogenation, Fe naphthenate (Fe Naph) was the most active while Fe stearate (Fe STR) showed equivalent activity at 425°C but lesser activity at 380°C (Table 1). Sulfur was required for any activity to be observed from either catalyst. The primary product obtained was dihydropyrene (DHP), the secondary products were hexahydropyrene (HHP), and small amounts of tetrahydropyrene (THP) were formed.

Of the other three slurry phase iron catalysts tested with sulfur, Fe AcAc reacted at 425°C was the only one which showed substantial pyrene hydrogenation of 9.3% and yielded the same products as Fe Naph. All of the other systems with sulfur, Fe citrate-hydrate (Fe CH) and Fe 2-ethylhexanoate (Fe 2-EH) showed limited activity for pyrene hydrogenation.

Reactions were also performed with Mo Naph with and without sulfur at 380 and 425°C for 30 min. The presence of sulfur in the reactor allowed the Mo released from Mo Naph to form finely divided MoS<sub>2</sub> which was an active catalyst for pyrene hydrogenation (Kim et al., 1989). At 380°C, without sulfur, the reaction with Mo Naph yielded 11.7% HYD with DHP

as the primary product and THP as the secondary product. At 380°C, with sulfur, the reaction with Mo Naph yielded 34.6% HYD of pyrene with HHP isomers being the primary products and a substantial amount of decahydroxyrene (DCHP) being formed.

At 425°C, the reaction of Mo Naph without sulfur showed less activity for pyrene hydrogenation than did the system with sulfur. Without sulfur the %HYD of pyrene was somewhat higher at 13.8% than at 380°C which yielded 11.7%. But the reaction at higher temperature, 425°C, with sulfur gave less activity than at 380°C with sulfur. At 425°C, thermodynamics are limiting the amount of pyrene conversion allowed and, hence, lower the amounts of partially saturated compounds produced in the reaction (Ting et al., 1992).

**Concentration of Iron Complexes at Liquefaction Conditions.** The iron complexes of Fe-CH, Fe Naph, Fe AcAc, and Fe 2-EH, each with an initial concentration of 1000 ppm Fe, were reacted at 380°C with an initial hydrogen charge of 1250 psig hydrogen introduced at ambient temperature. The concentration of each iron complex was determined by measuring the absorbance at two wavelengths and comparing the absorbance reading with a calibration curve for each complex obtained with the same solvent as was used with the reaction mixture. Each of the iron complexes disappeared very quickly at liquefaction conditions. After 5 min of reaction, all of the iron complexes were decomposed; in fact, all of them except Fe Naph were decomposed after 2 min of reaction. By contrast, Mo Naph remained in solution longer; after 10 min of reaction, more than half of the Mo Naph remained. However, Mo Naph had totally decomposed after 15 min of reaction.

**Comparison of Dispersion Methods for Activity of Fe Slurry Phase Catalysts.** Three methods of dispersion *in situ*, *ex situ*, and two stage batch processing were used to test the effect of dispersion on the catalytic activity of the generated catalysts (Table 2). Comparison of Fe Naph and Mo Naph activity for pyrene hydrogenation using the *in situ* method revealed that Mo Naph resulted in nearly three times as much hydrogenation as Fe Naph. HHP was the primary product for Mo Naph while DHP was the primary product for Fe Naph. The *ex situ* method, in which the catalyst produced in an *in situ* experiment was added to pyrene hydrogenation reaction system, resulted in less activity for both Fe Naph and Mo Naph. Fe Naph did not convert any pyrene while Mo Naph yielded about half the amount of hydrogenation observed in the *in situ* reaction.

Two-stage batch reactions were performed in which the catalyst precursor was introduced into hexadecane in the first stage and then reacted in the presence of sulfur and hydrogen for 30 min at 380°C. At that point, the reaction was quenched, gas released and pyrene and a new charge of hydrogen added. The system, including pyrene, was then reacted again for 30 min. The two-stage reaction with Fe Naph yielded about 6% conversion of pyrene to DHP so that its activity was much less than that of the *in situ* generated catalyst. By contrast, the two-stage reaction with Mo Naph yielded higher pyrene hydrogenation, 40% for the two-stage compared 34.6% for the *in situ* single-stage. Hence, the catalytic activity of Mo Naph appeared to increase with the two-stage treatment while Fe Naph did not.

**Effect of Combining Iron Complexes with Mo Naphthenate on the Reaction Products from Pyrene Hydrogenation.** Reactions were performed in which the catalyst precursors of the various iron complexes were combined with Mo Naph to determine if any synergism occurred in their catalytic activity for pyrene hydrogenation (Figure 1). Reactions were performed with 1000 ppm of the iron complex, 1000 ppm of Mo Naph, and with the combinations of 750 ppm iron complex with 250 ppm Mo Naph, 500 ppm with 500 ppm, and 250 with 750 ppm, respectively.

The combination of Fe Naph and Mo Naph at 75:25 and 50:50 Fe to Mo ratio yielded increased pyrene hydrogenation compared to either Mo Naph or Fe Naph alone. These results are presented in Figure 1 along with baseline experiments using Fe Naph and Mo Naph, individually. With Fe AcAc and Fe CH, each combined with Mo Naph, increased pyrene hydrogenation was observed at the combination of 25:75 Fe to Mo compared to the Mo Naph alone. By contrast, none of the combinations of Fe 2-EH with Mo Naph yielded increased conversions. In fact, the amount of pyrene hydrogenation increased with the amount of Mo Naph added; however, the amount of pyrene hydrogenation was less with Fe 2-EH than with Mo Naph alone at equivalent concentration levels. Therefore, for some combinations of Fe complexes and Mo Naph, synergism between the two catalyst precursors occurred resulting in increased pyrene hydrogenation, while another iron complex was detrimental to pyrene hydrogenation.

**Hydrocracking Reactions Using Fe Naphthenate and Fe Stearate.** Hydrocracking reactions using 1-methylnaphthalene (1-MN) and 2-hexylnaphthalene (2-HN) were performed using Fe Naph and Fe STR. The product distributions obtained with these reactions were compared to that obtained with naphthalene (NAP) (Table 3). The primary products obtained from 1-MN as shown in Table 3 were 5,6,7,8-tetrahydro-1-methylnaphthalene (5,6,7,8-1-MN) and 1,2,3,4-tetrahydro-1-methylnaphthalene (1,2,3,4-1-MN). For all catalysts the 5,6,7,8-1-MN isomer was the preferred product. At the higher reaction temperature, both iron complexes yielded NAP as a secondary product. If 1-methyldecalin is considered the most hydrogenated product, then the iron complexes both yielded between 6 and 7% hydrogenation of 1-MN but less than 3% hydrocracking. By contrast, Mo Naph yielded substantially more hydrogenation of ~26% but no hydrocracking. The baseline reaction using NAP only yielded tetralin (TET) as a product. No hydrocracking of the aromatic rings was obtained.

The reactions of 2-HN also given in Table 3 in the presence of Fe Naph, Fe STR and Mo Naph resulted in the production of two products: 2-hexyltetralin (2-HT) and 2-ethyltetralin (2-ET). For all three catalyst precursors, 2-HT was the primary product while 2-ET was the secondary product. Of all of the catalyst precursors, Mo Naph yielded the most hydrogenation and hydrocracking.

## SUMMARY

Slurry phase iron catalysts showed varying amounts of activity for pyrene hydrogenation reactions. Fe naphthenate and Fe stearate were the most active complexes although all of the Fe complexes broke down quickly at liquefaction conditions. By comparison, at the same reaction conditions, Mo naphthenate gave higher activity for pyrene hydrogenation. The activity of the slurry phase iron catalysts for pyrene hydrogenation depended upon the ligand type, reaction temperature and sulfur addition. The dispersion method also made a substantial difference in the activity of the catalyst. Fe naphthenate yielded the most activity using the *in situ* dispersion method and the least using the *ex situ* method. By contrast, Mo naphthenate showed the most activity with the two-stage process and the least with the *ex situ* method. Combination of some iron complexes with Mo naphthenate showed marked increases in activity for pyrene hydrogenation. In particular, the combination of Fe naphthenate with Mo naphthenate yielded increased yields of hydrogenated products from pyrene. Hydrocracking reactions revealed that the iron complexes promoted a small amount of hydrocracking with 1-methylnaphthalene and more with 2-hexylnaphthalene although Mo naphthenate promoted more hydrocracking of 2-hexylnaphthalene at equivalent reaction conditions.

## NOMENCLATURE

PYR = pyrene	Fe STR = iron stearate
DHP = dihydropyrene	Fe 2-EH = iron 2-ethylhexanoate
THP = tetrahydropyrene	Mo Naph = molybdenum naphthenate
HHP = hexahydropyrene	2-HN = 2-hexylnaphthalene
DCHP = decahydropyrene	2-HT = 2-hexyltetralin
1-MN = 1-methylnaphthalene	2-ET = 2-ethyltetralin
NAP = naphthalene	1,2,3,4-1-MN = 1,2,3,4-tetrahydro-1-methylnaphthalene
TET = tetralin	5,6,7,8-1-MN = 5,6,7,8-tetrahydro-1-methylnaphthalene
Fe Naph = iron naphthenate	%HYD = percent hydrogenation
Fe AcAc = iron acetylacetonate	
Fe CH = iron citrate hydrate	

## REFERENCES

- Cugini, A.V., Utz, B.R. Krustman, D., Hickey, R.I., Balsone, V. *ACS Fuel Chemistry Division Preprints*, 36(1), 91, 1991.
- Huffman, G.P., Ganguly, B., Taghili, M., Huggins, F.E. and Shah, N., *ACS Fuel Chemistry Division Preprints*, 36(2), 561, 1991.
- Kim, H., Curtis, C.W. *Energy and Fuels*, 4, 206-14, 1990.
- Kim, H., Curtis, C.W., *ACS Fuel Chemistry Division Preprints*, 35(4), 1990.
- Kim, H., Curtis, C.W., Cronauer, D.C., Sajkowski, *ACS Fuel Chemistry Division Preprints*, 34(4), 1431, 1989.
- Pellegrino, J.L., Curtis, C.W., *Energy and Fuels*, 3(2), 160, 1989.
- Pradhan, V.R., Herrick, D.E., Tierney, J.W., Wender, I. *Energy and Fuels*, 5(5), 712, 1991.
- Pradhan, V.R., Holder, G.D., Tierney, J.W. and Wender, I., "Modified Iron Oxide Catalysts in Coal Liquefaction," Fifth Annual Technical Meeting, Consortium for Fossil Fuel Liquefaction Science, Lexington, Kentucky, August, 1991.
- Stansberry, P., Zondlo, J.W., Yang, J., Stiller, A.H., Ragela, P., and Dadyburjor, D.B., "Ferric Sulfide as a Precursor for Coal Liquefaction," Fifth Annual Technical Meeting, Consortium for Fossil Fuel Liquefaction Science, Lexington, Kentucky, August, 1991.
- Suzuki, T., Yamada, H., Sears, P.L. and Watanabe, *Energy and Fuels*, 3, 707, 1989.
- Ting, P.S., Curtis, C.W., Cronauer, D.C. *Energy and Fuels*, 6, 511, 1992.

Table 1. Activity of Iron Complexes for Pyrene Hydrogenation

Product Distribution (mol %)	Fe Naphthenate		Fe Stearate		Fe Citrate-Hydrate		Fe Acetylacetonate		Fe 2-ethyl-Hexanoate	
	380°C	425°C	380°C	425°C	380°C	425°C	380°C	425°C	380°C	425°C
	3:1 S to Fe Ratio									
PYR	49.7±1.0	52.9±1.9	75.7±0.2	53.4±0.7	93.3±0.7	NP	95.6±0.7	61.6±0.6	100	90.5±0.7
DHP	32.1±0.5	29.1±0.5	18.2±0.2	26.7±0.6	6.7±0.7	NP	4.4±0.7	24.0±0.5	0	9.5±0.7
THP	2.9±0.1	3.2±0.3	0.0±0.0	3.2±0.4	0	NP	0	2.2±0.1	0	0
HHP	15.4±0.3	14.9±0.6	6.1±0.2	16.8±0.2	0	NP	0	12.3±0.2	0	0
% HYD	12.0±0.3	11.5±0.6	5.2±0.2	11.9±0.4	1.0±0.1	NP	0.6±0.1	9.3±0.1	0.0	1.4±0.1
	No Sulfur									
PYR	98.2±0.1	87.9±0.2	100.0	100.0	100.0±0	NP	98.8±0.8	93.1±0.5	100	94.2±0.2
DHP	1.8±0.1	12.1±0.2	0.0	0.0	0	NP	1.2±0.8	6.9±0.5	0	5.8±0.2
% HYD	0.3±0.0	1.7±0.0	0.0	0.0	0	NP	0.2±0.0	1.0±0.1	0.0	0.8±0.0

Reaction Conditions: 990-1100 ppm of Fe, 30 min, 1250 psig hydrogen pressure at ambient conditions, 2 wt % Pyrene in hexadecane.

Table 2. Comparison of Dispersion Methods of Iron and Molybdenum Precursors on Their Activity for Pyrene Hydrogenation

Product Distribution (mole %)	Fe Naphthenate			Mo Naphthenate		
	In Situ	Ex Situ	Two Stages	In Situ	Ex Situ	Two Stage
PYR	49.7±1.0	100.0±0.0	94.2±1.0	14.7±1.4	33.3	10.3±1.0
DHP	32.1±0.5	0.0	5.8±1.0	18.7±1.4	32.3	14.3±0.5
THP	2.9±0.1	0.0	0.0	7.5±0.6	9.1	6.2±0.3
HHP	15.4±0.3	0.0	0.0	43.5±0.9	25.5	45.8±0.8
DCHP	0.0	0.0	0.0	15.7±0.7	0.0	23.4±0.8
% HYD	12.0±0.3	0.0	0.8±0.1	34.7±1.7	18.1	40.2±0.6

**Table 3. Comparison of the Activity for the Hydrogenation and Hydrocracking of Naphthalene, 1-Methylnaphthalene, and 2-Hexylnaphthalene**

Product (mole %)				
	No Catalyst	Fe Stearate + S	Fe Naph + S	Mo Naph + S
<b>Naphthalene</b>				
NAP	100.0	85.5±0.4	83.9±0.5	
TET	0.0	14.5±0.4	16.1±0.5	
% HYD	0.0	5.8±0.1	6.4±0.1	
<b>1-Methylnaphthalene</b>				
1-MN	100±0.0	82.3±1.0	81.1±0.6	35.5±0.6
5,6,7,8-1-MN	0.0	11.9±1.0	10.8±0.5	39.2±0.8
1,2,3,4-1-MN	0.0	3.6±0.4	5.3±0.2	25.3±0.9
NAP	0.0	2.2±0.3	2.7±0.4	0.0
% HYD	0.0	6.3±0.4	6.6±0.3	25.8±0.4
<b>2-Hexylnaphthalene</b>				
2-HN	100.0±0.0	70.4±1.2	79.3±0.9	20.1±1.1
2-HT	0.0	16.5±1.2	11.1±0.9	43.5±1.0
2-ET	0.0	13.1±0.9	9.6±0.2	36.4±0.3
%HYD	0.0	14.8±0.7	10.4±0.8	40.0±1.0
%HYC	0.0	13.1±0.9	9.6±0.2	36.4±0.3

Reaction Conditions: 1250 psig H<sub>2</sub> introduced at ambient temperature; 30 minutes, 425°C, S to Fe ratio 3:1, S to Mo ratio 3:1.

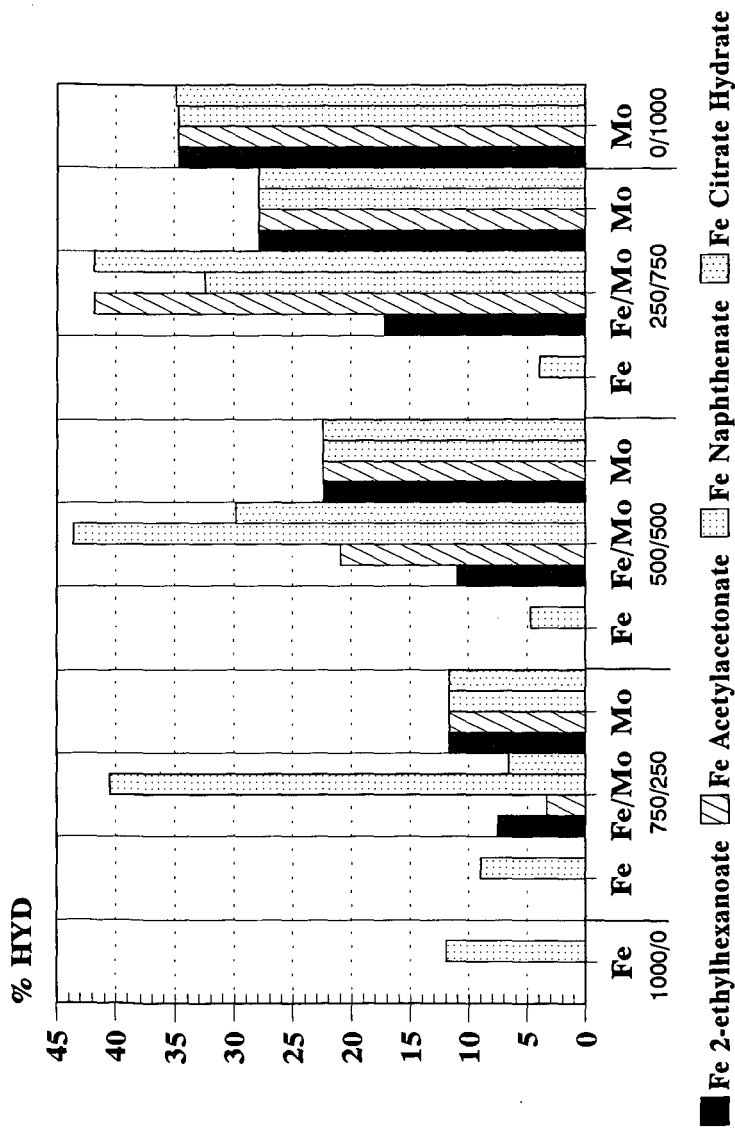


Figure 1. Synergism with Mo Naphthenate.

## CHARGE DISTRIBUTION ANALYSIS OF IRON OXIDE CATALYSTS\*

Friedemann Freund\* and Eun-Joo Whang

Department of Physics  
San Jose State University  
San Jose, CA 95192-0106

Keywords: Surface charge, Sign of charge carriers, Correlation with activity

### Abstract:

Catalytic reactions on solid contacts involve the exchange of charges across the solid/gas interfaces. Charge Distribution Analysis (CDA) is a new technique, capable of determining the generation of mobile charges in the bulk of materials and their appearance at the surface. By measuring the force acting on a sample in an electric field gradient, CDA derives unique information previously not available by any other technique. We have studied pressed pellets of two iron oxide catalysts supplied by the DOE Pittsburgh Energy Technology Center.  $\alpha$ - $\text{Fe}_2\text{O}_3$  (hematite), heated in  $\text{O}_2$ , behaves as a regular dielectric up to 450°C. The weakly negative surface charge indicates that electrons are the majority charge carriers. In  $\text{Fe}_3\text{O}_4$  (magnetite), heated in  $\text{N}_2$ , the surface is also weakly negative at ambient temperature, but evolves toward strongly positive values above 230°C. Upon cooling from 350°C this positive surface charge is firmly established, suggesting that defect electrons or holes have become the majority charge carriers. The trend toward positive surface charge continues up to 410°C when the composition of the magnetite sample starts to change. Between 275–410°C the magnetite is catalytically highly active toward dealkylation of 6-methyl-9-(1-methylethyl) dibenzo thiophene-4-ol. The fact that the catalytic activity toward dealkylation coincides with the appearance of a positive surface charge suggests that the active magnetite surface acts as an electron acceptor.

### INTRODUCTION

Whenever chemical reactions occur, they involve the transfer of electrical charges between reacting partners. When one of the partners is a solid and the reaction occurs catalytically at its surface, the onset of reactivity will be marked by the appearance of charge carriers in the bulk of the catalyst and their diffusive transport toward the active surface.

In principle, the appearance of charge carriers should be amenable to electrical conductivity measurements. However, conventional conductivity techniques require electrodes that are in direct contact with the sample surface. Obviously, this can cause many problems. If the electrode-sample contacts are good, the surfaces are no longer free and unperturbed. In the case of high surface area samples good physical contacts are impossible to establish. It is therefore fair to say that conventional electrical conductivity techniques appear not to be well suited to study catalytic reactivity – unless a method can be developed which allows contact-free measurement of the electrical conductivity.

\* Work supported by the ACS-Petroleum Research Fund under Grant #24335-AC5, the DOE Pittsburgh Energy Technology Center, and the NASA Ames Research Center.

\* Mailing address: NASA Ames Research Center, MS 239-4, Moffett Field, CA 94035-1000

## CHARGE DISTRIBUTION ANALYSIS - A POWERFUL NEW TECHNIQUE

*Charge Distribution Analysis* (CDA) is a non-contacting technique that allows conductivity measurements of insulating and semiconducting materials under minimum perturbation conditions <sup>1,2</sup>. CDA is based on the dielectric polarization at the limit of 0 Hertz. When a dielectric is placed in an external electric field of field strength  $E_{ext}$  it becomes polarized. Its polarization  $P$  is:

$$P = \frac{\epsilon_0(\epsilon-1)}{4\pi} E_{ext} \quad (1)$$

where  $\epsilon_0$  is the permittivity of vacuum and  $\epsilon$  the dielectric constant.  $P$  contains five contributions,  $P_{el} + P_{ion} + P_{local} + P_{space} + P_{surface}$ , of which the first two refer to the ideal dielectric.  $P_{el}$  reflects the electronic polarization of the electronic shells and  $P_{ion}$  the ionic polarization due to the field-induced atom displacement. The remaining three contributions arise from defects and impurities.  $P_{local}$  reflects local defects that change their intrinsic polarizability or dipolar defects that can rotate in the externally applied electric field.  $P_{space}$  arises from the space charge polarization due to mobile charges that can diffuse inside the sample.  $P_{surface}$  is uniquely related to the surface charge.

When a dielectric is placed in a field gradient along the  $z$  direction, a force  $F_z^\pm$  acts on the sample towards higher field density. Using Maxwell's equations,  $F_z^\pm$  is given to first approximation by:

$$F_z^\pm = - \int \nabla (P \cdot E_{ext}) dV \quad (2)$$

where the volume integral includes the sample but not the sources of the field. In the case of an ideal dielectric (only  $P_{el}$  and  $P_{ion}$ )  $F_z^\pm$  is invariant to the direction of the field gradient:  $F_z^\pm = F_z^+(E_{ext}) = F_z^(-E_{ext})$ . In a real dielectric the contributions from  $P_{local}$  and  $P_{space}$  also remain invariant. However, the  $P_{surface}$  term is variant to field gradient reversal. It causes an attraction to or repulsion from the region of higher field density, depending upon the sign of the surface charge. To separate ( $P_{el} + P_{ion} + P_{local} + P_{space}$ ) from  $P_{surface}$  we form the linear combinations:

$$F_\Sigma \equiv \frac{1}{2}(F^- + F^+) = - \frac{\epsilon_0(\epsilon-1)}{4\pi} \int \nabla \cdot E_{ext}^2 dV \quad (3)$$

$$F_\Delta \equiv \frac{1}{2}(F^- - F^+) = - \int \nabla (P_{surface} \cdot E_{ext}) dV. \quad (4)$$

To evaluate  $P_{surface}$ , we introduce  $a_\pm U^2$  where  $a_\pm$  is a constant:

$$F^\pm = F_1^\pm + a_\pm U^2 \quad (5)$$

$a_\pm U^2$  describes the ideal dielectric and the  $F_1^\pm$  are constants.  $F_\Sigma$  and  $F_\Delta$  are then given as:

$$F_\Sigma = \frac{1}{2}(F_1^- + F_1^+) + \frac{1}{2}(a_- + a_+) U^2 \quad (6)$$

$$F_\Delta = \frac{1}{2}(F_1^- - F_1^+) + \frac{1}{2}(a_- - a_+) U^2 \quad (7)$$

$F_\Sigma$  characterizes the bulk polarization and is sensitive to the generation of mobile charges.  $F_\Sigma$  is proportional to the square of the applied voltage.  $F_\Delta$  characterizes the surface, its charge density and the internal electric field.  $F_\Delta$  is linearly proportional to the applied voltage and its sign identifies the sign of the charge carriers, for instance electrons (negative) or holes (positive) that may be present in the catalyst sample.  $F_\Sigma$  and  $F_\Delta$  provide unique information about fundamental properties such as the on-set of chemical reactivity of a catalyst that is not available by any other known technique.

## EXPERIMENTAL

A PERKIN-ELMER TGS-2 thermobalance, equipped with a cup-shaped Pt-wound furnace (10 mm i.d. x 20 mm), was modified by the introduction of a circular bias electrode and a cylindrical ground electrode to create an asymmetrical capacitor of axial symmetry. The samples were suspended via a fused silica fiber, well insulated from ground, and placed into the region of the steepest electric field gradient, approximately 0.1–0.5 mm above the bias electrode. They were heated in 25°C increments, using a heating rate of 20°C/min. During the time at constant temperature the bias voltages were applied sequentially for 10–20 sec in increments of +20 V, 0 V and –20V. The forces were recorded as apparent weight changes in the sensitivity range 0.1–1 mg full scale.

The samples studied were coarse powders of  $\alpha$ -Fe<sub>2</sub>O<sub>3</sub> (hematite), labeled Catalyst #7, and Fe<sub>3</sub>O<sub>4</sub> (magnetite), which were both prepared by Dr. Malvina Farcasiu of the DOE Pittsburgh Energy Technology Center. The average grain size of the magnetite was 5  $\mu$ m and its specific surface area was of the order of 7 m<sup>2</sup>/g. Both powders were pressed dry into 6 mm diameter pellets, about 1.5 mm thick. The hematite was dried in N<sub>2</sub> at 150°C, heated in O<sub>2</sub> to 410°C, cooled to 380°C and reheated to 560°C. The magnetite was dried in N<sub>2</sub> to 150°C, then heated to 350°C ("2nd heating"). It was then cooled to 150°C and reheated to 500°C in N<sub>2</sub> with intermittent cooling from 400°C to 300°C and 450°C to 350°C ("3rd heating").

## RESULTS

$F_{\Sigma}$  of the hematite sample increased slightly and approximately linearly with temperature up to 500°C as shown in Fig. 1a. This suggests that up to 500°C, the sample behaved as a near-ideal insulator. Above 500°C, the  $F_{\Sigma}$  increased significantly, indicating that mobile charge carriers are being generated.  $F_{\Delta}$  was negative over the entire temperature range as shown in Fig. 1b, indicating that the surface charge of the hematite is dominated by electrons. A slight tendency towards positive  $F_{\Delta}$  values was noted after the intermittent cooling from 410°C to 380°C which, however, was overtaken by an even stronger trend towards negative  $F_{\Delta}$  values above 450°C. In conjunction with the pronounced increase in  $F_{\Sigma}$  above 500°C this response clearly suggests that the mobile charge carriers generated in the hematite above 450°C are electrons.

The magnetite exhibited a distinctly different behavior. As shown in Fig. 2a, the  $F_{\Sigma}$  values during the 2nd heating increased linearly with a lesser slope up to 230°C than above 230°C. This suggests the appearance of mobile charge carriers in the higher temperature range. During the 2nd heating,  $F_{\Delta}$  was initially very slightly negative and showed a trend towards more negative values up to 230°C as evidenced by Fig. 2b. Above 230°C, however, the trend reversed towards positive  $F_{\Delta}$  values.

After cooling to 150°C and subsequent reheating (3rd heating)  $F_{\Sigma}$  increased linearly from 230°C onward up to about 450°C with the same slope as during the 2nd heating as shown in Fig. 3a. During intermittent cooling and reheating cycles the  $F_{\Sigma}$  values were found to be successively higher, indicating that mobile charge had been generated during the heating cycles which did not disappear or recombine during cooling. Above 450°C,  $F_{\Sigma}$  increased more rapidly, but at the same time, the magnetite sample started to lose weight, probably due to changes in composition in the unbuffered N<sub>2</sub>

atmosphere. Experimentally this is seen in the fact that  $F_{\Sigma}$  is no longer proportional to the square of the applied bias voltage.

$F_{\Delta}$  remained positive during the 3rd heating as shown in Fig. 3b. Only at low bias voltage (20V) did  $F_{\Delta}$  still show the same trend towards negative values up to 230°C, followed by an evolution toward positive values. At the higher bias voltages the trend was towards positive values. During intermittent cooling up to about 410°C the positive  $F_{\Delta}$  values were further enhanced, indicating that the mobile charge carriers generated in the temperature interval 230–410°C have a positive sign. This in turn suggests that they are defect electrons or holes. The magnitude of  $F_{\Delta}$ , about 10% of  $F_{\Sigma}$ , indicates that the charge carrier density at the magnetite surface is rather high. However, quantitative data can be obtained only from single crystals, not from a pressed powder sample<sup>1</sup>. Above 410°C  $F_{\Delta}$  showed signs of degradation. Experimentally this is seen in the fact that  $F_{\Delta}$  was no longer linearly proportional to the applied bias voltage.

## DISCUSSION

The magnetite under study is active toward the dealkylation of 6-methyl-9-(1-methylethyl) dibenzo thiophene-4-ol in the presence of a hydrogen donor. In spite of its large average grain size (5  $\mu\text{m}$  diameter, 7  $\text{m}^2/\text{g}$  specific surface area), its catalytic activity is very high as illustrated in Fig. 4. The  $F_{\Delta}$  values shown (left ordinate) correspond to those measured during 2nd heating at 100V while the percentage dealkylation was achieved after 1 hour (right ordinate) using 25 mg catalyst and 25 mg 6-methyl-9-(1-methylethyl) dibenzo thiophene-4-ol. Trial runs performed by Dr. Farcasiu for 5 hrs at 150°C and 210°C did not produce an measurable dealkylation. Though we are still at an early stage of the investigation it appears that the catalytic activity of the magnetite may be directly related to the appearance of mobile charge carriers at its surface. The positive charge of the carriers identifies them as defect electrons or holes. Hence, the magnetite surface is expected to act as an electron acceptor.

Obviously, the holes are produced in the bulk of the magnetite crystals and diffuse to the surface where they become available for surface–gas reactions. To achieve the high turn–over number required for the observed degree of dealkylation, a large number of holes must flow from the bulk to the surface. By performing time–dependent CDA experiments it should also be possible in the future to measure the diffusive mobility of these active charges. Such measurements are of interest, if one tries to correlate the rate of a catalytic reaction with the density of charges at the solid surfaces.

On the basis of the data so far available, the CDA technique seems to be a promising tool to evaluate the activity of catalysts and to obtain valuable information about the nature of the charge carriers which participate in or are instrumental for catalytic reactions<sup>3</sup>.

## REFERENCES

- (1) Freund, M. M.; Freund, F.; Batllo, F. *Phys. Rev. Lett.* **1989**, *63*, 2096-2099.
- (2) Freund, F.; Batllo, F. *US Patent No. 4,884,031* **1989**,
- (3) Freund, F.; Maiti, G. C.; Batllo, F.; Baerns, M. *J. Chim. Phys.* **1990**, *87*, 1467-1477.

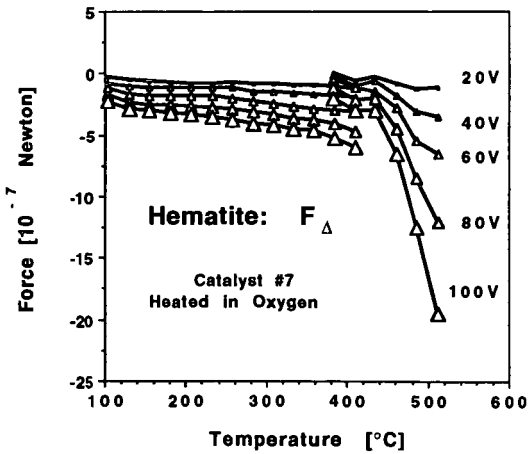
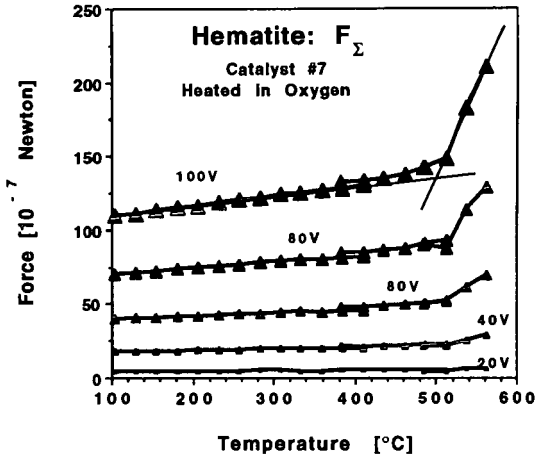


Fig. 1 a/b:  $F_{\Sigma}$  (top) and  $F_{\Delta}$  (bottom) of hematite (Catalyst #7) heated in  $O_2$ . The CDA response is typical for a near-ideal dielectric up to about 500°C. Throughout the temperature range studied, the dominant charge carriers are electrons.

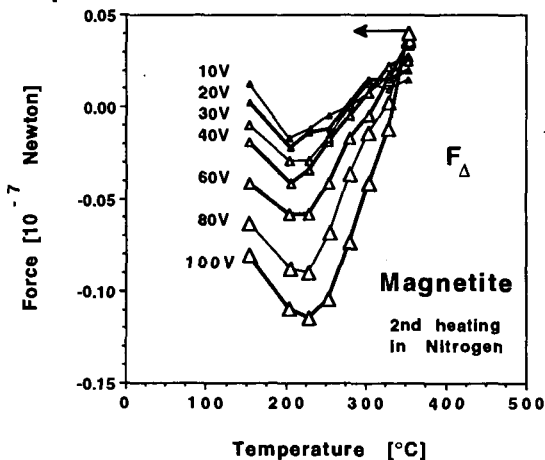
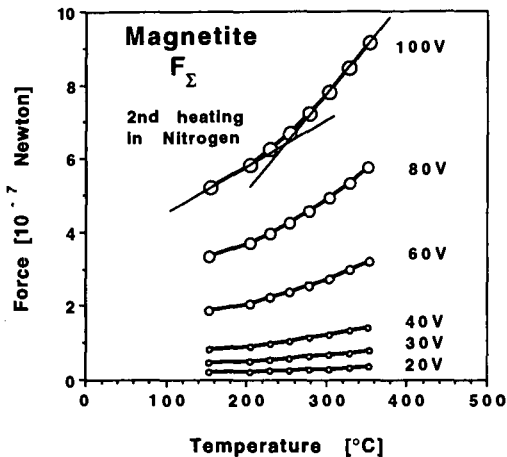


Fig. 2a/b:  $F_{\Sigma}$  (top) and  $F_{\Delta}$  (bottom) of magnetite heated in  $N_2$ . The CDA response suggests that, while electrons are the predominant charge carriers below 230 $^{\circ}$ C, defect electrons or holes start to dominate at the higher temperatures.

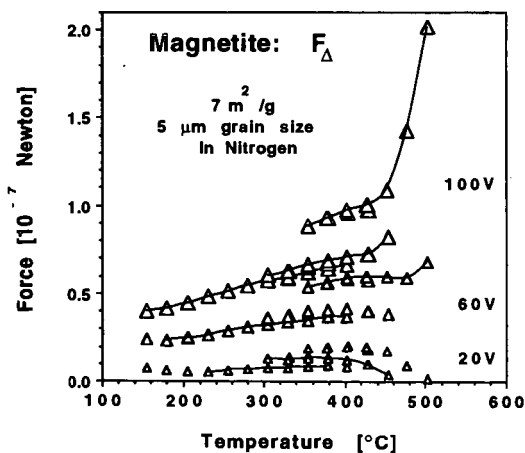
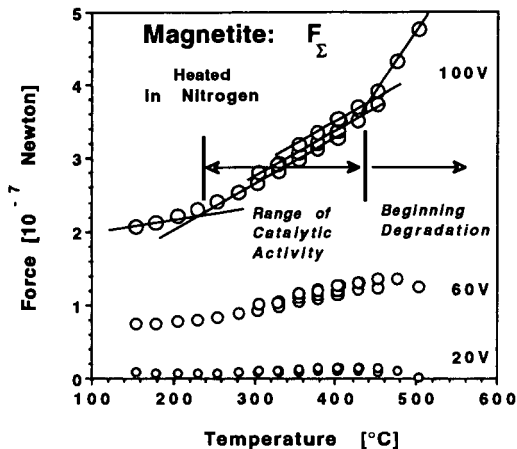


Fig. 3a/b:  $F_{\Sigma}$  (top) and  $F_{\Delta}$  (bottom) of magnetite heated and intermittently cooled in  $\text{N}_2$ . The CDA response of magnetite suggests that defect electrons or holes are the predominant charge carriers up to  $450^{\circ}\text{C}$  at which point decomposition sets in.

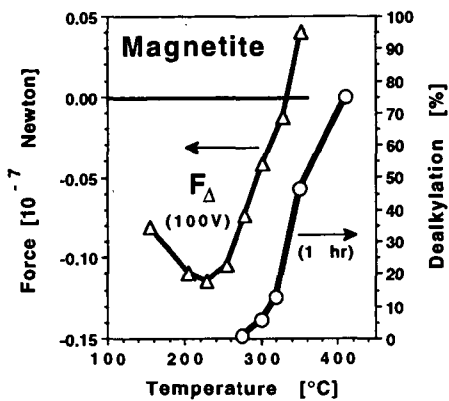


Fig. 4: Comparison between the surface charge of the magnetite sample in  $N_2$  as measured by CDA,  $F_{\Delta}$  (left scale), and the percentage of dealkylation of 6-methyl-9-(1-methylethyl) dibenzo thiophene-4-ol (right scale) after 1 hr. reaction time. At 150°C and 210°C no dealkylation occurred, even after 5 hrs. (Data courtesy of Dr. Malvina Farcasiu)

## FREE RADICAL INVESTIGATIONS OF DIRECT COAL LIQUEFACTION WITH Fe-BASED CATALYSTS USING ELECTRON SPIN RESONANCE SPECTROSCOPY

Manjula M. Ibrahim and Mohindar S. Seehra  
Physics Department, P.O. Box 6315  
West Virginia University, Morgantown, WV 26506-6315

Keywords: Coal hydrogenation; Free radicals; Fe-based catalysts

### ABSTRACT

Using a recently fabricated in-situ high pressure/high temperature electron spin resonance (ESR) apparatus, we report the variations of the ESR parameters of free radicals (density  $N$ , linewidth  $\Delta H$  and  $g$ -value) in the hydrogenation of Blind Canyon coal at 440°C and 415°C and as a function of  $H_2$  pressure up to 600 psi. More efficient hydrogenation is observed at 440°C as the decrease in  $N$  with  $H_2$  pressure is much higher at 440°C than at 415°C. A corresponding decrease in  $\Delta H$  with  $H_2$  pressure is also observed. Similar experiments but with loadings of  $Fe_2O_3/SO_4$  catalyst, elemental sulfur and hydrogen donor 9-10 dihydrophenanthrene are now being carried out.

### SUMMARY OF RESULTS/PROCEDURES

It is now generally accepted that direct coal liquefaction involves the interaction of thermally/catalytically generated free radicals in coals with the available hydrogen [1,2]. Some of these free radicals can be detected by in-situ electron spin resonance (ESR) spectroscopy. Recently we have fabricated a high pressure/high temperature in-situ ESR cavity system in order to investigate the free radical chemistry of direct coal liquefaction under more realistic conditions used in coal liquefaction experiments [3]. Experiments have been carried out from ambient to 500°C and for gaseous pressures up to 600 psi at X-band frequencies (~9 GHz). The density  $N$  of the free radicals and their  $g$ -values  $g$  and linewidth  $\Delta H$  are measured as a function of temperature and pressure. The experimental procedures for measuring these quantities have been described in a recent paper [4].

In Fig. 1, we show the variation of the free radical density  $N$  in Blind Canyon coal as a function of  $H_2$  pressure at two temperatures viz. 415°C and 440°C. The decrease in the free radical density with  $H_2$  pressure signifies hydrogenation since capture of  $H_2$  by free radicals quenches them and makes them undetectable by ESR. Comparing the results at 440°C with those at 415°C shows that hydrogenation is considerably more efficient at 440°C than at 415°C since considerably larger decrease in  $N$  with  $H_2$  pressure is observed at 440°C. The significance of these results is that these experiments are providing a direct evidence for the process of hydrogenation.

The variation of the  $g$ -value and the linewidth  $\Delta H$  of the free radicals with  $H_2$  pressure is shown in Fig. 2 for the experiments at 440°C. Whereas the  $g$ -value is essentially independent of  $H_2$  pressure, the linewidth decreases as the  $H_2$  pressure increases. The  $g$ -value, in favorable circumstances, can provide some information on the nature of the free radicals. However since there is no change in the observed  $g$ -value with  $H_2$  pressure (Fig. 2), no additional information on the chemical nature of free radicals is readily apparent from this experiment. The observed decrease in the linewidth with  $H_2$  pressure may be related to the decrease in the free radical density with  $H_2$  pressure observed in Fig. 1.

To simulate the conditions used in direct coal liquefaction, experiments are now underway in which the Blind Canyon coal is successively loaded with the catalyst (e.g.  $Fe_2O_3/SO_4$ ), elemental sulfur, and the hydrogen donor 9-10 dihydrophenanthrene (DHP). Free radical ESR

parameters are then monitored as a function of temperature in flowing H<sub>2</sub> gas and at fixed temperature as a function of H<sub>2</sub> pressure. In Fig. 3, we show one set of such results in flowing H<sub>2</sub> gas in which N vs T is plotted for the Blind Canyon coal, and for the coal loaded with Fe<sub>2</sub>O<sub>3</sub>/SO<sub>4</sub> and sulfur, and coal loaded with Fe<sub>2</sub>O<sub>3</sub>/SO<sub>4</sub>, sulfur and DHP. The loading by weight was in the ratio coal: Fe<sub>2</sub>O<sub>3</sub>/SO<sub>4</sub>:sulfur:DHP = 100:1.44:2.02:200. These loadings are chosen so as to give the ratios Fe/coal = 1/99 (~1%), Fe/S = 1/2, coal/DHP = 1/2. These preliminary results in Fig. 3 show that the catalyst and sulfur promote cracking since N is higher compared to the unloaded coal at all temperatures. With loading of DHP, magnitude of N is lowered as compared to the unloaded coal for temperatures below 260°C. Above this temperature, N values with DHP loading are essentially identical to the coal + catalyst + sulfur case as if the DHP is no longer present. To verify this, we carried out a thermogravimetric experiment on DHP in flowing H<sub>2</sub> gas. This experiment showed that by 290°C all DHP is evaporated, confirming the above argument. The lower values of N below 260°C in DHP are simply due to hydrogenation since it is well known that hydrogenation caps the free radicals, at least some of them. Experiments are now in progress under H<sub>2</sub> pressures up to 600 psi to simulate direct liquefaction conditions. Under H<sub>2</sub> pressures, evaporation of DHP at lower temperatures should be suppressed. Results of these experiments will be reported elsewhere in the near future.

#### ACKNOWLEDGMENTS

This research was supported in part by the U.S. Department of Energy through the Consortium for Fossil Fuel Liquefaction Science under DOE Contract No. DE-FC22-90PC90029.

#### REFERENCES

1. Neavel, R. C. *Fuel* 1976, 55, 237-242.
2. Petrakis, L. and Grandy, D. W. "Free Radicals in Coals and Synthetic Fuels" 1983 (Elsevier Science Publication Co. N.Y.).
3. Ibrahim, M. M. and Seehra, M. S., *ACS Div. Fuel Chem. Preprints*, 1992, 37, 1131-1140.
4. Seehra, M. S. and Ghosh, B. J. *Anal. Appl. Pyrolysis* 1988, 13, 209-220.

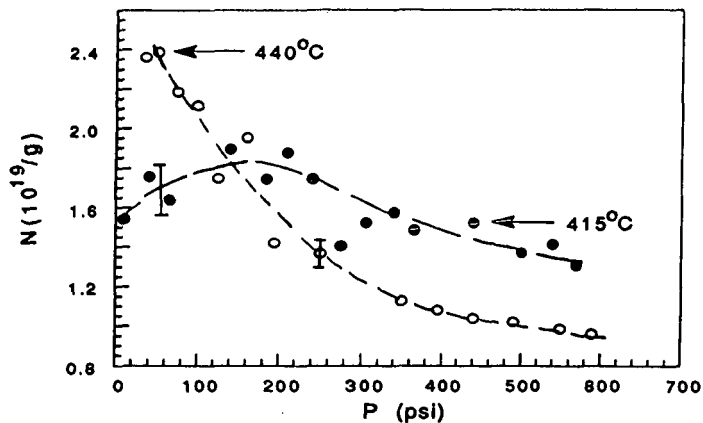


Fig. 1. Variation of N in Blind Canyon coal with  $H_2$  pressure at two temperatures.

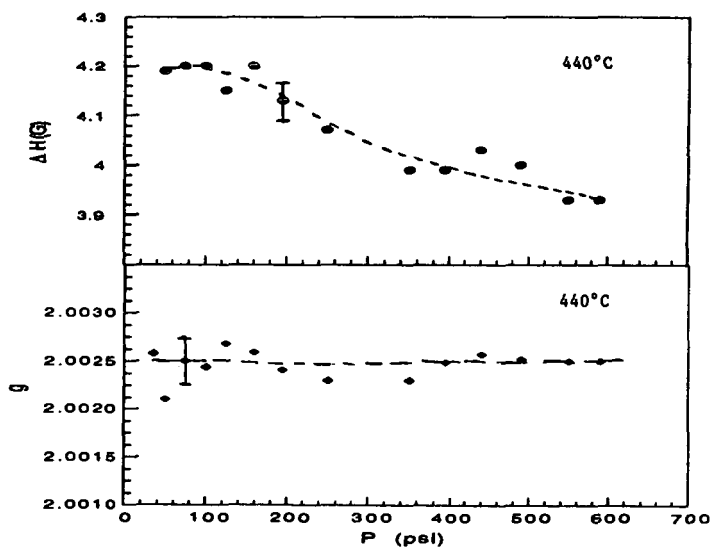


Fig. 2. Variations of the g-value and linewidth  $\Delta H$  with  $H_2$  pressure.

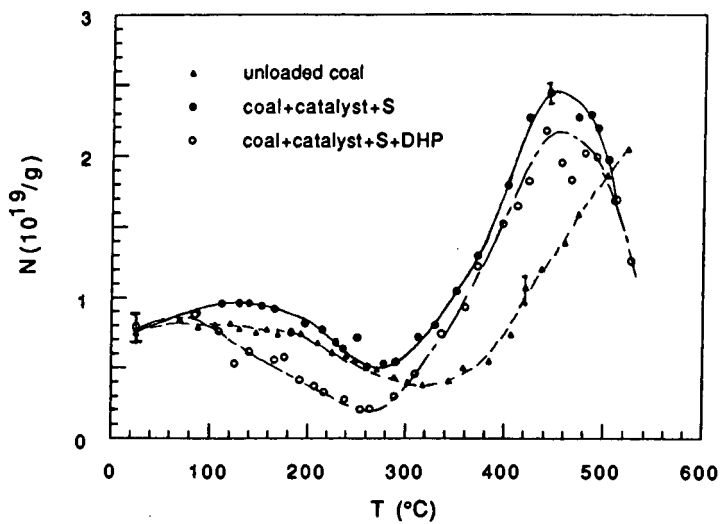


Fig. 3. Variation of free radical density  $N$  with temperature for unloaded and loaded coal. See text for details.

## AN EVALUATION OF PARTICLE SIZE MEASUREMENT TECHNIQUES FOR DISPERSED IRON CATALYSTS

V.U.S. Rao  
Department of Energy  
Pittsburgh Energy Technology Center  
P.O.Box 10940  
Pittsburgh, PA 15236.

Keywords: Highly dispersed catalysts, Direct coal liquefaction

### Abstract

Highly dispersed iron-based catalysts are being examined for the initial stage of direct coal liquefaction. Ultrafine (<10 nm) particles are produced by a variety of methods. Mössbauer spectroscopy, magnetometry, XAFS, electron microscopy, XRD line-broadening, and BET surface area measurement are used to estimate the particle size of the catalyst precursor and, in some instances, of the phases found consequent to the reaction process. With Mössbauer and magnetization techniques, data have to be obtained over a range of temperatures, usually from 4 K to 300 K. In addition, obtaining the particle size by Mössbauer spectroscopy requires a knowledge of the magnetic anisotropy energy. For some XRD lines, the broadening is a consequence of the presence of fault planes rather than crystallite size. The utility of the characterization techniques will be evaluated and comparative results that are available will be presented.

### Introduction

The use of inexpensive, ultrafine (<10 nm) iron catalysts for the initial stage of direct coal liquefaction [1] and the conversion of model compounds [2] has attracted attention in recent years. An advantage of using iron is that its disposal after use is not likely to present environmental problems. Hence the development of nanometer-sized, iron-based catalysts could eliminate the need for the expensive catalyst recovery step associated with the more conventional catalysts based on elements such as Mo, Co, Ni and W. Recent studies [1] indicate that ultrafine iron-based catalysts could be active for the first step in coal liquefaction, i.e., solubilization, in concentrations as low as 3,500 ppm with respect to coal.

To support research on the synthesis and testing of iron-based catalysts, it is necessary to have techniques to determine the composition, structural characteristics, and particle size distribution of the catalyst precursor, and more importantly, of the phases during and after the reaction. In the case of iron-based catalysts, the characterization techniques include Mössbauer spectroscopy, magnetometry, XAFS, electron diffraction, XRD, and BET surface area measurement. This paper will attempt to analyze the information that could be obtained from the above techniques and provide comparative results where available.

### Phases in Iron-Based Catalysts

It is frequently observed that an iron-based catalyst precursor that is not a sulfide is converted into a sulfided form during coal liquefaction if sufficient sulfur is present in the reaction mixture. The sulfur could be present in coal itself or added as  $H_2S$  or  $S$ .

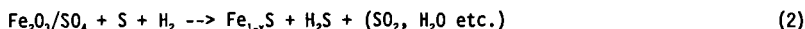
A significant fraction of the inorganic sulfur in coal is found as pyrite ( $FeS_2$ ) which is transformed into pyrrhotite ( $Fe_{1-x}S$ ) under liquefaction conditions according to



Depending on the reaction temperature and the partial pressures of  $H_2$  and  $H_2S$ , different pyrrhotites characterized by the value of  $x$  (typically .07-.12) are observed. The transformation of pyrite to pyrrhotite is slow below  $400^\circ C$  [3].

To investigate the influence of low concentrations of iron-based catalysts, a coal with a minimal quantity of pyrite must be used. For this reason, recent investigations [1] have focussed on the liquefaction of the low-pyrite Blind Canyon coal from Utah [4], which contains only 0.02 wt% pyritic sulfur, compared to 2.1 wt% in Illinois #6 and 0.17 wt% in Wyodak coal.

The approach to attaining ultrafine particle catalysts has been to increase the dispersion of the precursor. Complexes of iron [5], sulfate-promoted oxides [1], and carbides [6] have been used as precursors. In direct liquefaction, in the presence of sufficient sulfur, pyrrhotites are formed, for example [1],



For compositions ranging between  $FeS$  (troilite) and  $Fe_7S_8$  (monoclinic pyrrhotite), the compounds are referred to generally as pyrrhotites [7]. These include  $Fe_9S_{10}$ ,  $Fe_{10}S_{11}$ , and  $Fe_{11}S_{12}$  which are hexagonal, as is  $FeS$ . The hexagonal pyrrhotites are characterized crystallographically by their superstructures of the hexagonal NiAs structure.

It should be mentioned that the above phases are "low-temperature" pyrrhotites. Above  $308^\circ C$  and below its maximum melting point of  $1190^\circ C$ , pyrrhotite exhibits a rather wide homogeneity range as a single solid solution  $Fe_{1-x}S$  with the NiAs structure, extending from the stoichiometric  $FeS$  to a composition of approximately  $Fe_{0.9}S$ . Irrespective of the phases found at room temperature in used catalyst samples, it is evident that at liquefaction temperature ( $350-425^\circ C$ ) the solid solution  $Fe_{1-x}S$  is expected. Therefore, *in situ* characterization of the catalyst at reaction condition, although difficult to perform, is desirable.

### Mössbauer Relaxation Spectra

The technique of Mössbauer Spectroscopy can be used to detect iron-bearing phases in coal and in liquefaction catalysts [8]. Since the pyrrhotites show magnetic ordering, magnetic hyperfine splitting resulting in a sextet for each magnetically inequivalent Fe site is observed in the Mössbauer spectrum and can be used to identify the phases present [9, 10]. The spectra are frequently

interpreted in terms of three or four inequivalent Fe sites, which have internal magnetic fields in the range 230 to 300 kOe.

In magnetically ordered materials such as the pyrrhotites and  $\text{Fe}_3\text{O}_4$ , one would expect the sextet pattern to broaden and collapse to a quadruple doublet as the particle diameter decreases below a critical diameter,  $d_c$ . The corresponding particle volume is designated  $V_c$ . Below  $d_c$ , the particles exhibit superparamagnetic behavior owing to rapid relaxation of the particle spin system.  $V_c$  is given by

$$V_c = kT \ln(f_o/f_i) / K_a \quad (3)$$

where  $K_a$  is the magnetic anisotropy energy,  $f_i$  is the Larmor precession frequency of the  $^{57}\text{Fe}$  nucleus, and  $f_o$  is a frequency factor which has to be determined for each phase. The particle size distribution can be obtained from an analysis of the Mössbauer relaxation spectra [11].

From an analysis of the Mössbauer relaxation spectra, at temperatures from 10 K to 300 K, of a narrow-size range  $\text{Fe}_2\text{O}_3$  with the particle diameter centered at 3.2 nm, and using  $K_a = 0.55 \text{ J/m}^3$  [12], Huffman et al [10] have determined that  $f_o = 10^{12} \text{ s}^{-1}$ . The critical diameter  $d_c$  was determined to be 11.8 nm for  $\text{Fe}_2\text{O}_3$  at 300 K.

Using the above parameters, the particle size range of  $\text{Fe}_2\text{O}_3/\text{SO}_4$  precursors was determined [10] from the observed Mössbauer relaxation spectra. The size distribution showed that nearly 50% of the Fe was in particles that had diameters less than 11.8 nm. The methodology for determining particle size distribution of  $\text{Fe}_2\text{O}_3$  and related compounds such as  $\text{FeOOH}$  from Mössbauer relaxation spectra appears to have been established.

In contrast to the above, Mössbauer spectra of pyrrhotites, attributing the unresolved lines to superparamagnetic particles, have been reported in only a few instances [13-15]. Even in these cases, only room temperature spectra were reported; hence the interpretation of the unresolved lines is not unequivocal.

A possible reason for the paucity of confirmed Mössbauer relaxation spectra in pyrrhotites could be the high value of the magnetic anisotropy energy; for example,  $K_a = 10 \text{ J/m}^3$  for  $\text{Fe}_7\text{S}_8$  [16,17]. If  $f_o$  for  $\text{Fe}_7\text{S}_8$  is the same as that for  $\text{Fe}_2\text{O}_3$ , one estimates the critical diameter of  $\text{Fe}_7\text{S}_8$  as being  $d_c = 4 \text{ nm}$  at 300 K. It would appear that the samples that have been examined by Mössbauer spectroscopy do not have pyrrhotite particles whose diameter is less than 4 nm.

Recent progress in the synthesis of fine particles using novel techniques, such as the microemulsion method [18], provides the possibility of synthesizing uniform-size pyrrhotite particles in the 4 nm range. It would then be possible to determine  $f_o$  for the pyrrhotites as was done in the case of  $\text{Fe}_2\text{O}_3$ , and use the value of  $f_o$  thus derived to estimate the pyrrhotite particle size in liquefaction catalysts.

#### Magnetometry

In favorable cases particle size distribution can be determined from a measurement of magnetization in a range of applied fields and temperatures [19]. The technique is applicable when the particles in the sample are super-

paramagnetic. In the range of temperatures in which the sample exhibits superparamagnetic behavior, the magnetization is a function of  $H/T$  and obeys the Langevin equation:

$$M/M_s = L(M_s V H / kT), \quad L(x) = \coth x - 1/x \quad (4)$$

where  $M_s$  and  $M_s$  are, respectively, the saturation and spontaneous magnetizations per unit volume, and  $V$  is the volume of the particle.

Using a SQUID magnetometer, Ibrahim et al. [19] have determined the particle size distribution of  $Fe_2O_3/SO_4$  samples. A significant fraction of the sample consisted of particles in the 6-10 nm range. The results were in reasonable agreement with the particle size distribution obtained from Mössbauer relaxation spectra. The magnetometric method has not yet been used to determine the particle size of pyrrhotite samples.

#### XAFS Spectroscopy

Attempts are being made to use XAFS spectroscopy to obtain particle size information on Fe-based catalysts. The analysis of the XAFS spectra provides information on the interatomic distances and coordination numbers of the various neighbor shells to a given Fe atom. Spectra of bulk  $Fe_2O_3$  were compared with those of the fine-particle  $Fe_2O_3/SO_4$  catalyst precursor [10]. While the interatomic distances were similar for the two samples, the average coordination number of the catalyst precursor was significantly lower than that of the bulk sample. This indicated that the Fe atoms in the ultrafine particles that were on or near the surface had, on average, fewer Fe neighbors. Assuming a spherical shape for the particles, particle diameters in the range 1.2-1.8 nm were obtained. The significantly smaller particle diameter obtained using this technique was attributed to the possible nonspherical geometry of the particles.

#### XRD Line Broadening

The average crystallite dimension of small particles can be estimated from the line broadening of the Bragg peaks using the relation

$$d = 0.9 \lambda / B \cos \theta \quad (5)$$

where  $d$  = crystallite size,  $\lambda$  = wavelength,  $B$  = peak width at half-maximum, and  $\theta$  is the Bragg angle.

The technique has to be used with caution since faults or other defects can also result in line broadening [20]. Pollack and Spittler [21], who examined pyrrhotites produced in continuous liquefaction units, observed asymmetric Bragg peaks and attributed them to stacking disorder.

Ibrahim et al. [19] examined the XRD line broadening on the same sample of  $Fe_2O_3/SO_4$  on which the Mössbauer and magnetometric studies were performed and found good agreement between the particle size obtained by the different techniques.

## Electron Microscopy

Transmission electron microscopy (TEM), in combination with electron microdiffraction, is being employed to examine the particle size distribution and the structural characteristics of iron-based catalysts. In the case of  $\text{Fe}_2\text{O}_3/\text{SO}_4$ , the particle size distribution measured by TEM was in agreement with the results from Mössbauer, magnetometry, and XRD line broadening [10].

## BET Surface Area

Surface area measurement using the BET method requires a clean surface and is hence limited to the study of catalyst precursors. Pradhan et al. [1] found good correlation between the BET surface area and the average particle size from XRD and TEM on  $\text{Fe}_2\text{O}_3/\text{SO}_4$  samples. In the BET method, nitrogen adsorption at pressures upto 0.1 MPa is frequently used. Lambert et al. [22] have described a more sensitive BET method for measuring the surface area of pyrrhotites using krypton as the adsorbate at  $-196^\circ\text{C}$  and at pressures from 20 to 270 Pa.

## Conclusions

A number of characterization techniques are being successfully used to determine the particle size of iron-based catalyst precursors. In particular, the methods to measure the particle size of  $\text{Fe}_2\text{O}_3$  and related phases appear to be well established. There is a need to perform additional experimental and theoretical studies to develop methods to measure the particle size of pyrrhotites which seem to be catalytically very important. *In situ* techniques to measure particle size under reaction conditions have to be developed.

## Acknowledgements

The author would like to thank M. Farcasiu, S.S. Pollack, G.P. Huffman, F.E. Huggins, K.R.P.M. Rao, B. Ganguly, M.S. Seehra and C.D. Stinespring for helpful discussions.

## References

1. See for example, V.R. Pradhan, J.W. Tierney, and I. Wender, ACS Fuel Div. Preprints, 37, 254 (1992).
2. M. Farcasiu, C. Smith, V.R. Pradhan, and I. Wender, Fuel Process. Tech. 29, 199 (1991).
3. G.M. Schwab and J.J. Philnis, J. Am. Chem. Soc. 69, 2588 (1947).
4. Available from the Penn State Coal Research Bank.
5. D.E. Herrick, J.W. Tierney, I. Wender, G.P. Huffman and F.E. Huggins, Energy and Fuels 4, 231 (1990).
6. F. Derbyshire and T. Hager, ACS Fuel Chemistry Preprints, 37, 312 (1992).
7. L.F. Power and H.A. Fine, Minerals Sci. Eng. 8, 106 (1976).
8. See for example, P.A. Montano, Magn. Res. Rev. 7, 175 (1982).
9. J.C. Ward, Rev. Pure and Appl. Chem. 20, 175 (1970).
10. G.P. Huffman, B. Ganguly, J. Zhao, K.R.P.M. Rao, N. Shah, Z. Feng, M.M. Taghiei, F. Lu, I. Wender, V.R. Pradhan, J.W. Tierney, M.S. Seehra, M.M. Ibrahim, J. Shabtai, and E.M. Eyring, Energy and Fuels, in press.
11. V.U.S. Rao, F.E. Huggins and G.P. Huffman, J. Appl. Phys. 50, 2408 (1979).
12. A.M. van der Kraan, Phys. Stat. Sol. (a) 18, 215 (1973).

13. P. Bussiere, A. Newman and B.K. Sharma, *Hyperfine Interactions* **42**, 1211 (1988).
14. M. Jamond, R. Bacaud, P.Bussiere, H. Charcosset, and B. Nickel-Pepin-Donat, **52**, 297 (1989).
15. W. Sihao, J. Keyu, W. Zhaoming, G. Jinsheng, W. Youqing, W. Zhen, L. Diwan, Y. Yongquin, and Z. Changgen, *Hyperfine Interactions* **58**, 2617 (1990).
16. M.J. Besnus, G. Munsch, A.J.P. Meyer, *J. Appl. Phys.* **39**, 903 (1968).
17. K. Adachi and K. Sato, *J. Appl. Phys.* **39**, 1343 (1968).
18. See for example, J.C. Linehan, R.M. Beam, D.W. Matson, J.L. Fulton, and A.E. Crump, *ACS Fuel Div. Preprints*, **37**, 488 (1992).
19. M.M. Ibrahim, J. Zhao, and M.S. Seehra, *J. Mater. Res.* **7**, 1856 (1992).
20. J.M. Stencel, V.U.S. Rao, J.R. Diehl, K.R. Rhee, A.G. Dhere, and R.J. DeAngelis, *J. Catal.* **84**, 109 (1983).
21. S.S. Pollack and C.A. Spitler, *American Mineralogist* **66**, 1258 (1981).
22. J.M. Lambert, Jr., P.L. Walker, Jr., A.J. Perrotta, J.P. McCullough and H. Beuther, *Fuel* **62**, 1474 (1983).

## Mössbauer Studies of Fe-Based Ultrafine Coal Liquefaction Catalysts

Bhaswati Ganguly, Frank E. Huggins, K. R. P. M. Rao, and G. P. Huffman  
233 Mining and Mineral Resources Building  
University of Kentucky  
Lexington, Kentucky 40506.

### **ABSTRACT:**

$^{57}\text{Fe}$  Mössbauer spectroscopy has been used to investigate a variety of ultrafine iron-based direct coal liquefaction catalysts having either  $\text{Fe}_2\text{O}_3$  or  $\text{FeOOH}$  structure. The Mössbauer spectra of these catalysts showed pronounced superparamagnetic effects. The superparamagnetic relaxation spectra were analyzed as a function of temperature using a novel fitting model to determine the particle size distribution for these catalysts<sup>(1)</sup>. The resulting size distributions are in the nanometer range and agree reasonably well with size information obtained by Scanning Transmission Electron Microscopy (STEM), SQUID magnetometry, and X-Ray Diffraction (XRD).

### **INTRODUCTION:**

In recent years, there has been renewed interest in the use of iron-based catalysts for direct coal liquefaction (DCL)<sup>(2-7)</sup>. In their as-prepared form prior to liquefaction, such catalysts are normally in the form of highly dispersed iron oxides and oxyhydroxides. The Mössbauer spectra of such fine iron oxide and oxyhydroxide particles exhibit pronounced superparamagnetic relaxation effects, which have been extensively investigated<sup>(8-14)</sup>. Many of these studies of the superparamagnetic relaxation behavior of small particles have been based on an average particle volume or diameter<sup>(8,11-14)</sup>. Kundig et al.<sup>(9)</sup> were the first investigators to describe a method for determining the particle-size distribution of  $\alpha\text{-Fe}_2\text{O}_3$  by determining the percentage of the Mössbauer spectra in the form of magnetic hyperfine components as a function of temperature. The difficulty with this approach is that Mössbauer spectra are assumed to have sharp transitions from quadrupole doublets to magnetics on lowering the temperature. However, this transition occurs gradually, over a range of temperatures. We have used a similar technique to estimate particle size distributions, with a novel model for fitting the Mössbauer spectra that incorporates a superparamagnetic component as well as magnetic hyperfine and quadrupole components.

### **RESULTS AND DISCUSSIONS:**

When particles are small enough to behave superparamagnetically, the rapid relaxation of the particle spin system gives rise to complicated relaxation spectra which are superpositions of broadened magnetic hyperfine spectra, quadrupole doublets, and intermediate superparamagnetic (spm) spectra. Many papers have been written on the dependence of the shape of the Mössbauer spectra on the relaxation time<sup>(15-17)</sup>. As shown by such authors as Wickman<sup>(17)</sup>, the relaxation time dependent Mössbauer spectrum is given by:

$$I(\omega) = \sum_{i=1}^6 \frac{K_i [(1 + \tau \Gamma_i) P + QR]}{P^2 + Q^2} \quad (1)$$

where P, Q, R for a zero external magnetic field have the form

$$\begin{aligned} P &= \tau [\Gamma_i^2 - (\Delta - \omega)^2 + \delta_i] + \Gamma_i \\ Q &= \tau (\Delta - \omega) \\ R &= (\Delta - \omega)(1 + 2\tau \Gamma_i) \\ \delta_i &= \frac{1}{2}(\omega_{7,-i} - \omega_i), \quad \Delta = \frac{1}{2}(\omega_{7,-i} + \omega_i) \end{aligned} \quad (2)$$

where  $\tau$  is the relaxation time in sec,  $\omega$  is the frequency (in  $\text{sec}^{-1}$ ) corresponding to the Doppler energy of each data point in the Mössbauer spectrum, and  $\omega_i$  are the frequencies (in  $\text{sec}^{-1}$ ) corresponding to the six allowed transitions between the Zeeman split energy levels.  $K_i$  are the Clebsch-Gordon coefficients with  $K_6 = K_1 = 3$ ,  $K_5 = K_2 = 2$ , and  $K_4 = K_3 = 1$  for zero external magnetic field.  $\Gamma_i$  is the natural line width in  $\text{sec}^{-1}$  and is taken to be the same for all transitions.

A novel method of fitting the spectra is developed, based on the fact that the shape of the Mössbauer spectrum changes with the relaxation time, which in turn can be related to the size of the particle<sup>(1)</sup>. Figure 1 shows the theoretical Mössbauer spectra of  $\alpha\text{-Fe}_2\text{O}_3$  at room temperature as a function of particle-size, derived from Equation 1. It can be seen that at a given temperature, particles with a diameter exceeding some critical diameter,  $d_M$  exhibit a magnetic hyperfine spectrum, while particles with a diameter less than some other critical value,  $d_Q$ , exhibit a quadrupole doublet. Particles having diameters  $d$  such that  $d_Q < d < d_M$  exhibit spm relaxation spectra that are neither magnetic nor quadrupole in nature. A typical iron oxide catalyst will normally have a size distribution such that, over some range of temperature, some particles fall into all three size classifications, yielding spectra that are a mixture of magnetic, quadrupole, and spm relaxation spectra. The model consists of fitting the spectra with one or more magnetic hyperfine components corresponding to particles with  $d \geq d_M$ , one or more quadrupole components, representing particles with  $d < d_Q$ , and a single spm relaxation spectrum, representing particles for which  $d_Q < d < d_M$ .

To determine size distributions, the samples are run at several temperatures. The spectrum at each temperature is analyzed using the model mentioned above. The percentage of iron contributing to the magnetic hyperfine component is taken as the percentage of iron contained in particles of volume greater than the critical volume  $V_c$  at that temperature. Figure 2 shows an example of a fit obtained for a sulfated  $\text{Fe}_2\text{O}_3$  (run at room temperature) using this model, and the size distribution obtained by running this sample at different temperatures. The concept of assigning the percentage of iron contributing to the magnetic hyperfine spectra to particles exceeding a critical volume is similar to the approach of Kundig et al<sup>(8)</sup>. However, the incorporation of a spm relaxation component enables the magnetic and quadrupole components to be more accurately fit, leading to a correct magnetic percentage, rather than one which artificially incorporates a substantial amount of the spm spectral absorption. A more detailed discussion of this method and its application in determining the size distributions and structures

of a variety of iron-based coal liquefaction catalysts will be published elsewhere<sup>(1,18)</sup>.

#### SUMMARY:

Mössbauer spectroscopy has been used to derive the size dispersion of a variety of ultrafine iron based direct coal liquefaction catalysts which show superparamagnetic behavior. A novel method of fitting the spectra was developed, in which the larger particles were represented by magnetic hyperfine components, the smaller particles by quadrupole doublets, and particles of intermediate volume by a spm relaxation spectrum. The size distributions were determined by measuring the magnetic hyperfine percentage as a function of temperature, each temperature corresponding to a critical diameter required for a magnetic Mössbauer spectrum. Comparison of the size distributions determined in this manner to size information obtained from TEM, SQUID magnetometry and XRD gave reasonable agreement<sup>(1)</sup>. The advantage of this fitting model is that it does not assume any kind of standard distribution, but numerically fits the data itself as a combination of magnetic, quadrupole and spm component. Moreover, it is possible to obtain a rough estimate of the size distribution from a spectrum obtained at a single temperature, provided the spectrum exhibits a reasonable amount of all three spectral components (magnetic, quadrupole, and spm).

#### ACKNOWLEDGEMENTS:

This research was supported by the U.S. Department of Energy under DoE contract No. DE-FC22-90-PC90029, as part of the research program of the Consortium for Fossil Fuel Liquefaction Science. We are grateful to Bernard M. Kosowski of Mach I, Inc., for providing the sample used in this research.

#### REFERENCES:

1. Ganguly, B., Hugging, F.E., Rao, K.R.P.M., and Huffman, G.P.; "Determination of the Size of Iron Oxide Catalysts from Superparamagnetic Mössbauer Relaxation Spectra"; submitted to the Journal of Catalysis.
2. Suzuki, T.; Yamada, O.; Takehashi, Y.; Watanabe, Y., Fuel Process Technol., 1985, 10, 33.
3. Tanabe, K.; Yamaguchi, T.; Hattori, H.; Sanada, Y.; Yokoyama, S., Fuel Process. Technol., 1984, 8, 117.
4. Herrick, D.E.; Tierney, J.W.; Wender, I.; Huffman, G.P.; and Huggins, F.E., Energy & Fuels, 1991, 4, 231.
5. Pradhan, V.R.; Tierney, J.W.; Wender, I.; Huffman, G.P.; Energy & Fuels, 1991, 5, 497.
6. Cook, P.S.; Cashion, J.D., Fuel, 1987, 66, 661.
7. Huffman, G.P.; Huggins, F.E.; Ganguly, B.; Shah, N.; Taghiei, M.M.; Hager, G.T., Proceedings, 1991 International Conference on Coal Science, Newcastle, England, Ed. Int. Energy Agency, Butterworth-Heinemann Ltd., 1991, 826.
8. Shinjo, Teruya, J. Phys. Soc. Jap., 1966, 21(5), 917.
9. Kundig, W., Bommel, H., Constabaris, G., Lindquist, R.H., Phys Rev., 1966, 142, 327.
10. Van der Kraan, A.M., Phys. Stat. Sol. (a), 1973, 18, 215.

11. Vertes, A., Huang, T.C., Van der Hoff, J.W., Lazar, K., Bennetech, M., Reiff, W., Radiochem. Radioanal. Lett., 1983, 59(5-6), 307.
12. Van der Kraan, A.M., Thesis (1972).
13. Rodmacq, B., J. Phys. Chem. Solids, 1984, 45(11-12), 1119.
14. Roggwiler, P.; Kundig, W., Sol. State Comm., 1973, 12, 901.
15. Van der Woude, and Dekker, A.J., Phys. Stat. Sol., 1966, 13, 181.
16. Blume, M., and Tjon, J.A., Phys. Rev., 1968, 165, 446.
17. Wickman, H.H., "Mössbauer Effect Methodology", Vol II (ed. I.J. Gruverman), 1966, pp 39, Plenum Press, NY.
18. Huffman, G.P., et al.; "Structure and Dispersion of Iron-Based Catalysts for Direct Coal Liquefaction"; Energy and Fuels, in press.

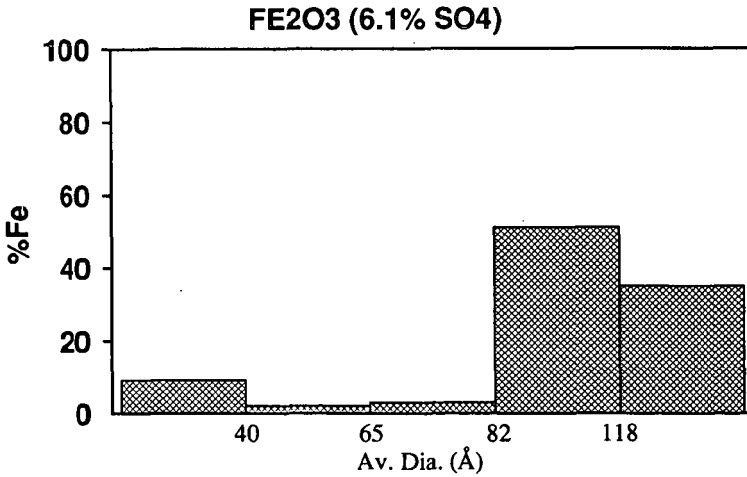
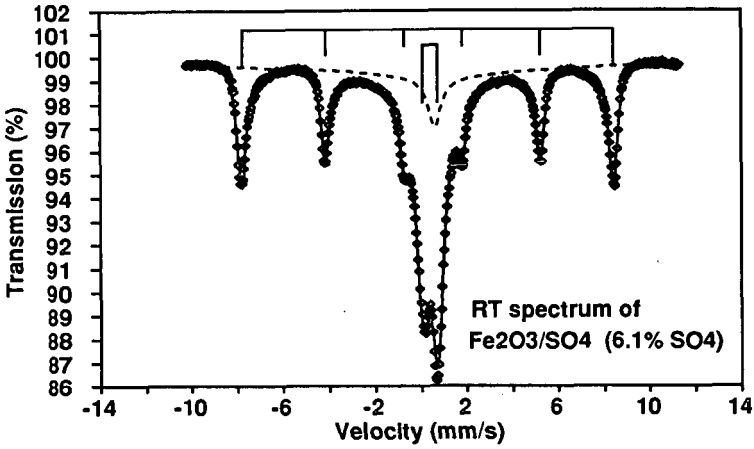


Figure 2. An example of a superparamagnetic fit and the size distribution obtained by running the sample at several temperatures.

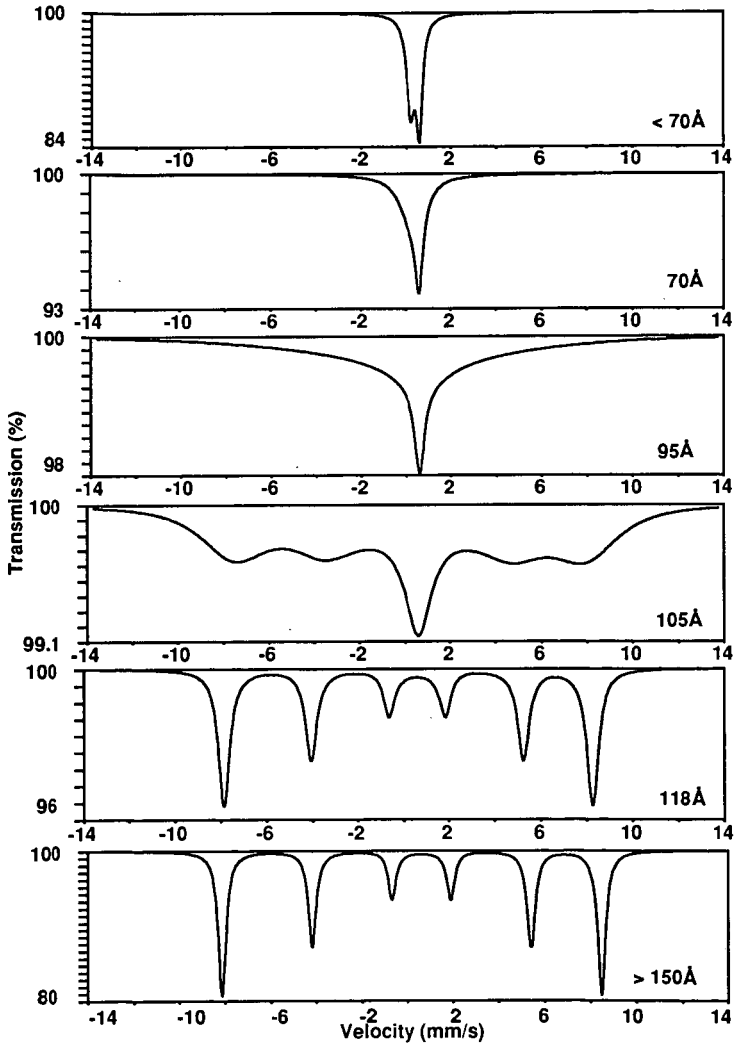


Figure 1. Theoretical plots of relaxation spectra of Fe<sub>2</sub>O<sub>3</sub> at room-temperature as a function of particle size.

## STRUCTURE AND PHASE TRANSITION OF AN ULTRAFINE IRON OXIDE CATALYST

J. Zhao, Z. Feng, F. E. Huggins, N. Shah and G. P. Huffman\*  
233 Mining and Mineral Research Building  
University of Kentucky  
Lexington, KY 40506

### I. Abstract

The structure and phase transitions of an iron oxide catalyst with average particle diameter of 30Å have been examined by means of X-ray absorption fine structure (XAFS) spectroscopy, thermal gravimetric analysis (TGA), Mossbauer spectroscopy, and transmission electron microscopy (TEM). The structure is found to be an FeOOH with surface iron ions at coordination unsaturated (CUS) sites or Lewis acid sites. At annealing temperatures of 250 to 350°C, the sample only partly converts to larger  $\alpha$ -Fe<sub>2</sub>O<sub>3</sub> particles. The conversion rate is greatly accelerated if the sample is exposed in air for several days. The results indicate that the 30Å particles become linked by water molecules adsorbed at the CUS sites after air exposure. At elevated temperature, these water molecules are evolved from between the particles, facilitating both agglomeration of the particles and phase transition to  $\alpha$ -Fe<sub>2</sub>O<sub>3</sub>.

### II. INTRODUCTION

In recent years, significant efforts have been made to produce highly dispersed iron catalysts for direct coal liquefaction (DCL), in order to increase surface area and minimize catalyst loading. Improved dispersion and conversion rate have been obtained by modifying the surface structure by adding small amount of sulfur and other elements to the catalyst [1]. Studies have shown that, at the sulfated iron oxide (Fe<sub>2</sub>O<sub>3</sub>/SO<sub>4</sub>) surface, coordination unsaturated (CUS) sites or Lewis acid sites are formed [2]. It has been suggested that a sulfated surface may prevent agglomeration of small catalyst particles during reaction [1]. The activity is also found to be sensitive to the surface conditions as determined by the moisture content of the catalysts [1,3]. These observation indicate that the surface structure and surface conditions are crucial for catalyst performance, although the exact mechanisms are still unclear.

### III. EXPERIMENTAL

The catalyst sample (NANOCAT™) is manufactured by Mach I, Inc. In addition to the as-received sample, several samples were prepared by annealing the as-received sample in air for 24 hrs at temperatures from 250 to 500°C. To observe the effect of moisture, part of the as-received sample was first exposed in air for five days at room temperature, and subsequently annealed at 250°C in air for 24 hrs.

X-ray absorption spectra were collected at the National Synchrotron Light Source (NSLS) on beam line X-19A at Brookhaven National Laboratory. All spectra were collected in the transmission mode and at liquid-nitrogen temperature.

Transmission electron micrographs and micro-diffraction patterns were obtained with a Hitachi H800 NA microscope. The operating voltage was set at 200kV for all samples.

Mössbauer spectra were recorded with a constant acceleration spectrometer. The

radioactive source consists of ~50 mCi of  $^{57}\text{Co}$  in Pd matrix. Spectra were recorded at 10 K with an Air Products displax cryogenic system.

Thermogravimetric analysis (TGA) were performed with a Seiko 320 TGA/DSC system.

### III. RESULTS

#### *Structure of the 30Å Catalyst*

The EXAFS radial structure functions (RSF) of the 30Å catalyst and several iron oxides and oxyhydroxides are shown in Figure 1. The position of the first Fe shell is close to that for oxyhydroxides. Least squares fitting for the 30Å catalyst gives first Fe coordination shell at 3.01 Å. By comparing with the first Fe shell distances of iron oxides (2.92-2.95 Å) and iron oxyhydroxides (3.01-3.05 Å), we conclude that the structure of the 30Å catalyst is oxyhydroxide ( $\text{FeOOH}$ ) like. The x-ray absorption near edge structure (XANES) for the 30Å catalyst is also similar to that for the oxyhydroxides.

Although both EXAFS and XANES for the 30Å catalyst indicates an  $\text{FeOOH}$  structure in which iron ions are coordinated by total six oxygens or hydroxyl groups, the intensity of pre-edge structure (Figure 2) of the catalyst is 1.7 times that for those octahedral oxides and oxyhydroxides, indicating that part of the iron ions have coordination less than six [4]. After an extended period of exposure of the sample to air, the average coordination number is increased as indicated by the decrease of the pre-edge peak. Therefore, these low coordination sites are likely to be at the particle surface. These sites, created by dehydroxylation on the oxide surface, are also known as CUS (coordination unsaturated) sites or Lewis acid sites. More details of the structure analysis are given in Ref. 5.

#### *Effect of Annealing*

The TGA curve for the fresh 30Å catalyst is compared to that of  $\alpha\text{-FeOOH}$  in Figure 3. At temperatures < 300°C,  $\alpha\text{-FeOOH}$  converts to  $\alpha\text{-Fe}_2\text{O}_3$  by releasing  $\text{H}_2\text{O}$ , resulting in 11% weight loss. For  $\alpha\text{-FeOOH}$ , the phase transition occurs between 200 to 270°C, as shown in the figure. For the 30Å catalyst, although a ~12% weight loss at  $T > 700^\circ\text{C}$  suggests that the above reaction does occur, no clear phase change was observed from room temperature up to 900°C.

TEM micrograph of the sample after 250°C annealing for 24 hrs indicates the coexistence of two phases (Figure 4a); the small particle 30Å  $\text{FeOOH}$  phase and a larger particle ( $d \approx 150\text{Å}$ )  $\alpha\text{-Fe}_2\text{O}_3$  phase. The volume fraction and average particle size of the larger  $\alpha\text{-Fe}_2\text{O}_3$  particles increases with annealing temperature. However, a considerable percentage of the 30Å particles appears to be unchanged even after 24 hrs annealing at temperatures up to 350°C which would completely convert  $\alpha\text{-FeOOH}$  to  $\alpha\text{-Fe}_2\text{O}_3$ . At annealing temperatures of 400°C and higher, larger particles dominates and the particle size becomes uniform. The phase transition rate is greatly accelerated if the 30Å catalyst is exposed to moist air before annealing. After annealing at 250°C in air for 24 hrs, the moisture exposed sample mainly consists of larger particles with diameters of ~150Å, as shown in TEM micrographs (Figure 4b).

The percentages of the two iron phases in the annealed samples are determined by Mossbauer spectroscopy [6]. After annealing at identical conditions, the as-received sample consists of 65% 30Å  $\text{FeOOH}$  phase and 34%  $\alpha\text{-Fe}_2\text{O}_3$  phase, whereas the air-exposed sample consists of 26% 30Å  $\text{FeOOH}$  phase and 73%  $\alpha\text{-Fe}_2\text{O}_3$  phase.

### IV. DISCUSSION

The difference of phase transition rates between the as-received and air exposed 30Å

FeOOH catalysts at elevated temperature is attributed to their surface conditions. A surface layer with CUS sites can effectively prevent not only the agglomeration of the small 30Å FeOOH particles, but also dehydroxylation in the sample bulk, thereby slowing down the phase transition. However, after moisture exposure, the small 30Å particles become linked by adsorbed H<sub>2</sub>O molecules on the surface. At elevated temperature, these water molecules are evolved from the particle joints, leading to agglomeration and phase transition to  $\alpha$ -Fe<sub>2</sub>O<sub>3</sub>. A diagram of this process is shown in Figure 5. It appears that the phase transition to  $\alpha$ -Fe<sub>2</sub>O<sub>3</sub> occurs immediately after the agglomeration takes place, as indicated by the TEM and Mössbauer results, which show no trace of larger FeOOH particles. At annealing temperatures below 350°C, the rate of phase transition is determined mainly by the coverage of the water molecules adsorbed on the particle surface. Agglomeration and phase transition take place mainly in those particles linked by water molecules. At T > 350°C, the transition to  $\alpha$ -Fe<sub>2</sub>O<sub>3</sub> is due to the dehydroxylation inside of the 30Å catalyst particle. It should be noted that only those H<sub>2</sub>O molecules adsorbed on the CUS sites may remain on the particle surface at T > 250°C or higher. Physisorbed H<sub>2</sub>O molecules, since their bonding to the particle surface is much weak, will be detached from the particle surface at temperature well below 250°C.

#### Acknowledgement

The support of the U.S. Department of Energy for this research under contract No. DE-FC22-90029 is gratefully acknowledged. This investigation was carried out as part of the cooperative research program of the Consortium for Fossil Fuel Liquefaction Science.

We would also like to acknowledge Dr. Aurora Rubel and Mr. Larry Rice, both at University of Kentucky, for their assistance with the TGA and TEM measurements.

#### References

1. Pradhan, V. R.; Tierney, J. W.; Wender, I., and Huffman, G. P., *Energy & Fuels*, **5**, 497 (1991).
2. Jin, Tuo; Yamaguchi, Y.; Tanabe, K., *J. Phys. Chem.* **90**, 4795 (1986).
3. Farcasiu, M., unpublished results.
4. Roe, A. L., et al., *J. Am. Chem. Soc.* **106**, 1676 (1984).
5. Zhao, J.; Huggins, F.E.; Feng, Z.; Lu, F.; Shah, N.; and Huffman, G. P.; to be published.
6. Feng, Zhen; Zhao, J.; Huggins, F.E.; and Huffman, G.P. to be published.

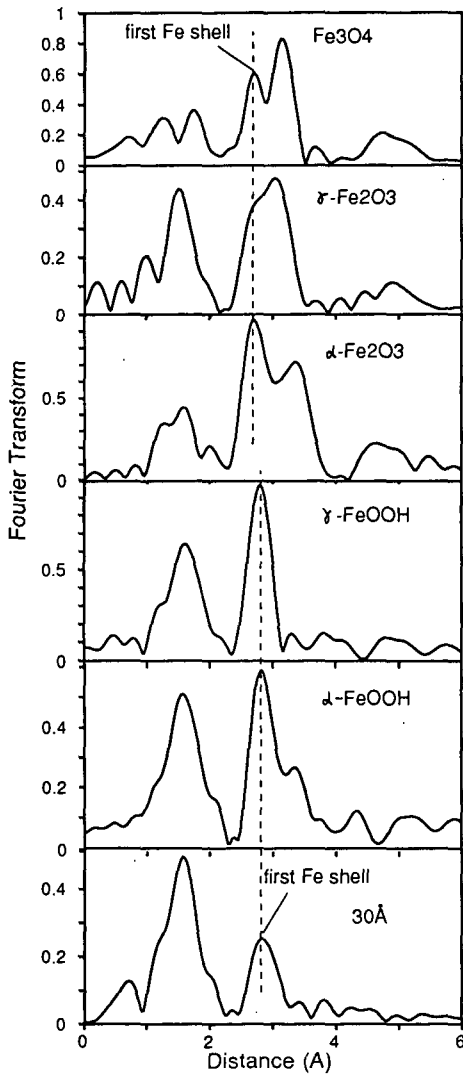


Figure 1. EXAFS RSF's for the 30Å catalyst and model compounds.

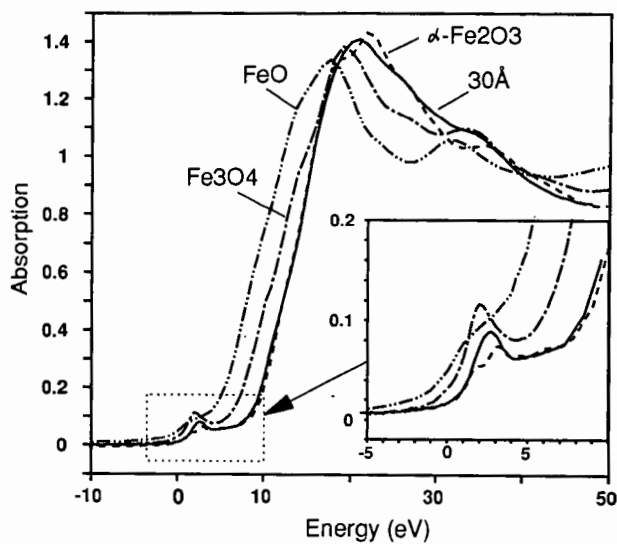


Figure 2. XANES pre-edge structures of the 30Å catalyst and model compounds.

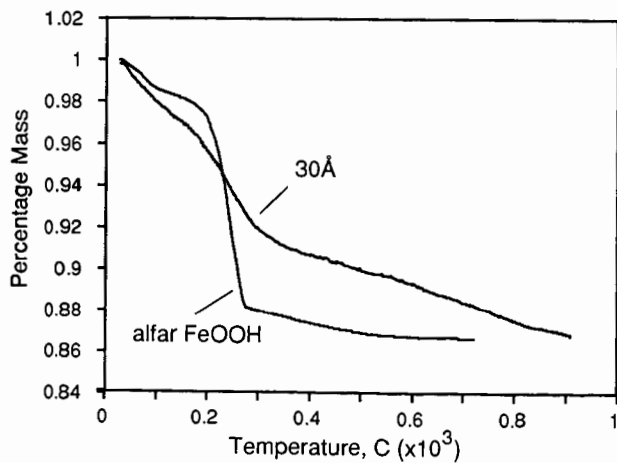


Figure 3. Thermogravimetric analysis for α-FeOOH and the 30Å catalyst.

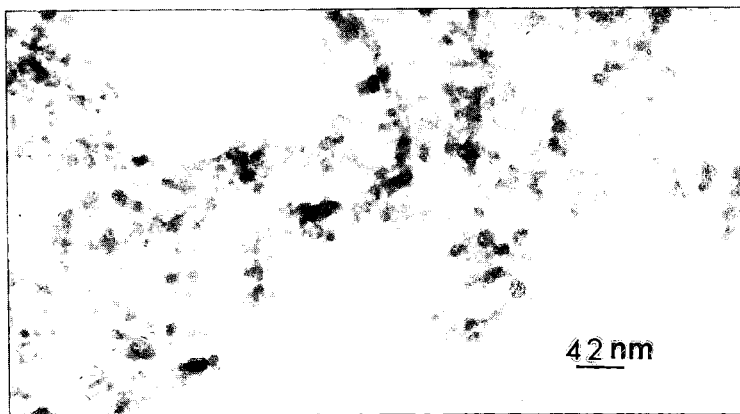
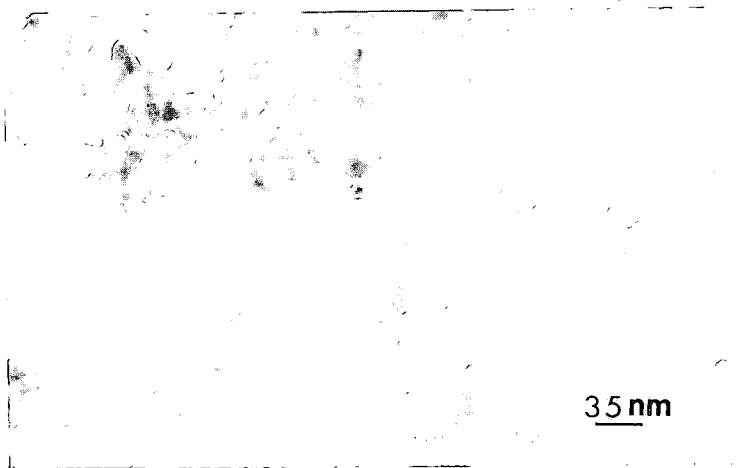


Figure 4. TEM micrographs of the as-received 30Å catalyst (top) and moist air exposed 30Å catalysts (bottom), after annealed at 250C for 24hrs.

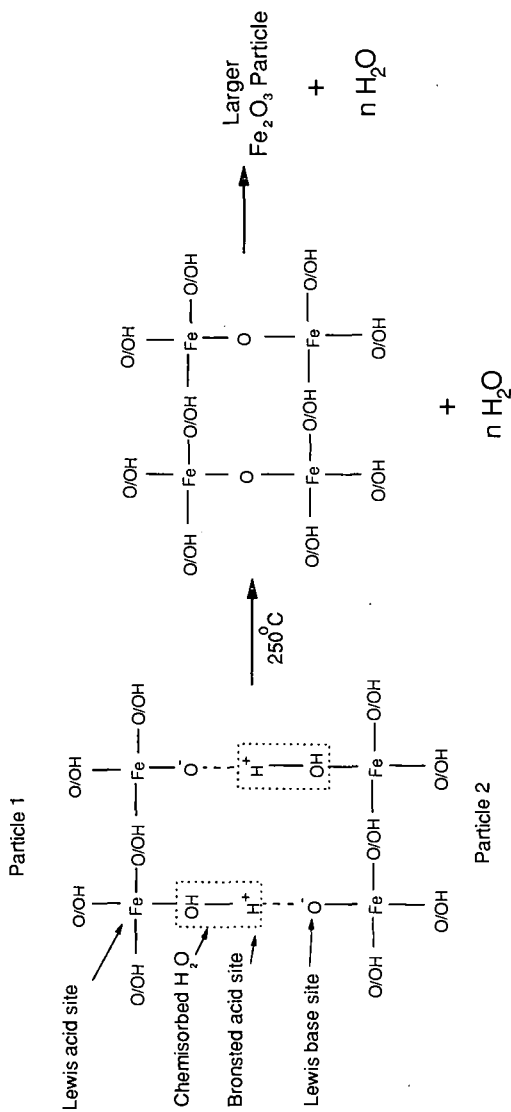


Figure 5. Proposed scheme of agglomeration and phase transition of the 30Å catalyst.

## CHARACTERIZATION OF SULFIDED IRON CATALYSTS

Ram Srinivasan, Robert A. Keogh, and  
Burtron H. Davis

Center for Applied Energy Research  
University of Kentucky  
3572 Iron Works Pike  
Lexington, KY 40511

### ABSTRACT

An ultrafine iron oxide and a FeOOH sample were sulfided using a H<sub>2</sub>S/N<sub>2</sub> mixture at room temperature. The sulfided samples obtained at room temperature were also run in a microautoclave reactor using a temperature of 200°C for 30 min. using a H<sub>2</sub>S/H<sub>2</sub> atmosphere and tetralin as a solvent. The sulfided iron catalysts were characterized by TEM and EDAX.

### INTRODUCTION

Coal liquefaction can be accomplished by thermolysis; however, it was quickly realized that improved yields could be obtained through the use of catalyst (1). One of the first catalysts studied was an iron oxide in one of several forms (1-3) and is still widely used today (4).

Initial coal liquefaction products may have very high molecular weights. These initial dissolution products are so large that they will not be able to diffuse into the smaller pores of most heterogeneous catalysts. It is therefore desirable that catalysts, especially those used in the reactor which involve the initial dissolution reactions, have the active component on the geometric surface of the catalyst particle. It is also desirable that these catalysts have a high surface area in order to obtain a high rate of conversion. These two factors indicate that the desirable catalyst will be one which is comprised of colloidal or smaller nonporous individual particles.

Although a large volume of work has been carried out to determine product yield, reaction conditions, etc., very limited work has been available in terms of microscopic characterization of catalyst powders. The results presented in this work used an ultrafine  $\gamma$ -Fe<sub>2</sub>O<sub>3</sub> (S.A. = 270 m<sup>2</sup>/g) and an  $\gamma$ -FeOOH precursor which have been sulfided at room temperature and at higher temperatures. The characterization of these catalysts are presented.

### EXPERIMENTAL

The  $\gamma$ -Fe<sub>2</sub>O<sub>3</sub> and  $\gamma$ -FeOOH were hydrated in a chamber saturated with H<sub>2</sub>O prior to sulfidation. Both catalyst precursors showed approximately a 28 wt.% gain in 48 hours. The dry samples could not be sulfided at room temperature. The catalyst precursors were sulfided using 5 mole % H<sub>2</sub>S in nitrogen. Approximately 2g of the hydrated precursors were placed in a flask containing ca. 20g of tetralin and the H<sub>2</sub>S/N<sub>2</sub> mixture was bubbled through the catalyst/tetralin slurry. The resulting sulfided samples were stored in the flask under the H<sub>2</sub>S/N<sub>2</sub> atmosphere prior to running at 200°C in the batch autoclave and

analysis. Aliquots of the sulfided catalysts/tetralin slurry were transferred to a 25cc microautoclave reactor. The reactor was pressurized to 800 psig (ambient) with a 10% H<sub>2</sub>S in H<sub>2</sub> and placed in a fluidized sand bath. The reaction was run at 200°C for 30 min.

The samples for electron transmission microscopy (TEM) analysis were prepared in the glovebox in flowing nitrogen. A few drops of the sample were transferred to a 100 cc beaker and washed with ethanol twice, and then ultrasonically agitated in ethanol. A drop of this suspension was placed on a carbon coated 200 mesh copper grids. Ethanol evaporated leaving a thin film of particles on the grids. These TEM grids were then transferred to a vacuum desiccator until they were inserted into the microscope. While transferring the samples into the microscope the samples were exposed to the atmosphere less than a minute.

For TEM analysis, a Hitachi H800 NA scanning microscope was used at 200 kV. Microdiffraction and energy-dispersive X-ray (EDX) analyses were carried out in a nanoprobe mode (5 nm). This implies that the microdiffraction and EDX data obtained were from a 5 nm regions of the sample. This microscope is equipped with a silicon-lithium diode detector (Link) and a multi-channel analyzer (Tracor 500). The X-rays emitted by the specimen were collected in the range 0-20 KeV for 60 seconds.

## RESULTS AND DISCUSSION

### Room Temperature Sulfidation of $\gamma$ -FeOOH

Many agglomerated large "blobs" were seen for this sample. Microdiffraction patterns could not be obtained from these blobs. A typical electron micrograph is presented in Figure 1. EDX from these blobs yielded very strong FeK $\alpha$  and SK $\alpha$  lines. These large blobs easily disintegrated under the beam giving rise to a good dispersion of small hexagonal particles. A representative micrograph from such a dispersed area of the sample is presented in Figure 2. EDX from these particles showed only FeK $\alpha$ , and these individual particles yielded microdiffraction patterns.

### $\gamma$ -FeOOH Sulfidation at 200°C

Contrary to the results of the above sample at room temperature, this sample contains large, thin hexagonal iron sulfide crystals. A typical micrograph of this sample is presented in Figure 3. EDX analysis of the large hexagonal crystals yielded strong signals for both FeK $\alpha$  and SK $\alpha$  lines. A typical electron microdiffraction pattern obtained from one such crystal is presented in Figure 4. This microdiffraction patterns indicates that the crystal is Fe<sub>7</sub>S<sub>8</sub> in [001]<sub>hcp</sub> orientation. Microdiffraction patterns and EDX data from several hexagonal particles consistently proved that these large hexagonal crystals are Fe<sub>7</sub>S<sub>8</sub>.

### Room Temperature Sulfidation of $\gamma$ -Fe<sub>2</sub>O<sub>3</sub>

This sample contains regions of free sulfur and needle-shaped  $\alpha$ -Fe<sub>2</sub>O<sub>3</sub>. A region containing long needles of  $\alpha$ -Fe<sub>2</sub>O<sub>3</sub> is shown in Figure 5. Electron microdiffraction pattern obtained from these particles indicated that these sticks are  $\alpha$ -Fe<sub>2</sub>O<sub>3</sub>. EDX data from these needles showed only FeK $\alpha$ . A typical region containing free sulfur in the form of flowers is shown in Figure 6. EDX from this region showed only sulfur. Also, regions containing hexagonal dense sulfur particles were evident as shown in Figure 7. No evidence for iron sulfide particles was obtained. Consequently, it appears that the  $\alpha$ -Fe<sub>2</sub>O<sub>3</sub> converts H<sub>2</sub>S to

S plus H<sub>2</sub>, more likely, that the sulfide formed is oxidized during the brief exposure to air during sample transfer.

#### $\gamma$ -Fe<sub>2</sub>O<sub>3</sub> Sulfidation at 200°C

This sample contained regions of both long, rectangular particles and the large hexagonal particles. As before, the large, thin hexagonal particles were found to be Fe<sub>7</sub>S<sub>8</sub> crystals both by electron microdiffraction and EDX analyses. A bright field electron micrograph (Figure 8) shows the presence of both these two kinds of particles. A typical electron microdiffraction pattern obtained from one of the large hexagonal crystals is presented in Figure 9, which is [001]<sub>hcp</sub> orientation. No free sulfur could be identified as was the case for the sample sulfided at room temperature.

#### **ACKNOWLEDGMENT**

This work was supported by the Commonwealth of Kentucky and DOE Contract No. DE-FC22-88PC8806 as part of the Consortium for Fossil Fuel Liquefaction Science (administered by the University of Kentucky).

#### **REFERENCES**

1. Bergius, F., "Chemical Reaction Under High Pressure", Nobel Lecture, May 21, 1932.
2. Stranges, A. N., *Fuel Proc. Tech.*, **1987**, 16, 205.
3. Wu, W. R. K.; Storch, H. H., "Hydrogenation of Coal and Tar", Bulletin 683, Bureau of Mines, U.S. Department of Interior, Washington, DC, 1968.
4. Lee, J. M.; Cantrell, C. E.; Gollakota, S. V.; Davies, O. L.; Corser, M. M.; Vimalchand, P., *ACS Div. Fuel Chem. Preprints*, **1991**, 36, 1915.

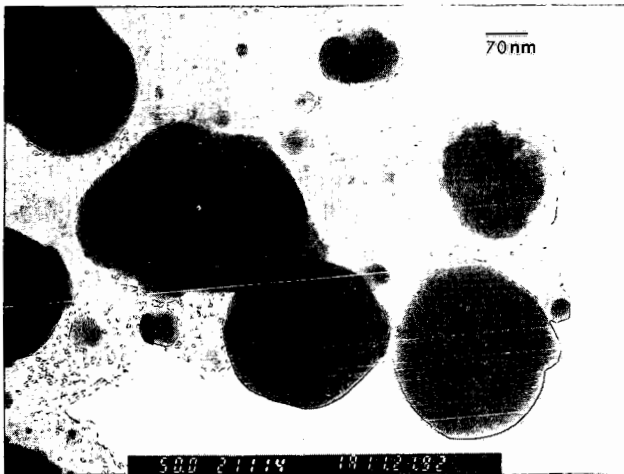


Figure 1. Typical micrograph of the "blobs" from the room temperature sulfidation of  $\gamma$ -FeOOH.

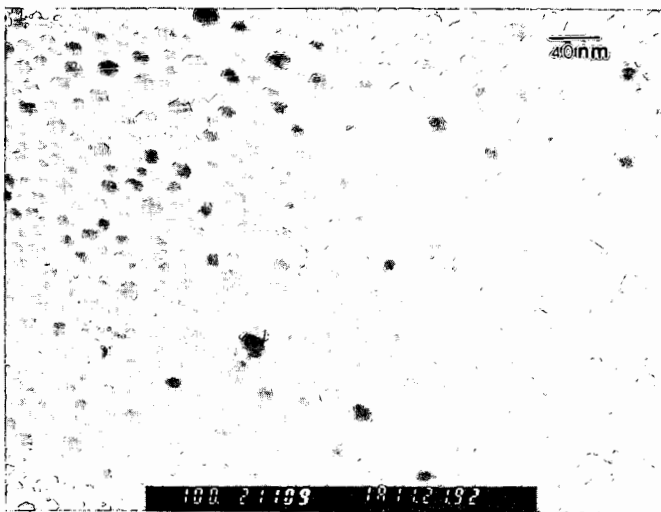


Figure 2. Micrograph of the disintegrated "blobs" using the electron beam.



Figure 3. Micrograph of the particles from the sulfidation of  $\gamma$ -FeOOH at 200°C.

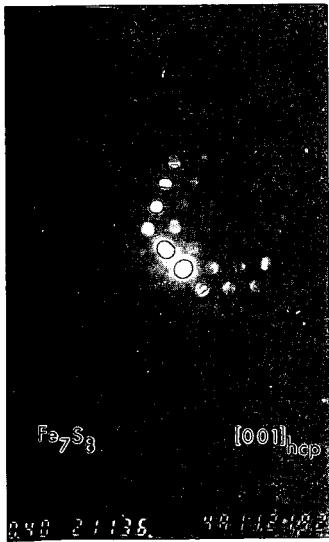


Figure 4. Microdiffraction pattern of the sulfided  $\gamma$ -FeOOH at 200°C.

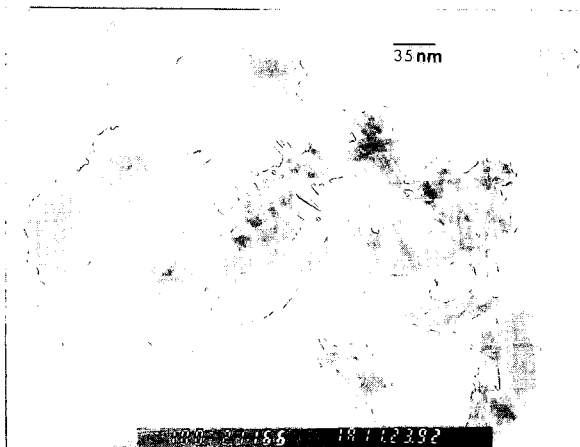


Figure 5. Micrograph of the particles from the room temperature sulfidation of  $\gamma$ - $\text{Fe}_2\text{O}_3$ .

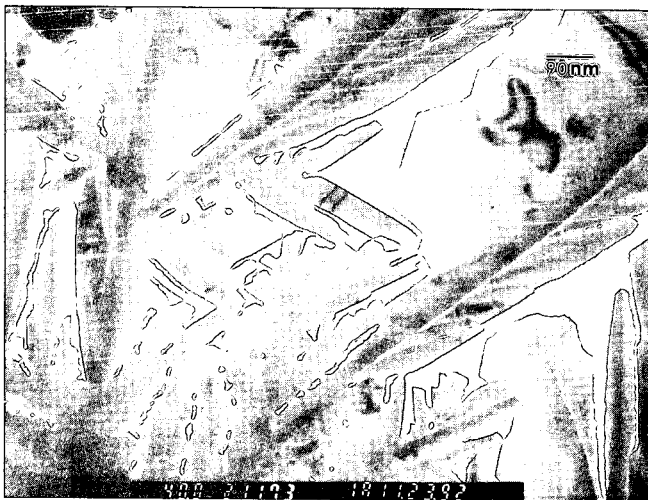


Figure 6. Micrograph of the region containing free sulfur from the room temperature sulfidation of  $\gamma$ - $\text{Fe}_2\text{O}_3$ .

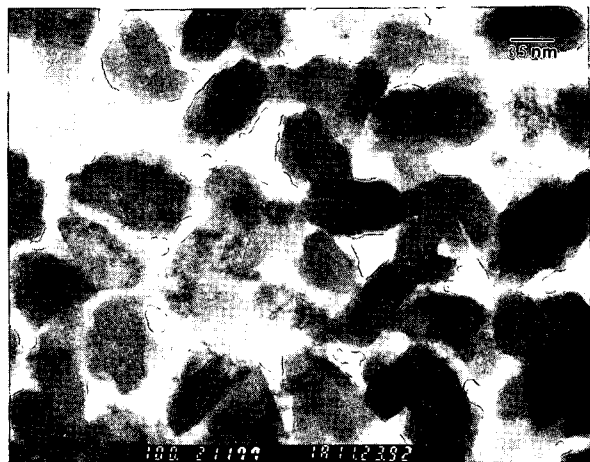


Figure 7. Micrograph of the region containing hexagonal sulfur from the room temperature sulfidation of  $\gamma\text{-Fe}_2\text{O}_3$ .

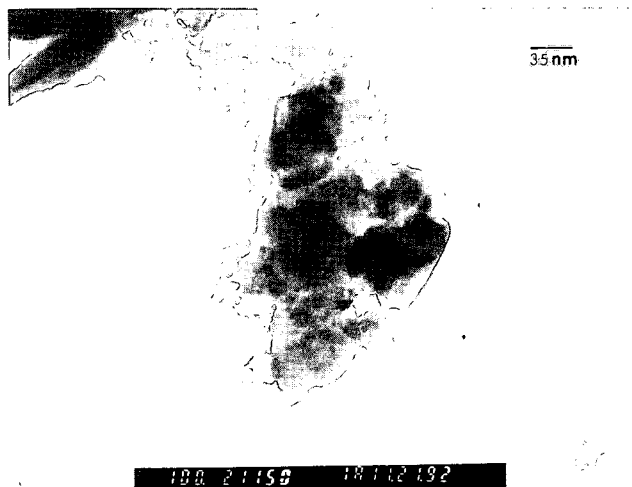


Figure 8. A bright field electron micrograph of the  $\gamma\text{-Fe}_2\text{O}_3$  sample sulfided at 200°C.

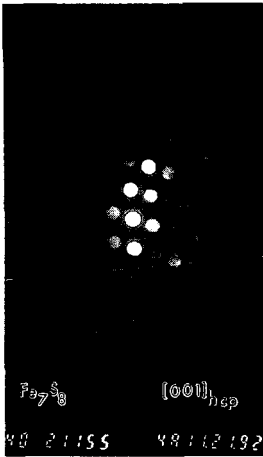


Figure 9. Microdiffraction pattern from the large hexagonal particles ( $\gamma\text{-Fe}_2\text{O}_3$ ) sulfidation at 200°C.

## TRACKING IRON CATALYSTS IN HYDROTREATED BLIND CANYON COAL

David A. Sommerfeld, Wisanu Tuntawiroon, Larry L. Anderson and Edward M. Eyring, Department of Chemistry and Department of Chemical and Fuels Engineering, University of Utah, Salt Lake City, UT 84112

### Introduction

In the past several years we have researched the dispersion of iron based catalysts within coal and coal macerals. This work has focussed not only upon the dispersion itself, but also upon the effect of the catalyst dispersion on the efficiency of the coal liquefaction process.

In experiments done with vitrinite and resinite macerals derived from Hiawatha (Utah) coal we found that an acetone soluble iron catalyst is more readily dispersed within the vitrinite than within the resinite maceral.<sup>1</sup> Using petrographic, IR spectroscopy and thermogravimetric analysis of the products, we determined that the vitrinite macerals had undergone a greater degree of depolymerization than the resinite maceral. In fact, the degree of aromaticity had increased in the resinite maceral indicating an overall loss of hydrogen during the hydrotreatment process. This retrograde process in the resinite maceral was attributed to the incomplete dispersion of the iron catalyst throughout this maceral.<sup>1</sup>

Further research with a suite of coals from the Argonne Premium Coal Sample Program indicated that the C, H, O elemental composition of the coal plays an important role in the catalyst dispersion and the efficiency of the liquefaction process.<sup>2</sup> It was

found that Wyodak, a low rank coal, gave a significantly greater yield of tetrahydrofuran (THF) solubles than does Pittsburgh #8, a higher rank coal. This result was attributed, in part, to the oxygen content of the coals. Wyodak coal has more oxygen, and this permits a greater degree of cross linking to occur during the hydrotreatment process. Cross linking preserves the pore structure of the coal thus facilitating the movement of the catalyst into the interior of the coal particle. In Pittsburgh #8, with a lower oxygen content than Wyodak coal, less cross linking occurs during hydrotreatment resulting in a poorer dispersion of the catalyst and a lower yield of THF solubles.<sup>3</sup>

In the past year we have been working with different forms of iron based coal liquefaction catalysts. The present paper covers some of our latest results that involve a comparison of catalyst efficiency and dispersion for various iron based catalysts with Blind Canyon (Utah) coal (DECS-17 from the Penn State Coal Sample Bank).

#### Experimental

The results reported in the present preprint were obtained using sealed glass tube reactors. Each reactor vessel contained 200 mg of catalyst impregnated DECS-17 coal and 400 mg of 9,10-dihydrophenanthrene which served as the hydrogen donor for the experiment. The catalyst loading for these experiments was 1 wt% by iron (and 1 wt% Mo or W in the case of the bimetallic catalyst systems). The sealed reaction vessels were then heated at 350°C for one hour. The THF solubles were obtained via soxhlet

extraction.

Catalysts were prepared in the following manner: If the catalyst was a dry, insoluble powder, the coal and catalyst were simply mixed together. Some coal samples were impregnated with catalysts derived from water soluble salts by an incipient wetness technique. The Mach 1 iron oxide catalyst was obtained from the Mach 1 Corporation (King of Prussia, PA). Presulfided Mach 1 was prepared in the following manner: 1 g of Mach 1 was placed in a tube oven. H<sub>2</sub>S gas (1 atm) was allowed to saturate the sample, which was then heated to 400°C for two hours; the Mach 1 powder turned black. Upon exposure to air the catalyst underwent combustion and returned to a rust color.

The degree of dispersion of the catalyst systems was determined by making electron probe microanalysis (EPMA) micrographs of the THF insoluble fraction of the product. EPMA is a technique which allows one to map the dispersion of a given chemical element within a sample by the detection of characteristic X-rays.<sup>4</sup> The coal samples were mounted in Petropoxy 154 and polished to the required smoothness on a Synttron diamond paste polisher. Visual images were obtained using both secondary electron images (SEM) and back-scattered electron images (BSE). EPMA micrographs were obtained for iron and sulfur, and when necessary for molybdenum and tungsten.

The glass tube studies reported here will be repeated using a shaken, horizontal, tubing bomb reactor. These tubing bomb reactions will be done at 350°C for one hour and 2000 psig H<sub>2</sub>. THF solubles yields and EPMA micrographs will be obtained.

## Results

The present results are for the glass tube experiments. Data from the tubing bomb reactions will be presented at the Denver meeting.

EPMA micrographs for raw, hydrotreated DECS-17 coal show very little background iron and no molybdenum. The expected sulfur background is seen evenly dispersed throughout the particle. The images obtained for the iron/molybdenum bimetallic, soluble salt derived catalyst exhibit the following pattern: The iron has fully penetrated the coal particle and maps onto the sulfur; the molybdenum has also entered the coal particle. To some extent the molybdenum has collected in two void spaces within the particle (Figures 1a and 1b). The EPMA micrographs of the iron/thiotungstate impregnated sample tell a different story. In this case the iron generally remains outside the coal particle (Figure 2a). The sulfur and tungsten EPMA micrographs map onto each other very nicely, but neither sulfur nor tungsten has fully penetrated the coal particle. Instead, the thiotungstate remains near the exterior of the coal particle forming a halo (Figure 2b).

Two other samples were examined using EPMA. Both of these samples involved catalysts that are made of finely granulated iron oxide powders: Mach 1 and an  $\text{Fe}_2\text{O}_3/\text{MoO}_4$  catalyst from the laboratory of Dr. Irving Wender (University of Pittsburgh). In the case of the presulfided Mach 1 catalyst the iron does not enter the coal particle. The iron and sulfur map onto each other indicating that some sulfur remains present even after the combustion process that

the catalyst underwent after presulfidation. The iron remains clumped together, a feature which was seen in samples treated with unsulfided Mach 1 (Figure 3). No molybdenum was added, and no molybdenum was found in the EPMA micrographs. According to EPMA micrographs (not shown), the catalyst provided by Irving Wender also did not enter the coal during hydrotreatment. The EPMA micrographs of the coal (not the catalyst) particles show typical native sulfur and iron backgrounds and no trace of molybdenum.

Due to the inherent uncertainties associated with the use of sealed glass tubes (i.e., loss of gaseous products and incomplete collection of the solid product), we do not report any THF solubles yields in this preprint. THF solubles yields will be reported at the Denver meeting for the reactions conducted in the tubing bomb reactors.

### Conclusions

Water soluble salts are the most completely dispersed catalysts in the coal particles. In the case of the iron/molybdenum combination, the metallic species have fully penetrated the coal particle. Even though Mach 1 exists as a very fine particulate (average diameter 30 Å) it does not enter the coal particle. If the efficiency of the coal liquefaction process depends upon catalyst dispersion then soluble catalysts introduced by the incipient wetness technique have a significant advantage over insoluble, particulate based catalyst systems.

### Acknowledgements

We would like to thank Dr. Irving Wender for samples of the  $\text{Fe}_2\text{O}_3/\text{MoO}_4$  catalyst and Ray Lambert for valuable technical assistance. Funding was provided by the Department of Energy Fossil Fuels Division through the Consortium for Fossil Fuel Liquefaction Sciences Contract No. UKRF-4-21003-86-24 (DE-FC22-89PC89851).

### References

1. H.P. Wang, R. Lo, D.A. Sommerfeld, H. Huai, R.J. Pugmire, J. Shabtai and E.M. Eyring, "Spectroscopic Studies of Coal Maceral Depolymerization Effected by an Iron-Based Catalyst," **Fuel**, 71, 723 (1992).
2. D.A. Sommerfeld, J. Jaturapitpornsakul, L.L. Anderson and E.M. Eyring, "Microscopic Studies on the Dispersion of Iron/Molybdenum Bimetallic Catalysts in Argonne Coals," (submitted to **Fuel Processing Technology**).
3. F. Derbyshire, "Vitrinite Structure: Alterations with Rank and Processing," **Fuel**, 70, 276, (1991).
4. D.E. Newbury, C.E. Flori, R.B. Marinenko, R.L. Myklebust, C.R. Swyt and D.S. Bright, "Compositional Mapping with the Electron Probe Microanalyzer: Part I," **Anal. Chem.**, 62, 1159A, (1990).



Figure 1a. This EPMA micrograph is  $45\mu\text{m}$  by  $45\mu\text{m}$ . The coal particle occupies the left and center of the image. Iron is well dispersed throughout this region. Note two void spaces circled in the figure.



Figure 1b. The EPMA micrograph is  $45\mu\text{m}$  by  $45\mu\text{m}$  and maps the Mo content of the coal particle. The coal particle occupies the left and center of the image. The Mo is well dispersed throughout the particle with two regions of greater concentration (circled) occurring in void spaces of the particle.

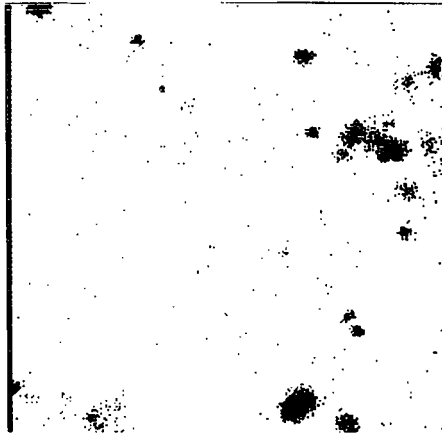


Figure 2a. The EPMA micrograph is  $45\mu\text{m}$  by  $45\mu\text{m}$  and represents the iron distribution in the coal particle. In this image the coal particle occupies the top and center. Only a small area has been penetrated by iron along the right side of the particle.

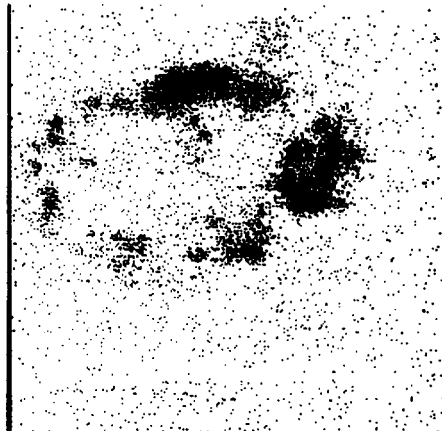


Figure 2b. The EPMA micrograph is  $45\mu\text{m}$  by  $45\mu\text{m}$  and represents the tungsten distribution within the coal particle. The tungsten has not fully penetrated the particle. Instead, it forms a halo at the edges of the coal particle.

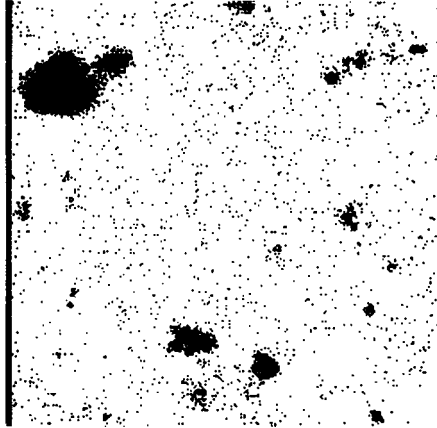


Figure 3. The EPMA micrograph is  $45\mu\text{m}$  by  $45\mu\text{m}$  and represents the iron distribution within the coal particle. In this image the coal particle occupies the center. The iron has not entered the particle and remains clumped outside the coal particle.

## DEPTH PROFILE STUDIES OF CATALYST/ LIQUEFIED COAL RESIDUES

J.Y. Kim, P.J. Reucroft and M. Taghei  
Department of Materials Science & Engineering,  
University of Kentucky, Lexington, KY 40506

V.R. Pradhan and I. Wender  
Chemical Petroleum Engineering Department,  
University of Pittsburgh, Pittsburgh, PA 15261

### INTRODUCTION

Iron based catalysts with a high specific surface area and fine particulate size can be utilized at small concentrations to achieve better performance in terms of overall coal conversion and selectivity to lighter products (oils) in direct coal liquefaction.<sup>1</sup> Since the surfaces of catalysts are the primary site of catalytic activity, efforts have been directed to characterizing catalyst surfaces in coal liquefaction environments. X-ray photoelectron spectroscopy (XPS) has been used to study the iron-based catalyst impregnated liquefied Blind Canyon coal residue samples at different liquefaction processing times (17, 30 and 60 minutes). It was shown that the concentration of elements at the outermost surface layer of samples measured by XPS is similar to that determined in the bulk by chemical analysis but differs from the bulk composition in some important respects.<sup>2</sup> In order to more carefully delineate the differences in the distribution of the elements and chemical changes between the surface and the bulk, the samples have been further analyzed by combining Ar<sup>+</sup> ion sputtering with XPS measurements. Special emphasis has been focused on the surface to bulk distributions of the catalytic elements iron and sulfur. The Fe peaks were not observed for most samples unless Ar<sup>+</sup> ion sputtering was carried out for long times. The S/Fe (catalyst element) ratio, which was initially greater than 1, decreased consistently to less than 1 as time of Ar<sup>+</sup> ion sputtering was increased.

### EXPERIMENTAL

Three different liquefaction processing times (17, 30 and 60 min.) of iron-based catalyst impregnated Blind Canyon coal samples were investigated in the surface characterization studies. Liquefaction conversion was carried out at 400 °C with tetralin as solvent (1:1.5 coal/solvent ratio) after adding Fe<sub>2</sub>O<sub>3</sub>/SO<sub>4</sub><sup>2-</sup>, so that the proportion of Fe was 5% by weight. Dimethyl disulfide was also added in amounts equivalent to Fe to promote sulfidation of the catalyst. The catalyst impregnated liquefied Blind Canyon coal residues were removed in liquid-like form after 17, 30 and 60 minutes and kept in a vacuum oven at 65 °C for 2 days to remove volatile material in the residue without exposing to an air atmosphere. The liquid-like samples were then mounted on the spectrometer probe tip by means of double-sided adhesive insulating tape. After heat treating at 65 °C for 10 hours in a pretreatment chamber to remove remaining volatile materials from the coal residues, the samples were inserted into an ultrahigh vacuum chamber for surface analysis. To exclude the possibility of recording contaminants associated with the tape, the tape was also analyzed separately. It was found that the constituents of tape were not detected by XPS, and that the photoionization signals were characteristic of the samples alone.

The samples were examined by XPS employing a Kratos XSAM 800 spectrometer using Mg K $\alpha$  ( $h\nu = 1253.6$  eV) radiation. The spectrometer was run in Fixed Analyzer Transmission (FAT) mode at pass energy of 11 kV and 13 mA. Under these conditions, the FWHM of Ag (3d<sub>5/2</sub>) peak is  $\approx 1.0$  eV. The system pressure never exceeded  $3 \times 10^{-6}$  torr during spectra acquisition. In situ Ar<sup>+</sup> ion sputtering of the residue samples was carried out using a differentially pumped and computer controlled 3M mini-beam ion gun. The ion beam was adjusted so that edge effects were minimized. Incident ion energy used was 3.5 kV and the sample currents were kept around 30  $\mu$ A (estimated etching rate was approximately 25 Angstroms/min, as determined from a SiO<sub>2</sub> standard film). The pressure in the main chamber was kept below  $4 \times 10^{-6}$  torr during ion sputtering. After ion sputtering, a consistent increase in the FWHM for all elements was found with increasing ion dose. No compensation was made for charging of the samples.

## RESULTS AND DISCUSSION

The initially recorded XPS spectra showed a distinct peak for each of the major elements, carbon, oxygen, and silicon, as well as the minor components, sulfur and nitrogen in each sample. Binding energies of these elements showed the expected values for the most stable oxidation state and were similar to those reported previously.<sup>2</sup> However, Fe was not observed initially in the surface regions of the liquefied coal residue particles. A relatively high oxygen concentration was determined initially at the surface by XPS before sputtering, but a sharp drop in oxygen concentration was subsequently observed. This surface enrichment of oxygen can be ascribed to air oxidation and the oxidized layer thickness was estimated to be 50-60 nm.

Two peak components were initially observed in the case of the surface sulfur XPS signal. The peak at 168 eV, can be ascribed to oxidized sulfur, i.e., organic plus inorganic (sulfate), while the other at 163 eV corresponded to inorganic sulfide plus the usual organic sulfur forms present in coal (thiophene, sulfides, mercaptans). As sputtering increased, the sulfate peak decreased and finally disappeared, while the sulfide peak showed an increase in intensity. This observation is in agreement with the decrease of oxygen concentration which was observed as the sputtering increased. These results are similar to those reported previously.<sup>2</sup>

The Fe peaks were not observed initially for most samples unless ion sputtering was carried out for at least 30 minutes. As the liquefaction reaction time increased from 17 to 60 min, sputtering time had to be further increased in order to observe the Fe peaks. Catalytic elements such as iron and sulfur showed a systematic trend towards higher concentrations of each sample after 30 min Ar<sup>+</sup> sputtering. The results are shown in Figures 1, 2, and 3. From these results, it can be concluded that the iron catalyst particles are well encapsulated in either oxide layers or within other organic materials from the coal residues.

The S/Fe (catalyst element) ratio, which was initially greater than 1, decreased consistently to less than 1 as time of Ar<sup>+</sup> ion sputtering was increased (Tables 1, 2 and 3). This is also shown in Figures 1, 2 and 3 for liquefaction times of 17, 30 and 60 minutes, respectively. EXAFS and Mossbauer studies have shown that under the liquefaction conditions that were employed i.e., after adding dimethyl disulfide to the catalyst/coal residue mixtures, the iron catalyst is converted to iron sulfide (pyrrhotite) within a few minutes of starting the reaction.<sup>3</sup> Further analysis is currently underway.

## SUMMARY AND CONCLUSIONS

Surface analysis combined with depth profiling shows that the sulfur/iron stoichiometry varies in iron catalyst/liquefied coal residues that have been extracted from coal liquefaction environments. The catalyst elements become increasingly more encapsulated in the carbonaceous material as the processing time increases. The S/Fe atomic ratio approaches 0.7 to 0.9 inside the coal residue particles.

## ACKNOWLEDGEMENT

We gratefully acknowledge financial support from the Consortium for Fossil Fuel Liquefaction Science, University of Kentucky under Dept. of Energy Contract No. DE-FC22-92 PC 90029. We also thank Dr. G.P. Huffman for his interest in this work.

## REFERENCES

1. F.J. Derbyshire, Catalyst in Coal Liquefaction: New Direction for Research , IEA Coal Research: London, 1988; IEA CR-08.
2. J.Y. Kim, P.J. Reucroft, V.R. Pradhan and I. Wender, American Chem. Soc., Div. of Fuel Chem. Preprints, 37, 756 (1992); to be published in Fuel Processing Technology.
3. M. Taghei, Private Communication.

**Table 1. XPS Catalyst Element Depth Profile for Ar<sup>+</sup> Sputtered 17 min Liquefied Coal Residues (atomic %)**

	0 min	10 min	20 min	30 min	40 min	50 min	60 min
S	0.38	0.48	0.76	0.50	0.58	0.73	0.89
Fe	-	-	-	0.40	0.73	0.89	1.24
S/Fe	-	-	-	1.25	0.79	0.82	0.72

**Table 2. XPS Catalyst Element Depth Profile for Ar<sup>+</sup> Sputtered 30 min Liquefied Coal Residues (atomic %)**

	0 min	10 min	20 min	30 min	40 min	50 min	60 min
S	0.25	0.23	0.34	0.43	0.51	0.72	0.97
Fe	-	-	-	0.20	0.45	0.69	1.12
S/Fe	-	-	-	2.15	1.13	1.04	0.87

**Table 3. XPS Catalyst Element Depth Profile for Ar<sup>+</sup> Sputtered 60 min Liquefied Coal Residues (atomic %)**

	0 min	10 min	20 min	30 min	40 min	50 min	60 min
S	0.62	0.53	0.42	0.38	0.37	0.62	0.63
Fe	-	-	-	0.17	0.23	0.52	0.74
S/Fe	-	-	-	2.24	1.61	1.19	0.85

Figure 1. Depth Profile of Elements for 17 min. Coal Liquefaction Residue

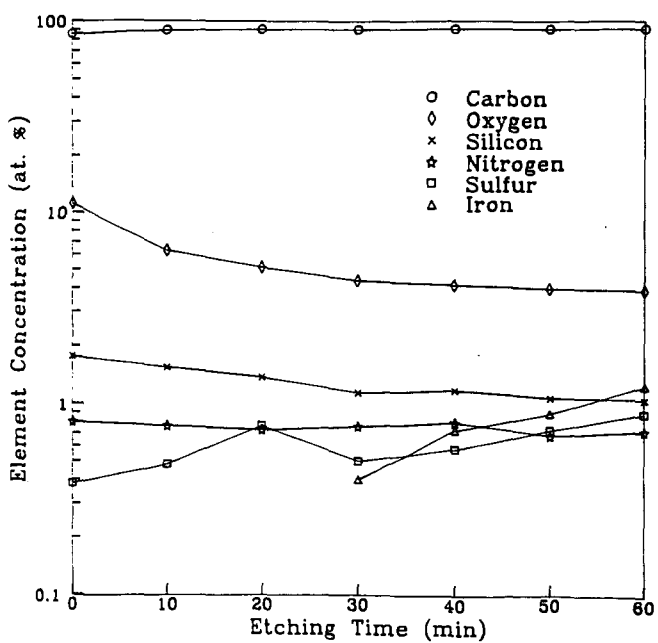


Figure 2. Depth Profile of Elements for 30 min. Coal Liquefaction Residue

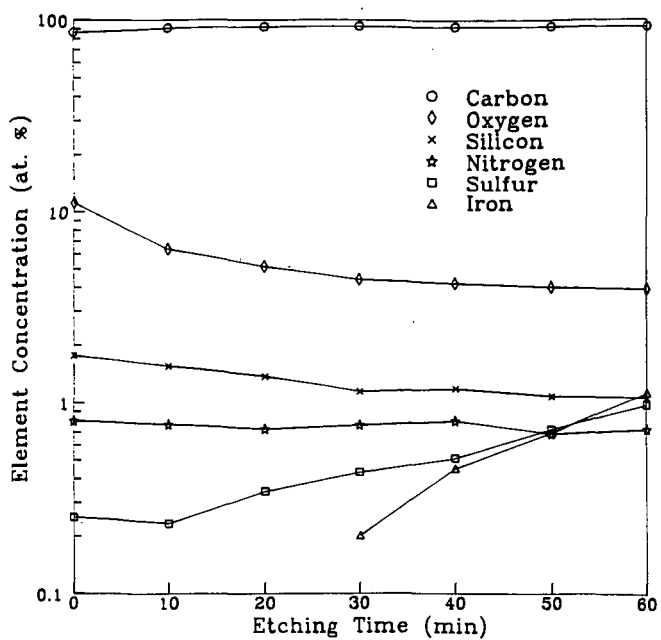
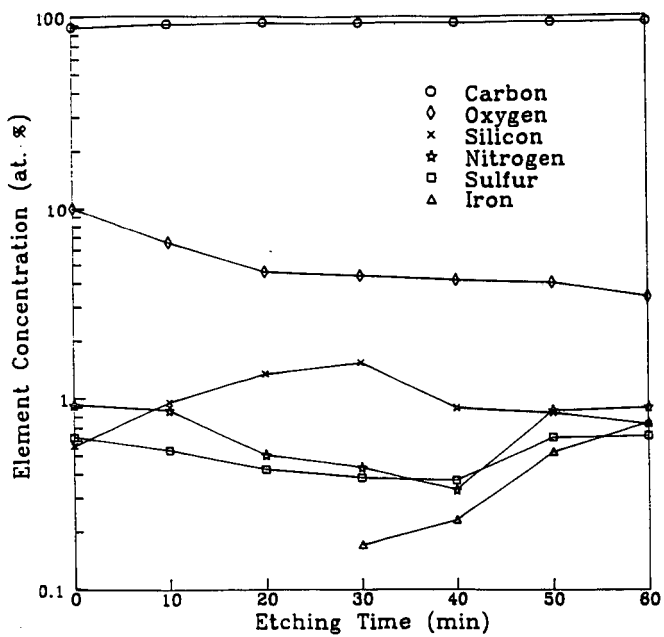


Figure 3. Depth Profile of Elements for 60 min. Coal Liquefaction Residue



ACTIVITY TESTING OF FINE-PARTICLE SIZE,  
UNSUPPORTED, IRON-BASED CATALYSTS\*

Frances V. Stohl  
Process Research Department 6212  
Sandia National Laboratories  
P.O. Box 5800  
Albuquerque, NM 87185

Keywords: Fine-particle catalysts; activity testing; statistical design

INTRODUCTION

The efficiency of the initial reactions of coal during coal liquefaction will have significant impacts on downstream processing (including catalyst usage, reaction severity, product yields, product quality) and hence on process economics. Reactions that result in compounds with low molecular weights and decreased boiling points are beneficial, whereas retrogressive reactions, which yield higher molecular weight compounds that are refractory to further processing, decrease process efficiency. Likewise, reactions that result in decreased sulfur, nitrogen, and oxygen contents and increased hydrogen contents in the products are beneficial. The use of unsupported fine-particle (<40 nm) catalysts during initial coal processing has the potential to enhance desired reactions and minimize retrogressive reactions. The potential advantages of using fine-particle size catalysts include improved dispersion of the catalyst, improved coal/catalyst contact, and the potential for using low amounts ( $\leq 0.5\%$  based on the weight of coal) of these novel catalysts due to their very high surface areas. These catalysts could be combined with the coal or coal-solvent mixture as either active catalysts or catalyst precursors that would be activated in situ. Several methods of combining catalyst and coal, such as physical mixing or using a catalyst-hydrogen donor slurry, are possible. Ideally the fine-particle catalysts would be inexpensive enough to be disposable.

The Pittsburgh Energy Technology Center's (PETC) Advanced Research (AR) Coal Liquefaction Program has many research projects to develop fine-particle size catalysts that are active for reactions of interest in direct coal liquefaction: hydrogenation, carbon-carbon bond breakage, and heteroatom removal. However, it is difficult to compare results among researchers because of the variety of testing procedures used including different reactors, reaction temperatures, reaction times, pressures, hydrogen donor solvents, solvent to coal ratios, and workup procedures. In addition, some catalyst developers in the AR program do not have any testing capabilities for direct liquefaction. The objectives of the work reported here are to develop standard coal liquefaction test procedures and to perform the testing of the novel fine-particle size catalysts being developed in the PETC AR Coal Liquefaction Program.

EXPERIMENTAL PROCEDURES

Materials

The coal being used in this project is the DECS-17 Blind Canyon Coal obtained from The Penn State Coal Sample Bank. The coal, which is packaged under an

\* This work was supported by the U. S. Department of Energy at Sandia National Laboratories under contract DE-AC04-76DP00789.

inert atmosphere in sealed foil bags with a plastic liner, is stored in a refrigerator prior to use. The coal is a HVA bituminous coal with 0.36% iron, 0.02% pyritic sulfur, and 7.34% mineral matter (on a dry basis). The particle size is -60 mesh. The coal is riffled three times with remixing prior to taking splits. 1,2,3,6,7,8-hexahdropyrene ( $H_6Py$ ) and 9,10-dihydrophenanthrene (DHP) were evaluated as hydrogen donors for use in the standard tests.  $H_6Py$  was obtained from Aldrich (98% purity), and DHP was obtained from either Aldrich (94% purity) or Janssen Chimica (97% purity). Pyrite (99.9% pure on a metals basis) with a -100 mesh particle size was obtained from Johnson-Matthey. An X-ray diffraction pattern taken on this material showed only pyrite. The surface area of the pyrite is 0.7 m<sup>2</sup>/g as measured using BET techniques. Stabilized tetrahydrofuran (THF) and heptane are used in product workups.

#### Reactors

The testing is being performed using batch microautoclaves consisting of a 0.75" OD Swagelok "T" connected to 0.375" OD high pressure stainless steel tubing. A Whitey plug valve at the top of the tubing is used for pressurizing and depressurizing the reactors. A thermocouple was inserted into the reactor, and a pressure transducer was attached. The total volume for a reactor is 43 cm<sup>3</sup> with a liquid capacity of up to 8 cm<sup>3</sup>. Four reactions can be run simultaneously. After being charged with the reactants (coal, hydrogen donor solvent, high pressure gas, and other additives required by the experimental design such as catalyst or sulfur), the reactors are rapidly heated to temperature in a fluidized-sand bath while being agitated at 200 cycles/sec with a wrist-action shaker. Temperatures and pressures are recorded with a digital data acquisition system during the course of the experiments. Following the heating period, the reactors are rapidly quenched in a water bath to ambient temperature, a gas sample is taken, and the liquid and solid products are removed for analysis.

#### Product Analyses

The primary criteria for evaluating catalysts are based on coal conversion. Reaction product analyses that are performed routinely include THF and heptane solvent solubility determinations, gas chromatographic (GC) analyses of the hydrogen donor, and analyses of gas products. Solvent solubilities are done using pressure filtration procedures with a Millipore 142 mm diameter pressure filtration device and Duropore (0.45 micron) filter paper. Quantitative GC analyses using methylnaphthalene as an internal standard are performed on the THF soluble material to determine the recovery of the hydrogen donor and the amounts of both DHP and phenanthrene present in the product. The quantity of each gas in the product is calculated using the ideal gas law, the mole percent in the gas sample as determined from a Carle GC using standard gas mixtures, and the post-reaction vessel temperature and pressure.

### RESULTS AND DISCUSSION

Two important aspects of the catalyst testing program are the development of standard test procedures and the development of a statistical experimental design.

#### Standard Test Procedures

The standard test procedures cover both performing the reactions and doing product workups.  $H_6Py$  and DHP were evaluated for use as hydrogen donors in the standard tests. DHP was chosen because it is less expensive than  $H_6Py$  and has a lower melting point (32-35°C) that could help ensure good mixing. It also performed well in experiments. Current coal liquefaction processing

configurations use approximately a 2:1 hydrogen donor solvent to coal ratio. In addition, some of the better recycle solvents from large-scale processes contain about 1% donatable  $H_2$ , which is considered very good. Use of DHP at a 2:1 donor solvent:coal ratio gives about 1% donatable hydrogen and a high liquid:coal ratio for aiding catalyst dispersion.

Procedures have been set up to obtain excellent temperature control during the course of the reactions. The average temperature is routinely within one degree of the desired temperature and the standard deviation is  $<1^\circ C$ . Heat-up times are about 3.5 minutes for  $400^\circ C$  reactions and quench times to temperatures  $<50^\circ C$  are about 2 minutes.

After the gas samples are collected, the reactors are opened and the Swagelok tees and end caps containing the product are sonicated in THF, soaked in THF overnight, and then sonicated again prior to filtration. The total time the liquid products are in THF is about 17 hours. The volume of THF used in this reactor cleaning is 200 ml. Typically, three filter papers are used for THF filtration. The filter cake is rinsed with THF prior to opening the device. After the filtration is complete, the filter paper is dried in a vacuum oven, cooled to room temperature and weighed to determine the insoluble portion. The THF solubles are then rotoevaporated to about 50 to 60 ml volume, quantitatively transferred to a 100 ml volumetric flask and brought to 100 ml volume after the solubles have cooled to room temperature. A 1 ml portion is removed and used for determination by GC of the hydrogen donor recovery, including both DHP and phenanthrene. The remaining 99 ml is rotoevaporated until there is no weight loss after 10 minutes of rotoevaporating. A stirring bar is added to the flask and 200 ml heptane is added with constant stirring. This heptane/product mixture is then pressure filtered to obtain the weight of heptane insolubles.

#### Statistical Experimental Design

There are two main reasons for using an experimental design: to enable good comparisons among novel catalysts and to obtain more information with fewer experiments. This procedure will give statistical information regarding the results and will yield optimum processing conditions for each catalyst over the ranges of the variables studied. The statistical experimental design (Figure 1) that was chosen evaluates the effects of three variables: time (20 to 60 minutes), temperature ( $350$  to  $400^\circ C$ ) and catalyst loading (0 to 1 wt% on a weight of as-received coal basis). These conditions are consistent with process conditions used in coal liquefaction. An additional advantage of using an experimental design is that the impacts of additives, such as sulfur required to activate an  $Fe_2O_3$  catalyst, can be easily evaluated by adding sulfur to the thermal baseline reactions.

#### Evaluation of the Statistical Design

This experimental design was evaluated by each of two operators using pyrite. Pyrite was chosen because it is a known iron catalyst in coal liquefaction, is commercially available, and is easy to work with.

The hydrogen donor recoveries (including both DHP and phenanthrene) were greater than 90% for all the reactions. At the lower severity conditions about 83% of the donor product was DHP, whereas at the higher severity conditions only 24% was DHP. The non-hydrogen gases detected in the reaction products were  $CO_2$ ,  $CO$ ,  $CH_4$ , and  $C_2H_6$ . The quantities of these gases produced ranged from 0.23% (dmwf coal basis) for the lowest severity conditions to 2.21% for the highest severity conditions. Table 1 shows the measured, gas

corrected THF conversions and heptane conversions obtained by each operator for the nine sets of process conditions in the experimental design. It also gives the average conversions and the standard deviations. The THF results show good reproducibility. The largest standard deviation is 4.09 for the center point of the cube. This high value is consistent with the fact that both operators indicated the products from runs made at these conditions are the most difficult to filter. The equation obtained by fitting the THF conversion data to a linear model is as follows:

$$\text{THF Conv}(\%) = 70.908(+/-)16.938(+/-)6.931(+/-)1.091(+/-)(+/-)(-1.956)$$

Where:

70.908	Center Point Conversion
16.938	Temperature Effect
6.931	Time Effect
1.091	Pyrite Effect
-1.956	Time x Temperature Interaction

The  $r^2$  value for the fit of the THF data to this equation is 0.987. To calculate the THF conversion for a given set of reaction conditions choose either the + or - in each (+/-). Use + for each high value: 400°C or 60 minutes or 1 wt% catalyst. Use - for each low value: 350°C or 20 minutes or no catalyst. This analysis shows that the largest effect is due to temperature, followed by time and finally pyrite addition. There is also some interaction between temperature and time. No other interactions were observed. The calculated THF values for the points on the cube are shown in Figure 2. The results show that the impact of a 1% pyrite addition is to increase the THF conversion by 2.2%, which is a statistically significant increase. It also shows that the effect is the same at both the lowest and highest severity conditions.

The measured heptane conversions in Table 1 show much greater variability than the THF conversions. Approximately halfway through the experimental design, it was observed that there was a systematic difference between the heptane conversion values obtained by the two operators. Therefore, the procedure was revised to ensure that both operators were doing the workups the same way. The results for the runs that were made after this change are indicated with an "\*". A comparison of the results from the revised procedure to those from the old procedure shows significant improvement in reproducibility. All of the measured heptane conversions were used in the linear modeling effort because there would not be enough data if the old workup procedure results were discarded. The equation obtained by fitting the heptane conversion data to a linear model is as follows:

$$\text{Heptane Conv}(\%) = 19.958(+/-)13.020(+/-)5.255(+/-)(+/-)2.406$$

Where:

19.958	Center Point Conversion
13.020	Temperature Effect
5.255	Time Effect
2.406	Time x Temperature Interaction

The  $r^2$  value for the fit of the heptane conversion data to this equation is 0.957. The calculated heptane values are shown in Figure 3. This analysis indicates that the largest effect is due to temperature, followed by time. Pyrite addition had no effect on heptane conversion. There is also an

interaction between temperature and time. No other interactions were observed. The estimates of standard errors associated with this data could probably be improved by repeating the experimental design using the new workup procedure for all experiments. This might show somewhat different results. The heptane conversion (4.09%) for 350°C for 20 minutes is equal to that obtained from the as-received coal.

Operator effects were also analyzed as part of the statistical analysis of the results. Operator effects include both effects between operators and within each operator. The results were as follows:

<u>SOURCE</u>	<u>ESTIMATES OF STANDARD DEVIATION</u>	
	<u>THF CONVERSIONS</u>	<u>HEPTANE CONVERSIONS</u>
Between Operators	0.23	0.31
Within Operators	1.78	0.95

These results show good reproducibility both between operators and within each operator and thus indicate that there are no systematic differences in the procedures used by the operators. Only the results from the new workup procedure were used in this analysis of the heptane conversions.

#### SUMMARY

The results of the experiments performed using pyrite have shown that small differences in activity can be detected by using a statistical experimental design. The differences in THF conversion were 2.2% between thermal and catalytic reactions. This difference was unaffected by changes in reaction time and temperature over the parameter ranges used in this study. The results also show that the experimental procedures (with the revised heptane conversion techniques) can be well duplicated between operators and within a single operator.

#### FUTURE WORK

Future work will include repeating the statistical experimental design to determine if the revised heptane procedure impacts the conclusions. The hydrogen donor to coal ratio will also be varied to determine the effects on catalyst activity. Efforts will be made to develop a procedure for obtaining information on the quality of the reaction products by performing elemental analyses on the THF and heptane insoluble materials. Testing of a novel catalyst being developed by I. Wender at the University of Pittsburgh will be initiated. This will be the first novel catalyst that will be evaluated using this experimental design.

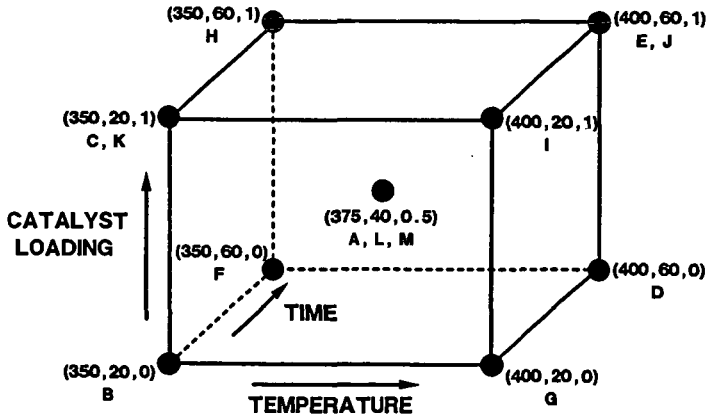
#### Acknowledgement

I would like to express my thanks to Jeff Kawola and Richard Jensen for performing the experimental work associated with this project. I would also like to thank Kathleen Diegert for determining the best experimental design and analyzing the results and Carlos Quintana for his efforts in setting up the new testing facility.

TABLE 1. MEASURED CONVERSIONS

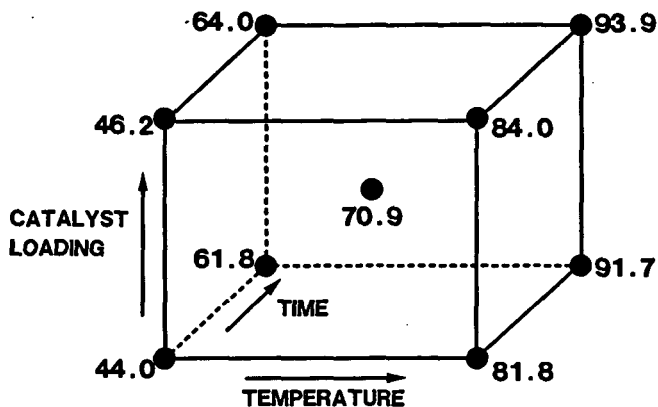
TEMP (°C)	TIME (min)	CAT (wt%)	THF RESULTS				HEPTANE RESULTS			
			OPERATOR		AVERAGE	STD DEV	OPERATOR		AVERAGE	STD DEV
			#1	#2			#1	#2		
350	20	0	42.5	44.0	43.2	1.05	3.0	6.6	4.8	2.55
400	20	0	82.2	79.2	80.7	2.16	25.6*	25.1*	25.3	0.33
350	60	0	61.4	60.9	61.1	0.34	6.6	13.0	9.8	4.53
400	60	0	93.0	91.6	92.3	0.72	37.8	48.4	42.1	4.58
			91.7				39.9*			
			92.9				42.5*			
375	40	0.5	74.6	74.9	71.8	4.09	15.7	22.2	17.2	3.07
			65.1				17.6*			
			70.6	73.7			14.1*	16.4*		
350	20	1	47.2	45.9	46.1	1.20	2.4	3.9	4.6	2.05
			44.5	46.9			4.9*	7.3*		
400	20	1	84.0	83.9	83.9	0.03	26.7*	27.4*	27.0	0.45
350	60	1	62.1	64.9	63.5	2.02	11.3*	11.7*	11.5	0.26
400	60	1	93.2	92.6	92.8	0.28	35.0	40.4	40.0	3.53
			92.7	92.7			41.9*	42.9*		

\* - Revised work up procedure



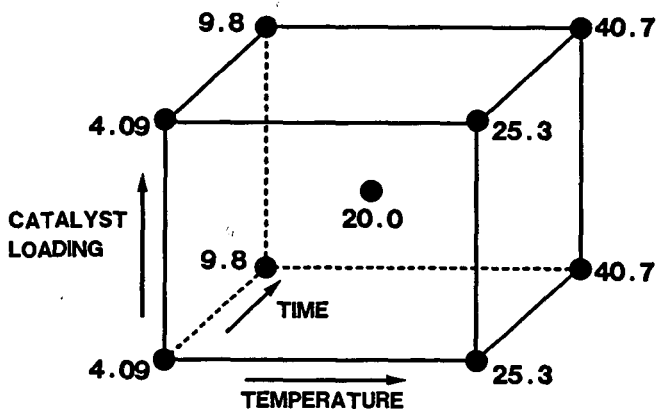
(TEMPERATURE = °C; TIME = MINUTES; CATALYST LOADING = WT % AR COAL)  
LETTERS = ORDER IN WHICH REACTIONS WERE PERFORMED

Figure 1: Statistical experimental design



(TEMPERATURE - °C; TIME - MINUTES; CATALYST LOADING - WT % AR COAL)

Figure 2. THF conversions: Calculated from the linear model



(TEMPERATURE - °C; TIME - MINUTES; CATALYST LOADING - WT % AR COAL)

Figure 3. Heptane conversions: Calculated from the linear model

## THE EFFECT OF CO COADSORPTION ON THE HYDROGENATION PROPERTIES OF IRON

R. T. K. Baker, M. S. Kim and N. M. Rodriguez  
Materials Research Laboratory  
The Pennsylvania State University  
University Park, PA, 16802

Keywords: Iron catalysts, hydrogenation catalysts, ethylene decomposition

### ABSTRACT

During the course of a series of reactions designed to examine the differences in carbon deposition characteristics exhibited by CO and C<sub>2</sub>H<sub>4</sub> over iron an unexpected pattern of behavior was found. Exposure of the metal to a C<sub>2</sub>H<sub>4</sub>-H<sub>2</sub> mixture at 600°C resulted in only minor decomposition of the olefin, however, upon addition of a small amount of CO to the system, there was a dramatic increase in the amount of filamentous carbon formed, of which the major fraction could be attributed to decomposition of C<sub>2</sub>H<sub>4</sub>. Maximum reactivity was achieved with a C<sub>2</sub>H<sub>4</sub>-CO-H<sub>2</sub> (3:1:1) mixture and it was apparent that CO was responsible for not only promoting the formation of solid carbon, but also inducing the conversion of C<sub>2</sub>H<sub>4</sub> to C<sub>2</sub>H<sub>6</sub>. Removal of CO from the system resulted in a rapid decline in catalytic activity, however, upon re-introduction of CO activity was restored to its initial high level, indicating that the reversible nature of the activation-deactivation processes. This behavior is rationalized in terms of a reconstruction of the iron surface in the presence of coadsorbed CO which results in the possible formation of various faces with differing reactivity characteristics, and a relaxation when CO is removed from the reactant.

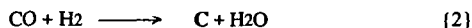
### INTRODUCTION

The high activity of iron with CO has only been observed when some additive gas such as hydrogen, water vapor or other oxygenates were mixed with the reactant [1-3]. Dry and coworkers [2] reported that in all the cases where enhancement of carbon deposition was observed then hydrogen was shown to be present within the catalyst bed. They suggested that the increase in solid carbon formation was related to the ability of hydrogen to strengthen the adsorption characteristics of CO to the iron and as a consequence increase its rate of decomposition.

It is known that disproportionation of CO takes place via the Boudouard equilibrium,



which favors the right side at temperatures below 700°C. The promotional effects of hydrogen on the decomposition of CO have been interpreted in two ways. The first, the occurrence of a secondary reaction (CO hydrogenation) to produce solid carbon [1,3]:



In addition to this process, hydrogen adsorbed on the metal surface was also found to catalyze the Boudouard reaction and this effect has been explained by the ability of hydrogen to decompose inactive metal carbides into the catalytically active metallic phase [1]. There have been numerous investigations which have dealt with the interaction of CO and hydrogen on transition metal surfaces and these have been comprehensively reviewed by Vannice [4]. It is generally agreed that the uptakes of CO and hydrogen are mutually enhanced by a coadsorption procedure compared to that of either gas alone and this aspect was rationalized in terms of the formation of a surface complex between the two adsorbate molecules.

Perhaps the clearest understanding of the interaction of CO-H<sub>2</sub> with iron comes from recent surface science studies performed by Madix and coworkers [5,6] of the coadsorption of CO and H<sub>2</sub> on Fe(100) surfaces. It was suggested that adsorbed CO induced a weakening in the strength of the Fe-H bond, which triggered the formation of a potentially more reactive hydrogen species. In a subsequent investigation Burke and Madix [7] demonstrated the validity of this argument in experiments where the introduction of CO onto an iron surface pre-saturated with hydrogen brought about the formation of ethane from coadsorbed ethylene, a reaction which did not occur in the absence of CO [8].

The current investigation was undertaken in an attempt to gain a fundamental understanding of the differences in the reactivity of ethylene-hydrogen mixtures both in the absence and presence of carbon monoxide, when passed over an iron catalyst.

## EXPERIMENTAL

The experiments reported here were carried out in a flow reactor system operated at 1 atm total pressure. There was provision for taking samples at various intervals during reaction for gas product analysis by gas chromatography. Powdered iron catalyst samples (50 mg) were held in a ceramic boat which was placed at the center of the reactor tube. After reduction of the sample in a 10% H<sub>2</sub>-He mixture for 2 hours at 600°C, the system was flushed with helium and then the reactant, either pure CO, CO-H<sub>2</sub>, C<sub>2</sub>H<sub>4</sub>-H<sub>2</sub> or CO-C<sub>2</sub>H<sub>4</sub>-H<sub>2</sub> mixtures, was introduced into the system and allowed to react with the iron catalyst at 600°C for periods of up to 5 hours. The total amount of carbon deposited during the experiment was determined by weight difference. The composition of the gas phase was monitored as a function of time from analysis performed in a Varian 3400 GC equipped with a 30 m megabore column (GS-Q). Iron powder (200 mesh) was obtained from Johnson Matthey Inc. (99.99% purity) and had a BET nitrogen surface area of 0.3 m<sup>2</sup>/g<sup>-1</sup> at -196°C. The gases used in this work CO (99.9%), hydrogen (99.999%), ethylene (99.99%) and helium (99.99%) were obtained from Alphagaz company and used without further purification.

## RESULTS AND DISCUSSION

### *Iron Catalyzed Decomposition of C<sub>2</sub>H<sub>4</sub>-H<sub>2</sub> and CO-C<sub>2</sub>H<sub>4</sub>-H<sub>2</sub> Mixtures*

When C<sub>2</sub>H<sub>4</sub>-H<sub>2</sub> (3:1) mixture was passed over iron at 600°C, the reactivity of the system was very low, only about 0.43% of solid carbon being produced with no detectable amounts of other products being formed. This is consistent with the notion that iron is not a very active hydrogenation catalyst in its pure form [8]. After a period of about 1 hour, CO was introduced into the feed gas in sufficient concentration to create a CO-C<sub>2</sub>H<sub>4</sub>-H<sub>2</sub> (1:3:1) mixture. The addition of CO to the reactant resulted in a dramatic increase in the percent of ethylene undergoing reaction, rising from 0.51 to 79.7%, over a 30 min period of time. It appears that the presence of CO induces changes in the surface of the iron catalyst which enhances its ability to adsorb and decompose ethylene.

In a further series of experiments, initially a CO-C<sub>2</sub>H<sub>4</sub>-H<sub>2</sub> (1:3:1) mixture was passed over an iron catalyst, and the same high levels of ethylene decomposition as those produced in the previous experiment were obtained. After 80 minutes reaction time, the CO flow was stopped and this action resulted in a dramatic decrease to around 0.5%, a level comparable to that obtained with a C<sub>2</sub>H<sub>4</sub>-H<sub>2</sub> (3:1) mixture in the previous experiment. When the CO flow was re-introduced into the feed 45 minutes later, the percentage of ethylene undergoing reaction was restored to the original high level. This sequence of events indicates that the catalyst activation-deactivation process is reversible and the high olefin decomposition activity occurs only when CO is present in the reactant mixture.

In order to investigate the details of the influence of CO on the decomposition of ethylene, the ratio of CO in CO-C<sub>2</sub>H<sub>4</sub>-H<sub>2</sub> mixtures was varied from 0 to 1 (CO fraction = CO/(CO+C<sub>2</sub>). The gaseous product distribution obtained with the various mixtures are presented in Table 1. Since the amount of methane produced was relatively small and that produced from CO was negligible with the feed containing a small portion of hydrogen, the error resulting from the approach should not be appreciable. Inspection of this data shows that coadsorption of CO on the iron catalyst not only promotes the formation of ethane via the hydrogenation step, but also has a tremendous impact on the fate of the carbon species produced on the metal surface from the C-C bond cleavage of the adsorbed ethylene molecules. It is known from previous studies [8] that in the absence of CO, ethylene adsorbs reversibly without dissociation on hydrogen pre-saturated iron surfaces and it is therefore not surprising to find that very little solid carbon is produced on the metal. In the presence of CO, the metal is activated towards ethylene decomposition and the carbon species formed at the surface proceed to dissolve into the bulk of the particle and eventual precipitation at the rear faces in the form of a filament. This is obviously a facile process since filamentous carbon is formed in abundance and its growth is sustained for relatively long periods of time.

When CO is removed from the reactant then the fraction of ethylene which decomposes declines to the level exhibited by the CO-free iron surface. On re-introduction of CO the amount of ethylene which is decomposed is quickly restored to a high level demonstrating the reversible nature of the promotional effect. It is possible that adsorption of CO induces reconstruction of the surface to a configuration which facilitates rupture of the C=C bond in ethylene. Elimination of CO from the system causes a relaxation of the reconstructed surface to a structure which no longer favors ethylene decomposition. It is also worth taking into consideration the possibility that the presence of CO produces electron perturbations which alter the bonding characteristics between the ethylene and metal surface atoms.

It is interesting to compare the relative amounts of methane formed in the present system with that produced from the decomposition of C<sub>2</sub>H<sub>4</sub>-H<sub>2</sub> mixtures over copper-nickel alloy particles [9] where over 20% of the ethylene decomposed to form methane. The excessive amount of methane generated in this latter system was purported to result from the formation of an "ethylidyne" intermediate. It would appear, therefore, that in the present system, where the methane yield under comparable conditions is less than 1%, the formation of an "ethylidyne" intermediate is not a favored step.

From a consideration of the product distribution it is possible to make certain speculations regarding the mode by which ethylene is adsorbed on the iron surface containing coadsorbed CO and H<sub>2</sub>. The formation of a relatively large amount of ethane from the CO-induced hydrogenation of the olefin suggests that there is a strong tendency for the ethylene molecules to bind in an arrangement in which the C=C bond is "parallel" to the metal surface, as depicted in Figure 1a. Conversely, the low amount of methane produced during this reaction indicates that there is a reluctance for ethylene to adsorb in the "end-on" configuration, where one of the carbon atoms in the molecule is attached to three metal atoms in the form of an "ethylidyne" conformation, as illustrated in Figure 1b.

## CONCLUSIONS

In the present investigation ethylene was used as a model hydrogen acceptor molecule. It was found that iron exhibited very little activity for the hydrogenation of the olefin, however, when as little as 7% CO was added to the hydrocarbon-hydrogen mixture, the hydrogenation activity of the metal was substantially enhanced. Such an increase in hydrogenation activity was observed over a wide range of temperature, however, at 600°C one has to contend with the concomitant formation of a large amount of solid carbon. The presence of coadsorbed CO induces a weakening in the strength of the metal-hydrogen bond, which gives rise to the formation of a very reactive hydrogen species. These model studies demonstrate that the introduction of a gas additive, such as CO, into the reactant stream can effectively convert a metal which in its pure state is relatively inert into an

extremely active hydrogenation catalyst, and we believe that this concept could be extended to hydrogenation of coal and its derivatives.

#### ACKNOWLEDGMENTS

Support for this work was provided by the National Science Foundation, under Grant CBT-8800931.

#### REFERENCES

1. Walker, Jr., P. L., Rakszaski, J. F., and Imperial, G. R., *J. Phys. Chem.* **63**, 140 (1959).
2. Dry, M. E., Shingles, T., Boschhoff, L. J., and Van H. Botha, C. S., *J. Catal.* **17** 347 (1970).
3. Turkdogan, E. T. and Vinters, J. V., *Met. Trans.* **5**, 11, 21, (1974).
4. Vannice, M. A., in "Catalysis Science and Technology" Vol. 3 (J. R. Anderson and M. Boudart ed.), Springer-Verlag, New York, 1982, p. 139.
5. Benziger, J. B., and Madix, R. J., *Surf. Sci.* **115**, 279 (1982).
6. Burke, M. L. and Madix, R. J., *Surf. Sci.* **237**, 20 (1990).
7. Burke, M. L. and Madix, R. J., *J. Am. Chem. Soc.* **113**, 1475 (1991).
8. Burke, M. L. and Madix, R. J., *J. Am. Chem. Soc.* **113**, 3675 (1991).
9. Kim, M. S., Rodriguez, N. M., and Baker, R. T. K., *J. Catal.* **131**, 60 (1991).

TABLE 1. EFFECT OF GAS COMPOSITION ON THE GASEOUS PRODUCT DISTRIBUTION FROM THE INTERACTION OF C<sub>2</sub>H<sub>4</sub>-CO-H<sub>2</sub> MIXTURES OVER IRON AFTER 60 MINUTES AT 600°C

C <sub>2</sub> H <sub>4</sub> :CO:H <sub>2</sub>	% C <sub>2</sub> H <sub>4</sub> Decomposition	% CH <sub>4</sub> formed	C <sub>2</sub> H <sub>6</sub> formed
80:0:20	0.51	-	-
73:7:20	29.53	0.73	8.5
68:12:20	60.28	0.58	9.4
60:20:20	79.47	1.07	10.3
38:42:20	76.10	2.7	5.5
17:63:20	54.30	2.6	5.8
0:80:20	21.95	0.05	--

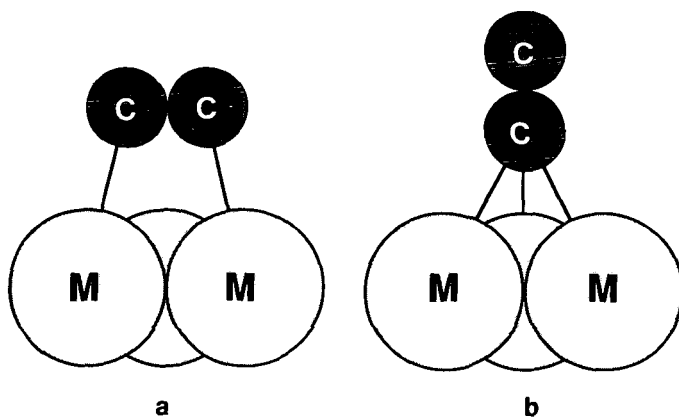


FIGURE 1. STRUCTURAL ARRANGEMENT FOR (a) ETHYLENE BONDED PARALLEL TO METAL SURFACE AND (b) ETHYLENE BONDED TO METAL IN THE STABLE "ETHYNYDYNE" CONFORMATION

## **Regulation of Air Toxics Under the 1990 Clean Air Act Amendments<sup>1/</sup>**

**Lee B. Zeugin  
Hunton & Williams  
2000 Pennsylvania Avenue, NW  
Suite 9000  
Washington, D.C. 20006**

Keywords: Clean Air Act, Section 112; Legal Requirements; Hazardous Air Pollutants

### **I. Introduction**

The 1990 Clean Air Act Amendments significantly revised the regulation of hazardous air pollutants under § 112. The old § 112 required EPA to identify hazardous air pollutants and promulgate health-based emission standards for each pollutant. The new § 112 requires EPA to regulate categories of sources using technology-based emission standards. Section 112 now specifically identifies 189 hazardous air pollutants, directs EPA to promulgate a list of the "major" and "area" source categories that emit those pollutants, and specifies a schedule within which EPA must promulgate emission standards for all source categories.

EPA has only just begun to implement the new air toxics provisions. This fall EPA promulgated a list of approximately 170 major and area sources including chemical manufacturers, polymers and resins producers, pharmaceutical producers, oil and natural gas producers, and petroleum refineries and proposed a schedule for regulating those sources. Synthetic organic chemical manufacturers will be among the first sources to be regulated. EPA's proposed hazardous organics national emission standard for hazardous air pollutants (hazardous organics NESHP or HON) may require synthetic organic chemical manufacturers to reduce emissions of as many as 149 hazardous air pollutants.

This paper will provide an overview of the new air toxics provisions including the HON, the early reductions program which enables sources to delay compliance with new regulations, and the modification provision which may compel sources to comply with new emission standards even sooner than otherwise required.

### **II. Overview of § 112**

The new § 112 establishes a list of 189 hazardous air pollutants that must be regulated under the air toxics program. Clean Air Act ("CAA") § 112(b). The statute directs EPA to issue a list of categories and subcategories of "major" and "area" sources that emit those pollutants. Last summer, EPA promulgated a list of approximately 170 source categories to be regulated. See 57 Fed. Reg. 31,591 (July 16, 1992).

Section 112 distinguishes between "major" and "area" emission sources. A "major source" is defined as "any stationary source or group of stationary sources located within a contiguous area and under common control that emits or has the potential to emit considering

---

<sup>1/</sup> The comments presented in this paper are those of the author and are not necessarily those of any client of Hunton & Williams. The author wishes to acknowledge Margaret L. Claiborne for her substantial contributions to this paper.

controls, in the aggregate 10 tons per year or more of any hazardous air pollutant or 25 tons per year or more of any combination of hazardous air pollutants." CAA § 112(a)(1). An "area source" is any source of hazardous air pollutants that is not a major source. CAA § 112(a)(2).

Once a source is on the list, it will be subject to technology-based emission standards. EPA must establish emission standards for every source category on the list by the year 2000. For major sources, the emission standards will be based on the maximum degree of reduction in air toxic emissions achievable based on the best technology currently available for the source category in question (maximum achievable control technology or MACT). Existing sources subject to MACT standards will have to achieve the average emissions limitation achieved by the best performing 12 percent of the existing sources or the average emission limitation achieved by the best performing five existing sources if less than 30 sources are in the category. New sources must meet the emissions limitation achieved by the best performing plant.

EPA must also promulgate technology-based emission standards for area sources. The Act directs EPA to establish standards for area sources based on "generally available control technology" (GACT). In practice, this standard will probably be less stringent than the MACT standard for major sources.

The statute establishes a timeframe within which EPA must promulgate these emission standards and then requires EPA to promulgate a more specific schedule based on its own source category list. Section 112(e) requires EPA to promulgate emission standards for 40 source categories by November 15, 1992, for 25 percent of all source categories by 1994, for 50 percent of all source categories by November 1997, and for the remaining source categories by November 15, 2000. EPA issued its proposed regulatory schedule in September 1992. See 57 Fed. Reg. 44,147 (Sept. 24, 1992). According to the proposal, synthetic organic chemical manufacturers must be regulated by November 15, 1992. EPA missed this deadline but hopes to promulgate a final rule by the end of 1993.

While the Amendments added the concept of technology-based standards, they did not completely abolish health-based emission standards. By November 1996, EPA must investigate and report to Congress on the risks to public health remaining, or likely to remain, after application of MACT standards and make recommendations for legislation necessary to control those risks. CAA § 112(f)(1). The Agency must adopt residual risk-based standards if any source in a source category presents a risk to the maximum exposed individual of more than one in one million ( $1 \times 10^6$ ). The risk-based standards must protect public health with an ample margin of safety and prevent adverse environmental effects. Furthermore, the Act contains a savings provision for the health-based emission standards promulgated under the old § 112. See CAA § 112(q). EPA must, however, review and revise those pre-1990 standards, if appropriate, before the year 2000.

### III. The Early Reductions Program

Sources may delay compliance with MACT standards by participating in the early reductions program under § 112(i). CAA § 112(i)(5); 57 Fed. Reg. 61,970 (December 29, 1992). An existing source can qualify for a six-year compliance extension by voluntarily reducing hazardous air pollutant emissions by 90 percent (95 percent for particulates) before EPA proposes a MACT standard applicable to the source. Sources subject to MACT standards

proposed before 1994, such as synthetic organic chemical manufacturers, may participate in the early reductions program by making an enforceable commitment to meet program requirements by January 1, 1994. Sources that qualify for the extension will be subject to an alternative emission limitation (AEL) which will be included in the sources' title V operating permit.

To encourage sources to participate, EPA has attempted to build some flexibility into this program. The final early reductions rule uses a flexible definition of "source" to enable a facility to choose whether to enroll the entire facility in the program or limit participation to certain process units provided that the emission reductions constitute significant reductions from the entire facility. The source may also choose the baseline year for calculating reductions, but it may be no earlier than 1987 unless the source can show that an earlier year (1985 or 1986) is more representative. Finally, a source may take credit for reductions taken for any reason, whether voluntary or involuntary.

Most sources interested in participating in the early reductions program may apply through the state's title V permit program. Sources subject to MACT standards proposed before 1994, however, may have to apply for a "specialty permit" through EPA because state title V permit programs will not likely be in place before January 1, 1994, the date by which those sources must make an enforceable commitment in order to participate in the program.

#### IV. Modifications & Reconstruction of "Major Sources"

While the early reductions program enables sources to delay compliance with MACT standards, some sources may become subject to MACT standards sooner than would otherwise be expected because of § 112's modification provision. Under § 112(g), once a state operating permit program is in place, if a modification to a "major source" is proposed and that modification would increase actual emissions of any hazardous air pollutant by more than a de minimis amount, then the modification cannot begin until the facility demonstrates that it will meet the MACT for existing sources. Because EPA has not yet defined "source" for purposes of MACT standards, it is unclear whether a modification would trigger MACT compliance for the specific emission point being modified or for the plant as a whole.

This modification provision differs from that under the new source review program in that not all modifications will trigger the rule, only those that will cause more than a de minimis increase in actual emissions. Section 112(a)(5) defines "modification" as "any physical change in, or change in the method of operation of, a major source which increases the actual emissions of any hazardous air pollutant emitted by such source by more than a de minimis amount or which results in the emission of any hazardous air pollutant not previously emitted by more than a de minimis amount." EPA has not yet defined de minimis for purposes of this section.

Even if the modification would cause more than a de minimis increase in emissions, sources making modifications can avoid demonstrating compliance with MACT standards by offsetting any increase in hazardous air pollutants by decreasing other hazardous emissions. More specifically, a physical or operational change that would otherwise fit the definition of modification will not be considered a "modification" if the owner or operator of the source shows that the "increase in the quantity of actual emissions of any hazardous air pollutant from

such source will be offset by an equal or greater decrease in the quantity of emissions of another hazardous air pollutant (or pollutants) from such source which is deemed more hazardous."<sup>27</sup>

One final point to note about the modification provision is that although it does not apply until after operating permit programs are in place, it has the effect of imposing MACT standards on sources even before EPA establishes MACT standards for that particular category or subcategory. In those cases, the emission limitation will be set on a case-by-case basis. CAA § 112(g)(2)(A).

While modifications under this provision may subject sources to MACT standards for existing sources, a major source that is reconstructed will be subject to MACT standards for new sources. The 1990 Amendments do not define "reconstruction," but EPA is likely to use the definition under the new source review provisions as a starting point for defining the term.

#### V. The Hazardous Organics NESHAP

The HON is the first major set of technology-based emission standards proposed under § 112 as amended and is therefore the best indication of how EPA plans to implement the new air toxics program. 57 Fed. Reg. 62,608 (Dec. 31, 1992). For example, this rule will indicate how EPA defines "source" in the context of MACT standards, how EPA determines the MACT floor, and how costs will be factored into the definition of MACT.

##### A. Definition of "Source"

The definition of "source" is important for a number of reasons. First, it describes the emission points to which each standard will apply. It is also important for defining the MACT floor, that is, the minimum emission level the source must meet, and finally, it is important for determining whether a particular source is a "major source" (i.e., whether the plant emits more than 10 tpy of any air toxic or 25 tpy of any combination of air toxics).

EPA has not adopted a general definition of "source" for purposes of § 112 but has indicated that it plans to define "source" within each MACT standard.<sup>28</sup> The HON as proposed defines "source" broadly. Under the HON, "source" will include all the process vents, storage vessels, transfer racks, wastewater collection and treatment operations, and equipment leaks in the organic hazardous air pollutant emitting chemical manufacturing processes that are located in a single facility covering a contiguous area under common control. The HON will apply to chemical manufacturers that produce one or more of the synthetic organic chemicals listed in the

---

<sup>27</sup> CAA § 112(g)(1)(A). EPA is in the process of developing regulations for the offset provision. The rule should include a ranking of the 189 hazardous air pollutants based on their effects on human health and the environment.

The offset provision applies only in the context of modifications and will not protect major sources from MACT standards once EPA has promulgated them for the source category.

<sup>28</sup> Sources should note that the definition may or may not be the same as the definition of "source" for purposes of the title V permit program.

rule and have an organic hazardous air pollutant as either: (1) a product, by-product, co-product, or intermediate or (2) a reactant.<sup>9</sup>

#### B. Definition of MACT

How EPA defines MACT is also important. For purposes of the HON, EPA determined the MACT floor by looking at each type of emission point, as opposed to the source as a whole, and developed a "reference control technology" (RCT) for each emission point that would satisfy the statutory maximum achievable control technology requirement. Affected sources will have to limit regulated emissions to the level that would be achieved using that RCT. How to achieve the emission limitations is up to each source. It may apply the RCT or another technology that will achieve the same standard. According to EPA, this standard takes into consideration the cost of controls.

The HON also allows sources to use emissions averaging to achieve the required emission limitations. This provision allows a source to average emissions from two or more emission points to achieve the overall emission reduction that would be achieved using the RCT. Therefore, by overcontrolling certain emission points, a source can undercontrol other emission points if the average satisfies the standard.

These requirements will be phased in over time. While the statute allows up to three years for compliance with air toxics emission standards, the HON will require certain process units to comply within six months of promulgation and others to comply within a year and a half after promulgation.

#### VI. The General Duty Clause

At least one regulatory provision of § 112 creates immediate obligations for industry. Congress enacted § 112(r) to prevent and detect accidental releases of hazardous air pollutants. This section applies to all owners and operators of stationary sources that produce, process, handle, or store certain "extremely hazardous" substances and imposes a "general duty" to prevent and respond to accidental releases of those substances.

The statute requires EPA to promulgate a list of not less than 100 substances "which, in the case of an accidental release, are known to cause or may reasonably be anticipated to cause death, injury, or serious adverse effects to human health or the environment."<sup>10</sup> Section 112(r) imposes an affirmative duty on owners and operators "to identify hazards which may result from [accidental] releases using appropriate hazard assessment techniques, to design and maintain a

---

<sup>9</sup> The equipment leak provisions of the HON will also apply to the following sources: styrene/butadiene rubber production, polybutadiene production, chlorine production, pesticide production, chlorinated hydrocarbon use, pharmaceutical production, and miscellaneous butadiene use.

<sup>10</sup> CAA § 112(r)(3). The statutory deadline for this list was November 15, 1992. EPA missed this deadline but hopes to propose a list along with the regulations under § 112(r) in 1993.

safe facility taking such steps as are necessary to prevent releases, and to minimize the consequences of accidental releases which do occur." CAA § 112(r)(1).

Although the statute requires EPA to promulgate regulations under this provision by November 1993, this "general duty" appears to be self-implementing. That is, it can be used as a basis for enforcement actions by EPA, even in the absence of any implementing regulations defining what steps are needed to comply with this "general duty."

#### **VII. Implementation of the Air Toxics Program**

The air toxics regulations will be implemented by the states under the title V operating permit program. Once the states have developed an EPA-approved operating permit program, all major sources under § 112 will be required to obtain a title V permit which specifies the applicable emission standards.

All major sources of hazardous air pollutants will be required to apply for a title V operating permit within 12 months of implementation of the state permit program, and those sources will have to report their air toxics emissions in their permit applications even if they are not yet subject to an emission standard under § 112. The title V permit rules require sources to describe in their permit application emissions of all "regulated air pollutants." "Regulated air pollutant" includes any air pollutant for which a § 112 standard has been established, regardless of whether the standard applies to the source submitting the permit application. That is, if a § 112 standard has been established for any source to limit emissions of a particular hazardous air pollutant, then all sources must report their emissions of that pollutant in their permit applications. See 40 C.F.R. § 70.2; 57 Fed. Reg. 32,295, 32,297 (July 21, 1992) (final title V permit rules). The list of "regulated air pollutants" for purposes of § 112 could become quite long very quickly; the HON alone may regulate as many as 149 of the 189 listed hazardous air pollutants.

#### **VIII. Issues to Watch**

In the next year, EPA will propose its general provisions under § 112 which will define basic terms and requirements that apply across MACT standards including monitoring, recordkeeping, and reporting requirements. EPA will also propose regulations under the modification provision, and in the next two years, EPA is scheduled to propose and promulgate MACT standards for over 40 source categories. Along with the HON, these rules will define the new air toxics program. Because the air toxics provisions of the statute leave many questions unanswered and because the way those questions are ultimately resolved can have a great impact on regulated entities, it will be important for industry to follow and participate these rulemakings.

**December 31, 1992**

## COAL CONVERSION AT THE K/T BOUNDARY: REMNANTS OF THE HAZARDOUS WASTE

Edwin S. Olson  
Universal Fuel Development Associates, Inc.  
Grand Forks, ND 58201

Key Words: K/T transition, coal gasification, amino acids

### ABSTRACT

The occurrence of large amounts of two nonprotein amino acids, aminobutyric acid (AIB) and isovaline (ISOVAL), in sediments near the Cretaceous/Tertiary (K/T) boundary was originally attributed to remnants of a bolide collision. However, these two amino acids are derived from the same two hydantoins that were isolated in large amounts from gasifier quench water, and we hypothesized that the K/T amino acids originated from a natural coal gasification process involving intrusion of magma into a coal seam. Condensation of the resulting gases, including carbon dioxide, ammonia, hydrogen cyanide, and ketones formed the hydantoin precursors for the amino acids. The K/T AIB/ISOVAL ratio corresponds to that observed for the corresponding hydantoins in gasifier quench water. The ratio of the ketones (acetone and 2-butanone) resulting from pyrolysis of a large variety of coals is also consistent with the AIB/ISOVAL ratio, although much larger amounts of the ketones are generated from low-rank coals.

### INTRODUCTION

At the close of the Cretaceous Period, a large number of species became extinct, most noteworthy, the dinosaurs. Many theories have been suggested to explain the mass extinction at the Cretaceous/Tertiary (K/T) boundary, including climate and land mass changes as well as collisions with a massive extraterrestrial object (bolide). The occurrence of nonprotein amino acids in sediments deposited before and after the K/T boundary was interpreted as evidence for an extraterrestrial event (1). Recently I established that the assumptions that led to that conclusion were erroneous, and that a more likely explanation for the occurrence of the amino acids, aminoisobutyric acid (AIB) and isovaline (ISOVAL), is that they formed from hydrolysis of hydantoins that were produced from coal-derived gases (2). This hypothesis is based on the finding of large amounts of hydantoins, mainly 5,5-dimethylhydantoin (DMH) and 5-ethyl-5-methylhydantoin (EMH), in condensate water from a coal gasification facility (3,4). The two major hydantoins (DMH and EMH) were present in concentrations of about 2000 and 500 mg/L, respectively, in condensate water from gasification of Indian Head lignite (4). Numerous other 5-substituted hydantoins were also identified at concentrations an order of magnitude smaller (3). The two major hydantoins produced as by-products of coal gasification are in fact those that generate AIB and ISOVAL on hydrolysis. Thus the AIB and ISOVAL isolated from the sediment samples may very likely have resulted from natural thermal processing of terrestrial coal sources via hydantoin formation and subsequent hydrolysis.

The K/T transition was accompanied by extensive magmatic intrusions and volcanic activity. Magmatic intervention in a coal seam may have generated the gases that condensed and reacted to form large amounts of the hydantoins. Many examples of thermal magmatic decomposition of coal have been reported in

geological investigations of coals from various locations (5). In order to ascertain which intrusion sites might be candidates for the generation of the precursor components required for hydantoin synthesis, a relationship between the chemical evidence in the K/T or near K/T deposits and potential coal progenitors must be demonstrated. The purpose of this paper is to present data that relates to the issue of coal-derived precursors for the amino acids.

## RESULTS AND DISCUSSION

The formation of hydantoin in the water from the slagging gasifier was demonstrated to have resulted from the complex Bucherer-Bergs reaction of ammonia, carbonate, hydrogen cyanide, and various ketones and aldehydes present in the gas cooling/condensing system (spray washer and tar-oil-water separator) of the gasifier and not from a high-temperature reaction in the gasifier itself (6,7). In the upper pyrolysis region of the slagging fixed-bed gasifier, hot gases produced in the high-temperature gasification zone heat the coal and release the ketones, as well as phenolics, alcohols, nitriles, and other volatile organic components. A large number of ketones are produced in coal pyrolysis, the major ones being acetone and 2-butanone, and these are present in significant concentrations in the condensate water, even after hydantoin formation has been completed (4). The ratio of acetone to 2-butanone was between 3 and 4 in the condensate water samples obtained from lignite (Indian Head, ND) gasification. This ratio corresponded closely to the DMH/EMH ratio observed in the condensate water. As much as 95% of the ketones were converted to hydantoin; but, in general, the limiting species in the Bucherer-Bergs reaction occurring in the condensate water is the hydrogen cyanide, owing to its lower solubility in water at the collection temperature. In the high-temperature gasification zone, ammonia and hydrogen cyanide are produced in about a 10 to 1 ratio (8). Carbon dioxide is generated by the reaction of oxygen with carbon in the hot zone and also by decarboxylation in the pyrolysis zone (in the case of low-rank coals).

If the AIB and ISOVAL in the K/T boundary sediments resulted from natural coal gasification via DMH and EMH, then the AIB/ISOVAL ratio should match the acetone/2-butanone ratio in the products from pyrolysis of the type of coal that was heated at the K/T transition. Pyrolysis products from a number of coal samples of different ranks were collected and analyzed in a pyrolysis/devolatilization project at the University of North Dakota Energy Research Center (9). Data from these analyses are given in Table 1. The ratio of acetone to 2-butanone from pyrolysis of the various coals is between 3 and 4 and is not rank dependent. The ratio of AIB to ISOVAL found in the sediment layers above and below the iridium layer at Stevns Klint was 3 and 4, respectively (1). This means that either a bituminous or lower rank coal could have been the source of the ketones which formed the amino acids found in the sediments.

A terrestrial coal source can account for production of a very large amount of amino acids. The total quantity of acetone and 2-butanone produced from coal pyrolysis is significantly large and is rank dependent (Table 1). Low-rank coals gave three times more ketones than bituminous coals. Thus the yield of hydantoin from 1 kg of lignite could have been as high as 4 g, if all the acetone and 2-butanone produced in pyrolysis were converted via a Bucherer-Bergs reaction in a condensed phase. Geothermal or volcanic gasification of a small coal seam of 1 km<sup>2</sup> by 10 m thickness could have generated  $6 \times 10^7$  kg of hydantoin.

A possible mechanism for natural coal gasification is suggested here. Since a low-rank coal may contain as much as 40% water and a high percentage of oxygen that could be converted to carbon dioxide, a source of intense heat is the main requirement for pyrolytic generation of ammonia, hydrogen cyanide, ketones, and carbon dioxide, which are the precursors for the hydantoins. However, ground or stream water may have played a role in furnishing steam, which could have effectively driven the gasification, and also in furnishing a coolant for the gas produced, so that the condensed gases could react to form the hydantoins. A second possibility is discharge and collection of gases into natural water reservoirs overlying the magma intrusion into the coal seam. Hydrolysis of hydantoins to the amino acids may have been microbially catalyzed or may have occurred over a long time period. Utilization of the 2-substituted amino acids by microorganisms is not likely, resulting in high stability for these compounds. Actually, the method for analysis of the sediments involved conditions that may have hydrolyzed hydantoins to the amino acids; therefore, we cannot rule out their existence in the sediments.

The location and extent of the natural coal gasification promises to be as interesting as the search for the alleged bolide collision site has been. One very important fact must be considered. Whereas the iridium anomaly specifically requires a mantle type of volcanic activity (or bolide), any kind of volcanic or magmatic intrusion into a coal field could have been responsible for the amino acid anomaly. Evidence was recently presented for a tectonic uplifting activity (10) and mantle hot-spot doming in the North Atlantic at the K/T transition (11). Alternatively the magmatic event may have been associated with the North American Laramide magmatic trend, such as the Raton, Colorado, area, where large quantities of char were observed (5). Natural coal gasification may have occurred in several localities, since coal deposits as well as geothermal activity were plentiful in the northern hemisphere.

Natural coal gasification may be only indirectly related to the extinctions that occurred at the K/T transition through volcanism or magmatic intrusions that accompanied a general climatic or sea level change scenario. The complex sequence of extinctions related to volcanism, sea level changes, and other global trends was recently reviewed by Officer (12). There is also a possibility that coal gasification may be related to extinctions during a period of intense volcanic activity. Drawing from the Lake Nyos disaster which involved conversion of a relatively small amount of carbon and evolution as carbon dioxide, we could speculate on another possible relationship. Many of the compounds generated as a result of coal gasification are highly toxic. Besides the ammonia and hydrogen cyanide discussed above, hydrogen sulfide is produced in copious amounts; however, the major component of coal gas by weight is carbon monoxide. Toxic compounds such as phenols and carcinogens such as polynuclear aromatics and amines are also formed. Hydantoins are well known as hypnotics and suspected carcinogens. Many of the organic products would have persisted for a long time. Thus the toxicity of coal gasification gases or other products may offer an alternative explanation for some of the extinctions that occurred in this period.

**Table 1** Yields of Ketones (micrograms/gram maf coal) from Pyrolysis of Coals

Coal	%C maf	%O (dif.)	Acetone	2-Butanone
Gascoyne Blue	59.8	32	1600	510
Center	70.0	23	1480	440
Indian Head	72.0	22	1420	400
Rosebud	76.3	16	930	320
Sufco	79.2	14	750	250
Illinois #6	77.2	11	500	120

Pyrolysis conditions were the following: heating rate of 45°C/min, max. 850°C, helium atmosphere, -60-mesh particle size, 5-g sample size (9).

## REFERENCES

1. Zhao, M. & Bada, J.L. Nature 339, 463-465 (1989).
2. Olson, E.S. Nature 357, 202 (1992).
3. Olson, E.S., Diehl, J.W. & Miller, D.J. Anal. Chem. 55, 1111 (1983).
4. Willson, W.G., Hendrikson, J.G., Mann, M.D., Mayer, G.G. & Olson, E.S. in Twelfth Biennial Lignite Symposium: Technology and Utilization of Low-Rank Coals, Proceedings, Vol. I, DOE/METC84-13 (Feb. 1984) (eds. Kube, W.R., Sondreal, E.A., & Rao, C.D.) 265-299.
5. Crelling, J.C. & Dutcher, R.R. Geol. Soc. of Amer. Bull. 79, 1375-1386 (1968).
6. Olson, E.S., Worman, J.J. & Diehl, J.W. ACS Div. of Fuel Chem. Preprints 30 (2), 288-290 (1985).
7. Diehl, J.W., Olson, E.S. & Worman, J.J. Fuel 64, 1019-1021 (1985).
8. Anastasia, L.J. in Advanced Techniques in Synthetic Fuels Analysis (eds. Wright, C.W., Wiemer, W.C., & Felix, W.D.) Tech. Inform. Ctr. USDOE, PNL-SA-11552 (DE83015528), 105-132 (1983).
9. Ross, S.F. Pyrolysis and Devolatilization of Low-Rank Coals Final Report for the Period Apr. 11, 1983 - June 30, 1986, Univ. of ND En. Res. Ctr. DOE/FE/60181-2129 (DE87001017).
10. Lewis, C.L.E., Green, P.F., Carter, A., and Hurford, A.J. Earth & Planetary Sci. Lett., 112, 131-145 (1992).
11. White, R.S. and McKenzie, D.P. J. Geophys. Res. 94 (B6), 7685-7730 (1989).
12. Officer, C.B. J. Geol. Educ. 38, 402-416 (1990).

## TRACE ELEMENT BEHAVIOR IN GASIFICATION SYSTEMS

Thomas A. Erickson and Steven A. Benson  
Energy and Environmental Research Center  
University of North Dakota  
Box 8213, University Station  
Grand Forks, North Dakota 58202.

**Keywords:** trace elements, coal gasification, modeling

### ABSTRACT

Research has been initiated to determine the behavior of trace elements in integrated gasification combined cycle (IGCC) and integrated gasification fuel cell (IGFC) systems. The goal is to identify and model the important physical and chemical transformation mechanisms of seven trace elements (arsenic, chromium, cadmium, mercury, nickel, selenium, and lead) during gasification as a function of coal composition (trace element abundance and association) and gasification conditions. Identification of the reactions and transformations of trace elements is being conducted in laboratory-scale coal gasification systems. This experimental work is coupled with the development of a computer model to predict the state of trace elements in gasification systems and to identify effective control technologies.

### INTRODUCTION

Trace element emissions pose a potential problem to two emerging coal gasification electric power generating systems: IGCC and IGFC. The potential problems associated with trace elements are the release of substances that are considered air toxics and the degradation of fuel cell efficiency due to contamination with minor elements. In order to develop effective technologies to control trace element emissions within anticipated regulatory requirements and to ensure the efficient operation of fuel cells, the type and quantity of trace elements emitted from coal gasification-based systems must be determined as a function of system, system conditions, and coal composition.

The fate of trace elements in coals used in IGCC and IGFC systems is closely tied to how the trace elements are associated in the coal and the gasification conditions. Trace elements in coals are associated in several forms, including organic associations, such as salts of carboxylic acid groups and organic coordination complexes, and mineral associations, such as sulfides, sulfates, silicates, phosphates, and carbonates. During gasification, these inorganic elements are partitioned into gases, liquids, and solids. The transformation of these trace elements into the various states and phases depends upon the fundamental characteristics of the elements and their association with minerals and coal particles. Minerals that are not directly associated with coal particles experience a different process environment than minerals that are intimately associated with coal particles during gasification.

Gasification conditions, such as reducing and oxidizing atmospheres, gas phase composition, pressure, and temperature, influence the partitioning of trace elements between various gases, liquids, and solid inorganic components as a function of location in the gasifier. In order to predict the form of the

inorganic species during gasification, it is essential that detailed information on the distribution of major mineral phases and organically associated inorganic elements be determined. This information is critical since the transformations and interactions during utilization impact the partitioning of trace elements. Modeling the transformations using thermochemical equilibrium calculations combined with various chemical and physical constraints to reach equilibrium can be effectively used to estimate the distribution of gas, liquid, and solid components as a function of gasification conditions.

#### EXPERIMENTAL APPROACH

The predicting of inorganic transformations (major and minor components) during coal combustion has long been the focus of many research programs.<sup>1-3</sup> In the program described in this paper, the predictive techniques that have been applied to combustion are being modified to predict inorganic transformations under gasification conditions. Many of the current trace element predictive techniques are based on the assumption of equilibrium conditions and not on actual kinetically constrained transformations that occur during coal utilization. The approach used in the program is to combine inorganic transformation algorithms and the thermochemical equilibrium calculations.<sup>4,5</sup> These techniques will be developed to predict the particle-size and composition distribution of the resulting coal ash particulate, along with the state of the vapor species at selected conditions for major, minor, and trace constituents.

The predictive techniques being applied to the modeling of trace elements during gasification require state-of-the-art analytical and experimental data. The modeling of trace elements requires particle-size and composition distributions of the trace constituents in relation to the major and minor species in the coal. To provide the necessary data, computer-controlled scanning electron microscopy (CCSEM) is being adapted to include trace element analysis through the use of wavelength dispersive x-ray spectrometers. Although the automated adaptations to the CCSEM technique will require significant development, generalized distributions of the trace elements can be made manually in conjunction with the CCSEM analysis. To generate the essential experimental data, a pressurized drop-tube furnace (PDTF) is being used to simulate coal gasification. Ash and vapor samples produced from the PDTF are characterized by CCSEM with wavelength adaptations for determining trace elements, wavelength and energy dispersive x-ray fluorescence, inductively coupled argon plasma spectroscopy (ICAP), and atomic adsorption (AA). The following sections discuss the three major developments taking place to produce a predictive methodology for trace element emissions during gasification: transformation modeling, microscopic sample characterization, and laboratory-scale coal gasification.

#### TRANSFORMATION MODELING

A computer model to predict the evolution of major, minor, and trace elements during the gasification of coal is being created based on the algorithm shown in Figure 1. The shaded boxes in Figure 1 represent the inputs required, while the boxes with a drop shadow are the outputs generated from the model.

The first task of the model is to determine the associations of the major, minor, and trace elements in the coal prior to utilization. The association of the elements prior to utilization will affect their phase, size, and composition distribution in the residual ash and gas streams. The three primary inorganic associations are water, organic, and mineral. Water-associated constituents are generally in the form of sulfates or chlorides present in the moisture of a coal particle. The organically associated constituents are generally found as the salts of carboxylic acid groups attached to the carbon matrix and as oxygen replacement (such as organic sulfur). The mineral associations are elements which comprise discrete minerals in the coal (such as clays, carbonates, and sulfides).

Due to the complexity of interaction of the inorganics during coal gasification, the mineral associations are further divided into mineral type, trace, minor and major element content, size, and juxtaposition. Juxtaposition refers to the association of the minerals with the coal and with other minerals. A locked mineral is intimately associated in the coal particle, while a liberated mineral is external to the carbon matrix. The detailed mineral classification is very important because different minerals behave differently. For instance, carbonates will commonly release  $\text{CO}_2$ . This will result in a greater potential for mineral fragmentation, depending on the system conditions. Clays which contain high levels of moisture may fragment initially due to the release of  $\text{H}_2\text{O}$  from their porous structure. Silicates are much less prone to fragmentation because they lack any of the previously discussed components.

Many of the mineral particles encountered in coal utilization are rarely free from trace and minor components. To predict the transformations of the trace and minor elements effectively, their distribution among the minerals is required. Whether a mineral is locked within the coal matrix or external to the coal can also have a large impact on its transformations. Locked minerals will be much more likely to coalesce with other minerals and organically associated constituents than the liberated minerals. The liberated particles will also experience a slightly different gas environment during coal gasification since they are not intimately in contact with the highly reducing, exothermic reaction of the carbon matrix.

Once a mass balance is performed around the coal input data, it is necessary to determine which of the inorganic components will be vaporized during the initial gasification process. These calculations will be performed with the use of a thermochemical equilibrium program, PHOEBE,<sup>4,5</sup> created at the Energy and Environmental Research Center (EERC). This code is currently being upgraded to include the appropriate trace element phases. With the exclusion of the vaporized species, the remaining constituents will be processed through algorithms for mineral fragmentation, coalescence of both minerals and organically associated species, and shedding of resulting particles.

The fragmentation, coalescence and shedding algorithms will be developed with the aid of data generated in the pressurized drop-tube furnace (PDTF). These algorithms are designed on various frequency distributions for each of the minerals and physical processes. The organically associated species which do not readily volatilize will also undergo coalescence with mineral particles as a function of the surface area of the minerals during coalescence. A portion of the organically associated species also homogeneously coalesces. The

liberated minerals undergo fragmentation, but do not appreciably coalesce with other minerals due to their lack of intimate contact with the coal.

The state of the volatile species at the resultant conditions will then be determined using the PHOEBE code again. The quantity of species that will condense prior to the resultant conditions are calculated from the PHOEBE data. The condensing species will then be homogeneously and heterogeneously condensed. The heterogeneous condensation will be based on the surface area of the particles. The resultant particulate and vapor species will be compiled and manipulated into various composition and size distributions as to the user's discretion. These distributions can be used to determine effective control technologies for a specific coal or to locate a coal compatible to a specific control technology.

Although the emphasis of this model is to aid in the control of trace element emissions, little attention is being given at this time to the effects of size and composition of inorganic ash components on control technologies. Once this model has been tested and verified, the next logical step will be to investigate the control technologies as a function of particulate and vapor properties.

#### **MICROSCOPIC SAMPLE CHARACTERIZATION**

Many of the computer models recently developed to predict the evolution of major and minor elements during coal gasification were made possible by the development on a highly quantitative analytical technique for coal analysis, CCSEM.<sup>6</sup> CCSEM provides a particle-size and composition distribution for the mineral contents of a particular coal for twelve major and minor elements. These raw CCSEM data are the primary input to the newest computer models ash formation. The CCSEM data are used in conjunction with a bulk ash determination (x-ray fluorescence or atomic absorption) to determine the content of nonmineral species by mass balance. The goal for trace element modeling is to provide particle-size and composition distributions for the trace elements and a bulk composition containing trace elements similar to the current data produced for major and minor species. The bulk trace element composition has long been attainable by ICAP or AA, and the size and composition distributions are nearly obtainable by combining the current CCSEM technique with wavelength dispersive x-ray analysis capabilities for trace elements.

The standard CCSEM technique uses an energy dispersive spectrometer (EDS) which allows for the simultaneous determination of major and minor species in the minerals. However, the EDS detector is not sufficiently sensitive to trace elements. A wavelength dispersive spectrometer is much more sensitive for trace elements, but can only characterize one element at a time, thus making it impractical for the time-consuming rigors of the CCSEM technique. By combining both detectors during a single analysis, trace, minor, and major elements can be recorded. This procedure is currently being developed, but is not expected to be fully operational until the second quarter of 1993.

In an initial effort to determine the generalized associations of trace elements with minerals, the standard CCSEM procedure is run on a coal. At the completion of each frame of analysis, the operator can locate the specific minerals and reanalyze them with the wavelength dispersive instrumentation.

The wavelength data analysis can then be manually compared to the standard CCSEM data to correlate the presence of trace elements with specific mineral species. A generalized trace element profile can then be created for a number of coals to be used for data correlations in the model until the more rigorous technique is completed. In addition, the chemical fractionation technique is being used to support the CCSEM by providing data on the general association of the seven trace metals.

#### LABORATORY-SCALE COAL GASIFICATION

The fate and distribution of trace elements under the effects of temperature, pressure, and gas composition in IGCC systems are important to the emerging technologies. Laboratory-scale experiments performed in the EERC PDTF are being used to study the partitioning of important trace elements and to enable the prediction of trace element emissions for IGCC and IGFC systems.

The PDTF furnace assembly, Figure 2, consists of a 2.875-inch ID alumina tube (55 inches long) with a slightly reduced end, used to support a flow accelerator in a fixed position, nested on top of a tube of the same dimensions (25 inches long). These tubes are concentrically surrounded by a tube of slightly larger dimensions. The tubes are heated externally by high-temperature tube furnaces equipped with Kanthal Super 33 elements. The entire reactor and the heating elements are housed in a water-jacketed pressure vessel. Coal is introduced into the reactor with a carrier gas through a traversing, water-cooled injector located in the center of the tube. Optional, secondary air enters the reactor at the top of the tube and flows through the tube around the injector assembly. The coal residue and process gases travel down the tube in a laminar flow regime and pass through the accelerator where they are collected by a water-cooled, nitrogen-quenching ash collection probe. Various collection devices can be attached to the collection probe to collect the solids. Size segregation of the ash is obtained using a multicyclone or impactor in conjunction with a final filter. A bulk filter is used to collect ash for bulk chemistry. A water-cooled deposition probe can also be inserted, in place of the ash collection probe, to simulate the deposition conditions in a utility boiler. The product gases are monitored on-line by O<sub>2</sub>, CO, and CO<sub>2</sub> gas analyzers or are intermittently sampled for a gas chromatograph (GC).

The PDTF can operate at temperatures as high as 1500°C and pressures up to 250 psi. Efforts are currently underway to attach an atomic absorption unit to the exiting gas line to acquire on-line mercury analysis from the furnace. Previous studies in the PDTF have produced very good gasification simulation results. Burnouts in excess of 95% with high carbon monoxide/carbon dioxide ratios have been produced under gasification conditions.

In this initial modeling effort, three coals will be run under multiple temperatures, pressures, gas compositions and residence times. The resultant samples will be collected in a three-stage multicyclone and characterized using scanning electron microscopy, wavelength dispersive x-ray fluorescence, inductively coupled plasma spectrometry, and atomic absorption. The data generated from the PDTF will support the development of the physical interaction algorithms in the model.

## CONCLUSIONS

A computer model to predict the transformations of trace, minor, and major elements during coal gasification is expected to be completed by late 1993. This model will generate the particle-size and composition distribution of the inorganic constituents as a function of the original coal content and system conditions. Advances in both analytical and experimental technologies are currently being made to provide added insight into the modeling of these inorganics during coal utilization.

## REFERENCES

1. Zygarlicke, C.J.; Ramanathan, M.; Erickson, T.A. "Fly Ash Particle-Size Distribution and Composition: Experimental and Phenomenological Approach," In *Inorganic Transformations and Ash Deposition During Combustion*; Benson, S.A., Ed.; American Society of Mechanical Engineers: New York, 1992, pp 525-544.
2. Wilemski, G.; Srinivaschar, S.; Sarofim, A.F. "Modeling of Mineral Matter Redistribution and Ash Formation in Pulverized Coal Combustion," In *Inorganic Transformations and Ash Deposition During Combustion*; Benson, S.A., Ed.; American Society of Mechanical Engineers: New York, 1992, pp 545-564.
3. Baxter, L.L. "Char Fragmentation and Fly Ash Formation During Pulverized-Coal Combustion," In *Combustion and Flame* 1992, 90, 174-184.
4. Ramanathan, M.; Ness, S.; Kalmanovitch, D.P. "New Techniques for Thermochemical Phase Equilibrium Predictions in Coal Ash Systems - I," 197<sup>th</sup> Annual Meeting of the American Chemical Society, April 9-14, 1989, Dallas, TX, 1989, p 7.
5. Ramanathan, M.; Kalmanovitch, D.P.; Ness, S. "New Techniques for Thermochemical Phase Equilibrium Predictions in Coal Ash Systems - II," Sixth International Conference on High Temperatures - Chemistry of Inorganic Materials, April 3-7, 1991, Gaithersburg, MD, p 17.
6. Steadman, E.N.; Zygarlicke, C.J.; Benson, S.A.; Jones, M.L. "A Microanalytical Approach to the Characterization of Coal, Ash, and Deposits," ASME Seminar on Fireside Fouling Problems, Brigham Young University, Provo, UT, Apr. 1990.
7. Benson, S.A.; Holm, P.L. "Comparison of the Inorganic Constituents in Three Low-Rank Coals," *Ind. Eng. Chem. Prod. Res. Dev.* 1985, 24, 145.

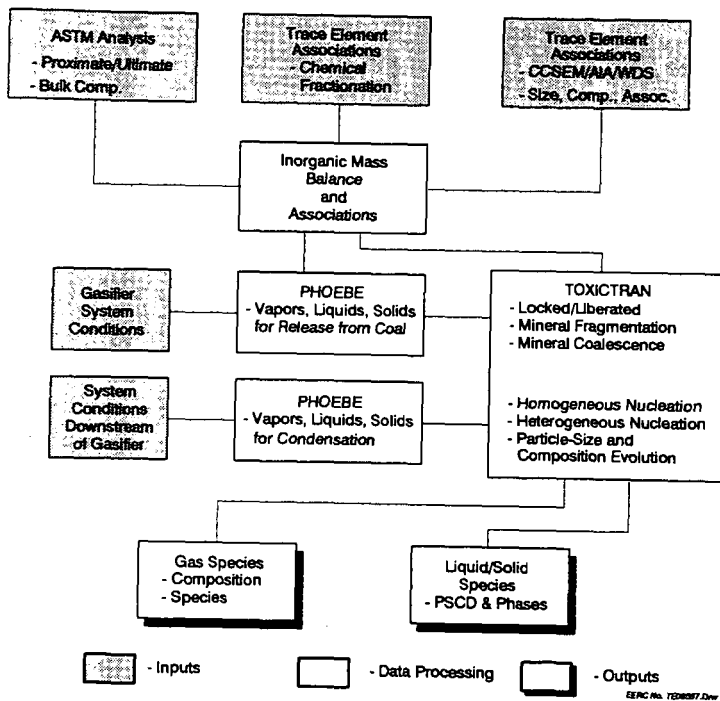


Figure 1. Trace element emissions model algorithm.

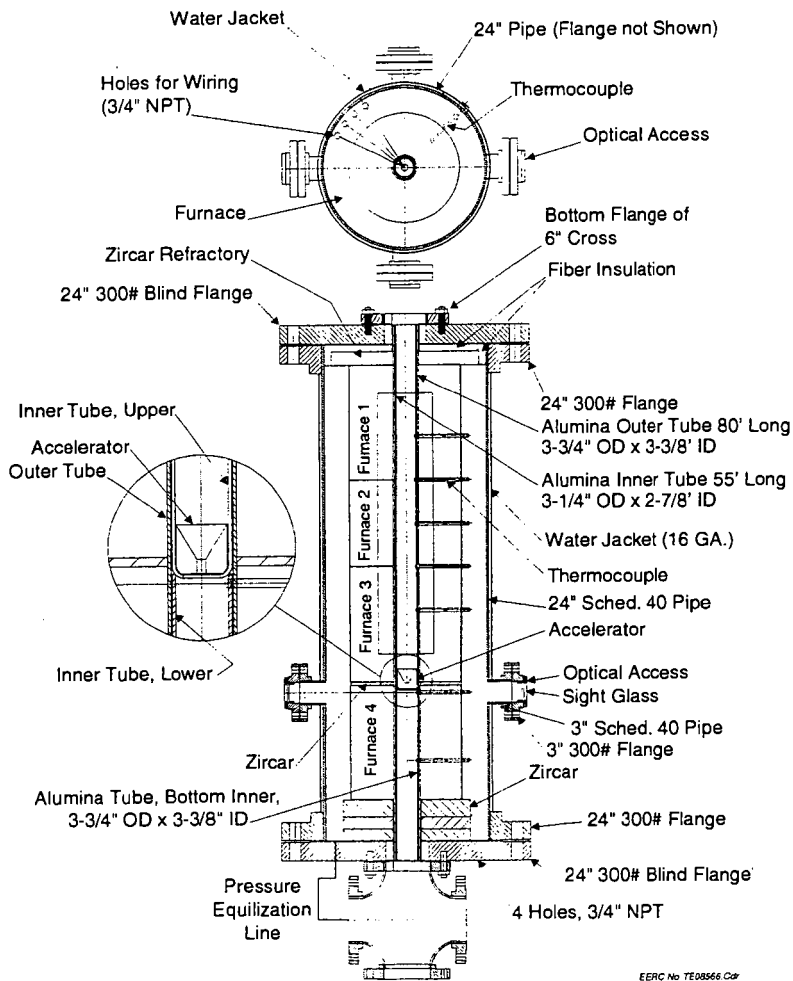


Figure 2. Pressurized drop-tube furnace assembly.

## TRACE ELEMENT BEHAVIOR DURING COAL COMBUSTION

J.J. Helble<sup>1</sup> and A.F. Sarofim<sup>2</sup>

<sup>1</sup>PSI Technology Co., Andover MA 01810

<sup>2</sup>MIT Dept. of Chemical Engineering, Cambridge MA 02139

**Keywords:** Trace elements, coal combustion, partitioning

### ABSTRACT

The emissions of trace elements from coal-powered processes depends to a large extent on the high temperature transformations of the trace species. In a laboratory study utilizing an Alabama bituminous coal, a Wyoming sub-bituminous coal, and a Montana lignite coal, trace element partitioning during coal combustion was examined. Experiments were conducted in an isothermal laminar flow drop tube furnace, using narrowly size-segregated coal samples to minimize particle to particle variation in the feed. In these experiments, the partitioning of the elements Zn, Mn, Cr, As, Sb, and Se among the various size fractions of ash particles was measured as a function of coal type and particle combustion temperature. Different fractions of each element were noted in the submicron ash, with Zn, As, Sb, and Se generally concentrated in the smallest ash particle size fractions.

### INTRODUCTION

Title III of the 1990 Amendments to the Clean Air Act identify 189 hazardous air pollutants whose emissions may be regulated [1]. A wide variety of stationary sources, including industrial and institutional combustion sources, are to be regulated as a result of this legislation. Coal-fired electricity-generating utility power plants are currently not regulated by Title III, the hazardous air pollutants portion of the legislation. Pending the results of an EPA study of power plant emissions, however, utility boilers may also be regulated.

Of these 189 hazardous air pollutants, 11 are trace metals contained in coal. For these metals - Sb, As, Be, Cd, Co, Cr, Hg, Pb, Mn, Ni, Se - the concentration in the stack gases strongly depends upon elemental partitioning during coal combustion. For example, volatile elements such as Hg are likely to leave the boiler with the flue gases, whereas relatively non-volatile elements such as Mn are likely to be collected with the fly ash or bottom ash. These are not firm "rules", however; for any element, variations in concentration in the various effluent streams have been reported [2-5].

Many of the observed differences in partitioning have been attributed to differences in coal type. This is likely due to differences in the form of an element in coal with rank. Elements associated with clays generally associate with fly ash, whereas elements associated with the organic matrix are more likely to volatilize. Consider chromium as an example. A typical chromium concentration in U.S. coal is 15 to 20 ppm [6,7], with the elemental forms uncertain. One study identified Cr within clays as a possibility, while another suggested that

50% organic association was possible [4,6]. These differences point to possible differences in partitioning for this element.

To investigate the importance of coal rank, and therefore indirectly investigate the effect of the elemental form on partitioning, a detailed laboratory study was conducted. In this paper, results from three U.S. coals are presented.

## EXPERIMENTAL

### Coal Selection

Experiments were conducted with three different parent coals: Illinois #6 and Alabama Rosa (bituminous), Wyoming Comanche (sub-bituminous), and a Montana lignite. A density-separated sample of the Montana lignite, treated to remove all coal particles with a specific gravity greater than 1.8, was also investigated to look for differences in behavior arising from reduced ash content. Selected trace element concentration data for these coals are presented in Table I. For most of the elements considered in this study, concentration of the element within the coal varied by factors of 2 to 20 with coal type.

### Laboratory Combustion Facility

All of the coal combustion experiments were conducted in the MIT laboratory scale laminar flow furnace [8]. A schematic diagram of this facility is presented in Figure 1. Coal particles, sized to 53/63, 75/90, or 125/150  $\mu\text{m}$  by dry sieving techniques, were injected at the top of the reactor through a water-cooled feeder probe. Feed rates of 0.01 to 0.03 g/min were used, with nitrogen serving as the entraining carrier gas. Combustion occurred in the heated zone of the laminar flow reactor, with coal particle temperatures controlled by the concentration of oxygen in the bulk gas. Reactor wall temperatures were held constant at 1750 K. At the conclusion of combustion, all ash particles and gaseous combustion products were extracted with a water-cooled, nitrogen-quenched sampling probe. Nitrogen gas was also transpired through a porous metal probe liner to minimize particle losses during sampling. Particles were size segregated on-line as needed through the use of an Andersen Mark 2 eight-stage cascade impactor.

### Chemical Analysis

Neutron activation analysis at the M.I.T. Nuclear Reactor Laboratory was used to determine the concentration of trace elements in all coal and ash samples examined in this study. Analysis of orchard leaves, a standard reference material obtained from NIST, was used for calibration.

## RESULTS AND DISCUSSION

The variation in the concentration of selected trace elements in the submicron ash was examined as a function of coal type, coal particle size, and coal particle combustion temperature. In addition, the concentration of selected trace elements as a function of ash particle size was examined.

### Trace Element Concentration as a Function of Ash Particle Size

The concentration of trace elements as a function of ash particle size was examined in a study of Wyoming Comanche sub-bituminous coal. A 75/90  $\mu\text{m}$  size fraction of the coal was used in these tests. Furnace wall temperature was maintained at 1750 K, with an oxygen partial pressure of 0.30 atmosphere (balance nitrogen). Trends observed for the elements vanadium, chromium, and manganese are presented in Figure 2. Vanadium was uniformly distributed among all particle size classes, whereas chromium was slightly enriched and manganese was significantly enriched in the submicron fraction of the ash. Chromium concentrations measured for ash generated from combustion of the density segregated Montana lignite in 20% oxygen show a similar trend to the chromium from the Wyoming coal.

Enrichment in the smallest size fraction is generally taken as a sign of vaporization. This is because condensation occurs preferentially on the smallest ash particles that provide most of the surface area. Non-volatile elements generally are concentrated in the largest ash particles. The concentration of Sc, presented for comparison in Figure 2, shows behavior typically associated with a highly refractory, non-vaporizing element. From this, we conclude that for the Wyoming sub-bituminous coal, 1) manganese vaporizes during combustion and condenses on the smallest ash particles; 2) chromium may partially volatilize during combustion; and 3) vanadium remains associated with the larger fly ash particles and hence is relatively non-volatile.

### Effect of Combustion Temperature

At the gas temperatures considered in this study, the combustion of pulverized coal is controlled by the diffusion of oxygen to the particle surface at the gas. The rate of combustion and hence the coal particle temperatures are therefore affected by the flux of oxygen to the surface, which in turn is controlled by the partial pressure of oxygen in the gas. Thus, by increasing oxygen partial pressure, the coal particle combustion temperature can be raised accordingly. Measurements and calculations have indicated that coal particle temperatures may increase from approximately 1900 to 2000 K in 20% oxygen to as high as 2600 to 2800 K in 80% oxygen [8].

The effect of coal particle combustion temperature on trace element concentration in the submicron ash was investigated in a study of the Wyoming coal. Results obtained for the elements V, Cr, As, and Sb are presented in Figure 3. Concentrations of Sc are again presented as an example of a non-volatile element. Vanadium, chromium, and scandium concentrations all increased with increasing oxygen concentration indicative of relative non-volatility. Arsenic and antimony concentrations, however, decreased with increasing temperature. This suggests that the majority of each of these elements vaporized at relatively low temperatures. The reduction in concentration is a diluent effect, resulting from additional vaporization of refractory species at higher temperatures.

### Effect of Feed Coal Particle Size

Trace element concentrations in the Montana lignite coal and combustion-derived submicron ash as a function of coal particle size are presented in Figure 4. Little difference was noted in the concentration of these elements in the coal or the ash for most elements. Chromium concentrations in the submicron ash, however, decreased as larger coal particles

were burned. This suggests that chromium in the largest coal particles was either retained by aluminosilicate minerals (ash particles), or was present in a more refractory form initially.

#### Effect of Coal Type

Enrichment of trace elements in the submicron ash was examined for the three parent coals considered in this study. As shown in Figure 5, enrichment was typically lowest for the sub-bituminous coal. Arsenic and vanadium were most volatile in the bituminous coal, whereas chromium was most volatile in the lignitic coal. For a given element, differences in enrichment factor as a function of coal type suggest differences in volatility. This in turn suggests differences in the predominant form of the element in the parent coals.

#### **ACKNOWLEDGEMENTS**

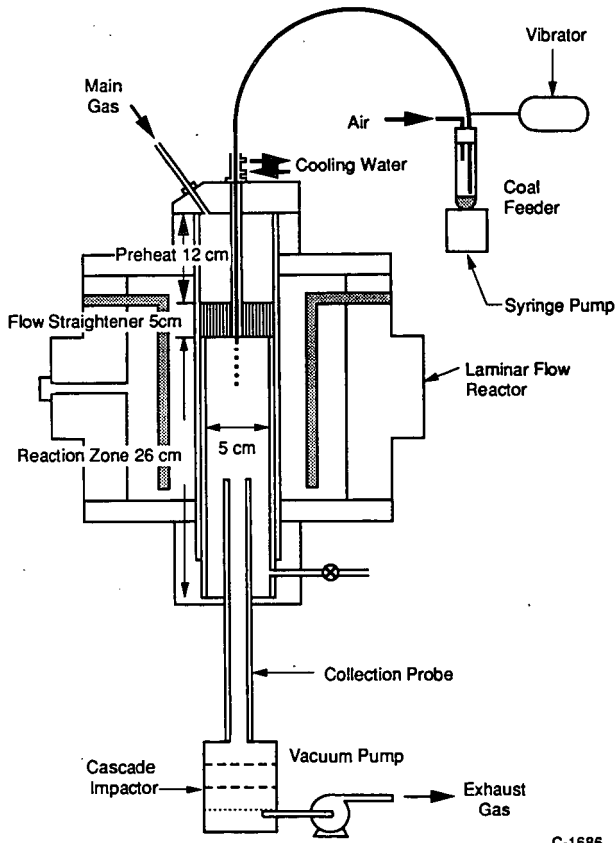
The authors acknowledge the National Institute for Environmental Health Science, the National Science Foundation, and DOE/PETC for their support of this project.

#### **REFERENCES**

1. Stensvaag, J.M., "Clean Air Act 1990 Amendments: Law and Practice," Wiley Law Publications, New York (1991).
2. Brooks, G., Radian Corporation Final Report submitted to the US EPA under contract number 68-02-4392, Report No. EPA-450/2-89-001 (1989).
3. Edwards, L.O., Muehla, C.A., Sawyer, R.E., Thompson, C.M., Williams, D.H., and Delleney, R.D., "Trace Metals and Stationary Conventional Combustion Processes," EPA Report No. EPA-600/S7-80-155 (1981).
4. Smith, R.D., *Progr. Energy Combust. Sci.* 6, 53 (1980).
5. Davison, R.L., Natusch, D.F.S., Wallace, J.R., and Evans Jr., C.A., *Env. Sci. and Tech.* 8(13), 1107 (1974).
6. Finkelman, R.B., in *Organic Geochemistry*, Engle, M., and Macko, F., eds., Plenum Publishing Co. (1992).
7. Raask, E., *Progr. Energy Combust. Sci.* 11, 97 (1985).
8. Helble, J.J., Ph.D. Thesis, M.I.T. Department of Chemical Engineering, May (1987).

Table 1. Coal Trace Element Data

	Alabama Bituminous (75/90 $\mu\text{m}$ )	Wyoming Sub-bituminous (75/90 $\mu\text{m}$ )	Montana Lignite (75/90 $\mu\text{m}$ )	Density- Graded M. Lignite*
Ash (wt%, dry)	7.3	5.2	6.9	5.9
Trace elements (ppm by weight of coal)				
Mn	20	25	78	66
Cr	14	11	3.8	6.1
As	30	1.6	4.0	-
Sb	1.4	-	0.6	-
Se	-	-	0.5	-
Co	9.2	2.4	0.9	-
V	17	16	5	-
Zn	23	-	8	-
U	-	0.9	0.5	-



C-1686

Figure 1. Laminar-entrained flow reactor used for combustion experiments.

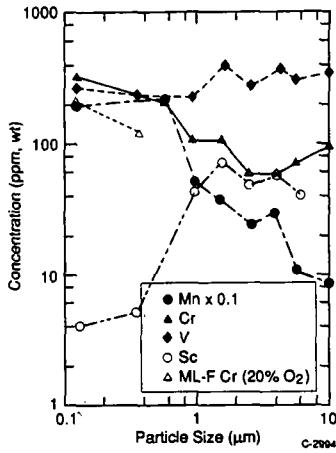


Figure 2. Concentration of trace elements in ash as a function of ash particle size for Wyoming and Montana coals. 75/90 μm, 1750 K, 30% O<sub>2</sub> except as noted.

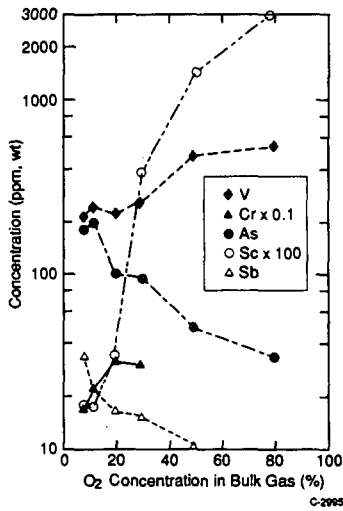


Figure 3. Concentration of trace elements in ash as a function of oxygen partial pressure. Wyoming coal, 75/90 μm, 1750 K.

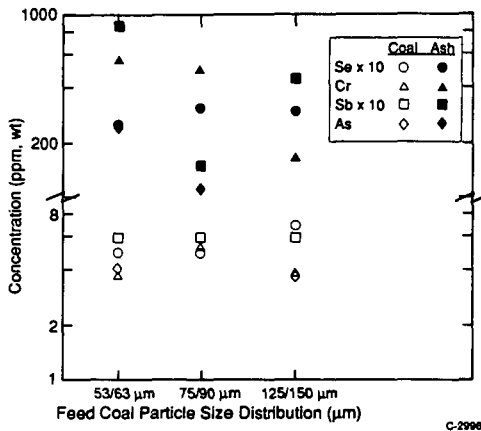


Figure 4. Concentration of trace elements in Montana lignite coal and ash as a function of coal particle size. 1750 K, 20% O<sub>2</sub>.

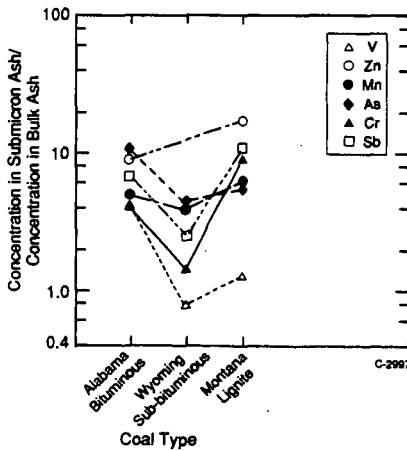


Figure 5. Relative concentration of trace elements in submicron ash as a function of coal type. 75/90 μm, 1750 K, 30% oxygen except Montana coal (20%).

## FORMS OF OCCURRENCE OF ARSENIC IN COAL AND THEIR BEHAVIOR DURING COAL COMBUSTION

Frank E. Huggins<sup>1</sup>, J. J. Helble<sup>2</sup>, N. Shah<sup>1</sup>, J. Zhao<sup>1</sup>,  
S. Srinivasachar<sup>2</sup>, J. R. Morency<sup>2</sup>, F. Lu<sup>1</sup>, and G. P. Huffman<sup>1</sup>,

<sup>1</sup>University of Kentucky, Lexington, KY 40506,

<sup>2</sup>PSI Technology Co., Andover, MA 01810.

**Keywords:** XAFS spectroscopy, arsenic, trace elements, coal, combustion

### ABSTRACT

New information from XAFS spectroscopy on the occurrence of arsenic in U.S. bituminous coals shows that arsenic may be present in one or more of three distinct forms: (i) arsenical pyrite; (ii) arsenopyrite (FeAsS); and (iii) arsenate ( $\text{AsO}_4^{3-}$ ), most probably as a result of oxidation. In ash samples analyzed to date by XAFS spectroscopy the arsenic is present predominantly as arsenate species. Some preliminary data on arsenic capture efficiency during combustion suggest that the presence of arsenate in the coal may facilitate the retention of arsenic in combustion solids.

### INTRODUCTION:

A recent comprehensive study of ash formation during combustion of U.S. coals [1] has indicated the importance of the form-of-occurrence of an element in the coal for determining the behavior of major elements during pulverized coal combustion. Similarly, information regarding the forms of occurrence of minor and trace elements in coal and ash must also be obtained to understand their behavior during combustion and to assess whether or not the release of these elements during combustion poses a significant environmental hazard. One of the more critical trace elements in this regard is arsenic as its behavior can be variable. For example, large variations (from <1% to >50% of the total arsenic flux) were reported for arsenic concentrations in the vapor phase at a U.S. power station [2]; and, in trace-element mass balance studies at commercial power plants, arsenic in bottom ash has been shown to vary from as little as 0.5% to as much as 10% of the total arsenic, with the balance in fly ash, except for a very small fraction (<0.5%) that escapes in the flue gas [3]. It is likely that one of the more important factors that might influence the behavior of arsenic during combustion is the form of occurrence of arsenic in the coal.

In his comprehensive review of trace elements in coal, Swaine [4] lists the probable major forms of occurrence of arsenic as arsenical pyrite and arsenopyrite (FeAsS) based on observations (and speculations) made on various coals from around the world. In the U.S., there have been a few direct observations made on the forms of occurrence of arsenic in coal: such observations have been made using scanning electron microscopy [5,6], the electron microprobe [7,8], and other less direct methods [9]. These findings by and large confirmed the occurrence of arsenic as arsenical pyrite in most U.S. coals. In recent work [10,11], we have demonstrated the potential of XAFS spectroscopy as a direct and nondestructive probe for forms-of-occurrence information about trace elements in coal and ash down to concentration levels as low as 10 ppm. In this study, we will present new data on arsenic occurrences in various U.S. coals and derived ash materials.

## EXPERIMENTAL:

Samples: Various coals from the Argonne Premium coal sample bank (APCSB), from the Department of Energy Coal Sample (DECS) bank administered by D. Glick and A. Davis (Pennsylvania State University), and from miscellaneous sources were used in this study. Ash samples were prepared from some of these coals in a drop-tube furnace at PSI Technology (PSIT) Company or in a larger-scale combustion unit at the University of Arizona (UAZ). The drop-tube furnace was run at 1750 K and an oxygen content in the furnace atmosphere of either 7% or 10.5%. Ash samples were collected on filters; in the case of the UAZ combustion unit, an Anderson impactor was used to segregate the ash particulate matter by size. Arsenic contents of the coals were determined by either instrumental neutron activation analysis (INAA) or by proton induced x-ray emission (PIXE), although we have relied on published INAA analyses [12] for the arsenic contents of the APCSB coals. The same techniques were also used to determine the arsenic contents of ash samples.

XAFS Spectroscopy: XAFS spectroscopy was performed at beam-line X-19A at the National Synchrotron Light Source, Brookhaven National Laboratory. For arsenic in coals and ash samples, the absorption of X-rays was measured over the spectral range from 11.75 keV to as high as 13.0 keV; over the XANES region (11.85 to 11.90 keV), absorption data were collected every 0.25 eV. Absorption of the X-rays was measured by means of a thirteen-element germanium array detector [13] that detected the fluorescent X-rays only in a specified tunable energy window that corresponded to the energy of the arsenic fluorescent  $K_{\alpha}$  X-rays. The arsenic K-edge XANES spectra shown in this report are calibrated with respect to a zero energy point (11.867 keV) defined as the position of the white line in the spectrum of  $As_2O_3$  that was run simultaneously with all arsenic spectra. Other details of XAFS experimentation for trace element studies are given elsewhere [10,11].

## RESULTS AND DISCUSSION:

### Arsenic in Coal:

Preliminary XAFS work on the speciation of arsenic in coal [10,11] has shown that it is relatively easy to distinguish among the different arsenic oxidation states likely to be found in coals and other geological materials. This work showed that arsenic was present either in association with iron as in arsenical pyrite, in which arsenic substitutes for sulfur in the pyrite structure, or as an arsenate ( $AsO_4^{3-}$ ) species, presumably formed as a result of oxidation.

However, it is also essential for speciation studies of arsenic in coal to be able to distinguish between the discrete arsenic mineral, arsenopyrite ( $FeAsS$ ), and arsenical pyrite ( $FeS_2$ ). These two forms-of-occurrence of arsenic have been postulated to be the likely major forms of arsenic in coal [4]. The As K-edge XAFS spectra of arsenopyrite and arsenical pyrite are quite similar, but there are subtle differences that can be used to discriminate successfully between these alternatives in both the XANES and EXAFS regions of the spectra. Figure 1 compares the XANES and radial structure function (derived by Fourier transform of the EXAFS function,  $k^2 \cdot CHI$ ) spectra from the two materials. There are clearly more distinctive features, in both magnitude and structure, in the radial structure function (RSF), which is the most processed of these spectra. But even in the XANES spectra there are sufficient differences to discriminate between arsenopyrite and arsenical pyrite simply by inspection.

Such distinctions can be seen in arsenic XANES spectra of coals down to at least 10 ppm. Figure 2 shows the normalized XANES spectra of arsenic in three coals that vary in arsenic content from 17 ppm to 434 ppm. Of these coals, the Pittsburgh seam coal is unique in that its XANES spectrum is closely similar to that of arsenopyrite, whereas the remainder of the coals have features consistent with As in solid solution in pyrite. For the two coals richest in arsenic,

the radial structure functions are shown in Figure 3 and, upon comparison with the RSFs shown in Figure 1, the RSF spectra confirm the inferences based on the XANES spectra. As indicated by the extra white-line peak in the XANES spectrum and also by the peak at about 1.4 Å in the RSF, the Jefferson coal contains a significant fraction of its arsenic as arsenate. Even with this complication, it is clear that remainder of the arsenic in this coal is present in substitutional form for sulfur in pyrite.

XAFS spectra of arsenic were reported previously [10,11] from a suite of float/sink fractions from newly opened vials of the APCSB Upper Freeport coal and showed that the dominant arsenic form-of-occurrence was arsenical pyrite. Similar XAFS spectra were also obtained from the same samples after a three month interval, during which time the samples were stored in glass (not air-tight) vials, and from previously opened vials that had been opened for a number of months. The spectra of these samples were found to be significantly different from those obtained previously. As can be seen from Figure 4, the arsenate contents of these Upper Freeport coal fractions are significantly higher after just three months' storage at room temperature in closed glass vials. These observations confirm that the oxidation of arsenical pyrite to arsenate can occur extremely rapidly, even during storage at room temperature.

The data presented here and in previous preliminary studies show that there are at least three forms of occurrence of arsenic that may be found in laboratory samples of U.S. coals. Based on the limited number of samples examined to date, arsenical pyrite appears to be the most common of these forms, with arsenate as the next most common (although it is conceivable that this form is only formed as a result of oxidation during processing and storage), and arsenopyrite as the least common.

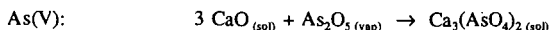
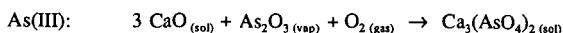
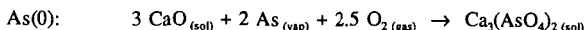
#### Arsenic in Ash:

The conversion of arsenic forms in coal to arsenic forms in ash as a result of combustion has been investigated for a number of ash samples prepared in the drop-tube furnace at PSIT Company or the combustion unit at UAZ. All of the ash samples derived from coal combustion that have been examined to date by XAFS spectroscopy contain arsenic predominantly, if not entirely, in the form of arsenate ( $\text{AsO}_4^{3-}$ ) complexes. Such complexes are readily recognized by the strong white line absorption at about 3 - 4 eV and the broad low intensity peak that is a maximum in the range 80 - 90 eV in the As XANES spectrum, and by the major peak at about 1.3 - 1.4 Å in the RSF of samples rich in arsenic. Figure 5 shows the As K-edge XANES spectra for the bottom ash collected in the UAZ combustion unit from combustion of Kentucky #9 coal and of the fly-ash samples collected in the same unit on an Anderson impactor, during combustion of Beulah (ND) lignite. In comparison to arsenate complexes of known crystal structure, the arsenic K-edge XANES spectra of this and similar bottom ash samples are relatively featureless: the white-line peak is relatively broad and there are no minor peaks in the 10 - 30 eV range and no obvious shoulders or inflection points on the broad peak in the range 50 - 100 eV. Such a lack of features is consistent with a mixture of different structural environments for arsenate complexes in these materials, such as those that might be expected if the arsenate complexes were assimilated in amorphous or glassy materials.

The spectra of the fly-ash samples collected in the UAZ combustion unit on an Anderson impactor, during combustion of Beulah (ND) lignite, begin to deviate from this pattern, particularly for the finer of the two fractions. In the spectrum of the fine fraction, the width of the white line is narrower and there is the obvious presence of a minor peak at about 20 eV in comparison to the coarse fraction. These observations are interpreted as indicating a significantly higher fraction of a crystalline arsenate occurrence in the finer fly-ash fraction than in the coarse fly-ash fraction.

Recent observations and theories on ash particulate formation involving major elements during pulverized coal combustion [1] have invoked two main mechanisms for ash particle formation: (1) evaporation of volatile species and condensation of phases from the vapor, and (2) partial or total fusion and agglomeration of mineral particles. The first mechanism commonly results in the formation of small particles of relatively well defined composition and crystallinity, such as alkali and alkaline-earth sulfates. The second mechanism results in the formation of partially molten aluminosilicate particles that incorporate varied amounts of basic elements. These latter particles tend to be much larger and are generally at least partially amorphous (glass) upon quenching. In such partially molten deposits, it is likely that  $AsO_4^{3-}$  species would be incorporated as a network former in aluminosilicate melts, in much the same way as phosphate anionic species ( $PO_4^{3-}$ ) are incorporated in such melts.

Alkaline-earth orthoarsenates are relatively stable compounds (calcium orthoarsenate melts only at temperatures above 1450°C and magnesium orthoarsenate would be expected to be almost as refractory) and consequently they are prime candidates as condensates from vapor phase arsenic species during combustion, especially of low-rank coals. Under combustion conditions, decomposition of arsenical pyrite or arsenopyrite will be rapid and release arsenic vapor, which should then readily oxidize to vaporous arsenic oxides. In the presence of oxygen, the following solid-vapor reactions will lead to the condensation of calcium orthoarsenate, depending on the oxidation state of arsenic in the vapor phase:



It is apparent that these reactions become simpler and involve fewer molecular species with increasing oxidation state of the arsenic. In particular, regardless of whether the transitory species in the vapor phase is the oxide,  $As_2O_5$ , or the anion species,  $AsO_4^{3-}$ , no additional oxygen is necessary in reactions involving the As(V) oxidation state as a reactant. Hence, the presence of arsenate in the coal might be expected to facilitate the formation of arsenate compounds during combustion and its capture on particulate matter. Furthermore, arsenate mineral species that are not associated with pyrite or arsenopyrite particles in the coal need not undergo vaporization, but may remain as discrete particles or be assimilated by partial fusion into other particles during combustion.

Comparison of the arsenic retention during combustion for the two DECS coals in the PSIT drop-tube experiments is tabulated below:

Coal	As (coal)	As (ash)	Wt% Ash	As cap. eff. <sup>1</sup>
Pittsburgh	70	31	10.0	0.04
Illinois #6	10	21	14.5	0.30

<sup>1</sup>Arsenic capture efficiency is defined as:  $As(ash)/(As(coal)/Wt\text{ fn. ash})$

It can be seen from this table that relatively little of the arsenic is captured on the filter and it is probable that arsenic in both vapor and submicron microparticulate matter may have avoided

the filter sampling process. From this tabulation, it would appear that the arsenic is captured more efficiently in the case of the Illinois #6 (DECS-2) coal than the Pittsburgh (DECS-12) coal. Although this would appear to be consistent with anticipated trends based on the forms of occurrence of arsenic in the original coals (the Pittsburgh coal contains virtually all arsenic as arsenopyrite, whereas about 40-50% of the arsenic in the Illinois #6 coal is oxidized to arsenate), it may be fortuitous because other factors in the combustion experiment and sampling process that might influence arsenic capture have not been considered.

#### CONCLUSIONS:

XAFS spectroscopy has identified three distinct arsenic occurrences in U.S. bituminous coals: (i) arsenical pyrite; (ii) arsenopyrite; and (iii) arsenate species, which may have formed from the other two forms by oxidation. This technique also indicates that, regardless of the original form of occurrence of arsenic in coal, all arsenic forms are oxidized to arsenate forms during combustion of coal. The presence of arsenate forms in the original coal may facilitate the retention of arsenic in ash; however, more work needs to be done to prove this point adequately.

#### Acknowledgements:

We acknowledge Prof. J. D. Robertson and Ms. Amy Wong for the PIXE determinations of arsenic in the DECS coals and corresponding ash samples. This study was supported by the Office of Exploratory Research of the Electric Power Research Institute (Palo Alto, CA) under EPRI Contract No. RP-8003-20, and by the U.S. Department of Energy (Pittsburgh, PA) under DOE Contract No. DE-AC22-86PC90751. The XAFS spectra were obtained at the National Synchrotron Light Source at Brookhaven National Laboratory, which is supported by the U.S. Department of Energy.

#### References:

1. J. J. Helble et al. in "Inorganic Transformations and Ash Deposition During Combustion" (Ed. S. A. Benson), pp. 209-228, pp. 229-248, AMSE, New York, (1992).
2. M. S. Germani, and W. H. Zoller, *Environ. Sci. Technol.* **22**, 1079-1085, (1988).
3. L. B. Clarke, and L. L. Sloss, "Trace Elements", Report IEACR/49, International Energy Agency Coal Research, London, 111 pp., (1992).
4. D. J. Swaine, "Trace Elements in Coal", Butterworth & Co., London, (1990).
5. R. B. Finkelman, in "Atomic and Nuclear Methods in Fossil Energy Research", (Eds. R.H. Filby, B.S. Carpenter, and R.C. Ragaini), 141-149, Plenum Press, New York, (1982).
6. R.B. Finkelman, and R.W. Stanton, *Fuel*, **57**, 763-768, (1978).
7. J.A. Minkin, E.C.T. Chao, and C.L. Thompson, *ACS Div. Fuel Chem. Preprints*, **24(1)**, 242-249, (1979).
8. L.F. Ruppert, J.A. Minkin, J.J. McGee, and C.B. Cecil, *Energy & Fuels*, **6**, 120-125, (1992).
9. R.B. Finkelman, C.A. Palmer, M.R. Krasnow, P.J. Aruscavage, G.A. Sellars, and F.T. Dulong, *Energy & Fuels*, **4**, 755-766, (1990).
10. F.E. Huggins, N. Shah, J. Zhao, F. Lu, and G.P. Huffman, *ACS Div. Fuel Chem. Preprints*, **37(2)**, 1110-1116, (1992).
11. F.E. Huggins, N. Shah, J. Zhao, F. Lu, and G.P. Huffman, submitted to *Energy & Fuels*, January, 1993.
12. C.A. Palmer, *Energy & Fuels*, **4**, 436-439, (1990).
13. S.P. Cramer, O. Tench, N. Yocum, and G.N. George, *Nucl. Instr. Meth.* **A266**, 586-591, (1988).

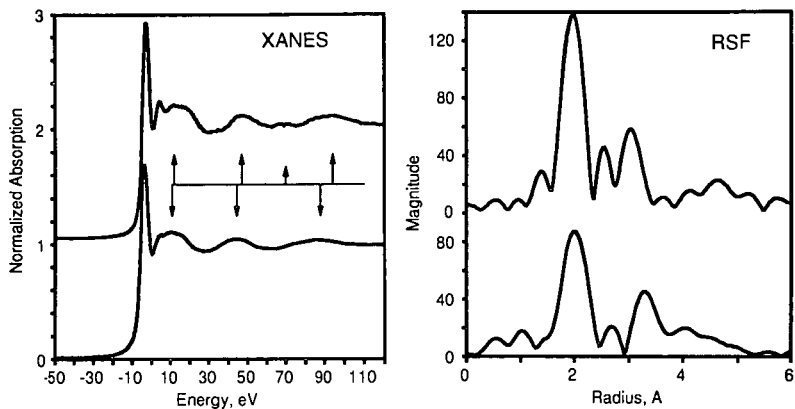


Figure 1: Comparison of XANES and RSF spectra for arsenic in arsenical pyrite (top) and arsenopyrite (bottom).

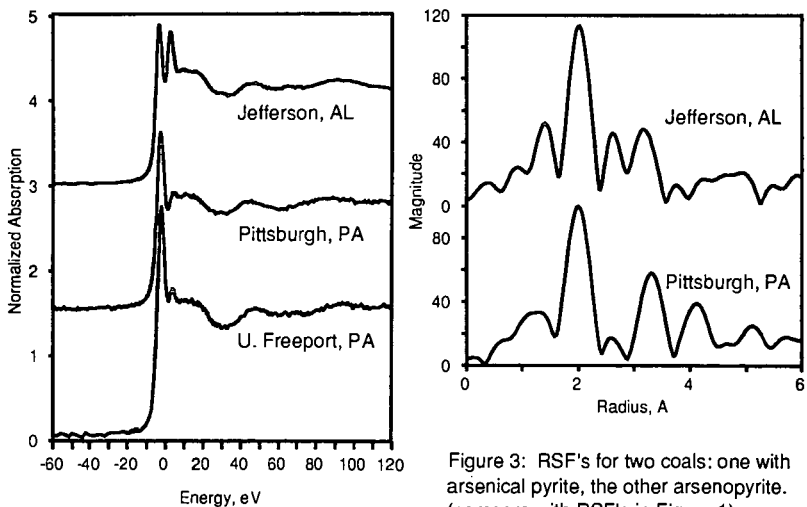


Figure 2: Arsenic K-edge XANES spectra for three U.S. bituminous coals

Figure 3: RSF's for two coals: one with arsenical pyrite, the other arsenopyrite. (compare with RSF's in Figure 1).

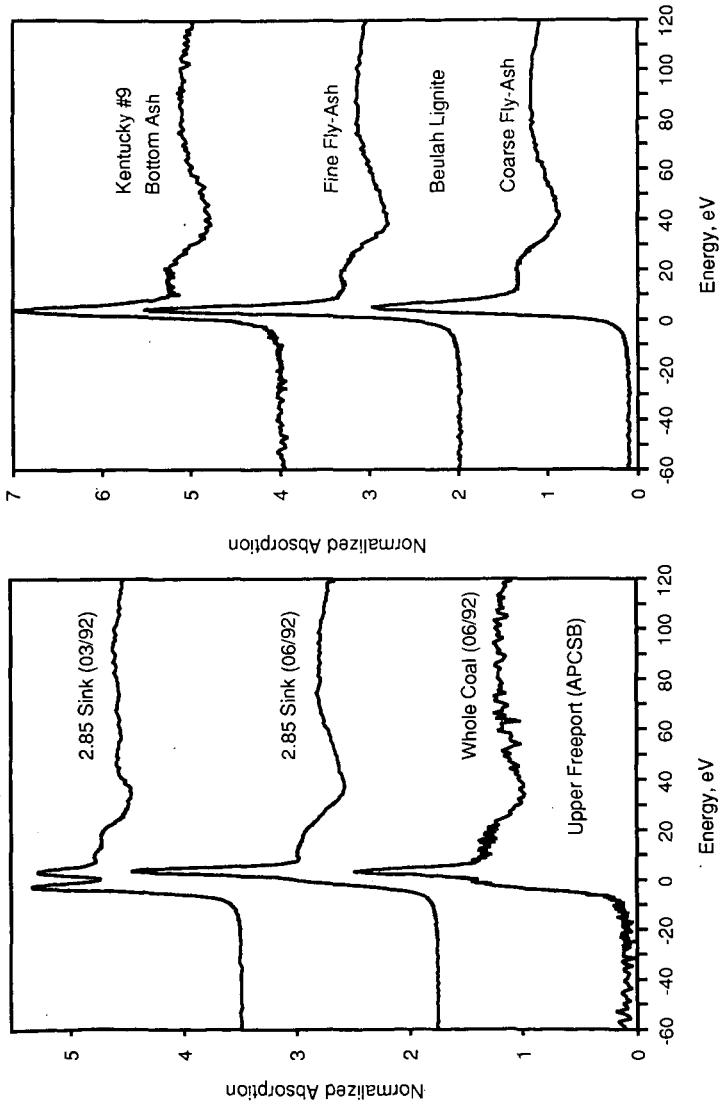


Figure 4: Arsenic K-edge XANES spectra for oxidized coals. (compare bottom spectra with that in Fig. 2)

Figure 5: Arsenic K-edge XANES spectra for ash samples collected in the University of Arizona combustion unit.

ON-LINE, MULTIELEMENT ICP SPECTROMETER FOR APPLICATION TO HIGH TEMPERATURE AND PRESSURE FOSSIL FUEL PROCESS STREAMS

Robert R. Romanosky, Anthony S. Viscomi \*, Steven S. Miller,  
William P. Chisholm

US Department of Energy, Morgantown Energy Technology Center,  
Morgantown, WV 26507-0880

\* current address: US Army Corps of Engineers, Ohio River Division  
Laboratory, 11275 Sebring Dr., Cincinnati, OH 45240

KEYWORDS: ICP, On-Line Analysis, Fossil Fuel Analysis

ABSTRACT: METC is developing a real-time, multielement ICP spectrometer system for application to high temperature and high pressure fossil fuel process streams. The ICP torch operates on a mixture of argon and helium with a conventional annular swirl flow plasma gas, no auxiliary gas, and a conventional sample stream injection through the base of the plasma flame. The base of the torch body is a unique design, allowing process gas at 650°C to be injected into the torch. The RF generator (40.68 MHz) can deliver 10 kW, but the best detection limits have been observed at 5 kW. The detection system is a quartz fiber optic bundle mated to a battery of one-tenth meter monochromators with photomultiplier tubes. A microcomputer controls scanning of the monochromators and data acquisition from the PMTs. The METC ICP system is modular and mobile, allowing the system to be operated in close proximity to any process of interest.

Rising concerns about the potential release of harmful elements into the environment from coal utilization have driven the development of new analytical capabilities. Especially useful to the suite of advanced technologies under development by the Morgantown Energy Technology Center, (METC), would be a process monitor to perform real-time, multi-element trace analysis in a high temperature and high pressure environment. The inductively coupled plasma (ICP) spectrometer has the potential to perform this kind of process monitoring.

The role of the inductively coupled plasma, (ICP) as a process stream monitor for trace elements is only beginning to be realized, although it has been widely used for a number of years as a spectrometric emission source in elemental analysis laboratories. Previous work by other researchers [1] focused on monitoring of liquid phase process streams and looked only at elements at a relatively high concentration. Process monitoring by ICP spectrometry under conditions relevant to METC's advanced technologies has not been previously reported. The principle reason for this lack of progress is the difficulty of sustaining a stable plasma discharge around a high flow of carbon-containing sample gas.

Conventional ICP systems cannot operate at sample flow rates greater than two liters per minute, nor do they operate well with carbon-containing gases in the sample stream. The low flow requirements limit the use of an ICP

argon plasma with particle-laden process streams, since at such low rates particles drop out of the gas stream before reaching the torch. Also, ICP plasmas quench when the carbon-containing gases of fossil fuel process streams are introduced, especially at high flow rates. Our torch design using a mixed gas plasma provides for operation at higher sample flow rates and for stable performance when analyzing samples of varied gas composition.

Prior work sponsored by METC, [2] was only partially successful in achieving this goal. On-line ICP analysis was attempted on a cleaned sample stream from METC's 107 cm diameter, (42 inch) fixed bed gasifier. An extracted gas stream was diluted with argon to 10% and introduced to the ICP torch at a flow rate of 1 l/min. Higher concentrations of gasifier gas extinguished the plasma, as did higher flow rates. The detection limits of this configuration were very poor. Consequently, METC began seeking methods that allow higher sample flow rates and concentrations while maintaining stable plasma conditions.

The conventional ICP excitation source is a plasma sustained at atmospheric pressure by coupling 27.12 MHz radio frequency power to a stream of argon. Almost all ICP systems use argon as the discharge medium, with aqueous solutions of unknowns nebulized into an argon sample stream injected into the argon plasma. This arrangement works well for power levels below 3 or 4 kilowatts, and for low flow sample streams that contain only argon and a small amount of aqueous aerosol.

Figure 1 shows METC's version of an ICP torch and the induction coil that transmits the high frequency power a radio frequency generator to the plasma. Similar to a conventional torch, it differs in some details because of the need to sustain a discharge with a high flow rate of carbon-containing gases in the sample stream. Also, the sample stream, coming from an industrial gasifier or combustor, is expected to vary widely in composition and particle loading on a timescale of seconds.

The torch uses conventional annular plasma gas injection. Auxiliary gas is not needed, and no provision for it is made in this design. The base of the torch is an unconventional construction, rather than the usual teflon, so a hot, high pressure sample line can be directly connected to the torch. The samples line can be maintained at an elevated (process) temperature to protect sample integrity by preventing tar condensation and particle dropout from loss of velocity. The sample injection tube is ceramic, and connects directly to the sample line through a drilled out compression fitting on the base. Graphite ferrules seal the compression fitting. The sample injection tube does not touch any teflon parts, and water cooling in the brass base protects the O-ring and adjacent teflon sections.

The presence of particles and carbon-containing polyatomic gases in the sample stream requires a high minimal power to sustain a stable discharge. Especially so, since the flow rate of sample gas into the discharge must be high to minimize particle dropout. Operation of argon ICP discharges above three or four kilowatts is difficult because the torch overheats. Our earlier work [2] reported configuration factors very close to unity generate a stable discharge with an argon and helium mixed gas plasma, but more recent work has shown that unusually small configuration factors, near 0.8, work well and

facilitate construction and adjustment of the torch. The mixed gas plasma can be used at up to ten kilowatts with a high flow rate of carbon-containing sample gas. Optimum detection limits were found at five kilowatts, and it is not difficult to sustain a stable discharge at this power level. It is also possible to operate with pure helium, but there is no advantage and it is more expensive.

A frequency of 40.68 MHz, (higher than the conventional 27.12 MHz) was chosen for this torch design so the skin depth in the plasma would be smaller. Hence the coupling of power to the discharge is confined to the outer edge of the plasma flame where it is minimally affected by variations in the properties of the injected sample stream.

The torchbox opens from both the top and front, and has dark glass observation windows on two sides. This arrangement greatly facilitates adjustment of the torch and load coil orientation. Two windows on the back side provide optical access for the detection system optics. There is a separate impedance matching network and a Tesla coil in a housing attached to the torchbox. By using screw latches on all the doors and maintaining clean conductive surfaces around the doors and windows, electromagnetic leakage is kept well below safe limits.

The detection system consists of a battery of six one-tenth meter monochromators equipped with photomultiplier tubes. Each monochromator is equipped with a 3600 or 4800 groove/mm diffraction grating optimized for a particular region of the spectrum. The monochromators are all computer controlled, scanned via stepper motor drivers. Two of the eight monochromators are equipped with a red and near infrared sensitive photomultiplier tube, the rest are equipped with an ultraviolet and visible sensitive photomultiplier tube. Photomultiplier tubes were chosen for their excellent sensitivity and dynamic range. Their principle drawback is the need for separate monochromators for each detector, hence the battery of monochromators. Using two different types of photomultipliers also necessitates two independent high voltage supplies. The photocurrent from the photomultiplier tubes is connected to an A/D card in a PC, where the voltage developed across a load resistor is digitized and stored for processing.

The six monochromators are mounted on a platform adjacent to the ICP torch. Light from the plasma is gathered by two  $f/2$ , 5 cm diameter quartz lenses and focused into two 3mm diameter quartz fiber optic bundles. Each bundle is randomly split into four branches, and one branch is mounted at the entrance slit of each monochromator. The divergence angle of light from the quartz fiber is such that the gratings are nearly exactly filled without any optic between the bundle output and the entrance slit. The photomultiplier tubes are bolted directly over the exit slit of the monochromators.

For purposes of calibration, an aerosol from standard aqueous solutions is injected into the torch sample stream. The aerosol is generated with an ultrasonic nebulizer, which is much more efficient than the common Babington type aerosol generator. The aqueous aerosol is passed vertically through a drying oven to remove all water from the aerosol, and then through a chiller section, which condenses and removes most of the water vapor from the gas flow. Then the dry aerosol is directed through the sample line into the ICP torch. Overall efficiency of the generator is better than 80%.

A single software package to control the monochromators, acquire the data, and to calculate concentrations was written in C by a resident programmer. When the system is started and a new wavelength calibration is needed, the operator uses a low pressure mercury lamp to generate a known spectrum. The software knows approximately where to drive the stepper motors for various mercury lines; it positions the monochromator wavelength near a mercury emission line and acquires a spectrum of that region. Then the software executes a peak search routine and recalibrates its wavelength exactly.

When the system is to be operated, the first task facing the operator is calibration of both wavelength and concentration. Wavelength calibration was described above; concentration calibration is done conventionally, by supplying standard solutions over a range of concentrations and calculating a calibration curve. To measure concentration the software moves the monochromator wavelength to the peak region and acquires data over a small region of the spectrum. Before and after the measurement, the software moves the monochromator wavelength to either side of the line to acquire a background intensity, and calculates the area of the background trapezoid. It requires approximately one-half hour to start up the system and go through a complete calibration routine. Calibrations are reliable for periods of eight hours or longer. Real-time data are collected at one kilohertz and digitally processed to remove artifacts, and then summed and stored at the rate of one data point per second.

One of the principle requirements of our on-line system was that it be readily adaptable to use in the field. This meant that the system had to be modular and mobile. The torchbox, detection system, and calibration system must all be located at the sampling site, since preservation of sample integrity requires that the length of sampling tube be as short as possible. On the other hand, there is no requirement that the radio frequency generator be close at hand, since power can be conducted over tens of meters of coaxial cable without undue difficulty or expense. Also, in many industrial process installations, the site where the sample is extracted is off-limits to personnel when the process is operating, and therefore all the controls and the computer must be remotely located. Figure 2 illustrates the various ICP modules.

The radio frequency generator is contained in a standard 19-inch cabinet, approximately two meters tall. The generator uses vacuum tubes for both stages of amplification and for the oscillator; the final stage is a single tube. This tube is very large and requires a large cooling air flow. Also, the separate vacuum tube stages require their own plate voltage, and therefore the power transformer is large and bulky. For these reasons, this unit is large, and until solid state technology advances, there is no prospect of obtaining a smaller one. There is a small, mobile transformer from which it is powered; the transformer takes 480 volts from a standard welding power receptacle and steps it down to 208 volts to operate the generator. This is convenient, since virtually all industrial facilities are equipped with 480 volt power. The generator also contains a full set of controls for power delivery.

The calibration rig is housed in a two meter high standard 19-inch rack, including the ultrasonic nebulizer, drying oven, cooling jacket, cooler, power supplies, and controllers. All these devices operate from standard low current 110 volt power.

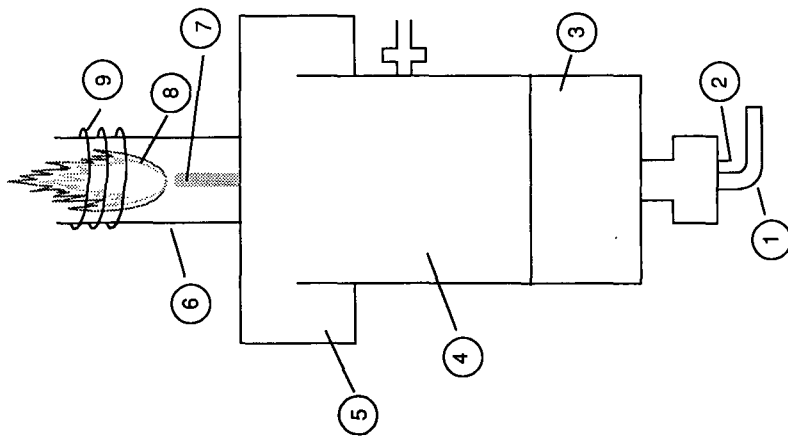
Typically, the computer that runs the monochromators, and the radio frequency power generator are located near each other, so that data acquisition and processing and power delivery are controlled from one location. Additional power controls are located underneath the torchbox to facilitate starting and calibrating the system prior to making measurements on unknowns.

The plasma gas is a mixture of helium and argon. The argon is usually delivered from a large liquid argon tank. Helium is delivered from cylinders on a manifold or from a liquid helium tank. The tanks and cylinders are connected via mass flow controllers and can be remotely located, either near the computer and RF generator or at another convenient location.

Future plans for this instrument include field testing on coal combustors and gasifiers, refinement of torch design to increase reliability and minimize maintenance, and development of a CCD array detection system.

#### References

- [1] M.W. Routh and J.D. Steiner, Spectrochimica Acta 40B, 177 (1985).
- [2] D.L. McCarty, R.R. Romanosky, W.P. Chisholm, Proceedings of the Advanced Research and Technology Development, Direct Utilization and Instrumentation & Diagnostics Contractors' Review Meeting, Pittsburgh, PA, September 6-9, (1988), p. 576 - 585.



- 1. Heated Sample Line
- 2. Compression Fitting
- 3. Base Section
- 4. Teflon Body
- 5. Teflon Nut

- 6. Quartz Tube
- 7. Ceramic Sample Injection Tube
- 8. Plasma "Flame"
- 9. Copper Tubing RF Load Coil

**Figure 1. ICP Torch with Load Coil and Plasma "Flame"**

M9300817

1. Torch Box
2. Access doors
3. Matching Network
4. Matching Network Control Panel
5. Heated Sample Line
6. Emergency Shutoff Control Box
7. Electronic Flow Controls and HV Power Supplies
8. Rotameters and Pressures Gauges
9. Chimney
10. 10 KW Radio Frequency Generator
11. Coax RF Power Cable
12. Mobile 480V to 208V Transformer
13. Chilled Water for ICP Load Coil
14. Ultrasonic Nebulizer, Standard Solution, and Peristaltic Pump
15. 500 °C Heater
16. Power Controller to Heater
17. 0 °C Condensor
18. 0 °C Chiller
19. Containment Vessel for Condensed Water
20. Sample Line to ICP Torch

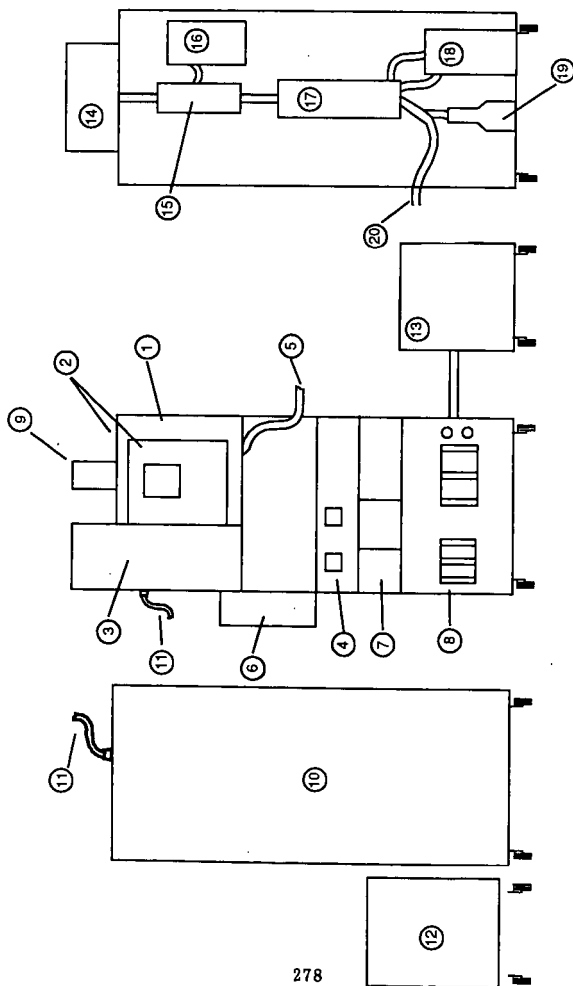


**Figure 2. Modular Arrangement of METC's Complete On Line ICP System**

M93000818

**RECENT ADVANCES IN SAMPLING AND ANALYSIS  
OF COAL-FIRED POWER PLANT EMISSIONS  
FOR AIR TOXIC COMPOUNDS**

JOHN A. COOPER  
Direct of Technology  
Air Quality Division  
Chester Environmental  
12242 S.W. Garden Place  
Tigard, Oregon 97223, U.S.A.

**Keywords:** Emissions, Toxics, Advances

## INTRODUCTION

The new Clean Air Act amendments (CAAs) require the evaluation of potential health effects due to emission of hazardous air pollutants (HAPs) from coal-fired power plant (CFPPs). The amendments also specifically require evaluation of mercury (Hg) emissions from CFPP. Although the CAAs specify these measurements be made, standard reference methods for testing all of the HAP emissions from CFPPs are not available and some of the methods currently being used have not been validated.

Previous studies have shown fly ash from coal combustion may be a potential source of HAPs. Samples for these previous studies, however, were collected using conventional methods which do not allow for the normal dilution and cooling that takes place in a plume. Organic compounds, for example, are typically in the vapor phase at stack temperatures and with conventional methods are collected separately from the particles by condensation and adsorption traps. There is evidence, however, that some polycyclic aromatic hydrocarbons (PAHs) can undergo chemical reactions and/or rearrangements when adsorbed on coal fly ash particles. As a result, samples collected with conventional methods may not be representative of CFPP emissions as they exist in the ambient environment. In addition, there are over a dozen different sampling and analysis methods required to measure HAPs from CFPPs each requiring separate probes and sampling teams. This negates to a great extent the possibility of simultaneous sample collection, greatly increases the cost of sampling and introduces the potential for greater uncertainties in the measurements.

Emission measurements of hazardous air pollutants requires an optimization of sampling and analysis methods. Recent advances in emissions measurements have resulted in major strides towards this optimization process. Two recent advances include the development of a plume simulating dilution sampling system using zero background dilutant for simultaneous measurement of the complete set of hazardous air pollutants and a new hazardous element sampling train.

## PLUME SIMULATING DILUTION SAMPLER

Chester Environmental's plume simulating dilution sampler is illustrated in Figure 1. The configuration illustrated is but one configuration that has been used for the simultaneous collection of both gas and particle phase HAPs. An isokinetic sample is drawn into the system through a cyclone preseparator and a heated stainless steel transfer tube. The hot stack gas is drawn from

the transfer tube (similar to a standard Method 5 transfer tube) into the instrument and blending module where it is surrounded by cooled dilution gas.

The dilution gas used for this sampling is nitrogen ( $N_2$ ) derived from evaporated liquid nitrogen but other mixtures such as an 80/20  $N_2/O_2$  mixture could be used. This provides a cool, bone-dry dilution gas with zero background for both particulate and vapor phase species. Keystone/NEA has been using evaporated liquid  $N_2$  for dilution gas with its PSDS for air toxic emission testing since 1988. This type of dilution gas is considered essential because of the need to minimize sulfate artifact formation and an oxygen mixture of dilutant gas is considered important to simulate the  $O_2$  concentration in a plume so as not to inhibit the formation of oxygenated compounds.

After blending and mixing, the diluted gas stream passes through an aging chamber. After exiting the aging chamber and before sample collection, the diluted gas stream passes through a section for determining the pressure, temperature, velocity, and relative humidity. The particle and gas phase samples are sampled downstream of this section.

The sample entering the inlet nozzle will pass through the transfer tube and the dilution chamber for dilution, aging, and collection. The transfer tube is maintained at stack temperature to prevent premature condensation. An S-type pitot tube and a thermocouple are installed on the transfer tube to monitor stack gas velocity and temperature. The flow rate through the transfer tube is established by the difference between the total stack pressure at the inlet nozzle and the static pressure in the dilution chamber. This pressure difference, monitored with a magnehelic gauge installed between the upstream port of the pitot and the dilution chamber, is referred to as chamber pressure. The chamber pressure/flow relationship is established by calibration of the nozzle/transfer tube assembly as an integrated unit. The operating chamber pressure will be determined on site using this calibration with the appropriate temperature and pressure corrections for the actual stack conditions encountered.

The dilution chamber facilitates mixing of the flue gas with dilution gas, cooling and aging of this mixture to simulate the dilution processes occurring in a plume, and distribution of the aged mixture to the various sampling devices. The chamber sections can be configured to affect a variety of dilution, aging, and sampling schemes. The chamber flows are balanced by throttling the dilution gas (supplied under pressure) as required to establish the operating chamber pressure (for the specified flue gas flow rate through the transfer tube) while maintaining the necessary sampling device flow rates (withdrawn under vacuum).

A wide range of sampling methods can be used with the PSDS. Particle loading, for example, can be determined by direct filtration and gravimetry. Both the 8 x 10-inch quartz fiber high-volume and teflon filters can be used to provide independent determination of the particle loading. Particle and gas phase elemental compositions are determined using a combination of sampling and analysis methods. The teflon filters are analyzed by x-ray fluorescence and neutron activation analysis for particle phase trace elements and charcoal traps are analyzed by the same methods for gas phase elements. This ultra-sensitive trace element procedure provides low detection limits (down to  $0.05 \mu\text{g}/\text{m}^3$ ) for a wide range of elements. The particulate phase elements measured by this method include Al, Si, P, S, Cl, K, Ca, Ti, V, Cr, Mn, Fe, Co, Ni, Cu, Zn, As, Se, Br, Rb, Sr, Zr, Mo, Cd, Sb, Ba, Hg, Pb, U, and Th. Of the four elements expected to have a significant gas phase component at plume-simulated conditions (As, B, Hg, and Se), three (As, Hg, and Se) can be sampled and measured by the charcoal trap method.

The gas concentration in the PSDS is typically reduced by about 30 fold from the stack concentration by dilution. To compensate for this lower concentration, larger volumes are sampled and more sensitive analytical methods used to provide improved detection limits.

#### HAZARDOUS ELEMENT SAMPLING TRAIN

Current EPA sampling and analysis methods for hazardous elements rely on method 101A for mercury and tentative method 29 for multiple metals testing. Both methods are based on EPA method 5 stack sampling probes and impinger trains. Method 101A uses potassium permanganate in sulfuric acid impingers to extract mercury from a gas stream. Tentative method 29 adds hydrogen peroxide-nitric acid impingers in front of the permanganate impingers to remove other metals. These impinger trains are difficult to run, somewhat dangerous, require complex sample recovery and analysis procedures and are costly. In addition, concerns for the validity of these methods have also been raised and extended sampling periods are required to achieve adequate detection levels.

A method has recently been developed to measure hazardous element emissions that combines activated charcoal impregnated filters (CIFs) and XRF analysis. This method is applicable to all of the elements on the EPA hazardous air pollutants (HAPs) list except beryllium which must be analyzed by inductively coupled argon plasma (ICAP) methods but can be done with the same hazardous element sampling train (HEST). This new, innovative method not only has the ability to measure mercury in CFPP emissions with sampling intervals as short as 10 minutes, but has the potential to achieve order of magnitude better detection limits for mercury and the other HAP elements that are now measured with tentative method 29. ◦

Chester Environmental's HEST is schematically illustrated in Figure 2 to collect both particulate and gas phase samples, and XRF and ICAP to determine elemental concentrations as illustrated with the flow diagram shown in Figure 3.

The sampling train uses a standard in-stack filter probe which draws in an isokinetic sample that passes through a filter pack. The filter pack holds three 47 mm diameter filters. Arranged as illustrated in Figure 2. A stainless steel washer at the filter pack entrance and a stainless steel washer/screen at the exit, hold the three stacked filters in place and prevent sticking to the filter holder O-rings. The first filter collects the particulate phase. Only quartz fiber filters have been used to date but optimum detection limits will be obtained with teflon filters. The second filter is a CIF used to collect gas phase elements. The second CIF is a backup which can be analyzed if there is concern for breakthrough. (To date, in-stack measurements have demonstrated CIF collection efficiencies in excess of 99.7% for total mercury).

The stack gas passes through the filter pack and to a series of impactors to remove water vapor before the flow and volume are monitored.

The filter pack, including the inlet nozzle, are separated from the probe at the end of a sampling period, capped and returned to the laboratory for analysis. In-field sample train rinsing and sample recovery steps are not required by this method. If repeated field tests are required, the filter may be transferred to petri slides and fresh filters loaded in the filter pack. Special filter treatment is not required after sample collection. (Mercury, for example, is not lost from the CIF even after 15 hours exposure to a vacuum of 150 microns of mercury at room temperature).

Upon receipt in the laboratory, the probe inlet is separated from the filter pack, the filters removed, placed in petri slides and archived. (This method does not require total filter deposit mass to be determined). The filters are removed from storage and analyzed first by nondestructive XRF analysis using a high powered modified Ortec Tefa III analyzer. The complete analysis which requires two excitation conditions (Mo anode and Mo x-ray filter at 50 KV, tungsten anode with Cu filter at 35 KV). The front particulate catch filter is then cut in half after nondestructive XRF. One half of the filter is archived and one half is analyzed for ICAP for Be by ICAP. The entire filter may be analyzed by ICAP if lower detection limits are required. Elemental detection limits of the HEST will range from about 10 to 100 ng/m<sup>3</sup>.

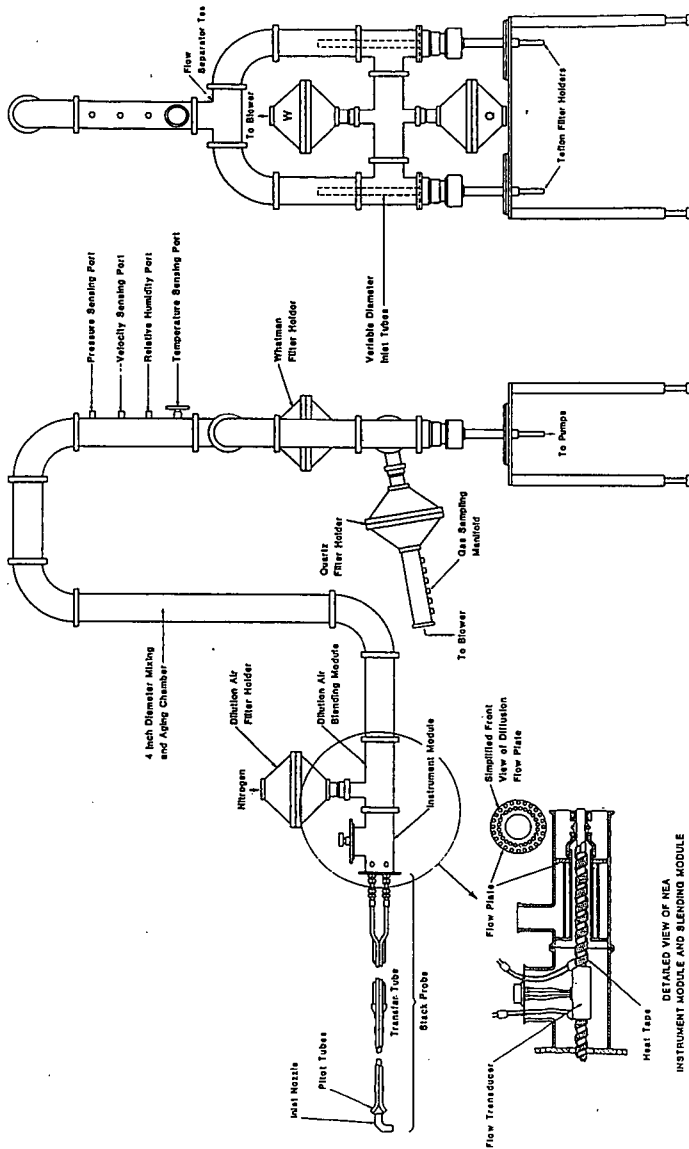
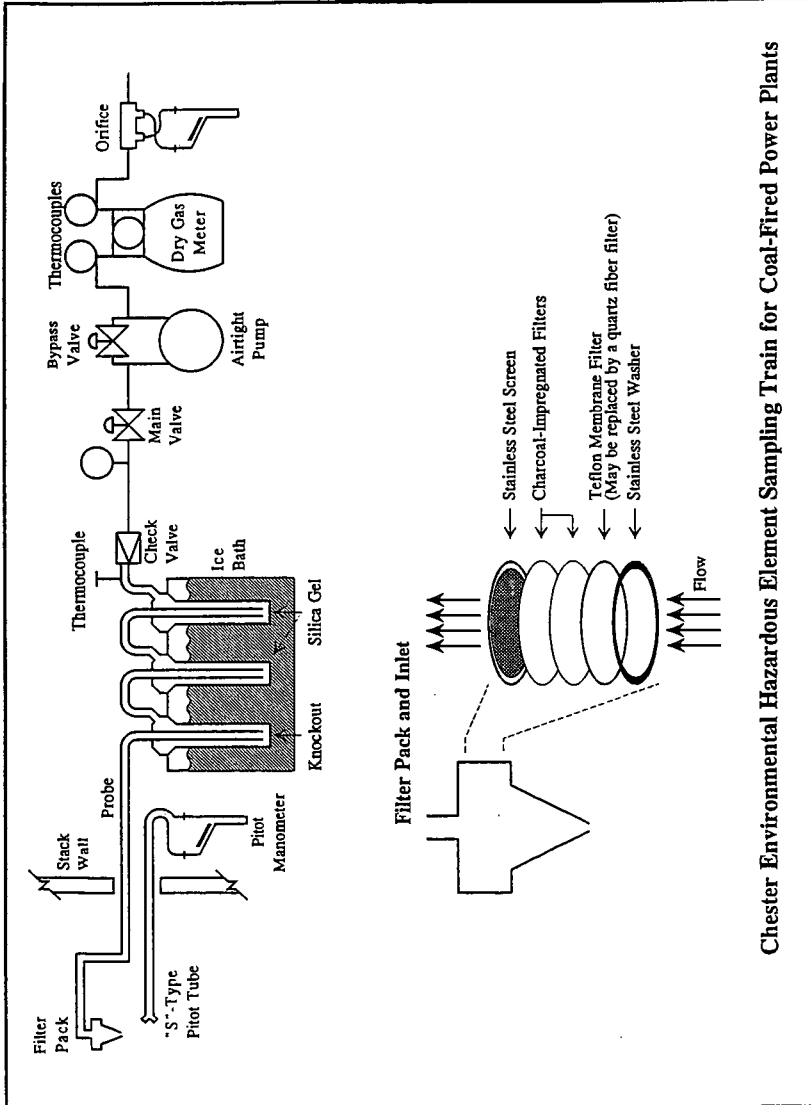


Figure 1. Schematic Representation of the Plume-Simulating Dilution Sampler (PSDS) for Simultaneous Collection of Particle and Gas Phase Hazardous Air Pollutants.



Chester Environmental Hazardous Element Sampling Train for Coal-Fired Power Plants

Figure 2.



## CHARACTERIZATION OF HAZARDOUS AIR POLLUTANTS FROM COAL-FIRED ELECTRIC UTILITIES

Thomas D. Brown and Charles E. Schmidt  
U.S. DOE/Pittsburgh Energy Technology Center  
P.O. Box 10940  
Pittsburgh, PA 15236-0940

Keywords: air toxic emissions, hazardous air pollutants

### ABSTRACT

This paper briefly describes both recent and ongoing studies being conducted to assess the emissions of hazardous and toxic substances from a variety of coal-fired electric utility power generation systems. Recent developments in the analytical methodology required to measure low levels of toxic metals associated with flyash are presented. Also, current and future U.S. Department of Energy plans to augment these assessments are discussed.

### INTRODUCTION

The trace elements associated with the mineral matter in coal and the various compounds formed during coal combustion have the potential to produce air toxic emissions from coal-fired electric utilities. The recently enacted Clean Air Act Amendments (CAAA) contain provisions that will set standards for the allowable emissions of 190 hazardous air pollutants (HAPS). These 190 air toxics can be associated with any number of source categories that emit pollutants to the environment. Many of these HAPS could possibly be emitted from coal-fired electric generating stations. Coal-fired electric utility boilers will be studied by the Environmental Protection Agency (EPA) to determine if regulation is appropriate and necessary.

When coal is combusted, trace elements associated with the mineral matter are released in both solid and vaporized forms. Those trace elements not vaporized during combustion will report to the bottom ash stream or exit the combustor as particulate matter. The trace elements that are vaporized during combustion will exit the combustor as gases, condense either as submicron particles, or on the surface of particulate matter in the flue gas stream. The condensation of trace elements on particles results in an enrichment in concentration of specific elements (1), as shown in Table 1.

During the first phase of a two-phase program, the Canadian Electric Association (2) conducted a study to examine air, water, and ash pathways for trace constituents released to the environment from four Canadian coal-fired generating stations. All the major input and output streams of the utility plant were sampled for up to 45 elements in addition to polycyclic aromatic hydrocarbons. Material balances were made based on the average of several runs. Material balance closures to within 20% were found for 37 elements. Closure was not obtained for fluorine, silicon, phosphorus, cadmium, mercury, and boron. Table 2 summarizes the emission of elements which are on the EPA HAPS list from the Canadian Electric Association study of coal-fired power plants. The second phase

of the program dealt with the environmental dispersion and biological implications of the release.

The Electric Power Research Institute (EPRI) has begun to assess the emissions from power plants under the PISCES (Power Plant Integrated Systems: Chemical Emission Studies) program. The first activity consisted of an exhaustive literature review to obtain as much existing data as possible on the emission of chemical species from power plants (3). This data was organized into a database that contains information on both individual power plants and on the chemical characteristics of various streams within those plants. The PISCES literature study also served to identify gaps in the existing data on power plant emissions. The second major activity within the PISCES program is the Field Chemical Emissions Monitoring project which involves the use of a consistent and comprehensive analytical protocol to evaluate all inputs and outputs of the pollution control subsystems and all the process streams at the utility for HAPS. To date, the EPRI study has gathered analytical information at ten utility sites for 24 of the 190 hazardous pollutants listed in Title III of the CAAA.

Conventional air pollution control subsystems have the potential to remove many of the air toxic emissions from flue gas generated from the combustion of coal. However, there is a lack of precise analytical data on the removal of toxics across environmental control devices, such as electrostatic precipitators, baghouses, and wet limestone scrubbers. The relative concentrations of some of the toxic materials could also be increased as a result of using these technologies, or toxics could be formed when chemicals are added to the flue gas stream to increase particulate collection efficiency. Further, some of the more advanced SO<sub>2</sub> and NO<sub>x</sub> mitigation technologies involve furnace injection of a sorbent and combustion modification, respectively, and could influence the distribution of toxics between the bottom ash and flue gas streams. To date, little information exists on the effects these advanced technologies have on the amounts of toxic substances formed in the combustion zone.

#### CURRENT DOE AIR TOXICS INVESTIGATIONS

The Pittsburgh Energy Technology Center (PETC) of the U.S. Department of Energy (DOE) has two current investigations, initiated before passage of the CAAA, that will determine the air toxic emissions from coal-fired electric utilities. DOE has contracted with Battelle Memorial Institute and Radian Corporation to conduct studies focusing on the potential air toxics, both organic and inorganic, associated with different size fractions of fine particulate matter emitted from power plant stacks. Table 3 indicates the selected analytes to be investigated during these studies. PETC is also developing guidance on the monitoring of HAPS to be incorporated in the Environmental Monitoring Plans for the demonstration projects in the DOE Clean Coal Technology Program.

#### Battelle Memorial Institute

Battelle Memorial Institute and its subcontractor, Keystone/NEA, will correlate the air toxics produced by a laboratory combustor with those from two operating coal-fired electric utility boilers. A characterization of air toxics associated with the surfaces of fine particles and vapor phase constituents of the stack flue gas of the selected coal-fired units will be made. Both the diluted, cooled flyash particles with adsorbed and condensed material on the surfaces and the hot

gas flyash particles will be collected in three size fractions from the stacks. These size fractions are <0.6, 0.6-2.0, and 2.0-0.5 microns.

An innovative source dilution sampler will be utilized to simulate plume cooling and collect the diluted, cooled particles that may have an increased concentration of certain toxic substances. The hot gas samples, particulate and vapor phase, will be collected by EPA Modified Method 5 procedures. The differences in the two samples will provide information on the characteristics of the overall composition of fine particles, particularly materials of air toxic concern.

Laboratory studies can be more useful under certain circumstances than full-scale studies because these studies provide the flexibility to examine emissions from developing pollution control technologies (i.e., furnace and duct sorbent injection, flue gas conditioning, and various combustion configurations). The coals used by the two coal-fired electric utilities will be used in the laboratory combustion studies, which will indicate the efficacy of using a well-controlled laboratory-scale combustor to simulate emissions from a full-scale unit. Additional results from the Battelle laboratory combustion work will include the further development of more advanced sampling methods for collection of flyash and vapor-phase constituents from flue gas. The results will also assist DOE and EPRI in determining which toxic substances to sample in future emissions characterization studies.

#### Radian Corporation

Radian Corporation will collect size-fractionated particles from the stack of a full-scale coal-fired utility boiler and characterize the particles for both bulk and surface chemical composition. The sampling will take place over two different time periods ranging from three to four weeks. This will enable the collection of fine particles during a high-load season (winter), a lower-load season (spring), and load swings. Particulate samples will be collected from the stack effluent under both hot-stack and dilution-cooled conditions.

A source dilution sampler will be utilized to simulate the cooling and dilution that the flue gases and particles experience while entering the atmosphere at the stack exit. A relationship will be sought between the chemical materials found and the size of particles. Also, the effects of cooling and dilution upon the surface condensation of volatile species will be evaluated and characterized. In addition, the carbon content of the particulate matter will be determined in an attempt to correlate any organic compounds found on the dilution-sample particulate with the amount of carbon in the flyash.

To date, Radian has evaluated several sample preparation and analysis procedures in order to select two bulk-composition and three surface-leaching techniques to use on the size-fractionated flyash samples collected from both the hot stack gas and the cooled stack gas from the dilution sampler. To accurately evaluate these methods, a coal flyash was selected that is certified by Brammer Standard Company for 29 trace metals ( $\mu\text{g/g}$ ) and 8 major metals (wt.%), and is sieved instead of ground to produce a homogenous sample of ash particles less than 80 microns in size. Metals targeted for analysis and low detection limits were arsenic, barium, beryllium, cadmium, chromium, copper, cobalt, lead, manganese, mercury, molybdenum, nickel, selenium, and vanadium. These metals were chosen because of their known toxic properties, presence on the CAAA's list of hazardous

substances, or suspected occurrence in flue gas streams from coal-fired utility boilers.

Total composition of the flyash particles was determined by neutron activation and glow discharge mass spectrometry (GDMS). Acceptable recoveries, defined as 80-120% of the standard's certified value, were obtained by neutron activation analysis for Ba, Co, Cu, Mn, and V. Chromium and arsenic recoveries were only slightly outside this range at 124 and 127 percent, respectively. The reproducibility was acceptable (less than 20% relative standard deviation, RSD) for all the target elements except Cd, Cu, and Hg. Cadmium, lead, and beryllium were not detected by neutron activation. GDMS analysis provided acceptable recovery (80-120%) for two elements, chromium and copper. Recovery of the remaining elements was biased low and ranged from 16 to 86% recovery. The reproducibility was acceptable (<20% RSD) for all target analytes except molybdenum and cadmium, which were not detected.

The primary focus of the methods evaluation plan was to determine methods that could leach or dissolve metals from the surface of flyash particles. The five leaching agents studied were chosen based on either selectivity for the metals of interest, the method's similarity to chemical or biological processes, or as modifications of an established method. The five methods were 1) a nitric acid digestion technique that indicates the maximum amount of material available from the alumina-silica flyash matrix (EPA Method 3050); 2) an acetic acid leaching solution prepared according to the Toxicity Characteristics Leaching Procedure to a pH of 4.93 to simulate environmental availability; 3) a simulated gastric fluid made from HCl, pepsin, and NaCl buffered to pH 1.2; 4) a simulated lung fluid prepared from phosphate buffered (pH 7.5) saline solution containing bovine serum (albumin) and dextrose; and 5) a chelating agent specific for arsenic and chromium consisting of buffered (pH 4.4) ammonium pyrrolidine-N-dithiocarbamate solution.

For all five methods, 100 mg of the certified flyash was treated. The three analytical techniques used for the analysis of the leachate samples included inductively coupled argon plasma emission spectrophotometry (ICP), graphite furnace atomic absorption spectrophotometry (GFAA), and inductively coupled argon plasma mass spectrometry (ICP-MS). Results of the ICP, GFAA, and ICP-MS analysis of these leachate samples provided a clear indication that the analytical method's sensitivity and precision are very important. ICP-MS provided lower detection limits than ICP or GFAA for all the matrices tested. ICP-MS has the advantage of detecting elements from Be to U (mass 9 to 238) with quantitation levels of 20 ng/mL to 0.1 mg/mL. Detection limits for 14 metals in this evaluation ranged from 0.002 to 0.13 ng/mL. The detection limits are 10 to 100 times lower than ICP or GFAA. By ICP-MS, the RSD for nitric acid digestion samples was <20% for all target elements except Cd (34% RSD), Cu (25% RSD), and Pb (36% RSD). These diluted samples had elemental concentrations less than 3 ng/mL for all target analytes. With respect to the ICP and GFAA analyses, only arsenic (1% RSD), beryllium (7% RSD), chromium (120% RSD), copper (27% RSD), lead (59% RSD), nickel (40% RSD), selenium (1900% RSD), and vanadium (5% RSD) were detected. Similar results were obtained on the other leachate samples, except the simulated lung fluid sample whose increased viscosity presented sample aspiration problems, indicating the superiority of the ICP-MS technique.

The nitric acid digestion, gastric fluid, and acetic acid leach are the three methods chosen based on the performance criteria when analyzed by ICP-MS. ICP-MS

provides lower detection limits and improved precision than previously obtained by conventional ICP or GFAA methods.

#### FUTURE TOXIC EMISSION STUDIES

A collaborative effort has been initiated by the DOE, the Utility Air Regulatory Group (UARG), EPRI, and the EPA to expand the study of hazardous pollutant emissions from utility boilers. This effort will involve measurements at a number of power plants having different boiler designs, NO<sub>x</sub> control methods, particulate control devices, and SO<sub>2</sub> removal systems (wet and dry). From these measurements, the EPA expects to predict the potential air toxic emissions from coal-fired boilers in 1995 and 2000 (after controls are installed to meet the requirements of the acid rain title of the CAAA). Measurements from plants firing bituminous or subbituminous coal will be used to evaluate the entire range of existing power plant configurations and will form the basis for this study.

DOE has issued a solicitation for proposals to assess selected hazardous/toxic pollutants from a number of utilities that utilize different pollution control and process subsystems while burning either bituminous or subbituminous coal. The power plant configurations addressed in this solicitation are given in Table 4. Objective of this solicitation are to determine the removal efficiencies of pollution control subsystems for selected pollutants and the concentrations of pollutants associated with the particulate fraction of the flue gas stream as a function of particle size. A further objective is to determine mass balances for selected pollutants for a variety of different input and output streams of the power plants and subsequently for the entire power plant.

Results from all the DOE studies will provide input to the congressionally mandated study being conducted by the EPA to assess the impacts of the listed HAPS emissions from coal-fired electric utilities, as required in Title III of the CAAA of 1990. In addition, the data will provide a basis for evaluating the potential effects of air toxics regulation on existing pollution control and auxiliary processes being utilized at electric utilities and on the commercialization of technologies demonstrated under the Clean Coal Technology Program.

#### REFERENCES

1. D.G. Coles, R.C. Rahaini, J.M. Ondov, G.L. Fisher, D. Silberman, and B.A. Prentice, "Chemical Studies of Stack Fly Ash from Coal-Fired Power Plant," Environmental Science and Technology, Vol 13, 4, April 1979.
2. J.C. Evans, K.H. Abél, K.B. Olsen, E.A. Lepell, R.W. Sanders, C.L. Wilkerson, and D.J. Hayes, "Characterization of Trace Constituents at Canadian Coal-Fired Plants - Phase I," Contract Number 001G194, Canadian Electrical Association, January, 1985.
3. F.B. Meserole and W. Chow, "Controlling Trace Species in the Utility Industry, paper presented at the conference Managing Hazardous Air Pollutants: State of the Art, Washington, D.C., November 4-6, 1991.

Table 1. Comparison of Elemental Concentrations in Size-Classified Flyash Fractions (Concentrations in  $\mu\text{g/g}$  unless indicated by %)

Element	Fraction 1, <u>18.5 <math>\mu\text{m}</math></u>	Fraction 2, <u>6.0 <math>\mu\text{m}</math></u>	Fraction 3, <u>3.7 <math>\mu\text{m}</math></u>	Fraction 4, <u>2.4 <math>\mu\text{m}</math></u>
Aluminum, %	13.8	14.4	13.3	13.9
Barium, %	0.168	0.245	0.31	0.41
Calcium, %	2.1	2.23	2.3	2.36
Iron, %	2.51	3.09	3.04	3.2
Magnesium, %	0.47	0.56	0.60	0.63
Potassium, %	0.74	0.80	0.82	0.81
Silicon, %	29.6	28.0	27.5	26.8
Sodium, %	1.22	1.75	1.81	1.85
Sulfur, %	0.101	0.304	0.425	0.711
Titanium, %	0.62	0.74	0.73	0.77
Antimony*	2.6	8.3	13.0	20.6
Arsenic*	13.7	56.0	87.0	132.0
Beryllium*	6.3	8.5	9.5	10.3
Cadmium*	0.4	1.6	2.8	4.6
Cerium	113.0	122.0	123.0	120.0
Cesium	3.2	3.7	3.7	3.7
Chromium*	28.0	53.0	64.0	68.0
Cobalt*	8.9	17.7	20.3	21.8
Copper	56.0	89.0	107.0	137.0
Dysprosium	6.9	8.5	8.1	8.5
Europium	1.0	1.2	1.2	1.3
Gallium	43.0	116.0	140.0	178.0
Hafnium	9.7	10.3	10.5	10.3
Lanthanum	62.0	68.0	67.0	69.0
Lead*	73.0	169.0	226.0	278.0
Manganese*	208.0	231.0	269.0	309.0
Neodymium	45.0	47.0	49.0	52.0
Nickel*	25.0	37.0	43.0	40.0
Rubidium	51.0	56.0	57.0	57.0
Samarium	8.2	9.1	9.2	9.7
Scandium	12.6	15.3	15.8	16.0
Selenium*	19.0	59.0	78.0	198.0
Strontium	410.0	540.0	590.0	700.0
Tantalum	2.06	2.3	2.5	2.7
Terbium	0.90	1.06	1.10	1.13
Thorium	25.8	28.3	29.0	30.0
Uranium	8.8	16.0	22.0	29.0
Vanadium	86.0	178.0	244.0	327.0
Tungsten	3.4	9.0	16.0	24.0
Ytterbium	3.4	4.1	4.0	4.2
Zinc	68.0	189.0	301.0	590.0

NOTE: These data were taken from Reference 1.

\*Denotes element is contained on EPA HAPS list.

\*\*Aerodynamic cut sizes.

Table 2. Flue Gas Trace Element Releases from Selected Canadian Coal-Fired Power Plants

<u>Element</u>	<u>% of Total Element in Coal Released with the Flue Gas</u>	
Chlorine	49	- 99.0
Chromium	0.1	- 8.7
Manganese	0.1	- 1.0
Cobalt	0.09	- 1.5
Arsenic	0.74	- 9.3
Selenium	3.5	- 73.0
Antimony	0.2	- 2.5
Mercury	79.0	- 87.0
Lead	0.2	- 1.4

Table 3. Compounds and Elements for the Battelle and Radian Air Toxics Studies

Arsenic	Ammonia
Barium	Radionuclides (Ra, Po, U, etc.)
Beryllium	Sulfates
Cadmium	
Chromium	Benzene
Chlorine (as Cl <sup>-</sup> )	Toluene
Cobalt	Formaldehyde
Copper	Polycyclic Aromatic Hydrocarbons
Cyanide	
Fluorine (as F <sup>-</sup> )	
Lead	
Manganese	
Mercury	
Molybdenum	
Nickel	
Phosphorus (as PO <sub>4</sub> <sup>3-</sup> )	
Selenium	
Vanadium	

TABLE 4.  
ELECTRIC UTILITY CONFIGURATIONS

Configuration	Coal Rank	Particulate Control	SO <sub>2</sub> Control	NO <sub>x</sub> Control <sup>1</sup>	Coal Preparation	Cooling Tower (Water) Streams
1	Bituminous	ESP	None	None		
2	Bituminous	ESP	Wet FGD	None		
3	Bituminous	ESP	Wet FGD	All	Yes	Yes
4	Bituminous	Baghouse	None	All		
5	Bituminous or Subbituminous	Baghouse	Wet or Dry FGD	All		
6	Bituminous or Subbituminous	ESP	Dry FGD	All		
7	Subbituminous	Baghouse	None	All		
8	Subbituminous	ESP	Wet FGD	All		

<sup>1</sup> All designation includes low NO<sub>x</sub> burners, overfire air, and "other."

SULFUR TRIOXIDE FORMATION IN THE PRESENCE OF  
RESIDUAL OIL ASH DEPOSITS IN AN ELECTRIC UTILITY BOILER

Peter M. Walsh,\* Dominick J. Mormile,† and Bruce F. Piper‡

\*Fuel Science Program  
Department of Materials Science and Engineering  
The Pennsylvania State University, University Park, PA 16802

†Office of Environmental Affairs  
The Consolidated Edison Co. of New York, Inc.  
4 Irving Place, New York, NY 10003

‡Energy Technology Consultants, Inc.  
51 Virginia Avenue, West Nyack, NY 10994

Keywords: residual oil ash, sulfur trioxide formation, utility boilers

A model is proposed for the catalytic oxidation of sulfur dioxide to sulfur trioxide over vanadium-containing ash deposits on heat exchanger tubes in the convective section of a residual oil-fired boiler. The model includes a global description of the rates of forward and reverse reactions at the deposit surface and mass transfer of the product  $SO_3$  from the deposit surface to free stream. The kinetic parameters for the chemical reaction and the ratio of active deposit surface area to geometric external area are the principal adjustable parameters. Conversion of  $SO_2$  to  $SO_3$  is strongly dependent on the surface area-temperature-residence time distribution in the convective section. The change in surface temperature with increasing deposit thickness accounts for a significant part of the increase in sulfur trioxide content of stack gas which occurs as ash accumulates on convective tubes.

#### INTRODUCTION

A few percent of the sulfur in residual fuel oil typically appears as sulfur trioxide in the stack gas from an electric utility boiler. Sulfur trioxide is completely converted to sulfuric acid vapor at approximately 500 K (440°F), and condenses as aqueous sulfuric acid at the dewpoint, near 400 K (260°F) (Halstead and Talbot, 1980). Adsorption of the acid on unburned coke particles and reaction with ash increases the particulate matter concentration in the combustion products, when measured by USEPA Method 5. Acid droplets contribute to the visual opacity of the stack plume. The distribution of sulfur oxides among gaseous species, droplets, and particles influences the dispersion, atmospheric reactions, and deposition of sulfate from the plume.

Vanadium, one of the most abundant inorganic impurities in many residual fuel oils, is the active ingredient of commercial catalysts for oxidation of sulfur dioxide to sulfur trioxide in the manufacture of sulfuric acid. The fraction of sulfur oxides emitted as sulfur trioxide from an oil-fired boiler has been observed to increase with increasing vanadium content of the fuel, with increasing excess oxygen in the flue gas, and with accumulation of vanadium-containing deposits on heat exchanger tubes. In the present paper we examine the effect of the deposit surface temperature on sulfur trioxide formation.

Reactions determining the formation and fate of  $SO_3$  in oil-fired boilers are shown as functions of temperature in Figure 1. In the flame and postflame regions, above about 1200 K (1700°F), the steady-state concentration of  $SO_3$  is approximately described by formation and destruction reactions of  $SO_2$  and  $SO_3$  with oxygen atoms (Merryman and Levy, 1971). Detailed discussions of the homogeneous reaction system are given by Cullis and Mulcahy (1972) and by Smith, Wang, Tseregounis, and

Westbrook (1983). The equilibrium distribution of sulfur oxides shifts toward SO<sub>3</sub> as temperature decreases, so the concentration of SO<sub>3</sub> just downstream from the furnace exit is determined by the relative rates of the formation reactions and cooling of the combustion products in this region. Typically 1 mol% of the sulfur oxides are thought to be present as SO<sub>3</sub> in furnace exit gas, i.e. on the order of 10 mol ppm in the products from combustion of 2 wt% sulfur oil. If SO<sub>3</sub> remained at this level, low temperature corrosion, plume opacity, and other problems associated with sulfuric acid would not be too troublesome.

Oxidation of SO<sub>2</sub> is catalyzed by iron- and vanadium-containing ash deposits in the convective section of a boiler. Conversion of SO<sub>2</sub> to SO<sub>3</sub> via heterogeneous reactions is greatest over a relatively narrow temperature range, from about 780 to 980 K (950 to 1300°F) (Wickert, 1963; Reid, 1971). At lower temperatures, formation of SO<sub>3</sub> is limited by the rate of the surface reaction; at higher temperatures it is limited by the equilibrium distribution of sulfur oxides, which increasingly favors the reactants, O<sub>2</sub> and SO<sub>2</sub>, as temperature increases. When the heterogeneous contribution to SO<sub>3</sub> formation is significant, problems associated with sulfate and sulfuric acid are more severe. Plume visibility due to acid mist increases as ash deposits accumulate (Reidick and Riefenhäuser, 1980). A model for SO<sub>3</sub> formation in boilers, including both homogeneous and heterogeneous reactions, was developed by Squires (1982). Release of SO<sub>3</sub> accumulated in ash deposits during operation at reduced load was proposed by Shareef, Ramsay, and Homolya (1986) and Shareef, Homolya, and Mormile (1990) to explain the increase in plume opacity associated with increase in load, following a period of low-load operation.

The formation of sulfuric acid vapor and liquid is shown at the bottom left in Figure 1. All four of the major sulfur-containing species, gaseous SO<sub>2</sub> and SO<sub>3</sub>, as well as liquid and vapor phase H<sub>2</sub>SO<sub>4</sub>, may react with metal oxides in the oil ash forming metal sulfates, processes which are shown at the bottom right in Figure 1. Little is known about the relative importance of these reactions, or the relative amounts of sulfate present in particulate matter as metal salts and adsorbed sulfuric acid (Halstead, 1978; Penfold and Smith, 1982). A conservative estimate of the contribution of sulfate to particulate matter would require that one place all of the SO<sub>3</sub> in the particulate, but a conservative estimate of the contribution of acid droplets to opacity would require one to assume that all of the SO<sub>3</sub> forms sulfuric acid mist! More experimental work on the distribution of these species is needed.

#### MODEL FOR CATALYTIC SO<sub>3</sub> FORMATION

The model is based on the assumption that only ash deposited on convective tubes contributes to SO<sub>3</sub> formation, according to the overall reaction



Ash particles suspended in the gas stream are neglected because their external surface area per unit of flue gas volume is much smaller than that of deposits. Some SO<sub>3</sub> is considered to be present in the gas entering the convective section, but flame and postflame homogeneous reactions are not included in the simulation.

The kinetics of heterogeneous oxidation of SO<sub>2</sub> were reviewed by Urbanek and Trela (1980). A global expression for the rate of formation of SO<sub>3</sub>, assuming a rate proportional to the mass fraction of vanadium oxides in deposits, is

$$r_{\text{SO}_3} = k Y_{\text{VO}_x} S_d C_{\text{O}_2}^a C_{\text{SO}_2}^b \left[ 1 - \frac{C_{\text{SO}_3, s}}{K C_{\text{SO}_2} C_{\text{O}_2}^{1/2}} \right] \quad (2)$$

The factor in brackets accounts for the approach of the rate to zero as the SO<sub>2</sub> concentration adjacent to the catalyst surface approaches its equilibrium value. Under conditions of interest in boilers the extent of reaction is small, so changes in the SO<sub>2</sub> and O<sub>2</sub> concentrations are negligible. When the system is steady, the rate of SO<sub>2</sub> formation at the deposit surface equals its rate of transport from the surface to the free stream:

$$r_{SO_2} = \frac{Sh_t D_{SO_2}}{d_t} A_t (C_{SO_2,s} - C_{SO_2}) \quad (3)$$

Elimination of the unknown concentration at the surface and integration over time, with the boundary condition, C<sub>SO<sub>2</sub></sub> = C<sub>SO<sub>2</sub>,o</sub> at t = 0, gives:

$$C_{SO_2} = K C_{O_2}^{1/2} C_{SO_2} + [C_{SO_2,o} - K C_{O_2}^{1/2} C_{SO_2}] \exp(-k' A_t t) \quad (4)$$

C<sub>SO<sub>2</sub>,o</sub> and C<sub>SO<sub>2</sub></sub> are the SO<sub>2</sub> concentrations entering and leaving, respectively, a region in which deposit surface temperature and composition are approximately constant. The effective rate coefficient, k', is given by:

$$\frac{1}{k'} = \frac{1}{Sh_t D_{SO_2}} + \frac{1}{\frac{k}{K} \frac{S_d}{A_t} Y_{VOx} C_{O_2}^{a-1/2} C_{SO_2}^{b-1}} \quad (5)$$

The kinetic parameters were estimated from the work of Glueck and Kenney (1968), who observed that the reaction over a vanadium oxide-potassium oxide melt was first order in SO<sub>2</sub> (b = 1), and zeroth order in O<sub>2</sub> (a = 0). After choosing the kinetic constants, the most important adjustable parameter in the model is the ratio of effective catalytic surface area to the geometric external surface area of deposits, S<sub>d</sub>/A<sub>t</sub>.

## RESULTS

A study of SO<sub>2</sub> formation was conducted by the Consolidated Edison Co. of New York at Arthur Kill Station (Piper and Kokoska, 1983; Shareef, Ramsay, and Homolya, 1986; Shareef, Homolya, and Mormile, 1990). The majority of testing was conducted on the superheat furnace of Arthur Kill Unit 20. This unit normally fires oil containing less than 0.3 wt% sulfur, but the testing for the SO<sub>2</sub> study was performed using oil containing 0.75 wt% sulfur. Measurements of SO<sub>2</sub> were made as functions of load during both transient and steady-state operation. Under steady full load conditions, the level of SO<sub>2</sub> in flue gas varied between 31 and 40 mol ppm over three days of tests. Gas temperatures, tube temperatures, gas velocities, and residence times were calculated for 14 separate tube bundles from the platen superheater inlet to economizer outlet (Piper and Kokoska, 1983; Piper, 1985).

The model described above was used to examine the influence of deposit accumulation on SO<sub>2</sub> formation, considering only the effect of deposit thickness on the surface temperature distribution, neglecting any change in the effective surface area of catalyst which might be associated with deposit growth. The increase in surface temperature with increasing deposit thickness was estimated by assuming that deposit was built on surfaces whose temperatures were fixed at the values calculated by Piper (1985). The deposition rate was assumed to be 1 g/m<sup>2</sup>-hour, distributed uniformly over the length and circumference of the tubes. Changes in deposition rate with changes in gas, tube, and surface temperatures were not considered. Equation 4 was applied to successive banks of convective tubes, from the furnace exit to economizer outlet. The calculated SO<sub>2</sub> profiles through the convective section after 0, 3, 6, and 12 months of continuous full load

operation are shown in Figure 2. Position in the convective passage is given as a fraction of the total gas residence time. The surface temperature distribution calculated by Piper (1985) is the base case, shown at the bottom of the figure. The calculated thickness of deposits after 12 months of continuous full load operation was 4 mm.

Under the conditions investigated, the temperature distribution is such that the rate of heterogeneous  $\text{SO}_3$  formation is low near the entrance to the convective section, then increases, and decreases as the combustion products move downstream. The model properly accounts for the observation that the rate of  $\text{SO}_3$  formation peaks in a narrow temperature window, the actual range of temperatures depending on conditions such as mass transfer between the free stream and catalyst surface, concentrations of  $\text{O}_2$  and  $\text{SO}_2$ , etc. As ash thickness and surface temperature increase, the activity of deposits near the entrance to the convective section decreases as their temperatures move farther from the optimum range. However, the decrease in  $\text{SO}_3$  formation rate at the entrance is more than compensated by an increase in rate in the larger surface area, higher gas velocity tube banks in the middle of the convective section, with the result that  $\text{SO}_3$  continuously increases with increasing fouling of the tubes. For the assumed conditions,  $\text{SO}_3$  at the economizer outlet (far right) increases from 33 to 44 mol ppm over the 12 month period. Changes in surface temperature distribution may therefore be a significant factor in the increase in sulfate emissions with time after cleaning of a unit, apart from any effect of an increase in effective surface area of deposits.

#### CONCLUSION

Simulation of the catalytic oxidation of  $\text{SO}_2$  to  $\text{SO}_3$  over vanadium-containing ash deposits, including chemical reaction between  $\text{SO}_2$  and  $\text{O}_2$  at the surface and diffusion of  $\text{SO}_3$  from the surface to free stream, shows that changes in deposit surface temperature associated with deposit growth may be a significant influence on  $\text{SO}_3$  formation. Using conditions in Arthur Kill Unit 20 as a baseline, and assuming deposit growth at the rate of  $1 \text{ g/m}^2\text{-hour}$  while firing 0.75 wt% sulfur oil, changes in deposit surface temperature resulting from the increase in deposit thickness were estimated to cause a 30% increase in  $\text{SO}_3$  at the economizer outlet over a period of 12 months at full load.

#### ACKNOWLEDGMENTS

This investigation was begun while the first author was a member of the research staff in the Energy Laboratory at the Massachusetts Institute of Technology, working with Professor János M. Beér. That research program was supported by Babcock and Wilcox Canada, Canadian Electrical Association, Consolidated Edison Co. of New York, Electric Power Research Institute, Empire State Electric Energy Research Corp., Florida Power & Light Co., Long Island Lighting Co., New England Power Service Co., Northeast Utilities Service Co., and Shell Development Co. Subsequent work, at the Pennsylvania State University, was supported by the Consolidated Edison Co. of New York, Electric Power Research Institute, Empire State Electric Energy Research Corp., and Florida Power & Light Co.

#### NOMENCLATURE

- a order of the heterogeneous reaction with respect to  $\text{O}_2$ , dimensionless
- $A_c$  geometric external surface area of tubes or deposits, per unit of gas volume,  $\text{m}^{-1}$
- b order of the heterogeneous reaction with respect to  $\text{SO}_2$ , dimensionless
- $C_i$  concentration of species  $i$ ,  $\text{kmol/m}^3$

- $d_t$  tube diameter, m
- $D_{SO_2}$  molecular diffusion coefficient of  $SO_2$  in combustion products,  $m^2/s$
- $k$  rate coefficient for the heterogeneous reaction between  $SO_2$  and  $O_2$ , the dimensions depend upon the orders of reaction, a and b
- $k'$  effective rate coefficient for  $SO_3$  formation, including surface reaction and boundary layer diffusion, m/s
- $K$  equilibrium constant, in terms of concentrations, for the reaction  $SO_2 + 1/2 O_2 = SO_3$ ,  $m^{3/2}/kmol^{1/2}$
- $r_{SO_3}$  rate of sulfur trioxide formation,  $kmol/m^3 \cdot s$
- $S_d$  effective surface area of catalytic deposits per unit of gas volume,  $m^{-1}$
- $Sh_t$  average Sherwood number for mass transfer between tube or deposit surface and free stream, dimensionless
- $t$  time, s
- $Y_{Vx}$  mass fraction of vanadium oxides in deposits, dimensionless

#### Subscripts

- $o$  initial value
- $s$  condition at the catalytic deposit surface

#### REFERENCES

- C. F. Cullis and M. F. R. Mulcahy, The Kinetics of Combustion of Gaseous Sulphur Compounds, *Combustion and Flame* **18** (1972) 225-292.
- A. R. Glueck and C. N. Kenney, The Kinetics of the Oxidation of Sulfur Dioxide over Molten Salts, *Chemical Engineering Science* **23** (1968) 1257.
- W. D. Halstead, The Nature of  $H_2SO_4$  in Deposits of Acid Contaminated Combustion Grits, *Journal of the Institute of Fuel* **51** (1978) 149-153.
- W. D. Halstead and J. R. W. Talbot, The Sulphuric Acid Dewpoint in Power Station Flue Gases, *Journal of the Institute of Energy* **53** (1980) 142-145.
- E. L. Merryman and A. Levy, Sulfur Trioxide Flame Chemistry -  $H_2S$  and  $COS$  Flames, Thirteenth Symposium (International) on Combustion, The Combustion Institute, Pittsburgh, PA, 1971, pp. 427-436.
- D. Penfold and A. C. Smith, The Analysis of Carbonaceous Material from Oil-Fired Boilers, *Journal of the Institute of Energy* **55** (1982) 98-101.
- B. Piper, 1985, Arthur Kill 20  $SO_3$  Model, Appendix B to Shareef, Ramsay, and Homolya, (1986).
- B. Piper and T. Kokoska, Opacity Study - Data to Support  $SO_3$  Formation Analysis, KVB 81-21620-1447, Report prepared by KVB, Inc., for the Consolidated Edison Co. of New York, Inc., 1983.

W. T. Reid, External Corrosion and Deposits, Boilers and Gas Turbines, American Elsevier, New York, 1971, pp. 75-114.

H. Reidick and R. Reifenhäuser, Catalytic SO<sub>3</sub> Formation as Function of Boiler Fouling, *Combustion*, Vol. 51, No. 8, February 1980, pp. 17-21.

G. S. Shareef, J. B. Homolya, and D. J. Mormile, SO<sub>3</sub> Formation over Fuel Oil Fly Ash Deposits, 1990 SO<sub>2</sub> Control Symposium, New Orleans, LA, May 8-11, 1990.

G. S. Shareef, G. G. Ramsay, and J. B. Homolya, Development and Calibration of a Prediction Model for the Formation of Sulfur Trioxide in a Residual Oil-Fired Boiler, Report prepared for the Consolidated Edison Co. of New York, Inc., by Radian Corp., Research Triangle Park, NC, 1986.

O. I. Smith, S.-N. Wang, S. Tseregounis, and C. K. Westbrook, The Sulfur Catalyzed Recombination of Atomic Oxygen in a CO/O<sub>2</sub>/Ar Flame, *Combustion Science and Technology* 30 (1983) 241-271.

R. T. Squires, The Kinetics of SO<sub>3</sub> Formation in Oil-Fired Boilers, *Journal of the Institute of Energy* 55 (1982) 41-46.

A. Urbanek and M. Trela, Catalytic Oxidation of Sulfur Dioxide, *Catalysis Reviews, Science and Engineering* 21 (1980) 73-133.

K. Wickert, The Oil-Firing Yearbook, Kopf, Stuttgart, 1963.

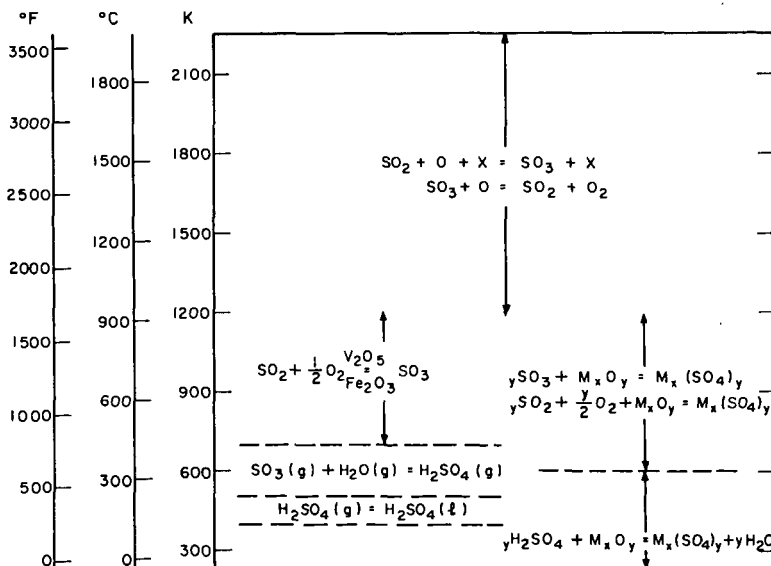


Figure 1. Processes contributing to formation of sulfur trioxide, sulfuric acid, and sulfates in residual oil-fired boilers.

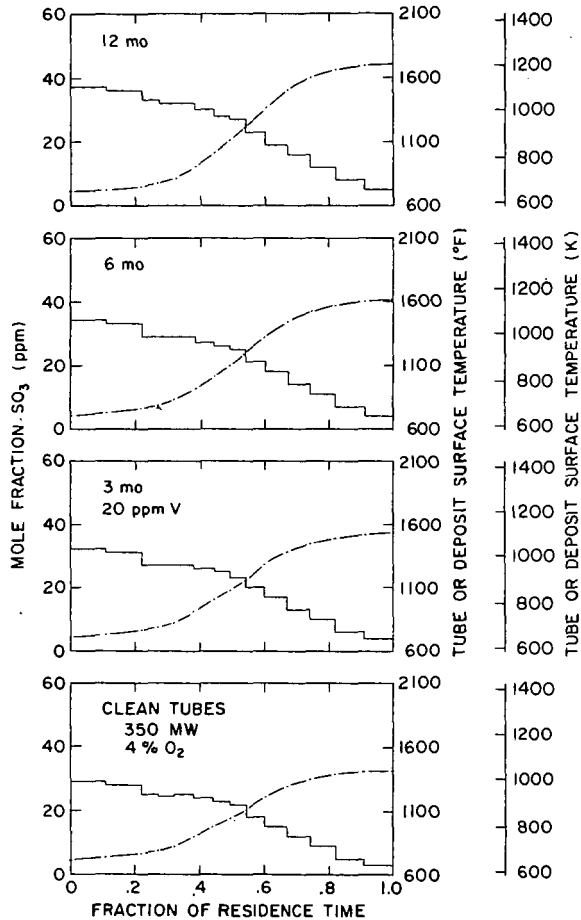


Figure 2. Expected change in SO<sub>3</sub> formation in Arthur Kill Unit 20 as ash deposits accumulate on the convective tubes. Solid line: surface temperature; dot-dash line: SO<sub>3</sub> mole fraction. The estimates are based on the gas temperature-tube temperature-tube area-gas velocity calculations of Piper and Kokoska (1983) and Piper (1985). The fuel oil sulfur content was 0.75 wt%, different from the 0.3 wt% sulfur oil normally fired in the unit. Ash deposits were assumed to grow at the rate of 1 g/m<sup>2</sup>-hour. As the thickness of deposits increases, the formation of SO<sub>3</sub> decreases at the entrance to the convective section because the equilibrium ratio of SO<sub>3</sub>/SO<sub>2</sub> decreases with increasing temperature. However, the ultimate mole fraction of SO<sub>3</sub> at the economizer outlet (far right) increases, because the contribution to SO<sub>3</sub> formation from the higher gas velocity, higher surface area region near the middle of the convective section increases.

## Precombustion Control of Hazardous Air Pollutants

Michael A. Nowak and Victoria L. McLean

U.S. Department of Energy  
Pittsburgh Energy Technology Center  
P.O. Box 10940  
Pittsburgh, PA 15236-0940

KEY WORDS: trace elements, air toxics, coal preparation

### INTRODUCTION

The air toxics provision of the 1990 Clean Air Act Amendments (CAAA) requires the Environmental Protection Agency (EPA) to promulgate regulations establishing emission standards for Hazardous Air Pollutants (HAP). Precursors of 13 of the HAPs are found in trace quantities in coal: As, Se, Hg, Pb, Cl, F, Be, Co, Ni, Cr, Sb, Cd, and Mn. The EPA is currently conducting a Congressionally mandated study of HAPs emissions from coal-fired power plants; the results of the study may lead to regulations governing the emissions of specific trace elements from coal. Influenced by the potential risk to coal utilization by possible future HAP emissions regulations, the Department of Energy, in cooperation with coal users and other government agencies, is seeking to evaluate the information on these elements of environmental concern in coal and to examine methods of measuring and controlling these emissions.

One control option is precombustion coal cleaning, which can significantly reduce mineral matter concentration and consequently has the ability to remove trace elements associated with the mineral matter liberated from the coal matrix. Primary factors controlling the precombustion removal of trace elements are the extent of association of the element with mineral matter within the coal matrix and the crushed coal particle size. The finer the coal is crushed, the more mineral matter is liberated and the further the trace elements associated with the mineral matter are reduced in the product coal.

The affinities of coal-related HAP precursors have been discussed extensively in the literature. This paper will review and summarize the literature on trace element affinities in coals, and the ability of precombustion coal cleaning to remove those trace elements from coals.

### TRACE ELEMENTS AND COAL CLEANING

Finkelman,<sup>1</sup> in his 1980 dissertation, examined in depth the Waynesburg and Upper Freeport seam coals. In addition, he briefly examined 80 U.S. coals from every major basin and an additional 20 coals from around the world. He relied on a Scanning Electron Microscope equipped with an Energy Dispersive X-ray detector (SEM/EDX) to determine the mode of occurrence. His analysis discusses the problems associated with using float-sink testing as an analytical tool. Finkelman's float-sink data for the Waynesburg and Upper Freeport coals showed that, in general, trace element separation is dependent on mesh size, and, for the trace elements examined, approximately one-half of each trace element found in the whole coal was retained in the fractions with a specific gravity less than 1.50.

Finkelman summarized the literature that evaluated float-sink studies. His summary covered 12 float-sink studies involving a number of trace elements in several specific gravity fractions and whole coal samples for over 60 coals.

Finkelman briefly reviewed a number of studies that discussed the use of various leaching agents, including HCl, HF, HNO<sub>3</sub>, and pyridine. His summary suggests that organic affinity index determinations may be exaggerated due to experimental error and indicates that a common error in each study is the assumption that the leaching was quantitative. In his discussion of correlation of trace elements, several studies on coals from around the globe are cited. His conclusion was that correlation coefficients do not necessarily reflect the mode of occurrence, but rather a common original source of the element. For example, Hg and As have very high correlation coefficients for pyrite and for each other. Finkelman's SEM/EDX experiments found that Hg and As are in solid solution with pyrite, (probably as sulfides) thus suggesting that the Hg and As had a common source. For any given trace element, there does not appear to be any coefficient that indicates a correlation between that trace element's concentration in coal and any other coal constituent's concentration that can be applied to more than one coal.

In summarizing his findings on the trace elements in coal, Finkelman states:

- Most trace elements appear to have an inorganic association in most high-rank coals.
- The organic complexing of trace elements, however, is not unimportant.
- Even in any one coal, the mode of occurrence can vary.

According to Gluskoter<sup>2</sup> and Ruch et al.<sup>3</sup>, organic affinity numerical values change with particle size distribution of the coal. The reason for this interpreted behavior is due to the misuse of the term "organic affinity." Gluskoter and Ruch developed the organic affinity index as a single numerical value to replace washability curves in an effort to simplify comparison of trace element reductions among different coals. Some researchers have misinterpreted the term to imply that trace elements may be chemically bound to the organic matrix, i.e., as in organometallic complexes, porphyrins, etc., but the vast majority of the organically associated trace elements in coal are very fine mineral particles that are dispersed and are difficult to liberate and separate. Examining the inorganic material frequently referred to as syngenetic, authigenic, or inherent mineral matter, Nicholls<sup>4</sup> noted that some elements appear to be predominantly dispersed in the organic fraction, that is, the concentration of the element is constant with rising ash content. This suggests that those trace elements were present when the plant material was deposited prior to coalification and not introduced through later mineral deposition.

Kuhn et al.<sup>5</sup> examined the trace elements of Davis, Blue Creek, Pittsburgh, Illinois No. 6, Rosebud, and Black Mesa coals. They examined the trace element concentrations of whole coal and float-1.40 sp. gr. fractions for 33 elements and the effects of acid leaching with HNO<sub>3</sub>, HCl, and HF, and reactions with lithium aluminum hydride (LAH) on demineralization. They also examined Cr in five specific gravity fractions of Illinois No. 6 coal. Trace element concentrations and organic affinities were determined. With regard to the trace elements that

are potential precursors to HAPs cited in the 1990 CAAA, the following can be extracted from their summary:

- Be and Sb are consistently associated with the organic matrix.
- As and Cd are found with pyrite and can usually be substantially reduced with pyrite by gravity methods.
- Hg, Pb, and Mn have a high degree of inorganic association and are removed rather easily by conventional coal cleaning.

Akers<sup>6,7</sup> examined conventional coal cleaning as a control method for trace elements. Akers' studies may be summarized by the following:

- Upper Freeport coal was found to be relatively high in As, Cd, and Cr. Conventional cleaning reduced As, Ba, Cd, Cr, F, Pb, Hg, Ag, and Zn by at least 50%. A significant reduction in Ni also occurred. An increase in Se concentration (ca. 30%) was noted.
- Conventional cleaning of Rosebud/McKay subbituminous coals showed significant reductions in As, Ba, and Ni. Small reductions of Cd and Se were observed. The Cr concentration was reported as increasing from 6 ppm to 10 ppm.
- Conventional cleaning of samples from the Croweburg seam indicated significant reductions in As, Ba, Cd, Cr, Pb, Ni, and Zn. In some cases, but not in others, reductions in F, Hg, and Ag correlate with ash reduction.
- A comparison of advanced coal cleaning to conventional cleaning was made with Sewickley seam coal. The Custom Coals International process (density separation of fine coal) was found to provide further reduction of all trace elements, except Hg, which is in disagreement with Kuhn's<sup>5</sup> findings that Hg is readily removed with the ash. In one example, As was reduced from 14 ppm to 4 ppm (70%).
- Physical coal cleaning is effective in reducing the concentration of many trace elements, especially if they are in high concentration. Trace element removal is not, however, always proportional to ash removal. Potential changes in plant flow sheets and operating parameters may not lead to reduction in the ash content of the coal but may reduce trace element concentrations. Trace element reduction appears to be coal-specific, relating in part to the degree of liberation and the trace-element-bearing mineral matter. Thus, advanced coal cleaning methods that process more finely ground coals may provide greater reductions than conventional technologies.
- Conventional cleaning of Kentucky No. 11 coal led to large reductions in all trace elements measured.
- The Midwest Ore process, which involves extraction with hot perchloroethylene (PERC) followed by gravity separation in PERC, reduced nine trace elements by two-thirds or more.

White et al.<sup>8</sup> prepared a very extensive report for the EPA that covered the entire coal utilization cycle, including a review of the literature on the following topics: occurrence of trace elements in U.S. coals; organic affinity studies, including the PETC Study<sup>9</sup>; photomicrographic studies; conceptual models for trace element modes of occurrence; coal washing, particularly partitioning of trace elements; and leaching of coal wastes.

The report concluded that:

- Organic affinity data are usually acquired by specific gravity fractionation, although acid leaching has also been used. The literature describing characterization and trace element washability of up to 27 elements was reviewed. Organic affinities and trace element concentrations for mineral-matter-free coals derived from reviewing the literature, including the work of Boyer et al.<sup>10</sup>, are presented in tables. The Boyer et al.<sup>10</sup> report has a complete bibliography of 1,076 publications covering the fate of trace elements during mining, preparation, and utilization. The report cites earlier key studies by Buroff et al.<sup>11,12</sup> and Miller et al.<sup>13</sup>, and includes where trace element removal at coal cleaning plants are cited, with a note that mass balances were not done.
- Although a thorough understanding of the response of various coals to sulfur and trace element removal does not yet exist, significant insight has been developed.
- Coals containing dispersed fine-grained minerals or free-swelling clays are more difficult to clean.
- A logical step in the process of better understanding trace element reduction potential is further statistical assessment of existing data.
- A statistical evaluation of existing ISGS and DOE data was performed. Linear correlations and regressions gave correlation coefficients (CC)  $\geq 0.70$  for the occurrence of several clustered groups of elements: As, Cd, Pb, Sb, and Zn; Al, Si, Ti, K, Co, V, and Cr; Fe and S; F with Al, K, Si, Ti, Cr, Cu, Be, and Ni. Regarding trace element reduction, a large number of elements showed coefficients greater than 0.70 and appeared to suggest that ash removal was more important than the removal of any individual element. Arsenic, Hg, and Fe reductions had CCs between 0.50 and 0.70 for pyrite removal and As, Co, Hg, Pb, Se, and Fe reductions had CCs greater than 0.50 for sulfur reduction. Efforts to correlate trace element reductions with an element's concentration in the whole coal were unsuccessful, except for the elements in the clays, suggesting that abundance of clays, and not the concentration of the element, determines the extent to which the element can be removed. Analysis of trace element removal data indicated elements in coal occur in two groups: 1) those associated with Al, K, Na, Si, Ti, Be, Cr, Cu, Mn, Ni, V, and ash; or 2) those associated with Fe, As, Hg, and pyrite.

- There is considerable disagreement among coal scientists on the methods of analysis and interpretation of the results of trace element studies of coal. A detailed framework for predicting trace element occurrence for a seam based on existing samples and associated geologic, geochemical, or paleoenvironmental data is lacking. Therefore, research priority needs for the coal resource appear to be in interpreting these data on a regional or seam basis. Given the magnitude of the U.S. coal resource base, combined with the extent and variability of existing data, collection and analysis of further samples (except as they relate to the evaluation of new mines and coal-using facilities) will provide little additional information.
- Pyritic sulfur and trace elements associated with pyrite and extraneous clays can be removed with relatively high efficiency by coal cleaning. Other trace elements are generally not removed during conventional cleaning. Variability in cleanability between regions or seams can be explained by the mode of occurrence, but the geologic processes responsible for these variations are poorly understood. Based on available (and in most cases, limited) data, it appears that the removal of most of the common trace elements can be reasonably correlated with the removal of ash and sulfur from coal using standard washability tests. For the chalcophile elements, the removal of sulfur is a better estimator of trace element removal than is the removal of ash. Removal of chalcophile elements from Allegheny formation coals is generally higher than from other U.S. coals. Interior Province coals exhibit significant variation in cleanability. Using a number of statistical techniques on existing washability data, White et al<sup>5</sup> determined partitioning coefficients describing the relationship between trace element reduction and both sulfur and ash reduction for six major coal-producing regions of the U.S.
- Before additional data compilations on coal characteristics are made, the procedures for evaluating samples must be standardized.
- The trace element washability of forty-four coals was examined and compared to sulfur washability data for 750 coal samples. The authors concluded that specific attention should be given to major coal seams that are currently being washed or which are likely to be washed. Washability and statistical analysis studies similar to those described should be done, including analysis of minerals in the coals.
- Certain trace elements (e.g., V and Fe) have the potential for the catalytic conversion of  $SO_2$  to  $SO_3$ . Because of the increased efficiency by which  $SO_3$  is absorbed onto the surface of fly ash particles, this catalytic effect may be important but has not been extensively investigated.

Conzemius et al.<sup>14</sup> described the partitioning of 75 trace elements, sulfur, and ash in Illinois No. 6 and Upper Freeport coals processed in two dense-medium cyclone plants at sp. gr. of 1.4 and 1.6. Approximately two-thirds or more of Be, B, Cr, Mn, Co, Ni, As, Se, Cd, Sb, Hg, and Pb were removed. Chlorine and radionuclide concentrations were cut approximately by one-half and Mo by one-third.

The ISGS<sup>15</sup> flotation studies on Illinois No. 6 coal have shown average reductions of selected trace elements of 58% and 77% for froth flotation and aggregate flotation, respectively.

Norton et al.<sup>16</sup> described trace element reduction for a Texas lignite. Coal passing a 25- x 9.5-mm (1-in. x 3/8-in.) screen was cleaned by dense-medium cyclone and 9.5- x 0.15-mm (3/8-in. x 100 mesh) material cleaned on a concentrating table. Mercury, Ni, and Pb (3, 29, and 27 ppm in the feed coal, respectively) were reduced to below detectable levels. Selenium concentration was reduced by one-half.

Bechtel National<sup>17</sup> performed a study on microbubble flotation for DOE and reported the trace element analyses for ROM, conventionally cleaned, and deeply cleaned Pittsburgh No. 8, Illinois No. 6, and Upper Freeport coals. The sources for the concentration data reported are not known, and no discussion of the data in the tables was available. The data presented indicate, that, except for arsenic reduced at every stage of processing, the trace element concentrations in the deeply cleaned coal were significantly lower than in the ROM coal, but higher than the conventionally cleaned coal used as the feed to the flotation unit.

A recent report prepared by Coal Technology Corporation<sup>18</sup> for DOE describes the washability of coal for development of advanced cyclone processes. Four coals, Meigs No. 9, Illinois No. 6, Upper Freeport, and Pittsburgh No. 8, were ground to below 0.15 mm (minus 100 mesh) and deep cleaned using gravimetric techniques at a sp. gr. of 1.5. Deep cleaning of a plant-washed sample of Meigs No. 9 coal resulted in a change in ash content from 12.71% to 6.41%; a major (more than 50%) reduction of As, Mn, and V concentrations; a minor reduction (less than 50%) in Co, Se, and Zn concentrations; essentially no change in the Cd and Hg concentrations and an increase in concentration of Sb, Be, Cr, Cu, Pb and Ni. The ash content of the Illinois No. 6 coal was reduced from 11.05% to 4.7% and resulted in major reductions of As, Cd, Mn, Zn, and Hg concentrations; minor reductions in Co, Pb, Se, Ni, and V concentrations; and an increase in Sb, Be and Cu concentrations. Deep cleaning the Upper Freeport coal reduced the ash content from 23.49% to 4.49%; significantly reduced the Cd, Cr, Co, Pb, Mn, Hg, Ni and Zn concentrations; and mildly reduced Be and V concentrations; and increased the Sb, As and Se concentrations. The ash content of Pittsburgh No. 8 was reduced from 10.31% to 4.36% and provided major reductions in As, Mn and Hg; provided minor reductions in Cd, Cr, Co, Pb, Ni, Se and Zn; and increased Sb, Be, Cu, and V concentrations.

In examining the mode of occurrence and concentration of trace elements in U.S. and U.K. coals, Raask<sup>19</sup> concluded that trace elements in bituminous coals are present chiefly in the mineral matter fraction and, in particular, a large number of chalcophilic elements are present. He also concluded that high-sulfur coals in the U.S. are relatively rich in Cd and Zn, the chalcophilic elements are preferentially removed upon coal cleaning, and between 40% to 50% of Be, Cd, Cu, Pb, Hg, and Zn are removed by reducing the ash content of cleaned coals to below 15%.

Norton et al.<sup>20</sup> examined the trace elements in chemically cleaned coals and concluded that hot aqueous carbonate, molten NaOH/KOH, and acid treatments can

effectively remove trace elements from coals. However, they cautioned that corrosion of the reaction vessels may elevate certain trace elements in the treated coals.

A project completed by the EPA's Industrial Environmental Research Laboratory and summarized by Harvey et al.<sup>21</sup> investigated the distribution of trace elements in the Illinois No. 6 and Illinois No. 5 coals of the Illinois Basin. It was found that elements of environmental concern were present in the following concentrations: Pb (28 ppm), Cr and Ni (18 ppm), Cu (12.5 ppm), As (11 ppm), Mo (9.2 ppm), and Se (2.4 ppm). The other trace elements found in these specific coals average less than 2.4 ppm. From washability tests completed on the same coals, As, Cd, Mo and Pb were found to be trace elements associated with the mineral matter and were typically reduced by 50% or more. Some trace elements (Be, Ni and Sb) appear to be associated with the organic portion of the coal. Reductions in concentration of these elements were more difficult to achieve, their concentrations being reduced by less than 10%. Reductions in concentration of 15% to 30% were noted for several trace elements (Co, Cr, F, Hg, Se and Th) and those trace elements are assumed to be associated with both the mineral matter and the organic portion of the coal.

Researchers at Conso<sup>22,23</sup> have assembled an extensive database characterizing trace element concentrations of ROM and coal preparation plant products. The database contains over 850 composite samples and 3,400 individual trace element analyses for 225 commercial coals. The Conso researchers concluded that:

- Individual trace elements are weakly to moderately correlated to ash content, but no correlation was noted for sulfur.
- Coal cleaning to remove ash is effective in removing a portion of many trace elements. The degree of trace element removal is often similar to the overall ash rejection.

#### SUMMARY AND CONCLUSIONS

The literature concerning the trace element concentration of U.S. coals, and coal preparation as it relates to trace element removal, is extensive. The subject has been of interest for at least 40 years and is of vital interest today. A computer search of papers published in the last decade on topics related to the subject readily revealed 200 citations on trace element concentrations in coals and their removal by physical methods. Nearly 100 additional references were found that address chemical and biological methods for removing trace elements from coal. Approximately 100 references were found that deal with the issue of trace element analyses of coal. A considerable amount of the material is contained in EPA reports and the EPRI PISCES Database.

The U.S. coal reserves are reasonably well characterized in terms of their trace element concentrations. However, there seems to be a great deal of inconsistency with regard to trace element washability of coal. As an example, it was noted in the discussion section that some authors report Hg as associated with the organic matrix (difficult to remove) while others report Hg as associated with the mineral matter (easy to remove). Inconsistencies like this suggest that each coal seam must be evaluated individually with respect to trace element washability.

Another example of an apparent inconsistency is the decrease in Cr concentration when Upper Freeport coal was cleaned, while Cr concentrations increased when Rosebud/McKay seam coal was subjected to cleaning. While it is possible that more carbon could be rejected than finely disseminated Cr, in this case the magnitude of Cr concentration increase suggests analytical errors. In reviewing the trace element literature, it is difficult to compare different research findings and determine where the errors may lie. Much of the trace element literature fails to discuss attempts at mass balance closure. Historically, a number of analytical techniques have been applied to trace element analysis of coal and older research efforts may have used analytical techniques which have subsequently been found to be lacking in accuracy. Even when newer methods were used, sampling procedures and sample preparation methods are often not discussed. There exist today analytical techniques which are capable of determining quite accurately trace element concentrations of homogeneous samples. It appears that coal sampling, good sample preparation techniques, and additional analytical standards appear to be the major obstacles to overcome in achieving good trace element analyses of coal.

There is a reasonable correlation between trace element removal during coal cleaning and ash rejection. This is apparently due to the "organic affinity" of certain trace elements. Some trace elements are so finely disseminated throughout the coal matrix that they are not removed by coal preparation methods in common practice. A conclusion based on a review of the literature is that all trace elements can be readily reduced by 40 to 50% by physical coal cleaning and any further characterization that may be deemed desirable should rely on statistical analysis of existing concentration and washability data. Further reductions could be achievable by advanced physical coal preparation methods which separate the mineral matter that has been more effectively liberated by grinding coal to finer particle sizes. To comply with potential regulation of HAPs from coal-fired power plants, it may be desirable to develop methods of removing specific trace elements, such as mercury or arsenic, which would suggest the need for chemical or biochemical coal cleaning methods.

#### ACKNOWLEDGMENTS

We gratefully acknowledge the financial assistance provided by the Oak Ridge Associated Universities Research Associate Program in which Victoria McLean participated.

#### DISCLAIMER

References in this report to any specific commercial process, product, or service is to facilitate understanding and does not necessarily imply its endorsement or favoring by the United States Department of Energy.

## REFERENCES

1. Robert B. Finkelman, "Modes of Occurrence of Trace Elements in Coal," Ph.D. Dissertation, University of Maryland, 1980.
2. H.J. Gluskoter, "Mineral Matter and Trace Elements in Coal," in Trace Elements in Fuel, S.P. Babu, ed., ACS Advances in Chemistry Series 141, ACS, Washington D.C., 1975.
3. R.R. Ruch, H.J. Gluskoter, and N.F. Shimp, "Occurrence and Distribution of Potentially Volatile Trace Elements in Coal," Environmental Geology Notes No. 74, ISGS, 1974.
4. G.C. Nicholls, "The Geochemistry of Coal-Bearing Strata," in D. Muchison and T.S. Westoll, eds., Coal and Coal-Bearing Strata: American Edition, American Elsevier, New York, 1968, pp. 269-307.
5. J.K. Kuhn, F.L. Fiene, R.A. Cahill, H.J. Gluskoter, and N.F. Shimp, "Abundance of Trace and Minor Elements in Organic and Mineral Fractions of Coal," Environmental Geology Notes, No. 88, ISGS, 1980.
6. D.J. Akers, "Precombustion Control of Trace Elements," Presented at the Sixteenth Annual Conference on Fuel Science, Palo Alto, June 18-19, 1990.
7. D.J. Akers, "Coal Cleaning: A Trace Element Control Option," Preprint for the EPRI Conference on Managing Hazardous Air Pollutants: State of the Art, Washington, D.C., November 4-6, 1991.
8. D.M. White, L.O. Edwards, A.G. Eklund, D.A. Eklund, D.A. DuBose, F.D. Skinner, and D.L. Richmann, Radian Corp., "Correlation of Coal Properties with Environmental Control Technology Needs for Sulfur and Trace Elements," U.S. EPA Final Report EPA 600/7-84-066, June 1984.
9. J.A. Cavallaro, A.W. Duerbrouck, G. Gibbon, E.A. Hattman, H. Schultz, and J.C. Dickerman, "A Washability and Analytical Evaluation of Potential Pollution from Trace Elements in Coal," EPA-600/7-78-038, March 1978.
10. J.F. Boyer, J.P. Constantino, C.T. Ford, V.E. Gleason, and K.A. Rosnick, "Evaluation of the Effect of Coal Cleaning on Fugitive Elements, Phase II, Part III, State-of-the-Art: Fate of Trace Elements In Coal During Mining, Preparation, and Utilization," U.S. Department of Energy Report No. De-AC22-77EV04427, 1981, 263 pp.
11. J.M. Buroff, J. Straus, A. Jung, and L. McGilvray, Environmental Assessment: Source Test and Evaluation Report: Coal Preparation Plant No. 1, VERSAR, Inc., Springfield, Va., U.S. Environmental Protection Agency Report No. EPA-600/7-81-071a, 1981, 287 pp.
12. J.M. Buroff, J. Straus, A. Jung, and L. McGilvray, Environmental Assessment: Source Test and Evaluation Report- Coal Preparation Plant No. 2, VERSAR, Inc., Springfield, Va., U.S. Environmental Protection Agency Report No. EPA-600/7-81-071b, 1981, 290 pp.

13. F.A. Miller, T.L. Bell, R.C. Patyrak, and J.M. Wyatt, Environmental Studies on a Level C Coal Cleaning Plant, Tennessee Valley Authority, Chattanooga, Tenn., U.S. Environmental Protection Agency Report No. TVA/OP/EDT-81/46, 1981, 137 pp.
14. R.J. Conzemius, C.D. Chriswell and G.A. Junk, Fuel Processing Technology, 1988, 19, pp. 95-106.
15. R.B. Read, R.R. Ruch, H.P. Ehrlinger, P.J. DeMaris, D.M. Rapp, L.R. Camp, and J.A. Fitzpatrick, "ISGS Aggregate Flotation Fine-Coal Cleaning Process," Technical Report for January 1, 1983 - August 31, 1986, CRSC.
16. G.A. Norton, W.H. Buttermore, R. Markuszewski, and D.J. Akers, "The Removal and Control of Trace Elements in Coal and Coal Wastes," Proceedings of the EPRI Seminar on Reducing Power Plant Emissions by Controlling Coal Quality, Bethesda, Md., October 27-28, 1987.
17. Advanced Physical Fine Coal Cleaning: Microbubble Flotation, DOE Final Report DE-AC22-85PC81205, Bechtel National, Inc., September 1988.
18. Coal Technology Corporation, Phase I Report, DOE Contract DE-AC222-90PC90177, June 1992.
19. E. Raask, "The Mode of Occurrence and Concentration of Trace Elements in Coal," Prog. Energy Combust. Sci., 1985, 11, pp. 97-118.
20. G.A. Norton, R. Markuszewski, and H.G. Araghi, "Chemical Cleaning of Coal: Effect on the Removal of Trace Elements," Am. Chem. Soc. Symposium Series 319, Fossil Fuels Utilization: Environmental Concerns, R. Markuszewski, and B.D. Blaustein, eds., ACS, Washington, 1986.
21. R.D. Harvey, R.A. Cahill, C.L. Chou, and J.I. Steele, Mineral Matter and Trace Elements in the Herrin and Springfield Coals, Illinois Basin Coal Field, EPA Report No. EPA-600/S7-84-036, 1984.
22. P.R. Tumati and S.M. DeVito, Trace Element Emissions from Coal Combustion - A Comparison of Baghouse and ESP Collection Efficiency, Proceedings of the EPRI Conference on the Effect of Coal Quality on Power Plants, August 25-27, 1992, San Diego, Ca.
23. E.L. Obermiller, V.B. Conrad, and J. Lengyel, "Trace Element Contents of Commercial Coals," EPRI Conference on Managing Hazardous Air Pollutants: State-of-the-Art, Washington, D.C. November 1991.

## THE GAS-PHASE DERIVATIZATION OF COAL

A.W. Wells, R.F. Frank, and K. Waldner

U.S. Department of Energy  
Pittsburgh Energy Technology Center  
Pittsburgh, Pennsylvania 15236

### Introduction

Most of the spectroscopies employed to study reactive functionalities on the surface of coal suffer because a high percentage of adsorption from bulk or subsurface functional groups are included. For example, photoacoustic infrared Fourier transform (PAIFT) spectroscopy, while one of the most surface selective of the infrared spectroscopies, still has a thermal diffusion length of approximately 20 micrometers for a coal particle of 150 micrometers radius under typical experimental conditions.<sup>1</sup> Spectroscopic techniques are also limited in their ability to provide accurate quantification due to difficulties in estimating adsorption coefficients and the need to employ such techniques as curve deconvolution.

An alternative approach is to employ a probe molecule that will interact with reactive functional groups on the surface of coal and to quantify the degree of interaction. Although this approach is in its infancy, some success has been demonstrated for flow microcalorimetry using acidic and basic probes.<sup>2,3,4</sup> A logical extension to this approach would be to employ probe molecules that react with specific surface functionalities to form products that can be accurately quantified without the use of surface spectroscopies. Information on total surface functionality content should also provide complementary information to surface functionality densities obtained from spectroscopies such as X-ray photoelectron spectroscopy.<sup>5,6</sup> It was the purpose of this investigation to test the feasibility of this approach using the gas-solid phase silylation of hydroxyl groups on coal with hexamethyldisilazane (HMDS) in nitrogen.

The kinetics of the chemisorption of HMDS vapors into 100-mesh Illinois No. 6 coal particles were followed by periodic removal from the reactor of portions of the coal. The coal was subsequently analyzed for its trimethylsilyl ether content. The kinetics were evaluated using a mathematical model applied by Berens and Hopfenberg to describe the sorption of vinyl chloride monomer, acetone, and methanol vapors into powder samples of polyvinyl chloride.<sup>7</sup> For experiments in which "glassy" polymers were continuously exposed to relatively large concentrations of sorbate, a striking two-phase sorption process was observed by News<sup>8</sup> and by Long and Richman.<sup>9</sup> The two stages were separated in time and consisted of an initial, rapid Fickian diffusion process that was followed by a much slower relaxation process. Berens and Hopfenberg interpreted the diffusion process as involving migration of penetrant molecules into preexisting void space, and the relaxation process as related to swelling, resulting from large-scale segmental motions of the polymer.<sup>7</sup>

These preliminary investigations attempted to exploit the two-stage sorption kinetics to define reaction parameters that would result in a high level of surface selectivity while minimizing relaxation and swelling of the bulk of the coal's macromolecular structure. The effects of particle size were evaluated by Enscoe et al.<sup>10</sup> who demonstrated that under proper conditions of temperature and penetrant activity, n-hexane sorption into about 200 micrometer diameter polystyrene spheres was dominated by a relaxation mechanism whereas sorption into submicron polystyrene spheres was predominantly by way of Fickian diffusion. As suggested by Vrentas et al.,<sup>11</sup> the relaxation process is independent of the particle size of the polymer but the Fickian diffusion time frame varies with the square of the particle size. Two-stage behavior, therefore, can be approached by increasing the diffusion rate through increased reagent activity and by reducing the diffusive path length by decreasing the particle size. Ideally, the Fickian diffusion coefficient should be at least an order of magnitude greater than the first-order relaxation rate constant for the predominant relaxation mode.

A corollary consideration in designing experiments to elicit two-stage behavior would be to reduce the relaxation rate by selecting penetrants with a low solubility in the polymer. Ritgar and Peppas<sup>12</sup> modeled the sorption of pyridine vapors by thin films of bituminous coals using the Berens and Hopfenberg equation and found that the process could be modeled using a single first-order relaxation term. The relaxation rate constant remained nearly the same over a range of coal carbon content and sample thickness, indicating the process to be mechanistically characteristic of the penetrant. The relatively rapid relaxation of coal by pyridine vapor would presumably make it difficult to construct experimental conditions where two-phase behavior would be observed. Two-phase behavior was observed by Hsieh and Duda for the sorption of toluene vapor by pyridine extracted bituminous coal powders.<sup>13</sup> The removal of the "mobile phase" in coal by pyridine extraction decreased penetrant uptake. Hsieh and Duda also observed an initial rapid adsorption onto the surface of the coal particles.<sup>13</sup> These observations of two-stage behavior suggest an approach to obtaining surface selectivity. HMDS was selected as a suitable vapor phase chemisorption probe, in part, because of a low solubility in bituminous coals.

The Berens and Hopfenberg model is a linear combination of a Fickian diffusion component and of one or more first-order relaxation components.

$$M_t = M_\infty \left\{ 1 - \frac{6}{\pi^2} \sum_{n=1}^{\infty} \frac{1}{n^2} \exp(-n^2 k_r t) \right\} + \sum_i M_{s,i} \left[ 1 - \exp(-k_{s,i} t) \right]$$

Where:  $M_t$  is the total sorption due to Fickian diffusion,  
 $M_{x,i}$  is the total sorption due to the  $i$ th relaxation mode,  
 $M_t$  is the total sorption at time  $t$ ,  
 $k$ , is the Fickian rate constant, and  
 $k_{x,i}$  is the first-order rate constant for the  $i$ th relaxation mode.

The relaxation components in this model are driven by the release of stresses within the polymeric macromolecule through penetrant-induced swelling. The relaxation processes are, unlike Fickian diffusion, unrelated to particle size.

### Experimental

The gas-solid phase silylation reactions were carried out in a 250-mL, three-necked, round-bottom, nitrogen-flushed flask. For kinetic studies, coal samples were periodically removed from the reactor through an "entrance port" fitting. The fitting directly above the coal sample was used for reagent addition. This fitting supported a Mininert valve above the reactor and a 1 mL, "evaporation" beaker which could be heated by being lowered against the bottom interior of the reaction flask. A glass capillary tube connected the Mininert valve to the evaporation beaker. The capillary tube could be raised or lowered through an O-ring fitting. The bottom of the flask was placed into a heating mantle and the temperature was monitored using a thermocouple. All fittings were Teflon with Viton O-ring seals to avoid the use of sealants that might contaminate the surface of the coal particles.

The coal sample (0.8 g of Argonne premium Illinois No. 6 coal) was spread out on the bottom of the flask and the flask flushed with nitrogen. The reaction was initiated by addition of 500 microliters of HMDS, which was rapidly volatilized. Saturation with HMDS was maintained throughout the experiment. Approximately 70-mg coal samples were removed at various time intervals for analysis. Their trimethylsilyl ether content was determined after 3 hours of vacuum drying to remove physically adhering reagent. The trimethylsilyl ether content was determined using a fluoride cleavage-G.C. headspace procedure. Gas-solid-phase silylations were carried out at coal temperatures of 123, 163, 178, and 196 degrees C. Ten mL of a solution of 65% THF, 25% concentrated HF, and 10% water (by volume) were used to cleave the trimethylsilyl ethers in a 30-mL Teflon test tube fitted with a Mininert cap, valve, and septum assembly. The reaction was carried out at room temperature. In the reaction, hydrofluoric acid cleaves the trimethylsilyl ethers, converting them into trimethylfluorosilane, which is largely soluble in the reaction solution. The coal-hydroxyl groups are regenerated in the process. One-half milliliter of headspace was sampled and analyzed for trimethylfluorosilane on a Poropak P column maintained isothermally at 185°C. The trimethylfluorosilane peak area was calibrated against a standard curve generated by fluoride cleavage of various amounts of the TMS ether of 1-naphthol (Figure 1). As shown in Figure 1, deviations from Henry's law (linearity) begin at 20 microliters of standard. Sample weights were adjusted to utilize the linear range of the standard curve. The TMS ether of 1-naphthol was obtained by refluxing 1-naphthol in a 1:1:2.5 mixture of HMDS:TMCS:Pyridine, and distilling the crude product at 90 -91°C under 1 mm of nitrogen.

## Results and Discussion

The Berens and Hopfenberg model was modified slightly by the addition of a separate term,  $M_1$ , to describe a rapid, initial chemisorption occurring within the first few minutes and presumably resulting from the unimpeded contact of reagent vapors with the surface of larger pores. The computer-assisted curve fitting process for obtaining equation parameters was essentially the same as that described by Berens and Hopfenberg.<sup>7</sup> A computer program was used to minimize the summed-squares deviations between measured values and the corresponding values generated from the equation by adjusting the constants.

A comparison between the equation and measurements obtained at 178°C is shown in Figure 2 together with curves representing contributions from individual terms of the equation. Two-stage behavior was clearly evident for curves generated over the reaction temperature range of 123° to 196°C. Appropriate, early termination of the reaction would result in the initial and diffusion terms constituting an average of 89% of the total chemisorption. The time required to reach diffusion equilibrium was less at 196°C, 3 hours to reach 93% of maximum, than at lower temperatures where 6 hours were required to reach 93% of maximum. The total contributions at infinity for the two relaxation terms,  $M_{r_1}$  and  $M_{r_2}$ , for the Fickian diffusion term,  $M_f$ , and for the summation of terms,  $M_{total}$ , are given as a function of reaction temperature in Figure 3. The Fickian diffusion term plateaued at 178°C as did the principle relaxation mode,  $r_2$ . The minor relaxation mode,  $r_1$ , does not plateau over the temperature range.

While specific polymeric motions cannot be identified with  $r_1$  or  $r_2$  relaxations, a case can be made for a linkage between the diffusion term and  $r_2$  relaxation (Figure 2.) Pore deformation and a corresponding expansion of the nascent void space might result from chemical modification of the pore surface, the disruption of intrapore hydrogen bonding, or from steric interactions as the pores are filled. Gethner<sup>8</sup> utilized light scattering to probe changes in the larger pores of an Illinois No. 6 coal when immersed in each of 7 different liquids and concluded that such pores were not rigid but easily deformed. Void-structure alterations were clearly evident and resulted in an increase of the total void-volume contributing to the light scattering. Information on sorbate-induced polymeric rearrangements or conformational transformations associated with the relaxation of coal cannot be obtained directly from phenomenological measurements of sorbate uptake. Coal relaxation linked to solvent or vapor sorption is, however, invariably correlated to coal swelling. In the chemisorption of HMDS into Illinois No. 6 coal, a single relaxation term accounts for the majority of reagent uptake and is assumed to reflect the gradual 'opening' of the macromolecular coal networks. For gas-phase, surface-limited applications, however, the silylation is terminated before appreciable polymeric relaxation and corresponding penetration of the coal matrix has occurred. This should presumably reduce opportunities for matrix entrapment of reagent.

The kinetic studies were used to define 'standard' conditions for surface-limited derivatizations of 178°C and a 6 hour reaction time. Ten replicate determinations under these conditions gave a total surface hydroxyl content of 0.76 hydroxyl groups / 100 carbon atoms with a standard deviation of 0.02 hydroxyl groups / 100 carbon atoms. This compares with a total hydroxyl content for Illinois No. 6 premium coal of 4.7 hydroxyl groups / 100 carbon atoms determined from liquid phase silylation reactions. This technique could be very

useful in following changes in coal surface chemistry when the surface is subjected to modification.

While the concept of coal surface is defined through the choice of experimental conditions and probe, an approach based upon limiting relaxation of the coal structure is reasonable. In contrast to spectroscopies, molecular probes should access the surface of pore systems where much of the liquid-solid and gas-solid interfacial chemistry of coal processing technologies occur. The gas-solid phase derivatization approach to coal surface analysis should result in an improved ability to quantify surface functionality content and to obtain a greater level of chemical selectivity through functionality specific reactions.

#### References

1. T. Zerlita *Applied Spectroscopy* 1986, 40, 214.
2. F.M. Fowkes, K.L. Jones, L. Guozhen, and T.B. Lloyd *Prepr. Pap. - Am. Chem. Soc., Div. Fuel Chem.* 1987, 32(1), 216.
3. D.W. Fuerstenau, G.C. Yang, and S. Chander *Prepr. Pap. - Am. Soc., Div. Fuel Chem.* 1987, 32(1), 209.
4. D. Brooks, A. Finch, P.J. Gardner, and R. Harington *Fuel* 1986, 65, 1750.
5. D.L. Perry and A. Grint *Fuel* 1983, 62, 1024.
6. D.T. Clark and R. Wilson *Fuel* 1983, 62, 1034.
7. A.R. Berens and H.B. Hopfenberg *Polymer*, 1978, 19, 489.
8. A.C. Newns *Trans. Faraday Soc.* 1956, 52, 1533. (Ref. 9(12))
9. F.A. Long and D. Richman *J. Am. Chem. Soc.* 1960, 82, 513. (Ref. 7(14))  
10.D.J. Enscoe, H.B. Hopfenberg, and V.T. Stannett *Polymer* 1977, 18, 793. (Ref. 7(8))
11. J.S. Vrentas, C.M. Jarzebski, and J.L. Duda *AIChE J.* 1975, 21, 894. (Ref. 7(7))
12. P.L. Ritger and N.A. Peppas *Fuel* 1987, 66, 1379.
13. S.T. Hsieh and J.L. Duda *Fuel* 1987, 66, 170.
14. J.S. Gethner *Prepr. Pap. - Am. Chem. Soc., Div. Fuel Chem.* 1987, 32(1), 239.
15. H. Marsh *Carbon* 1987, 25(1), 49.

FIGURE 1

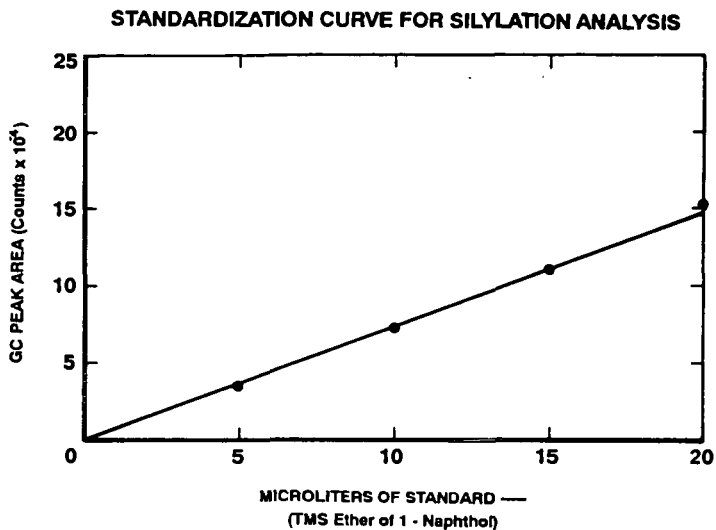


FIGURE 2

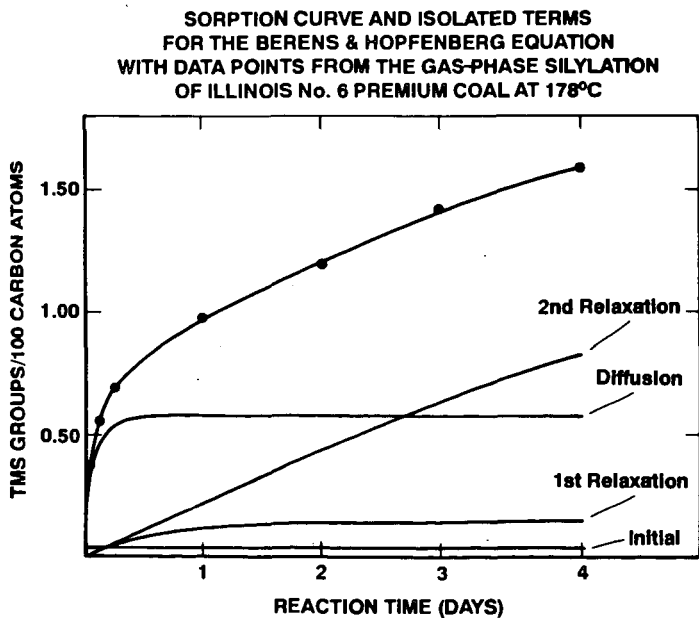
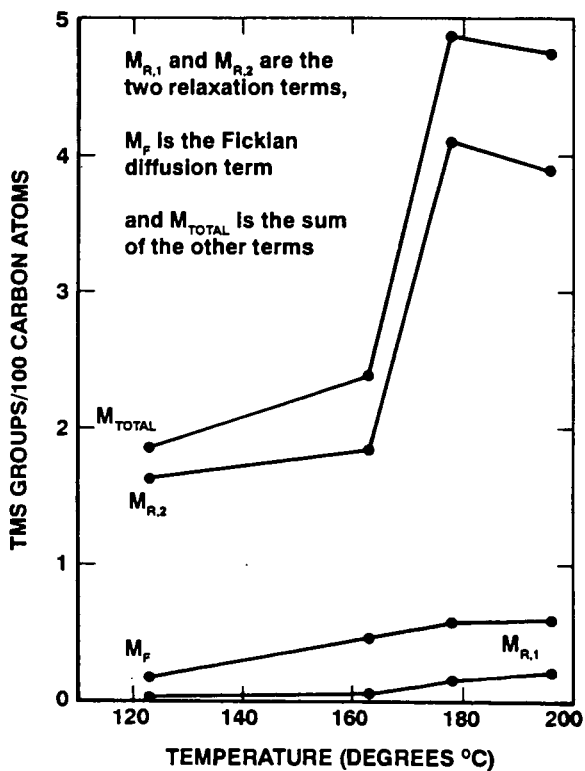


FIGURE 3

TEMPERATURE PROFILE OF TERMS  
FROM THE BERENS & HOPFENBERG EQUATION  
AT INFINITY FOR THE GAS-PHASE SILYLATION  
OF ILLINOIS No. 6 PREMIUM COAL



**LASER DESORPTION ION TRAP MASS SPECTROMETRY  
OF THE MACROMOLECULAR COMPONENT OF COAL**

John A. Burroughs, Brian M. Cadre, and Luke Hanley  
University of Illinois at Chicago  
Department of Chemistry, m/c 111  
Chicago, IL 60607-7061

Keywords: coal, laser desorption, mass spectrometry

**INTRODUCTION**

The structure of coal has been proposed to be a macromolecular network in which smaller molecules are confined [1]. It follows that a portion of the organic sulfur and other heteroatoms present in coal are covalently bound to this network. This paper describes efforts to measure high molecular weight mass spectra representative of this macromolecular network and ultimately, determine the chemical structure of organic sulfur contained therein.

Indirect evidence for the existence of a two component coal structure has been provided by solvent swelling, nuclear magnetic resonance, and various other measurements [1,2]. Size exclusion chromatography (SEC) has been used to determine that the number average molecular weight ( $M_n$ ) of polymers extracted from coal with pyridine and other solvents ranges from 1000 to above 10,000 amu [3-5]. However, SEC experiments on coal polymers are limited by the difficulty in calibrating the retention time of what are essentially unknown chemical compounds. Thus,  $M_n$  values obtained by SEC differ by ~20% from values obtained with vapor phase osmometry [4]. Furthermore, only the soluble portion of the coal sample is analyzed by these methods and SEC has not provided a detailed chemical description of these coal polymers. Mass spectrometry is a logical method for measuring  $M_n$  of coal polymers. Nevertheless, experiments which have utilized ion bombardment [6], pyrolysis [7,8], electric field gradients [9], or pulsed lasers [10-12] for desorption and ionization of coal polymers have only formed low molecular weight ions via thermal degradation and chemical transformation rather than intact, high molecular weight ions.

The experiments described here attempt to exploit recent advances in high molecular weight mass spectrometry to generate representative ions of coal polymers. Infrared and ultraviolet laser desorption methods are applied to pyridine solvent extracts of high sulfur coals, where any ions formed are detected by an ion trap mass spectrometer. Ion trap mass spectrometers can measure the mass to charge ( $m/z$ ) ratio of ions over a wide mass range, can perform collision induced dissociation experiments for structural analysis of ions, and can be operated in a high resolution mode [13].

**EXPERIMENTAL DETAILS**

A schematic diagram of the experimental apparatus is shown in Figure 1. To obtain a mass spectrum up to ~650  $m/z$ , ions formed by laser desorption from a coal sample are injected through holes in the end cap of the ion trap into its center [13]. The ions are contained

inside the trap by an initial radio frequency voltage applied to the ring electrode while the end cap electrodes are held at ground potential. After the ions have undergone many collisions with a helium buffer gas, the radio frequency amplitude is ramped linearly, causing ions of increasing  $m/z$  values to be ejected from the trap through holes in the end caps. The ions which exit the ion trap are detected by a conversion dynode/channeltron ion detector.

The mass range of the ion trap is extended via the application of an auxiliary frequency across the end cap electrodes concurrent with the rf amplitude ramp. Ions up to 10,000  $m/z$  have been detected with this apparatus to date and future experiments should extend this towards the theoretical limit of ~40,000  $m/z$ . Trapping of individual mass ions has also been accomplished, as a predecessor to collision induced dissociation experiments.

The ion trap mass spectrometer was constructed by mounting the electrodes from an commercially available ion trap detector (Finnigan MAT ITD 700) inside a diffusion pumped vacuum chamber with a base pressure of  $\sim 2 \times 10^{-8}$  Torr. A 6 kV conversion dynode is located adjacent to the channeltron near the exit end cap electrode to allow for high mass detection. Roughly  $10^{-3}$  Torr of helium buffer gas is introduced into the trap via a leak valve. Experimental timing sequences and data acquisition are controlled with an IBM compatible 80386 microcomputer interfaced to the commercial ion trap electronics via plug-in multifunction data acquisition boards (National Instruments models AT-MIO-16F-5 and PC-TIO-10). The end cap electrodes are connected to a function generator (Stanford Research Systems DS345) through a homemade buffer amplifier.

To perform infrared laser desorption experiments, pulses of 1064 nm radiation of ~7 ns duration from a Nd:YAG laser (Continuum Surelite) are focussed onto the sample probe resulting in power densities of  $10^9$ - $10^{10}$  W/cm<sup>2</sup>. The power density is calculated by visual estimation of the laser spot diameter on the sample probe tip and by measuring the unfocussed laser power with a pyroelectric joulemeter (Molelectron). For ultraviolet laser desorption, fourth harmonic generation of the Nd:YAG fundamental wavelength gives 266 nm pulses in the  $10^9$ - $10^{10}$  W/cm<sup>2</sup> power density range.

Solvent extracts from coal are prepared by dissolving powdered coal in pyridine and allowing the samples to equilibrate for three days at room temperature, then filtering out the insoluble portion which remains. Experiments were performed using Pocahontas No. 3 and Illinois No. 6 coal from the Argonne Premium Coal Sample Program and Herrin No. 6 (IBC 101) coal from the Illinois Basin Coal Sample Program.

## RESULTS AND DISCUSSION

Laser desorption MS using infrared radiation has been used for the analysis of various nonvolatile organic molecules, biomolecules, and synthetic polymers [14]. The technique usually involves irradiating the sample at power densities from  $10^7$ - $10^{10}$  W/cm<sup>2</sup>. In many cases the sample is doped with an inorganic salt to assist the formation of cation-attached molecular ions. Here, infrared laser

desorption was used to generate spectra from a series of poly(ethyleneglycol) standards of known molecular weight (American Polymer Standards) doped with KCl. Cation-attached molecular ions up to  $\sim 10,000$  m/z were successfully formed and detected using this method.

Laser desorption experiments utilizing infrared radiation to desorb and ionize either disburbed solid coal or solvent extracts of same have been unsuccessful in generating any meaningful information regarding the macromolecular structure of coal. The only observable peaks above  $\sim 300$  m/z in these spectra were due to the presence of carbon cluster ions, as verified by comparison with similar clusters formed in laser desorption of graphite samples. Attempts to dope the coal samples with KCl, NaCl, and CsCl to enhance the formation of cation attached ions have all failed to produce intact molecular ions. It is concluded that regardless of the sample preparation method, infrared laser desorption of coal and coal extracts is not a useful method for generating the desired high molecular weight ions, in agreement with previous experiments along these lines [10-12].

Ultraviolet matrix assisted laser desorption/ionization (UVMALDI) has recently emerged as a useful tool for forming intact molecular ions up to  $300,000$  m/z of various biopolymers including proteins and carbohydrates as well as synthetic polymers [15-17]. The technique requires that the analyte molecule, usually exhibiting only moderate optical absorption at the desorption wavelength, be sparsely dispersed in a strongly absorbing matrix [15]. Much lower power densities (i.e.  $10^6$ - $10^7$  W/cm<sup>2</sup>) are used in a typical UVMALDI experiment than with infrared laser desorption [18], but the former method is capable of desorbing intact far larger and more labile species than the latter. Although time-of-flight mass spectrometers are most often employed in such experiments, ion traps have been used to detect ions formed by UVMALDI [19-21].

The matrix which was used for both test compounds and for coal extract samples is 2,5-dihydroxybenzoic acid (DHB). For the first test sample, gramicidin S was dissolved in a water/ethanol solution in a 1000:1 molar mixture of matrix/analyte. A second test sample of bovine insulin was similarly prepared in a 5000:5000:1 DHB/d-fructose/bovine insulin mixture. Intact molecular ion peaks from gramicidin S (1140 m/z) and bovine insulin (5733 m/z) have been formed and detected with UVMALDI and the spectra for the later is shown in Figure 2; The intact molecular ion and the ionized chain B portion of the molecule are present, but no other fragments are observed.

Unfortunately, attempts to generate intact macromolecular ions from the pyridine soluble portion of various coals using the UVMALDI technique have not yet been successful. Detection of sample molecules using UVMALDI requires that the analyte molecule be capable of forming a stable ion in the gas phase, presumably by accepting or donating a proton or other cation. The various proposed structures of coal all contain numerous ionizable groups such as S or N-containing heterocyclic rings, hydroxides, or sulfides [22]. Therefore, it should be possible to produce intact molecular ions from coal using UVMALDI.

It is postulated that the failure of UVMALDI to generate intact ions from coal polymers derives from improper sample preparation. Preparing a proper sample of a new compound for UVMALDI is at present

a trial and error process in which matrix type, matrix-to-analyte ratio, and concentration of cation donating dopants are all varied [15,23]. Furthermore, while some samples produce positive ions, others generate only negative ions. To date, only positive ions have been sought in these experiments. New sample preparations and negative ion formation are presently under exploration. Therefore, a final conclusion cannot yet be drawn regarding the applicability of laser desorption ion trap mass spectrometry to the study of polymers from coal.

#### ACKNOWLEDGEMENTS

This work was prepared with the support, in part, by grants made possible by the Illinois Department of Energy and Natural Resources through its Coal Development Board and Illinois Clean Coal Institute, and by the U.S. Department of Energy (Contract Number DE-FG22-91PC91334). However, any opinions, findings, conclusions, or recommendations expressed herein are those of the authors and do not necessarily reflect the views of IDENR, ICCI, or DOE.

#### REFERENCES

- 1) P.H. Given, A. Marzec, W.A. Barton, L.J. Lynch, and B.C. Gerstein, *Fuel* **65** (1986) 155.
- 2) F. Derbyshire, A. Marzec, H.-R. Schulten, M.A. Wilson, A. Davis, P. Tekely, J.-J. Delpuech, A. Jurkiewicz, C.E. Bronnimann, R.A. Wind, G.E. Maciel, R. Narayan, K. Bartle, and C. Snape, *Fuel* **68** (1989) 1091.
- 3) J.L. Wong in "Coal Science and Chemistry", A. Volborth, ed., Elsevier (Amsterdam, 1987) 461.
- 4) D.H. Buchanan, L.C. Warfel, S. Bailey, and D. Lucas, *Energy Fuels* **2** (1988) 32.
- 5) J.W. Larsen and Y.-C. Wei, *Energy Fuels* **2** (1988) 344.
- 6) J.M. Lytle, G.L. Tingey, and R.D. Macfarlane, *Anal. Chem.* **54** (1982) 1881.
- 7) R.E. Winans and P.H. Neill, in "Geochemistry of Sulfur in Fossil Fuels", W.L. Orr and C.M. White, eds., ACS (Washington, 1990) 249.
- 8) P.J.J. Tromp, J.A. Moulijn, and J.J. Boon in "New Trends in Coal Science", Y. Yurum, ed., Kluwer Academic (Dordrecht, 1988) 241.
- 9) J.A.G. Drake, D.W. Jones, D.E. Games, and J.L. Gower, *Fuel* **63** (1984) 634.
- 10) J.E. Hunt, K.R. Lykke, and R.E. Winans, *Fuel Chem. Div. Am. Chem. Soc.* **36** (1991) 1325.
- 11) T. Mauney, *Anal. Chim. Acta* **195** (1987) 337.
- 12) P.F. Greenwood, M.G. Strachan, H.J. El-Nakat, G.D. Willett, M.A. Wilson, and M.I. Attalla, *Fuel* **69** (1990) 257.
- 13) R.G. Cooks, G.L. Glish, S.A. McLuckey, and R.E. Kaiser, *Chem. Eng. News* **69:12** (1992) 26.
- 14) R.B. Cody, A. Bjarnason, and D.A. Weil in "Lasers and Mass Spectrometry", D.M. Lubman, ed., Oxford University (New York, 1990) 316.
- 15) F. Hillenkamp, M. Karas, R.C. Beavis, and B.T. Chait, *Anal. Chem.* **63** (1991) 1193A.

- 16) U. Bahr, A. Deppe, M. Karas, F. Hillenkamp, and U. Giessmann, *Anal. Chem.* **64** (1992) 2866.
- 17) P.O. Danis, D.E. Karr, F. Mayer, A. Holle, and C.H. Watson, *Org. Mass Spectrom.* **27** (1992) 843.
- 18) B.U.R. Sundqvist, *Int. J. Mass Spectrom. Ion Proces.* **118/119** (1992) 265.
- 19) M.E. Bier, J.C. Schwartz, I. Jardine, and G. Stafford; *Proc. 40th ASMS Conf. Mass Spectrom. and Allied Topics*, Washington, DC, 31 May - 5 June 1992, 117.
- 20) D.M. Chambers, D.E. Goeringer, S.A. McLuckey, and G.L. Glish; *Proc. 40th ASMS Conf. Mass Spectrom. and Allied Topics*, Washington, DC, 31 May - 5 June 1992, 1747.
- 21) V. Doroshenko, T. Cornish, and R.J. Cotter; *Proc. 40th ASMS Conf. Mass Spectrom. and Allied Topics*, Washington, DC, 31 May - 5 June 1992, 1753.
- 22) G.A. Carlson and B. Granoff, in "Coal Science II", H.H. Schobert, K.D. Bartle, and L.J. Lynch eds., ACS (Washington, 1991) 159.
- 23) T-W.D. Chan, A.W. Colburn, P.J. Derrick, D.J. Gardiner, and M. Bowden, *Org. Mass Spectrom.* **27** (1992) 188.

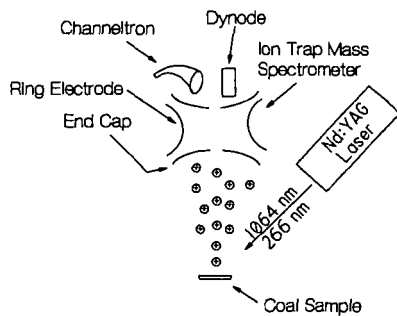


**Figure 1:** Schematic diagram of the laser desorption ion trap mass spectrometer.

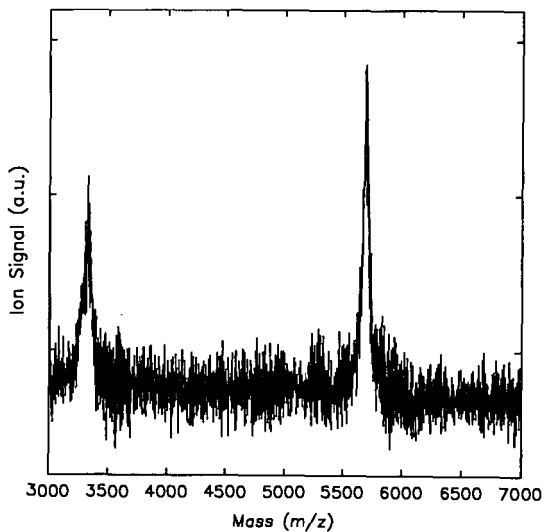


**Figure 2:** UVMALDI spectrum of a trial compound, bovine insulin, demonstrating the feasibility of the method for labile high molecular weight compounds such as coal polymers.

## MEASUREMENT OF THE ADSORPTION AND CRACKING OF MODEL COMPOUNDS OVER PROCESSED OIL SHALE PARTICLES

Darrell N. Taulbee,  
Center for Applied Energy Research,  
3572 Iron Works Pike,  
Lexington, KY 40511, (606) 257-0238

**Keywords:** Cracking reactions, adsorption-desorption, oil shale.

A parallel reactor system has been constructed to monitor adsorption, desorption, and/or cracking/coking of vapor phase model compounds over solid substrates at elevated temperatures. In this study, selected hydrocarbons ranging from benzene to n-decane were passed across pyrolyzed, gasified, or combusted oil shale particles at temperatures between 270 °C and 650 °C. A vapor phase hydrocarbon, Ar tracer gas, and N<sub>2</sub> carrier are combined and routed through a heated switching valve to a sand-packed tube reactor positioned within a tube furnace. A parallel line routes N<sub>2</sub> gas through a second tube reactor packed with substrate. After exiting the tube reactors, the two lines are combined and sampled by a heated capillary connected to the inlet of a quadrupole mass spectrometer (QMS). A typical run entails establishing a QMS baseline with the model compound passing through the sand-packed reactor, switching the valve so the model compound passes through the substrate bed, then returning to the sand-packed reactor to re-establish the QMS baseline.

**Introduction.** The utilization of fluidized bed retorting technology for the processing of the Eastern US oil shale deposits has been under investigation at the CAER since about 1982. Development has progressed from small independent grams/hours pyrolysis, combustion, and gasification reactors, through operation of an integrated, 3-stage, 5-lb/hr unit and currently, construction of an integrated 50-lb/hr pilot plant representing the most recent effort to provide proof of concept for KENTORT II. KENTORT II is designed to maximize oil and gas production and to fully utilize the carbon contained in Eastern US oil shales without resorting to exotic or high pressure atmospheres<sup>1,2</sup> and to do so in an environmentally acceptable manner.

In the KENTORT II reactor, pyrolysis heat is provided by recycling hot gasified or combusted particles to the pyrolysis zone. Thus, of particular interest are those reactions that can be attributed to the recycling of hot solids and which impact oil yield, i.e., cracking and coking reactions. Within limits, the detrimental effect of recycling hot solids to the retort can be minimized by varying the relative proportion of gasified versus combusted particles or by selecting the optimum recycle rate/particle temperature, i.e., fewer high temperature vs. more low temperature particles.

A previous study<sup>3-4</sup> focused on the kinetics of shale oil coking as a function of substrate type and temperature using gasified, combusted, and pyrolyzed shales. In a similar manner, the current study will focus on product adsorption and cracking. However, unlike the coking study which utilized freshly generated shale oil, the measurement of adsorption and cracking kinetics in the system described here dictated the use of model compounds.

**Experimental. Reactor System.** A simplified schematic of the reactor system is shown in Figure 1. High purity N<sub>2</sub> is introduced to a heated valve oven (275 °C) at 100 psig, split into parallel carrier lines and routed through a pair of metering valves. From the metering valves to the reactor, all carrier/transfer lines are constructed of 1/16" x 0.03" 304 ss.

One of the carrier lines, termed the bypass line, is routed through a switching valve, an 18" heat traced transfer line, a 48" preheater coil, and into one of the parallel tube reactors positioned in a 2"

x 15" Lindberg tube furnace. In the initial "bypass" mode, this line is routed through the substrate-packed reactor (substrate reactor).

High purity Ar is introduced at 100 psig and metered to the parallel HC carrier line just downstream from the N<sub>2</sub> metering valve. A Waters model 6000A LC pump is used to dispense the liquid hydrocarbon (HC) which first passes through a restriction coil to maintain pump back pressure (and thus constant flow), then into the valve oven where it passes through a downward spiraling volatilization/surge suppressor coil before connecting to the HC carrier line. The HC line parallels the bypass line to the reactor furnace where, in the initial valve position, it passes through the sand-packed bypass reactor.

After passing through the parallel reactors, both lines are combined and continuously sampled just inside the reactor furnace by a heated capillary connected to the inlet of a VG/Fisons Sensorlab 300D quadrupole mass spectrometer (QMS). The QMS may be operated in either a log histogram mode which monitors all mass intensities at 1-amu resolution from zero to a selected upper limit (usually just above the molecular ion of the model compound) or in a selected ion monitoring (SIM) mode which records up to 16 selected ion intensities at approximately 1 second intervals. The latter is the preferred operating mode due to a more rapid sampling rate but with the trade-off that not all ion intensities are monitored.

The tube reactors are constructed of 9" x 3/8" -o.d. (1/4" i.d.) 316 ss. One of the reactors, the bypass, is packed with 6-gm of sand while the second, the substrate reactor, is packed with 4-gm of one of the substrates listed in Table 1. Quartz wool is used to hold the solids in place. Substrates are centered in the reactor tubes with an approximate 2" void on each end. A type K thermocouple is placed into each reactor tube, 2.5" from the entrance to the bypass tube and 4" from the entry to the substrate tube. The substrate was removed following each run, crushed, and submitted for elemental analysis. The bypass sand was replaced after each 650 °C run (or when the model compound or study substrate was changed).

**Study Substrates.** The three substrates examined in this study (Table 1) originated from the CLE-003 master sample taken from Fleming County, Ky.<sup>1-3</sup> These materials represent the three types of solids present in the pyrolysis section of the KENTORT II reactor to which the vapor phase shale oil is exposed. All three substrates were prepared in a fluid-bed reactor using N<sub>2</sub>, steam, or air as the fluidizing media (Table 1). All three substrates were screened to 20 x 60 mesh. The Ottawa sand was screened to 20 x 30 mesh.

**Run Conditions and Procedure.** A nominal model compound flow of either 0.1 or 0.2-mL/min was used for all runs. A total gas flow of 150 mL/min (ambient temperature) was maintained through each reactor. This flow was comprised solely of N<sub>2</sub> in the bypass line. For the HC carrier line, Ar tracer gas flow was set to 50 mL/min; the volume of the gas phase model compound was calculated assuming ideal gas behavior; and the cumulative flow adjusted to 150 mL/min with high purity N<sub>2</sub>.

Run preparation entailed packing 4-gm of substrate to the substrate reactor and 6-gm of sand to the bypass reactor, setting the Lyndberg furnace controller to the target temperature with the reactors in place, and initiating carrier gas and model compound flow. QMS data collection was initiated following a minimum 2-minute equilibration at temperature. The substrate thermocouple reading was manually maintained within ±2 °C of the target temperature for the duration of the run. After a minimum of 100 data points were collected in the SIM mode (or at least 2 minutes in the log histogram mode), the valve was rotated so that the HC carrier passed through the substrate reactor (make-up line is simultaneously switched to the bypass reactor). Following the selected exposure time, the valve was returned to the initial position and the QMS baseline reestablished. Control runs were made by packing both the bypass and substrate reactor tubes with sand to ensure acceptable system operation.

**Data Management.** Following data collection, the QMS data files are imported to a spreadsheet where the model compound's molecular ion (and/or selected cracking product) intensity is ratioed to

the Ar intensity. These ratios are then exported to a curve-fitting software routine (Sigma Plot) where a linear equation was fitted to the data points collected in the bypass mode (before and after HC/substrate exposure). A function containing both linear and decaying exponential terms (eq. 1) was fitted to the molecular ion/Ar ratio obtained during substrate exposure:

$$\text{Eq. 1} \quad y = -a \cdot \exp(-bt) + c \cdot t + d$$

The difference in the integrated area between the linear and exponential equations over the substrate exposure interval represents either product loss due to cracking/coking reactions for the high temperature runs ( $\sim 500^\circ\text{C}$ ), to HC adsorption for low temperature runs ( $\sim 400^\circ\text{C}$ ), or to a combination of these at the mid temperature ( $\sim 400\text{--}500^\circ\text{C}$ ). Further, since the HC flow is known, HC loss can be expressed on an absolute basis, i.e., gms HC/gm substrate.

**RESULTS AND DISCUSSION:** A typical run sequence in which cyclohexene was passed through gasified shale at  $500^\circ\text{C}$  is shown graphically in Figure 2a. The response as plotted shows the ion intensity for the molecular ion of cyclohexene ratioed to the Ar ion intensity. Data are displayed as ratios instead of absolute intensities in order to correct for changing conditions during a run, e.g., QMS drift, pressure fluctuations, etc. The first segment represents QMS response in the initial valve position (bypass mode) in which the model compound is flowing through the sand-packed bypass bed. The second segment shows QMS response with the valve switched so that the model compound passes through the substrate reactor. The third segment shows the return to bypass mode at which time the QMS baseline is reestablished.

There is no measurable desorption in the data of Figure 2a following return to bypass suggesting that all product loss is attributable to cracking or coking losses. Evidence that this loss is due in large part to cracking reactions can be found in Figure 2b, which shows a substantial increase in the mass 42 (largely propene) to mass 82 (cyclohexene) ratio during exposure.

The high initial HC loss followed by a gradual decline to constant response was characteristic of the high temperature runs (Figure 4). Generally, substrate reactivity followed the order of gasified > combusted  $\geq$  pyrolyzed. Also, cyclic aliphatics were found to be more susceptible to induced reaction than were straight chain aliphatics with aromatics generally exhibiting the greatest stability. As of this writing, carbon analysis of the substrates is incomplete and thus product loss due to coking versus cracking cannot yet be differentiated. However, it is believed that cracking reactions (i.e., thermal cleavage with little or no coke deposition) are much more prevalent for aliphatics (particularly cyclic aliphatics) than aromatics which more likely undergo a higher proportion of coking reactions in the initial interaction. To help differentiate between cracking and coking losses, future runs are planned in which the total product stream will be combusted with the resulting  $\text{CO}_2$  and  $\text{H}_2\text{O}$  products monitored with the QMS. It is anticipated that this approach will unambiguously determine coking losses with cracking losses determined by difference.

Figure 3 shows a similar cyclohexene/Ar ion intensity plot at a lower temperature of  $300^\circ\text{C}$ . HC loss in this run is attributed solely to adsorption since 1) the QMS response during the bypass mode and the latter portion of the expose mode are equivalent and 2) the desorption curve following return to bypass is equal in magnitude to the HC loss observed in the initial stages of substrate exposure. Generally, adsorption capacity followed the order of gasified  $\gg$  combusted  $\geq$  pyrolyzed shale. Adsorption was so extensive for many of the low temperature gasified shale runs that QMS response dropped off-scale resulting in a delay in data collection of up to 2 minutes in some instances.

**SUMMARY.** The reactor system described in this manuscript provides a rapid means of measuring HC reaction kinetics. The system is flexible in that direct comparisons of solid substrate reactivities may be compared over a wide temperature range with a variety of hydrocarbons. Though

not discussed, fixed gases are also amenable to adsorption/desorption studies by this technique. Future plans include: 1) examination of the liquid products and ultimate analysis of the solid substrates following exposure in order to help elucidate reaction mechanisms and differentiate between predominantly cracking versus predominantly coking reactions and 2) examining mixtures of two or more hydrocarbons to determine differential adsorption/desorption kinetics.

**Acknowledgments.** The author gratefully acknowledge the work of D.McLean, G. Thomas, and M. Moore for analytical support and S. Carter for providing the oil shale substrates and for valuable discussions. This work was supported in part by the Morgantown Energy Tech. Ctr., USDOE, under Coop. Agreement DE-FC21-90MC27286 (such support does not constitute an endorsement by the USDOE of the views expressed in this manuscript).

1. Carter, S.D., Taulbee, D.N., Rubel, A.R., Abner, R.T., *Proc.: 1988 Eastern Oil Shale Symp.,IMMR88/101*, Inst. Min. & Minerals Res., Lexington, Ky., May., 1989, p. 333-340.
2. Carter, S.D., Robl, T.L., Rubel, A.M., and Taulbee, D.N., *Fuel*, 1990, 69, p 1124.
3. Taulbee, D.N. and Carter, S.D., *Proc.: ACS Div. of Fuel Chem. 37, #2*, Fuel Chem. Div of ACS, pub., San Francisco, CA, April, 1992, pp. 800-809.
4. Carter, S.D., and Taulbee, D.N., *Fuel*, 71, #12, 1992, 1421-26.

---

Table 1. Study Substrates. Substrates dry screened to 20X60 mesh.

<u>Substrate</u>	<u>Origin</u>	<u>Reactor Load (g)</u>	<u>Preparation/comment</u>
Pyrolyzed Shale	Cleveland oil shale	4-g	530C in N <sub>2</sub> /10 min
Gasified Shale	Cleveland oil shale	4-g	800C in Steam/20 min
Combusted Shale	Cleveland oil shale	4-g	700C in air/10 min
Sand	Ottawa, Canada	6-g	20X30 mesh

---

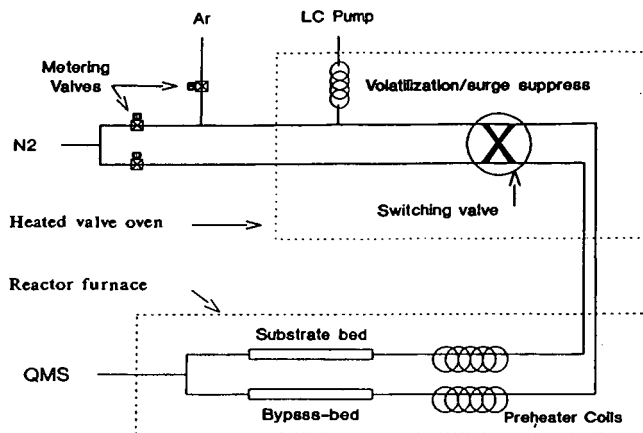


Figure 1. Adsorption/Cracking Reactor Schematic.

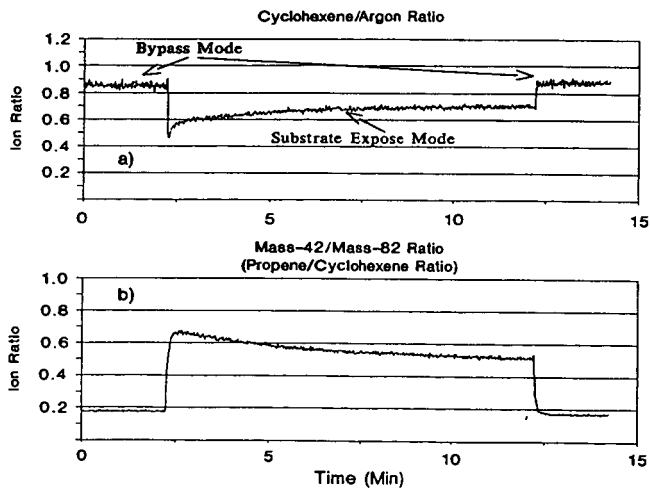
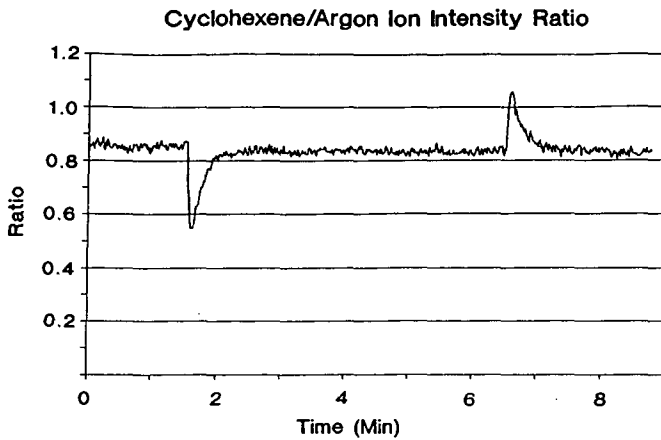
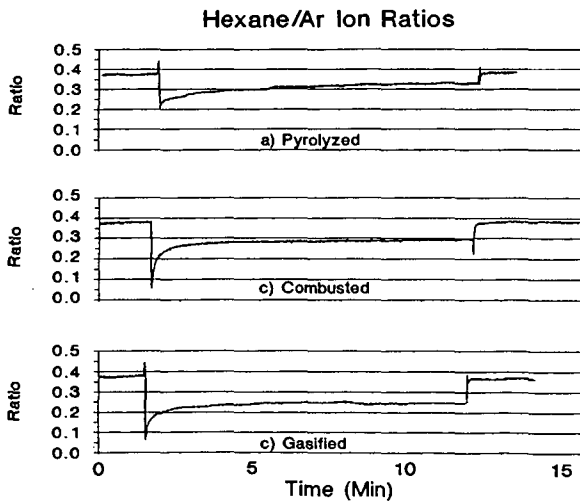


Figure 2. Gasified shale, 500 °C, 10 min exposure, ~10 vol% cyclohexene in Ar/N<sub>2</sub> carrier. a) Cyclohexene/Ar (82/20) ion ratios, b) Mass 42/mass 82 (largely propene).



**Figure 3.** Cyclohexene/Ar ion intensity during gasified shale substrate run at 300 °C, 5 minute exposure. Otherwise, same conditions as Figure 2.



**Figure 4.** Hexane/Ar ion ratios for 650 °C, 10 min exposure runs, ~10 vol% hexane in Ar/N<sub>2</sub> carrier. a) pyrolyzed b) combusted and c) gasified substrate.

## THE ROLE OF CATALYST PRECURSOR ANIONS IN CHAR REACTIVITY

Lillian L. Sims, Godfried M. K. Abotsi and Kofi B. Bota  
Research Center for Science and Technology  
Clark Atlanta University  
Atlanta, GA 30314

**Key words:** Anions, zeta potential, metal adsorption

### INTRODUCTION

Coal gasification activity is generally attributed to the metal components of catalyst precursors. However, there is evidence that the anion of the catalytic salt plays a significant role in the performance of the catalyst. It has been reported (1) that for the same metal, the chlorides, acetates, or hydroxides of sodium, potassium, magnesium, and calcium exhibited different char reactivities. The catalysts were loaded from aqueous solution. For example, at 1223K, the order of reactivity for the sodium compounds was  $\text{NaOH} > \text{NaAc} > \text{NaCl}$ . These findings were rationalized in terms of the influence of the various anions on the diffusivities of the cations ( $\text{Na}^+$ ,  $\text{K}^+$ ,  $\text{Mg}^{2+}$ , and  $\text{Ca}^{2+}$  produced by dissociation of the metal precursors at gasification temperatures) through the pores of the chars. The variations in the activities of the catalysts were also ascribed to differences in the extent of deactivation as a result of the catalyst reaction with inorganic materials in the coal, and to the presence or absence of coal surface metal-oxygen complexes which have been hypothesized as prerequisites for coal char reactivity (2-7). It has also been suggested that the metal ion of the catalyst salt reacts with the carbon in the char to form active intermediates for gasification and that the anion of the salt favorably modifies the structure of the active species. However, the composition and structure of the active intermediates are unknown (8).

Since coal is normally impregnated with catalyst from solution, the variations in the activities of different catalyst precursors may be due to the influence of different anions during the adsorption of the metal ions onto the coal. The surface charge properties of aqueous suspensions of coal is well known. The electrical potential on a coal particle decreases rapidly with distance from the charged coal surface. The effective thickness is the distance from the charged surface into the solution within which most of the electrical interactions with the surface occur (9,10). The effective thickness,  $1/K$ , (or the Debye length) is given by the expression (9,10):

$$1/K = \left[ (\epsilon_r RT) / (4\pi F^2 \sum_i C_i Z_i^2) \right]^{1/2} \quad (1)$$

where  $\epsilon_r = \epsilon/\epsilon_0$  = the relative static permittivity or dielectric constant of the solution ( $\epsilon$  = the static permittivity of the solution and  $\epsilon_0$  = the permittivity of a vacuum),  $R$  = the gas constant,  $T$  = the absolute temperature,  $F$  = the Faraday constant,  $C_i$  = the molar concentration of any ion in solution. The above equation shows that  $1/K$  is inversely proportional to both the valence ( $Z$ ) of the ions in solution and to the square root of their ionic concentrations. Also, in the presence of an electrolyte, the electrical effects are experienced over shorter distances (due to the compression of the electrical double layer) than in the absence of an electrolyte. Thus, the Debye length decreases rapidly with increasing ionic strength, given by  $1/2\sum C_i Z_i^2$  (10).

In relation to catalyzed coal gasification, it is apparent from the above discussion that when different catalyst precursor electrolytes containing the same metal (e.g. KCl and  $K_2CO_3$ ) are dissolved in aqueous solution and separately introduced into coal, the degree of coal-metal ion contact will be different for the various catalyst precursors due to differences in the double layer thickness. This will produce different metal adsorption densities and possibly different catalyst dispersion and gasification activities. Variations in catalyst uptake by coals can also occur as a result of differences in the pHs of the impregnating metal solutions. This work reports on the effects of catalyst precursor anions and pH on coal electrokinetic properties and catalyst adsorption by various calcium and potassium catalyst precursors.

## EXPERIMENTAL

The surface electrokinetic properties of the raw coal (North Dakota Hagel lignite, PSOC 1482) in the presence or absence of acetate ( $CH_3COO^-$ ), chloride ( $Cl^-$ ), nitrate ( $NO_3^-$ ), carbonate ( $CO_3^{2-}$ ) or sulfate ( $SO_4^{2-}$ ) anion was investigated by dispersing 300 mg of the coal (-200 mesh sieve size) in a liter of distilled water containing  $10^{-1}$ ,  $10^{-2}$  or  $10^{-3}$  mol/L of each anion. The potassium compound of each anion was used as the source of the anion while the acetate, chloride or nitrate of calcium was applied. The slurries were divided into 50.0 mL portions and the pHs were adjusted with a few drops of dilute nitric acid or ammonium hydroxide solution. The slurries were mechanically agitated for 3h to attain equilibrium followed by determination of the pHs and the zeta potentials using "Pen Kem model 501 Lazer Zee Meter."

The effects of the surface charge properties of the coal on the adsorption of potassium from  $CH_3COOK$ , KCl,  $KNO_3$ ,  $K_2CO_3$  or  $K_2SO_4$  solution has been ascertained by agitation (for 24h) of 4.0 g of the coal with 100 mL of solution containing  $10^{-1}$  mol/L potassium metal. The catalyst precursors were used separately. Following the adsorptions, the coal particles were filtered and the potassium content in the coal samples was determined by Galbraith Laboratories, Inc.

## RESULTS AND DISCUSSION

The effects of chloride anion concentration on the zeta potentials of the coal particles are shown in Figures 1 and 2, respectively, for  $CaCl_2$  and KCl catalyst precursors. As can be observed from Figure 1, the charge density on the coal particles becomes progressively more negative, in the absence of added chloride anions, as the pH

of the slurry was raised from acidic to basic. However, addition of  $10^{-2}$  or  $10^{-3}$  mol/L chloride anion significantly reduced the net negative surface charge on the coal particles, especially at the higher chloride anion concentration. At  $\sim$  pH 10, for instance, the zeta potential of the coal is about -78 mV in the absence of chloride anion, but decreased to -15 and -40 mV, for the  $10^{-2}$  and  $10^{-3}$  mol/L  $\text{Cl}^-$  concentrations, respectively. Since the original coal particles are negatively charged, chloride anion adsorption will be hindered as a result of electrostatic repulsion between the coal surface and the chloride anion. Thus, the reduction in surface charge density must arise from the adsorption of calcium ions produced from the dissociation of calcium chloride, the driving force for the adsorption being coulombic attraction between the anionic coal surface and the calcium cations.

As in the case of the  $\text{CaCl}_2$  precursor, Figure 2 shows that the zeta potentials of the coal particles decrease with increase in pH when KCl is used as the  $\text{Cl}^-$  source. It is also observed that, within experimental error, addition of KCl produces a less negative zeta potential compared to that on the coal without KCl addition. The development of surface charge on coal particles in aqueous media has been attributed to the dissociation of coal surface carboxylic and hydroxyl groups as discussed by several investigators (9,11-13). Comparison of Figures 1 and 2 shows that the reduction in the negative zeta potentials is more prominent, at similar chloride concentrations, for  $\text{CaCl}_2$  than KCl. This behavior is consistent with equation (1) which predicts that the Debye length should be shorter in the presence of  $\text{CaCl}_2$  than for KCl due to the higher ionic charge on  $\text{Ca}^{2+}$  compared to that on  $\text{K}^+$ . This compression of the double layer promotes higher  $\text{Ca}^{2+}$  than  $\text{K}^+$  uptake and results in a greater reduction in the net negative surface charge density in the presence of  $\text{CaCl}_2$ . Similar trends were observed for the other corresponding calcium and potassium salts. To maintain a constant double layer thickness in studies involving interfacial phenomena, an excess of a 1:1 supporting electrolyte is normally added to the system. However, a supporting electrolyte was not applied in the current study in order to determine the influence of the various catalyst precursor anions or cations on coal surface chemistry.

The dependence of zeta potentials on pH and carbonate anion concentration, when using  $\text{K}_2\text{CO}_3$  as  $\text{CO}_3^{2-}$  source, is provided in Figure 3. Similar zeta potentials were obtained in the presence or absence of  $\text{CO}_3^{2-}$ , particularly around  $\sim$  pH 2 - 4.5, for the  $10^{-2}$  or  $10^{-3}$  mol/L  $\text{CO}_3^{2-}$  concentration. However, significant reductions in the negative zeta potentials occurred at  $10^{-1}$  mol/L  $\text{CO}_3^{2-}$ . The influence of the surface electrical properties of the coal on potassium adsorption from aqueous solutions of the potassium compounds is presented in Figure 4. The potassium uptake shows two distinct features: (1) a strong dependence on coal slurry pH, and (2) a dependence on the potassium salt used. For all the compounds, potassium adsorption was minimum around pH 2, it was maximum at  $\sim$  pH 10 and intermediate at pHs between 5 and 6. From Figure 4, it appears that at a given pH, the metal uptake can be classified into three groups according to the potassium precursor used: KCl,  $\text{KNO}_3$  and  $\text{K}_2\text{SO}_4$  fall into one group, while  $\text{KOOCCCH}_3$  and  $\text{K}_2\text{CO}_3$  belong to separate groups. It is evident from Figure 4 that the highest potassium loading was obtained at all pHs when adsorption was effected using potassium carbonate solution. The second highest metal uptake occurred when potassium acetate was used and approximately the same level of potassium was adsorbed from potassium chloride, potassium nitrate and potassium acetate solutions. As can be seen from Figure 3, the net negative surface charge density on the coal is significantly reduced in  $10^{-1}$  mol/L  $\text{CO}_3^{2-}$  solution when  $\text{K}_2\text{CO}_3$  was used as the carbonate anion precursor. The observed potassium loadings from this salt is in agreement with the zeta potential results. Thus, the surface charge on the coal clearly plays a role in potassium uptake. However,

the reasons for the variations in metal adsorption as a function of anion type are not known at this time and are the subjects of continuing research.

In conclusion, it has been shown that the negative charge density on a North Dakota lignite is reduced in the presence of  $\text{CH}_3\text{COOK}$ ,  $\text{KCl}$ ,  $\text{KNO}_3$ ,  $\text{K}_2\text{CO}_3$  or  $\text{K}_2\text{SO}_4$  solutions. For each compound, the reduction becomes more prominent as the salt concentration is increased, the phenomenon being particularly distinct for  $\text{K}_2\text{CO}_3$ . Adsorption studies show that the highest potassium adsorption occurs from aqueous  $\text{K}_2\text{CO}_3$  solution, thus confirming the zeta potential results which were least negative at  $10^{-1}$  mol/L  $\text{CO}_3^{2-}$  when using  $\text{K}_2\text{CO}_3$  salt. The reported superior activity of  $\text{K}_2\text{CO}_3$  in char reactivity may reside in its stronger interaction with the coal surface during catalyst loading from solution. Fourier transform infrared studies are also in progress to gain insight into the interaction between the coal surface and the various ions.

#### ACKNOWLEDGEMENT

Financial support for this research was provided by the U. S. Department of Energy under contract number DE-FG22-91PC91286.

#### REFERENCES

1. Calahorro, C. V.; Gonzalez, C. F.; Garcia, A. B.; Serrano, V. G., *Fuel* 1987, 66, 216.
2. Wigmans, T.; Haringa, H., Moulijn, J. A., *Fuel* 1983, 62, 185.
3. Hashimoto, K.; Miura, K.; Xu, J. J.; Watanabe, A.; Masukami, H. *Fuel* 1986, 65, 489.
4. Wigmans, T.; van Craneburgh, H.; Elfring, R.; Moulijn, J. A., *Carbon* 1983, 21, 23.
5. Yuh, S. J.; Wolf, E. E., *Fuel* 1983, 62, 252.
6. Fredriks, I. L. C.; van Wechem, H. M. H.; Stuiver, J. C. M.; Bouwman, R., *Fuel* 1981, 60, 463.
7. Mims, C. A.; Rose, K. D.; Melchior, M.-T.; Pabst, J. K., *J. Am. Chem. Soc.*, 1982, 104, 6886.
8. Wood, B. J. and Sancier, K. M. *Catal. Rev. Sci. Eng.* 1984, 26(2), 233.
9. Laskowski, J. S., Parfit, G. D., In "Interfacial Phenomena in Coal Technology," Botsaris, G. D. and Glazman, Y. M., Eds., Marcel Dekker, New York, 1988, p. 279.
10. Rosen, M. J., "Surfactants and Interfacial Phenomena," John Wiley, New York, 1978, p. 31.

11. Kelebek, S., Salman, T.; Smith, G. W., *Canad. Metal. Quart.* 1982, 21, 205.
12. Abotsi, G. M. K., Bota, K. B., Saha, G., *Energy & Fuels* 1992, 6, 779.
13. Fuerstenau, D. W.; Rosenbaum, J. M.; Laskowski, J., S., *Coll. Surf.* 1983, 8, 137.

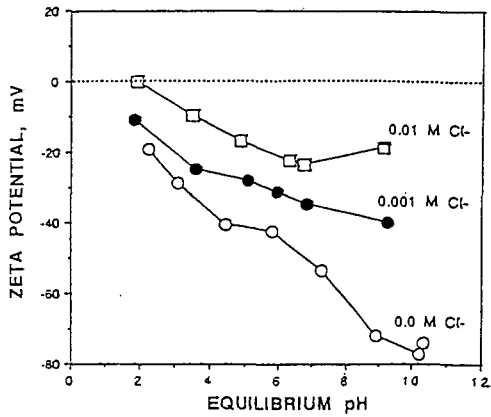


Figure 1. Dependence of zeta potential on the coal slurry pH and chloride anion concentration using  $\text{CaCl}_2$  as the source of chloride. Coal: North Dakota lignite.

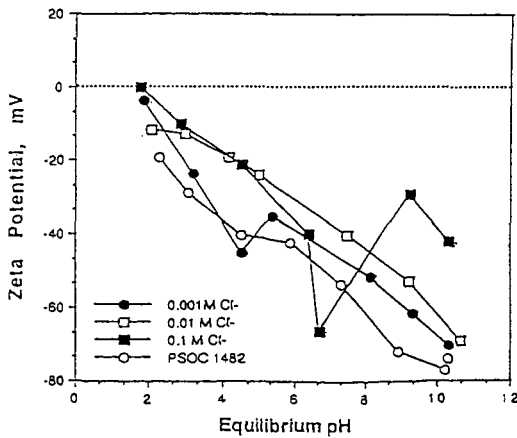


Figure 2. Dependence of the coal's zeta potential on pH and chloride anion concentration. KCl as source of chloride.

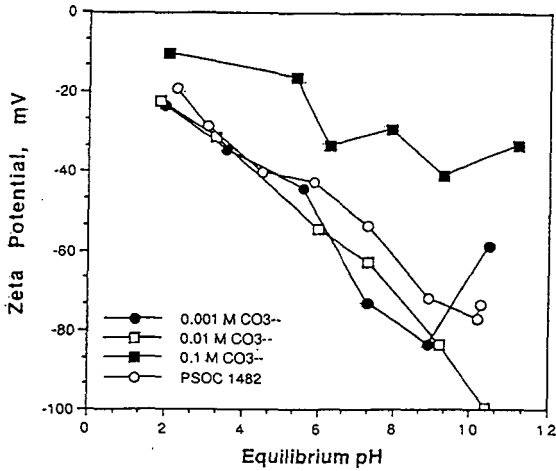


Figure 3. Variation of the coal's zeta potential with pH and carbonate anion concentration. K<sub>2</sub>CO<sub>3</sub> as source of carbonate anion.

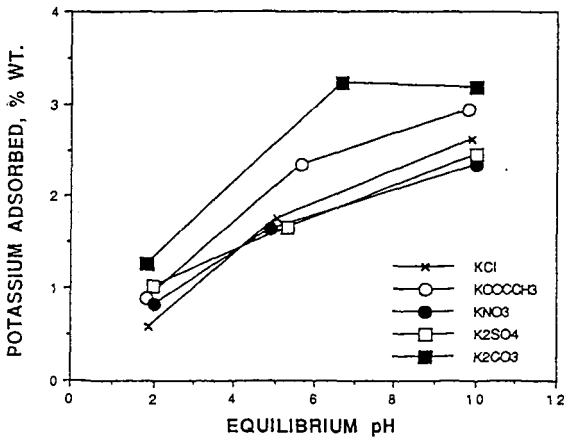


Figure 4. Influence of various potassium salts and pH on potassium adsorption by the coal.

Partial Oxidation of Ethane and Ethylene in the  
Presence and Absence of  $^{13}\text{C}$  Labeled Methane  
on Reducible and Non-Reducible Oxide Catalysts

Abolghasem Shamsi  
United States Department of Energy  
Morgantown Energy Technology Center  
P.O. Box 880  
Morgantown, WV 26507-0880

**Keywords:** Catalysis; Oxidative coupling; Relative reactivity

## INTRODUCTION

In recent years, there has been considerable progress in the development of catalysts for the conversion of natural gas to more useful chemicals and fuels. Oxidative coupling of methane to ethane and ethylene, and subsequent conversion of these chemicals to liquid fuel, is one approach that has attracted great interest in recent years (Liu et al., 1984; Yates and Zlotin, 1988; Otsuka et al., 1986). We have shown that by proper cation substitution in pervoskite-type oxides, active and selective catalysts for the oxidative coupling of methane to higher hydrocarbons can be obtained (France et al., 1988 (a and b); Shamsi and Zahir, 1989; Siriwardane and Shamsi, 1990). Recent studies have shown that gas-phase reactions, especially at higher pressures, play a significant role in the partial oxidation of methane (Labinger and Ott, 1987; Lane and Wolf, 1988; Shamsi and Zahir, 1989).

Despite intensive research on oxidative coupling of methane, no one has yet achieved a single pass yield large enough for a process to be economical. McCarty (1992) has evaluated several approaches for achieving higher yield in methane conversion processes. He has concluded that oxidative coupling of methane into desirable products is limited by two types of side reactions: "1) direct oxidation of reactive intermediates, and 2) the parallel conversion of desired metastable products into deep oxidation by-products."

Mazanec et al. (1992) studied methane conversion to higher hydrocarbons using electrocatalytic cells. They have concluded that "there is a fundamental mechanistic limitation to the conversion of methane to higher hydrocarbons." Olsbye et al. (1992) studied the effects of adding ethane and ethylene to an oxidative coupling reaction and found that methane is formed from the  $\text{C}_2$  products. They suggested that the  $\text{C}_2$  products are more reactive to form methane than the reverse methane coupling reaction. Mazanec et al. (1992) and Labinger (1992) have proposed a simple two-step "ABC" model. In this model, A is the reactants, B is the desired products, and C is the by-products. In this simplified model where

$$\text{A} \xrightarrow{k_1} \text{B} \xrightarrow{k_2} \text{C},$$
 the  $k_2/k_1$  ratio is used to estimate the desired  $\text{C}_2$  yield.

The challenging problem in converting methane to ethane and ethylene is the reactivity of methane relative to its products. There are at least three vital points in converting methane to ethane and ethylene using oxidative coupling. First, at high temperature and pressure, both homogeneous and heterogeneous reactions occur during oxidative coupling of methane, and the major precursors are produced in the gas phase (Shamsi and Zahir, 1989; Liu et al., 1984). Consequently, under these conditions it is difficult to change the product distribution entirely by tailoring the catalyst. Second, methane is much less reactive than its products, ethane and ethylene. Therefore, high conversion with high selectivity is very difficult to obtain. Third, complete oxidation of intermediates to carbon dioxide becomes increasingly important at higher pressure, which is required for a commercial process. The first and third problems could be overcome by developing a catalyst to activate methane at temperatures below 600°C and by designing a process that operates at 1 atm pressure. However, neither the catalyst nor the process design can solve the second problem. Ethane and ethylene, depending on their partial pressures, will compete for active species in the gas phase and for active centers on the catalyst surfaces as will be discussed later.

## EXPERIMENTAL

See publication by Shamsi, A. and Zahir, K., (1989) for details.

## RESULTS AND DISCUSSION

Earlier studies on oxidative coupling of methane indicated that the activation of methane occurs both in the gas phase and on the surfaces of the catalyst (Shamsi and Zahir, 1989). The results also showed that contact time, temperature, pressure, and methane-to-oxygen ratio are the major factors affecting conversion and selectivity in the presence and absence of the catalyst. Before investigating the catalytic oxidation, the effects of pressure, temperature, and contact time on partial oxidation of ethane and ethylene in an empty reactor were studied. This will determine the extent of gas-phase contribution to the overall reactions at various experimental conditions.

Ethane was partially oxidized by co-feeding ethane, helium, and oxygen into the reactor. The dependence of conversion and selectivity on temperature, pressure, and contact time is shown in Tables 1, 2, and 3. Ethane oxidation commenced at temperatures higher than 550°C. Higher ethane and oxygen conversions were obtained at higher temperatures, pressures, and contact times. Ethylene is the major product at low ethane conversion, and its concentration decreased with increasing temperature, pressure, and contact time. The amounts of CO and CO<sub>2</sub>, carbon monoxide being predominant, also increased with increasing conversion. Methane, higher hydrocarbons, and formaldehyde were also detected at higher temperatures, pressures, and contact times, indicating that ethylene further reacts with oxygen to form formaldehyde and carbon oxides.

Ethylene was mixed with helium and oxygen and co-feed into the reactor. The dependence of conversion and selectivity on temperature, pressure, and contact time is shown in Tables 4, 5, and 6. Ethylene oxidation commences at temperatures higher than 500°C, about 50°C lower than required for ethane activation. Higher ethylene and oxygen conver-

sions were observed at higher temperatures, pressures, and contact times. Furthermore, at low ethylene conversion, ethylene oxide and formaldehyde are the major products, and their concentrations decreased with increasing conversion. The amount of CO increased with increasing conversion. This indicates that formaldehyde and ethylene oxide underwent further reactions to form carbon monoxide. Methane and higher hydrocarbons were also detected at higher temperatures, pressures, and contact times. Comparison with ethane shows that ethylene in an empty reactor, mainly gas-phase reactions, is oxidized more easily than ethane. These results are in good agreement with those reported by Burch and Tsang (1990). However, they have reported neither formaldehyde nor ethylene oxide.

Temperature-programmed partial oxidation of ethane, ethylene, and  $^{13}\text{C}$  labeled methane was studied separately. Results are shown in Figures 1. The temperature was raised from 400 to 700°C at 40°C/min. Abundance of  $^{12}\text{CO}_2$ ,  $^{13}\text{CO}_2$ , and oxygen were monitored using a GC with an MSD. The temperature at which 50% of the oxygen converted during oxidation of ethane and ethylene is significantly less than the temperature at which 50% of the oxygen converted during oxidation of methane. The rates of activation of these hydrocarbons on sodium promoted  $\text{Sm}_2\text{O}_3$  decrease in the order of ethane > ethylene >> methane. Using these results and those in the literature to compare the reactivity of ethane and ethylene with methane would be misleading. According to the results shown in this graph, ethane and ethylene are activated at significantly lower temperatures than that required for methane activation. Therefore, any ethane or ethylene formed during oxidative coupling of methane would be consumed before any methane could be activated. The earlier results in this laboratory and elsewhere showed that this is not correct. Therefore, the relative reactivity of ethane and ethylene are different in the presence of methane and the catalyst as will be discussed later.

A mixture of ethylene in  $^{13}\text{C}$  labeled methane were co-fed with oxygen and helium into the reactor (total flow rate of 17.5 cm<sup>3</sup>/min; hydrocarbon:oxygen ratio=2:1) containing 0.5 grams of 1.4 wt% sodium promoted  $\text{Sm}_2\text{O}_3$ . The temperature of the catalyst bed was raised from 400 to 700°C at 40°C/min and held for 7.5 min at 720°C. The abundance (concentration, a.u.) of  $^{12}\text{CO}_2$  and  $^{13}\text{CO}_2$  was monitored using GC with an MSD. The concentrations of ethylene varied from 5 to 50 vol%. When the ethylene concentration was about 5 vol%,  $^{13}\text{CO}_2$  was slightly more abundant than  $^{12}\text{CO}_2$ . However, increasing the concentrations of ethylene to 10 and 50 vol% formed more  $\text{CO}_2$  from ethylene than from methane. No significant amount of carbon dioxide was detected at temperatures of less than 400°C and ethylene concentration of less than 10 vol%. However, when the concentration increased to more than 10 vol%, ethylene was activated at temperatures less than 400°C.

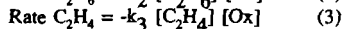
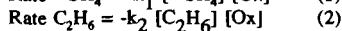
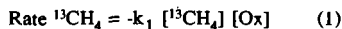
A plot of  $^{12}\text{CO}_2$  to  $^{13}\text{CO}_2$  ratios versus ethylene concentrations is shown in Figure 2. These data were obtained at steady state conditions of 720°C and 1 atm pressure. At a lower ethylene concentration of 5 vol%, ethylene was 7.8 times more reactive than methane. However, as the concentrations of ethylene increased to 10 and 50 vol%, the reactivity of ethylene decreased to 7.5 and 3.6, respectively. The relative reactivity was calculated based on the assumption that at equal reactivity and replacing 5, 10, and 50 vol% of  $^{13}\text{C}$  labeled methane by  $^{12}\text{C}$  ethylene, the  $^{12}\text{CO}_2$  to  $^{13}\text{CO}_2$  ratios will increase to 0.105, 0.222, and 2.0,

respectively. In all cases, when a mixture of methane and ethylene partially oxidized over quartz or the catalyst, higher ratios of  $^{12}\text{CO}_2$  to  $^{13}\text{CO}_2$  were obtained.

Temperature-programmed partial oxidation of mixtures of ethane in  $^{13}\text{C}$  labeled methane over 1.4 wt% sodium promoted  $\text{Sm}_2\text{O}_3$  were also studied. The temperature of the catalyst bed was raised from 400 to 700°C at 40°C/min and held for 7.5 min at 730°C. The abundance of  $^{12}\text{CO}_2$  and  $^{13}\text{CO}_2$  was monitored using GC with an MSD. The concentrations of ethane varied from 5 to 50 vol%. When the ethane concentration was about 5 vol%, the  $^{13}\text{CO}_2$  was slightly more abundant than the  $^{12}\text{CO}_2$ , indicating that more than two moles of methane were converted to carbon dioxide per one mole of ethane. Increasing the concentrations of ethane to 10 and 50 vol% formed more carbon dioxide from ethane than from methane.

A plot of  $^{12}\text{CO}_2$  to  $^{13}\text{CO}_2$  ratios versus ethane concentrations is shown in Figure 3. These data were obtained at steady state conditions of 730°C and 1 atm pressure. At a lower ethane concentration of 5 vol%, ethane was about 5.5 times more reactive than methane. However, as the concentrations of ethane increased to 10 and 50 vol%, the relative reactivity of ethane decreased to 4.7 and 3.5, respectively. Comparing with ethylene mixtures, ethane at concentrations less than 10 vol% is about 1.5 times less reactive than ethylene. However, at concentrations of more than 10 vol%, ethane and ethylene show a similar reactivity and were about 3.5 times more reactive than methane.

Mazanec et al.(1992) have proposed that at the relative rates of methane and ethylene activation,  $k_2/k_1$ , in equations (1) and (2) determine the upper limit of  $\text{C}_2$  yield, considering ethane can be converted to ethylene readily by "non-oxidative pyrolysis".



They have also reported that "ethylene is more stable than ethane and the rate of ethylene activation is considered to be the limiting feature." However, the results obtained by passing a mixture of methane (34.7%), ethane (19.4%), ethylene (13.1%), and oxygen (32.8%) over a catalyst containing reducible oxides of transition metals (Ca/Ni/K= 2:1:0.1) show that almost all the ethylene was consumed while the concentration of ethane was reduced to 13.3% at 600°C and 1 atm pressure. When this similar mixture was passed over quartz chips at the same conditions, the concentrations of methane and ethylene increased to 42.7 and 19.1%, respectively. Therefore, rate equation (3) was added to explain the relative reactivity of methane and ethylene as the ratio of  $k_3/k_1$ .

## CONCLUSION

This study was conducted to understand the relative reactivity of ethane and ethylene compared to methane and to determine whether a catalyst could be designed to overcome the limitation in yield required for an economical process to convert natural gas to liquid fuels.

The most widely acceptable mechanism for activation of methane appears to be the reaction of methane from the gas phase with surface oxygen, which abstracts hydrogen from methane to form methyl radicals (Ahmed and Moffat, 1990). The methyl radicals are released into the gas phase and form ethane. However, the reaction pathways for activation of ethane and ethylene are not well established. The relative H-abstraction rates for hydroxyl radicals in the gas phase for  $C_2H_6/CH_4$  and  $C_2H_4/CH_4$  are reported by McCarty (1992). From these data and suggestion from Lunsford that the C-H bond strength in ethylene is greater than methane, the relative gas-phase reactivity can be estimated to be in the order of  $C_2H_6 > CH_4 > C_2H_4$ . However, this order was not observed in this study, and it has been reported only for  $LiCl/MnO_x$  catalyst (Burch and Tsang, 1990), indicating that the H-abstraction is not the only pathway for ethane and ethylene activation. Likewise, depending on the catalyst and the experimental conditions, C-C and C=C bonds are also attacked by the active centers on the catalyst and by the active species in the gas phase. Therefore, the relative reactivity of ethane and ethylene compared to methane appears to strongly depend on the partial pressures of reactants and the type of catalysts used.

The relative reactivities are in the order of ethylene > ethane >> methane for reactions in the gas phase and on the catalysts containing reducible oxides of transition metals such as Ca/Ni/K. However, this order changed to ethane > ethylene >> methane for a non-reducible catalyst such as sodium promoted  $Sm_2O_3$ . Oxidation of ethane and ethylene in the presence of methane and catalyst show that methane and ethylene, depending on their partial pressures, compete for active centers, and neither formaldehyde nor ethylene oxide were detected in the presence of methane and the catalyst.

#### LITERATURE CITED

- Ahmed, S.; Moffat, J.B., *Journal of Catalysis* 1990, 125, 54.  
Burch, R.; Tsang, S. C., *Applied Catalysis*, 1990, 65, 259.  
France, J.E.; Shamsi, A.; Ahsan, M.Q.; Headley, L.C., *Energy Progress* 1988 (a), 8(4), 185.  
France, J.E.; Shamsi, A.; Ahsan, M.Q., *Energy & Fuels* 1988(b), 2(2), 235.  
Labinger, J. A.; Ott, K. C., *J. Phys. Chem.* 1987, 91(2), 682.  
Labinger, J.A., *Preprints-Symposia* 1992, 37(1), 289. ACS, 5-10 April, San Francisco, CA.  
Lane, G.; Wolf, E. E., *Journal of Catalysis* 1988, 113, 144.  
Liu, H.-F.; Liu, K. Y.; Johnson, R. E.; Lunsford, J. H., *J. Am. Chem. Soc.* 1984, 106(4), 117.  
Mazanec, T.J.; Cable, T. L.; Frye, J. G. Jr., *Preprints-Symposia* 1992, 37(1), 135. ACS, 5-10 April, San Francisco, CA.  
McCarty, J. G., *Preprints-Symposia* 1992, 37(1), 153. ACS, 5-10 April, San Francisco, CA.  
Otsuka, K.; Jinno, K.; Morikawa, A., *Journal of Catalysis* 1986, 100, 353.  
Olsbye, U.; Desgrandchamps, G.; Jens, K.-J.; Kolboe, S., *Preprints-Symposia* 1992, 37(1), 180. ACS, 5-10 April, San Francisco, CA.  
Pereira, P.; Lee, S.H.; Somorjai, G.A.; Heinemann, H., *Catalysis Letters* 1990, 6, 255.  
Shamsi, A.; Zahir, K., *Energy & Fuels* 1989, 3(6), 727.  
Siriwardane, R.V.; Shamsi, A., *Applied Catalysis* 1990, 60, 119.  
Yates, D. J. C.; Zlotin, N.E., *Journal of Catalysis* 1988, 111, 317.

Table 1. Effect of Temperature on Ethane Conversion and Selectivity in an Empty Alumina Reactor at 1 atm Pressure,  $C_2H_6/He/O_2=20/20/10$  cm<sup>3</sup>/min NPT Flow Rates, Contact Time = 2.4 s

	Temperature (°C)		
	550	580	610
Conversion, Mol%			
Ethane	2.1	23.1	58.6
Oxygen	1.4	26.4	99.3
Product Distribution, Carbon Mol%			
C <sub>2</sub> H <sub>4</sub>	100	84.9	54.2
CH <sub>4</sub>	0.0	2.1	8.3
CO	0.0	7.3	26.3
CO <sub>2</sub>	0.0	0.6	1.2
C <sub>3</sub> <sup>+</sup>	0.0	2.9	7.4
HCHO	0.0	2.3	2.6

Table 2. Effect of Pressure on Ethane Conversion and Selectivity in an Empty Alumina Reactor at 550°C,  $C_2H_6/He/O_2=20/20/10$  cm<sup>3</sup>/min NPT Flow Rates, Contact Time = 2.4 s

	Pressure (atm)		
	1.0	1.7	2.4
Conversion, Mol%			
Ethane	2.1	8.1	57.4
Oxygen	1.4	7.5	99.4
Product Distribution, Carbon Mol%			
C <sub>2</sub> H <sub>4</sub>	100	92.5	49.8
CH <sub>4</sub>	0.0	1.2	10.2
CO	0.0	1.9	27.2
CO <sub>2</sub>	0.0	0.9	1.4
C <sub>3</sub> <sup>+</sup>	0.0	2.1	7.2
HCHO	0.0	1.5	4.3

Table 3. Effect of Contact Time on Ethane Conversion and Selectivity in an Empty Alumina Reactor at 550°C, 1 atm Pressure,  $C_2H_6/He/O_2=20/20/10$  cm<sup>3</sup>/min NPT Flow Rates

	Contact Time (s)		
	2.4	4.8	9.6
Conversion, Mol%			
Ethane	2.1	10.9	47.8
Oxygen	1.4	11.5	99.3
Product Distribution, Carbon Mol%			
C <sub>2</sub> H <sub>4</sub>	100	92.2	55.5
CH <sub>4</sub>	0.0	1.4	6.6
CO	0.0	3.3	23.9
CO <sub>2</sub>	0.0	0.3	1.3
C <sub>3</sub> <sup>+</sup>	0.0	0.0	8.3
HCHO	0.0	2.7	4.4

Table 4. Effect of Temperature on Ethylene Conversion and Selectivity in an Empty Alumina Reactor at 1 atm Pressure,  $C_2H_4/He/O_2=20/20/10$  cm<sup>3</sup>/min NPT Flow Rates, Contact Time = 2.4 s

	Temperature (°C)			
	500	538	546	560
Conversion, Mol%				
Ethylene	2.1	10.0	14.0	46.9
Oxygen	3.0	19.7	30.2	96.4
Product Distribution, Carbon Mol%				
C <sub>2</sub> H <sub>6</sub>	0.0	0.7	0.0	2.4
CH <sub>4</sub>	0.2	0.7	1.0	14.3
CO	15.8	39.4	46.2	70.5
CO <sub>2</sub>	3.8	2.2	2.3	4.4
C <sub>3</sub> <sup>+</sup>	2.2	5.9	5.8	2.6
HCHO	26.0	19.4	14.8	2.4
C <sub>2</sub> H <sub>4</sub> O	52.0	31.7	29.9	3.4

Table 5. Effect of Pressure on Ethylene Conversion and Selectivity in an Empty Alumina Reactor at 500°C, C<sub>2</sub>H<sub>4</sub>/He/O<sub>2</sub>=20/20/10 cm<sup>3</sup>/min NPT Flow Rates, Contact Time = 2.4 s

	Pressure (atm)			
	1.0	1.7	2.4	3.0
Conversion, Mol%				
Ethylene	0.9	5.7	18.1	44.4
Oxygen	1.3	6.1	37.6	90.2
Product Distribution, Carbon Mol%				
C <sub>2</sub> H <sub>6</sub>	0.0	0.0	0.3	2.7
CH <sub>4</sub>	0.2	0.0	0.5	16.4
CO	15.8	23.7	37.9	66.3
CO <sub>2</sub>	3.8	3.1	4.4	5.0
C <sub>3</sub> <sup>+</sup>	2.2	3.1	6.1	2.2
HCHO	26.0	22.3	14.6	3.6
C <sub>2</sub> H <sub>4</sub> O	52.0	47.8	36.1	3.6

Table 6. Effect of Contact Time on Ethylene Conversion and Selectivity in an Empty Alumina Reactor at 500°C, 1 atm Pressure, C<sub>2</sub>H<sub>4</sub>/He/O<sub>2</sub>=20/20/10 cm<sup>3</sup>/min NPT Flow Rates

	Contact Time (s)			
	2.4	3.2	4.8	9.6
Conversion, Mol%				
Ethylene	4.2	5.3	7.8	21.1
Oxygen	2.7	4.7	10.6	51.0
Product Distribution, Carbon Mol%				
C <sub>2</sub> H <sub>6</sub>	0.0	0.0	0.0	0.6
CH <sub>4</sub>	0.2	0.3	0.5	1.0
CO	15.8	24.6	31.2	46.0
CO <sub>2</sub>	3.8	2.4	2.5	3.3
C <sub>3</sub> <sup>+</sup>	2.2	2.8	4.1	5.7
HCHO	26.0	21.5	18.1	10.3
C <sub>2</sub> H <sub>4</sub> O	52.0	48.4	43.6	33.2

**Figure 1.** Temperature-Programmed Oxidation of Ethane, Ethylene and  $^{13}\text{C}$  Labeled Methane Over Sodium Promoted  $\text{Sm}_2\text{O}_3$

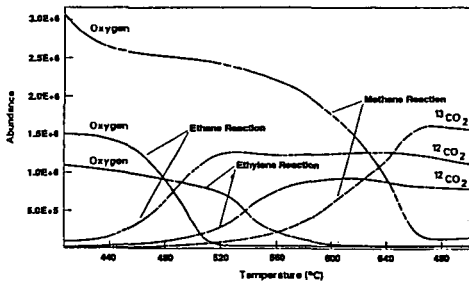


**Figure 2.** Effect of Ethylene Concentration in  $^{13}\text{C}$  Labeled Methane on  $\text{CO}_2$  Formation Over Sodium (1.4wt%) Promoted  $\text{Sm}_2\text{O}_3$  at  $725^\circ\text{C}$  and 1 Atm Pressure

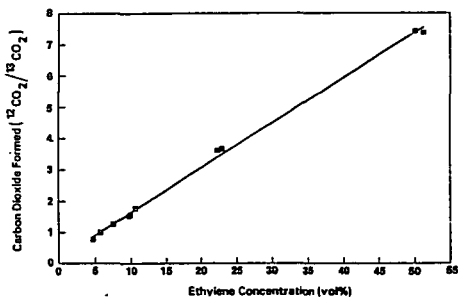
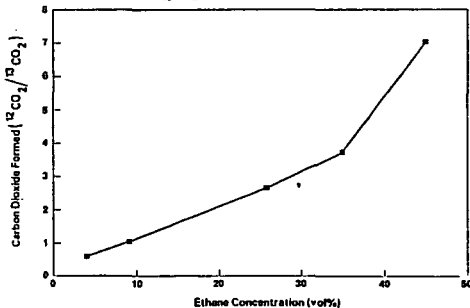


**Figure 3.** Effect of Ethane Concentration in  $^{13}\text{C}$  Labeled Methane on  $\text{CO}_2$  Formation Over Sodium (1.4wt%) Promoted  $\text{Sm}_2\text{O}_3$  at  $725^\circ\text{C}$  and 1 Atm Pressure



## PHOTODECOMPOSITION OF HYDRAZINE FUELS

Ghanshyam L. Vaghjiani  
University of Dayton Research Institute  
Phillips Laboratory, PL/RKFA  
Edwards AFB, CA 92523

UV photometric measurement at 253.65 nm of hydrazine ( $N_2H_4$ ) concentration in the gas phase has been used to study its 248.3-nm laser-photodissociation at 296 K. H-atoms, the major product in the photolysis, were directly detected by cw-resonance fluorescence. The primary quantum yield of  $H(^2S)$  formation was measured to be  $0.85 \pm 0.15$ . The reaction,  $H + N_2H_4 \rightarrow$  products; ( $k_1$ ), that is initiated by the laser-flash was studied in the temperature range 296-222 K. The Arrhenius temperature dependence was determined to be  $k_1 = (7.57 \pm 1.55) \times 10^{-12} \exp[-(1150 \pm 50)/T] \text{ cm}^3 \text{ molec}^{-1} \text{ s}^{-1}$ .

### INTRODUCTION

Hydrazine ( $N_2H_4$ ), methylhydrazine ( $CH_3NNH_2$ ), and unsymmetrical dimethylhydrazine ( $(CH_3)_2NNH_2$ ), are an important class of nitrogen-based compounds that have positive standard enthalpies of formation. Decomposition of these compounds offer a wide variety of industrial applications such as in electrical power cells, fuels for thruster engines aboard the Space Shuttle and the Titan launch vehicles, as a mono-propellant, and in explosives. In addition to the above immediately practical reasons of studying hydrazine chemistry, the understanding of its laboratory photochemical decomposition is relevant to combustion because both processes can involve common reaction intermediates.<sup>1-4</sup> In this study we report the nature of the near ultraviolet absorption spectrum of  $N_2H_4$  in the region 191-291 nm, the dissociation modes in the laser-photolysis at 248.3 nm, and the kinetics of the elementary reaction,  $H + N_2H_4 \rightarrow$  products, which is an important reaction in the pyrolysis of hydrazine fuels. Several previous studies on this reaction have all reported a different temperature dependence for this atom-molecule reaction. Our carefully chosen experimental conditions indicate that all but one previous study had interference from secondary reactions. Using our data and that of Stief and Payne<sup>5</sup>, it is now possible, for the first time, to make a recommendation for the Arrhenius activation energy and the pre-exponential factor for this reaction.

### EXPERIMENTAL TECHNIQUE

The apparatus used to measure the ultraviolet absorption spectrum of  $N_2H_4$  vapor is similar to that previously employed by Vaghjiani and Ravishankara,<sup>6</sup> and the present experimental procedures are fully described elsewhere.<sup>7</sup> The relative UV absorbance spectrum of a column of slowly flowing mixture of  $N_2H_4$ /helium was monitored in a 100-cm-long Pyrex absorption cell using a diode-array spectrometer. The relative absorbance data was converted to absolute cross sections by using the 253.65 nm absorption cross section value determined in a separate experiment. In this experiment, as before, the 253.65 nm absorbance was monitored in a column of  $N_2H_4$ /He, and the hydrazine

concentration in the experiment quantified by passing the eluting mixture through a series of Pyrex traps maintained at 77 K, and titrating the collected  $N_2H_4$  with standard  $KIO_3$  solution in 6 M HCl acid solution. The Beer-Lambert law,  $A_{253.65} = \ell \sigma_{253.65} [N_2H_4]$ , where  $A_{253.65}$  is the measured absorbance at 253.65 nm, and  $\ell$  the cell path length, was used to calculate the absorption cross section,  $\sigma_{253.65}$ , from the volumetrically determined hydrazine concentration,  $[N_2H_4]$ . The spectrum determined in this work together with data from previous work is shown in Figure 1.

The photodissociation of  $N_2H_4$  was studied in a flash-photolysis apparatus of a design similar to that of *Vaghjiani and Ravishankara*.<sup>8</sup> The formation of  $H(2S)$  in the pulsed-laser photolysis (under optically thin conditions) of  $N_2H_4$  was directly monitored by cw-resonance fluorescence detection of the ( $2^2P^0 \rightarrow 1^2S$ ) transition in H-atoms at 121.6 nm. All experiments were carried out under slow-flow conditions, and under pseudo-first-order conditions in  $[H]$  with the photolyte in an excess such that the temporal profile of  $[H]_t$  immediately after photolysis followed an exponential relationship:

$$[H]_t = [H]_0 e^{-kt} \quad (1)$$

$[H]_t$  and  $[H]_0$  are the concentrations of H-atoms at time  $t$  and zero, respectively.  $k = k_1[N_2H_4] + k_d + \sum_i k_i[i]$ , and is the pseudo-first-order rate coefficient for loss of  $[H]$  in the gas mixture.  $k_1$  is the second-order rate coefficient for the reaction  $H + N_2H_4$ ,  $k_d$  is the first-order rate coefficient for diffusion of  $[H]$  out of the detection zone, and  $k_i$  is the second-order rate coefficient for the reaction of H with minute impurities,  $i$ , in the gas mixture. Typical  $[H]$  temporal profiles obtained are shown in Figure 2. The slopes of the decays give values for the pseudo-first-order rate coefficient,  $k$ , and the intercepts,  $S_{0N}$  (at time zero), a measure for the initial amount of H-atoms produced in the photolyses. The intercept in a given hydrazine photolysis is compared to the intercept,  $S_{0R}$ , obtained in a back-to-back photolysis of a known amount of  $CH_3SH$  under similar experimental conditions. The  $[CH_3SH]$  is determined from the measured flow rates and the measured cell pressure. The  $[N_2H_4]$  was directly determined by photometry at 253.65 nm. The observed initial signals,  $S_{0N}$  and  $S_{0R}$  need to be corrected for the attenuation of the detected 121.6 nm resonance fluorescence by the presence of the excess photolyte, and normalized by the photolytic energies,  $E_N$  and  $E_R$ , employed, respectively, in the two experiments.<sup>9,10</sup> The plots in Figure 3 show how the observed signals, when normalized for the amount of photolyte present and photolysis energy employed, vary with the concentration employed. It can be shown that the primary  $H(2S)$  quantum yield,  $\Phi_N$ , in hydrazine photolysis is given by:

$$\Phi_N = \Phi_R \times \sigma_R / \sigma_N \times \exp(I_N) / \exp(I_R) \quad (2)$$

$\Phi_N$ ,  $\Phi_R$ ,  $\sigma_N$ ,  $\sigma_R$ ,  $I_N$ , and  $I_R$  are the primary quantum yields for  $H(2S)$  production, the absorption cross sections at 248.3 nm, and the intercepts in Figure 3, respectively, for each of the photolytes,  $N_2H_4$  and  $CH_3SH$ . The values of the absorption cross sections used in this work are summarized in Table 1. Any revision in these values will directly affect the  $H(2S)$  quantum yield computed in this study.

The kinetics of the reaction,  $\text{H} + \text{N}_2\text{H}_4 \rightarrow \text{products}$ ; ( $k_1$ ), was studied by measuring the pseudo-first-order rate coefficient,  $k$ , as a function of  $[\text{N}_2\text{H}_4]$ . A typical result at 296 K is shown in Figure 4. The straight line is a linear-least-squares fit to the data points whose slope yields a value for  $k_1(296 \text{ K})$ .  $k_1$  was also measured at 273, 250, 232, 230, and 222 K.<sup>11,12</sup> The Arrhenius temperature dependence of  $k_1$  is shown in Figure 5. The straight line is a linear-least-squares fit to the data points. The temperature dependences obtained in previous studies are also shown in Figure 5.

## RESULTS AND DISCUSSION

The absorption cross section at 253.65 nm,  $\sigma_{253.65}$ , was calculated to be  $(2.86 \pm 0.17) \times 10^{-20} \text{ cm}^2 \text{ molec}^{-1}$  at 296 K. The normalized absorption spectrum in the region 191–291 nm is shown in Figure 1. The relative shape and the absolute values of this work and that of Biehl and Stuhl<sup>13</sup> are in reasonable agreement to within  $\pm 20\%$  in the wavelength region 195–230 nm. Becker and Welge's, discrete values in the vacuum-UV are also in good agreement.<sup>14</sup> We are therefore confident that our photometric measurements at 253.65 nm give accurate absolute  $\text{N}_2\text{H}_4$  number densities, to within  $\pm 6\%$  (where the error is 1-sigma, precision plus systematic), in the photodissociation and kinetics experiments.

The continuous spectrum observed is indicative of absorption to one or more dissociative states. A variety of possible primary products can result on absorption of UV light.<sup>7</sup>  $\text{H} + \text{N}_2\text{H}_3$ ,  $\text{NH}_2 + \text{NH}_2$ ,  $\text{NH} + \text{NH}_3$ ,  $\text{NH}_2(\tilde{\text{A}}^2\text{A}_1) + \text{NH}_2$ , and  $\text{N}_2\text{H}_2 + \text{H}_2$  can energetically form for photolysis wavelengths,  $\lambda$ , < 248.3 nm. We have measured directly, for the first time, an H-atom quantum yield,  $\Phi_{\text{H}}$ , of 0.85  $\pm$  0.15 (where the error is 1-sigma, precision plus systematic) at 248.3 nm ( $\Phi_{\text{H}}$  in  $\text{CH}_3\text{SH}$  is unity).<sup>15</sup> The quantum yield was independent of laser fluences of up to  $1.25 \text{ mJ cm}^{-2} \text{ pulse}^{-1}$  employed, and of the linear flow rate of the gas mixture ( $2\text{--}8 \text{ cm s}^{-1}$ ) through the reaction zone. This indicates that 2-photon processes or subsequent photolyses of the reaction products formed in previous laser pulses, that may produce secondary H-atoms, is unimportant in our experiments. Our result is in excellent agreement with the indirect studies of Schurath and Schindler,<sup>16</sup> who reported a yield of  $0.97 \pm 0.10$  at 206.2 nm. Ramsay's,<sup>17</sup> and Husain and Norrish's<sup>18</sup> suggestion that  $\text{NH} + \text{NH}_3$  and  $\text{NH}_2 + \text{NH}_2$  are the major primary products in their flash-photolyses experiments is not consistent with our measured H-atom quantum yield. These latter intermediates are thought to be formed in subsequent secondary reactions after the initial flash. Within our experimental uncertainties, unit dissociation of hydrazine is suggested for absorption of 248.3 nm radiation due to a weak electronic transition to the lowest dissociative singlet,  $\tilde{\text{A}}^1\text{A}$ , state.

The Arrhenius temperature dependence of the reaction,  $\text{H} + \text{N}_2\text{H}_4 \rightarrow \text{products}$ ; ( $k_1$ ), is shown in Figure 5, and is given by  $k_1 = (7.57 \pm 1.55) \times 10^{-12} \exp[-(1150 \pm 50)/T] \text{ cm}^3 \text{ molec}^{-1} \text{ s}^{-1}$ . This is in excellent agreement with  $(9.87 \pm 1.17) \times 10^{-12} \exp[-(1200 \pm 50)/T] \text{ cm}^3 \text{ molec}^{-1} \text{ s}^{-1}$  reported by Stief and Payne.<sup>5</sup> However, the other three studies of Gehring et al.,<sup>19</sup> Francis and Jones,<sup>20</sup> and Schiavello and Volpi<sup>21</sup> all give different temperature dependences. These are also shown in Figure 5. The interference from secondary reactions at high radical concentrations, and or errors in estimating  $[\text{N}_2\text{H}_4]$  employed in these later studies may be responsible for the differences in the reported values.

In this kinetic investigation of  $k_1$ , we have minimized the importance of secondary chemistry by keeping  $[\text{N}_2\text{H}_4]/[\text{H}]$  ratio high, typically  $5 \times 10^4$ , and  $[\text{H}]$  low, typically  $1 \times 10^{11}$  molec  $\text{cm}^{-3}$ , and have used excess He buffer gas to thermalize the initially produced translationally hot H-atoms in the photodissociation of  $\text{N}_2\text{H}_4$ . Using our data and that of Stief and Payne,<sup>5</sup> the recommended Arrhenius temperature dependence is derived to be  $k_1 = (10.28 \pm 1.22) \times 10^{-12} \exp[-(1220 \pm 30)/T]$   $\text{cm}^3 \text{molec}^{-1} \text{s}^{-1}$ . An activation energy of  $(2.4 \pm 0.1)$  kcal  $\text{mol}^{-1}$  is obtained for this metathesis reaction in which the products are thought to be  $\text{H}_2 + \text{N}_2\text{H}_3$ .

We are currently looking at the temperature dependence of  $k_1$  for  $T > 296$  K, and the photodissociation of  $\text{N}_2\text{H}_4$  at  $\lambda < 248.3$  nm to get a through understanding of the dissociation mechanism(s) involved in hydrazine photolysis by UV light.

#### REFERENCES

- (1) Hepler, W. A.; Smith, O. I. *Symp. (Int.) Combust. Proc.* **1988**, *22*, 1799.
- (2) McHale, E. T.; Knox, B. E.; Palmer, H. B. *Symp. (Int.) Combust. Proc.* **1965**, *10*, 341.
- (3) Michel, K. W.; Wagner, H. Gg. *Symp. (Int.) Combust. Proc.* **1965**, *10*, 353.
- (4) Gray, P.; Lee, J. C.; Leach, H. A.; Taylor, D. C. *Symp. (Int.) Combust. Proc.* **6**, 255 (1956).
- (5) Stief, L. J.; Payne, W. A. *J. Chem. Phys.* **1976**, *64*, 4892.
- (6) Vaghjiani, G. L.; Ravishankara, A. R. *J. Geophys. Res.* **1989**, *94*, 3487.
- (7) Vaghjiani, G. L. *J. Chem. Phys.* **1993**, *98*, in press.
- (8) Vaghjiani, G. L.; Ravishankara, A. R. *J. Chem. Phys.* **1990**, *92*, 996.
- (9) Turnipseed, A. A.; Vaghjiani, G. L.; Gierczak, T.; Thompson, J. E.; Ravishankara, A. R. *J. Chem. Phys.* **1991**, *95*, 3244.
- (10) Talukdar, R. K.; Vaghjiani, G. L.; Ravishankara, A. R. *J. Chem. Phys.* **1992**, *96*, 8194.
- (11) Vaghjiani, G. L.; Ravishankara, A. R. *J. Phys. Chem.* **1989**, *93*, 7833.
- (12) Vaghjiani, G. L. *J. Phys. Chem.* **1993**, *97*, to be submitted.
- (13) Biehl, H.; Stuhl, F. *J. Photochem. Photobiol. A: Chem.* **1991**, *59*, 135.
- (14) Becker, Von K. H.; Welge, K. H. *Z. Naturforsch. Teil A* **1964**, *19*, 1006.
- (15) Wine, P. H.; Nicovich, J. M.; Hynes, A. J.; Well, J. R. *J. Phys. Chem.* **1986**, *90*, 4033.
- (16) Schurath, U.; Schindler, R. N. *J. Phys. Chem.* **1970**, *74*, 3188.
- (17) Ramsay, D. A. *J. Phys. Chem.* **1953**, *57*, 415.
- (18) Husain, D.; Norrish, R. G. W. *Proc. R. Soc. London, Ser. A* **1963**, *273*, 145.
- (19) Gehring, M.; Hoyeremann, K.; Wagner, H. Gg.; Wolfrum, J. *Ber. Bunsenges. Phys. Chem.* **1971**, *75*, 1287.
- (20) Francis, P. D.; Jones, A. R. *J. Chem. Phys.* **1971**, *54*, 5085.
- (21) Schiavello, M.; Volpi, G. G. *J. Chem. Phys.* **1962**, *37*, 1510.

**Table I:** Absorption cross section values used in this work  
 $\sigma(10^{-20} \text{ cm}^2 \text{ molec}^{-1})$

$\lambda$ (nm)	$\text{CH}_3\text{SH}$	$\text{N}_2\text{H}_4$
253.65	.....	2.86
248.3	30.0	5.88

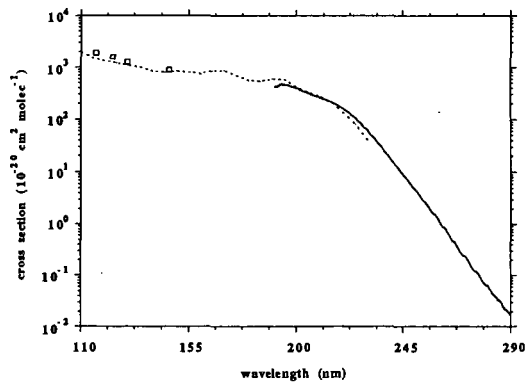


**Figure 1.** UV absorption cross sections of  $\text{N}_2\text{H}_4$ . Solid line is this work, dashed line is from ref. 13, and squares are from ref. 14.

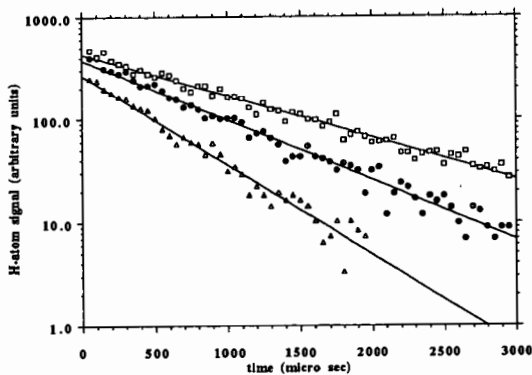


Figure 2. Typical [H] temporal profiles at 296 K. Each data point is the signal collected in 50- $\mu$ sec dwell-time and co-added over 5000 photolytic pulses. The slopes yield values for  $k$  and the intercepts values for  $S_{0N}$ .

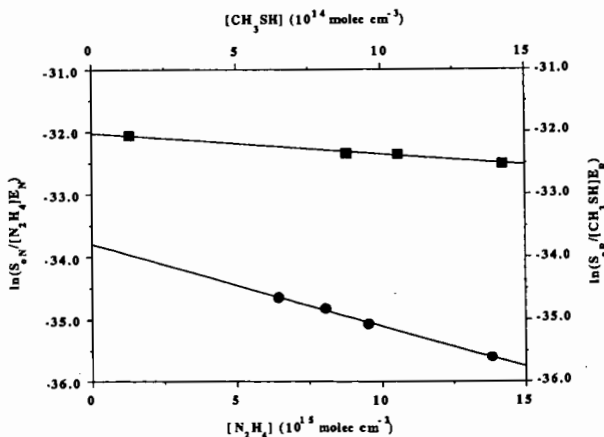


Figure 3. Variation of the log of normalized  $S_{0N}$  and  $S_{0R}$  signals with  $[N_2H_4]$  (circles) and  $[CH_3SH]$  (squares), respectively. Intercepts yield values for  $I_N$  and  $I_R$ , respectively, for the two photolytes.

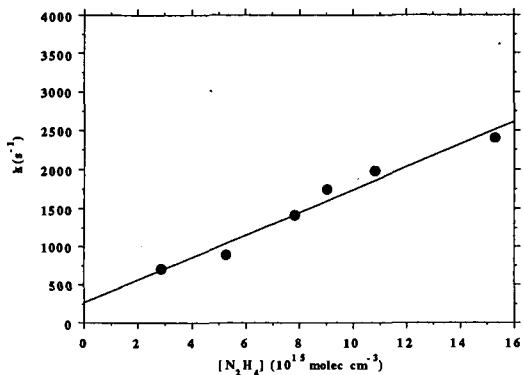


Figure 4. Plot of  $k$  versus  $[N_2H_4]$ . The slope yields a value for  $k_1(296\text{ K})$ .

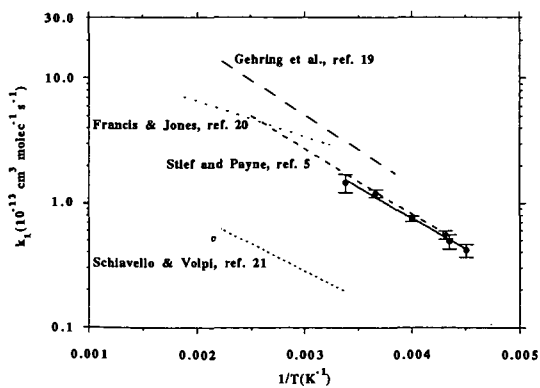


Figure 5. Arrhenius temperature dependences of  $k_1$ . Data points are from this study.

## POROUS $\gamma$ -ALUMINA MEMBRANES MODIFIED WITH ULTRAFINE ZIRCONIA PARTICLES PREPARED BY REVERSED MICELLES METHOD

Katsuki Kusakabe, Takeyuki Yamaki, Hideaki Maeda and Shigeharu Morooka  
Department of Chemical Science and Technology,  
Kyushu University, Fukuoka 812 Japan

**Keywords:** Gas separation, Inorganic membrane, Reversed micelles

### INTRODUCTION

Inorganic membranes have great potential as gas separation devices at elevated temperatures, but they have been little used to date. A major reason is that selectivity and permeability of inorganic membranes are not simultaneously achieved at an acceptable cost. If a high selectivity is requested in gas separation process, micropores in the membrane should be close to the size of gas molecules. This often reduces the permeability of that membrane. Porous inorganic membranes obtainable commercially have pore diameters ranging from 4 to 50 nm, where permselectivity is fundamentally controlled by Knudsen diffusion mechanism. Thus it is essential to develop a new membrane that shows an enough selectivity among small molecule gases without sacrificing the permeability.

In the present study, the outer surface of an  $\alpha$ -alumina support membrane is coated with a thin layer of  $\gamma$ -alumina particles prepared by a sol-gel method. Further, micropores of the  $\gamma$ -alumina are narrowed with ultrafine  $ZrO_2$  particles formed by a reversed micelles technique. The membrane obtained is evaluated with gas separation tests.

### FORMATION OF ULTRAFINE ZIRCONIA PARTICLES

Zirconium tetrabutoxide ( $Zr(OC_4H_9)_4$ , Tri-chemicals) was used as zirconia source. The surfactant was dioleoyl phosphoric acid (DOLPA), which was synthesized according to the method of Goto et al. (1989). Water content in reversed micelles formed with DOLPA was decreased by two orders of magnitude when the pH value was decreased from 6 to 3.5 (Goto et al. 1990). This implies the reversed micelles can be destroyed by acidification.

**Figure 1** shows the flow chart for the production of ultrafine zirconia particles by the reversed micelles technique. Ammonia and KCl was dissolved in a part of water to optimize ionic strength and pH. The same part of isooctane, in which DOLPA was dissolved, was placed on the top of the aqueous solution, and the aqueous phase was gently stirred at 303 K for 24 h. Stable reversed micelles were formed in the isooctane phase, which was recovered with a separation funnel. A butanol solution of zirconium tetrabutoxide was mixed to the isooctane solution. Zirconium tetrabutoxide was transferred to micro water pool in reversed micelles and then hydrolyzed to zirconia. After stirred at 303 K for 24 h, the reversed micelles were destroyed by adding an aqueous nitric acid solution, and finally the organic and aqueous phases were separated.

The concentration of zirconium in the aqueous phase was tried to determine with ICP-AES (SEIKO I. SPS-1200VR), but no zirconium was detected. It was also impossible to recover

zirconia particles into the aqueous solution by adding copper or nickel ions forming strong coordination bond with normal surfactants. The presence of zirconium in the organic phase, on the other hand, was confirmed by x-ray luminescence analysis. These results mean that ultrafine zirconia particles were stabilized in the organic phase with DOLPA molecules coordinated to hydroxyl group of zirconia.

The average size of water pools formed in the organic phase was 5 nm from the results of the dynamic laser scattering measurement (Photal DLS-7000). If one zirconia particle is formed in each micelle, the particle size, calculated from the number of micelles formed, is on the order of 0.1 nm. Since the zirconia concentration in the organic phase is as low as  $3.0 \times 10^{-5} \text{ mol} \cdot \text{L}^{-1}$ , the size of the particles formed in the reversed micelles is estimated to be less than 1 nm. This was assured from the observation of zirconia particles with a TEM (JOEL JEM-200CX).

#### PREPARATION OF COMPOSITE MEMBRANE

Porous  $\alpha$ -alumina hollow fibers supplied by NOK Corp. were used as the support. The outer surface of the support was coated with a thin layer of  $\gamma$ -alumina by the following procedure: A boehmite ( $\gamma$ - $\text{Al}(\text{OOH})$ ) sol was formed by adding aluminium isopropoxide into water and peptizing the suspension with hydrochloric acid (Yoldas, 1975). The concentration of the sol was  $0.6 \text{ Al} \cdot \text{mol} \cdot \text{L}^{-1}$ . The hollow fiber, whose lower end was closed, was dipped in the sol for several minutes, dried overnight in the atmosphere and heated to 1023 K at  $50 \text{ K} \cdot \text{h}^{-1}$  in an air stream. This dipping-firing procedure was repeated 4 times.

The concept of modifying the  $\gamma$ -alumina membrane with zirconia particles is illustrated in Fig. 2. The  $\gamma$ -alumina-coated hollow fiber support, one end was plugged and the other was connected to a vacuum line, was dipped in the organic phase where zirconia particles were suspended. Ultrafine zirconia particles were trapped in the  $\gamma$ -alumina layer by suction for 1 h. The treated hollow fiber was heated at  $50 \text{ K} \cdot \text{h}^{-1}$  and kept at 673 or 873 K in an air stream. This procedure was repeated 6 times.

#### GAS PERMEATION

Gas permeation experiments were performed at 373-673 K using hydrogen, nitrogen and methane. The unnecessary surface of the support fiber except for the test part was coated with a  $\text{SiO}_2$ - $\text{B}_2\text{O}_3$ - $\text{Na}_2\text{O}$  sealant. The permeating gas from the outside to the inside of the membrane was carried with argon. The flow rate was measured with a soap-film flow meter, and gas compositions were analyzed by gas chromatography. The total pressure in the both side of the membrane was kept at atmosphere pressure.

The gas permeability largely decreased with increasing number of dipping-firing cycle when the calcination was carried out at 673 K for 2 h. The membrane surface was grayish, and it was suspected that micropores were blocked with carbonaceous matters which were not removed at this temperature. Then the calcination temperature was raised to 873 K. As shown in Fig. 3, the gas permeability remained at about 5 % of that of the initial  $\gamma$ -alumina membrane after six repetitions of the dipping-firing cycle, and was still larger than that of Vycor glass membranes (Tsapatsis et al., 1991). From the observation of a fractured

section with an FE-SEM (Hitachi S-900), the thickness of the  $ZrO_2/\gamma-Al_2O_3$  layer hardly changed after the six repetitions. The line analysis of Zr across the fractured surface indicates that most of  $ZrO_2$  particles were collected in micropores of the  $\gamma$ -alumina layer. The top surface of the membrane was gradually smoothed by repeating the impregnation cycle.

**Figure 4** shows the effect of the zirconium concentration, based on the volume of the organic phase, on the permeability after three or six repetitions of the dipping-firing cycle. The permeability decreased with increasing zirconium concentration in the range lower than  $2 \times 10^{-5} \text{ mol}\cdot\text{L}^{-1}$ . Smaller particles were packed more tightly in micropores, and the selectivity for hydrogen became large. In the present experiment, the separation factor of hydrogen to nitrogen was about 4.5 after the sixth impregnation cycle at a zirconia concentration of  $1 \times 10^{-5} \text{ mol}\cdot\text{L}^{-1}$  as shown in **Fig.5**. The separation factor obtained exceeded the value of the  $\gamma$ -alumina membrane, 3.4. The gas permeability was independent of the pressure drop across the membrane and the permeation temperature.

## CONCLUSION

Ultrafine zirconia particles were formed by hydrolysis of zirconium tetrabutoxide in reversed micelles with a novel surfactant, DOLPA. By repeating the dipping-firing cycle, micropores of a  $\gamma$ -alumina membrane were plugged with the zirconia particles. The permeability of the membrane was ca. 5 % of that of the initial  $\gamma$ -alumina membrane after the six repetition. The permselectivity of hydrogen to nitrogen was increased to 4.5 from the initial value 3.4. The membrane was stable at 673 K.

## REFERENCES

1. Goto, M., Kondo, K and Nakashio, F. *J. Chem. Eng. Japan* 1989, **22**, 79.
2. Goto, M., Kondo, K and Nakashio, F. *J. Chem. Eng. Japan* 1990, **23**, 513.
3. Yoldas, B.E. *Am. Ceram. Soc. Bull.* 1975, **54**, 289.
4. Tsapatsis, M., Kim, S., Nam, S.W. and Gavalas, G. *Ind. Eng. Chem. Res.* 1991, **30**, 2152.

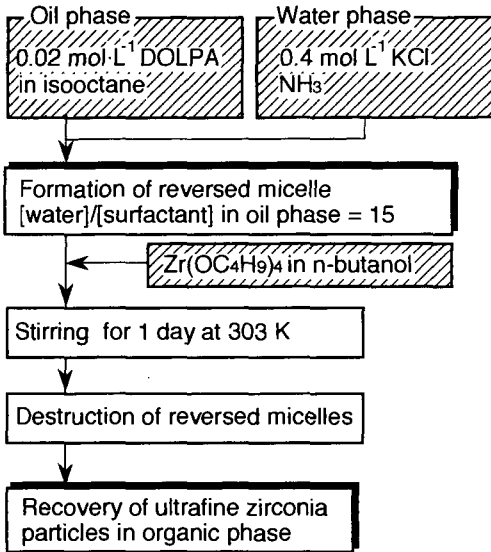


Fig. 1 Preparation of ultrafine zirconia particles by reversed micelles method

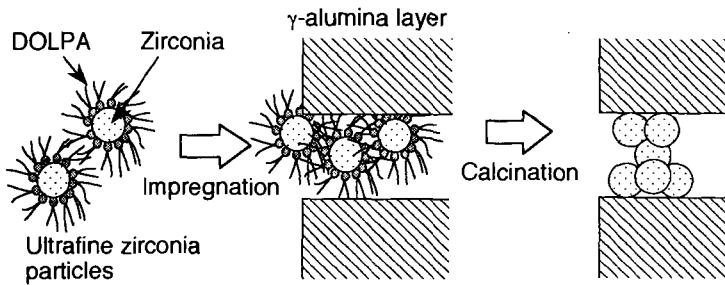


Fig.2 Preparation of zirconia/γ-alumina membrane

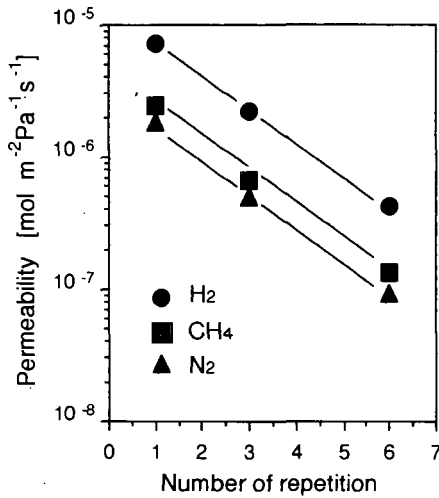


Fig. 3 Effect of repetition number of dipping-firing cycle on gas permeability. Permeation temperature = 373K, Zirconium concentration in organic phase =  $1.0 \times 10^{-5} \text{ mol} \cdot \text{L}^{-1}$

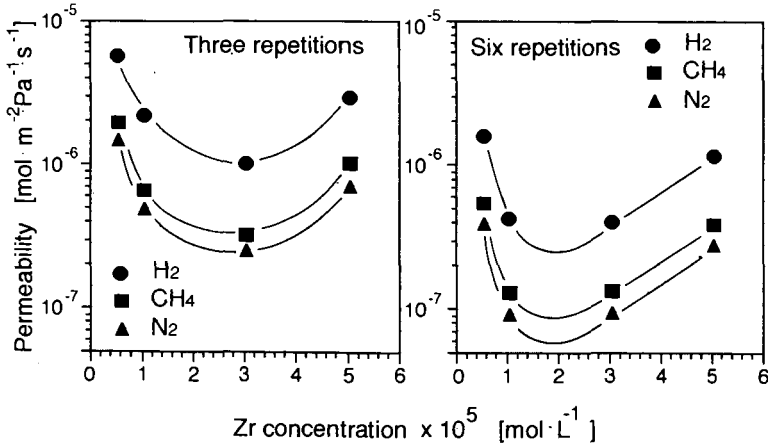


Fig. 4 Effect of zirconia concentration in organic phase on gas permeability. Permeation temperature = 373 K

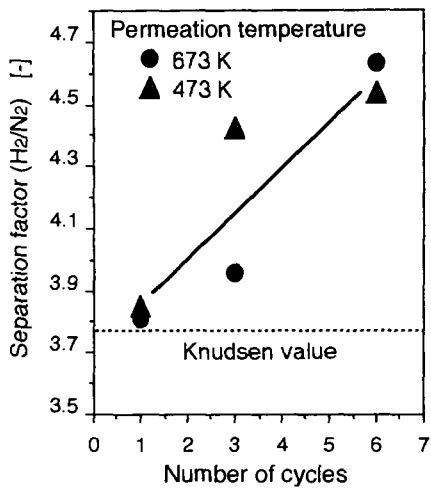


Fig. 5 Effect of repetition number of dipping-firing cycle on separation factor. Zirconium concentration in organic phase =  $1.0 \times 10^{-5} \text{ mol} \cdot \text{L}^{-1}$